Methods in Molecular Biology 1339

Springer Protocols

Vicente Andrés
Beatriz Dorado *Editors*

Methods in Mouse Atherosclerosis

Humana Press

METHODS IN MOLECULAR BIOLOGY

Series Editor
John M. Walker
School of Life and Medical Sciences
University of Hertfordshire
Hatfield, Hertfordshire, AL10 9AB, UK

For further volumes:
http://www.springer.com/series/7651

Methods in Mouse Atherosclerosis

Edited by

Vicente Andrés

Laboratory of Molecular and Genetic Cardiovascular Pathophysiology, Centro Nacional de Investigaciones Cardiovasculares Carlos III (CNIC), Madrid, Spain

Beatriz Dorado

Laboratory of Molecular and Genetic Cardiovascular Pathophysiology, Centro Nacional de Investigaciones Cardiovasculares Carlos III (CNIC), Madrid, Spain

Humana Press

Editors
Vicente Andrés
Laboratory of Molecular and Genetic Cardiovascular Pathophysiology
Centro Nacional de Investigaciones Cardiovasculares Carlos III (CNIC)
Madrid, Spain

Beatriz Dorado
Laboratory of Molecular and Genetic Cardiovascular Pathophysiology
Centro Nacional de Investigaciones Cardiovasculares Carlos III (CNIC)
Madrid, Spain

ISSN 1064-3745 ISSN 1940-6029 (electronic)
Methods in Molecular Biology
ISBN 978-1-4939-2928-3 ISBN 978-1-4939-2929-0 (eBook)
DOI 10.1007/978-1-4939-2929-0

Library of Congress Control Number: 2015948251

Springer New York Heidelberg Dordrecht London

Printed on acid-free paper

Humana Press is a brand of Springer
Springer Science+Business Media LLC New York is part of Springer Science+Business Media (www.springer.com)

Preface

Atherosclerosis and associated cardiovascular disease (CVD), most prominently manifesting as myocardial infarction or stroke, constitute the main cause of morbidity and mortality in industrialized countries. In spite of major advances in our understanding of the genetic, molecular, and cellular determinants of CVD, its incidence and prevalence are expected to increase significantly over the coming decades owing to the progressive aging of our societies (aging is the dominant cardiovascular risk factor) and the consequences of modern unhealthy lifestyle habits, such as a high-fat diet, smoking, and lack of physical exercise. Moreover, many manifestations of CVD are not predicted by "traditional" cardiovascular risk factors. It is therefore of the utmost importance to increase our knowledge about the genetic, molecular, and cellular mechanisms involved in atherosclerosis, in order to improve the prevention, diagnosis, and treatment of the disease. In this necessary basic and preclinical research, genetically modified mouse models continue to be an essential tool in many laboratories due to their relatively short life-span, ease of handling, and low cost.

This book begins with introductory chapters that briefly review the available mouse models of atherosclerosis, basic aspects of disease initiation and progression, and the visualization of atherosclerotic lesions with invasive and noninvasive techniques that are widely used both in basic research and in the clinic. Subsequent chapters catalogue a wide range of in vitro and in vivo experimental methods used for atherosclerosis research, including thorough protocols and valuable notes based on the authors' personal wet lab experience. We hope that this book will be a valuable working guide for researchers performing mouse-based atherosclerosis studies.

Madrid, Spain

Vicente Andrés, Ph.D.
Beatriz Dorado, Ph.D.

Contents

Contributors

Vicente Andrés • *Centro Nacional de Investigaciones Cardiovasculares Carlos III (CNIC), Madrid, Spain*

M. Jesús Andrés-Manzano • *Centro Nacional de Investigaciones Cardiovasculares Carlos III (CNIC), Madrid, Spain*

Alicia Arranz • *Institute for Biomedical Engineering, Swiss Federal Institute of Technology (ETH), Zurich, Switzerland*

Marina Benito • *Centro Nacional de Investigaciones Cardiovasculares Carlos III (CNIC), Madrid, Spain; CIBER de Enfermedades Respiratorias (CIBERES), Madrid, Spain*

Martin R. Bennett • *Division of Cardiovascular Medicine, Addenbrooke's Centre for Clinical Investigation, University of Cambridge, Cambridge, UK*

Izaskun Bilbao • *Centro Nacional de Investigaciones Cardiovasculares Carlos III (CNIC), Madrid, Spain; Universidad Complutense de Madrid and CIBER de Enfermedades Respiratorias (CIBERES), Madrid, Spain*

Francisco Blanco-Vaca • *Institut de Recerca de l'Hospital de la Santa Creu i Sant Pau, Institut d'Investigacions Biomèdiques (IIB) Sant Pau, Barcelona, Spain; CIBER de Diabetes y Enfermedades Metabólicas Asociadas, CIBERDEM, Madrid, Spain; Departament de Bioquímica i Biologia Molecular, Universitat Autònoma de Barcelona, Barcelona, Spain*

Rune Carlsson • *Department of Biomedicine, Pulmonary and Cardiovascular Pharmacology, Aarhus University, Aarhus, Denmark*

Lídia Cedó • *Institut de Recerca de l'Hospital de la Santa Creu i Sant Pau, Institut d'Investigacions Biomèdiques (IIB) Sant Pau, Barcelona, Spain; CIBER de Diabetes y Enfermedades Metabólicas Asociadas, CIBERDEM, Madrid, Spain*

Yung Chih Chen • *Atherothrombosis & Vascular Biology, Baker IDI Heart and Diabetes Institute, Melbourne, Australia; Departments of Medicine and Immunology, Monash University, Melbourne, Australia*

Raphäel Chévre • *Department of Atherothrombosis, Imaging and Epidemiology, CNIC (Spanish National Cardiovascular Research Center), Madrid, Spain*

Robin P. Choudhury • *Division of Cardiovascular Medicine, Radcliffe Department of Medicine, John Radcliffe Hospital, University of Oxford, Oxford, UK*

Alba de Juan • *Walter Brendel Center for Experimental Medicine, Ludwig-Maximilians-Universität, Munich, Germany*

Lara del Campo • *Centro Nacional de Investigaciones Cardiovasculares Carlos III (CNIC), Madrid, Spain*

Beatriz Dorado • *Centro Nacional de Investigaciones Cardiovasculares Carlos III (CNIC), Madrid, Spain*

Joan Carles Escolà-Gil • *Institut de Recerca de l'Hospital de la Santa Creu i Sant Pau, Institut d'Investigacions Biomèdiques (IIB) Sant Pau, Barcelona, Spain; CIBER de Diabetes y Enfermedades Metabólicas Asociadas, CIBERDEM, Madrid, Spain;*

Departament de Bioquímica i Biologia Molecular, Universitat Autònoma de Barcelona, Barcelona, Spain

Samuel España • *Centro Nacional de Investigaciones Cardiovasculares Carlos III (CNIC), Madrid, Spain*

Mercedes Ferrer • *Department of Physiology, Faculty of Medicine, Universidad Autónoma de Madrid, Madrid, Spain*

Nichola L. Figg • *Division of Cardiovascular Medicine, Addenbrooke's Centre for Clinical Investigation, University of Cambridge, Cambridge, UK*

Edward A. Fisher • *Marc and Ruti Bell Vascular Biology Program, Division of Cardiology, Department of Medicine, New York University School of Medicine, New York, NY, USA*

José J. Fuster • *Whitaker Cardiovascular Institute, Boston University School of Medicine, Boston, MA, USA*

Valentín Fuster • *Centro Nacional de Investigaciones Cardiovasculares Carlos III (CNIC), Madrid, Spain; The Zena and Michael A. Wiener Cardiovascular Institute/ Marie-Josee and Henry R. Kravis Center for Cardiovascular Health, Icahn School of Medicine, New York, NY, USA*

Matthew Gage • *Centre for Clinical Pharmacology, Division of Medicine, University College London, London, UK*

Elena V. Galkina • *Department of Microbiology and Molecular Cell Biology, Eastern Virginia Medical School, Norfolk, VA, USA*

Godfrey S. Getz • *Department of Pathology, University of Chicago, Chicago, IL, USA*

Marion J. Gijbels • *Department of Pathology, Cardiovascular Research Institute Maastricht, Maastricht University, Maastricht, The Netherlands; Department of Molecular Genetics, Cardiovascular Research Institute Maastricht, Maastricht University, Maastricht, The Netherlands; Department of Medical Biochemistry, Amsterdam Medical Center, Amsterdam, The Netherlands*

Anton Gisterå • *Department of Medicine, Center for Molecular Medicine, Karolinska University Hospital, Karolinska Institute, Stockholm, Sweden*

Breanne N. Gjurich • *Department of Microbiology and Molecular Cell Biology, Eastern Virginia Medical School, Norfolk, VA, USA*

Jose M. González-Granado • *Centro Nacional de Investigaciones Cardiovasculares Carlos III (CNIC), Madrid, Spain*

Herminia González-Navarro • *Institute of Health Research INCLIVA, Valencia, Spain*

Andreas Habenicht • *Institute for Cardiovascular Prevention, Ludwig-Maximilians-University, Munich, Germany*

Magda R. Hamczyk • *Centro Nacional de Investigaciones Cardiovasculares Carlos III (CNIC), Madrid, Spain*

Sylvia Heeneman • *Department of Pathology, Cardiovascular Research Institute Maastricht, Maastricht University, Maastricht, The Netherlands*

Andrés Hidalgo • *Centro Nacional de Investigaciones Cardiovasculares Carlos III (CNIC), Madrid, Spain; Institute Cardiovascular Prevention, Ludwig-Maximilians-University, Munich, Germany*

Desheng Hu • *Institute of Molecular Immunology, Helmholtz Zentrum München, Munich, Germany*

Salvador Iborra • *Centro Nacional de Investigaciones Cardiovasculares Carlos III (CNIC), Madrid, Spain*

Jesús Jiménez-Borreguero • *Centro Nacional de Investigaciones Cardiovasculares Carlos III (CNIC), Madrid, Spain; Hospital Universitario de La Princesa, Madrid, Spain*
Josep Julve • *Institut de Recerca de l'Hospital de la Santa Creu i Sant Pau, Institut d'Investigacions Biomèdiques (IIB) Sant Pau, Barcelona, Spain; CIBER de Diabetes y Enfermedades Metabólicas Asociadas, CIBERDEM, Madrid, Spain; Departament de Bioquímica i Biologia Molecular, Universitat Autònoma de Barcelona, Barcelona, Spain*
Daniel F.J. Ketelhuth • *Department of Medicine, Center for Molecular Medicine, Karolinska University Hospital, Karolinska Institute, Stockholm, Sweden*
Pascal J.H. Kusters • *Department of Medical Biochemistry, Academic Medical Center, Amsterdam, The Netherlands*
Miriam Lee-Rueckert • *Wihuri Research Institute, Helsinki, Finland*
Esther Lutgens • *Department of Medical Biochemistry, Academic Medical Center, University of Amsterdam, Amsterdam, The Netherlands; Institute for Cardiovascular Prevention (IPEK), Ludwig Maximilians University (LMU), Munich, Germany*
Zhe Ma • *Institute for Cardiovascular Prevention, Ludwig-Maximilians-University, Munich, Germany*
Jesús Mateo • *Centro Nacional de Investigaciones Cardiovasculares Carlos III (CNIC), Madrid, Spain*
Martina A. McAteer • *Midatech Ltd., Begbroke Science Park, Oxfordshire, UK*
Remco T.A. Megens • *Institute for Cardiovascular Prevention, LMU Munich, Munich, Germany; Cardiovascular Research Institute Maastricht, Maastricht University, Maastricht, The Netherlands*
Prashanthi Menon • *Marc and Ruti Bell Vascular Biology Program, Division of Cardiology, Department of Medicine, New York University School of Medicine, New York, NY, USA*
Sarajo Mohanta • *Institute for Cardiovascular Prevention, Ludwig-Maximilians-University, Munich, Germany*
Pedro Molina-Sánchez • *Centro Nacional de Investigaciones Cardiovasculares Carlos III (CNIC), Madrid, Spain*
Oscar M. Pello • *Centre for Clinical Pharmacology, Division of Medicine, University College London, London, UK; Department of Hematology, John Goldman Centre for Cellular Therapy, Hammersmith Hospital, London, UK*
Karlheinz Peter • *Atherothrombosis & Vascular Biology, Baker IDI Heart and Diabetes Institute, Melbourne, Australia; Departments of Medicine and Immunology, Monash University, Melbourne, Australia*
Inés Pineda-Torra • *Centre for Clinical Pharmacology, Division of Medicine, University College London, London, UK*
Catherine A. Reardon • *Department of Pathology, University of Chicago, Chicago, IL, USA*
Jorge Ripoll • *Department of Bioengineering and Aerospace Engineering, Universidad Carlos III of Madrid, Madrid, Spain; Experimental Medicine and Surgery Unit, Instituto de Investigación Sanitaria Gregorio Marañón, Madrid, Spain*
Cristina Rius • *Centro Nacional de Investigaciones Cardiovasculares Carlos III (CNIC), Madrid, Spain*
Jennifer Rivera • *Atherothrombosis & Vascular Biology, Baker IDI Heart and Diabetes Institute, Melbourne, Australia*

José Rivera-Torres • *Centro Nacional de Investigaciones Cardiovasculares Carlos III (CNIC), Madrid, Spain*
Markus Rudin • *Institute for Biomedical Engineering, Swiss Federal Institute of Technology (ETH), Zurich, Switzerland*
Jesús Ruiz-Cabello • *Centro Nacional de Investigaciones Cardiovasculares Carlos III (CNIC), Madrid, Spain; Universidad Complutense de Madrid and CIBER de Enfermedades Respiratorias (CIBERES), Madrid, Spain*
David Santos • *Institut de Recerca de l'Hospital de la Santa Creu i Sant Pau, Institut d'Investigacions Biomèdiques (IIB) Sant Pau, Barcelona, Spain; CIBER de Diabetes y Enfermedades Metabólicas Asociadas, CIBERDEM, Madrid, Spain*
Javier Sanz • *The Zena and Michael A. Wiener Cardiovascular Institute/Marie-Josee and Henry R. Kravis Center for Cardiovascular Health, Icahn School of Medicine, New York, NY, USA*
Maria J. Sanz • *Department of Pharmacology, Faculty of Medicine, University of Valencia, Valencia, Spain; Institute of Health Research-INCLIVA, Valencia, Spain*
Olav L. Schjørring • *Department of Biomedicine, Pulmonary and Cardiovascular Pharmacology, Aarhus University, Aarhus, Denmark; Department of Anesthesiology, Aalborg University Hospital, Aalborg, Denmark*
Ulf Simonsen • *Department of Biomedicine, Pulmonary and Cardiovascular Pharmacology, Aarhus University, Aarhus, Denmark*
Judith C. Sluimer • *Department of Pathology, Cardiovascular Research Institute Maastricht, Maastricht University, Maastricht, The Netherlands*
Oliver Soehnlein • *Institute for Cardiovascular Prevention, LMU Munich, Munich, Germany; Department of Pathology, Academic Medical Center, Amsterdam University, Amsterdam, The Netherlands; DZHK (German Centre for Cardiovascular Research), partner site Munich Heart Alliance, Munich, Germany*
Vinatha Sreeramkumar • *Centro Nacional de Investigaciones Cardiovasculares Carlos III (CNIC), Madrid, Spain*
Parésa L. Taghavie-Moghadam • *Department of Microbiology and Molecular Cell Biology, Eastern Virginia Medical School, Norfolk, VA, USA*
Juan José Vaquero • *Departamento de Bioingeniería & Ingeniería Aeroespacial, Universidad Carlos III Madrid, Madrid, Spain; Instituto de Investigación Sanitaria Gregorio Marañón, Madrid, Spain*
Ricardo Villa-Bellosta • *Centro Nacional de Investigaciones Cardiovasculares Carlos III (CNIC), Madrid, Spain*
Ángela Vinué • *Institute of Health Research, INCLIVA, Valencia, Spain*
Christian Weber • *Institute for Cardiovascular Prevention, Ludwig-Maximilians-University, Munich, Germany*
Falk Weih • *(Deceased)*
Changjun Yin • *Institute for Cardiovascular Prevention, Ludwig-Maximilians-University, Munich, Germany*
Carlos Zaragoza • *Cardiovascular Research Unit, Hospital Ramón y Cajal, Universidad Francisco de Vitoria, Madrid, Spain*

Chapter 1

Use of Mouse Models in Atherosclerosis Research

Godfrey S. Getz and Catherine A. Reardon

Abstract

Cardiovascular disease is the major cause of death in most developed nations and the social and economic burden of this disease is quite high. Atherosclerosis is a major underlying basis for most cardiovascular diseases including myocardial infarction and stroke. Genetically modified mouse models, particularly mice deficient in apoprotein E or the LDL receptor, have been widely used in preclinical atherosclerosis studies to gain insight into the mechanisms underlying this pathology. This chapter reviews several mouse models of atherosclerosis progression and regression as well as the role of immune cells in disease progression and the genetics of murine atherogenesis.

Key words apoE deficient, LDL receptor deficient, Atherosclerosis, Genetics, Regression, Immune system

Atherosclerosis is a chronic inflammatory disease of the intima of medium and large arteries that develops over months, years, or decades. Atherosclerotic plaques occur in susceptible regions of the blood vessels involved, mostly attributable to the local hemodynamics, characterized by low shear stress. Thus, for example, lesions form in the lesser curvature of the aortic arch while the greater curvature is relatively resistant. The evolution of atherosclerotic lesions occurs at different rates at each of the susceptible regions [1]. In humans, atherosclerosis underscores most of the cardiovascular disease affecting the coronary, carotid, and aortic arteries. Clinically it is complicated by the instability of the atheromatous plaques, with superimposed thrombosis, resulting in partial or complete occlusion of the vessel lumen and downstream ischemia, such as in myocardial infarction and stroke. Atherosclerosis and its pathogenesis may be studied in a variety of mammalian species [2], as the basic mechanisms for this pathology is similar in most of them. However, for reasons explored below, the mouse has become the preferred species for preclinical studies.

Vicente Andrés and Beatriz Dorado (eds.), *Methods in Mouse Atherosclerosis*, Methods in Molecular Biology, vol. 1339, DOI 10.1007/978-1-4939-2929-0_1,

1 Brief Survey of the Cellular Pathology of the Atherosclerotic Plaque

Early atheromatous lesions are made up of clusters of subendothelial macrophages. These macrophages are loaded with cholesteryl esters sequestered in intracytoplasmic lipid droplets, giving rise to the canonical foam cell of the lesion. These cells arise from infiltrating circulating monocytes. In the context of hyperlipidemia, monocytes gain access to the subintima as a result of the activation of endothelial cells in the lesion prone regions of the aorta leading to the expression of adhesion molecules and the production of chemotactic molecules such as monocyte chemotactic protein-1 (MCP-1) [3, 4]. The elevated plasma low-density lipoproteins (LDLs) also enter the subintimal space where they are subject to modification by reactive oxygen species or enzymes expressed by the intimal cells. The infiltrated monocytes differentiate into macrophages under the influence of monocyte colony stimulating factor (M-CSF) produced locally. These macrophages express cell surface scavenger receptors, which are able to bind and endocytose sufficiently modified lipoprotein. Not only do these modifications of lipoproteins allow for the recognition by macrophage receptors, but they also represent neoantigens that stimulate the adaptive immune system to produce antibodies [5]. The endocytosed lipoproteins gain access to the endolysosomal network with the degradation of the ingested lipids and proteins. The liberated cholesterol travels to the endoplasmic reticulum, where it can either enter the cholesterol regulatory pool leading to changes in expression of genes in lipid metabolism [6] or serve as a substrate for the cholesterol-esterifying enzyme acyl cholesterol acyl transferase (ACAT) producing the cholesteryl esters that are sequestered in the cytoplasmic lipid droplets. In the event that the activity of this enzyme is suboptimal, the accumulation of free cholesterol in the endoplasmic reticulum may elicit the unfolded protein response and apoptosis [7]. These apoptotic cells may be phagocytosed by other macrophages removing pro-inflammatory signals and also increasing the sterol load of the efferocyte [8]. Apoptotic cells that are not efficiently removed may undergo secondary necrosis, contributing to necrotic core formation in lesions, thus enhancing plaque's inflammation and instability.

The accumulation of lesional macrophages is the resultant of several processes: recruitment from the blood stream, active retention and local proliferation [4]. The macrophages present in the lesion are a source of a variety of mediator molecules, such as cytokines and chemokines and may present neoantigens to the adaptive immune system. Collectively these processes lead to the recruitment to the plaque or aortic adventitia of other inflammatory cells, such as T and B cells and their respective subsets, all of which contribute to the local plaque inflammatory environment [9, 10].

As the lesion progresses, smooth muscle cells from the media migrate into the intima, where they may adopt a synthetic rather than contractile phenotype. "Synthetic" smooth muscle cells produce high levels of collagen, proteoglycans and other matrix molecules, accounting for the formation of the fibrous cap, which, if intact, protects the lesion from rupture and the activation of the prothrombotic system.

From the above brief survey of the nature of the atherosclerotic plaque, it is clear that it is a complex network of cells and molecules that may vary as a function of the evolution of the plaque. A good deal of the understanding of the mechanisms of the evolution of the plaque derives from the study of mouse models.

2 Mouse Models

Animal models used for the investigation of atherosclerosis have included rabbits, pigs, and nonhuman primates, each of which has its advantages and disadvantages, as has been reviewed recently [2]. The current favored species is the mouse, which is small, has a relatively short life span, is relatively inexpensive to maintain for longer term experiments, and by far most important are the relative ease of introducing a wide range of genetic manipulations, including transgenesis, gene knockout and knock-in and the temporal or tissue specific manipulation of gene expression and the simultaneous modification of more than one gene in a single animal model due to the relative ease of breeding (Table 1).

Table 1
Some advantages and limitations to the use of mouse models of atherosclerosis

Advantages
Atherosclerosis develops over a period of months
Relative ease of genetic manipulation to allow for investigation of multiple cell types or proteins, including temporal or cell specific expression, on atherogenic process
Relatively short gestation time
Lower amounts of drugs/reagents needed due to small size
Limitations
Does not develop unstable plaques characteristic of human lesions
Does not readily develop coronary artery atherosclerosis
Develops significant atherosclerosis in the aortic sinus, which is not a common site of lesion formation in humans
Lipoprotein profile is not identical to humans: need to significantly increase apoB-containing lipoproteins and plasma cholesterol levels to develop atherosclerosis; does not express CETP; HDL subclass profiles are different
Amount of tissue obtainable for analysis is limited by small size
Immune system is not identical to humans

It is reassuring that mechanisms of atherogenesis appear to have much in common between humans and mice, including those driven by hemodynamic stresses. This said, the murine models and their analysis have important limitations (Table 1). First, the currently intrinsic limitation is that murine lesions seldom develop the instability characteristic of the advanced human lesions that account for much of clinically significant atherosclerotic cardiovascular disease. Also the precise distribution of lesions is not identical for murine and human lesions. Mice seldom develop atherosclerosis in the coronary artery, a major site of lesion development in humans. In addition, the aortic root is one of the earliest sites for the development of lesions in the mouse and is seldom involved in humans. This is likely due to the more rapid heartbeat in the mouse. The aortic root has been the most frequently analyzed site of lesion development, but fortunately investigators are examining now more than one arterial site and often at multiple experimental time points. This allows for a better understanding of the impact of the genetic manipulation or therapeutic treatment at different stages of plaque evolution and if there are site-specific effects. Mice also differ in lipoprotein metabolism, with wild-type mice predominantly accumulating cholesterol in HDL particles, not expressing cholesteryl ester transfer protein (CETP), and producing apoB48, the edited version of apoB100, in the liver as well as the intestine, unlike humans where only the intestine is involved in the editing of the apoB transcript.

The initial study of vascular lesions in rodents began more than 60 years ago with the feeding of cholesterol and cholate containing diets to rats [11]. However, the use of mice for such investigations really took off after Jan Breslow's laboratory [12] and Nabuyo Maeda's laboratory [13] independently described the apolipoprotein E (apoE) deficient mouse ($Apoe^{-/-}$), which develops atherosclerosis even while being fed standard rodent chow diets. With maturation these lesions can be quite complex [14]. This model has been very widely used for the preclinical study of atherosclerosis. The other widely employed murine model is the LDL receptor deficient ($Ldlr^{-/-}$) mouse, which is a murine model of human familial hypercholesterolemia [15]. Both of these models are characterized by hypercholesterolemia which is prerequisite for the development of atherosclerosis in murine models. However, these two models differ in significant ways from one another as will be apparent from what follows.

2.1 The ApoE Deficient Model

ApoE is carried on plasma lipoproteins, mostly chylomicron remnants, VLDL and large HDL. It serves as a ligand for the hepatic uptake of non-HDL lipoproteins by members of the LDL receptor superfamily of receptors. The lipoprotein phenotype of $Apoe^{-/-}$ mice consists of a predominance of remnant lipoproteins that are enriched in cholesteryl ester and apoB48. Though atherosclerosis

develops when *Apoe*$^{-/-}$ mice are fed a standard low fat chow diet, the development can be accelerated by feeding the fat and cholesterol enriched Western type diet (WTD). Lesions develop at the aortic root, the aortic arch, the innominate artery, the carotid arteries and other arterial sites depending on the diet and the duration of feeding [14]. Note that in this model there is little or no coronary artery lesion. However, the combination of apoE and scavenger receptor BI deficiencies leads to a model having profound coronary lesions with lumenal obstruction [16].

Although the presence of hyperlipidemia is a prerequisite for atherogenesis in mice, the modern concept of atherogenesis focuses on inflammation as the other major component of its pathogenesis. Bone marrow transplantation is a technique often used to assess the involvement of specific cells or cell products of the immune system in atherogenesis. Fixed tissue macrophages e.g., Kupffer cells are not completely eliminated by irradiation that destroys the cells of the bone marrow of the recipient mouse, but this can be effected by treatment with clodronate liposomes following reconstitution of the bone marrow in the recipient mice [17]. However, there is a limitation to using bone marrow transplantation studies in *Apoe*$^{-/-}$ mice. The clearance of chylomicron remnants is quite sensitive to the concentration of apoE in the plasma, with plasma levels ~10 % of normal being sufficient to effect virtually normal lipoprotein clearance [18]. While the hepatocyte is the major site of synthesis of apoE, it is also produced by macrophages, as well as steroidogenic cells, astrocytes and adipocytes [19]. The complementation of hyperlipidemic *Apoe*$^{-/-}$ mice with bone marrow from wild type mice largely rescues the hyperlipidemic and atherosclerosis phenotype, even though the plasma concentration of apoE barely reaches 10 % of normal levels [20]. The reduction in plasma lipids by macrophage-derived apoE likely contributes to the reduced atherosclerosis. However, apoE has a number of non-lipoprotein metabolism related functions as well that likely influence atherosclerosis, including promoting lipid efflux from macrophages and anti-inflammatory actions [19]. Studies involving the transplantation of bone marrow from *Apoe*$^{-/-}$ mice [21, 22] or from apoE expressing mice under conditions that did not alter plasma lipid levels [23, 24] demonstrate a plasma lipid-independent effect of apoE expressed by bone marrow-derived cells, primarily macrophages, on atherosclerosis. Thus, its local presence within the lesion in the artery wall also contributes to atherosclerosis phenotype. As a result, the bone marrow transplantation approach to the study of cells and genes of the immune system on atherosclerosis is somewhat limited if using *Apoe*$^{-/-}$ recipient mice by the need to use bone marrow donors that are themselves apoE deficient. However, not all sources of apoE are equally effective in rescuing the hyperlipidemic atherosclerosis phenotype of *Apoe*$^{-/-}$ mice. Though apoE expressed by adipose tissue transplants results in a

plasma apoE concentration similar to that induced by bone marrow transplantation, it does not improve either the hyperlipidemia or the atherosclerosis of the *Apoe*$^{-/-}$ host [25]. The basis for this distinction is not clear.

2.2 The LDL Receptor Deficient Mouse

The LDL receptor is a widely expressed plasma membrane protein that is responsible for the clearance of plasma lipoproteins containing either apoB100 or apoE. From the pioneering and continuing work of Brown, Goldstein and their colleagues in Dallas, we know that the major function of this receptor is to mediate the hepatic clearance of these lipoproteins and modulation of receptor biogenesis is a major indirect target of the statin group of drugs used to control hyperlipidemia in patients at risk of developing atherosclerotic heart disease. Since the hepatic LDL receptor is primarily responsible for the uptake and clearance of apoB/apoE -containing lipoproteins, the absence of the hepatic LDL receptor is mostly responsible for the accumulation of apoB100 containing LDL particles in the *Ldlr*$^{-/-}$ mice fed standard chow diet. But the liver has other uptake pathways for VLDL and remnants, which accounts for the modest hypercholesterolemia and small lesions that develop only in aged *Ldlr*$^{-/-}$ mouse upon feeding chow diet [26]. Therefore, this model is most often employed with the feeding of a high-fat, high-cholesterol diet, leading to an accumulation of VLDL remnants as well as LDL. In contrast to the *Apoe*$^{-/-}$ mouse, the VLDL of the *Ldlr*$^{-/-}$ mouse is richer in triglyceride and apoB100. Lesions in *Ldlr*$^{-/-}$ mice develop in each of the vascular sites where lesions are seen in the *Apoe*$^{-/-}$ model, within a time frame exceeding at least 6 weeks of high-fat diet feeding.

Although the WTD is most widely employed atherogenic diet, a variety of high-fat diets have been used [27]. This includes diets containing quite high cholesterol content [28] or others that induce obesity and diabetes, such as the high-fat, high-sucrose, cholesterol-supplemented diet [29], which may induce even larger lesions than does the WTD [30]. There are also diets in which the composition of the dietary fat is varied. The WTD is usually associated with the presence of insulin resistance, which can be avoided by feeding a diet enriched in cholesterol with low fat [31].

The *Ldlr*$^{-/-}$ mouse is much more useful for bone marrow transplantation studies, as the LDL receptor expressed on bone marrow derived cells is not critical for the clearance of apoB containing lipoproteins [32]. Thus, in contrast to the situation with the *Apoe*$^{-/-}$ model, the donor bone marrow can express the LDL receptor without significantly influencing atherosclerosis burden in the chimeric mouse.

2.3 Other Murine Models of Atherosclerosis

In addition to *Apoe*$^{-/-}$ mice, several models in which variants of apoE are expressed have also been used in atherosclerosis research. In humans there are three major apoE isoforms, designated apoE2,

apoE3, and apoE4. These different isoforms can profoundly modify the metabolic phenotype of the individual. A series of targeted gene replacement mice in which the mouse apoE gene was replaced with one of the human apoE isoforms have been engineered [33], allowing for the exploration of the mechanisms by which these isoforms may modify arterial vessel functions that impact on atherogenesis. While mice expressing *APOE3* and *APOE4* genes are relatively protected from development of atherosclerosis, *APOE2* knock-in mice spontaneously develop atherosclerosis. Likewise, transgenic mice expressing the *APOE*3-Leiden* variant, which has low affinity for the LDL receptor, develop atherosclerosis when fed a high-fat diet and have been used by several groups [34].

There are a number of variants of the *Ldlr*$^{-/-}$ model that will develop atherosclerosis while being fed standard chow. These include apoB100 transgenic/*Ldlr*$^{-/-}$ mice [35] and *Apobec*$^{-/-}$*Ldlr*$^{-/-}$ mice [36]. This latter model lacks the enzyme responsible for the editing of the apoB100 mRNA transcript to yield apoB48 and hence the apoB expressed in these mutant mice is exclusively the apoB100 variant. Young and colleagues have also developed apoB100 only mice by mutating the codon in the mouse apoB gene that is edited to generate apoB48. These mice were crossed with *Ldlr*$^{-/-}$ or *Apoe*$^{-/-}$ mice to explore the role of plasma lipoprotein size on atherogenesis [37]. These studies were partly informed by the finding that cholesterol fed rabbits had more atherosclerosis than similar fed rabbits that were diabetic [38]. The diabetic rabbits had more chylomicron cholesterol, i.e., larger particles, which were thought to have more limited access to the arterial intima [39]. When Young and colleagues compared the two apoB100 only models fed standard chow at similar plasma cholesterol levels, they found that the *Apob100* only, *Ldlr*$^{-/-}$ mice, whose plasma cholesterol was carried primarily in LDL particles, had much more lesion than the *Apob100* only, *Apoe*$^{-/-}$ mice which had most of their plasma cholesterol in larger remnant particles. Thus, a large number of small apoB-containing particles (i.e., LDL) were more atherogenic than a smaller number of large particles (i.e., VLDL/chylomicron remnants). However, a model in which chylomicrons are very poorly lipolyzed and accumulate in the plasma (due to deficiency of glycosyl phosphatidyl inositol anchoring HDL binding protein required for binding of lipoprotein lipase to the capillary wall) indicates that large chylomicrons may be atherogenic albeit at a much slower rate and extent than for elevated LDL [40]. As mentioned above, mice lack CETP, which facilitates the exchange of lipids between HDL and apoB-containing lipoproteins leading to a reduction in HDL levels. Mice transgenic for human CETP expressed in the *Ldlr*$^{-/-}$ mouse [41] and *Apob100* transgenic mouse [42] as well as in *Apoe*$^{-/-}$ [41] and *APOE*3-Leiden* [43] mice have been used to examine the impact of CETP expression on atherogenesis.

3 Immune Cells in Atherogenesis

The macrophage is the most abundant cell type of the atherosclerotic plaque, especially in the early plaque which is predominantly a foam cell lesion. The importance of macrophages was highlighted by the profound reduction in lesion growth in the absence of M-CSF [44]. Monocytes in the blood are the source of lesional macrophages and we now know that monocytes and macrophages are heterogeneous [4, 45]. In murine blood, the monocytes are divided into two major subpopulations, the inflammatory Ly6C^{hi} cells and patrolling Ly6C^{lo} monocytes. Hypercholesterolemia in *Apoe*$^{-/-}$ mice increased the level of Ly6C^{hi} monocytes [46]. This subpopulation is also the major monocyte population that infiltrates the atherosclerotic lesion [46, 47]. Within the atherosclerotic lesions, signals within the microenvironment promote the polarization of macrophages to M1-like inflammatory macrophages and alternatively activated M2-like less inflammatory macrophages, although macrophages with other phenotypes are also observed [4, 48]. The M1-like macrophages are the predominant cells in developing atherosclerotic plaques and are likely derived from infiltrating Ly6C^{hi} monocytes and conversion of M2-like macrophages in response to signals within the lesion. Activated inflammatory macrophages in the plaques are one source of pro-inflammatory cytokines, such as IFNγ, and chemokines such as MCP-1. The M2-like cells probably participate in healing that occurs within chronic plaques and are enriched in plaques undergoing regression [49].

Recently there has been much evidence showing that mouse models of atherosclerosis, particularly *Apoe*$^{-/-}$ mice fed a WTD, have monocytosis [50]. Indeed in humans monocytosis constitutes a risk factor for atherosclerotic heart disease [51]. Among the regulators of monocytosis in the setting of atherosclerosis is the stimulation of growth factor-mediated proliferation in the hematopoietic stem and multiple progenitor cells (HSPC) in the bone marrow in response to dysregulated cholesterol homeostasis [52]. The mechanism appears to involve an increase in plasma membrane cholesterol leading to increased lipid rafts and the concentration of growth factor receptors, particularly IL-3/GM-CSF receptors which share a common subunit. This occurs, for example, in HSPC of cholesterol efflux deficient *Abca1*$^{-/-}$ *Abcg1*$^{-/-}$ mice. Thus, the cells are more responsive to cell proliferation in the presence of IL-3 and GM-CSF. The enhanced proliferation of these cells is attenuated by HDL [53]. In addition, monocytes may be mobilized from the spleen where extramedullary hematopoiesis may add to the numbers of these cells in circulation, i.e., the spleen may function as a reservoir from which cells are mobilized into the plaques [54].

Neutrophils have been recently implicated in the progression of human and murine atherosclerosis as well as contributing to

plaque instability in humans [55]. *Apoe*$^{-/-}$ mice fed WTD also have a neutrophilia [50]. This effect on neutrophil levels involves extramedullary hematopoiesis and the IL-23/IL-17/G-CSF signaling axis [52].

Many cells of the adaptive immune system are also found in the plaque and influence its evolution [9, 56]. In the complete absence of mature T and B cells, as for example in the recombination activation gene deficient animals (*Rag*$^{-/-}$), atherogenesis in the aortic root is reduced, but this is not observed when animals are fed a WTD for an extended period [57–59]. As a first approximation this argues that cells of the adaptive immune system are not required for the development of robust atherosclerosis. The immune cells may be either pro-inflammatory or anti-inflammatory. The fact that immune deficient mouse models generally exhibit either smaller or similar sized lesions suggests that their predominant effect is pro-inflammatory, although other effects may occur under certain circumstances. For example, in the chow fed *Apoe*$^{-/-}$*Rag*$^{-/-}$ model the innominate artery atherosclerosis is actually increased (unpublished data), arguing that in this context the predominant cell removed is anti-inflammatory.

Among B cells there are several subsets; B-2 cells, B-1 cells, and B regulatory cells. B-2 cells are the primary antibody producing cells and they also are capable of presenting antigen. Their role in atherosclerosis is primarily proatherogenic as evidenced by the effect of their removal or interruption of their signaling in murine models of atherosclerosis [60, 61]. On the other hand, the B-1 cells of the innate immune system produce atheroprotective natural IgM antibodies, such as those targeting oxidized phospholipids [5, 62]. A number of investigators have immunized atherosclerosis susceptible murine models with relevant antigens (e.g., apoB peptides) with resulting attenuation of atherosclerosis [63].

T cells also have the potential to contribute various influences on atherogenesis. There are many subsets of T cells, among which are Th1 cells, Th2 cells, Th17 cells, T regulatory cells and natural killer T (NKT) cells. The Th1 cells generally are proatherogenic, by functioning as helper cells or producing proinflammatory cytokines, such as IFNγ. Their adoptive transfer into immune deficient atherosclerosis susceptible hosts promotes lesion development [64]. The role of Th2 cells is less clear, although they appear to be antiatherogenic. Similarly, Th17 cells have been shown to be proatherogenic and antiatherogenic in different studies in mouse models [65]. T regulatory cells are notably antiatherogenic, predominantly by secreting anti-inflammatory cytokines, of which IL-10 and TGFβ are most prominent and most studied [66]. NKT cells are of particular interest with respect to atherosclerosis in that they recognize lipid antigens presented by CD1 molecules on antigen presenting cells. Although they come in at least two varieties, invariant or group I NKT cells that express relatively invariant

T cell receptors and group II NKT cells with more diverse T cell receptors, both groups of cells are CD1d restricted in the mouse [67]. The group I NKT cells are most prominent, particularly in the liver, and they have been most studied. They are proatherogenic as demonstrated in several ways, including their adoptive transfer into immune deficient *Ldlr*$^{-/-}$ recipients [68]. The type II NKT cells are much less abundant and their role in atherogenesis is much less clear. Their direct study is not easy for lack of specific targetable markers.

The stimulation of the adaptive immune system requires two signals; an antigen signal and a second signal involving a variety of interacting co-stimulatory molecules on T cells and antigen presenting cells. The role of many of these costimulatory molecules have been studied in murine atherogenesis models [69]. For the most part, these molecules are pro-atherogenic, consistent with the pro-atherogenic role of T and B cells.

4 Genetics of Murine Atherogenesis

Much of the work reviewed above has been carried out in a single strain of mice: the C57BL/6 strain which is the most atherosusceptible strain. The focus has been primarily on the examination of the effect of overexpression or deletion of a large number of genes on atherogenesis. In a recent review, the effect of the deletion of about 100 genes on atherosclerosis in C57BL/6 mice, mostly in the *Apoe* or *Ldlr* deficient backgrounds, has been surveyed [70]. About a third of these genes affect plasma lipids, which may be mediating the role of that gene product in atherosclerosis. A less biased approach to the identification of genes that impact on atherosclerosis has involved genetic crosses between the atherosusceptible C57BL/6 mice and one or other resistant strains, e.g., FVB, again frequently in the *Apoe* or *Ldlr* deficient background. This has resulted in the identification of a number of loci (>40) having an impact on lesion development that are mapped to a variety of chromosomes. This emphasizes the complexity of genetic influences on atherogenesis. It should be noted that in most cases, each putative locus contains multiple neighboring genes. In very few cases has a particular gene been identified by this approach. However, recently the subcongenic analysis of the *Ath11* locus in a cross between C57BL/6 *Apoe*$^{-/-}$ and FVB *Apoe*$^{-/-}$ mice has identified a single gene, *Raet1e* encoding a major histocompatibility class 1-like molecule, whose expression level regulates aortic root atherosclerosis [71]. This conclusion was confirmed by the targeted overexpression of one of the alleles of this gene, resulting in the predicted atherosclerosis phenotype. A particularly interesting outcome of the comparison of mouse strains involved the study of 129S6/SvEvTac *Apoe*$^{-/-}$ strain which exhibited a surprising increase in

aortic arch atherosclerosis relative to C57BL/6 *Apoe*$^{-/-}$ mice. The aortic root in the 129S6/SvEvTac strain is more atheroresistant, but this strain has a sharper angle of curvature for the arch and this appears to induce a difference in shear stress at this vascular site resulting in a hemodynamic environment that promotes lesion initiation and growth [72]. The development of large panels of recombinant inbred strains offers the potential for the dissection of high-resolution genetic control of various lipid and atherosclerosis phenotypes [73].

5 Regression of Atherosclerosis

It is important to appreciate that development of the atherosclerotic plaque is a highly dynamic chronic inflammatory process. The susceptibility of plaques to regression is a very good indication of this. There are several examples of the regression of established murine lesions [74]. The clearest indication of plaque regression is seen in the transplantation of an atherosclerotic aortic arch into a naïve non-atherosclerotic, normolipidemic host. In this model, both early and advanced lesions regress [75, 76] and this regression is enhanced by the overexpression of apoA-I, suggesting that apoA-I/HDL mediated cholesterol efflux may be an important mechanism promoting regression [77]. Indeed, the induction of regression following agonism of miR-33 which leads to increased expression of the ABCA1 transporter involved in macrophage cholesterol efflux and hepatic biogenesis of HDL [78] or treatment of mice with LXR agonists [79] that also promote expression of ABCA1 along with ABCG1 and apoE support the concept that enhancement of macrophage cholesterol efflux promotes atherosclerosis regression. Given that hypercholesterolemia plays such a critical role in lesion development, the substantial reduction of plasma cholesterol level likely contributed to the lesion reduction in the transplant model. Plasma cholesterol reduction can be accomplished by switching from a high-fat to low-fat diet, thus reducing apoB-containing lipoproteins. Another mechanism to reduce the secretion of apoB-containing lipoproteins is achieved by targeting microsomal triglyceride transfer protein (MTP), a protein involved in the lipidation of apoB. The conditional attenuation of the *Mtp* gene expression in the *Apob100* only/*Ldlr*$^{-/-}$ model or the inhibition of MTP activity in *Ldlr*$^{-/-}$ mice along with a return to a standard chow diet represents an effective strategy to achieve regression [80, 81]. Similarly, the conditional induction of apoE expression in the hypomorphic *Apoe/Mx1-Cre* model also promotes regression of lesions in high-fat diet fed mice [82]. During lesion regression associated with lowering the cholesterol burden, macrophage cells alter their phenotype and are thought to emigrate from the lesion to the draining lymph nodes [75]. This process is enhanced by the

increased expression of the chemokine receptor CCR7 [83], now recognized as a cholesterol responsive gene [84]. Murine models of atherosclerosis are also being used to demonstrate that immune cells other that macrophages, such as T cells and T regulatory cells [85, 86], can also participate in lesion regression. Thus, cells of the immune system participate in many aspects of the atherogenic process.

6 Conclusions

The study of murine models of atherogenesis over the last two decades has been extremely valuable in revealing the mechanisms that are operative in initiating lesion development as well as their progression and regression. As lesion development occurs over an extended time, it is likely that the dominance of pathways may vary over the evolution of the plaque, which adds to the requirement for examination of the effect of genetic manipulation at different stages of lesion development. Murine atherosclerotic models are also valuable for the dissection of mechanisms operative in response to potential therapeutic interventions. It is clear from the information so far acquired that there are many genes and processes implicated in the pathogenesis of atherosclerosis, involving a great deal of cross talk between cells and their gene products, and this in turn may change with lesion maturation. With the rapid advance in gene sequencing and analysis technology as well as associated data processing one can expect even more appreciation of these mechanisms, involving not only single genetic targets but system analysis [87]. The more frequent employment of conditional gene deletions such as the Cre-Lox system and inducible expression systems to temporally turn on or off gene expression, will add greatly to our understanding of the mechanisms involved. While studies in mice have and will continue to provide insight into the mechanisms of the pathogenesis of atherosclerosis, it needs to be kept in mind that there are limitations to the use of mouse models, particularly that the arterial sites where lesions develop are not identical to humans, that mice do not develop unstable plaques characteristic of human lesions, and that significant hypercholesterolemia is needed to induce atherosclerosis in these models.

References

1. VanderLaan PA, Reardon CA, Getz GS (2004) Site specificity of atherosclerosis: site-selective responses to atherosclerotic modulators. Arterioscler Thromb Vasc Biol 24:12–22
2. Getz GS, Reardon CA (2012) Animal models of atherosclerosis. Arterioscler Thromb Vasc Biol 32:1104–1115
3. Glass CK, Witztum JL (2001) Atherosclerosis. the road ahead. Cell 104:503–516
4. Moore KJ, Sheedy FJ, Fisher EA (2013) Macrophages in atherosclerosis: a dynamic balance. Nat Rev Immunol 13:709–721
5. Witztum JL, Lichtman AH (2014) The influence of innate and adaptive immune

responses on atherosclerosis. Annu Rev Pathol 9:73–102

6. Brown MS, Goldstein JL (2009) Cholesterol feedback: from Schoenheimer's bottle to Scap's MELADL. J Lipid Res 50(Suppl):S15–S27
7. Scull CM, Tabas I (2011) Mechanisms of ER stress-induced apoptosis in atherosclerosis. Arterioscler Thromb Vasc Biol 31:2792–2797
8. Thorp E, Subramanian M, Tabas I (2011) The role of macrophages and dendritic cells in the clearance of apoptotic cells in advanced atherosclerosis. Eur J Immunol 41:2515–2518
9. Lichtman AH, Binder CJ, Tsimikas S, Witztum JL (2013) Adaptive immunity in atherogenesis: new insights and therapeutic approaches. J Clin Invest 123:27–36
10. Hansson GK, Hermansson A (2011) The immune system in atherosclerosis. Nat Immunol 12:204–212
11. Wissler RW, Eilert ML, Schroeder MA, Cohen L (1954) Production of lipomatous and atheromatous arterial lesions in the albino rat. AMA Arch Pathol 57:333–351
12. Plump AS, Smith JD, Hayek T, Aalto-Setala K, Walsh A, Verstuyft JG, Rubin EM, Breslow JL (1992) Severe hypercholesterolemia and atherosclerosis in apolipoprotein E-deficient mice created by homologous recombination in ES cells. Cell 71:343–353
13. Zhang SH, Reddick RL, Piedrahita JA, Maeda N (1992) Spontaneous hypercholesterolemia and arterial lesions in mice lacking apolipoprotein E. Science 258:468–471
14. Nakashima Y, Plump AS, Raines EW, Breslow JL, Ross R (1994) ApoE-deficient mice develop lesions of all phases of atherosclerosis throughout the arterial tree. Arterioscler Thromb 14:133–140
15. Ishibashi S, Goldstein JL, Brown MS, Herz J, Burns DK (1994) Massive xanthomatosis and atherosclerosis in cholesterol-fed low density lipoprotein receptor-negative mice. J Clin Invest 93:1885–1893
16. Braun A, Trigatti BL, Post MJ, Sato K, Simons M, Edelberg JM, Rosenberg RD, Schrenzel M, Krieger M (2002) Loss of SR-BI expression leads to the early onset of occlusive atherosclerotic coronary artery disease, spontaneous myocardial infarctions, severe cardiac dysfunction, and premature death in apolipoprotein E-deficient mice. Circ Res 90:270–276
17. Bradshaw G, Gutierrez A, Miyake JH, Davis KR, Li AC, Glass CK, Curtiss LK, Davis RA (2005) Facilitated replacement of Kupffer cells expressing a paraoxonase-1 transgene is essential for ameliorating atherosclerosis in mice. Proc Natl Acad Sci U S A 102:11029–11034
18. Hasty AH, Linton MF, Swift LL, Fazio S (1999) Determination of the lower threshold of apolipoprotein E resulting in remnant lipoprotein clearance. J Lipid Res 40:1529–1538
19. Getz GS, Reardon CA (2009) Apoprotein E as a lipid transport and signaling protein in the blood, liver, and artery wall. J Lipid Res 50(Suppl):S156–S161
20. Linton MF, Fazio S (1999) Macrophages, lipoprotein metabolism, and atherosclerosis: insights from murine bone marrow transplantation studies. Curr Opin Lipidol 10:97–105
21. Fazio S, Babaev VR, Murray AB, Hasty AH, Carter KJ, Gleaves LA, Atkinson JB, Linton MF (1997) Increased atherosclerosis in mice reconstituted with apolipoprotein E null macrophages. Proc Natl Acad Sci U S A 94: 4647–4652
22. Van Eck M, Herijgers N, Vidgeon-Hart M, Pearce NJ, Hoogerbrugge PM, Groot PH, Van Berkel TJ (2000) Accelerated atherosclerosis in C57Bl/6 mice transplanted with ApoE-deficient bone marrow. Atherosclerosis 150:71–80
23. Hasty AH, Linton MF, Brandt SJ, Babaev VR, Gleaves LA, Fazio S (1999) Retroviral gene therapy in ApoE-deficient mice: ApoE expression in the artery wall reduces early foam cell lesion formation. Circulation 99:2571–2576
24. Fazio S, Babaev VR, Burleigh ME, Major AS, Hasty AH, Linton MF (2002) Physiological expression of macrophage apoE in the artery wall reduces atherosclerosis in severely hyperlipidemic mice. J Lipid Res 43:1602–1609
25. Huang ZH, Reardon CA, Subbaiah PV, Getz GS, Mazzone T (2013) ApoE derived from adipose tissue does not suppress atherosclerosis or correct hyperlipidemia in apoE knockout mice. J Lipid Res 54:202–213
26. Teupser D, Persky AD, Breslow JL (2003) Induction of atherosclerosis by low-fat, semisynthetic diets in LDL receptor-deficient C57BL/6J and FVB/NJ mice: comparison of lesions of the aortic root, brachiocephalic artery, and whole aorta (en face measurement). Arterioscler Thromb Vasc Biol 23:1907–1913
27. Getz GS, Reardon CA (2006) Diet and murine atherosclerosis. Arterioscler Thromb Vasc Biol 26:242–249
28. Curtiss LK, Black AS, Bonnet DJ, Tobias PS (2012) Atherosclerosis induced by endogenous and exogenous toll-like receptor (TLR)1 or TLR6 agonists. J Lipid Res 53:2126–2132
29. Subramanian S, Han CY, Chiba T, McMillen TS, Wang SA, Haw A 3rd, Kirk EA, O'Brien KD, Chait A (2008) Dietary cholesterol worsens adipose tissue macrophage accumulation

and atherosclerosis in obese LDL receptor-deficient mice. Arterioscler Thromb Vasc Biol 28:685–691

30. Subramanian S, Turner MS, Ding Y, Goodspeed L, Wang S, Buckner JH, O'Brien K, Getz GS, Reardon CA, Chait A (2013) Increased levels of invariant natural killer T lymphocytes worsen metabolic abnormalities and atherosclerosis in obese mice. J Lipid Res 54:2831–2841
31. Hartvigsen K, Binder CJ, Hansen LF, Rafia A, Juliano J, Horkko S, Steinberg D, Palinski W, Witztum JL, Li AC (2007) A diet-induced hypercholesterolemic murine model to study atherogenesis without obesity and metabolic syndrome. Arterioscler Thromb Vasc Biol 27:878–885
32. Boisvert WA, Spangenberg J, Curtiss LK (1997) Role of leukocyte-specific LDL receptors on plasma lipoprotein cholesterol and atherosclerosis in mice. Arterioscler Thromb Vasc Biol 17:340–347
33. Pendse AA, Arbones-Mainar JM, Johnson LA, Altenburg MK, Maeda N (2009) Apolipoprotein E knock-out and knock-in mice: atherosclerosis, metabolic syndrome, and beyond. J Lipid Res 50(Suppl):S178–S182
34. van Vlijmen BJ, van den Maagdenberg AM, Gijbels MJ, van der Boom H, HogenEsch H, Frants RR, Hofker MH, Havekes LM (1994) Diet-induced hyperlipoproteinemia and atherosclerosis in apolipoprotein E3-Leiden transgenic mice. J Clin Invest 93:1403–1410
35. Sanan DA, Newland DL, Tao R, Marcovina S, Wang J, Mooser V, Hammer RE, Hobbs HH (1998) Low density lipoprotein receptor-negative mice expressing human apolipoprotein B-100 develop complex atherosclerotic lesions on a chow diet: no accentuation by apolipoprotein(a). Proc Natl Acad Sci U S A 95:4544–4549
36. Powell-Braxton L, Veniant M, Latvala RD, Hirano KI, Won WB, Ross J, Dybdal N, Zlot CH, Young SG, Davidson NO (1998) A mouse model of human familial hypercholesterolemia: markedly elevated low density lipoprotein cholesterol levels and severe atherosclerosis on a low-fat chow diet. Nat Med 4:934–938
37. Veniant MM, Withycombe S, Young SG (2001) Lipoprotein size and atherosclerosis susceptibility in Apoe(−/−) and Ldlr(−/−) mice. Arterioscler Thromb Vasc Biol 21:1567–1570
38. Duff GL, Mc MG (1948) The inhibition of experimental cholesterol atherosclerosis by alloxan diabetes in the rabbit. Am Heart J 36:469
39. Nordestgaard BG, Zilversmit DB (1988) Large lipoproteins are excluded from the arterial wall in diabetic cholesterol-fed rabbits. J Lipid Res 29:1491–1500
40. Weinstein MM, Yin L, Tu Y, Wang X, Wu X, Castellani LW, Walzem RL, Lusis AJ, Fong LG, Beigneux AP, Young SG (2010) Chylomicronemia elicits atherosclerosis in mice – brief report. Arterioscler Thromb Vasc Biol 30:20–23
41. Plump AS, Masucci-Magoulas L, Bruce C, Bisgaier CL, Breslow JL, Tall AR (1999) Increased atherosclerosis in ApoE and LDL receptor gene knock-out mice as a result of human cholesteryl ester transfer protein transgene expression. Arterioscler Thromb Vasc Biol 19:1105–1110
42. Zuckerman SH, Evans GF, Schelm JA, Eacho PI, Sandusky G (1999) Estrogen-mediated increases in LDL cholesterol and foam cell-containing lesions in human ApoB100xCETP transgenic mice. Arterioscler Thromb Vasc Biol 19:1476–1483
43. de Vries-van der Weij J, Zadelaar S, Toet K, Havekes LM, Kooistra T, Rensen PC (2009) Human CETP aggravates atherosclerosis by increasing VLDL-cholesterol rather than by decreasing HDL-cholesterol in APOE*3-Leiden mice. Atherosclerosis 206:153–158
44. Smith JD, Trogan E, Ginsberg M, Grigaux C, Tian J, Miyata M (1995) Decreased atherosclerosis in mice deficient in both macrophage colony-stimulating factor (op) and apolipoprotein E. Proc Natl Acad Sci U S A 92: 8264–8268
45. Swirski FK, Weissleder R, Pittet MJ (2009) Heterogeneous in vivo behavior of monocyte subsets in atherosclerosis. Arterioscler Thromb Vasc Biol 29:1424–1432
46. Swirski FK, Libby P, Aikawa E, Alcaide P, Luscinskas FW, Weissleder R, Pittet MJ (2007) Ly-6Chi monocytes dominate hypercholesterolemia-associated monocytosis and give rise to macrophages in atheromata. J Clin Invest 117:195–205
47. Tacke F, Alvarez D, Kaplan TJ, Jakubzick C, Spanbroek R, Llodra J, Garin A, Liu J, Mack M, van Rooijen N, Lira SA, Habenicht AJ, Randolph GJ (2007) Monocyte subsets differentially employ CCR2, CCR5, and CX3CR1 to accumulate within atherosclerotic plaques. J Clin Invest 117:185–194
48. Koltsova EK, Hedrick CC, Ley K (2013) Myeloid cells in atherosclerosis: a delicate balance of anti-inflammatory and proinflammatory mechanisms. Curr Opin Lipidol 24:371–380
49. Feig JE, Vengrenyuk Y, Reiser V, Wu C, Statnikov A, Aliferis CF, Garabedian MJ, Fisher EA, Puig O (2012) Regression of atherosclerosis is characterized by broad changes in the

plaque macrophage transcriptome. PLoS One 7:e39790

50. Tall AR, Yvan-Charvet L, Westerterp M, Murphy AJ (2012) Cholesterol efflux: a novel regulator of myelopoiesis and atherogenesis. Arterioscler Thromb Vasc Biol 32:2547–2552
51. Soehnlein O, Swirski FK (2013) Hypercholesterolemia links hematopoiesis with atherosclerosis. Trends Endocrinol Metab 24:129–136
52. Westerterp M, Gourion-Arsiquaud S, Murphy AJ, Shih A, Cremers S, Levine RL, Tall AR, Yvan-Charvet L (2012) Regulation of hematopoietic stem and progenitor cell mobilization by cholesterol efflux pathways. Cell Stem Cell 11:195–206
53. Yvan-Charvet L, Pagler T, Gautier EL, Avagyan S, Siry RL, Han S, Welch CL, Wang N, Randolph GJ, Snoeck HW, Tall AR (2010) ATP-binding cassette transporters and HDL suppress hematopoietic stem cell proliferation. Science 328:1689–1693
54. Robbins CS, Chudnovskiy A, Rauch PJ, Figueiredo JL, Iwamoto Y, Gorbatov R, Etzrodt M, Weber GF, Ueno T, van Rooijen N, Mulligan-Kehoe MJ, Libby P, Nahrendorf M, Pittet MJ, Weissleder R, Swirski FK (2012) Extramedullary hematopoiesis generates Ly-6C(high) monocytes that infiltrate atherosclerotic lesions. Circulation 125:364–374
55. Woollard KJ (2013) Immunological aspects of atherosclerosis. Clin Sci (Lond) 125:221–235
56. Libby P, Lichtman AH, Hansson GK (2013) Immune effector mechanisms implicated in atherosclerosis: from mice to humans. Immunity 38:1092–1104
57. Reardon CA, Blachowicz L, Lukens J, Nissenbaum M, Getz GS (2003) Genetic background selectively influences innominate artery atherosclerosis: immune system deficiency as a probe. Arterioscler Thromb Vasc Biol 23:1449–1454
58. Daugherty A, Pure E, Delfel-Butteiger D, Chen S, Leferovich J, Roselaar SE, Rader DJ (1997) The effects of total lymphocyte deficiency on the extent of atherosclerosis in apolipoprotein E–/– mice. J Clin Invest 100: 1575–1580
59. Dansky HM, Charlton SA, Harper MM, Smith JD (1997) T and B lymphocytes play a minor role in atherosclerotic plaque formation in the apolipoprotein E-deficient mouse. Proc Natl Acad Sci U S A 94:4642–4646
60. Sage AP, Tsiantoulas D, Baker L, Harrison J, Masters L, Murphy D, Loinard C, Binder CJ, Mallat Z (2012) BAFF receptor deficiency reduces the development of atherosclerosis in mice – brief report. Arterioscler Thromb Vasc Biol 32:1573–1576
61. Kyaw T, Tay C, Khan A, Dumouchel V, Cao A, To K, Kehry M, Dunn R, Agrotis A, Tipping P, Bobik A, Toh BH (2010) Conventional B2 B cell depletion ameliorates whereas its adoptive transfer aggravates atherosclerosis. J Immunol 185:4410–4419
62. Tsiantoulas D, Gruber S, Binder CJ (2012) B-1 cell immunoglobulin directed against oxidation-specific epitopes. Front Immunol 3:415
63. Nilsson J, Bjorkbacka H, Fredrikson GN (2012) Apolipoprotein B100 autoimmunity and atherosclerosis - disease mechanisms and therapeutic potential. Curr Opin Lipidol 23:422–428
64. Zhou X, Robertson AK, Hjerpe C, Hansson GK (2006) Adoptive transfer of CD4+ T cells reactive to modified low-density lipoprotein aggravates atherosclerosis. Arterioscler Thromb Vasc Biol 26:864–870
65. Butcher M, Galkina E (2011) Current views on the functions of interleukin-17A-producing cells in atherosclerosis. Thromb Haemost 106:787–795
66. Tedgui A, Mallat Z (2006) Cytokines in atherosclerosis: pathogenic and regulatory pathways. Physiol Rev 86:515–581
67. Bendelac A, Savage PB, Teyton L (2007) The biology of NKT cells. Annu Rev Immunol 25:297–336
68. Getz GS, Vanderlaan PA, Reardon CA (2011) Natural killer T cells in lipoprotein metabolism and atherosclerosis. Thromb Haemost 106:814–819
69. Gotsman I, Sharpe AH, Lichtman AH (2008) T-cell costimulation and coinhibition in atherosclerosis. Circ Res 103:1220–1231
70. Stylianou IM, Bauer RC, Reilly MP, Rader DJ (2012) Genetic basis of atherosclerosis: insights from mice and humans. Circ Res 110:337–355
71. Rodriguez JM, Wolfrum S, Robblee M, Chen KY, Gilbert ZN, Choi JH, Teupser D, Breslow JL (2013) Altered expression of Raet1e, a major histocompatibility complex class 1-like molecule, underlies the atherosclerosis modifier locus Ath11 10b. Circ Res 113:1054–1064
72. Tomita H, Hagaman J, Friedman MH, Maeda N (2012) Relationship between hemodynamics and atherosclerosis in aortic arches of apolipoprotein E-null mice on 129S6/SvEvTac and C57BL/6J genetic backgrounds. Atherosclerosis 220:78–85
73. Ghazalpour A, Rau CD, Farber CR, Bennett BJ, Orozco LD, van Nas A, Pan C, Allayee H, Beaven SW, Civelek M, Davis RC, Drake TA,

Friedman RA, Furlotte N, Hui ST, Jentsch JD, Kostem E, Kang HM, Kang EY, Joo JW, Korshunov VA, Laughlin RE, Martin LJ, Ohmen JD, Parks BW, Pellegrini M, Reue K, Smith DJ, Tetradis S, Wang J, Wang Y, Weiss JN, Kirchgessner T, Gargalovic PS, Eskin E, Lusis AJ, LeBoeuf RC (2012) Hybrid mouse diversity panel: a panel of inbred mouse strains suitable for analysis of complex genetic traits. Mamm Genome 23:680–692

74. Williams KJ, Feig JE, Fisher EA (2008) Rapid regression of atherosclerosis: insights from the clinical and experimental literature. Nat Clin Pract Cardiovasc Med 5:91–102
75. Trogan E, Feig JE, Dogan S, Rothblat GH, Angeli V, Tacke F, Randolph GJ, Fisher EA (2006) Gene expression changes in foam cells and the role of chemokine receptor CCR7 during atherosclerosis regression in ApoE-deficient mice. Proc Natl Acad Sci U S A 103:3781–3786
76. Reis ED, Li J, Fayad ZA, Rong JX, Hansoty D, Aguinaldo JG, Fallon JT, Fisher EA (2001) Dramatic remodeling of advanced atherosclerotic plaques of the apolipoprotein E-deficient mouse in a novel transplantation model. J Vasc Surg 34:541–547
77. Feig JE, Rong JX, Shamir R, Sanson M, Vengrenyuk Y, Liu J, Rayner K, Moore K, Garabedian M, Fisher EA (2011) HDL promotes rapid atherosclerosis regression in mice and alters inflammatory properties of plaque monocyte-derived cells. Proc Natl Acad Sci U S A 108:7166–7171
78. Rayner KJ, Sheedy FJ, Esau CC, Hussain FN, Temel RE, Parathath S, van Gils JM, Rayner AJ, Chang AN, Suarez Y, Fernandez-Hernando C, Fisher EA, Moore KJ (2011) Antagonism of miR-33 in mice promotes reverse cholesterol transport and regression of atherosclerosis. J Clin Invest 121:2921–2931
79. Levin N, Bischoff ED, Daige CL, Thomas D, Vu CT, Heyman RA, Tangirala RK, Schulman IG (2005) Macrophage liver X receptor is required for antiatherogenic activity of LXR agonists. Arterioscler Thromb Vasc Biol 25:135–142
80. Lieu HD, Withycombe SK, Walker Q, Rong JX, Walzem RL, Wong JS, Hamilton RL, Fisher EA, Young SG (2003) Eliminating atherogenesis in mice by switching off hepatic lipoprotein secretion. Circulation 107: 1315–1321
81. Hewing B, Parathath S, Mai CK, Fiel MI, Guo L, Fisher EA (2013) Rapid regression of atherosclerosis with MTP inhibitor treatment. Atherosclerosis 227:125–129
82. Raffai RL, Loeb SM, Weisgraber KH (2005) Apolipoprotein E promotes the regression of atherosclerosis independently of lowering plasma cholesterol levels. Arterioscler Thromb Vasc Biol 25:436–441
83. Feig JE, Pineda-Torra I, Sanson M, Bradley MN, Vengrenyuk Y, Bogunovic D, Gautier EL, Rubinstein D, Hong C, Liu J, Wu C, van Rooijen N, Bhardwaj N, Garabedian M, Tontonoz P, Fisher EA (2010) LXR promotes the maximal egress of monocyte-derived cells from mouse aortic plaques during atherosclerosis regression. J Clin Invest 120: 4415–4424
84. Feig JE, Shang Y, Rotllan N, Vengrenyuk Y, Wu C, Shamir R, Torra IP, Fernandez-Hernando C, Fisher EA, Garabedian MJ (2011) Statins promote the regression of atherosclerosis via activation of the CCR7-dependent emigration pathway in macrophages. PLoS One 6:e28534
85. Kita T, Yamashita T, Sasaki N, Kasahara K, Sasaki Y, Yodoi K, Takeda M, Nakajima K, Hirata K (2014) Regression of atherosclerosis with anti-CD3 antibody via augmenting a regulatory T-cell response in mice. Cardiovasc Res 102:107–117
86. Foks AC, van Puijvelde GH, Bot I, ter Borg MN, Habets KL, Johnson JL, Yagita H, van Berkel TJ, Kuiper J (2013) Interruption of the OX40-OX40 ligand pathway in LDL receptor-deficient mice causes regression of atherosclerosis. J Immunol 191:4573–4580
87. Civelek M, Lusis AJ (2014) Systems genetics approaches to understand complex traits. Nat Rev Genet 15:34–48

Chapter 2

Cytokines and Immune Responses in Murine Atherosclerosis

Pascal J.H. Kusters and Esther Lutgens

Abstract

Atherosclerosis is an inflammatory disease of the vessel wall characterized by activation of the innate immune system, with macrophages as the main players, as well as the adaptive immune system, characterized by a Th1-dominant immune response. Cytokines play a major role in the initiation and regulation of inflammation. In recent years, many studies have investigated the role of these molecules in experimental models of atherosclerosis. While some cytokines such as TNF or IFNγ clearly had atherogenic effects, others such as IL-10 were found to be atheroprotective. However, studies investigating the different cytokines in experimental atherosclerosis revealed that the cytokine system is complex with both disease stage-dependent and site-specific effects. In this review, we strive to provide an overview of the main cytokines involved in atherosclerosis and to shed light on their individual role during atherogenesis.

Key words Atherosclerosis, Cytokines, Experimental atherosclerosis

1 Introduction

Atherosclerosis, the underlying cause of many cardiovascular diseases, including coronary artery disease, stroke, and peripheral arterial disease, is responsible for a major health burden in the western world. Atherosclerosis is a lipid-driven, chronic inflammatory disease in which both the innate and adaptive immune system play an essential role.

The initiation of atherosclerosis is characterized by endothelial activation and dysfunction, caused by shear stress and increased permeability for low-density lipoproteins (LDL), and modification of the infiltrated lipids in the arterial wall. Subsequent induction of adhesion molecules and secretion of inflammatory mediators by endothelial cells and adherent platelets induce recruitment of immune cells to the arterial wall. Innate immune cells, such as monocytes, macrophages, neutrophils, dendritic cells, mast cells, and natural killer T-cells (NKT) migrate towards the intima, phagocytose (modified) lipids, and produce additional

Vicente Andrés and Beatriz Dorado (eds.), *Methods in Mouse Atherosclerosis*, Methods in Molecular Biology, vol. 1339, DOI 10.1007/978-1-4939-2929-0_2,

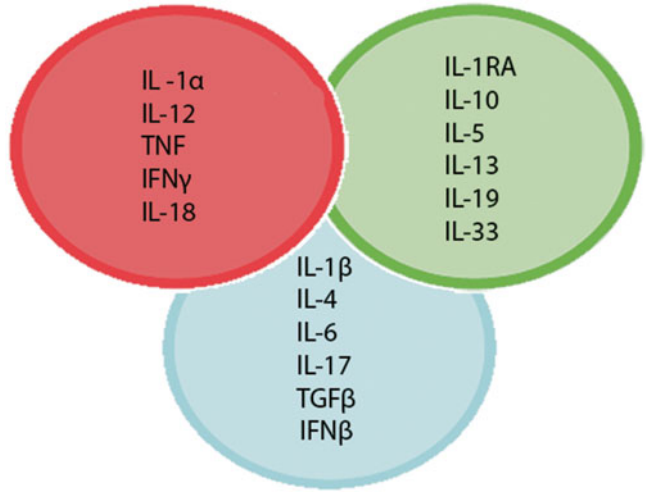

Fig. 1 The primary cytokines involved in atherosclerosis. In *red*: atherogenic cytokines. In *green*: atheroprotective cytokines. In *blue*: exact role still under investigation

inflammatory mediators. Simultaneously, the adaptive immune system is activated. Several subsets of T-cells (Thelper1, 2, and 17 cells (Th1, Th2, Th17) and regulatory T-cells (Treg)) and B-cells (B1 and B2) are found in the arterial wall, and have been shown to play a major role in atherosclerosis [1].

Cytokines are a family of small proteins (5–20 kDa) that consists of chemokines, interleukins, lymphokines, interferons, and tumor necrosis factor (TNF). Cytokines play a role in (inter)cellular communication in the immune system and thereby mediate activation and resolution of inflammation (Fig. 1). They are able to enact various cellular responses, act in synergy with one another and can function in an autocrine, paracrine, or juxtacrine manner (Fig. 2). Cytokines play a crucial role in the initiation and propagation of atherosclerosis and, combined with their receptors, have been found in large quantities in atherosclerotic plaques where they regulate immune reactions and inflammation.

In this review, we aim to give a structural overview of the cytokines involved in atherosclerosis (Table 1), with special focus on the interleukin family and mouse studies.

2 The Interleukin Family

2.1 Interleukin 1

Interleukin 1 is part of the Interleukin 1 family, which consists of 11 members that have a similar gene structure, and all play a role in acute immune responses. Of these members, IL-1α, IL-1β, IL-1 receptor antagonist (IL-1Ra), IL-18, IL-33, and IL-37 are important in atherosclerosis.

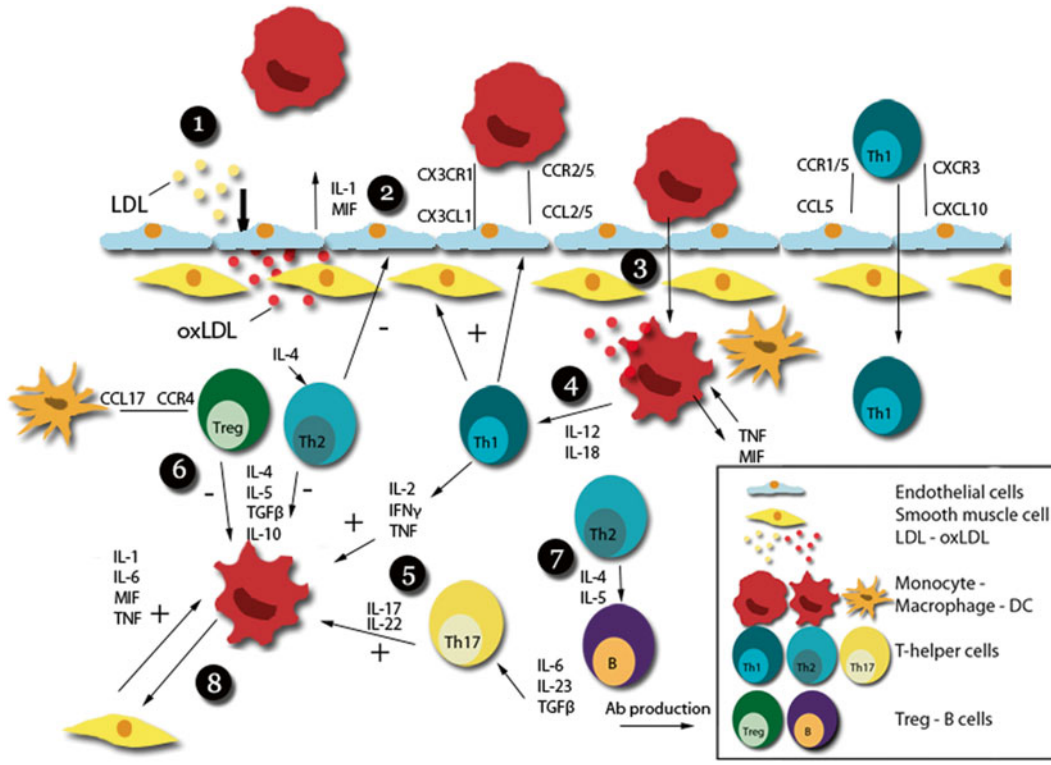

Fig. 2 Cytokines in the immune response of atherosclerosis. (*1*) LDL enters the vessel wall, and transforms into oxLDL by the action of enzymes and reactive oxygen species. (*2*) oxLDL induces immune cell chemotaxis and adhesion by endothelial cells. (*3*) Adhesion and diapedesis of monocytes and subsequent transformation into oxLDL-phagocyting macrophages producing autocrine cytokines such as TNF and MIF. (*4*) Aggravation of the initial immune response via macrophage-T-cell interactions propagating a Th1-based immune response via IL-12 and IL-18. (*5*) Th1-related cytokines such as IFNγ, but also IL-17 produced by Th17 cells, exacerbate the immune response by further stimulating macrophages. (*6*) Th2 cells and Tregs produce anti-inflammatory cytokines such as IL-10, dampening the immune response. (*7*) Th2 cells, formed under the influence of IL-4, induce B-cell proliferation and antibody production via IL-4 and 5. (*8*) Further exacerbation of the immune response occurs via macrophage-SMC interactions

Using hyperlipidemic LDL receptor ($ldlr^{-/-}$) or apolipoprotein E ($apoE^{-/-}$) null mice deficient in IL-1α, it was clearly shown that IL-1α exacerbates atherosclerosis [2–5]. IL-1α deficient macrophages were found to secrete lower levels of IL-1β and higher levels of IL-10 [3]. Interestingly, fatty acids, in particularly oleic acid, have been found to induce IL-1α production, further indicating a direct role of this cytokine in the pathophysiology of atherosclerosis [5].

Although the majority of studies reported a similar atherogenic effect for IL-1β [3, 6, 7], other studies found no effect on lesion size in the absence of IL-1β [2, 5]. One of these studies which has compared IL-1α and IL-1β deficient mice, found that bone

Table 1
Overview of cytokines in mouse atherosclerosis models

Cytokine	Receptor	Models	Diet	Outcome	Reference
IL-1α	IL-1r	IL-1α$^{-/-}$	AD	– Atherosclerosis↓	[2]
		IL-1α$^{-/-}$, induction	CC	– NS neointima	[182]
		IL-1α$^{-/-}$, apoE$^{-/-}$	CC	– Atherosclerosis↓	[3]
		IL-1α+/–, apoE$^{-/-}$	CC	– Atherosclerosis↓	[3]
		IL-1α/β$^{-/-}$, ldlr$^{-/-}$	AD	– Atherosclerosis↓	[11]
		apoE$^{-/-}$, IL-1α vaccine(IL-1α-C-Qβ)	AD	– Atherosclerosis↓	[4]
		IL-1α$^{-/-}$, ldlr$^{-/-}$	AD	– Atherosclerosis↓	[5]
IL-1β	IL-1r (1/2)	IL-1β$^{-/-}$	AD	– NS	[2]
		IL-1β$^{-/-}$, induction	CC	– Neointima↓	[182]
		IL-1β$^{-/-}$, apoE$^{-/-}$	CC	– Atherosclerosis↓	[3, 6]
		IL-1β$^{-/-}$, ldlr$^{-/-}$	AD	– NS	[5]
		apoE$^{-/-}$, anti-IL-1β (XMA052 MG1K)	AD	– Atherosclerosis↓	[7]
	IL-1r1	IL-1r1$^{-/-}$, induction	CC	– Neointima↓	[182]
		IL-1r1$^{-/-}$, apoE$^{-/-}$	AD/CC	– Atherosclerosis↓	[183–185]
			AD(WD)	– NS	[184]
			CC	– NS	[184]
		IL-1r1$^{-/-}$, apoE+/–	AD	– Atherosclerosis↓	[186]
			CC	– NS	[186]
		IL-1r1$^{-/-}$, apoE+/–, induction	AD/CC	– Atherosclerosis↓	[186]
IL-1Ra	IL-1r	IL-1Ra$^{-/-}$	AD	– NS	[187]
		IL-1Ra$^{-/-}$, induction	CC	– Neointima↑	[188]
		IL-1Ra treatment, induction	CC	– Neointima↓	[182]
		IL-1Ra$^{-/-}$, apoE$^{-/-}$	CC	– Atherosclerosis↑	[189]
		IL-1Ra+/–, apoE$^{-/-}$	CC	– Atherosclerosis↑	[189]
		IL-1RaTg, ldlr$^{-/-}$	AD	– Atherosclerosis↓	[187]
			AD(WD)	– NS	[187]
		IL-1RaTg(ic/s), apoE$^{-/-}$	AD	– Atherosclerosis↓	[190]
		apoE$^{-/-}$, rhIL-1Ra	AD	– Atherosclerosis↓	[191]
IL-2	IL-2r CD25	apoE$^{-/-}$, IL-2/anti-IL-2 mAb	AD	– Atherosclerosis↓	[16]
		apoE$^{-/-}$, rIL-2	AD	– Atherosclerosis↑	[15]
		apoE$^{-/-}$, anti-mIL-2	AD	– Atherosclerosis↓	[15]
IL-4	IL-4r	IL-4$^{-/-}$, ldlr$^{-/-}$	AD	– Atherosclerosis↓	[22]
				– NS	[25]
		IL-4$^{-/-}$, induction	AD	– Atherosclerosis↓	[23]
		IL-4$^{-/-}$	AD	– NS	[23]
		IL-4T$^{-/-}$	AD	– NS	[26]
		IL-4$^{-/-}$, apoE$^{-/-}$	CC	– Atherosclerosis↓	[24]
			AD/CC	– NS	[25]
		IL-4$^{-/-}$, apoE$^{-/-}$, induction	CC	– NS	[25]
		WT, IL-4 treatment	AD	– Atherosclerosis↓	[27]
		apoE$^{-/-}$, rIL-4	AD/CC	– NS	[25]
IL-5	IL-5r	IL-5$^{-/-}$, ldlr$^{-/-}$	AD	– Atherosclerosis↑	[30]

(continued)

Table 1
(continued)

Cytokine	Receptor	Models	Diet	Outcome	Reference
IL-6	IL-6r (gp130)	IL-6$^{-/-}$	AD	– Atherosclerosis↑	[37]
		IL-6$^{-/-}$, apoE+/–	AD	– Atherosclerosis↑	[38]
		IL-6$^{-/-}$, apoE+/–, induction	AD/CC	– Atherosclerosis↑	[38]
		IL-6$^{-/-}$, ldlr$^{-/-}$	AD/CC	– NS	[192]
		IL-6$^{-/-}$, apoE$^{-/-}$	CC	– Atherosclerosis↑	[39, 40]
			CC(16w)	– NS	[40]
		IL-6+/–, apoE$^{-/-}$	CC(16w)	– NS	[40]
		apoE$^{-/-}$, IL-6 lentivirus, induction	AD	– Size NS, plaque destabilization↑	[193]
		apoE$^{-/-}$, rIL-6	CC	– Atherosclerosis↓	[41]
		apoE$^{-/-}$, rIL-6	AD/CC	– Atherosclerosis↑	[35]
		WT, rIL-6	AD	– Atherosclerosis↑	[35]
		ldlr$^{-/-}$, sgp130Fc	AD	– Atherosclerosis↓	[194]
		Hepatocyte-specific gp130$^{fl/fl}$, apoE$^{-/-}$	AD	– Atherosclerosis↓	[36]
IL-10	IL-10r	IL-10$^{-/-}$	AD	– Atherosclerosis↑	[45, 46]
		IL-10$^{-/-}$, ldlr$^{-/-}$	AD	– Atherosclerosis↑	[43]
		IL-10$^{-/-}$, apoE$^{-/-}$	CC	– Atherosclerosis↑	[44]
		apoE$^{-/-}$, mIL-10lv	AD	– Atherosclerosis↓	[47]
		mIL-10Tg	AD	– Atherosclerosis↓	[45]
		IL-10Tg, ldlr$^{-/-}$	AD	– Atherosclerosis↓	[48]
		AAV2-hIL-10, ldlr$^{-/-}$	AD	– Atherosclerosis↓	[49]
		AAV5-mIL-10, apoE$^{-/-}$	AD	– Atherosclerosis↓	[50]
		mIL-10-HVJ, apoE$^{-/-}$	AD	– Atherosclerosis↓	[51]
		AAV8-hIL-10, ldlr$^{-/-}$	AD	– Atherosclerosis↓	[52]
IL-12	IL-12r (β1/β2)	IL-12$^{-/-}$, apoE$^{-/-}$	CC	– Atherosclerosis↓	[24]
		apoE$^{-/-}$, rIL-12	CC	– Atherosclerosis↑	[58]
		ldlr$^{-/-}$, IL-12 vaccine (PADRE), induction	AD	– Atherosclerosis↓	[53]
IL-13	IL-13r	ldlr$^{-/-}$, preexistent lesions, IL-13 treatment	AD	– Size NS, stable phenotype	[59]
		IL-13$^{-/-}$, ldlr$^{-/-}$	AD	– Atherosclerosis↑	[59]
IL-17 (A-F)	IL-17r (A-E)	IL-17a$^{-/-}$	AD	– Atherosclerosis↓	[71]
		IL-17a$^{-/-}$, ldlr$^{-/-}$	AD	– NS	[68, 72]
		IL-17a$^{-/-}$, ldlr$^{-/-}$, nephrectomy	AD	– Atherosclerosis↓	[68]
		IL-17a$^{-/-}$, apoE$^{-/-}$	AD	– Atherosclerosis↓	[69, 70]
				– Atherosclerosis↑	[67]
				– NS	[73]
			Paigen	– NS	[69]
			CC	– NS	[69, 70]
		IL-17a$^{-/-}$, apoE$^{-/-}$, induction	AD	– NS	[73]
		IL-17a$^{-/-}$, apoE$^{-/-}$, induction, anti-IL-17f	AD	– NS	[73]

(continued)

Table 1
(continued)

Cytokine	Receptor	Models	Diet	Outcome	Reference
		IL-17a$^{-/-}$, induction	AD	– Atherosclerosis↓	[71]
		apoE$^{-/-}$, anti-IL-17a ab, induction	AD	– Atherosclerosis↓	[74]
		apoE$^{-/-}$, anti-IL-17a ab	AD	– Atherosclerosis↓	[74]
			CC	– Atherosclerosis↓	[72, 75]
				– NS	[72]
		ldlr$^{-/-}$, anti-IL-17a ab	AD	– NS	[78]
		ldlr$^{-/-}$, T-cell SOCS3 del, anti-IL-17a ab	AD	– Atherosclerosis↑	[78]
		apoE$^{-/-}$, Ad-IL-17RA:Fc	AD	– Atherosclerosis↓	[76]
		ldlr$^{-/-}$, rIL-17a	AD	– Atherosclerosis↓	[78]
		apoE$^{-/-}$, rIL-17a	AD	– Atherosclerosis↑	[74]
		apoE$^{-/-}$, rIL-17a, (IL-17a$^{-/-}$)	AD	– Atherosclerosis↓	[67]
		IL-17r$^{-/-}$, ldlr$^{-/-}$	AD	– Atherosclerosis↓	[77]
		IL-17ra$^{-/-}$, apoE$^{-/-}$	AD	– Atherosclerosis↓	[70]
			CC	– NS	[70]
IL-18	IL-18r	IL-18$^{-/-}$, apoE$^{-/-}$	CC	– Atherosclerosis↓	[81]
			AD	– Atherosclerosis↑	[195]
		apoE$^{-/-}$, rIL-18	CC	– Atherosclerosis↑	[82]
		apoE$^{-/-}$, pcDNA3-mIL18BP	CC	– Atherosclerosis↓	[196]
		SCID/apoE$^{-/-}$, rIL-18	CC	– Atherosclerosis↑	[80]
		SHL, pCAGGS-IL-18	AD	– Atherosclerosis↑	[79]
			CC	– NS	[79]
TNF	TNFr, (p55/p75)	TNF$^{-/-}$	AD	– Atherosclerosis↓	[89]
				– NS	[96]
		tmTNF	AD	– NS	[89]
		TNF$^{-/-}$, apoE$^{-/-}$	AD/CC	– Atherosclerosis↓	[90–93, 95]
			CC	– NS	[90]
		tmTNF-KI, apoE$^{-/-}$	AD	– Atherosclerosis↓	[90]
			CC	– NS	[90]
		TNF$^{-/-}$, apoE*3-leiden	AD	– Advanced plaque↓, size NS	[94]
		apoE$^{-/-}$, TNFbp	AD	– NS	[191]
		p55$^{-/-}$	AD	– Atherosclerosis↑	[96, 97]
		p75$^{-/-}$	AD	– NS	[96]
		p55$^{-/-}$, ldlr$^{-/-}$	AD	– Atherosclerosis↓	[98, 99]
		p55$^{-/-}$ carotid graft, apoE$^{-/-}$	CC	– Atherosclerosis↓	[100]
		p55$^{-/-}$, apoE$^{-/-}$	CC	– NS	[101]
		p55$^{-/-}$, c. pneumonia	AD	– No effect c.pneumonia	[197]
		apoE$^{-/-}$, chimeric murine sTNF-RI/Fc	CC	– Atherosclerosis↓	[91]

(continued)

Table 1
(continued)

Cytokine	Receptor	Models	Diet	Outcome	Reference
IFNγ	IFNGR	IFNγ$^{-/-}$, ldlr$^{-/-}$	AD	– Atherosclerosis↓	[105]
		IFNγ$^{-/-}$, apoE$^{-/-}$	AD/CC	– Atherosclerosis↓ (male, female ns)	[106]
		apoE$^{-/-}$, sIFNγr plasmid	AD	– Atherosclerosis↓	[107, 109]
		IFNγ$^{-/-}$, apoE$^{-/-}$, angII induction	CC	– Atherosclerosis↓	[108]
		IFNγr$^{-/-}$, apoE$^{-/-}$	AD	– Atherosclerosis↓	[110]
		apoE$^{-/-}$, rIFNγ	CC	– Atherosclerosis↑	[198]
IFNβ	IFNAR	ldlr$^{-/-}$, rIFNβ	AD	– Atherosclerosis↑	[111]
		apoE$^{-/-}$, IFNβ treatment	CC	– NS	[113]
		apoE$^{-/-}$, rIFNβ, collar	AD	– Atherosclerosis↑	[111]
			CC	– NS	[113]
		apoE$^{-/-}$, IFNβ, angII (+/− collar)	CC	– Atherosclerosis↓	[113]
		ldlr$^{-/-}$, IFNAR1$^{-/-}$ myeloid BMT	AD	– Atherosclerosis↓	[111]
		IFNAR$^{-/-}$, apoE$^{-/-}$	AD	– Atherosclerosis↓	[199]
TGFβ (1-3)	TGFβR (1-3)	AdrTGFβ	CC	– Neointima↑	[122]
		AAV/TGFβ$_1^{ACT}$, ldlr$^{-/-}$	AD	– Atherosclerosis↓	[123]
		apoE$^{-/-}$,TGFβ$_1$ overexpr (heart/macrophages)	AD	– Atherosclerosis↓	[124, 125]
		apoE$^{-/-}$, B6-TgAlb/TGFβ	CC	– Atherosclerosis↑	[126]
		apoE$^{-/-}$, anti-hTGFβ$_{1,2,3}$	CC	– Atherosclerosis↑	[116]
		ldlr$^{-/-}$, anti-TGFβ, induction	AD	– Atherosclerosis↓	[118]
		ldlr$^{-/-}$, anti-TGFβ	AD	– NS	[118]
		TGFβRII:Fc, apoE$^{-/-}$	CC	– Atherosclerosis↑	[117]
		TGFβRII neg. T-cells (CD4dnTGFβRII), apoE$^{-/-}$	CC	– Atherosclerosis↑	[119]
		TGFβRII neg. T-cells (CD2-dnTGFβRII), ldlr$^{-/-}$	AD	– Atherosclerosis↓	[120]
		CD11c-dnTGFβRII, apoE$^{-/-}$	CC	– Atherosclerosis↑	[121]
		CD4Cre^{+} Smad7$^{fl/fl}$, ldlr$^{-/-}$	AD	– Atherosclerosis↑	[200]
IL-27	IL-27r (IL-27ra + gp130)	IL-27$^{-/-}$(Ebi3), ldlr$^{-/-}$	AD	– Atherosclerosis↑	[201]
		IL-27ra$^{-/-}$, ldlr$^{-/-}$	AD	– Atherosclerosis↑	[201, 202]
		ldlr$^{-/-}$, rIL-27 (IL-27$^{-/-}$)	AD	– Atherosclerosis↓	[201]
IL-19	IL-20r1/2	ldlr$^{-/-}$ or apoE$^{-/-}$, rIL-19	AD	– Atherosclerosis↓	[203]
IL-33	IL-33r	apoE$^{-/-}$, rIL-33	AD	– Atherosclerosis↓	[86]
		apoE$^{-/-}$, sST2	AD	– Atherosclerosis↑	[86]

AD = atherogenic diet; CC = control chow; NS = non-significant effect on plaque area; induction = induction of atherosclerosis (non-diet)

marrow-derived macrophages from mice deficient in IL-1β also produce lower amounts of IL-1α, even after addition of recombinant IL-1β, suggesting that the effects seen in IL-1β-deficient mice are IL-1α-dependent [5].

The IL-1-receptor antagonist (IL-1Ra), that inhibits the effects exerted by IL-1α and IL-1β, has been extensively studied as well. Not only have murine studies conclusively shown an atheroprotective role for IL-1Ra, but also a recombinant protein of IL-1Ra, Anakinra, has been used successfully to treat rheumatoid arthritis. Recently it has been shown that the cardiovascular system in rheumatoid arthritis patients also benefits from Anakinra treatment, with a reduction in oxidative stress, endothelin and IL-6 production and improved left ventricular function [8, 9]. Currently, a clinical trial is underway investigating the effects of Anakinra treatment in patients with non-ST elevated acute coronary syndrome [10].

In innate immune cells, the NLRP3 inflammasome plays a key role in the maturation of IL-1β and IL-18 by caspase-1-dependent cleavage of their pro-forms [11, 12]. Cholesterol crystals present in atherosclerotic lesions can induce inflammation via these NLRP3 inflammasomes and thus provide an early proinflammatory factor [11]. Indeed, disabling the NLRP3 inflammasome in ldlr−/− mice markedly reduced atherosclerotic lesions size and IL-18 production thus further establishing an important role for inflammasome-associated cytokine production in atherosclerosis via interleukin 1 family members [11].

Conclusively, cytokines of the interleukin 1 family have been found to play a vital role in the initiation and propagation of atherosclerosis and could potentially provide targets for future treatment.

2.2 Interleukin 2

Interleukin 2 is required for the growth, proliferation, and differentiation of (thymic) T-cells to effector cells, and for the maturation of regulatory T-cells [13]. In humans, serum IL-2 levels correlate with carotid intima-media thickness, and thus with atherosclerosis [14]. ApoE−/− mice treated with IL-2 were found to have an increased plaque burden while mice treated with anti-IL-2 antibody featured smaller lesions [15]. Furthermore, a reduction in atherosclerosis was observed in an apoE−/− mouse model treated with an IL-2/anti-IL-2 mAb complex that was able to expand the pool of Tregs [16]. Tregs express CD25, the receptor for IL-2. When mice were treated with an anti-IL-2r (CD25) antibody, Treg development was hampered and atherosclerosis increased [17–19]. Although further research with selective targeting of IL-2 or CD25 is necessary to evaluate the net effect of IL-2 in atherosclerosis, it is clear that IL-2 plays a role in T-cell-mediated inflammation through both T helper cells and Tregs.

2.3 Interleukin 4

Interleukin 4 is secreted by T helper 2 (Th2) cells and induces T- and B-cell proliferation as well as a shift towards alternatively activated M2 macrophages, which are believed to play a protective role in atherosclerosis [20, 21]. In vascular disease, IL-4 plays an ambivalent role. Since the Th2 response is considered antiatherogenic, IL-4 was long believed to have anti-inflammatory properties. However, experimental studies have revealed a more complex role for IL-4 in the pathogenesis of atherosclerosis. IL-4 increases VCAM-1 expression in endothelial cells and increases endothelial cell turnover [20]. Furthermore, IL-4 induces the synthesis of MCP-1 and IL-6 [20], and is able to induce endothelial damage via the generation of reactive oxygen species (ROS) [20]. Accordingly, experimental atherosclerosis studies have unveiled an atherogenic role for IL-4 [22–24]. However, others have found no effects in models with genetic defects of IL-4 [25, 26], or found that IL-4 treatment induced a Th2 response and indeed decreased atherosclerosis [27]. Therefore, the role of IL-4 in atherosclerosis still remains to be fully elucidated.

2.4 Interleukin 5

Interleukin 5 is secreted by Th2 cells as well as mast cells [28]. B-cells express IL-5 receptor and IL-5 plays a role in B-cell proliferation and differentiation, immunoglobulin class switching and the production and secretion of IgM and IgA [28]. Furthermore, IL-5 induces the generation of eosinophils and drives allergic reactions [28]. In humans, a single nucleotide polymorphism (SNP) for IL-5 has been associated with cardiovascular disease [29]. In experimental studies, ldlr−/− mice receiving IL-5−/− bone marrow had increased amounts of atherosclerosis [30]. Additionally, IL-5 was found to be responsible for the generation of atheroprotective T15/EO6 antibodies by B-cells. Indeed, IL-5-knockout mice featured lower plasma levels of T15/EO6 antibodies and significantly larger lesions [30].

2.5 Interleukin 6

IL-6 and its receptor, gp130, exhibit both pro- and anti-inflammatory functions. IL-6 is secreted by a plethora of cells, including T-cells, monocytes and macrophages, but also endothelial cells, B-cells, adipocytes, fibroblasts, smooth muscle cells (SMCs) and hepatocytes [31, 32]. Once upregulated via NF-κB following trauma, infections or other sources of stress, IL-6 exerts its effects on a large variety of cell types. IL-6 signaling induces cell migration and proliferation, matrix metalloproteinase (MMP) production, B-cell differentiation and reduces Treg formation [31, 33, 34]. In atherosclerosis, IL-6 is produced both locally in atherosclerotic lesions as well as systemically. It can aggravate atherosclerosis through endothelial dysfunction, the recruitment as well as activation of inflammatory cells and the migration and proliferation of SMCs [31]. IL-6 can also exert effects on the receptors responsible

for the uptake of LDL, the scavenger receptors SR-A and CD36 [31]. Interestingly, while these findings point towards a clear pro-inflammatory role of IL-6 in atherosclerosis, animal experiments indicate a more complex system. Studies have shown that knocking out IL-6 signaling in hepatocytes decreases atherosclerosis and that treating mice with recombinant IL-6 increases atherosclerosis [35, 36]. However, other studies showed contradictory results. For example, multiple studies found that knocking out IL-6 increases lesion size [37–40] or that recombinant IL-6 reduces lesion size [41]. These conflicting results could point towards a dual role of IL-6 in atherosclerosis although most studies indicate a predominantly antiatherogenic role for IL-6. Regardless, systemic inhibition of IL-6 seems an unlikely therapeutic method to limit atherosclerosis development, and further investigation into downstream signaling and potential site-specific effects is necessary to fully elucidate the role of IL-6 in atherosclerosis.

2.6 Interleukin 10

IL-10 is one of the most intensively studied cytokines in atherosclerosis. IL-10 is able to inhibit the presentation of antigens, block the secretion of cytokines and the expression of costimulatory molecules as well as MHC-II. It is also able to modify chemokine secretion and chemokine receptor expression [42]. IL-10 is produced by macrophages, but also by Tregs. Both knockout and overexpression strategies have revealed a protective role for IL-10 in atherosclerosis [43–52]. This makes modulation of IL-10, or its downstream modulators, a highly interesting target for future treatments.

2.7 Interleukin 12

IL-12, a cytokine consisting out of a 35-kDa light chain and a 40-kDa heavy chain, forms a bridge between the innate and adaptive immune response and promotes a Th1 based proatherogenic phenotype [53–55]. It is secreted by activated monocytes, macrophages, neutrophils and dendritic cells [56]. Furthermore, in combination with IL-18, it drives the production of IFNγ by T-cells [53, 57]. In concert with its proposed polarization towards a Th1-based response, animal studies have universally shown a pro-inflammatory and pro-atherogenic role for IL-12, as revealed in studies with IL-12 knockout mice, IL-12-treated mice and mice vaccinated against the IL-12 p40 subunit [24, 53, 58].

2.8 Interleukin 13

Similar to IL-4, IL-13 is predominantly produced by Th2 T-cells [59, 60]. Although intracellular signaling occurs via similar pathways as IL-4, IL-13 is believed to possess not just overlapping but also unique effects, including the production of TGF-β by macrophages [59, 61–63]. A recent study using ldlr$^{-/-}$ mice with preexisting lesions showed that treatment with IL-13 decreased plaque macrophages and adhesion molecule expression, and produced a shift from atherogenic M1 macrophages towards M2 macrophages

[59]. Furthermore, IL-13−/− ldlr−/− mice fed an atherogenic diet showed significantly larger atherosclerotic lesions, indicating a protective role for IL-13 in atherosclerosis [59].

2.9 Interleukin 17

IL-17 is predominantly produced by Th17 cells, which also produce IL-21 and IL-22 [64, 65]. Th17 cells develop upon stimulation of naïve T-cells with TGFβ, IL-6, and IL-23 [66]. In recent years, it has become clear that IL-17 has an important role in atherosclerosis, although its exact effects remain elusive since several studies have reported both atherogenic and atheroprotective actions. These effects are mediated by the effects IL-17 has on both pro- and anti-inflammatory cytokines and chemokines as well as MMPs and adhesion molecules [66]. In accordance with this, studies investigating atherosclerosis in IL-17 deficient mice have yielded conflicting results regarding lesion size, including increase [67], reduction [68–71], or no effect at all [72, 73]. The use of antibodies has yielded more consistent results, with blocking antibodies reducing lesion size [72, 74–76]. Similarly, knocking out the IL-17 receptor appears to decrease lesion size [70, 77]. However, other studies using IL-17 antibodies or recombinant IL-17 also point towards a more complex, regulatory role reflecting the diverse effects IL-17 has on inflammation [67, 74, 78]. It is currently believed that the specific effects IL-17 has on atherosclerosis are dependent on the region in which IL-17 is released. IL-17 appears to have clear proatherogenic effects inside of the microenvironment of an inflammatory atherosclerotic plaque [66]. However, Th17 cells differentiating in the presence of TGF-β and IL-6 are found to produce IL-17 and IL-10, which might suppress Th1 cell differentiation [64, 66]. Conclusively, although most studies appear to point towards a proatherogenic role of IL-17, results of animal studies are inconclusive and indicate a complex, site-specific role of IL-17 and its receptors in atherosclerosis.

2.10 Interleukin 18

As discussed above, IL-18 is a member of the IL-1 family and is closely related to IL-1β, both in terms of release patterns as well as its receptors. Similar to IL-12, IL-18 has been found to be a potent inducer of the Th1 response as well as IFNγ [79–81]. The majority of animal studies point towards a proatherogenic role for IL-18. This has been validated through multiple modalities including IL-18−/− apoE−/− mice, apoE−/− mice treated with recombinant IL-18, recombinant IL-18 treatment of apoE−/− mice with severe combined immunodeficiency (SCID) and spontaneously hyperlipidemic (SHL) mice supplied with IL-18 via in vivo gene transfer, although in the latter, only mice on a high-fat diet showed a significant phenotype [79–82]. In addition to the described effects on atherosclerosis, multiple of these studies have also confirmed the importance of IFNγ in IL-18-mediated atherosclerosis. For example, the increase in atherosclerosis linked to IL-18

treatment in an apoE−/− background was nullified in mice lacking IFNγ [82]. Similarly, IL-18 knockout mice featured lower amounts of both IFNγ and Th1 cells but high Th2 counts [81]. Finally, recombinant IL-18 was found to induce IFNγ production by macrophages, NKT-cells as well as vascular cells [80]. This suggests a prominent role of IL-18 in atherosclerosis, mediated via the production of IFNγ.

2.11 Interleukin 33

IL-33 is a relatively recently discovered cytokine of the IL-1 family which is expressed in multiple cell types including endothelial cells, fibroblasts, macrophages and DCs [83]. It is believed to play a role in many auto-immune diseases and produces a Th2-based response by stimulating the production of cytokines including IL-5 and IL-13 [83–85]. Treatment of apoE−/− mice with IL-33 decreases atherosclerotic lesion size [86]. Furthermore, IL-33 increases the levels of Th2 related cytokines such as IL-4, 5, 6 and 13, as well as decreases levels of IFNγ. When IL-33 was combined with a neutralizing IL-5 antibody, which induces anti-oxLDL antibodies, the protective effect of IL-33 was nullified, indicating that IL-33 exerts its atheroprotective effects via IL-5-induced anti-oxLDL antibodies [86, 87].

3 Tumor Necrosis Factor

TNF, formerly known as TNFα, plays a role in many inflammatory diseases. Monocytes and macrophages are the main source of TNF. TNF binds two receptors, p55 and p75, of which p55 (TNFRSF1A) controls the major functions of TNF [88]. Multiple studies have shown that TNF deficiency decreases atherosclerosis in mice [89–95]. However, the role of p55 in atherosclerosis is less well established, with studies reporting both atherogenic as well as antiatherogenic effects. For example, mice only deficient in p55 were found to have increased lesion size in two studies [96, 97]. Other studies investigating mice deficient in both p55 and LDLr or apoE, however, found a decrease in lesion size [98–100], while another study found no effect [101]. The discrepancy in findings between p55 and TNF-deficient mice might be explained by p55 binding a variety of other ligands aside from TNF. The differences between various studies examining p55 are less easily explained but might be ascribed to variation in animal models. Interestingly, as observed above, mouse models featuring a deficiency in either LDLr or apoE next to p55 appeared to show different results. Perhaps the difference in homeostasis compared to mice only deficient in p55 could explain the different effects of p55 found in these studies.

4 Interferons

IFNγ plays a crucial role in immune responses and is secreted by many cells in the atherosclerotic plaque including Th1 cells, monocytes, macrophages, and NKT-cells [88, 102]. Despite its strong pro-inflammatory effects, IFNγ also exhibits anti-inflammatory characteristics and, accordingly, is able to manipulate the secretion of both pro- as well as anti-inflammatory signaling molecules [103]. In atherosclerosis, IFNγ promotes monocyte infiltration and differentiation into macrophages, foam cell formation and induces a Th1-driven response by the adaptive immune system [104]. Animal studies have confirmed this pro-inflammatory model for IFNγ in atherosclerosis. Without exception, all animal studies, using a variety of models including mice deficient in IFNγ or in IFNγ receptor as well as LDLr or apoE, show that suppressing IFNγ signaling reduces lesion size [105–110]. However, its therapeutic potential is limited due to the potential anti-inflammatory effects IFNγ has on other tissues as well as the importance of IFNγ in the immune response.

IFNβ, a member of the type I interferon family, is produced by immune cells following pathogenic challenging and plays an important role in inflammation [111, 112]. IFNβ induces chemotactic signals from macrophages and adhesion of leukocytes [111]. In experimental animal studies of atherosclerosis, the role of IFNβ remains unclear. Thus, IFNβ treatment reduced plaque development in apoE−/− mice in which atherosclerosis was accelerated by angiotensin II [113], but increased atherosclerosis in ldlr-/- and apoE−/− mice with implanted constrictive cuffs [111]. Furthermore, deletion of the receptor for IFNβ, IFNAR1, in myeloid cells using bone marrow transplant, was found to reduce the development of atherosclerosis [111]. In conclusion, IFNγ has been clearly found to induce atherosclerosis, but further studies are required to underscore the exact role of IFNβ.

5 TGFβ

TGFβ is produced by a multitude of cells including macrophages and Tregs. It plays an important role in many physiological processes, e.g., embryonic development and proliferation, differentiation, migration, adhesion, and apoptosis of cells [114]. TGFβ has also been implicated in many diseases including autoimmune diseases, cancer and cardiovascular disease [114]. Furthermore, TGFβ has an important function in angiogenesis with genetic defects in TGFβ causing vascular abnormalities [114]. In atherosclerosis, TGFβ was originally believed to exert an anti-inflammatory role [114, 115]. However, animal studies have shown inconsistent

results. Mouse models examining TGFβ or TGFβ receptor (TGFβR) inhibition have yielded both higher [116, 117] as well as lower [118] amounts of atherosclerosis. Similar conflicting results have been found with mice lacking TGFβR in T-cells featuring increased or decreased atherosclerosis while mice lacking TGFβR in CD11c+ cells were found to have increased atherosclerosis [119–121]. Finally, studies investigating TGFβ overexpression have also found varying results [122–126]. Thus, although an antiatherogenic function was initially attributed to TGFβ, animal studies have been inconclusive. This could in part be explained by the plethora of functions TGFβ has in both murine and human physiology.

6 Chemokines

Chemokines are members of the cytokine-family that are specialized in the chemotaxis of immune cells. Many chemokines and combinations of chemokines with their respective receptors are able to form specific patterns of cell attraction. The most thoroughly examined chemokine couple in atherosclerosis is CCL2/CCR2. CCL2, also known as macrophage chemotactic protein-1 (MCP-1), is produced primarily by monocytes, macrophages, endothelial cells, and SMCs. The expression of CCL2 and CCR2 is upregulated in hyperlipidemic conditions and CCL2 is present in murine and human atherosclerotic lesions [127–132]. A clear proatherogenic role for CCL2 was established many years ago. Since then, many studies have consistently shown that inhibiting either CCL2 or CCR2 is protective against atherosclerosis [133–154]. Similarly CCL5, also known as RANTES, is widely expressed in the atherosclerotic plaque [127, 155, 156]. Inhibition of the CCL5-CCR5 interaction has clearly been found to decrease atherosclerosis in mice [157–164]. Other examples of chemokines shown to induce atherosclerosis in mice studies include macrophage migration inhibitory factor (MIF), CX3CL1, CXCR3, and CXCL4 [133, 149, 165–181].

7 Conclusion

As highlighted in this chapter, a significant amount of research has been done on the role of cytokines in atherosclerosis. Several cytokines have been identified as being clearly atherogenic, such as IL-1α, IL-12, TNF, IFNγ, and IL-18, or atheroprotective, such as IL-10 and IL-1Ra. However, aside from a large consensus on the effects of different cytokines, the functions of others are still ambivalent (Fig. 1).

Cells of the immune system communicate with one another using cytokines and induce the immune reactions leading to atherosclerosis (Fig. 2). Individual cytokines can enact multiple effects in these signaling pathways as well as have site- or disease stage-specific effects. In addition to current data, future research should be aimed at further evaluating downstream signaling cascades and at attempting to discover potential targets which can be manipulated for therapeutic purposes with minimal systemic effects.

References

1. Legein B, Temmerman L, Biessen EA et al (2013) Inflammation and immune system interactions in atherosclerosis. Cell Mol Life Sci70(20):3847–3869. doi:10.1007/s00018-013-1289-1
2. Kamari Y, Werman-Venkert R, Shaish A et al (2007) Differential role and tissue specificity of interleukin-1alpha gene expression in atherogenesis and lipid metabolism. Atherosclerosis 195(1):31–38. doi:10.1016/j.atherosclerosis.2006.11.026
3. Kamari Y, Shaish A, Shemesh S et al (2011) Reduced atherosclerosis and inflammatory cytokines in apolipoprotein-E-deficient mice lacking bone marrow-derived interleukin-1alpha. Biochem Biophys Res Commun 405(2):197–203. doi:10.1016/j.bbrc.2011.01.008
4. Tissot AC, Spohn G, Jennings GT et al (2013) A VLP-based vaccine against interleukin-1alpha protects mice from atherosclerosis. Eur J Immunol 43(3):716–722. doi:10.1002/eji.201242687
5. Freigang S, Ampenberger F, Weiss A et al (2013) Fatty acid-induced mitochondrial uncoupling elicits inflammasome-independent IL-1alpha and sterile vascular inflammation in atherosclerosis. Nat Immunol 14(10):1045–1053. doi:10.1038/ni.2704
6. Kirii H, Niwa T, Yamada Y et al (2003) Lack of interleukin-1beta decreases the severity of atherosclerosis in ApoE-deficient mice. Arterioscler Thromb Vasc Biol 23(4):656–660. doi:10.1161/01.ATV.0000064374.15232.C3
7. Bhaskar V, Yin J, Mirza AM et al (2011) Monoclonal antibodies targeting IL-1 beta reduce biomarkers of atherosclerosis in vitro and inhibit atherosclerotic plaque formation in Apolipoprotein E-deficient mice. Atherosclerosis 216(2):313–320. doi:10.1016/j.atherosclerosis.2011.02.026
8. Ikonomidis I, Lekakis JP, Nikolaou M et al (2008) Inhibition of interleukin-1 by anakinra improves vascular and left ventricular function in patients with rheumatoid arthritis. Circulation 117(20):2662–2669. doi:10.1161/CIRCULATIONAHA.107.731877
9. Mertens M, Singh JA (2009) Anakinra for rheumatoid arthritis: a systematic review. J Rheumatol 36(6):1118–1125. doi:10.3899/jrheum.090074
10. Crossman DC, Morton AC, Gunn JP et al (2008) Investigation of the effect of Interleukin-1 receptor antagonist (IL-1ra) on markers of inflammation in non-ST elevation acute coronary syndromes (The MRC-ILA-HEART Study). Trials 9:8. doi:10.1186/1745-6215-9-8
11. Duewell P, Kono H, Rayner KJ et al (2010) NLRP3 inflammasomes are required for atherogenesis and activated by cholesterol crystals. Nature 464(7293):1357–1361. doi:10.1038/nature08938
12. Xie Q, Shen WW, Zhong J et al (2014) Lipopolysaccharide/adenosine triphosphate induces IL1beta and IL-18 secretion through the NLRP3 inflammasome in RAW264.7 murine macrophage cells. Int J Mol Med 34(1):341–349. doi:10.3892/ijmm.2014.1755
13. Gaffen SL, Liu KD (2004) Overview of interleukin-2 function, production and clinical applications. Cytokine 28(3):109–123. doi:10.1016/j.cyto.2004.06.010
14. Elkind MS, Rundek T, Sciacca RR et al (2005) Interleukin-2 levels are associated with carotid artery intima-media thickness. Atherosclerosis 180(1):181–187. doi:10.1016/j.atherosclerosis.2004.11.015
15. Upadhya S, Mooteri S, Peckham N et al (2004) Atherogenic effect of interleukin-2 and antiatherogenic effect of interleukin-2 antibody in apo-E-deficient mice. Angiology 55(3):289–294
16. Dinh TN, Kyaw TS, Kanellakis P et al (2012) Cytokine therapy with interleukin-2/anti-interleukin-2 monoclonal antibody complexes

expands CD4+CD25+Foxp3+ regulatory T cells and attenuates development and progression of atherosclerosis. Circulation 126(10):1256–1266. doi:10.1161/CIRCULATIONAHA.112.099044

17. Ait-Oufella H, Salomon BL, Potteaux S et al (2006) Natural regulatory T cells control the development of atherosclerosis in mice. Nat Med 12(2):178–180. doi:10.1038/nm1343
18. Kita T, Yamashita T, Sasaki N et al (2014) Regression of atherosclerosis with anti-CD3 antibody via augmenting a regulatory T-cell response in mice. Cardiovasc Res 102(1):107–117. doi:10.1093/cvr/cvu002
19. Takeda M, Yamashita T, Sasaki N et al (2010) Oral administration of an active form of vitamin D3 (calcitriol) decreases atherosclerosis in mice by inducing regulatory T cells and immature dendritic cells with tolerogenic functions. Arterioscler Thromb Vasc Biol 30(12):2495–2503. doi:10.1161/ATVBAHA.110.215459
20. Lee YW, Kim PH, Lee WH et al (2010) Interleukin-4, oxidative stress, vascular inflammation and atherosclerosis. Biomol Ther (Seoul) 18(2):135–144. doi:10.4062/biomolther.2010.18.2.135
21. Van Dyken SJ, Locksley RM (2013) Interleukin-4- and interleukin-13-mediated alternatively activated macrophages: roles in homeostasis and disease. Annu Rev Immunol 31:317–343.doi:10.1146/annurev-immunol-032712-095906
22. King VL, Szilvassy SJ, Daugherty A (2002) Interleukin-4 deficiency decreases atherosclerotic lesion formation in a site-specific manner in female LDL receptor–/– mice. Arterioscler Thromb Vasc Biol 22(3):456–461
23. George J, Shoenfeld Y, Gilburd B et al (2000) Requisite role for interleukin-4 in the acceleration of fatty streaks induced by heat shock protein 65 or Mycobacterium tuberculosis. Circ Res 86(12):1203–1210
24. Davenport P, Tipping PG (2003) The role of interleukin-4 and interleukin-12 in the progression of atherosclerosis in apolipoprotein E-deficient mice. Am J Pathol 163(3):1117–1125. doi:10.1016/S0002-9440(10)63471-2
25. King VL, Cassis LA, Daugherty A (2007) Interleukin-4 does not influence development of hypercholesterolemia or angiotensin II-induced atherosclerotic lesions in mice. Am J Pathol 171(6):2040–2047. doi:10.2353/ajpath.2007.060857
26. George J, Mulkins M, Shaish A et al (2000) Interleukin (IL)-4 deficiency does not influence fatty streak formation in C57BL/6 mice. Atherosclerosis 153(2):403–411
27. Huber SA, Sakkinen P, David C et al (2001) T helper-cell phenotype regulates atherosclerosis in mice under conditions of mild hypercholesterolemia. Circulation 103(21):2610–2616
28. Takatsu K (2011) Interleukin-5 and IL-5 receptor in health and diseases. Proc Jpn Acad Ser B Phys Biol Sci 87(8):463–485
29. Miller VM, Petterson TM, Jeavons EN et al (2013) Genetic polymorphisms associated with carotid artery intima-media thickness and coronary artery calcification in women of the Kronos Early Estrogen Prevention Study. Physiol Genomics 45(2):79–88. doi:10.1152/physiolgenomics.00114.2012
30. Binder CJ, Hartvigsen K, Chang MK et al (2004) IL-5 links adaptive and natural immunity specific for epitopes of oxidized LDL and protects from atherosclerosis. J Clin Invest 114(3):427–437. doi:10.1172/JCI20479
31. Schuett H, Luchtefeld M, Grothusen C et al (2009) How much is too much? Interleukin-6 and its signalling in atherosclerosis. Thromb Haemost 102(2):215–222. doi:10.1160/TH09-05-0297
32. Panesar N, Tolman K, Mazuski JE (1999) Endotoxin stimulates hepatocyte interleukin-6 production. J Surg Res 85(2):251–258. doi:10.1006/jsre.1999.5648
33. Lin G, Wang J, Lao X et al (2012) Interleukin-6 inhibits regulatory T cells and improves the proliferation and cytotoxic activity of cytokine-induced killer cells. J Immunother 35(4):337–343. doi:10.1097/CJI.0b013e318255ada3
34. Bettelli E, Carrier Y, Gao W et al (2006) Reciprocal developmental pathways for the generation of pathogenic effector TH17 and regulatory T cells. Nature 441(7090):235–238. doi:10.1038/nature04753
35. Huber SA, Sakkinen P, Conze D et al (1999) Interleukin-6 exacerbates early atherosclerosis in mice. Arterioscler Thromb Vasc Biol 19(10):2364–2367
36. Luchtefeld M, Schunkert H, Stoll M et al (2007) Signal transducer of inflammation gp130 modulates atherosclerosis in mice and man. J Exp Med 204(8):1935–1944. doi:10.1084/jem.20070120
37. Van Lenten BJ, Wagner AC, Navab M et al (2001) Oxidized phospholipids induce changes in hepatic paraoxonase and ApoJ but not monocyte chemoattractant protein-1 via interleukin-6. J Biol Chem 276(3):1923–1929. doi:10.1074/jbc.M004074200
38. Madan M, Bishayi B, Hoge M et al (2008) Atheroprotective role of interleukin-6 in diet- and/or pathogen-associated atherosclerosis

using an ApoE heterozygote murine model. Atherosclerosis 197(2):504–514. doi:10.1016/j.atherosclerosis.2007.02.023

39. Schieffer B, Selle T, Hilfiker A et al (2004) Impact of interleukin-6 on plaque development and morphology in experimental atherosclerosis. Circulation 110(22):3493–3500. doi:10.1161/01.CIR.0000148135.08582.97
40. Elhage R, Clamens S, Besnard S et al (2001) Involvement of interleukin-6 in atherosclerosis but not in the prevention of fatty streak formation by 17beta-estradiol in apolipoprotein E-deficient mice. Atherosclerosis 156(2):315–320
41. Tous M, Ribas V, Escola-Gil JC et al (2006) Manipulation of inflammation modulates hyperlipidemia in apolipoprotein E-deficient mice: a possible role for interleukin-6. Cytokine 34(3-4):224–232. doi:10.1016/j.cyto.2006.05.007
42. Pestka S, Krause CD, Sarkar D et al (2004) Interleukin-10 and related cytokines and receptors. Annu Rev Immunol 22:929–979. doi:10.1146/annurev.immunol.22.012703.104622
43. Potteaux S, Esposito B, van Oostrom O et al (2004) Leukocyte-derived interleukin 10 is required for protection against atherosclerosis in low-density lipoprotein receptor knockout mice. Arterioscler Thromb Vasc Biol 24(8):1474–1478. doi:10.1161/01.ATV.0000134378.86443.cd
44. Caligiuri G, Rudling M, Ollivier V et al (2003) Interleukin-10 deficiency increases atherosclerosis, thrombosis, and low-density lipoproteins in apolipoprotein E knockout mice. Mol Med 9(1-2):10–17
45. Pinderski Oslund LJ, Hedrick CC, Olvera T et al (1999) Interleukin-10 blocks atherosclerotic events in vitro and in vivo. Arterioscler Thromb Vasc Biol 19(12):2847–2853
46. Mallat Z, Besnard S, Duriez M et al (1999) Protective role of interleukin-10 in atherosclerosis. Circ Res 85(8):e17–e24
47. Sun J, Li X, Feng H et al (2011) Magnetic resonance imaging of bone marrow cell-mediated interleukin-10 gene therapy of atherosclerosis. PLoS One 6(9):e24529. doi:10.1371/journal.pone.0024529
48. Pinderski LJ, Fischbein MP, Subbanagounder G et al (2002) Overexpression of interleukin-10 by activated T lymphocytes inhibits atherosclerosis in LDL receptor-deficient Mice by altering lymphocyte and macrophage phenotypes. Circ Res 90(10):1064–1071
49. Liu Y, Li D, Chen J et al (2006) Inhibition of atherogenesis in LDLR knockout mice by systemic delivery of adeno-associated virus type 2-hIL-10. Atherosclerosis 188(1):19–27. doi:10.1016/j.atherosclerosis.2005.10.029
50. Yoshioka T, Okada T, Maeda Y et al (2004) Adeno-associated virus vector-mediated interleukin-10 gene transfer inhibits atherosclerosis in apolipoprotein E-deficient mice. Gene Ther 11(24):1772–1779. doi:10.1038/sj.gt.3302348
51. Namiki M, Kawashima S, Yamashita T et al (2004) Intramuscular gene transfer of interleukin-10 cDNA reduces atherosclerosis in apolipoprotein E-knockout mice. Atherosclerosis 172(1):21–29
52. Cao M, Khan JA, Kang BY et al (2012) Dual AAV/IL-10 Plus STAT3 Anti-Inflammatory Gene Delivery Lowers Atherosclerosis in LDLR KO Mice, but without Increased Benefit. Int J Vasc Med 2012:524235. doi:10.1155/2012/524235
53. Hauer AD, Uyttenhove C, de Vos P et al (2005) Blockade of interleukin-12 function by protein vaccination attenuates atherosclerosis. Circulation 112(7):1054–1062. doi:10.1161/CIRCULATIONAHA.104.533463
54. Hsieh CS, Macatonia SE, Tripp CS et al (1993) Development of TH1 CD4+ T cells through IL-12 produced by Listeria-induced macrophages. Science 260(5107):547–549
55. Manetti R, Parronchi P, Giudizi MG et al (1993) Natural killer cell stimulatory factor (interleukin 12 [IL-12]) induces T helper type 1 (Th1)-specific immune responses and inhibits the development of IL-4-producing Th cells. J Exp Med 177(4):1199–1204
56. Trinchieri G (2003) Interleukin-12 and the regulation of innate resistance and adaptive immunity. Nat Rev Immunol 3(2):133–146. doi:10.1038/nri1001
57. Munder M, Mallo M, Eichmann K et al (1998) Murine macrophages secrete interferon gamma upon combined stimulation with interleukin (IL)-12 and IL-18: a novel pathway of autocrine macrophage activation. J Exp Med 187(12):2103–2108
58. Lee TS, Yen HC, Pan CC et al (1999) The role of interleukin 12 in the development of atherosclerosis in ApoE-deficient mice. Arterioscler Thromb Vasc Biol 19(3):734–742
59. Cardilo-Reis L, Gruber S, Schreier SM et al (2012) Interleukin-13 protects from atherosclerosis and modulates plaque composition by skewing the macrophage phenotype. EMBO Mol Med 4(10):1072–1086. doi:10.1002/emmm.201201374
60. Oliphant CJ, Barlow JL, McKenzie AN (2011) Insights into the initiation of type 2 immune responses. Immunology 134(4):378–385. doi:10.1111/j.1365-2567.2011.03499.x

61. Kuperman DA, Schleimer RP (2008) Interleukin-4, interleukin-13, signal transducer and activator of transcription factor 6, and allergic asthma. Curr Mol Med 8(5):384–392
62. Chomarat P, Banchereau J (1998) Interleukin-4 and interleukin-13: their similarities and discrepancies. Int Rev Immunol 17(1-4):1–52
63. Fichtner-Feigl S, Strober W, Kawakami K et al (2006) IL-13 signaling through the IL-13alpha2 receptor is involved in induction of TGF-beta1 production and fibrosis. Nat Med 12(1):99–106. doi:10.1038/nm1332
64. Ghoreschi K, Laurence A, Yang XP et al (2011) T helper 17 cell heterogeneity and pathogenicity in autoimmune disease. Trends Immunol 32(9):395–401. doi:10.1016/j.it.2011.06.007
65. Ouyang W, Kolls JK, Zheng Y (2008) The biological functions of T helper 17 cell effector cytokines in inflammation. Immunity 28(4):454–467. doi:10.1016/j.immuni.2008.03.004
66. Liuzzo G, Trotta F, Pedicino D (2013) Interleukin-17 in atherosclerosis and cardiovascular disease: the good, the bad, and the unknown. Eur Heart J 34(8):556–559. doi:10.1093/eurheartj/ehs399
67. Danzaki K, Matsui Y, Ikesue M et al (2012) Interleukin-17A deficiency accelerates unstable atherosclerotic plaque formation in apolipoprotein E-deficient mice. Arterioscler Thromb Vasc Biol 32(2):273–280. doi:10.1161/ATVBAHA.111.229997
68. Ge S, Hertel B, Koltsova EK et al (2013) Increased atherosclerotic lesion formation and vascular leukocyte accumulation in renal impairment are mediated by interleukin-17A. Circ Res 113(8):965–974. doi:10.1161/CIRCRESAHA.113.301934
69. Usui F, Kimura H, Ohshiro T et al (2012) Interleukin-17 deficiency reduced vascular inflammation and development of atherosclerosis in Western diet-induced apoE-deficient mice. Biochem Biophys Res Commun 420(1):72–77. doi:10.1016/j.bbrc.2012.02.117
70. Butcher MJ, Gjurich BN, Phillips T et al (2012) The IL-17A/IL-17RA axis plays a proatherogenic role via the regulation of aortic myeloid cell recruitment. Circ Res 110(5):675–687. doi:10.1161/CIRCRESAHA.111.261784
71. Chen S, Shimada K, Zhang W et al (2010) IL-17A is proatherogenic in high-fat diet-induced and Chlamydia pneumoniae infection-accelerated atherosclerosis in mice. J Immunol 185(9):5619–5627. doi:10.4049/jimmunol.1001879
72. Cheng X, Taleb S, Wang J et al (2011) Inhibition of IL-17A in atherosclerosis. Atherosclerosis 215(2):471–474. doi:10.1016/j.atherosclerosis.2010.12.034
73. Madhur MS, Funt SA, Li L et al (2011) Role of interleukin 17 in inflammation, atherosclerosis, and vascular function in apolipoprotein e-deficient mice. Arterioscler Thromb Vasc Biol 31(7):1565–1572. doi:10.1161/ATVBAHA.111.227629
74. Gao Q, Jiang Y, Ma T et al (2010) A critical function of Th17 proinflammatory cells in the development of atherosclerotic plaque in mice. J Immunol 185(10):5820–5827. doi:10.4049/jimmunol.1000116
75. Erbel C, Chen L, Bea F et al (2009) Inhibition of IL-17A attenuates atherosclerotic lesion development in apoE-deficient mice. J Immunol 183(12):8167–8175. doi:10.4049/jimmunol.0901126
76. Smith E, Prasad KM, Butcher M et al (2010) Blockade of interleukin-17A results in reduced atherosclerosis in apolipoprotein E-deficient mice. Circulation 121(15):1746–1755. doi:10.1161/CIRCULATIONAHA.109.924886
77. van Es T, van Puijvelde GH, Ramos OH et al (2009) Attenuated atherosclerosis upon IL-17R signaling disruption in LDLr deficient mice. Biochem Biophys Res Commun 388(2):261–265. doi:10.1016/j.bbrc.2009.07.152
78. Taleb S, Romain M, Ramkhelawon B et al (2009) Loss of SOCS3 expression in T cells reveals a regulatory role for interleukin-17 in atherosclerosis. J Exp Med 206(10):2067–2077. doi:10.1084/jem.20090545
79. Imai T, Oikawa Y, Shimada A et al (2011) Proatherogenic effect of interleukin-18 is exerted with high-fat diet, but not with normal diet in spontaneously hyperlipidemic mice. J Atheroscler Thromb 18(12):1090–1101
80. Tenger C, Sundborger A, Jawien J et al (2005) IL-18 accelerates atherosclerosis accompanied by elevation of IFN-gamma and CXCL16 expression independently of T cells. Arterioscler Thromb Vasc Biol 25(4):791–796. doi:10.1161/01.ATV.0000153516.02782.65
81. Elhage R, Jawien J, Rudling M et al (2003) Reduced atherosclerosis in interleukin-18 deficient apolipoprotein E-knockout mice. Cardiovasc Res 59(1):234–240
82. Whitman SC, Ravisankar P, Daugherty A (2002) Interleukin-18 enhances atherosclerosis in apolipoprotein E(−/−) mice through release of interferon-gamma. Circ Res 90(2):E34–E38

83. Pei C, Barbour M, Fairlie-Clarke KJ et al (2014) Emerging role of interleukin-33 in autoimmune diseases. Immunology 141(1):9–17. doi:10.1111/imm.12174
84. Kurowska-Stolarska M, Kewin P, Murphy G et al (2008) IL-33 induces antigen-specific IL-5+ T cells and promotes allergic-induced airway inflammation independent of IL-4. J Immunol 181(7):4780–4790
85. Stolarski B, Kurowska-Stolarska M, Kewin P et al (2010) IL-33 exacerbates eosinophil-mediated airway inflammation. J Immunol 185(6):3472–3480. doi:10.4049/jimmunol.1000730
86. Miller AM, Xu D, Asquith DL et al (2008) IL-33 reduces the development of atherosclerosis. J Exp Med 205(2):339–346. doi:10.1084/jem.20071868
87. Hulthe J (2004) Antibodies to oxidized LDL in atherosclerosis development – clinical and animal studies. Clin Chim Acta 348(1-2):1–8. doi:10.1016/j.cccn.2004.05.021
88. Kleemann R, Zadelaar S, Kooistra T (2008) Cytokines and atherosclerosis: a comprehensive review of studies in mice. Cardiovasc Res 79(3):360–376. doi:10.1093/cvr/cvn120
89. Canault M, Peiretti F, Mueller C et al (2004) Exclusive expression of transmembrane TNF-alpha in mice reduces the inflammatory response in early lipid lesions of aortic sinus. Atherosclerosis 172(2):211–218. doi:10.1016/j.atherosclerosis.2003.10.004
90. Canault M, Peiretti F, Poggi M et al (2008) Progression of atherosclerosis in ApoE-deficient mice that express distinct molecular forms of TNF-alpha. J Pathol 214(5):574–583. doi:10.1002/path.2305
91. Branen L, Hovgaard L, Nitulescu M et al (2004) Inhibition of tumor necrosis factor-alpha reduces atherosclerosis in apolipoprotein E knockout mice. Arterioscler Thromb Vasc Biol 24(11):2137–2142. doi:10.1161/01.ATV.0000143933.20616.1b
92. Xiao N, Yin M, Zhang L et al (2009) Tumor necrosis factor-alpha deficiency retards early fatty-streak lesion by influencing the expression of inflammatory factors in apoE-null mice. Mol Genet Metab 96(4):239–244. doi:10.1016/j.ymgme.2008.11.166
93. Ohta H, Wada H, Niwa T et al (2005) Disruption of tumor necrosis factor-alpha gene diminishes the development of atherosclerosis in ApoE-deficient mice. Atherosclerosis 180(1):11–17. doi:10.1016/j.atherosclerosis.2004.11.016
94. Boesten LS, Zadelaar AS, van Nieuwkoop A et al (2005) Tumor necrosis factor-alpha promotes atherosclerotic lesion progression in APOE*3-Leiden transgenic mice. Cardiovasc Res 66(1):179–185. doi:10.1016/j.cardiores.2005.01.001
95. Kober F, Canault M, Peiretti F et al (2007) MRI follow-up of TNF-dependent differential progression of atherosclerotic wall-thickening in mouse aortic arch from early to advanced stages. Atherosclerosis 195(2):e93–e99. doi:10.1016/j.atherosclerosis.2007.06.015
96. Schreyer SA, Vick CM, LeBoeuf RC (2002) Loss of lymphotoxin-alpha but not tumor necrosis factor-alpha reduces atherosclerosis in mice. J Biol Chem 277(14):12364–12368. doi:10.1074/jbc.M111727200
97. Schreyer SA, Peschon JJ, LeBoeuf RC (1996) Accelerated atherosclerosis in mice lacking tumor necrosis factor receptor p55. J Biol Chem 271(42):26174–26178
98. Xanthoulea S, Gijbels MJ, van der Made I et al (2008) P55 tumour necrosis factor receptor in bone marrow-derived cells promotes atherosclerosis development in low-density lipoprotein receptor knock-out mice. Cardiovasc Res 80(2):309–318. doi:10.1093/cvr/cvn193
99. Xanthoulea S, Thelen M, Pottgens C et al (2009) Absence of p55 TNF receptor reduces atherosclerosis, but has no major effect on angiotensin II induced aneurysms in LDL receptor deficient mice. PLoS One 4(7):e6113. doi:10.1371/journal.pone.0006113
100. Zhang L, Peppel K, Sivashanmugam P et al (2007) Expression of tumor necrosis factor receptor-1 in arterial wall cells promotes atherosclerosis. Arterioscler Thromb Vasc Biol 27(5):1087–1094. doi:10.1161/ATVBAHA.0000261548.49790.63
101. Blessing E, Bea F, Kuo CC et al (2004) Lesion progression and plaque composition are not altered in older apoE−/− mice lacking tumor necrosis factor-alpha receptor p55. Atherosclerosis 176(2):227–232. doi:10.1016/j.atherosclerosis.2004.05.033
102. Harvey EJ, Ramji DP (2005) Interferon-gamma and atherosclerosis: pro- or anti-atherogenic? Cardiovasc Res 67(1):11–20. doi:10.1016/j.cardiores.2005.04.019
103. Muhl H, Pfeilschifter J (2003) Anti-inflammatory properties of pro-inflammatory interferon-gamma. Int Immunopharmacol 3(9):1247–1255. doi:10.1016/S1567-5769(03)00131-0
104. McLaren JE, Ramji DP (2009) Interferon gamma: a master regulator of atherosclerosis. Cytokine Growth Factor Rev 20(2):125–135. doi:10.1016/j.cytogfr.2008.11.003
105. Buono C, Come CE, Stavrakis G et al (2003) Influence of interferon-gamma on the extent

and phenotype of diet-induced atherosclerosis in the LDLR-deficient mouse. Arterioscler Thromb Vasc Biol 23(3):454–460. doi:10.1161/01.ATV.0000059419.11002.6E

106. Whitman SC, Ravisankar P, Daugherty A (2002) IFN-gamma deficiency exerts gender-specific effects on atherogenesis in apolipoprotein E−/− mice. J Interferon Cytokine Res 22(6):661–670. doi:10.1089/10799900260100141
107. Koga M, Kai H, Yasukawa H et al (2007) Postnatal blocking of interferon-gamma function prevented atherosclerotic plaque formation in apolipoprotein E-knockout mice. Hypertens Res 30(3):259–267. doi:10.1291/hypres.30.259
108. King VL, Lin AY, Kristo F et al (2009) Interferon-gamma and the interferon-inducible chemokine CXCL10 protect against aneurysm formation and rupture. Circulation 119(3):426–435. doi:10.1161/CIRCULATIONAHA.108.785949
109. Koga M, Kai H, Yasukawa H et al (2007) Inhibition of progression and stabilization of plaques by postnatal interferon-gamma function blocking in ApoE-knockout mice. Circ Res 101(4):348–356. doi:10.1161/CIRCRESAHA.106.147256
110. Gupta S, Pablo AM, Jiang X et al (1997) IFN-gamma potentiates atherosclerosis in ApoE knock-out mice. J Clin Invest 99(11):2752–2761. doi:10.1172/JCI119465
111. Goossens P, Gijbels MJ, Zernecke A et al (2010) Myeloid type I interferon signaling promotes atherosclerosis by stimulating macrophage recruitment to lesions. Cell Metab 12(2):142–153. doi:10.1016/j.cmet.2010.06.008
112. Yarilina A, Park-Min KH, Antoniv T et al (2008) TNF activates an IRF1-dependent autocrine loop leading to sustained expression of chemokines and STAT1-dependent type I interferon-response genes. Nat Immunol 9(4):378–387. doi:10.1038/ni1576
113. Zhang LN, Velichko S, Vincelette J et al (2008) Interferon-beta attenuates angiotensin II-accelerated atherosclerosis and vascular remodeling in apolipoprotein E deficient mice. Atherosclerosis 197(1):204–211. doi:10.1016/j.atherosclerosis.2007.03.019
114. Pardali E, Ten Dijke P (2012) TGFbeta signaling and cardiovascular diseases. Int J Biol Sci 8(2):195–213. doi:10.7150/ijbs.3805
115. Grainger DJ (2004) Transforming growth factor beta and atherosclerosis: so far, so good for the protective cytokine hypothesis. Arterioscler Thromb Vasc Biol 24(3):399–404. doi:10.1161/01.ATV.0000114567.76772.33
116. Mallat Z, Gojova A, Marchiol-Fournigault C et al (2001) Inhibition of transforming growth factor-beta signaling accelerates atherosclerosis and induces an unstable plaque phenotype in mice. Circ Res 89(10):930–934
117. Lutgens E, Gijbels M, Smook M et al (2002) Transforming growth factor-beta mediates balance between inflammation and fibrosis during plaque progression. Arterioscler Thromb Vasc Biol 22(6):975–982
118. Tang T, Wilson PG, Thompson JC et al (2013) Prevention of TGFbeta induction attenuates angII-stimulated vascular biglycan and atherosclerosis in Ldlr−/− mice. J Lipid Res 54(8):2255–2264. doi:10.1194/jlr.P040139
119. Robertson AK, Rudling M, Zhou X et al (2003) Disruption of TGF-beta signaling in T cells accelerates atherosclerosis. J Clin Invest 112(9):1342–1350. doi:10.1172/JCI18607
120. Gojova A, Brun V, Esposito B et al (2003) Specific abrogation of transforming growth factor-beta signaling in T cells alters atherosclerotic lesion size and composition in mice. Blood 102(12):4052–4058. doi:10.1182/blood-2003-05-1729
121. Lievens D, Habets KL, Robertson AK et al (2013) Abrogated transforming growth factor beta receptor II (TGFbetaRII) signalling in dendritic cells promotes immune reactivity of T cells resulting in enhanced atherosclerosis. Eur Heart J 34(48):3717–3727. doi:10.1093/eurheartj/ehs106
122. Otsuka G, Agah R, Frutkin AD et al (2006) Transforming growth factor beta 1 induces neointima formation through plasminogen activator inhibitor-1-dependent pathways. Arterioscler Thromb Vasc Biol 26(4):737–743. doi:10.1161/01.ATV.0000201087.23877.e1
123. Li D, Liu Y, Chen J et al (2006) Suppression of atherogenesis by delivery of TGFbeta1ACT using adeno-associated virus type 2 in LDLR knockout mice. Biochem Biophys Res Commun 344(3):701–707. doi:10.1016/j.bbrc.2006.04.010
124. Frutkin AD, Otsuka G, Stempien-Otero A et al (2009) TGF-[beta]1 limits plaque growth, stabilizes plaque structure, and prevents aortic dilation in apolipoprotein E-null mice. Arterioscler Thromb Vasc Biol 29(9):1251–1257. doi:10.1161/ATVBAHA.109.186593
125. Reifenberg K, Cheng F, Orning C et al (2012) Overexpression of TGF-ss1 in macrophages reduces and stabilizes atherosclerotic plaques in ApoE-deficient mice. PLoS One 7(7):e40990. doi:10.1371/journal.pone.0040990

126. Buday A, Orsy P, Godo M et al (2010) Elevated systemic TGF-beta impairs aortic vasomotor function through activation of NADPH oxidase-driven superoxide production and leads to hypertension, myocardial remodeling, and increased plaque formation in apoE(−/−) mice. Am J Physiol Heart Circ Physiol 299(2):H386–H395. doi:10.1152/ajpheart.01042.2009
127. Wan W, Murphy PM (2013) Regulation of atherogenesis by chemokines and chemokine receptors. Arch Immunol Ther Exp (Warsz) 61(1):1–14. doi:10.1007/s00005-012-0202-1
128. Zernecke A, Weber C (2010) Chemokines in the vascular inflammatory response of atherosclerosis. Cardiovasc Res 86(2):192–201. doi:10.1093/cvr/cvp391
129. Yu X, Dluz S, Graves DT et al (1992) Elevated expression of monocyte chemoattractant protein 1 by vascular smooth muscle cells in hypercholesterolemic primates. Proc Natl Acad Sci U S A 89(15):6953–6957
130. Han KH, Tangirala RK, Green SR et al (1998) Chemokine receptor CCR2 expression and monocyte chemoattractant protein-1-mediated chemotaxis in human monocytes. A regulatory role for plasma LDL. Arterioscler Thromb Vasc Biol 18(12):1983–1991
131. Nelken NA, Coughlin SR, Gordon D et al (1991) Monocyte chemoattractant protein-1 in human atheromatous plaques. J Clin Invest 88(4):1121–1127. doi:10.1172/JCI115411
132. Rayner K, Van Eersel S, Groot PH et al (2000) Localisation of mRNA for JE/MCP-1 and its receptor CCR2 in atherosclerotic lesions of the ApoE knockout mouse. J Vasc Res 37(2):93–102. doi:10.1159/000025720
133. Combadiere C, Potteaux S, Rodero M et al (2008) Combined inhibition of CCL2, CX3CR1, and CCR5 abrogates Ly6C(hi) and Ly6C(lo) monocytosis and almost abolishes atherosclerosis in hypercholesterolemic mice. Circulation 117(13):1649–1657. doi:10.1161/CIRCULATIONAHA.107.745091
134. Gosling J, Slaymaker S, Gu L et al (1999) MCP-1 deficiency reduces susceptibility to atherosclerosis in mice that overexpress human apolipoprotein B. J Clin Invest 103(6):773–778. doi:10.1172/JCI5624
135. Rull A, Beltran-Debon R, Aragones G et al (2010) Expression of cytokine genes in the aorta is altered by the deficiency in MCP-1: effect of a high-fat, high-cholesterol diet. Cytokine 50(2):121–128. doi:10.1016/j.cyto.2010.02.010
136. Gu L, Okada Y, Clinton SK et al (1998) Absence of monocyte chemoattractant protein-1 reduces atherosclerosis in low density lipoprotein receptor-deficient mice. Mol Cell 2(2):275–281
137. Ni W, Egashira K, Kitamoto S et al (2001) New anti-monocyte chemoattractant protein-1 gene therapy attenuates atherosclerosis in apolipoprotein E-knockout mice. Circulation 103(16):2096–2101
138. Inoue S, Egashira K, Ni W et al (2002) Anti-monocyte chemoattractant protein-1 gene therapy limits progression and destabilization of established atherosclerosis in apolipoprotein E-knockout mice. Circulation 106(21):2700–2706
139. de Waard V, Bot I, de Jager SC et al (2010) Systemic MCP1/CCR2 blockade and leukocyte specific MCP1/CCR2 inhibition affect aortic aneurysm formation differently. Atherosclerosis 211(1):84–89. doi:10.1016/j.atherosclerosis.2010.01.042
140. Ni W, Kitamoto S, Ishibashi M et al (2004) Monocyte chemoattractant protein-1 is an essential inflammatory mediator in angiotensin II-induced progression of established atherosclerosis in hypercholesterolemic mice. Arterioscler Thromb Vasc Biol 24(3):534–539. doi:10.1161/01.ATV.0000118275.60121.2b
141. Schepers A, Eefting D, Bonta PI et al (2006) Anti-MCP-1 gene therapy inhibits vascular smooth muscle cells proliferation and attenuates vein graft thickening both in vitro and in vivo. Arterioscler Thromb Vasc Biol 26(9):2063–2069. doi:10.1161/01.ATV.0000235694.69719.e2
142. Aiello RJ, Bourassa PA, Lindsey S et al (1999) Monocyte chemoattractant protein-1 accelerates atherosclerosis in apolipoprotein E-deficient mice. Arterioscler Thromb Vasc Biol 19(6):1518–1525
143. Ohman MK, Wright AP, Wickenheiser KJ et al (2010) Monocyte chemoattractant protein-1 deficiency protects against visceral fat-induced atherosclerosis. Arterioscler Thromb Vasc Biol 30(6):1151–1158. doi:10.1161/ATVBAHA.110.205914
144. Liu XL, Zhang PF, Ding SF et al (2012) Local gene silencing of monocyte chemoattractant protein-1 prevents vulnerable plaque disruption in apolipoprotein E-knockout mice. PLoS One 7(3):e33497. doi:10.1371/journal.pone.0033497
145. Meisner JK, Song J, Price RJ (2012) Arteriolar and venular remodeling are differentially regulated by bone marrow-derived cell-specific CX3CR1 and CCR2 expression. PLoS One 7(9):e46312. doi:10.1371/journal.pone.0046312

146. Martinez HG, Quinones MP, Jimenez F et al (2011) Critical role of chemokine (C-C motif) receptor 2 (CCR2) in the KKAy+Apoe−/− mouse model of the metabolic syndrome. Diabetologia 54(10):2660–2668. doi:10.1007/s00125-011-2248-8

147. Boring L, Gosling J, Cleary M et al (1998) Decreased lesion formation in CCR2−/− mice reveals a role for chemokines in the initiation of atherosclerosis. Nature 394(6696):894–897. doi:10.1038/29788

148. Dawson TC, Kuziel WA, Osahar TA et al (1999) Absence of CC chemokine receptor-2 reduces atherosclerosis in apolipoprotein E-deficient mice. Atherosclerosis 143(1):205–211

149. Saederup N, Chan L, Lira SA et al (2008) Fractalkine deficiency markedly reduces macrophage accumulation and atherosclerotic lesion formation in CCR2−/− mice: evidence for independent chemokine functions in atherogenesis. Circulation 117(13):1642–1648. doi:10.1161/CIRCULATIONAHA.107.743872

150. Guo J, Van Eck M, Twisk J et al (2003) Transplantation of monocyte CC-chemokine receptor 2-deficient bone marrow into ApoE3-Leiden mice inhibits atherogenesis. Arterioscler Thromb Vasc Biol 23(3):447–453. doi:10.1161/01.ATV.0000058431.78833.F5

151. Ishibashi M, Egashira K, Zhao Q et al (2004) Bone marrow-derived monocyte chemoattractant protein-1 receptor CCR2 is critical in angiotensin II-induced acceleration of atherosclerosis and aneurysm formation in hypercholesterolemic mice. Arterioscler Thromb Vasc Biol 24(11):e174–e178. doi:10.1161/01.ATV.0000143384.69170.2d

152. Okamoto M, Fuchigami M, Suzuki T et al (2012) A novel C-C chemokine receptor 2 antagonist prevents progression of albuminuria and atherosclerosis in mouse models. Biol Pharm Bull 35(11):2069–2074

153. Olzinski AR, Turner GH, Bernard RE et al (2010) Pharmacological inhibition of C-C chemokine receptor 2 decreases macrophage infiltration in the aortic root of the human C-C chemokine receptor 2/apolipoprotein E−/− mouse: magnetic resonance imaging assessment. Arterioscler Thromb Vasc Biol 30(2):253–259. doi:10.1161/ATVBAHA.109.198812

154. Guo J, Van Eck M, de Waard V et al (2005) The presence of leukocyte CC-chemokine receptor 2 in CCR2 knockout mice promotes atherogenesis. Biochim Biophys Acta 1740(3):453–459. doi:10.1016/j.bbadis.2004.10.007

155. Pattison JM, Nelson PJ, Huie P et al (1996) RANTES chemokine expression in transplant-associated accelerated atherosclerosis. J Heart Lung Transplant 15(12):1194–1199

156. Krohn R, Raffetseder U, Bot I et al (2007) Y-box binding protein-1 controls CC chemokine ligand-5 (CCL5) expression in smooth muscle cells and contributes to neointima formation in atherosclerosis-prone mice. Circulation 116(16):1812–1820. doi:10.1161/CIRCULATIONAHA.107.708016

157. Quinones MP, Martinez HG, Jimenez F et al (2007) CC chemokine receptor 5 influences late-stage atherosclerosis. Atherosclerosis 195(1):e92–e103. doi:10.1016/j.atherosclerosis.2007.03.026

158. Braunersreuther V, Zernecke A, Arnaud C et al (2007) Ccr5 but not Ccr1 deficiency reduces development of diet-induced atherosclerosis in mice. Arterioscler Thromb Vasc Biol 27(2):373–379. doi:10.1161/01.ATV.0000253886.44609.ae

159. Zernecke A, Liehn EA, Gao JL et al (2006) Deficiency in CCR5 but not CCR1 protects against neointima formation in atherosclerosis-prone mice: involvement of IL-10. Blood 107(11):4240–4243. doi:10.1182/blood-2005-09-3922

160. Cipriani S, Francisci D, Mencarelli A et al (2013) Efficacy of the CCR5 antagonist maraviroc in reducing early, ritonavir-induced atherogenesis and advanced plaque progression in mice. Circulation 127(21):2114–2124. doi:10.1161/CIRCULATIONAHA.113.001278

161. Veillard NR, Kwak B, Pelli G et al (2004) Antagonism of RANTES receptors reduces atherosclerotic plaque formation in mice. Circ Res 94(2):253–261. doi:10.1161/01.RES.0000109793.17591.4E

162. Braunersreuther V, Steffens S, Arnaud C et al (2008) A novel RANTES antagonist prevents progression of established atherosclerotic lesions in mice. Arterioscler Thromb Vasc Biol 28(6):1090–1096. doi:10.1161/ATVBAHA.108.165423

163. Arnaud C, Beguin PC, Lantuejoul S et al (2011) The inflammatory preatherosclerotic remodeling induced by intermittent hypoxia is attenuated by RANTES/CCL5 inhibition. Am J Respir Crit Care Med 184(6):724–731. doi:10.1164/rccm.201012-2033OC

164. Major TC, Olszewski B, Rosebury-Smith WS (2009) A CCR2/CCR5 antagonist attenuates an increase in angiotensin II-induced CD11b+ monocytes from atherogenic ApoE−/− mice. Cardiovasc Drugs Ther 23(2):113–120. doi:10.1007/s10557-008-6157-0

165. Pan JH, Sukhova GK, Yang JT et al (2004) Macrophage migration inhibitory factor deficiency impairs atherosclerosis in low-density lipoprotein receptor-deficient mice. Circulation 109(25):3149–3153. doi:10.1161/01.CIR.0000134704.84454.D2

166. Verschuren L, Kooistra T, Bernhagen J et al (2009) MIF deficiency reduces chronic inflammation in white adipose tissue and impairs the development of insulin resistance, glucose intolerance, and associated atherosclerotic disease. Circ Res 105(1):99–107. doi:10.1161/CIRCRESAHA.109.199166

167. Burger-Kentischer A, Gobel H, Kleemann R et al (2006) Reduction of the aortic inflammatory response in spontaneous atherosclerosis by blockade of macrophage migration inhibitory factor (MIF). Atherosclerosis 184(1):28–38. doi:10.1016/j.atherosclerosis.2005.03.028

168. Schober A, Bernhagen J, Thiele M et al (2004) Stabilization of atherosclerotic plaques by blockade of macrophage migration inhibitory factor after vascular injury in apolipoprotein E-deficient mice. Circulation 109(3):380–385. doi:10.1161/01.CIR.0000109201.72441.09

169. Chen Z, Sakuma M, Zago AC et al (2004) Evidence for a role of macrophage migration inhibitory factor in vascular disease. Arterioscler Thromb Vasc Biol 24(4):709–714. doi:10.1161/01.ATV.0000119356.35748.9e

170. Teupser D, Pavlides S, Tan M et al (2004) Major reduction of atherosclerosis in fractalkine (CX3CL1)-deficient mice is at the brachiocephalic artery, not the aortic root. Proc Natl Acad Sci U S A 101(51):17795–17800. doi:10.1073/pnas.0408096101

171. Veillard NR, Steffens S, Pelli G et al (2005) Differential influence of chemokine receptors CCR2 and CXCR3 in development of atherosclerosis in vivo. Circulation 112(6):870–878. doi:10.1161/CIRCULATIONAHA.104.520718

172. van Wanrooij EJ, de Jager SC, van Es T et al (2008) CXCR3 antagonist NBI-74330 attenuates atherosclerotic plaque formation in LDL receptor-deficient mice. Arterioscler Thromb Vasc Biol 28(2):251–257. doi:10.1161/ATVBAHA.107.147827

173. van Wanrooij EJ, Happe H, Hauer AD et al (2005) HIV entry inhibitor TAK-779 attenuates atherogenesis in low-density lipoprotein receptor-deficient mice. Arterioscler Thromb Vasc Biol 25(12):2642–2647. doi:10.1161/01.ATV.0000192018.90021.c0

174. Sachais BS, Turrentine T, Dawicki McKenna JM et al (2007) Elimination of platelet factor 4 (PF4) from platelets reduces atherosclerosis in C57Bl/6 and apoE−/− mice. Thromb Haemost 98(5):1108–1113

175. Koenen RR, von Hundelshausen P, Nesmelova IV et al (2009) Disrupting functional interactions between platelet chemokines inhibits atherosclerosis in hyperlipidemic mice. Nat Med 15(1):97–103. doi:10.1038/nm.1898

176. Lesnik P, Haskell CA, Charo IF (2003) Decreased atherosclerosis in CX3CR1−/− mice reveals a role for fractalkine in atherogenesis. J Clin Invest 111(3):333–340. doi:10.1172/JCI15555

177. Liu P, Yu YR, Spencer JA et al (2008) CX3CR1 deficiency impairs dendritic cell accumulation in arterial intima and reduces atherosclerotic burden. Arterioscler Thromb Vasc Biol 28(2):243–250. doi:10.1161/ATVBAHA.107.158675

178. Combadiere C, Potteaux S, Gao JL et al (2003) Decreased atherosclerotic lesion formation in CX3CR1/apolipoprotein E double knockout mice. Circulation 107(7):1009–1016

179. Landsman L, Bar-On L, Zernecke A et al (2009) CX3CR1 is required for monocyte homeostasis and atherogenesis by promoting cell survival. Blood 113(4):963–972. doi:10.1182/blood-2008-07-170787

180. Poupel L, Boissonnas A, Hermand P et al (2013) Pharmacological inhibition of the chemokine receptor, CX3CR1, reduces atherosclerosis in mice. Arterioscler Thromb Vasc Biol 33(10):2297–2305. doi:10.1161/ATVBAHA.112.300930

181. Bernhagen J, Krohn R, Lue H et al (2007) MIF is a noncognate ligand of CXC chemokine receptors in inflammatory and atherogenic cell recruitment. Nat Med 13(5):587–596. doi:10.1038/nm1567

182. Chamberlain J, Evans D, King A et al (2006) Interleukin-1beta and signaling of interleukin-1 in vascular wall and circulating cells modulates the extent of neointima formation in mice. Am J Pathol 168(4):1396–1403

183. Shemesh S, Kamari Y, Shaish A et al (2012) Interleukin-1 receptor type-1 in non-hematopoietic cells is the target for the pro-atherogenic effects of interleukin-1 in apoE-deficient mice. Atherosclerosis 222(2):329–336. doi:10.1016/j.atherosclerosis.2011.12.010

184. Chamberlain J, Francis S, Brookes Z et al (2009) Interleukin-1 regulates multiple atherogenic mechanisms in response to fat feeding. PLoS One 4(4):e5073. doi:10.1371/journal.pone.0005073

185. Alexander MR, Moehle CW, Johnson JL et al (2012) Genetic inactivation of IL-1 signaling

enhances atherosclerotic plaque instability and reduces outward vessel remodeling in advanced atherosclerosis in mice. J Clin Invest 122(1):70–79. doi:10.1172/JCI43713

186. Chi H, Messas E, Levine RA et al (2004) Interleukin-1 receptor signaling mediates atherosclerosis associated with bacterial exposure and/or a high-fat diet in a murine apolipoprotein E heterozygote model: pharmacotherapeutic implications. Circulation 110(12):1678–1685. doi:10.1161/01.CIR.0000142085.39015.31
187. Devlin CM, Kuriakose G, Hirsch E et al (2002) Genetic alterations of IL-1 receptor antagonist in mice affect plasma cholesterol level and foam cell lesion size. Proc Natl Acad Sci U S A 99(9):6280–6285. doi:10.1073/pnas.092324399
188. Isoda K, Shiigai M, Ishigami N et al (2003) Deficiency of interleukin-1 receptor antagonist promotes neointimal formation after injury. Circulation 108(5):516–518. doi:10.1161/01.CIR.0000085567.18648.21
189. Isoda K, Sawada S, Ishigami N et al (2004) Lack of interleukin-1 receptor antagonist modulates plaque composition in apolipoprotein E-deficient mice. Arterioscler Thromb Vasc Biol 24(6):1068–1073. doi:10.1161/01.ATV.0000127025.48140.a3
190. Merhi-Soussi F, Kwak BR, Magne D et al (2005) Interleukin-1 plays a major role in vascular inflammation and atherosclerosis in male apolipoprotein E-knockout mice. Cardiovasc Res 66(3):583–593. doi:10.1016/j.cardiores.2005.01.008
191. Elhage R, Maret A, Pieraggi MT et al (1998) Differential effects of interleukin-1 receptor antagonist and tumor necrosis factor binding protein on fatty-streak formation in apolipoprotein E-deficient mice. Circulation 97(3):242–244
192. Song L, Schindler C (2004) IL-6 and the acute phase response in murine atherosclerosis. Atherosclerosis 177(1):43–51. doi:10.1016/j.atherosclerosis.2004.06.018
193. Zhang K, Huang XZ, Li XN et al (2012) Interleukin 6 destabilizes atherosclerotic plaques by downregulating prolyl-4-hydroxylase alpha1 via a mitogen-activated protein kinase and c-Jun pathway. Arch Biochem Biophys 528(2):127–133. doi:10.1016/j.abb.2012.09.007
194. Schuett H, Oestreich R, Waetzig GH et al (2012) Transsignaling of interleukin-6 crucially contributes to atherosclerosis in mice. Arterioscler Thromb Vasc Biol 32(2):281–290. doi:10.1161/ATVBAHA.111.229435
195. Pejnovic N, Vratimos A, Lee SH et al (2009) Increased atherosclerotic lesions and Th17 in interleukin-18 deficient apolipoprotein E-knockout mice fed high-fat diet. Mol Immunol 47(1):37–45. doi:10.1016/j.molimm.2008.12.032
196. Mallat Z, Corbaz A, Scoazec A et al (2001) Interleukin-18/interleukin-18 binding protein signaling modulates atherosclerotic lesion development and stability. Circ Res 89(7):E41–E45
197. Campbell LA, Nosaka T, Rosenfeld ME et al (2005) Tumor necrosis factor alpha plays a role in the acceleration of atherosclerosis by Chlamydia pneumoniae in mice. Infect Immun 73(5):3164–3165. doi:10.1128/IAI.73.5.3164-3165.2005
198. Whitman SC, Ravisankar P, Elam H et al (2000) Exogenous interferon-gamma enhances atherosclerosis in apolipoprotein E−/− mice. Am J Pathol 157(6):1819–1824
199. Thacker SG, Zhao W, Smith CK et al (2012) Type I interferons modulate vascular function, repair, thrombosis, and plaque progression in murine models of lupus and atherosclerosis. Arthritis Rheum 64(9):2975–2985. doi:10.1002/art.34504
200. Gistera A, Robertson AK, Andersson J et al (2013) Transforming growth factor-beta signaling in T cells promotes stabilization of atherosclerotic plaques through an interleukin-17-dependent pathway. Sci Transl Med 5(196):196ra100. doi:10.1126/scitranslmed.3006133
201. Hirase T, Hara H, Miyazaki Y et al (2013) Interleukin 27 inhibits atherosclerosis via immunoregulation of macrophages in mice. Am J Physiol Heart Circ Physiol 305(3):H420–H429. doi:10.1152/ajpheart.00198.2013
202. Koltsova EK, Kim G, Lloyd KM et al (2012) Interleukin-27 receptor limits atherosclerosis in Ldlr−/− mice. Circ Res 111(10):1274–1285. doi:10.1161/CIRCRESAHA.112.277525
203. Ellison S, Gabunia K, Kelemen SE et al (2013) Attenuation of experimental atherosclerosis by interleukin-19. Arterioscler Thromb Vasc Biol 33(10):2316–2324. doi:10.1161/ATVBAHA.113.301521

Chapter 3

Intravital Microscopy for Atherosclerosis Research

Remco T.A. Megens and Oliver Soehnlein

Abstract

Recruitment of leukocytes into arteries is a hallmark event throughout all stages of atherosclerosis and hence stands out as a primary therapeutic target. To understand the molecular mechanisms of arterial leukocyte subset infiltration, real-time visualization of recruitment processes of leukocyte subsets at high resolution is a prerequisite. In this review we provide a balanced overview of optical imaging modalities in the more commonly used experimental models for atherosclerosis (e.g., mouse models) allowing for in vivo display of recruitment processes in large arteries and further detail strategies to overcome hurdles inherent to arterial imaging. We further provide a synopsis of techniques allowing for non-toxic, photostable labeling of target structures. Finally, we deliver a short summary of ongoing developments including the emergence of novel labeling approaches, the use of superresolution microscopy, and the potentials of opto-acoustic microscopy and intravascular 2-dimensional near-infrared fluorescence microscopy.

Key words Intravital microscopy, Optical imaging, Atherosclerosis, Arterial cell recruitment, In vivo labeling strategies

1 Inflammatory Processes in Atherosclerosis

Atherosclerosis is a chronic inflammatory disease of the arterial wall resulting from a dysbalanced lipid metabolism and a maladaptive inflammatory response. Large clinical studies lend strong support to the association between plasma lipid levels and the risk for cardiovascular events [1, 2]. In particular, low-density lipoprotein (LDL) levels correlate with the risk of cardiovascular events in human populations and augment the individual susceptibility to atherosclerosis and its complications. Mechanistically, LDL increases expression of endothelial cell adhesion molecules and primes circulating leukocytes, thus increasing the likeliness for arterial leukocyte infiltration [3]. The accumulation of leukocytes within the arterial wall is a hallmark of all stages of atherosclerosis [4]. During early atherosclerosis, inflammatory monocytes and neutrophils infiltrate the arterial wall by a process that is largely reminiscent of the classical recruitment cascade. Endothelial cell adhesion molecules, such as P-selectin, intercellular adhesion mol-

Vicente Andrés and Beatriz Dorado (eds.), *Methods in Mouse Atherosclerosis*, Methods in Molecular Biology, vol. 1339, DOI 10.1007/978-1-4939-2929-0_3,

ecule 1 (ICAM1), and vascular cell adhesion molecule 1 (VCAM1), facilitate the firm arrest of inflammatory cells along the arterial wall, while chemokines released from endothelial cells, inflammatory macrophages, or activated platelets crucially facilitate leukocyte adhesion and further guide neutrophils and monocytes into the lesion via mechanisms involving CCR1, CCR2, CCR5, and CXCR2 [5, 6]. In particular activation of platelets and subsequent release of preformed chemokines such as CCL5 induces adhesion and recruitment of myeloid cells [6]. The cationic nature of CCL5 facilitates its immobilization on the arterial cell surface. In this location CCL5 is presented to cells rolling along the arterial wall and when recognized by its receptors an intracellular signaling cascade sets in inducing the activation of integrins. Similarly, neutrophils contain granule proteins with chemotactic activities. As an example, neutrophils deposit azurocidin and cathelicidin on endothelial cells thus promoting monocyte adhesion and recruitment and subsequent atherosclerotic lesion formation [7–9]. During the later stages of atherosclerosis, accumulation of leukocytes is aggravated by the local proliferation of plaque resident macrophages, and possibly hampered egress of inflammatory cells [10, 11]. While arterial leukocyte infiltration in mouse models of atherosclerosis may during early stages of atherosclerosis primarily occur via the arterial vessel lumen, at advanced stages this may shift towards neovessels as primary entry site [12]. Indeed, newly formed plaque vasculature originating from vasa vasorum in the adventitia not just sustains inflammatory leukocyte influx but also cholesterol accumulation, and the supply with erythrocyte-derived phospholipids, thus contributing to plaque instability. Hence, neovascularization and intraplaque hemorrhage have recently been established as independent predictors of future adverse cardiovascular outcomes [13]. Intraplaque vessels are characterized by an immature structure with a reduced number of mural pericytes and SMCs covering the ECs, hence contributing to increased leakiness and rupture susceptibility [14]. Subsequent to their recruitment, monocytes differentiate towards macrophages which eventually undergo apoptosis. These apoptotic cells are not effectively cleared due to an impairment of clearance capacity in advanced atherosclerosis, and thus transit into secondary necrosis. Over time, secondary necrosis feeds the necrotic core and is a driver of plaque destabilization [15]. The plaque is shielded from the blood stream by a matrix-containing smooth muscle cell-rich fibrous cap which is covered by endothelial cells. Weakening of the fibrous cap by the continuous production and release of matrix degrading proteases from activated macrophages makes the atherosclerotic lesion more prone to plaque rupture. Consequent exposure of thrombogenic material to the blood stream causes platelet activation and blood clotting clinically observed as myocardial infarction or stroke.

As atherosclerosis is a disease largely driven by leukocyte influx in the vessel wall, visualizing leukocyte subset behavior in vivo along large arteries is the Holy Grail for those interested in understanding leukocyte migration. Major progress has been made in developing intravital microscopy approaches to study leukocyte movement and models, labeling techniques, and microscopes have improved over the last decades for several tissues, including the spleen, the skin, the lungs, and the heart [16–19]. However, studying arterial leukocyte recruitment is still hampered by many aspects including difficulties to access arteries and the large movement artifacts and hence people have largely extrapolated findings from the microcirculation to the macrocirculation. However, differences between these two vascular beds may provide a powerful entrance strategy for therapeutic approaches. Hence, this review provides an overview of techniques and labeling strategies that allow for intravital imaging of arterial leukocyte recruitment.

2 Optical Imaging Techniques for Visualization of Arterial Recruitment

Atherosclerosis is a chronic disease of the large arteries where both innate (atherogenesis) and adaptive (progression and destabilization) immunity responses are involved [4]. The general idea of luminal cell recruitment by the vessel wall leading to atherogenesis, plaque progression, and plaque destabilization is extrapolated from in vitro, histological or microcirculatory intravital studies. Models for microcirculatory intravital microscopy such as the cremaster muscle, mesentery, or skin offer an entrance for studying processes involved in cell rolling, cell recruitment, and cell migration into the vessel wall [20–23]. However, since the vascular structure, cellular functions and flow and shear stress milieu in the microcirculation are very different from macrocirculatory arteries, it is crucial to verify findings in a true atherosclerotic prone environment, i.e. in the large arteries. This however comes with difficulties: the arterial wall of large arteries is much thicker and therefore less easily penetrable with light. Moreover the arterial wall is subject to strong motion due to the heart and respiratory cycles [24]. All these aspects complicate intravital microscopy of large arteries dramatically.

The studies utilizing classical/conventional fluorescence intravital imaging (Fig. 1a) of exposed large arteries offer great overview of the artery and as such allow for easy quantification of luminal cell recruitment [25–28]. Additionally conventional fluorescence microscopy is relatively easy to apply and tissue motion disturbs imaging only to a limited extent (as a result of the non-scanned camera-based image acquisition and the lower magnification and numerical aperture objectives often used). However, conventional intravital microscopy often lacks the image quality required to study the process of phagocyte recruitment in more

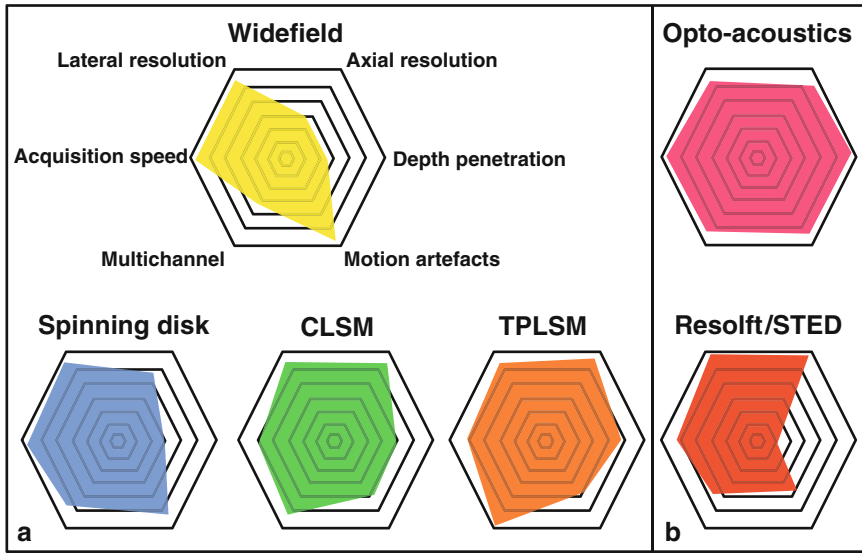

Fig. 1 Overview of image modalities for intravital microscopy. (**a**) comparison of characteristic image properties (i.e., axial and lateral resolution, acquisition speed, depth penetration multichannel detection, and motion artifact vulnerability) of the most widely used microscope modalities for intravital microscopy in atherosclerotic research. The color coded areas (wide field, *yellow*; spinning disk, *blue*; CLSM, *green*; TPLSM, *orange*) represent the differences and advantages of each modality for intravital imaging. (**b**) Properties of novel image modalities with potential future application for intravital imaging of atherosclerosis; multiscale opto-acoustics (*purple*) and the nanoscopic techniques STED and RESOLFT (*red*)

detail nor does it provide optical sectioning and thus 3-dimensional information. Furthermore, visualization of more than one target or cell type is challenging since most of the microscopic setups typically do not support simultaneous imaging of two or more channels or, if they do, require tedious alignment (Fig. 2) [6, 7]. In order to overcome the limitations of penetration depth into the vascular wall, as with all microscopes that make use of conventional fluorescence excitation, there is a need for strong fluorescence signals derived from the target structure(s). As such one can detect cells adhering or interacting to the arterial vessel wall but cannot judge whether cells are adhering to or are recruited into the vessel wall.

An alternative approach is confocal microscopy (Fig. 1a), a modality that offers optical sectioning by blocking out of focus light, and thus enables 3D imaging. There are basically two types of confocal microscopy that can be applied for intravital microscopy offering fast multichannel 3D imaging. The most often applied intravital confocal modality is spinning disk microscopy [29] where a so-called Nipkow disk generates the confocal effect with multiple foci [30]. Spinning disk confocal microscopy is a fast modality and, dependent on the system layout and settings, the optical resolution is mainly improved in depth (maximum axial resolution ≈ 5 μm).

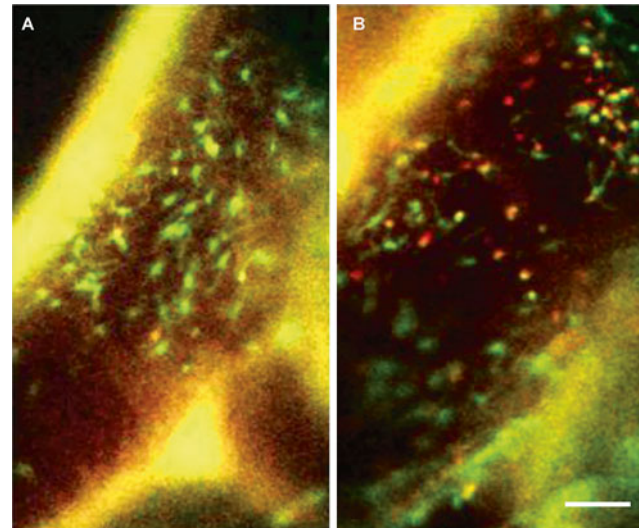

Fig. 2 Dual-channel conventional fluorescence intravital microscopy of carotid arteries. *Apoe*$^{-/-}$ mice were transplanted with *Cx3cr1gfp*$^{/}$*wtCcr2rfp*$^{/}$*wt* bone marrow. Local treatment of carotid artery with saline (**a**) or TNF (**b**) for 4 h. Scale bar represents 75 μm. Arterial wall is visible in both channels (*yellow*; autofluorescence)

Moreover, two or more spectral channels are typically available for simultaneous detection of multiple targets. Yet, the imaging of structures deep in or at the luminal border of the large arteries is still restricted due to the limited penetration depth. Moreover the increased cross talk between multiple foci that may occur potentially reduces the signal-to-noise ratio especially when imaging at depth in tissues. A second confocal approach is the use of a single focus, fast confocal laser scanning microscopy (CLSM) which makes use of pinhole(s) to block out of focus light and a scanhead enabling xy-scanning at resonant speeds. A state-of-the-art commercially available resonant scanned CLSM enables image acquisition at a rate of >30 Hz [31]. Combined with a piezo-driven z-positioner it is possible to obtain 3D xyz-stacks of the arterial wall at high speeds (typically 0.1–0–3 Hz) [32] (Fig. 3). Combined with powerful excitation laser sources and several sensitive emitted light detectors such as photo multipliers or (hybrid) diodes, these systems allow intravital imaging of circulation as well as the processes and structures in the tunica adventitia and media of large arteries [33]. Yet, even powerful CLSM systems lack the penetration depth that is required for studying cell recruitment at the luminal border of large arteries [33]. Fast two-photon laser scanning microscopy (TPLSM) offers a similar system layout as fast CLSM or makes use of multiplication of the excitation laser beam (1–64 beams) [34, 35], to enable high-speed acquisition without a negative impact on the overall image quality, size of the field of view, nor the image resolution.

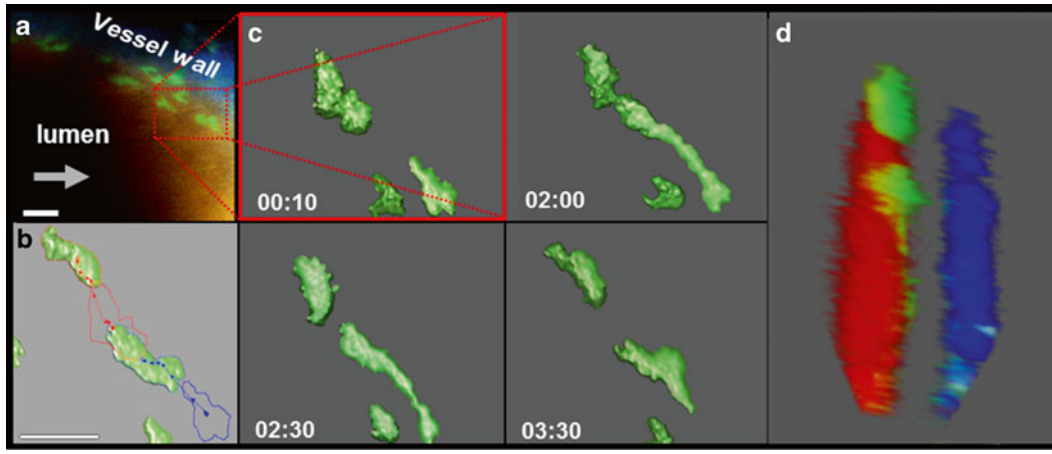

Fig. 3 Luminal tracking of myeloid cells in the stabilized carotid artery. TPLSM obtained 4D datasets (XYZT) of the stabilized carotid artery of Lysm$^{egfp/egfp}$ Apoe$^{-/-}$ mice presented over time as 2D extended depth of field pictures using maximum intensity projection (**a**), cell tracking (**b**) or as 3D reconstructions with (**b**, **c**) or without (**d**) isosurface rendering. *Arrows* indicate the direction of flow, *green* are myeloid cells, *blue* is collagen derived second harmonics generation in the tunica adventitia, *red* is 150 kDa Tritc-Dextran in the circulating blood representing the lumen. Scale bar = 25 μm. Figure was adapted from Chevre et al. [32]

However, unlike conventional fluorescence microscopy, TPLSM makes use of a different excitation process where near simultaneous absorption of two photons of approximately half the energy (and thus double the wavelength) causes fluorescent molecules to move from the ground state to a higher energy state (in most cases similar fluorophores as those used with conventional fluorescence) [36]. The subsequent decay causes the molecule to fall back to its ground state while emitting fluorescent light of a slightly lower energy (i.e., longer wavelength). To achieve two-photon excitation, a less scattering, pulsed, near-infrared laser source is used which increases light penetration into the artery while reducing the overall energy load on the tissue. Moreover, since the two-photon excitation and the resulting fluorescence decay of (intrinsic) fluorophores only occurs in the focal spot, all the detected fluorescence signal can be used for image reconstruction. As a result, there is no need for pinhole(s) and as such the detection efficiency and the signal-to-noise ratio are further improved, enabling imaging at greater depth in the arteries or detection of slightly weaker or more vulnerable fluorescent targets [33].

Microscopes offering high spatial and axial resolution have in common that they suffer severely from motion artifacts that are present in living specimen. When studying murine cardiovascular samples such as the large arteries, the motion disturbances are a consequence of the cardiac (6–9 Hz) and respiratory (2–4 Hz) cycles (depending on applied anesthesia) [37]. The cardiac cycle is the most prominent disturbance due to its higher frequency but

causes a somewhat smaller tissue drift; only the artery moves as a consequence of the blood pressure wave. The respiratory cycle motion causes the whole thorax to move and results in a more pronounced focus drift but at a lower frequency. As a result of the tissue motion, microscopic imaging suffers from both intra-frame and inter-frame motion artifacts. The intra-frame motion artifacts only occur with laser scanning microscopes that utilize pixel by pixel image construction where a gradient in time difference between the first scanned pixel in the left top corner of the image matrix and the last scanned pixel at the right bottom corner is present. As such, the tissue in focus may vary within the time required for acquisition of one single image, causing a shift in tissue in focus and thus a deterioration of the tissue in view due to the actual motion and loss of focus [24, 32]. The tissue motion also causes a difference of the tissue in focus between subsequent images. As a result, accurate tracking of objects over time or generation of 3-dimensional reconstructions (either in depth or over time) is almost impossible without any motion suppressing aid since subsequent optical sections do not contain the same tissue over time or are not only in axially (z) shifted but also spatially (xy). In order to reduce the impact of motion on imaging, optimization of the microscope hardware (fast acquisition and high sensitivity) combined with adaptions to the experimental layout are required.

There are several strategies to (partially) overcome both artifacts: (a) utilize the cardiac and respiratory cycle to manually guide the imaging by timing of the TPLSM acquisition in a time window where the motion will be limited; (b) record the moving tissue randomly, apply extensive post-processing of the images series to detect comparable tissue representations over time; (c) trigger the acquisition by using the cardiac and respiratory signals (triggered acquisition); and (d) stabilize and (partially) isolate the artery from the surrounding tissue with specifically designed tools to suppress the impact of motion. These strategies are discussed below:

1. Manual timing of the image acquisition between the tissue movements by means of timed recording is a logical step to (partially) overcome in vivo motion artifacts. Provided the image acquisition frequency is higher than the movement frequencies, it is possible to record a single image without intra-image artifacts. Timing of image acquisition has been performed for imaging of the lung using intravital laser scanning microscopy [38, 39]. By mechanically controlling the respiration, a stable respiration motion frequency is obtained that allows image acquisition in between the respiration frequency without intra-image artifacts (only when acquisition frequency is higher than motion frequency). When respiratory motion frequencies are unstable or when the motion is also caused by the cardiac cycle, as is the case in the large arteries, it is impossible to block

the impact of motion by simple timing of acquisition in the respiration-free time window.

2. When randomly recording a vast amount of single xy-images over time at 10–30 Hz, the resultant image datasets mainly consists of motion disturbed optical slices. Such datasets can be subjected to extensive post-processing of the images series in order to detect comparable tissue representations over time. In most cases, the (partially) stable images have a rhythmic appearance (dependent on acquisition frequency and type of motion disturbances) which is beneficial for the selection process. Additionally, non-moving structures or cells within the selected images have to be compared using overlays, edge detection, or co-localization protocols. The matching images may then be combined and used for evaluation of myeloid cell recruitment [5], vasa vasorum [40, 41], or biological structures such as presence of luminal neutrophil extracellular traps in atherosclerotic arteries [42]. The post-processing method can be performed manually but without automatic (structure recognition based) image processing protocols, it is very time consuming and tedious work with an unclear outcome; it is unclear whether the analyzed time series contain enough stable and comparable images to reconstruct cellular processes over time. Hence, there is a need for (development of) automatic processing protocols to automatically analyze in vivo datasets. To generate multidimensional microscopic datasets it is also required to have knowledge on the motion frequencies and tissue shifts which further complicates the post-processing procedures even more. Moreover, the time course of the resulting movie is not stable because of its dependency on the tissue in the focal plane.
3. By measuring both the respiratory and cardiac cycle signals using a balloon pressure and an ECG or blood pressure probe it is possible to determine a time gate where the motion of both cycles is limited. Image acquisition of each single image in the time gate of the combined cycles (by coupling the single-trigger pulse directly into the microscope hardware in order to avoid software jitter) results in a strong reduction of both intra- and inter-frame artifacts [24]. Moreover, the acquired images of both cardiac and respiratory triggered microscopy are less influenced by small irregularities that occur in both motion frequencies due to the possibility to apply trigger thresholds or trigger delays for each signal separately as well as the overall trigger output signal to start the image acquisition. As a result, double triggered acquisition holds potential for multidimensional microscopy, especially when combined with fast (>10 Hz) spinning disk or laser scanning microscopes in order to further suppress intra-frame artifacts.

A disadvantage of double-triggered acquisition is the reduction of overall imaging rates since the relatively small time gates of each individual cycle must be (partially) overlapping in order to achieve image stability. In practice, an overall acquisition frequency of 0.5–1.0 Hz is maximum achievable [24], which limits its applicability for studying fast biological processes.

4. Besides the rather non physiological procedures of physical suppression of the tissue motion either by adapting the surgical preparation method in order to temporary stoppage of the respiration [43] or blood flow [44], more subtle stabilization of arteries can be beneficial to reduce motion impact. Attempts to stabilize arteries by embedding the exposed carotid artery in stiffened material such as low percentage agarose in buffer, have up till now failed since they do not suppress the motion disturbances sufficiently (own observations). Chevre et al. [32] used a surgical layout similarly as applied by Yu et al. [44] but stabilized the carotid artery without the dramatic alterations to the blood flow by making use of a thin steel plate to carefully lift the artery up from the surrounding tissue, and part of a cover slip to gently squeeze the artery to further reduce motion while creating a imaging window. As a result, conventional intravital microscopy with a high magnification and numerical aperture objective could be applied to study several classes of leukocytes, including monocytes, lymphocytes, and platelets, using a combination of fluorescent reporter genes and fluorescently labeled antibodies that were injected intravenously before imaging. The authors used the artery-stabilizing protocol also in combination with multichannel fast TPLSM. For application of TPLSM the method required additional triggering to further suppress the impact of the respiratory cycle on imaging. Nevertheless the combination of physical stabilization of the sample with respiration controlled image acquisition enabled recording of multidimensional datasets with relatively high frequency (0.1–0.3 Hz per z-stack) for prolonged time (>30 min) and for the first time demonstrated the feasibility of 3D tracking of cells and their function in atherosclerotic prone arteries in vivo [45].

As is evident, the described techniques have their advantages and disadvantages, and ultimately the optimal technique offers the best balance between acquisition speed, sensitivity, and (3D) resolution. The latter will depend on the research question at hand as well as the availability of the various techniques. Quantification of cell adhesion and cell-arterial wall interactions are best performed using conventional fluorescence microscopy due to its ease of use. Studies focused on tissue structure would greatly profit from the most stable imaging layout with a double triggering protocol and using modalities with optical sectioning. Fast processes however,

such as multidimensional tracking of cells in the arterial system, may benefit more from artery stabilization (combined with respiratory triggering) since triggering-based techniques would result in too slow acquisition for proper assessment of real-time dynamics. In the near future, continuous imaging combined with automated post processing may enable more researchers to apply advanced microscopic techniques in strongly motional samples and indirectly obtain an improved image quality without the need for trigger adapted setups.

3 Strategies to Label Target Structures

Early intravital microcopy studies analyzing myeloid cell extravasation used bright field microscopy. Such techniques were typically employed in tissues that were thin enough to allow white light transmittance through the sample. However, as this is not possible for optical imaging of large arteries in vivo fluorescence microscopy is widely used benefiting from an ever-growing array of available fluorophores that can be used to label cells and tissue structures. These fluorophores can roughly be divided into two categories: endogenous reporters, i.e., fluorescent proteins expressed by cells of interest (Table 1); and exogenous probes, i.e., chemicals that interact with cellular or tissue components.

Table 1
List of mouse strains with fluorescent phagocyte subsets

Strain name	Fluorescent cell type	Reference
c-fms-gfp	GFP in mononuclear phagocytes	[96]
Cx3cr1-gfp	GFP expression correlates with CX_3CR1 transcription. Inflammatory monocytes are GFP^{lo}, resident monocytes are GFP^{hi}, NK cell subsets, microglia, and DCs are GFP^{int}	[46]
Lysm-gfp	GFP expression correlates with the transcription of Lysozyme M. Circulating neutrophils are GFP^{hi}, while monocytes are GFP^{lo}	[97]
MhcII-gfp	DCs are GFP^{hi}, B cells are GFP^{int}, and macrophages are GFP^{lo}	[98]
Cx3cr1-gfpCcr2-rfp	Inflammatory monocytes are $GFP^{lo}RFP^{+}$, resident monocytes are $GFP^{hi}RFP^{-}$	[48]
Ly6G-gfp-cre	This mouse strain is currently being developed by Dr. Matthias Gunzer (University of Duisburg-Essen, Germany); reported to carry tdTomato and Cre in neutrophils, only	Unpublished
hCD68-gfp	This mouse strain is currently being characterised by Dr. David R. Greaves (University of Oxford, UK); the eGFP transgene under control of the human CD68 promoter is expressed in circulating monocytes and resident and inflammatory macrophages	Unpublished

Irrespective of the nature of the probe, fluorophores for in vivo use are ideally nontoxic, photostable, with sufficient quantum yields to generate a signal detectable through living tissues.

The use of transgenic mice expressing fluorescent proteins in a cell-specific fashion is an elegant method for specific cell labeling and is widely accepted to track individual leukocyte subsets. A variety of strains has been created to allow for tracking of myeloid cell populations in vivo (Table 1). However, care has to be taken when using mice where the gene encoding for a fluorescent protein has been knocked into the locus of a gene involved in recruitment. This is the case for Cx3cr1-egfp mice or Ccr2-rfp mice, where homozygous mice lack these receptors and thus recruitment of monocyte subsets may be affected [46, 47].

The generation of blue/yellow-shifted GFP variants (blue, cyan, and yellow fluorescent proteins), together with the discovery- and mutation-based development of red fluorescent proteins has expanded the palette of colors available and has allowed the development of more complex reporter strategies. This development has led to the establishment of reporter mice for multiple cell types or cell subsets. An example herein is the *Cx3cr1gfp/wtCcr2rfp/wt* mouse allowing for in vivo tracking of monocyte subsets [48]. Apart from simultaneous visualization of multiple cell types, the extended palette of fluorescent proteins available has led to some very elegant applications from labelling different phases of the cell cycle to different clones of cells within a tissue. For instance, the FUCCI reporter system allows real-time visualization of cell cycle progression in living cells. Recently, a new type of FUCCI reporter strategy, based on the use of mCherry and Venus fluorescent proteins, has allowed similar studies to be performed within live, cultured mouse embryos [49]. Although the FUCCI technology has not been used in adult tissues (not to mention atherosclerosis research) this strategy could be important to study the dynamics of cell proliferation within atherosclerotic lesions. Several additional strategies for genetic labelling of cells are available. However, most of these have only been tested in cancer research and their use for optical imaging of atherosclerosis is at its infancy. Such approaches include confetti transgenic mice [50] for studying tissue dynamics, Forster resonance energy transfer (FRET)-based strategies to study signaling events [51, 52], and the use of photoswitchable or photoconvertible fluorescent proteins allowing for labeling of specific cells to be identified through multiple imaging sessions [53, 54]. On the other hand, the clear advantages of fluorescent protein-encoding mouse strains over adoptive transfer approaches is that the target cells are not subjected to ex vivo handling and that the fluorescent tags do not become diluted or fade in dividing cells.

Dyes present a variety of different challenges and limitations in comparison with endogenously expressed fluorescent proteins, ranging from higher cytotoxicity to rapid dilution upon cell proliferation.

However, they is often chosen because of their ease of use and the wide array of colours they provide. Moreover, a good staining strategy may be applied in any transgenic mouse model and as such offers great flexibility in usage since there is no need to generate novel transgenic mouse lines with multiple reporters. Cytoplasmic and nuclear dyes are, in principle, ideal for in vivo single-cell tracking because they should provide the most uniform staining; however, they tend to present higher cytotoxicity and are rarely used for intravital microscopy. Carboxyfluorescein succinimidyl ester (CFSE) and carboxyfluorescein diacetate succinimidyl ester (CFDA-SE) are amine-reactive probes that penetrate cells, where they are metabolized to amine-reactive chemicals, which then covalently bind to cytosolic components. High concentrations of CFSE have been associated with severe toxicity [55]; however, once carefully optimized, CFSE labelling enables in vivo cell tracking over a long period of time because it is very efficiently retained within the cytoplasm [56]. Amine-reactive dyes, available with a wide spectral range and in far red-shifted variants, overcome the limitations of CFSE/CFDA-SE and have been successfully used for confocal intravital microscopy (IVM) experiments.

Dyes with high affinity for double-stranded DNA provide a bright nuclear signal, and therefore should be ideal for tracking cells within densely clustered populations and in deep tissues, but have been consistently reported to have a number of limitations when applied to in vivo single-cell resolution imaging. In fact, DNA-binding dyes can interfere with fundamental biological processes, including DNA replication and transcription, and can induce DNA damage. For example, Hoechst 33342 has been reported to inhibit the proliferation of mammalian cells at high concentrations [56] and DRAQ5 was shown to interfere with DNA-binding proteins such as histones, DNA repair, replication, and transcription factors as well as essential cellular enzymes resulting in the inhibition of cellular functions [57]. Hoechst 33342 has the advantage of absorbing light in the UV range, excitable by two-photon microscopy, and is resistant to quenching. For these reasons, it has therefore been widely used to study leukocyte migration, a process uncoupled from DNA dynamics and therefore not affected by nuclear dyes. Moreover, Hoechst 33342 has been successfully used to visualize apoptosis in vivo [58]. The vital cell DNA binding dyes from the SYTO series are very stable and available with a variety of spectral properties. SYTO13 (green spectral range) and SYTO41 (blue spectral range) have been used for (in vivo) imaging of large arteries and are an alternative for Hoechst 33342 [24]. Propidium iodide also binds to DNA by intercalating between the bases with no sequence preference. As it is cell impermeable it is a good dye for in vivo detection of cell death or for detection of extracellular DNA [42].

Lipophilic, carbocyanine fluorescent tracking dyes, whose aliphatic portion binds to the cell membrane lipid bilayer, have been widely used by the scientific community and seem to have lower cytotoxicity than cytoplasmic and nuclear dyes [59]. PKH lipophilic dyes such as PKH2, PKH67 (green), PKH3 and PKH26 (red) have been extensively used for tracking leukocytes in vivo. These dyes stain the whole plasma membrane of cells through lateral diffusion, and also spread to intracellular organelles as a consequence of membrane turnover. More recently, another series of carbocyanine lipophilic dyes (DiO, DiI, DiD and DiR, with green, red, far-red, and near-infrared emission, respectively) have become increasingly popular and are now routinely used for in vivo tracking and imaging studies [60, 61]. They all follow the same labeling principle and cover a large spectral range, thus facilitating tracking of multiple cell populations simultaneously through multicolor imaging. Some of these dyes, for example DiR, are highly photostable, and all are easy and rapid to apply. Most importantly, despite the fact that they heavily intercalate within the lipid bilayer of cell membranes, they have not been reported to cause serious cytotoxicity at concentrations that provide strong, uniform staining.

In recent years, the use of mice expressing fluorescent proteins and fluorescent dyes has been complemented by the application of fluorescent antibodies towards myeloid cell subsets. The injection of antibodies to Gr1 and CD115 or F4/80 allows for labeling neutrophils or monocytes [6, 62] independently of the genetic background of the mice. However, one has to bear in mind that some antibodies may affect leukocyte behavior. In the case of antibodies to Gr1 it has been shown that higher doses of this antibody induce depletion of neutrophils, so that low concentrations have to be used to avoid such depletion [63]. In addition, antibodies may induce signaling events that impair cell function. In this context it has recently been reported that injection of low doses of anti-Ly6G antibody to label neutrophils disturbs their recruitment [64]. An alternative antibody-based approach is the conjugation of antibodies to fluorescent microbeads. Endothelial immobilization of such beads allows for detection and even quantification of cell adhesion molecule (CAM) expression, whereof the amount of immobilized beads correlates with luminal CAM expression [65] or luminally deposited chemotactic molecules (Fig. 4) [5, 7, 8]. The main challenges raised by the use of intact antibodies for in vivo labeling of cells and tissue structures are tissue penetration (i.e., the efficiency of labelling is likely to rapidly decrease with distance from vasculature), potential nonspecific signal and aberrant immune cell responses. The last two problems, both due to the antibodies binding and activating cellular Fc receptors, can be alleviated by removal of the Fc part of the antibodies [66]. An alternative to antibodies may be provided by aptamers, short nucleotide or peptide sequences that can recognize specific protein domains.

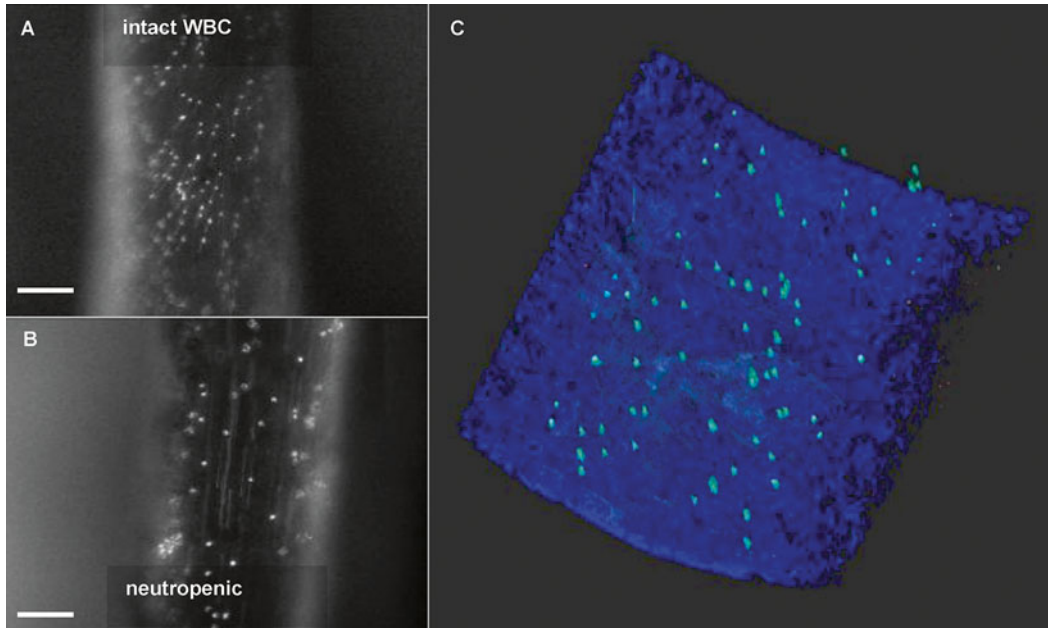

Fig. 4 Detection of luminally immobilized molecules. Conventional fluorescence intravital microscopy of anti-CRAMP fluorescent bead complex deposition in the injured carotid artery of *Apoe*$^{-/-}$ mice with intact white blood cell counts (**a**) and neutropenia (**b**). Directly after intravital microscopy, luminal presence was confirmed in the arteries ex vivo (**c**) using the 3-dimensional properties of TPLSM combined with intrinsic fluorescence derived from the arterial wall. Adapted from [26]

Because aptamers are small and change conformation upon binding of their target, they can be engineered so that specific binding releases a quencher or generates a FRET pair, thus reducing non-specific staining [67]. So far, aptamers have been used to label mesenchymal stem and progenitor cells ex vivo and to visualize them in mouse bone marrow following transplantation [67].

4 Current and Future Developments

In vivo imaging of cell biology processes has been increasingly rewarding, thanks to the constant improvement of fluorophores, both proteins and chemical, and to parallel technological advances. Recent developments in these fields are already providing indications on the future avenues of IVM studies. For example, fluorescent proteins emitting in the near-infrared region (such as Neptune and eqFP650/670) and the infrared region (such as iRFP) are becoming popular because they are more efficiently excited and detected in living tissues, where light scattering, autofluorescence and absorption are highest at lower wavelengths. These proteins have so far been successfully used for whole-body imaging experiments in mice [68–70].

Furthermore, near-infrared dyes are ideal candidates to enable multimodal optical imaging, for example a combination of fluorescence molecular tomography (FMT) modality offering a macroscopic view combined with CLSM or conventional fluorescence microscopy to study the same target at a subcellular resolution level. While red fluorophores are currently imaged through confocal microscopy, optical parametric oscillator (OPO) technology is making red and far-red fluorophores amenable to TPLSM [71], the ideal IVM modality as it reduces phototoxicity and increases contrast and resolution especially at higher tissue depths. Future generations of OPO technology are more flexible because of a continuous power output at the full tuning range (from 800 to 1300 nm) and as such are more easy to use and will further contribute to make the family of near-infrared fluorophores more easily detectable with multiphoton excitation. Moreover, the optical hardware will be further improved to enhance the sensitivity of near-infrared emission. Alternatively, the development of fluorophores that are excitable by short wavelengths but emit far red and near-infrared signals provides an ideal labelling strategy for IVM. Keima as well as LSS-mKate1 and LSS-mKate2 are proteins engineered with a large Stokes shift, e.g., to absorb similarly to CFP but emit above 600 nm, and other fluorescent proteins could be similarly engineered to allow two-photon excitation [72].

Superresolution microscopy or optical nanoscopy modalities offer resolving powers beyond the diffraction limit of light as described by Ernst Abbe in 1873 [73, 74]. For IVM, stimulated emission depletion (STED) and reversible saturable optical fluorescence transitions (RESOLFT) are of interest because of the fast acquisition rates while lacking the need for extensive post processing of the data to reconstruct a resultant image, as with other nanoscopy modalities (Fig. 1b) [75]. STED makes use of a "donut shaped" fluorescence depletion laser(s) that is overlapping the excitation laser(s) in order to reduce the volume of the emitted light area (point spread function engineering). Since STED microscopy is based on (fast) confocal laser scanning microscopic systems, it holds potential for multidimensional in vivo applications [76, 77]. However, since STED only yields fluorescence emission from a very small focus volume and the nanometer resolution requires the use of smaller pixels to match the Nyquist criterion, it is uncertain if one can detect sufficient amounts of photons per pixel for image reconstruction at the higher imaging rates that are desired for intravital imaging. Moreover, since the resolution improvement amongst others depends on the power of the "donut" depletion laser(s), it will only occur at limited depths since scattering and light absorption will deteriorate the image quality with increasing depth. Currently, commercially available STED systems appear not yet suited for IVM. Nevertheless the ongoing development of the hardware such as stronger red-shifted depletion lasers, dedicated

STED water immersion objectives, and improved detection sensitivity STED has potential for future application in IVM. Moreover the development of dedicated STED dyes [78] and improved sample preparation will further improve the applicability of STED in general but also its performance in vivo. Another promising nanoscopic modality for intravital application is RESOLFT [79, 80], a combination of point spread function engineering with switchable fluorophores [81]. A parallelized scanning RESOLFT system offers a (targeted) large field of nanoscopy with much lower light intensities as compared with STED which are strong assets for high resolution in vivo imaging [80, 82]. Moreover, the first commercial RESOLFT systems are now available which makes the modality more easily accessible for atherosclerotic research groups. However, since RESOLFT requires the use of reversible switchable fluorescent proteins (rsFPs) its future applicability for intravital imaging will mainly depend on the availability of more rsFPs and their possible incorporation in transgenic (mouse) models [83].

An exciting new development for in vivo studying of the macro- and microcirculation is opto-acoustic microscopy (Fig. 1b). In opto-acoustic imaging, ultrasounds, generated from the absorption of light energy, are used to map the optical absorption in tissues [84]. This combines the contrast and versatility of contrast agents and molecular markers designed for optical imaging, with the low scattering and diffusion of ultrasonic waves deep in tissues, thus achieving high-resolution 3-dimensional (3D) imaging of optical absorption at depths beyond the optical limits, even in diffusive tissue. Opto-acoustics is a multiscale imaging modality, where the resolution can be tailored to the degree and penetration depths required. It can be utilized for macroscopic, mesoscopic and microscopic preclinical and clinical applications [85–92]. Microscopic opto-acoustics describes the opto-acoustic signal generated from an optically focused beam. Since focused optical beams (lasers) are used, the spatial resolution is defined by the characteristics of the optical focusing system such as the wavelength of excitation and the characteristics of the objective lens (<1 μm), whereas the axial resolution is still defined by the bandwidth of the ultrasound transducer (5–10 μm; [93]). Opto-acoustic microscopy enables studying of the absorption properties of biological tissue on a microscopic level. Combined with an optical modality such as TPLSM, new hybrid imaging modalities is created that can detect multiple contrast mechanisms simultaneously [90]. Thus, opto-acoustic modalities hold great potential for in vivo imaging of the circulation. The possibility to collect both intrinsic (absorption properties of the various tissues) and extrinsic (fluorophores) information offers high flexibility and specificity. Moreover, its greatly improved depth penetration may enable less invasive preparation procedures and its multiscale character will boost validation of novel treatment targets from discovery up to preclinical level.

Intravascular 2D-near-infrared fluorescence (2D-NIRF) holds great potential for clinical applications and is also compatible with some experimental models of atherosclerosis due to its thin and flexible optical fiber (<0.5 mm) [94, 95]. 2D-NIRF makes use of far-red-shifted fluorophores for improved penetration depths and enables studying of atherosclerosis from a luminal point of view in vivo in the aortic root and arch as well as large arteries, which have until recently been inaccessible to high-resolution imaging. However, it remains to be seen if the fiber does not influence the in vivo environment too much by damaging the endothelial lining or altering the blood flow in the more commonly used experimental models for atherosclerosis (e.g., mouse models).

Acknowledgements

The work of the authors' is supported by the DFG (SO876/3-1, SO876/6-1, SFB914 TP B08, SFB1123 TPs A06, B05, Z01, INST409/97-1), the Else Kröner Fresenius Stiftung, the NWO (VIDI project 91712303), the LMUexcellence, and the FöFoLe program of the LMU Munich.

Conflict of interest

None declared.

References

1. Aulchenko YS, Ripatti S, Lindqvist I et al (2009) Loci influencing lipid levels and coronary heart disease risk in 16 European population cohorts. Nat Genet 41:47–55
2. Willer CJ, Sanna S, Jackson AU et al (2008) Newly identified loci that influence lipid concentrations and risk of coronary artery disease. Nat Genet 40:161–169
3. Soehnlein O, Drechsler M, Hristov M et al (2009) Functional alterations of myeloid cell subsets in hyperlipidaemia: relevance for atherosclerosis. J Cell Mol Med 13:4293–4303
4. Weber C, Noels H (2011) Atherosclerosis: current pathogenesis and therapeutic options. Nat Med 17:1410–1422
5. Drechsler M, Megens RT, van Zandvoort M et al (2010) Hyperlipidemia-triggered neutrophilia promotes early atherosclerosis. Circulation 122:1837–1845
6. Soehnlein O, Drechsler M, Doring Y et al (2013) Distinct functions of chemokine receptor axes in the atherogenic mobilization and recruitment of classical monocytes. EMBO Mol Med 5:471–481
7. Wantha S, Alard JE, Megens RT et al (2013) Neutrophil-derived cathelicidin promotes adhesion of classical monocytes. Circ Res 112:792–801
8. Doring Y, Drechsler M, Wantha S et al (2012) Lack of neutrophil-derived cramp reduces atherosclerosis in mice. Circ Res 110:1052–1056
9. Soehnlein O, Xie X, Ulbrich H et al (2005) Neutrophil-derived heparin-binding protein (hbp/cap37) deposited on endothelium enhances monocyte arrest under flow conditions. J Immunol 174:6399–6405
10. Llodra J, Angeli V, Liu J et al (2004) Emigration of monocyte-derived cells from atherosclerotic lesions characterizes regressive, but not progressive, plaques. Proc Natl Acad Sci U S A 101:11779–11784
11. Robbins CS, Hilgendorf I, Weber GF et al (2013) Local proliferation dominates lesional macrophage accumulation in atherosclerosis. Nat Med 19:1166–1172
12. Eriksson EE (2011) Intravital microscopy on atherosclerosis in apolipoprotein e-deficient mice establishes microvessels as major entry pathways for leukocytes to advanced lesions. Circulation 124:2129–2138
13. Hellings WE, Peeters W, Moll FL et al (2010) Composition of carotid atherosclerotic plaque

is associated with cardiovascular outcome: a prognostic study. Circulation 121:1941–1950

14. Sluimer JC, Kolodgie FD, Bijnens AP et al (2009) Thin-walled microvessels in human coronary atherosclerotic plaques show incomplete endothelial junctions relevance of compromised structural integrity for intraplaque microvascular leakage. J Am Coll Cardiol 53: 1517–1527
15. Silvestre-Roig C, de Winther MP, Weber C et al (2014) Atherosclerotic plaque destabilization: mechanisms, models, and therapeutic strategies. Circ Res 114:214–226
16. Lee S, Vinegoni C, Feruglio PF et al (2012) Real-time in vivo imaging of the beating mouse heart at microscopic resolution. Nat Commun 3:1054
17. Lammermann T, Afonso PV, Angermann BR et al (2013) Neutrophil swarms require ltb4 and integrins at sites of cell death in vivo. Nature 498:371–375
18. Looney MR, Thornton EE, Sen D et al (2011) Stabilized imaging of immune surveillance in the mouse lung. Nat Methods 8:91–96
19. Leuschner F, Panizzi P, Chico-Calero I et al (2010) Angiotensin-converting enzyme inhibition prevents the release of monocytes from their splenic reservoir in mice with myocardial infarction. Circ Res 107:1364–1373
20. van Gestel MA, Heemskerk JW, Slaaf DW et al (2003) In vivo blockade of platelet adp receptor p2y12 reduces embolus and thrombus formation but not thrombus stability. Arterioscler Thromb Vasc Biol 23:518–523
21. Proebstl D, Voisin MB, Woodfin A et al (2012) Pericytes support neutrophil subendothelial cell crawling and breaching of venular walls in vivo. J Exp Med 209:1219–1234
22. Soehnlein O, Zernecke A, Eriksson EE et al (2008) Neutrophil secretion products pave the way for inflammatory monocytes. Blood 112:1461–1471
23. Kempf T, Zarbock A, Widera C et al (2011) Gdf-15 is an inhibitor of leukocyte integrin activation required for survival after myocardial infarction in mice. Nat Med 17:581–588
24. Megens RT, Reitsma S, Prinzen L et al (2010) In vivo high-resolution structural imaging of large arteries in small rodents using two-photon laser scanning microscopy. J Biomed Opt 15:011108
25. Reitsma S, Oude Egbrink MG, Heijnen VV et al (2011) Endothelial glycocalyx thickness and platelet-vessel wall interactions during atherogenesis. Thromb Haemost 106:939–946
26. Soehnlein O, Wantha S, Simsekyilmaz S et al (2011) Neutrophil-derived cathelicidin protects from neointimal hyperplasia. Sci Transl Med 3:103ra198
27. Lutgens E, Lievens D, Beckers L et al (2010) Deficient cd40-traf6 signaling in leukocytes prevents atherosclerosis by skewing the immune response toward an antiinflammatory profile. J Exp Med 207:391–404
28. Massberg S, Gawaz M, Gruner S et al (2003) A crucial role of glycoprotein VI for platelet recruitment to the injured arterial wall in vivo. J Exp Med 197:41–49
29. Yipp BG, Petri B, Salina D et al (2012) Infection-induced netosis is a dynamic process involving neutrophil multitasking in vivo. Nat Med 18:1386–1393
30. Wilson T (2010) Spinning-disk microscopy systems. Cold Spring Harb Protoc 2010:pdb. top88
31. Fan GY, Fujisaki H, Miyawaki A et al (1999) Video-rate scanning two-photon excitation fluorescence microscopy and ratio imaging with cameleons. Biophys J 76:2412–2420
32. Chevre R, Gonzalez-Granado JM, Megens RT et al (2014) High-resolution imaging of intravascular atherogenic inflammation in live mice. Circ Res 114:770–779
33. van Zandvoort M, Engels W, Douma K et al (2004) Two-photon microscopy for imaging of the (atherosclerotic) vascular wall: a proof of concept study. J Vasc Res 41:54–63
34. Niesner RA, Andresen V, Gunzer M (2008) Intravital two-photon microscopy: focus on speed and time resolved imaging modalities. Immunol Rev 221:7–25
35. Kurtz R, Fricke M, Kalb J et al (2006) Application of multiline two-photon microscopy to functional in vivo imaging. J Neurosci Methods 151:276–286
36. Denk W, Strickler JH, Webb WW (1990) Two-photon laser scanning fluorescence microscopy. Science 248:73–76
37. Janssen BJ, De Celle T, Debets JJ et al (2004) Effects of anesthetics on systemic hemodynamics in mice. Am J Physiol Heart Circ Physiol 287:H1618–H1624
38. Kreisel D, Nava RG, Li W et al (2010) In vivo two-photon imaging reveals monocyte-dependent neutrophil extravasation during pulmonary inflammation. Proc Natl Acad Sci U S A 107:18073–18078
39. Lockett AD, Brown MB, Santos-Falcon N et al (2014) Active trafficking of alpha 1 antitrypsin across the lung endothelium. PLoS One 9: e93979
40. Rademakers T, Douma K, Hackeng TM et al (2013) Plaque-associated vasa vasorum in aged apolipoprotein e-deficient mice exhibit

proatherogenic functional features in vivo. Arterioscler Thromb Vasc Biol 33:249–256

41. Schmitt MM, Megens RT, Zernecke A et al (2014) Endothelial junctional adhesion molecule-a guides monocytes into flow-dependent predilection sites of atherosclerosis. Circulation 129:66–76
42. Megens RT, Vijayan S, Lievens D et al (2012) Presence of luminal neutrophil extracellular traps in atherosclerosis. Thromb Haemost 107:597–598
43. Reutelingsperger CP, Dumont E, Thimister PW et al (2002) Visualization of cell death in vivo with the annexin a5 imaging protocol. J Immunol Methods 265:123–132
44. Yu W, Braz JC, Dutton AM et al (2007) In vivo imaging of atherosclerotic plaques in apolipoprotein e deficient mice using nonlinear microscopy. J Biomed Opt 12:054008
45. Nahrendorf M, Swirski FK (2014) Fluorescent leukocytes enter plaque on the microscope stage. Circ Res 114:740–741
46. Jung S, Aliberti J, Graemmel P et al (2000) Analysis of fractalkine receptor cx(3)cr1 function by targeted deletion and green fluorescent protein reporter gene insertion. Mol Cell Biol 20:4106–4114
47. Tacke F, Alvarez D, Kaplan TJ et al (2007) Monocyte subsets differentially employ ccr2, ccr5, and cx3cr1 to accumulate within atherosclerotic plaques. J Clin Invest 117:185–194
48. Saederup N, Cardona AE, Croft K et al (2010) Selective chemokine receptor usage by central nervous system myeloid cells in ccr2-red fluorescent protein knock-in mice. PLoS One 5:e13693
49. Abe T, Sakaue-Sawano A, Kiyonari H et al (2013) Visualization of cell cycle in mouse embryos with fucci2 reporter directed by rosa26 promoter. Development 140:237–246
50. Livet J, Weissman TA, Kang H et al (2007) Transgenic strategies for combinatorial expression of fluorescent proteins in the nervous system. Nature 450:56–62
51. Stockholm D, Bartoli M, Sillon G et al (2005) Imaging calpain protease activity by multiphoton fret in living mice. J Mol Biol 346: 215–222
52. Kardash E, Reichman-Fried M, Maitre JL et al (2010) A role for rho gtpases and cell-cell adhesion in single-cell motility in vivo. Nat Cell Biol 12:47–53, sup pp 1–11
53. Kedrin D, Gligorijevic B, Wyckoff J et al (2008) Intravital imaging of metastatic behavior through a mammary imaging window. Nat Methods 5:1019–1021
54. Victora GD, Schwickert TA, Fooksman DR et al (2010) Germinal center dynamics revealed by multiphoton microscopy with a photoactivatable fluorescent reporter. Cell 143:592–605
55. Last'ovicka J, Budinsky V, Spisek R et al (2009) Assessment of lymphocyte proliferation: Cfse kills dividing cells and modulates expression of activation markers. Cell Immunol 256:79–85
56. Parish CR (1999) Fluorescent dyes for lymphocyte migration and proliferation studies. Immunol Cell Biol 77:499–508
57. Zhao H, Traganos F, Dobrucki J et al (2009) Induction of DNA damage response by the supravital probes of nucleic acids. Cytometry A 75:510–519
58. Mempel TR, Pittet MJ, Khazaie K et al (2006) Regulatory t cells reversibly suppress cytotoxic t cell function independent of effector differentiation. Immunity 25:129–141
59. Horan PK, Slezak SE (1989) Stable cell membrane labelling. Nature 340:167–168
60. Lo Celso C, Fleming HE, Wu JW et al (2009) Live-animal tracking of individual haematopoietic stem/progenitor cells in their niche. Nature 457:92–96
61. Joseph C, Quach JM, Walkley CR et al (2013) Deciphering hematopoietic stem cells in their niches: a critical appraisal of genetic models, lineage tracing, and imaging strategies. Cell Stem Cell 13:520–533
62. Chiang EY, Hidalgo A, Chang J et al (2007) Imaging receptor microdomains on leukocyte subsets in live mice. Nat Methods 4:219–222
63. Daley JM, Thomay AA, Connolly MD et al (2008) Use of ly6g-specific monoclonal antibody to deplete neutrophils in mice. J Leukoc Biol 83:64–70
64. Wang JX, Bair AM, King SL et al (2012) Ly6g ligation blocks recruitment of neutrophils via a beta2-integrin-dependent mechanism. Blood 120:1489–1498
65. Kunkel EJ, Chomas JE, Ley K (1998) Role of primary and secondary capture for leukocyte accumulation in vivo. Circ Res 82:30–38
66. Moreau HD, Lemaitre F, Terriac E et al (2012) Dynamic in situ cytometry uncovers t cell receptor signaling during immunological synapses and kinapses in vivo. Immunity 37:351–363
67. Zhao W, Schafer S, Choi J et al (2011) Cell-surface sensors for real-time probing of cellular environments. Nat Nanotechnol 6:524–531
68. Shcherbo D, Shemiakina II, Ryabova AV et al (2010) Near-infrared fluorescent proteins. Nat Methods 7:827–829
69. Shu X, Royant A, Lin MZ et al (2009) Mammalian expression of infrared fluorescent

proteins engineered from a bacterial phytochrome. Science 324:804–807

70. Filonov GS, Piatkevich KD, Ting LM et al (2011) Bright and stable near-infrared fluorescent protein for in vivo imaging. Nat Biotechnol 29:757–761
71. Herz J, Siffrin V, Hauser AE et al (2010) Expanding two-photon intravital microscopy to the infrared by means of optical parametric oscillator. Biophys J 98:715–723
72. Kawano H, Kogure T, Abe Y et al (2008) Two-photon dual-color imaging using fluorescent proteins. Nat Methods 5:373–374
73. Abbe E (1873) Ueber einen neuen beleuchtungsapparat am mikroskop. In: Schultze M (ed) Archive für mikrosckopische anatomie. Verlag von Max Cohen Sohn, Bonn, pp 469–481
74. Hell SW (2007) Far-field optical nanoscopy. Science 316:1153–1158
75. Muller T, Schumann C, Kraegeloh A (2012) Sted microscopy and its applications: new insights into cellular processes on the nanoscale. ChemPhysChem 13:1986–2000
76. Lauterbach MA, Keller J, Schonle A et al (2010) Comparing video-rate sted nanoscopy and confocal microscopy of living neurons. J Biophotonics 3:417–424
77. Berning S, Willig KI, Steffens H et al (2012) Nanoscopy in a living mouse brain. Science 335:551
78. Wurm CA, Kolmakov K, Göttfert F et al (2012) Novel red fluorophores with superior performance in sted microscopy. Opt Nanoscopy 1:1–7
79. Lavoie-Cardinal F, Jensen NA, Westphal V et al (2014) Two-color resolft nanoscopy with green and red fluorescent photochromic proteins. ChemPhysChem 15:655–663
80. Grotjohann T, Testa I, Leutenegger M et al (2011) Diffraction-unlimited all-optical imaging and writing with a photochromic gfp. Nature 478:204–208
81. Grotjohann T, Testa I, Reuss M et al (2012) Rsegfp2 enables fast resolft nanoscopy of living cells. eLife 1:e00248
82. Chmyrov A, Keller J, Grotjohann T et al (2013) Nanoscopy with more than 100,000 'doughnuts'. Nat Methods 10:737–740
83. Nienhaus K, Nienhaus GU (2014) Fluorescent proteins for live-cell imaging with super-resolution. Chem Soc Rev 43:1088–1106
84. Ntziachristos V, Razansky D (2010) Molecular imaging by means of multispectral optoacoustic tomography (msot). Chem Rev 110:2783–2794
85. Buehler A, Herzog E, Razansky D et al (2010) Video rate optoacoustic tomography of mouse kidney perfusion. Opt Lett 35:2475–2477
86. Ma R, Taruttis A, Ntziachristos V et al (2009) Multispectral optoacoustic tomography (msot) scanner for whole-body small animal imaging. Opt Express 17:21414–21426
87. Razansky D, Vinegoni C, Ntziachristos V (2009) Imaging of mesoscopic-scale organisms using selective-plane optoacoustic tomography. Phys Med Biol 54:2769–2777
88. Razansky D, Deliolanis NC, Vinegoni C et al (2012) Deep tissue optical and optoacoustic molecular imaging technologies for pre-clinical research and drug discovery. Curr Pharm Biotechnol 13:504–522
89. Omar M, Gateau J, Ntziachristos V (2013) Raster-scan optoacoustic mesoscopy in the 25-125 mhz range. Opt Lett 38:2472–2474
90. Tserevelakis GJ, Soliman D, Omar M et al (2014) Hybrid multiphoton and optoacoustic microscope. Opt Lett 39:1819–1822
91. Taruttis A, Ntziachristos V (2012) Translational optical imaging. AJR Am J Roentgenol 199:263–271
92. Ntziachristos V, Razansky D (2013) Optical and opto-acoustic imaging. Recent Results Cancer Res 187:133–150
93. Yao J, Wang LV (2013) Photoacoustic microscopy. Laser Photon Rev 7:758
94. Jaffer FA, Calfon MA, Rosenthal A et al (2011) Two-dimensional intravascular near-infrared fluorescence molecular imaging of inflammation in atherosclerosis and stent-induced vascular injury. J Am Coll Cardiol 57:2516–2526
95. Calfon MA, Rosenthal A, Mallas G, et al (2011) In vivo near infrared fluorescence (nirf) intravascular molecular imaging of inflammatory plaque, a multimodal approach to imaging of atherosclerosis. J Vis Exp (54):e2257
96. Sasmono RT, Oceandy D, Pollard JW et al (2003) A macrophage colony-stimulating factor receptor-green fluorescent protein transgene is expressed throughout the mononuclear phagocyte system of the mouse. Blood 101:1155–1163
97. Faust N, Varas F, Kelly LM et al (2000) Insertion of enhanced green fluorescent protein into the lysozyme gene creates mice with green fluorescent granulocytes and macrophages. Blood 96:719–726
98. Boes M, Cerny J, Massol R et al (2002) T-cell engagement of dendritic cells rapidly rearranges mhc class ii transport. Nature 418:983–988

Chapter 4

Noninvasive Molecular Imaging of Mouse Atherosclerosis

Martina A. McAteer and Robin P. Choudhury

Abstract

Molecular imaging offers great potential for noninvasive visualization and quantitation of the cellular and molecular components involved in atherosclerotic plaque stability. In this chapter, we review emerging molecular imaging modalities and approaches for quantitative, noninvasive detection of early biological processes in atherogenesis, including vascular endothelial permeability, endothelial adhesion molecule up-regulation, and macrophage accumulation, with special emphasis on mouse models. We also highlight a number of targeted imaging nanomaterials for assessment of advanced atherosclerotic plaques, including extracellular matrix degradation, proteolytic enzyme activity, and activated platelets using mouse models of atherosclerosis. The potential for clinical translation of molecular imaging nanomaterials for assessment of atherosclerotic plaque biology, together with multimodal approaches is also discussed.

Key words Adhesion molecules, Atherosclerosis, Inflammation, Magnetic resonance imaging, Molecular imaging

1 Introduction

Early detection of atherosclerosis may help to prevent clinical sequelae such as acute myocardial infarction (MI) and ischemic stroke. Conventional clinical imaging using X-ray angiography can accurately detect advanced atherosclerotic plaques that cause arterial luminal stenosis. However, most acute coronary events are caused by rupture or erosion of non-flow-limiting vulnerable plaques [1], which are not readily identified by X-ray angiography. Vulnerable plaques typically exhibit high level of inflammation and are classically characterized by a thin fibrous cap overlying a large lipid core and macrophage accumulation in the shoulder regions of the plaque [2, 3]. However, disruption of the arterial endothelium overlying atherosclerotic plaques rich in smooth muscle cells and extracellular matrix, with a relative paucity of inflammation, macrophages, and extracellular lipid, may also result in 8–30 % of acute coronary events [4]. This complexity and heterogeneous nature of atherosclerotic plaques requires the development of sensitive, diagnostic tools for noninvasive characterization of atherosclerotic

Vicente Andrés and Beatriz Dorado (eds.), *Methods in Mouse Atherosclerosis*, Methods in Molecular Biology, vol. 1339, DOI 10.1007/978-1-4939-2929-0_4,

disease and monitoring of responses to therapeutic interventions. Noninvasive characterization of atherosclerotic plaques can be achieved using magnetic resonance imaging (MRI), positron emission tomography (PET) or single-photon emission computed tomography (SPECT). Multi-slice computed tomography (CT) can discriminate calcified and non-calcified plaque burden but has low sensitivity for soft plaque characterization. Invasive imaging techniques, such as intravascular ultrasound (IVUS) and optical coherence tomography (OCT), are also used for characterizing atherosclerotic plaque composition [5–9], but do not readily report specifically on the molecular processes that drive atherosclerotic lesion development.

Genetically engineered hyperlipidemic mice, such as the apolipoprotein E knockout (apoE$^{-/-}$) and LDL-receptor knockout (LDLR$^{-/-}$) mice, have become the preeminent animal models for studies into the mechanisms driving the progression and regression of atherosclerosis [10]. The disease develops predictably at atherosclerosis-susceptible sites in the aorta including the aortic root, the inner curvature of the aortic arch and its branch points and later in the abdominal aorta [11, 12]. The brachiocephalic artery in fat-fed apoE$^{-/-}$ mice has been reported to develop advanced plaques, with features suggestive of fibrous cap disruption and intra-plaque hemorrhage [13–16]. The rapid development of atherosclerotic disease, accelerated by high-fat feeding in mice enables studies to be undertaken in months, in contrast with the human disease, which progresses over decades. Murine models have emphasized the central role of inflammation in atherogenesis and have been instrumental in the identification of molecular and cellular processes such as adhesion molecule up-regulation and monocyte recruitment to the vessel wall, as well as macrophage scavenger receptors, chemokines, and other macrophage activation receptors [17].

Appreciation of the molecular and cellular processes of atherosclerosis, thrombosis, and vascular inflammation has led to the identification of new targets for imaging. The goals of molecular imaging are to accelerate and refine diagnosis of the disease, provide insights into disease diversity and to guide and monitor therapeutic interventions [18]. Rapid advances in nanotechnology have led to the development of an array of imaging contrast agents, which can be functionalized with targeting ligands, such as antibodies, peptides, or aptamers for molecular imaging of biomarkers. In this chapter, we review molecular imaging modalities and approaches for noninvasive detection of mouse atherogenesis including vascular endothelial permeability, adhesion molecule up-regulation, and macrophage accumulation. We also highlight strategies for molecular imaging of biomarkers of advanced atherosclerosis including extracellular matrix (ECM) degradation, proteolytic enzymes, and activated platelets.

2 Imaging modalities

Molecular imaging modalities include MRI, nuclear imaging, contrast-enhanced ultrasound (CEU), and optical or fluorescence imaging techniques. Nuclear imaging using PET or SPECT allows quantitative measurements of atherosclerotic plaques with high sensitivity. PET has higher temporal resolution and sensitivity relative to SPECT, and can detect radiotracers such as ^{18}F in the nanomolar (10^{-9} M) to picomolar (10^{-12} M) range. Although PET is highly sensitive, the poor yield of anatomical information requires co-evaluation with another imaging modality, usually CT (PET-CT) or MRI (PET-MRI). Current clinical PET imaging approaches use exogenously administered radionuclides, such as 2-[^{18}F]-fluoro-2-deoxy-D-glucose (FDG), a glucose analogue that has been shown to accumulate in metabolically active tissue, yielding a signal that is proportional to local glycolytic activity. FDG has been shown to accumulate in macrophage-rich atherosclerotic plaques by PET imaging [19] and can detect foam cell formation in vitro [20] and in vivo [21]. FDG has also been shown by SPECT/CT to track glucose uptake in macrophages and co-localizes with macrophage-rich inflamed sites in atherosclerosis in mice and humans [22]. However, FDG may be taken up by other metabolically active cell types such as polymorphonuclear leukocytes [23]. Furthermore, in vitro studies suggest that FDG accumulation by macrophages may reflect hypoxia rather than inflammation per se [24]. Recently, radioactive tracer ^{18}F-sodium fluoride was reported to enable detection more sensitive detection of unstable plaques in human carotid and coronary arteries by in vivo PET-CT imaging than FDG, which tracked with the process of active calcification [25]. SPECT and PET imaging modalities however remain limited by their substantial ionizing radiation exposure, poor spatial resolution, expense, and relatively cumbersome reagents of finite longevity and there is an additional constraint of limited availability of PET hardware.

Contrast-enhanced ultrasound (CEU) is an easily accessible, low-cost technique that has been applied for molecular imaging of vascular inflammation in atherosclerosis [26–28] and activated platelets in advanced atherosclerotic plaques [29] in mice using targeted microbubbles. However, CEU is inherently limited by the need for acoustic windows and ultrasound cannot reliably penetrate bony structures. Optical imaging such as OCT provides high spatial resolution real-time images, at relatively low cost and does not expose the patient to ionizing radiation. However, OCT cannot penetrate beyond a soft tissue depth of ~1 mm [30]. Photoacoustic tomography (PAT), also known as optoacoustic tomography, is a hybrid imaging modality that provides stronger optical absorption contrast with high ultrasonic resolution [30].

Gold nanoparticles (GNPs) have shown promise as PAT contrast agents due to their optically tunable properties in the NIR region. GNPs have allowed in vivo PAT imaging of macrophage accumulation [31] and targeted detection of VCAM-1 in mouse atherosclerosis [32]. Fluorescence imaging techniques in the near-infrared spectrum (NIR) combine low autofluorescence and useful tissue penetration (millimetres to centimeters) for imaging arteries in mice.

MRI is the leading noninvasive imaging modality for assessment of atherosclerotic plaques as it can provide high spatial (submillimeter) and temporal resolution images of the vessel wall, with excellent soft tissue contrast without ionizing radiation. The inherent low sensitivity of MRI can be improved by using paramagnetic gadolinium (Gd) or super-paramagnetic iron oxide contrast agents that enhance the T_1 or T_2 MRI contrast effects, respectively. Hybrid imaging modalities using combinations of PET-MRI, MRI-optical imaging, or PET-CT are also being developed. The integration or combination of imaging modalities and the development of multimodal contrast agents offer the potential to overcome the sensitivity and resolution limitations that a single imaging approach may have. For example, PET-MRI offers the possibility to integrate the highly sensitive PET images with high-resolution anatomical images provided by MRI to define the anatomical origin of radioactive PET signals, with high spatial resolution and without the use of additional radiolabels.

3 MRI Gadolinium-Based Contrast Agents

Paramagnetic Gd chelates shorten T_1 longitudinal relaxation times, providing positive contrast on T_1-weighted MR images. Conventional Gd chelates confer relatively low sensitivity (in the micromolar range), which is usually inadequate for molecular imaging applications. To overcome this, Gd-based nanoparticles which carry substantial payloads of amphipathic Gd chelates embedded in their outer membrane have been developed. These include liposomes [33], perfluorocarbon lipid emulsions [34], micelles [35, 36], and high-density lipoprotein (HDL)-like nanoparticles [37, 38] which have demonstrated potential for molecular MRI of abundant targets such as macrophages in atherosclerotic lesions as well as fibrin-rich clots. HDL-like particles have the advantages of being endogenous and biodegradable, do not trigger immune reactions and are not recognized by the reticulo-endothelial system [39–43]. Gd-based agents conjugated to Sialyl Lewis^x (sLe^X) have been reported to detect early endothelial activation of E-selectin by in vivo MRI [44]. Detection of intercellular adhesion molecule-1 (ICAM-1) has also been reported by ex vivo MRI (9.4 T) using antibody-conjugated paramagnetic liposomes [45]. However, the quantities of Gd that can be delivered to

the endothelial monolayer and the T_1 positive MRI contrast effects achievable are relatively modest [46]. Gd chelates has also been shown to increase risk of nephrogenic systemic fibrosis in patients with renal impairment [47, 48]. To address these safety concerns, newer MRI contrast agents use Gd-DOTA instead of gadolinium diethylenetriamine pentaacetic acid (Gd-DTPA) chelates due to the significantly better stability of DOTA chelates [49].

Recently, a target-specific, Gd-based contrast agent gadofosveset has been approved for clinical use [50]. Gadofosveset is an albumin-binding agent which has shown promise for in vivo detection of vascular endothelial permeability, which is increased in the early stages of atherosclerosis, in response to abnormal blood flow or systemic inflammation [51]. Gadofosveset reversibly binds to serum albumin in the blood and can enter the vessel wall through leaky neovessels or damaged endothelium, thus acting as a surrogate marker for endothelial permeability. Gadofosveset has been shown to detect increased plaque burden, endothelial permeability, and widening of the gap junctions in the brachiocephalic artery of $ApoE^{-/-}$ mice fed a high-fat diet by delayed enhancement MRI, while $ApoE^{-/-}$ mice treated with statins showed reduced endothelial damage and plaque burden [52]. Gadofosveset has also been applied to monitor the efficacy of the tetracycline antibiotic minocycline and the synthetic antioxidant ebselen, in reducing vascular endothelial permeability and plaque burden in the brachiocephalic artery of $ApoE^{-/-}$ mice using delayed enhancement MRI (Fig. 1) [53]. Flow cytometry confirmed that both treatments reduced the monocyte/macrophage content within the brachiocephalic artery, with significant attenuation of the pro-inflammatory Ly6C high subtype of monocytes. This clinically approved contrast agent shows promise for screening interventions to reduce endothelial permeability and restore/improve endothelial function in patients with cardiovascular disease.

4 Iron Oxide-Based Contrast Agents

Iron oxide-based contrast agents include nano-sized, ultra-small super-paramagnetic particles of iron oxide (USPIO) (20–50 nm), super-paramagnetic particles of iron oxide (SPIO) (60–250 nm) and micron-sized microparticles of iron oxide (MPIO) (0.9–4.5 μm). These contrast agents create hypo-intense signal or "negative" contrast areas on MR images, by shortening T_2 and T_2^* relaxation times, providing greater MRI contrast sensitivity compared to Gd chelates [54, 55]. USPIO have become popular owing to their long blood half-life compared to Gd agents, which is a positive attribute for applications such as measurement of changes in cerebral perfusion. However, this property may cause high background contrast for an extended period, thus reducing its visibility.

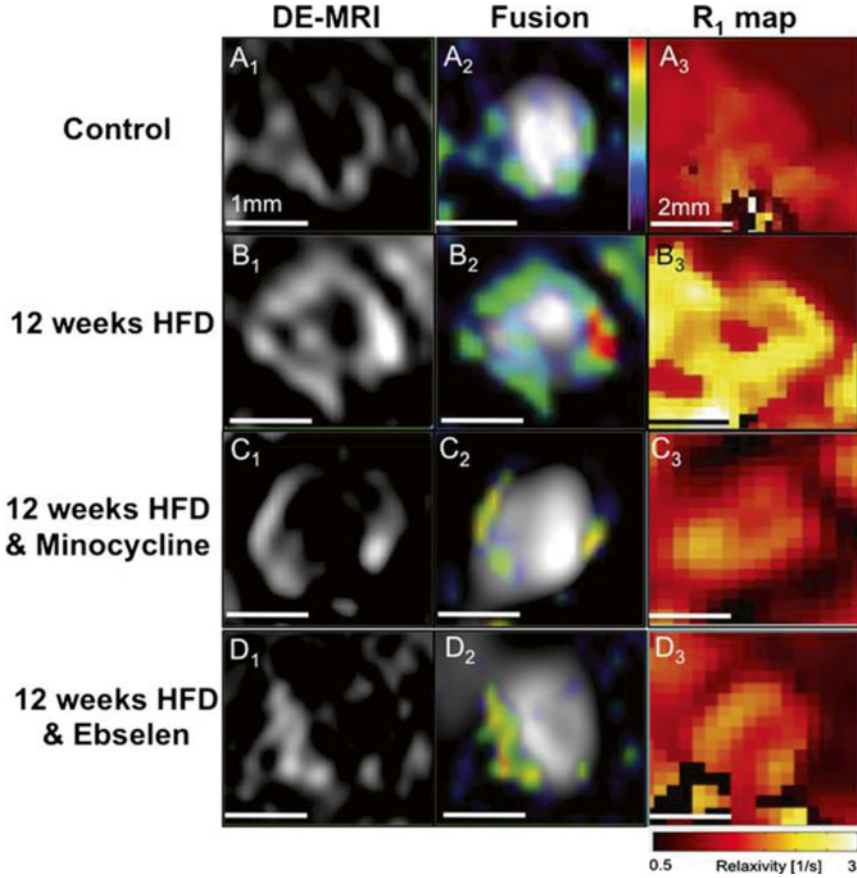

Fig. 1 Treatment with minocycline and ebselen reduced endothelial permeability, plaque burden, and gadofosveset uptake. *A1* through *D1* and *A2* through *D2*, Cross-sectional delayed enhancement magnetic resonance imaging (DE-MRI) fused with magnetic resonance angiography (MRA) images of the brachiocephalic artery. ApoE$^{-/-}$ mice on a high fat diet showed increased vessel wall enhancement corresponding to plaque progression, whereas minocycline- and ebselen-treated ApoE$^{-/-}$ mice showed less enhancement. *A3* through *D3*, Corresponding R1 maps quantify the amount of gadofosveset within the vessel wall. Intense *yellow* signal indicates increased gadofosveset concentration

Furthermore, UPSIO contrast is manifest in T_2*-weighted images as indistinct low-signal areas that may be difficult to distinguish from normal tissue heterogeneity and other susceptibility artifacts. To overcome this limitation, positive contrast techniques have been developed [56], which generate positive MRI signals and improves detection of USPIO accumulation in macrophages [57].

MPIO carry the highest payload of iron oxide (typically 0.1–1.6 pg iron/MPIO particle), which is orders of magnitude greater than nano-sized iron oxide particles [58]. MPIO produce a hypointense contrast "blooming effect" on MR images that extends up to 50 times the physical diameter of the microparticle. This produces strong contrast effects by in vivo MRI enabling detection of

single cells with high sensitivity, using only small numbers of MPIO [59, 60]. The rapid clearance of MPIO from the circulation (within minutes) [61, 62] minimizes background contrast enabling MRI to commence immediately after MPIO administration [63] as opposed to USPIO, which require up to 48 h to clear from the circulation. MPIO are less susceptible to vascular egress or uptake by endothelial cells due to their size and incompressible nature. MPIO can be readily functionalized with single or multiple targeting ligands, such as monoclonal antibodies, peptides or sugar ligands, providing a versatile contrast agent for molecular MRI of endovascular targets such as endothelial adhesion molecules and activated platelets [64].

5 Macrophage imaging

USPIO are typically phagocytosed by plaque-resident or blood-born macrophages and have been shown to accumulate in macrophage-rich atheroma in rabbits [65]. Enhanced USPIO retention has been demonstrated when monocyte recruitment is promoted by cytokine injection in mice [66]. Clinical studies in symptomatic patients scheduled for carotid endarterectomy showed preferential USPIO uptake in macrophage-rich plaques by histology and electron microscopy. USPIO uptake was higher (75 %) in ruptured and rupture-prone lesions compared to stable lesions (7 %) [67]. Targeted MRI of macrophages in atherosclerotic plaques in apoE$^{-/-}$ mice has been achieved using paramagnetic Gd-containing micelles targeted against macrophage scavenger receptor-A (MSR-A) [35]. Bimodal MSR-A-targeted micelles containing Gd chelates and a fluorescent label (either rhodamine-conjugated lipid in the micelle or quantum dots in the micelle corona) have also been developed and applied for in vivo MRI of macrophages in mice. Pronounced MR signal enhancement of up to 200 % was observed in the abdominal aorta of apoE$^{-/-}$ mice injected with MSR-A-targeted micelles, with minimal SE in mice injected with nontargeted micelles [68]. Ex vivo imaging with UV illumination confirmed quantum dot accumulation in regions with high macrophage content.

Nanoparticles conjugated with radiolabeled elements (^{64}Cu, ^{18}F) and/or fluorescent dyes have also been developed for multimodal imaging of macrophages which may decrease the detection threshold and nanoparticle dose required compared to MRI. Nahrendorf and colleagues have synthesized a tri-reporting cross-linked iron oxide nanoparticles (CLIO), decorated with diethylene triamine pentaacetic acid (DTPA) to transchelate radiolabel ^{64}Cu [69]. The ^{64}Cu-CLIO detected macrophages in inflammatory atherosclerotic lesions by PET/SPECT imaging, using an iron dose that was ~100 times lower as compared to MRI. Jarrett et al. have

also designed multimodal nanoparticle probes for PET and MRI containing either Gd or iron oxide conjugated to ^{64}Cu which identified regions of macrophage accumulation in apoE$^{-/-}$ mice with vascular inflammation induced by ligation [70]. The disadvantage of ^{64}Cu is that it is not widely available, whereas ^{18}F is more widely available, and has higher sensitivity, shorter half-life, and the ability of irreversible covalent bonding [71]. PET-CT imaging using ^{18}F-radiolabeled CLIO detected significantly higher PET signal in murine aortic aneurysms compared to normal aorta, due to enhanced uptake by macrophages within the aneurysm [72].

6 Vascular Endothelial Dysfunction in Atherosclerosis

Vascular endothelial dysfunction promotes atherosclerotic lesion development through endothelial activation and increased endothelial permeability, leukocyte and monocyte arterial infiltration, platelet activation, and smooth muscle cell proliferation [73]. The deposition of oxidized low-density lipoprotein in the vascular wall leads to localized endothelial expression of pro-inflammatory cytokines, such as interleukin-1β and tumor necrosis factor-α [74]. The localized increase in cytokine levels results in up-regulation of cell adhesion molecules, such as vascular cell adhesion molecule-1 (VCAM-1), and intercellular adhesion molecule-1 (ICAM-1), as well as P-selectin and E-selectin, expressed on the activated endothelial surface. This in turn promotes monocyte recruitment to the vessel wall, with initial monocyte rolling along activated endothelium mediated by interactions between endothelial P-selectin and its ligand, P-selectin glycoprotein ligand-1 (PSGL-1) integrin, expressed on monocytes. Firm adhesion of monocytes is mediated by VCAM-1 (CD106) and it ligand, very late antigen-4 (VLA-4, also known as $\alpha_4\beta_1$ integrin) [75]. In the following sections, we examine targeted molecular imaging approaches, which harness these adhesion molecule signals used for leukocyte recruitment during atherosclerotic lesion development.

7 Molecular MRI Using VCAM-1-Targeted Nanoparticles

VCAM-1 has been at the center of attention for molecular imaging of vascular inflammation since it is not constitutively expressed on the normal vascular endothelium but is rapidly up-regulated upon endothelial activation. Its endothelial location makes it readily accessible for targeted blood borne contrast agents [76]. VCAM-1 is expressed by vascular endothelial cells in both early and advanced atherosclerotic lesions [77] and is also up-regulated by macrophages and smooth muscle cells in atherosclerotic plaques. The expression of VCAM-1 is confined to predisposed arterial regions

such as the inner curvature of the aortic arch and its bifurcations, which are exposed to disturbed blood flow and low shear stress [78, 79]. Several generations of targeted nanoparticles have been developed for molecular imaging of VCAM-1. The first VCAM-1 targeted nanoparticles were based on CLIO conjugated to either VCAM-1 monoclonal antibody [80] or VCAM-1-targeting peptides, identified by phage display, with homology to VLA-4 [81, 82]. In vivo MRI studies confirmed detection of VCAM-1 expression using VCAM-1-targeted CLIO in a murine ear inflammation model and in the aortic root of atherosclerotic apoE$^{-/-}$ mice fed a high-fat diet [82]. However, these nanoparticles were also susceptible to non-specific uptake by macrophages, due to their small size and long blood clearance time (48 h). USPIO conjugated to a VCAM-1 targeting cyclic peptide, termed P03011, have recently been reported to detect VCAM-1 expression in early and advanced atherosclerotic lesions using in vivo ultrahigh-field strength MRI (17.6 T), with minimal nonspecific macrophage uptake of nontargeted USPIO [83]. The lack of nonspecific uptake of nontargeted USPIO may be due to the shorter blood clearance time or differences in their surface properties, size, or dose compared to previous USPIO studies. VCAM-1-targeted USPIO were observed to co-localize with macrophages, luminal endothelial-like cells and medial smooth muscle cells using high-resolution Stokes Raman scattering (SECARS) microscopy.

USPIO targeted to novel peptides targeting VCAM-1 (USPIO-R832) have also been reported to enable rapid in vivo MRI (4.7 T) detection of aortic VCAM-1 expression in advanced atherosclerotic plaques in apoE$^{-/-}$ mice at ~30 min, which was maintained until 90 min [84]. The use of USPIO (27 nm) covalently conjugated to PEG as opposed to previously reported dextran coated USPIO formulations was reported to act as a stealth coating to reduce nonspecific uptake into atherosclerotic plaques and enable rapid blood clearance. Co-localization of the USPIO-R832 agent was primarily to macrophage-rich areas of advanced atherosclerotic plaques, which is a downstream target compared to endothelial-specific imaging provided by targeted MPIO.

The targeted nanoparticles developed for molecular imaging of VCAM-1 are generally spherical in shape. However, nonspherical nanoparticles may enable improved margination to the vessel wall and therefore enhance presentation of targeting ligands. Bruckman et al. have exploited the elongated tubular structure of the tobacco mosaic plant virus (TMV) (300 × 18 nm) to engineer a novel Gd-based, near-infrared fluorescent nanoparticle, conjugated with VCAM-1-targeting peptides for dual-MRI-optical imaging of VCAM-1 expression in the aorta of atherosclerotic ApoE$^{-/-}$ mice (Fig. 2) [85]. VCAM-TMV were rapidly cleared from the circulation within minutes and reached rapid steady-state accumulation at the target site, with maximal signal-to-noise ratio

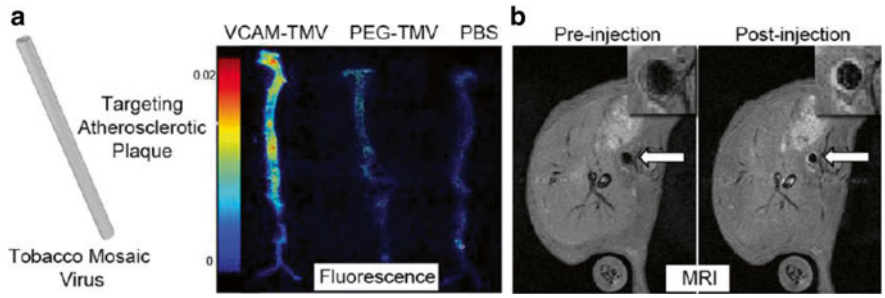

Fig. 2 (**a**) Ex vivo fluorescence of aortas from ApoE$^{-/-}$ mice injected with (from *left* to *right*) VCAM-TMV, PEG-TMV, PBS. (**b**) Pre- and post-injection MRI scans of VCAM-TMV in ApoE$^{-/-}$ mouse. The *inset* is a magnified image of the abdominal aorta region of interest [85]

(SNR) achieved 90 min post-VCAM-TMV injection. The Gd dose of VCAM-TMV was 400 times lower than the Gd dose used for clinical MR angiography, demonstrating the utility of targeted nanoparticle delivery for improved Gd detection. Non-targeted PEG-TMV showed negligible passive accumulation in atherosclerotic aortas by MRI and immunofluorescence imaging confirmed significantly greater VCAM-TMV accumulation at the intima-media interface. However, while these VCAM-1-targeted nanoparticle approaches can give insights into the vascular inflammatory processes in atherosclerosis, they lack specificity for specific cell types and their cellular uptake has potential for toxicity.

8 Molecular Imaging of Endothelial Adhesion Molecules Using Targeted MPIO

Targeted MPIO, due to their large micron size and conspicuous MRI contrast effects, offer a tool for specific targeting of endothelial molecular biomarkers, such as endothelial adhesion molecules [86, 87]. We have developed VCAM-1-targeted MPIO (1 μm diameter) (VCAM-MPIO) and applied them for in vivo MRI of acute cerebral endothelial activation in mice [88]. In vivo T_2*-weighted MR images showed potent, hypo-intense contrast effects in the activated cerebral hemisphere, corresponding to VCAM-MPIO binding, with no contrast effects observed in the non-activated cerebral hemisphere or in animals injected with VCAM-1 blocking antibody. Importantly, this technique also enabled 3-D volumetric mapping of VCAM-MPIO binding throughout the brain at a time when conventional, clinically used MRI techniques do not reveal abnormalities (Fig. 3a) [88]. In addition, inflammatory foci of leukocytes around vessels were shown to be VCAM-MPIO positive but Gd-DTPA negative [89]. Targeted VCAM-MPIO have also been applied for in vivo molecular MRI of endothelial activation following recent ischemia, in mouse

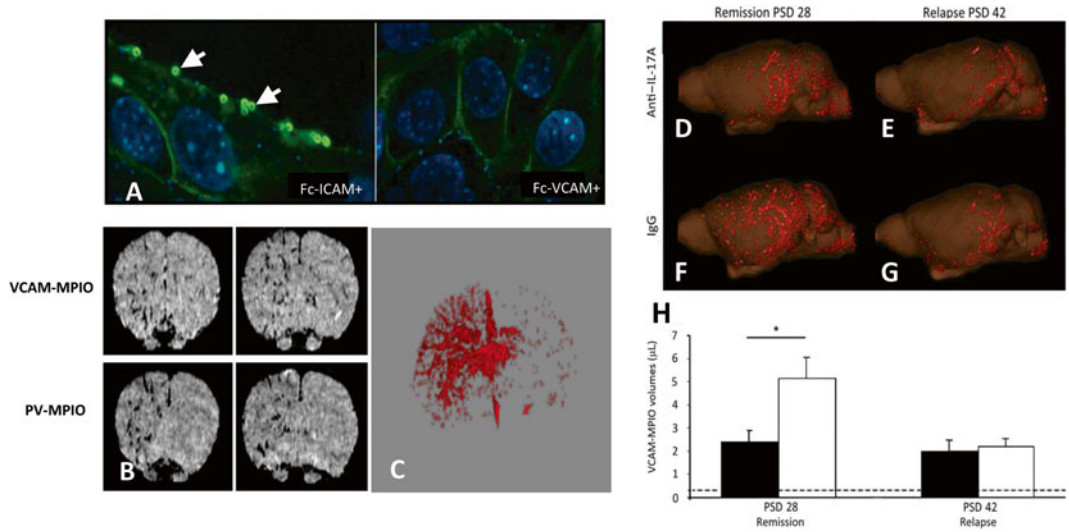

Fig. 3 (**a**) VCAM-MPIO binding (autofluorescent spheres (see *arrows*)) on the surface of sEND-1 cells, stimulated with TNF-α co-localizes with VCAM-1 immunofluorescence. Preincubation of VCAM-MPIO with Fc-VCAM-1 abolished VCAM-MPIO binding, despite cell surface expression of VCAM-1, as confirmed by immunofluorescence while pre-incubation with FcICAM-1 did not inhibit VCAM-MPIO binding. (**b**) T_2*-weighted 3-D gradient echo MR image showing intense low-signal areas on the left IL-1β-stimulated brain hemisphere reflecting specific VCAM-MPIO with virtually absent contrast effects in the contralateral hemisphere. Similar, unilateral contrast effects were observed in mice administered dual-targeted VCAM-1 and P-selectin MPIO (PV-MPIO). (**c**) 3-D volumetric map of segmented VCAM-MPIO contrast delineating the architecture of inflamed cerebral vasculature in the left IL-1β-stimulated hemisphere with absence of binding on the contralateral side [88]. Three-dimensional reconstruction showing that anti-IL-17A treatment of mice with chronic relapsing experimental autoimmune encephalitis (CR-EAE) mice (**d**) exhibited less MPIO binding during remission (post-sensitization day (PSD) 28) than IgG-treated mice (**f**). On PSD 42, no significant differences in MPIO binding were observed (**e** and **g**, respectively). (**h**) A significant reduction in VCAM-MPIO binding in anti-IL-17A-treated animals (*black bars*) was found compared with IgG-treated controls (*white bars*) on PSD 28, but no significant difference was observed on PSD 42. Data are shown as means SEM. *$P < 0.05$. *Dashed lines* represented baseline VCAM-MPIO binding in naive animals

models of unilateral renal ischemia-reperfusion injury (IRI) [90], experimental stroke [91], and myocardial IRI [92]. VCAM-MPIO have also demonstrated efficacy for discriminating reductions in endothelial activation following ischemic pre-conditioning [91] and for monitoring anti-interleukin 17A (IL-17A) therapeutic treatment in a chronic relapsing EAE mouse model [93]. Anti-IL-17A treatment was shown to delay relapse, and improve functional scores, and was associated with reduced VCAM-MPIO binding on the cerebral vasculature during remission compared to IgG treated animals (Fig. 3b). No significant differences in levels of Gd-DTPA- or VCAM-MPIO-positive lesions were observed during relapse. Therefore, VCAM-MPIO may be a more sensitive marker of disease activity than Gd-DTPA.

9 Molecular MRI of adhesion molecules in atherosclerosis

Targeted endovascular imaging of large arteries, such as the aorta, is more challenging since the contrast agent must bind to the endothelial monolayer in sufficient quantity and with high affinity and specificity, under conditions of high shear stress [94]. To address these challenges, we have developed dual-targeted MPIO (4.5 μm diameter), conjugated to VCAM-1 and P-selectin monoclonal antibodies (50:50 ratio) to mimic in vivo leukocyte-binding pathways [95]. Dual-targeted MPIO enabled high-resolution ex vivo MRI (9.4 T) detection of endothelial inflammation in advanced atherosclerotic plaque in the aortic root of apoE$^{-/-}$ mice fed a high-fat diet. However, the numbers of MPIO retained on the aortic root were thought to be insufficient for in vivo molecular MRI using acceptable iron doses. We therefore constructed a second generation of smaller 1 μm diameter, dual-targeted MPIO which we hypothesized would be less buoyant under high shear stress enabling more effective ligand presentation and improved MPIO binding, using lower iron doses [63]. In vitro flow chamber studies confirmed that dual VCAM-1 and P-selectin antibody-conjugated MPIO enabled greater binding affinity and specificity to activated endothelial cells compared to VLA-4 or PSGL-1 integrin-targeted MPIO. Dual-PV-MPIO produced strong signal enhancement post-contrast compared to pre-contrast images. Rapid dual PV-MPIO binding to the aortic root endothelium in chow-fed apoE$^{-/-}$ mice was demonstrated by in vivo MRI (11.7 T), with steady state accumulation reached within 30 min of MPIO injection, and maintained at 60 min (Fig. 4). Dual-PV-MPIO tracked closely with the burden and distribution of plaque macrophages, not merely plaque size, at different stages of lesion development. Flow cytometry of aortas confirmed that dual-ligand MPIO binding was predominantly to VCAM-1-positive endothelial cells. *En face* immunofluorescence microscopy confirmed co-localization of dual-PV-MPIO binding to VCAM-1 positive endothelial cells in the atherosclerosis-susceptible inner curvature of the aortic arch with no MPIO binding observed in the atherosclerosis-resistant outer curvature or descending aorta. MPIO have been shown be sequestered by the liver and spleen, with no evidence of tissue infarction, inflammation, or hemorrhage [95, 96]. Therefore, targeted MPIO offer potential as leukocyte-mimetic agents to track atherosclerotic disease.

A similar approach targeting ultrasound microbubbles to vascular endothelium used a combination of sLe^{X} and ICAM-1 antibody, though binding efficiency was increased only marginally, possibly due to stearic limitation from size mismatch between the two ligands [97]. Dual-targeted approaches have also been applied

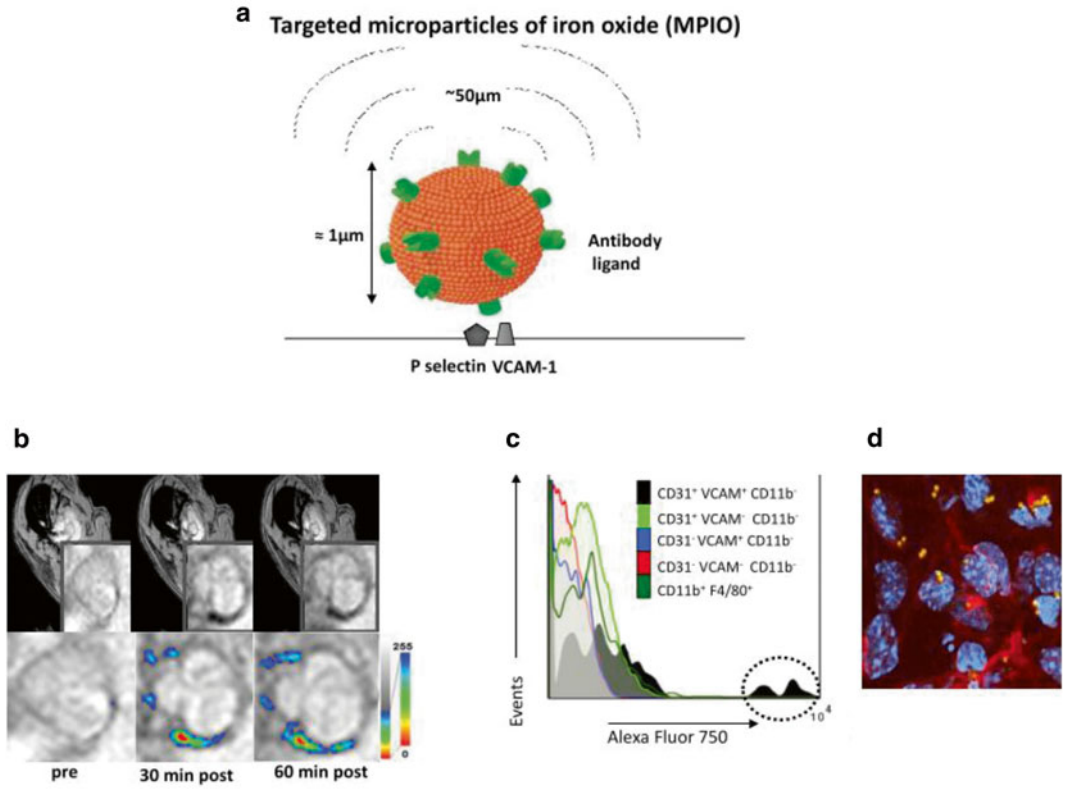

Fig. 4 (**a**) Schematic of dual-targeted MPIO conjugated with P-selectin and VCAM-1 monoclonal antibodies (PV-MPIO, 1 µm diameter). MPIO produce strong MRI contrast effects which can extend a distance of up to 50 times the diameter of the particle, known as the "MRI contrast blooming effect". (**b**) In vivo MRI shows rapid low MR signal intensity areas in the aortic root of chow-fed apoE−/− mice 30 min after PV-MPIO injection, which are maintained at 60 min. (**c**) Flow cytometry shows predominant binding of near-infrared fluorescently labeled dual-ligand MPIO to activated aortic endothelial cells (CD31+ VCAM+ CD11b−) with minimal signal in macrophages (CD11b+ F4/80+) or other cell types. (**d**) Dual-ligand MPIO binding localizes to activated endothelial cells in atherosclerosis-susceptible sites of the aortic arch [63]

to enhance the detection of vascular inflammation using optical imaging with fluorescent microspheres conjugated to recombinant PSGL-1 and ICAM-1 antibody [98] and photoacoustic imaging with E-selectin and ICAM-1 antibody conjugated gold nanorods [99]. In order to attenuate immunogenicity of monoclonal antibodies, Van Kasteren et al. developed iron oxide glyconanoparticles functionalized with a glycan ligand (sLe^X) that binds with high affinity to E and P-selectin [100]. This agent enabled molecular MRI of early endothelial inflammation in mouse models of acute cerebral vascular inflammation, EAE, and focal cerebral stroke. The sLe^X sugar ligand has the advantage of transferable cross-species utility that is difficult to achieve with antibodies.

10 Targeted Radioisotope Imaging of Adhesion Molecules

A number of radiolabeled peptides have been developed for molecular PET and SPECT imaging of endothelial adhesion molecule expression in atherosclerosis. Radiolabeled cyclic linear peptide, ^{18}F-4V, has been reported to detect in vivo VCAM-1 expression in atherosclerotic plaques in mice using hybrid PET-CT imaging [101]. Reduced atherosclerotic lesion uptake of ^{18}F-4V was detected in mice treated with atorvastatin, which corresponded to reduced aortic VCAM-1 mRNA expression. The rapid clearance of ^{18}F-4V from the circulation allowed imaging to commence 1 h after ^{18}F-4V administration, with minimal background signal. Radiolabeled nanobodies have also been investigated as potential targeted agents for imaging of atherosclerosis [102, 103]. Nanobodies are single-domain antibody fragments that occur naturally in sharks and camelids. Noninvasive SPECT–CT imaging using ^{99m}Tc-radiolabeled VCAM-1 nanobodies enabled detection of VCAM-1 expression in aortic arch atherosclerosis in apoE$^{-/-}$ mice [102]. Fucoidan, a naturally occurring polysaccharide mimetic of sLe^{x} derived from brown seaweed, has also been investigated as a targeting ligand for P-selectin. Radiolabeled ^{99m}Tc-labeled fucoidan was shown to detect endothelial activation in ischemic myocardium 2 h after reperfusion in rats [104]. However, PET tracers are limited in specificity since they also produce high background signal which may be difficult to distinguish specific contrast.

11 Molecular Imaging of Activated Platelets in Atherosclerois

In addition to endothelial cell inflammation, platelet-endothelial interactions play an important role in the pathogenesis of atherosclerosis. For example, platelet-endothelial interactions mediated by P-selectin have been shown to facilitate the initiation of atherosclerotic lesion formation in mice [105], platelets are involved in the advanced stages of atherosclerotic plaque rupture and microembolism [106], and ruptured atherosclerotic plaques and vulnerable rupture-prone plaques on the vessel wall are lined with activated platelets [107]. Glycoprotein GP IIb/IIIa receptors (CD41/CD61; also known as αIIbβ3 integrin) on activated platelets mediate the final common pathway of platelet aggregation via fibrinogen and are key to thrombus formation [108]. A single-chain antibody that specifically recognizes ligand-induced binding sites (LIBS) on GP IIb/IIIa receptors, which become exposed only upon activation by receptor-ligand binding, has been developed offering the opportunity to target activated platelet adhesion [109, 110]. The LIBS single-chain antibody binds specifically to GP IIb/IIIa on activated platelet aggregates or platelets adherent to damaged

endothelium, and does not bind to circulating platelets. However, in contrast to fibrin-rich thrombi, which form complex 3D reticular structures with high abundance of epitope, activated platelet thrombi may be only partially occlusive and localized at the surface of the ruptured atherosclerotic plaque, presenting a challenge to targeted contrast delivery. MPIO (1 μm diameter), conjugated to the histidine tag of LIBS single-chain antibodies (LIBS-MPIO) have been shown to overcome this challenge, enabling detection of activated platelets in a mouse model of endovascular platelet aggregation by ex vivo MRI (11.7 T) [96]. LIBS-MPIO have also allowed in vivo MRI detection of small, platelet-rich thrombi in a mouse model of wall-adherent carotid thrombosis, and reliably detected reductions in thrombus size in response to thrombolysis treatment with urokinase [111, 112]. The potential of LIBS-MPIO for human use has also been investigated in explanted symptomatic carotid artery plaque specimens by ex vivo MRI (9.4 T) [111] and human platelet-rich clots in vitro using a 3 T clinical MRI scanner [112]. MPIO targeting platelet-rich thrombi may also overcome the limitation of a previous in vivo MRI study using USPIO coupled to a cyclic arginine-glycine-aspartic acid (RGD) peptide, in which the in vivo spatial resolution ($0.2 \times 0.2 \times 1$ mm) and sensitivity were seen as potentially limiting for clinical application [113]. The use of single-chain antibodies as targeting ligands is attractive for human application since they have low immunogenicity due to a lack of Fc regions. Single-chain antibodies can also be tailored in size and produced in large quantities at low cost [114].

12 Molecular Imaging of Extracellular Matrix Proteins

ECM proteins, such as collagen and elastin, are major components of atherosclerotic lesions [23]. A high abundance of elastin during plaque development and changes in elastin content can provide a quantitative marker of plaque burden and plaque stability. In vivo molecular MRI of elastin was recently confirmed in apoE$^{-/-}$ mice using an elastin-specific small molecular weight Gd-based MR agent (ESMA) [115]. ESMA uptake by atherosclerotic plaques produced strong MRI signal intensity changes, which allowed accurate assessment of plaque burden and characterization by quantification of intra-plaque elastin content. Successful translation into the coronary arteries has been demonstrated in a swine model of coronary injury [116], offering potential for non-invasive assessment of coronary artery wall remodeling and plaque burden in patients with suspected coronary artery disease or in-stent restenosis. Imaging of plaque collagen has also been demonstrated using paramagnetic liposomes functionalized with the collagen adhesion protein CNA35, both in vitro [117] and in vivo in a mouse model of aortic aneurysm [118].

13 Proteolytic Enzymes

Molecular imaging of macrophage products has been demonstrated by targeted imaging of extracellular released enzymes, matrix metalloproteinase (MMP) or myeloperoxidases (MPO). Matrix metalloproteinases (MMPs) produced by macrophages and smooth muscle cells are thought to mediate the progression of stable atherosclerotic lesions to an unstable phenotype that is prone to rupture through the destruction of strength-giving ECM [119–121]. Activatable fluorescent probes, radiolabeled inhibitors, and nanoparticles are being investigated for molecular imaging of protease activity [122]. Recently, a Gd-based agent conjugated to the small MMP targeting peptide P947 has been shown to facilitate discrimination of MMP-rich atherosclerotic plaques compared to MMP-poor plaques by in vivo MRI in apoE$^{-/-}$ mice [123, 124], in hyperlipidemic rabbits [125] and by histologically evaluation of human carotid artery endarterectomy specimens [123]. The plasma half-life of this small peptide was only 30 min and the concentrations in artery specimens were three times as high as those achieved after injection of Gd-DOTA, with prolonged retention at least until 22 h after injection [123]. An MPO targeted Gd-based contrast agent has also enabled targeted imaging of MPO in the aortic wall of New Zealand White rabbits [126] and mice [127, 128]. Focal areas of increased signal intensity due to MPO (Gd) binding, co-localized with myeloperoxidase-rich areas infiltrated by macrophages [126]. MPO-Gd have also been applied for dual PET/MRI imaging of MPO-rich inflammatory leukocyte recruitment following nanoparticle-facilitated, siRNA therapy in atherosclerosis-prone apoE$^{-/-}$ mice after MI. A 75 % decrease in MPO-Gd signal following monocyte subset-targeted siRNA therapy was observed by PET-MRI [129].

14 Summary and Future Directions

Molecular imaging of atherosclerosis promises to provide improved diagnosis and prognosis of atherosclerotic plaques as well as monitoring of therapeutic efficacy. The development of imaging agents with potential for clinical translation is already under way. Small-molecular-weight Gd-based contrast agents can mainly image high abundance targets such as fibrin, elastin, collagen and albumin, while nano-sized particles and radiolabels have shown potential for imaging low-abundance targets or cells such as adhesion molecules and macrophages. MPIO offer a versatile platform for MRI of endothelial cell-specific biomarkers, such as VCAM-1, due to their size, exceptional potent T_2* contrast effects, as well as their rapid blood clearance and rapid binding to target. The MPIO used in

our studies are non-biodegradable due to their polyurethane coat. However, the basic iron contrast mechanism is potentially transferable to humans with suitable adaptation of the surface coat. Iron-dextran nanoparticles are already in clinical use and the synthesis of biodegradable MPIO is under development [130–133]. In particular, biocompatible MPIO based on a multiple iron oxide nanoparticle platform covalently coupled through a peptide linker and cleavable by intracellular macrophage proteases have shown promise for in vivo MRI of endothelial-specific inflammation [134, 135]. Extensive toxicological profiling and synthesis of sterile, clinical-grade targeted MPIO according to good manufacturing practise (GMP) will be required before clinical translation is feasible. Although targeted nano-sized agents, such as VCAM-1 targeted nanomaterials, lack cellular specificity and bind not only to endothelial cells but also smooth muscle cells and macrophages, these agents may still reveal important biological processes in atherosclerosis, through enhanced detection of inflammatory imaging signals [136]. However, more studies are required to comprehensively investigate the in vivo biological behavior and cellular processing of nano- and micro-materials as well as organ clearance of the core material and its coating.

With the recent approval of gadofosveset, a promising albumin-binding agent for detection of vascular endothelial permeability, and ferumoxytol, a super-paramagnetic ultra small iron oxide particle, and promising phase II results of EP-2104R, a fibrin-binding contrast agent, molecular MRI has entered the clinical arena [137]. The use of high MRI field strengths together with the introduction of multifunctional and multimodal nanoparticles offers great potential for future integration of diagnosis, treatment, and tracking of atherosclerotic plaque responses to therapy.

References

1. Virmani R, Burke AP, Farb A et al (2006) Pathology of the vulnerable plaque. J Am Coll Cardiol 47:C13–C18
2. Falk E, Shah PK, Fuster V (1995) Coronary plaque disruption. Circulation 92:657–671
3. Stary HC, Chandler AB, Dinsmore RE et al (1995) A definition of advanced types of atherosclerotic lesions and a histological classification of atherosclerosis. A report from the Committee on Vascular Lesions of the Council on Arteriosclerosis, American Heart Association. Circulation 92:1355–1374
4. Fishbein MC (2010) The vulnerable and unstable atherosclerotic plaque. Cardiovasc Pathol 19:6–11
5. Hattori K, Ozaki Y, Ismail TF et al (2012) Impact of statin therapy on plaque characteristics as assessed by serial OCT, grayscale and integrated backscatter-IVUS. JACC Cardiovasc Imaging 5:169–177
6. Miyamoto Y, Okura H, Kume T et al (2011) Plaque characteristics of thin-cap fibroatheroma evaluated by OCT and IVUS. JACC Cardiovasc Imaging 4:638–646
7. Christoph M, Herold J, Berg-Holldack A et al (2015) Effects of the PPARgamma agonist pioglitazone on coronary atherosclerotic plaque composition and plaque progression in non-diabetic patients: a double-center, randomized controlled VH-IVUS pilot-trial. Heart Vessels 30(3):286–295
8. van Velzen JE, Schuijf JD, de Graaf FR et al (2009) Plaque type and composition as evaluated non-invasively by MSCT angiography and invasively by VH IVUS in relation to the degree of stenosis. Heart 95:1990–1996

9. Jefferson A, Wijesurendra RS, McAteer MA et al (2011) Molecular imaging with optical coherence tomography using ligand-conjugated microparticles that detect activated endothelial cells: rational design through target quantification. Atherosclerosis 219:579–587
10. Meir KS, Leitersdorf E (2004) Atherosclerosis in the apolipoprotein-E-deficient mouse: a decade of progress. Arterioscler Thromb Vasc Biol 24:1006–1014
11. Itskovich VV, Choudhury RP, Aguinaldo JG et al (2003) Characterization of aortic root atherosclerosis in ApoE knockout mice: high-resolution in vivo and ex vivo MRM with histological correlation. Magn Reson Med 49: 381–385
12. Choudhury RP, Fayad ZA, Aguinaldo JG et al (2003) Serial, noninvasive, in vivo magnetic resonance microscopy detects the development of atherosclerosis in apolipoprotein E-deficient mice and its progression by arterial wall remodeling. J Magn Reson Imaging 17:184–189
13. Rosenfeld ME, Polinsky P, Virmani R et al (2000) Advanced atherosclerotic lesions in the innominate artery of the ApoE knockout mouse. Arterioscler Thromb Vasc Biol 20:2587–2592
14. Sato K, Nakano K, Katsuki S et al (2012) J Atheroscler Thromb 19:986–998
15. Bond AR, Jackson CL (2011) The fat-fed apolipoprotein E knockout mouse brachiocephalic artery in the study of atherosclerotic plaque rupture. J Biomed Biotechnol 2011: 379069
16. Calara F, Silvestre M, Casanada F et al (2001) Spontaneous plaque rupture and secondary thrombosis in apolipoprotein E-deficient and LDL receptor-deficient mice. J Pathol 195: 257–263
17. McNeill E, Channon KM, Greaves DR (2010) Inflammatory cell recruitment in cardiovascular disease: murine models and potential clinical applications. Clin Sci (Lond) 118:641–655
18. Choudhury RP, Fisher EA (2009) Molecular imaging in atherosclerosis, thrombosis, and vascular inflammation. Arterioscler Thromb Vasc Biol 29:983–991
19. Rudd JH, Elkhawad M, Fayad ZA (2009) Vascular imaging with 18F-FDG PET/CT: optimal 18F-FDG circulation time? J Nucl Med 50:1560, author reply 1560–1561
20. Ogawa M, Nakamura S, Saito Y et al (2012) What can be seen by 18F-FDG PET in atherosclerosis imaging? The effect of foam cell formation on 18F-FDG uptake to macrophages in vitro. J Nucl Med 53:55–58
21. Ishino S, Ogawa M, Mori I et al (2014) (18) F-FDG PET and intravascular ultrasonography (IVUS) images compared with histology of atherosclerotic plaques: (18)F-FDG accumulates in foamy macrophages. Eur J Nucl Med Mol Imaging 41:624–633
22. Graebe M, Pedersen SF, Borgwardt L et al (2009) Molecular pathology in vulnerable carotid plaques: correlation with [18]-fluorodeoxyglucose positron emission tomography (FDG-PET). Eur J Vasc Endovasc Surg 37: 714–721
23. Leuschner F, Nahrendorf M (2011) Molecular imaging of coronary atherosclerosis and myocardial infarction: considerations for the bench and perspectives for the clinic. Circ Res 108:593–606
24. Folco EJ, Sheikine Y, Rocha VZ et al (2011) Hypoxia but not inflammation augments glucose uptake in human macrophages: implications for imaging atherosclerosis with 18fluorine-labeled 2-deoxy-D-glucose positron emission tomography. J Am Coll Cardiol 58:603–614
25. Joshi NV, Vesey AT, Williams MC et al (2014) 18F-fluoride positron emission tomography for identification of ruptured and high-risk coronary atherosclerotic plaques: a prospective clinical trial. Lancet 383:705–713
26. Kaufmann BA, Carr CL, Belcik JT et al (2010) Molecular imaging of the initial inflammatory response in atherosclerosis: implications for early detection of disease. Arterioscler Thromb Vasc Biol 30:54–59
27. Kaufmann BA, Sanders JM, Davis C et al (2007) Molecular imaging of inflammation in atherosclerosis with targeted ultrasound detection of vascular cell adhesion molecule-1. Circulation 116:276–284
28. Khanicheh E, Mitterhuber M, Xu L et al (2013) Noninvasive ultrasound molecular imaging of the effect of statins on endothelial inflammatory phenotype in early atherosclerosis. PLoS One 8:e58761
29. Liu Y, Davidson BP, Yue Q et al (2013) Molecular imaging of inflammation and platelet adhesion in advanced atherosclerosis effects of antioxidant therapy with NADPH oxidase inhibition. Circ Cardiovasc Imaging 6:74–82
30. Wang LV (2008) Prospects of photoacoustic tomography. Med Phys 35:5758–5767
31. Qin H, Zhou T, Yang S et al (2013) Gadolinium(III)-gold nanorods for MRI and photoacoustic imaging dual-modality detection of macrophages in atherosclerotic inflammation. Nanomedicine (Lond) 8:1611–1624
32. Rouleau L, Berti R, Ng VW et al (2013) VCAM-1-targeting gold nanoshell probe for

photoacoustic imaging of atherosclerotic plaque in mice. Contrast Media Mol Imaging 8:27–39

33. Sipkins DA, Cheresh DA, Kazemi MR et al (1998) Detection of tumor angiogenesis in vivo by alphaVbeta3-targeted magnetic resonance imaging. Nat Med 4:623–626
34. Yu X, Song SK, Chen J et al (2000) High-resolution MRI characterization of human thrombus using a novel fibrin-targeted paramagnetic nanoparticle contrast agent. Magn Reson Med 44:867–872
35. Amirbekian V, Lipinski MJ, Briley-Saebo KC et al (2007) Detecting and assessing macrophages in vivo to evaluate atherosclerosis noninvasively using molecular MRI. Proc Natl Acad Sci U S A 104:961–966
36. Lipinski MJ, Amirbekian V, Frias JC et al (2006) MRI to detect atherosclerosis with gadolinium-containing immunomicelles targeting the macrophage scavenger receptor. Magn Reson Med 56:601–610
37. Frias JC, Williams KJ, Fisher EA et al (2004) Recombinant HDL-like nanoparticles: a specific contrast agent for MRI of atherosclerotic plaques. J Am Chem Soc 126:16316–16317
38. Glickson JD, Lund-Katz S, Zhou R et al (2008) Lipoprotein nanoplatform for targeted delivery of diagnostic and therapeutic agents. Mol Imaging 7:101–110
39. Cormode DP, Briley-Saebo KC, Mulder WJ et al (2008) An ApoA-I mimetic peptide high-density-lipoprotein-based MRI contrast agent for atherosclerotic plaque composition detection. Small 4:1437–1444
40. Cormode DP, Chandrasekar R, Delshad A et al (2009) Comparison of synthetic high density lipoprotein (HDL) contrast agents for MR imaging of atherosclerosis. Bioconjug Chem 20:937–943
41. Cormode DP, Fisher EA, Stroes ES et al (2013) High-density lipoprotein is a nanoparticle, but not all nanoparticles are high-density lipoprotein. Proc Natl Acad Sci U S A 110:E3548
42. Cormode DP, Frias JC, Ma Y et al (2009) HDL as a contrast agent for medical imaging. Clin Lipidol 4:493–500
43. Skajaa T, Cormode DP, Falk E et al (2010) High-density lipoprotein-based contrast agents for multimodal imaging of atherosclerosis. Arterioscler Thromb Vasc Biol 30:169–176
44. Sibson NR, Blamire AM, Bernades-Silva M et al (2004) MRI detection of early endothelial activation in brain inflammation. Magn Reson Med 51:248–252
45. Sipkins DA, Gijbels K, Tropper FD et al (2000) ICAM-1 expression in autoimmune encephalitis visualized using magnetic resonance imaging. J Neuroimmunol 104:1–9
46. Winter PM, Morawski AM, Caruthers SD et al (2003) Molecular imaging of angiogenesis in early-stage atherosclerosis with alpha(v) beta3-integrin-targeted nanoparticles. Circulation 108:2270–2274
47. Stratta P, Canavese C, Aime S (2008) Gadolinium-enhanced magnetic resonance imaging, renal failure and nephrogenic systemic fibrosis/nephrogenic fibrosing dermopathy. Curr Med Chem 15:1229–1235
48. Lim YL, Lee HY, Low SC et al (2007) Possible role of gadolinium in nephrogenic systemic fibrosis: report of two cases and review of the literature. Clin Exp Dermatol 32:353–358
49. Bousquet JC, Saini S, Stark DD et al (1988) Gd-DOTA: characterization of a new paramagnetic complex. Radiology 166:693–698
50. Alhadad A, Akesson M, Lehti L et al (2014) Safety aspects of gadofosveset in clinical practice - analysis of acute and long-term complications. Magn Reson Imaging 32:570–573
51. Phinikaridou A, Andia ME, Indermuehle A et al (2014) Vascular remodeling and plaque vulnerability in a rabbit model of atherosclerosis: comparison of delayed-enhancement MR imaging with an elastin-specific contrast agent and unenhanced black-blood MR imaging. Radiology 271:390
52. Phinikaridou A, Andia ME, Protti A et al (2012) Noninvasive magnetic resonance imaging evaluation of endothelial permeability in murine atherosclerosis using an albumin-binding contrast agent. Circulation 126: 707–719
53. Phinikaridou A, Andia ME, Passacquale G et al (2013) Noninvasive MRI monitoring of the effect of interventions on endothelial permeability in murine atherosclerosis using an albumin-binding contrast agent. J Am Heart Assoc 2:e000402
54. Mendonca Dias MH, Lauterbur PC (1986) Ferromagnetic particles as contrast agents for magnetic resonance imaging of liver and spleen. Magn Reson Med 3:328–330
55. Renshaw PF, Owen CS, McLaughlin AC et al (1986) Ferromagnetic contrast agents: a new approach. Magn Reson Med 3:217–225
56. Dahnke H, Liu W, Herzka D et al (2008) Susceptibility gradient mapping (SGM): a new postprocessing method for positive contrast generation applied to superparamagnetic iron oxide particle (SPIO)-labeled cells. Magn Reson Med 60:595–603
57. Briley-Saebo KC, Mani V, Hyafil F et al (2008) Fractionated Feridex and positive contrast: in vivo MR imaging of atherosclerosis. Magn Reson Med 59:721–730

58. Shapiro EM, Skrtic S, Koretsky AP (2005) Sizing it up: cellular MRI using micron-sized iron oxide particles. Magn Reson Med 53:329–338
59. Shapiro EM, Sharer K, Skrtic S et al (2006) In vivo detection of single cells by MRI. Magn Reson Med 55:242–249
60. Heyn C, Ronald JA, Mackenzie LT et al (2006) In vivo magnetic resonance imaging of single cells in mouse brain with optical validation. Magn Reson Med 55:23–29
61. Yang Y, Yanasak N, Schumacher A et al (2010) Temporal and noninvasive monitoring of inflammatory-cell infiltration to myocardial infarction sites using micrometer-sized iron oxide particles. Magn Reson Med 63:33–40
62. Ye Q, Wu YL, Foley LM et al (2008) Longitudinal tracking of recipient macrophages in a rat chronic cardiac allograft rejection model with noninvasive magnetic resonance imaging using micrometer-sized paramagnetic iron oxide particles. Circulation 118:149–156
63. McAteer MA, Mankia K, Ruparelia N et al (2012) A leukocyte-mimetic magnetic resonance imaging contrast agent homes rapidly to activated endothelium and tracks with atherosclerotic lesion macrophage content. Arterioscler Thromb Vasc Biol 32:1427–1435
64. McAteer MA, von Zur Muhlen C, Anthony DC et al (2011) Magnetic resonance imaging of brain inflammation using microparticles of iron oxide. Methods Mol Biol 680:103–115
65. Ruehm SG, Corot C, Vogt P et al (2002) Ultrasmall superparamagnetic iron oxide-enhanced MR imaging of atherosclerotic plaque in hyperlipidemic rabbits. Acad Radiol 9(Suppl 1):S143–S144
66. Litovsky S, Madjid M, Zarrabi A et al (2003) Superparamagnetic iron oxide-based method for quantifying recruitment of monocytes to mouse atherosclerotic lesions in vivo: enhancement by tissue necrosis factor-alpha, interleukin-1beta, and interferon-gamma. Circulation 107:1545–1549
67. Kooi ME, Cappendijk VC, Cleutjens KB et al (2003) Accumulation of ultrasmall superparamagnetic particles of iron oxide in human atherosclerotic plaques can be detected by in vivo magnetic resonance imaging. Circulation 107:2453–2458
68. Mulder WJ, Strijkers GJ, Briley-Saboe KC et al (2007) Molecular imaging of macrophages in atherosclerotic plaques using bimodal PEG-micelles. Magn Reson Med 58:1164–1170
69. Nahrendorf M, Keliher E, Marinelli B et al (2010) Hybrid PET-optical imaging using targeted probes. Proc Natl Acad Sci U S A 107:7910–7915
70. Jarrett BR, Correa C, Ma KL et al (2010) In vivo mapping of vascular inflammation using multimodal imaging. PLoS One 5:e13254
71. Devaraj NK, Keliher EJ, Thurber GM et al (2009) 18F labeled nanoparticles for in vivo PET-CT imaging. Bioconjug Chem 20: 397–401
72. Nahrendorf M, Keliher E, Marinelli B et al (2011) Detection of macrophages in aortic aneurysms by nanoparticle positron emission tomography-computed tomography. Arterioscler Thromb Vasc Biol 31:750–757
73. Choudhury RP, Fuster V, Fayad ZA (2004) Molecular, cellular and functional imaging of atherothrombosis. Nat Rev Drug Discov 3: 913–925
74. Oksjoki R, Kovanen PT, Pentikainen MO (2003) Role of complement activation in atherosclerosis. Curr Opin Lipidol 14:477–482
75. Dansky HM, Barlow CB, Lominska C et al (2001) Adhesion of monocytes to arterial endothelium and initiation of atherosclerosis are critically dependent on vascular cell adhesion molecule-1 gene dosage. Arterioscler Thromb Vasc Biol 21:1662–1667
76. Nahrendorf M, Sosnovik DE, French BA et al (2009) Multimodality cardiovascular molecular imaging, Part II. Circ Cardiovasc Imaging 2:56–70
77. Carlos TM, Schwartz BR, Kovach NL et al (1990) Vascular cell adhesion molecule-1 mediates lymphocyte adherence to cytokine-activated cultured human endothelial cells. Blood 76:965–970
78. Nakashima Y, Raines EW, Plump AS et al (1998) Upregulation of VCAM-1 and ICAM-1 at atherosclerosis-prone sites on the endothelium in the ApoE-deficient mouse. Arterioscler Thromb Vasc Biol 18:842–851
79. Ramos CL, Huo Y, Jung U et al (1999) Direct demonstration of P-selectin- and VCAM-1-dependent mononuclear cell rolling in early atherosclerotic lesions of apolipoprotein E-deficient mice. Circ Res 84: 1237–1244
80. Tsourkas A, Shinde-Patil VR, Kelly KA et al (2005) In vivo imaging of activated endothelium using an anti-VCAM-1 magnetooptical probe. Bioconjug Chem 16:576–581
81. Kelly KA, Allport JR, Tsourkas A et al (2005) Detection of vascular adhesion molecule-1 expression using a novel multimodal nanoparticle. Circ Res 96:327–336
82. Nahrendorf M, Jaffer FA, Kelly KA et al (2006) Noninvasive vascular cell adhesion molecule-1 imaging identifies inflammatory

activation of cells in atherosclerosis. Circulation 114:1504–1511

83. Michalska M, Machtoub L, Manthey HD et al (2012) Visualization of vascular inflammation in the atherosclerotic mouse by ultrasmall superparamagnetic iron oxide vascular cell adhesion molecule-1-specific nanoparticles. Arterioscler Thromb Vasc Biol 32:2350–2357
84. Burtea C, Ballet S, Laurent S et al (2012) Development of a magnetic resonance imaging protocol for the characterization of atherosclerotic plaque by using vascular cell adhesion molecule-1 and apoptosis-targeted ultrasmall superparamagnetic iron oxide derivatives. Arterioscler Thromb Vasc Biol 32:e36–e48
85. Bruckman MA, Jiang K, Simpson EJ et al (2014) Dual-modal magnetic resonance and fluorescence imaging of atherosclerotic plaques in vivo using VCAM-1 targeted tobacco mosaic virus. Nano Lett 14: 1551–1558
86. McAteer MA, Akhtar AM, von Zur Muhlen C et al (2010) An approach to molecular imaging of atherosclerosis, thrombosis, and vascular inflammation using microparticles of iron oxide. Atherosclerosis 209:18–27
87. McAteer MA, Choudhury RP (2009) Chapter 4 - Applications of nanotechnology in molecular imaging of the brain. Prog Brain Res 180:72–96
88. McAteer MA, Sibson NR, von Zur Muhlen C et al (2007) In vivo magnetic resonance imaging of acute brain inflammation using microparticles of iron oxide. Nat Med 13:1253–1258
89. Serres S, Mardiguian S, Campbell SJ et al (2011) VCAM-1-targeted magnetic resonance imaging reveals subclinical disease in a mouse model of multiple sclerosis. FASEB J 25:4415–4422
90. Akhtar AM, Schneider JE, Chapman SJ et al (2010) In vivo quantification of VCAM-1 expression in renal ischemia reperfusion injury using non-invasive magnetic resonance molecular imaging. PLoS One 5:e12800
91. Hoyte LC, Brooks KJ, Nagel S et al (2010) Molecular magnetic resonance imaging of acute vascular cell adhesion molecule-1 expression in a mouse model of cerebral ischemia. J Cereb Blood Flow Metab 30: 1178–1187
92. Grieve SM, Lonborg J, Mazhar J et al (2013) Cardiac magnetic resonance imaging of rapid VCAM-1 up-regulation in myocardial ischemia-reperfusion injury. Eur Biophys J 42:61–70
93. Mardiguian S, Serres S, Ladds E et al (2013) Anti-IL-17A treatment reduces clinical score and VCAM-1 expression detected by in vivo magnetic resonance imaging in chronic relapsing EAE ABH mice. Am J Pathol 182:2071–2081
94. McAteer MA, Choudhury RP (2013) Targeted molecular imaging of vascular inflammation in cardiovascular disease using nano- and micro-sized agents. Vascul Pharmacol 58:31–38
95. McAteer MA, Schneider JE, Ali ZA et al (2008) Magnetic resonance imaging of endothelial adhesion molecules in mouse atherosclerosis using dual-targeted microparticles of iron oxide. Arterioscler Thromb Vasc Biol 28:77–83
96. von zur Muhlen C, Peter K, Ali ZA et al (2009) Visualization of activated platelets by targeted magnetic resonance imaging utilizing conformation-specific antibodies against glycoprotein IIb/IIIa. J Vasc Res 46:6–14
97. Weller GE, Villanueva FS, Tom EM et al (2005) Targeted ultrasound contrast agents: in vitro assessment of endothelial dysfunction and multi-targeting to ICAM-1 and sialyl Lewisx. Biotechnol Bioeng 92:780–788
98. Sun D, Nakao S, Xie F et al (2010) Superior sensitivity of novel molecular imaging probe: simultaneously targeting two types of endothelial injury markers. FASEB J 24:1532–1540
99. Ha S, Carson A, Agarwal A et al (2011) Detection and monitoring of the multiple inflammatory responses by photoacoustic molecular imaging using selectively targeted gold nanorods. Biomed Opt Express 2:645–657
100. van Kasteren SI, Kramer HB, Gamblin DP et al (2007) Site-selective glycosylation of proteins: creating synthetic glycoproteins. Nat Protoc 2:3185–3194
101. Nahrendorf M, Keliher E, Panizzi P et al (2009) 18F-4V for PET-CT imaging of VCAM-1 expression in atherosclerosis. JACC Cardiovasc Imaging 2:1213–1222
102. Broisat A, Hernot S, Toczek J et al (2012) Nanobodies targeting mouse/human VCAM1 for the nuclear imaging of atherosclerotic lesions. Circ Res 110:927–937
103. Nahrendorf M, McCarthy JR, Libby P (2012) Over a hump for imaging atherosclerosis: nanobodies visualize vascular cell adhesion molecule-1 in inflamed plaque. Circ Res 110:902–903
104. Rouzet F, Bachelet-Violette L, Alsac JM et al (2011) Radiolabeled fucoidan as a p-selectin targeting agent for in vivo imaging of platelet-rich thrombus and endothelial activation. J Nucl Med 52:1433–1440

105. Jacobin-Valat MJ, Deramchia K, Mornet S et al (2011) MRI of inducible P-selectin expression in human activated platelets involved in the early stages of atherosclerosis. NMR Biomed 24:413–424
106. Gawaz M, Stellos K, Langer HF (2008) Platelets modulate atherogenesis and progression of atherosclerotic plaques via interaction with progenitor and dendritic cells. J Thromb Haemost 6:235–242
107. Gawaz M (2004) Role of platelets in coronary thrombosis and reperfusion of ischemic myocardium. Cardiovasc Res 61:498–511
108. Peter K, Ahrens I, Schwarz M et al (2004) Distinct roles of ligand affinity and cytoskeletal anchorage in alphaIIbbeta3 (GP IIb/IIIa)-mediated cell aggregation and adhesion. Platelets 15:427–438
109. Stoll P, Bassler N, Hagemeyer CE et al (2007) Targeting ligand-induced binding sites on GPIIb/IIIa via single-chain antibody allows effective anticoagulation without bleeding time prolongation. Arterioscler Thromb Vasc Biol 27:1206–1212
110. Schwarz M, Katagiri Y, Kotani M et al (2004) Reversibility versus persistence of GPIIb/IIIa blocker-induced conformational change of GPIIb/IIIa (alphaIIbbeta3, CD41/CD61). J Pharmacol Exp Ther 308:1002–1011
111. von Elverfeldt D, Meissner M, Peter K et al (2012) An approach towards molecular imaging of activated platelets allows imaging of symptomatic human carotid plaques in a new model of a tissue flow chamber. Contrast Media Mol Imaging 7:204–213
112. von Zur Muhlen C, von Elverfeldt D, Choudhury RP et al (2008) Functionalized magnetic resonance contrast agent selectively binds to glycoprotein IIb/IIIa on activated human platelets under flow conditions and is detectable at clinically relevant field strengths. Mol Imaging 7:59–67
113. Johansson LO, Bjornerud A, Ahlstrom HK et al (2001) A targeted contrast agent for magnetic resonance imaging of thrombus: implications of spatial resolution. J Magn Reson Imaging 13:615–618
114. Schwarz M, Meade G, Stoll P et al (2006) Conformation-specific blockade of the integrin GPIIb/IIIa: a novel antiplatelet strategy that selectively targets activated platelets. Circ Res 99:25–33
115. Makowski MR, Wiethoff AJ, Blume U et al (2011) Assessment of atherosclerotic plaque burden with an elastin-specific magnetic resonance contrast agent. Nat Med 17:383–388
116. Makowski MR, Preissel A, von Bary C et al (2012) Three-dimensional imaging of the aortic vessel wall using an elastin-specific magnetic resonance contrast agent. Invest Radiol 47:438–444
117. Sanders HM, Strijkers GJ, Mulder WJ et al (2009) Morphology, binding behavior and MR-properties of paramagnetic collagen-binding liposomes. Contrast Media Mol Imaging 4:81–88
118. Klink A, Heynens J, Herranz B et al (2011) In vivo characterization of a new abdominal aortic aneurysm mouse model with conventional and molecular magnetic resonance imaging. J Am Coll Cardiol 58:2522–2530
119. Shah PK, Galis ZS (2001) Matrix metalloproteinase hypothesis of plaque rupture: players keep piling up but questions remain. Circulation 104:1878–1880
120. Johnson JL (2007) Matrix metalloproteinases: influence on smooth muscle cells and atherosclerotic plaque stability. Expert Rev Cardiovasc Ther 5:265–282
121. Newby AC (2006) Matrix metalloproteinases regulate migration, proliferation, and death of vascular smooth muscle cells by degrading matrix and non-matrix substrates. Cardiovasc Res 69:614–624
122. Quillard T, Croce K, Jaffer FA et al (2011) Molecular imaging of macrophage protease activity in cardiovascular inflammation in vivo. J Thromb Haemost 105:828–836
123. Lancelot E, Amirbekian V, Brigger I et al (2008) Evaluation of matrix metalloproteinases in atherosclerosis using a novel noninvasive imaging approach. Arterioscler Thromb Vasc Biol 28:425–432
124. Amirbekian V, Aguinaldo JG, Amirbekian S et al (2009) Atherosclerosis and matrix metalloproteinases: experimental molecular MR imaging in vivo. Radiology 251:429–438
125. Hyafil F, Vucic E, Cornily JC et al (2011) Monitoring of arterial wall remodelling in atherosclerotic rabbits with a magnetic resonance imaging contrast agent binding to matrix metalloproteinases. Eur Heart J 32: 1561–1571
126. Ronald JA, Chen JW, Chen Y et al (2009) Enzyme-sensitive magnetic resonance imaging targeting myeloperoxidase identifies active inflammation in experimental rabbit atherosclerotic plaques. Circulation 120: 592–599
127. Chen JW, Querol Sans M, Bogdanov A Jr et al (2006) Imaging of myeloperoxidase in mice by using novel amplifiable paramagnetic substrates. Radiology 240:473–481
128. Pulli B, Ali M, Forghani R et al (2013) Measuring myeloperoxidase activity in biological samples. PLoS One 8:e67976

129. Majmudar MD, Keliher EJ, Heidt T et al (2013) Monocyte-directed RNAi targeting CCR2 improves infarct healing in atherosclerosis-prone mice. Circulation 127: 2038–2046
130. Hamoudeh M, Fessi H (2006) Preparation, characterization and surface study of poly-epsilon caprolactone magnetic microparticles. J Colloid Interface Sci 300:584–590
131. Hemmingsson A, Carlsten J, Ericsson A et al (1987) Relaxation enhancement of the dog liver and spleen by biodegradable superparamagnetic particles in proton magnetic resonance imaging. Acta Radiol 28:703–705
132. Zhu D, White RD, Hardy PA et al (2006) Biocompatible nanotemplate-engineered nanoparticles containing gadolinium: stability and relaxivity of a potential MRI contrast agent. J Nanosci Nanotechnol 6:996–1003
133. Chen HH, Le Visage C, Qiu B et al (2005) MR imaging of biodegradable polymeric microparticles: a potential method of monitoring local drug delivery. Magn Reson Med 53: 614–620
134. Perez-Balderas F, Davis BG, Van Kasteren SI, Khrapichev A, Anthony DC, Sibson NR (2010) Multimeric iron oxide micro particles: novel high sensitivity and biodegradable MRI contrast agents. Int Soc Magn Reson Med 18:1899
135. Perez-Balderas F, Davis BG, van Kasteren SI, Khrapichev A, Jefferson A, Bristow C, Serres S, Choudhury RP, Anthony DC, Sibson NR (2011) New biodegradable multimeric MPIO contrast agent shows rapid in vitro and in vivo degradation and high sensitivity contrast. Proc Int Soc Magn Reson Med 19:1689
136. Quillard T, Libby P (2012) Molecular imaging of atherosclerosis for improving diagnostic and therapeutic development. Circ Res 111: 231–244
137. Phinikaridou A, Andia ME, Lacerda S et al (2013) Molecular MRI of atherosclerosis. Molecules 18:14042–14069

Chapter 5

Oil Red O and Hematoxylin and Eosin Staining for Quantification of Atherosclerosis Burden in Mouse Aorta and Aortic Root

M. Jesús Andrés-Manzano, Vicente Andrés, and Beatriz Dorado

Abstract

Methods for staining tissues with Oil Red O and hematoxylin-eosin are classical histological techniques that are widely used to quantify atherosclerotic burden in mouse tissues because of their ease of use, reliability, and the large amount of information they provide. These stains can provide quantitative data about the impact of a genetic or environmental factor on atherosclerotic burden and on the initiation, progression, or regression of the disease, and can also be used to evaluate the efficacy of drugs designed to prevent or treat atherosclerosis. This chapter provides protocols for quantifying atherosclerotic burden in mouse aorta and aortic root, including methods for dissection, Oil Red O staining, hematoxylin-eosin staining, and image analysis.

Key words Atherosclerosis, Oil Red O, Hematoxylin-eosin, Dissection, Aorta, Aortic root

1 Introduction

If you are conducting a project related to atherosclerosis and plan to perform in vivo experiments with mice, it is likely that one of the questions you will try to answer is if a specific drug or a risk factor (genetic, environmental, related to behavior, etc.) has an impact on the atherosclerotic burden in the model under study (most frequently apolipoprotein E knockout or low-density lipoprotein receptor knockout mice) [1, 2]. An easy way to answer this question is first to detect the presence of atherosclerotic plaques and second to evaluate the size, stage, and number of those plaques at different endpoints. These kinds of data will help you to conclude either that a drug or factor has no effect on the disease or, on the contrary, that it contributes to the initiation, progression, or regression of atherosclerosis. Among the methods available to accomplish this task, one of the best approaches is to use classical histological techniques such as staining with Oil Red O (ORO) and hematoxylin-eosin (H&E).

Vicente Andrés and Beatriz Dorado (eds.), *Methods in Mouse Atherosclerosis*, Methods in Molecular Biology, vol. 1339, DOI 10.1007/978-1-4939-2929-0_5,

These techniques not only visualize atherosclerotic lesions but also yield reliable quantitative information about the area of the aorta affected by atherosclerotic lesions, the area of each individual lesion, and the aortic intima/media ratio. Another likely concern will be where to start looking for lesions. The small size of mice makes it impractical to search in the coronary arteries as you would in humans, and it is easier to focus on the aortic root and the aorta. The more prominent lesions usually develop in the aortic arch and the arterial bifurcation, whereas lesions tend to be smaller in the descending thoracic and abdominal aorta.

In any histological staining procedure it is advantageous to know something about the chemical properties of the tissue or structure you are trying to visualize and of the stain solution being used. Visualization of lipids is challenging because they are relatively inert and, even when unsaturated, have very few sites to which stain molecules can bind. The prerequisite for any dye used to stain lipids is that it must be more soluble in the target lipid than in the vehicular solvent. The stain ORO is a fat-soluble bright red diazo dye that works simply as a pigment (an oil-soluble colorant), without forming any bond with the lipid components. ORO effectively stains the most hydrophobic and neutral lipids in cells (such as triglycerides, diacylglycerols and cholesterol esters) but does not stain membranes because it does not stain polar lipids such as phospholipids, sphingolipids, and ceramides. Analysis with ORO is moreover inexpensive and requires only basic laboratory equipment and standard computer-based software. For these reasons, ORO is widely used to identify pathological fat deposits in tissues (e.g., atheroma plaques in artery walls) or in cultured cells (abnormal accumulation of lipid droplets). ORO staining can be conducted with fresh, frozen, or formalin-fixed samples, but not with paraffin-embedded samples because the chemicals used for the deparaffinization process will also wash out most of the fats from the samples themselves. To visualize plaque lesions in paraffin sections H&E can be used.

Hematoxylin is a relatively colorless natural product that forms a functional dye when oxidized to hematein and subsequently bound to a mordant like aluminum (Al^{3+}), iron (Fe^{3+}), or chromium (Cr^{3+}). Conversion of hematoxylin to hematein used to be accomplished with the natural, spontaneous and slow action of atmospheric oxygen. To speed up the process, most current formulations incorporate a chemical oxidant. For example, the Harris formulation (the hematoxylin solution used for the protocol presented in this chapter) for many years included mercury (II) oxide as the oxidant, which has since been replaced, due to environmental concerns, with sodium iodate (Harris modified formulations). Functional hematoxylin solutions produce a blue-purple staining of cell nuclei. The specific mechanism of the staining is not totally clear, but it is believed that the color is formed through the

interaction of the positively charged metal-ion–hematein complexes with the negatively charged phosphate groups in DNA. Hematoxylin can also stain acid mucins (e.g., in goblet cells of the gastrointestinal tract) and proteoglycans.

Hematoxylin solutions can be used for progressive or regressive staining. In progressive staining solutions are prepared with 1–4 g of hematoxylin per liter, with the intention of staining primarily the nucleus, with a much lesser extent of coloring in the cytoplasm. With this procedure, there is no overstaining regardless of the length of staining time, and there is no need for differentiation afterwards by diluting in an acid bath. In contrast, regressive staining (often performed with the Harris formulation) requires a much more concentrated solution (5 or more grams of hematoxylin per liter) and is intended to overstain both nuclei and cytoplasm within minutes of exposure, requiring subsequent decolorizing of the cytoplasm (differentiation) and removal of excess hematoxylin from the nucleus with dilute acid. In this procedure, omission or non-completion of differentiation will leave residual excess hematoxylin that will visually obscure fine details of nuclear chromatin and prevent the uptake of eosin. It is important to realize that hematoxylin formulations initially stain tissues a dull-looking red, and immersion in a "bluing solution" at pH5 or above is required to change the final color to bright blue. In fact, most public tap waters are sufficiently alkaline (pH 5.4–9.8) to convert the color from red to blue ("bluing") and are often used as a regular reagent in the procedure.

Eosin Y (Y for yellowish) is a synthetic dye derived from fluorescein and is the main component of the eosin stain, referred to in the H&E procedure as a counterstain. Due to its acidic, anionic nature, the Eosin Y molecule binds to positively charged proteins in the cytoplasm and connective tissue. Eosin thus stains nearly everything that hematoxylin does not. In addition, if used correctly, eosin staining can generate three shades of color, enabling the distinction of several tissue elements, for example red blood cells in dark reddish-orange, collagen in pastel pink, and smooth muscle in bright pink.

This chapter presents basic protocols for the dissection of mouse aorta and heart, paraffin embedding of tissues and microtome sectioning, ORO and H&E staining, and image analysis.

2 Materials

1. Mice.
2. CO_2 chamber.
3. Paper towels.
4. Cork board.

5. 25 G needles (or pins or adhesive tape).
6. Ethanol (EtOH):
   (a) Absolute (100 %).
   (b) 70 % EtOH in distilled water.
   (c) 80 % EtOH in distilled water.
   (d) 96 % EtOH in distilled water.
7. Dissection tools (*see* Fig. 1).
8. 10 ml syringes.
9. 1.5 ml Eppendorf tubes.
10. Phosphate-buffered saline (PBS): 1.54 mM KH_2PO_4, 155.17 mM NaCl, 2.70 mM Na_2HPO_4, pH 7.4.
11. Regular plastic dishes.
12. Dissecting dish (e.g., Electron Microscopy Science, Cat. No. 70540).
13. Microscope with camera (e.g., Olympus BX41 with Olympus UC30).
14. Fixation solution: 4 % paraformaldehyde (PFA) in PBS. For 500 ml, heat 400 ml PBS in a fume hood to approximately 60 °C on a hot plate with a magnetic stirrer, add 20 g of paraformaldehyde, and then add 1 M NaOH dropwise until all powder is dissolved. Make up to 500 ml with PBS, cool the solution, filter and adjust pH to 7.4. Use fresh or store frozen at −20 °C.
15. Fridge (or 4 °C cold room).
16. 0.2 % ORO solution (w/v): Dissolve 0.07 g ORO in 25 ml 100 % methanol mixed with 10 ml 1 M NaOH (*see* **Note 1**).
17. Glass funnel.
18. 0.45 μm filter paper.

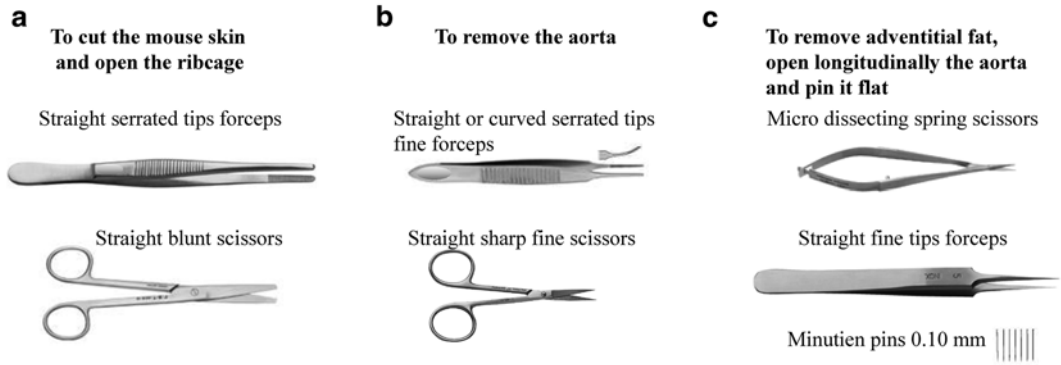

Fig. 1 Dissection tools

19. Methanol:
    (a) 78 % methanol in distilled water.
    (b) 100 % methanol.
20. Roller and tilted mixer.
21. Histosec paraffin (paraffin enriched with polymers).
22. Oven with temperature range 1–180 °C (e.g., Memmert 100-800).
23. Paraffin-embedding station.
24. Histology supplies:
    (a) Tissue processing/embedding cassettes with lids.
    (b) Pencil.
    (c) Biopsy foam pads.
    (d) Metal or plastic base molds.
    (e) Superfrost microscope slides.
    (f) Glass cover slides.
    (g) Slide storage boxes.
    (h) Slide-staining racks and jars.
    (i) Fine paintbrush.
    (j) Forceps.
25. Microtome.
26. Stainless steel microtome blades.
27. Histology paraffin bath with temperature range 0–100 °C (e.g., Termofin, PSelecta).
28. Ice bucket.
29. Xylene.
30. Fume hood.
31. Harris-modified hematoxylin solution (e.g., Sigma, Cat. No. HHS32).
32. Eosin Y alcoholic solution (e.g., Shandon, Cat. No. 6766008).
33. 1 % acetic acid in distilled water.
34. Xylene-based mounting medium: 45 % acrylic resin and 55 % xylene.
35. Stereomicroscope fitted with a digital camera and cold light (e.g., Olympus SZX10 with Olympus UC30 and Olympus KL1500 Compact).
36. Computer.
37. Software for bright-field image capture (e.g., Olympus Soft Imaging Solutions).
38. Software for image analysis and quantification (e.g., SigmaScan Pro 0.5).

3 Methods

3.1 Dissection of the Mouse Thoracic Aorta, Aortic Arch and Heart

1. Keep clean dissection tools to hand (*see* Fig. 1).
2. Euthanize the mouse in a CO_2 chamber.
3. Immobilize the mouse body before dissection: with the mouse facing up, pin down (e.g., with syringe needles) the fore and hind limbs to a cork board covered with 3–4 layers of paper towels.
4. Clean and wet the mouse fur to minimize its interference: spray a small volume of 70 % ethanol over the mouse abdomen.
5. Using blunt scissors and forceps, cut the mouse skin from the base of the abdomen to the top of the thorax.
6. Open the abdominal wall below the ribcage.
7. Lift the sternum with forceps and cut the diaphragm.
8. Open the ribcage bilaterally until the thymus and lungs are exposed.
9. Remove the esophagus and lungs to expose the heart and gain better access to the aorta.
10. Make 2–3 small incisions in the liver for drainage.
11. Wash out the blood from all organs using a 10 ml syringe loaded with PBS and fitted with a 25 G needle: introduce the needle into the apex of the heart left ventricle and gently depress the plunger to pump 10 ml of PBS.
12. Gently dry the dissection area with paper towels.
13. Using fine scissors and forceps, grip the segment of the diaphragm that is attached to the end of the thoracic aorta, and cut the connective tissue between the aorta and thoracic cavity muscle wall to expose the aortic arch area.
14. Cut the left and right carotid arteries and the left subclavian artery to give free access to the heart and aorta (*see* Fig. 2a).
15. Dissect out heart and aorta and place them in a regular plastic dish containing PBS.
16. Under a stereomicroscope, dissect the aorta by cutting at the point where it emerges from the heart.
17. Place the aorta in a 1.5 ml Eppendorf tube, add 1 ml of freshly prepared fixation solution, and leave the tube at 4 °C overnight or up to 24 h (*see* **Note 2**).
18. At this stage, the heart can either be processed directly for paraffin embedding (Subheading 3.4, **step 1**) or placed in a tube containing 5 ml of freshly prepared fixation solution and left at 4 °C for at least 48 h (*see* **Note 3**) and then processed from **step 3** in Subheading 3.4.

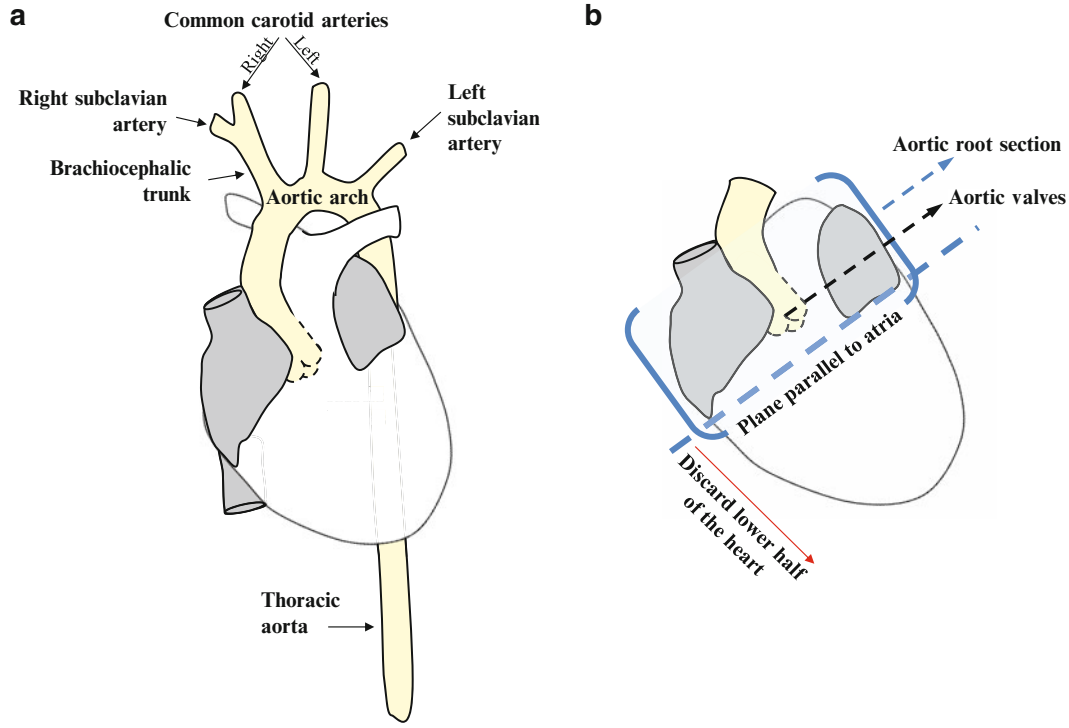

Fig. 2 Schemes for guiding aorta dissection (**a**) and aortic root sectioning (**b**)

19. The aorta can either be paraffin embedded (Subheading 3.4, **step 3**) or processed for ORO staining (Subheading 3.2). For ORO staining, you will need to clean the aorta by removing all adventitial fat under a stereomicroscope.
    - Place the aorta in a dissecting dish, taking care to maintain it wet at all times with PBS.
    - Pull away the adventitial fat very carefully with small forceps, avoiding excessive manipulation of the tissue.
    - Cut the branches of the brachiocephalic trunk, left carotid, and left subclavian arteries around 2 mm away from where they emerge.
20. Place cleaned and fixed aortas in 1.5 ml Eppendorf tubes containing PBS at 4 °C and proceed with Subheading 3.2.

3.2 Staining of Aorta with ORO to Visualize Atherosclerotic Lesions

Work at room temperature.

1. Place the cleaned and fixed aortas in 1.5 ml Eppendorf tubes, one aorta per tube.
2. Add 1 ml of 78 % methanol to each tube and place it on a tilted roller with gentle movement for 5 min. Replace the methanol solution and repeat this step twice.

3. Discard the methanol and add 1 ml of fresh ORO solution.
4. Incubate the tube on the tilted roller for 50–60 min (*see* **Note 4**).
5. Transfer the aorta to a clean tube and wash twice with 1 ml of 78 % methanol for 5 min each on the tilted roller.
6. Discard the methanol and refill the tube with 1 ml of PBS. If necessary, at this step aortas can be stored at 4 °C.

3.3 Quantification of Atherosclerotic Burden in ORO-Stained Aortas (See Fig. 3)

1. Using fine forceps, place the stained aorta on the dark surface of the dissecting dish (*see* **Note 5**).
2. Under the stereomicroscope, carefully remove any small piece of stained remnant adventitial fat that might be attached to the outer part of the adventitia.
3. Cut the aorta longitudinally: introduce the tips of a pair of microdissecting spring scissors into the artery lumen and cut the outer curvature of the aortic arch from the ascending arch to the left subclavian artery. Then continue cut along the length of the thoracic aorta.
4. Pin the aorta flat and lumen side up on the dissecting dish with steel minutien pins; insert the pins into the aorta at a small angle to minimize the shadow that they will cast on the illuminated aorta.

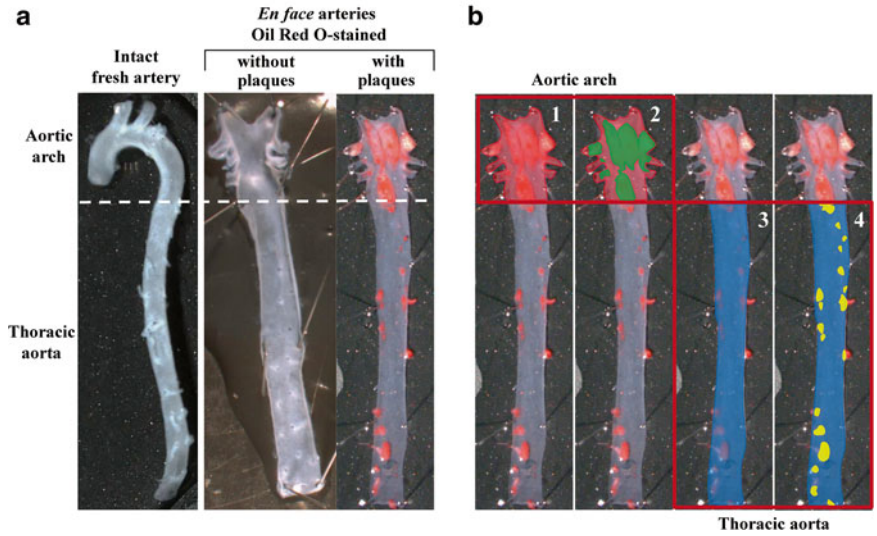

Fig. 3 Oil Red O staining and quantification of atherosclerosis burden. (**a**) Example of a freshly dissected intact aorta and ORO-stained aortas with and without atherosclerotic plaques. (**b**) Images illustrating the process for computer-assisted quantification of the area of vessel covered with atherosclerotic plaques in the aortic arch (*1*, *2*) and thoracic aorta (*3*, *4*). *1*: total aortic arch area rendered in *red*; *2*: area of aortic arch occupied by plaques rendered in *green*; *3*: total thoracic aorta area rendered in *blue*; *4*: area of thoracic aorta occupied by plaques rendered in *yellow*. Atherosclerosis burden is typically quantified as ORO-stained area as a percentage of total area

5. With a digital camera attached to the stereomicroscope and connected to a computer, capture a bright-field image (*see* **Note 6**).
6. Use appropriate software for image analysis and quantification to convert the staining in selected areas into relative quantitative data (*see* **Note 7**).

3.4 Preparation of Tissues for Paraffin Embedding (see Fig. 4)

1. For aortic root analysis, carefully trim the heart by locating the left and right atria and cutting the bottom half of the heart off with a sharp razor-blade along a plane parallel to the atria. Discard the lower half of the heart (*see* Fig. 2B and **Note 8**).
2. Immerse freshly dissected aortas and trimmed hearts in fixation solution overnight at 4 °C (*see* **Note 9**).
3. Introduce each fixed tissue sample into an individual pencil-labeled histology cassette (*see* **Notes 10** and **11**). Place the aortas between foam biopsy pads inside the cassette (*see* **Note 12).**
4. Immerse cassettes containing fixed tissues in 70 % EtOH in a container with a lid.

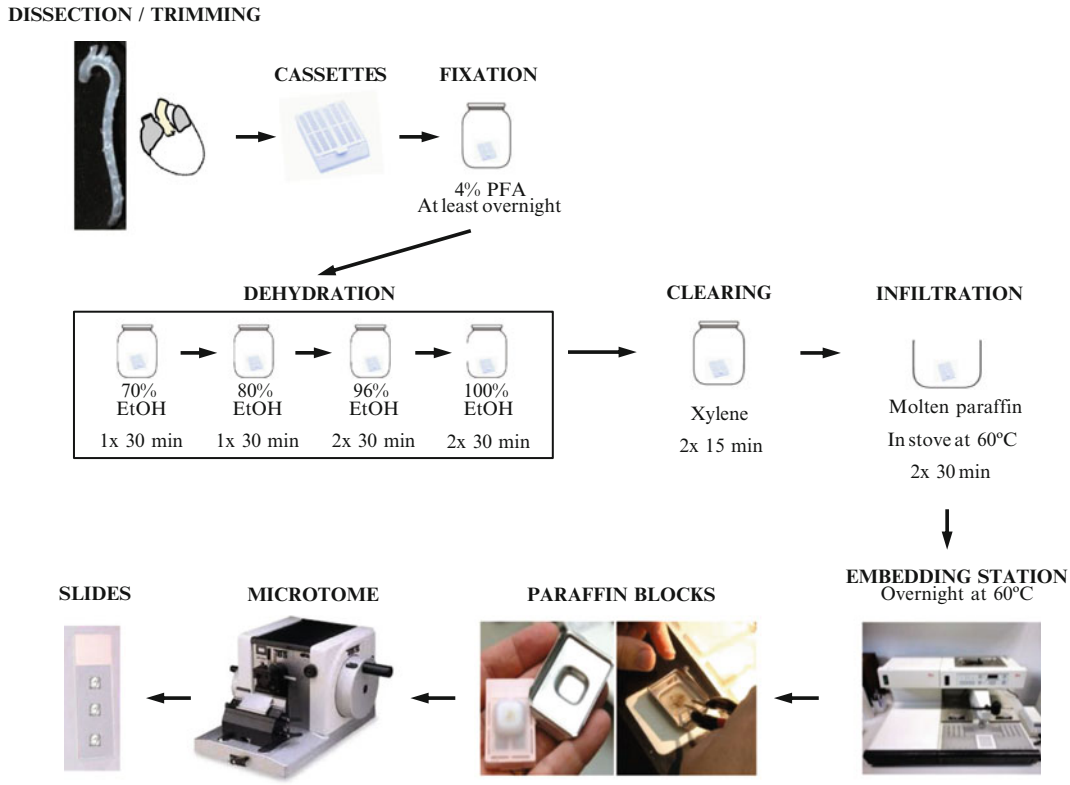

Fig. 4 Overview of the protocol for paraffin embedding and sectioning of aorta or heart (to obtain sections through the aorta and aortic root, respectively); see Subheadings 3.4 and 3.5

5. Dehydrate tissues by immersing them in solutions with increasing concentrations of EtOH (*see* **Notes 13** and **14**):

   30 min in 70 % EtOH.

   30 min in 80 % EtOH.

   30 min in 96 % EtOH (repeat this step).

   30 min in 100 % EtOH (repeat this step).

6. In a fume hood, clear tissues by immersing the cassettes in xylene for 15 min (repeat this step once, changing the xylene).
7. Infiltrate the tissues with molten paraffin by immersing the cassettes in paraffin at 60 °C for 30 min in an oven (*see* **Note 15**). Discard the molten paraffin and repeat this step once.
8. Transfer the cassettes to an embedding station containing molten paraffin and incubate at 58–60 °C overnight.
9. The next day, open the cassettes, discard the non-labeled lid, and choose the type of base mold (plastic or metal) that best fits the size of the sample, allowing an extra 2 mm spacing around all sides of the tissue.
10. Dispense a small amount of molten paraffin from the reservoir of the embedding station into the chosen mold.
11. Using warm forceps, transfer the tissue from the labeled cassette lid into the base mold, taking care to position the tissue in the desired orientation.
12. Transfer the mold to a cold plate to allow solidification of a thin layer of paraffin, which will hold the tissue in place.
13. To support the tissue and ensure its identification at later steps, place the labeled cassette lid on top of the mold so that they stick and stay together (*see* **Note 16**).
14. Once the paraffin has cooled down and hardened to a solid, separate the paraffin block from its mold (*see* **Note 17**).

3.5 Microtome Sectioning of Paraffin-Embedded Aortas and Hearts

1. Fill a water bath with deionized water and set it to a temperature 5–9 °C below the melting point of the paraffin (in preparation for the final steps of this method).
2. Cool down the paraffin blocks by placing them on the surface of melting ice for a few minutes (*see* **Note 18**).
3. Cut away any excess paraffin from the support cassette to facilitate secure clamping of the block in the following steps.
4. Insert the paraffin block into the specimen clamp so that the block faces the blade and is aligned in the vertical plane.
5. Before starting to trim the block, fit a new blade on the microtome (*see* **Note 19**) and adjust its angle to between 1° and 5°.
6. Trim the paraffin block roughly by cutting at thicknesses 10–30 μm (*see* **Note 20**).

7. When you arrive to the position in the block where sections begin to be of interest, change the microtome setting to 3–5 μm thickness and polish the surface of the block by gently cutting a few thin sections.
8. Using a part of the blade that has not been used for rough trimming, cut in the desired tissue plane and discard the paraffin ribbon (*see* **Note 21**).
9. Pick up the desired sections with forceps or a fine paintbrush.
10. Flatten the sections by floating them onto the water bath with a gentle sweeping hand movement. Make sure that the smooth/shiny side of the section is facing the water (*see* **Note 22**).
11. Collect the sections onto the surface of clean glass slides (free of grease and dust).
12. Remove the slides from the water in a vertical movement to drain off excess water.
13. Place the slides with the paraffin sections on a warming block or in a 65 °C oven for 10–30 min to allow bonding of the tissue to the glass.
14. Store ready-to-use slides at room temperature in appropriate boxes.

3.6 Hematoxylin-Eosin Staining of Paraffin-Embedded Sections

1. Warm slides with paraffin-embedded section in a dry oven at 55 °C for 5–10 min.

   From this step on work at room temperature, in a fume hood, and use slide jars for convenience.
2. Deparaffinize the sections: fill a slide jar with xylene and immerse the slides for 5 min. Repeat this step twice, changing the xylene each time (*see* **Note 23**).
3. Rehydrate sections by passing slides through a series of decreasing concentrations of EtOH as follows (*see* **Note 24**):
   - Two changes of absolute EtOH, 5 min each.
   - Two changes of 95 % EtOH, 5 min each.
   - Two changes of 70 % EtOH, 2 min each.
4. Wash briefly in distilled water (*see* **Note 25**).
5. Stain with Harris-modified hematoxylin solution for 3 min, monitoring the development of staining under a microscope (*see* **Note 26**).
6. Wash off excess stain with running tap water for 5–10 min.
7. Differentiate by immersing in 1 % acetic acid for 30 s.
8. Rinse in running tap water for 5 min to turn the stain blue.
9. Wash in 95 % EtOH for 30 s.
10. Counterstain in eosin alcoholic solution (diluted 1/10 in 95 % EtOH) for 0.5–1 min.

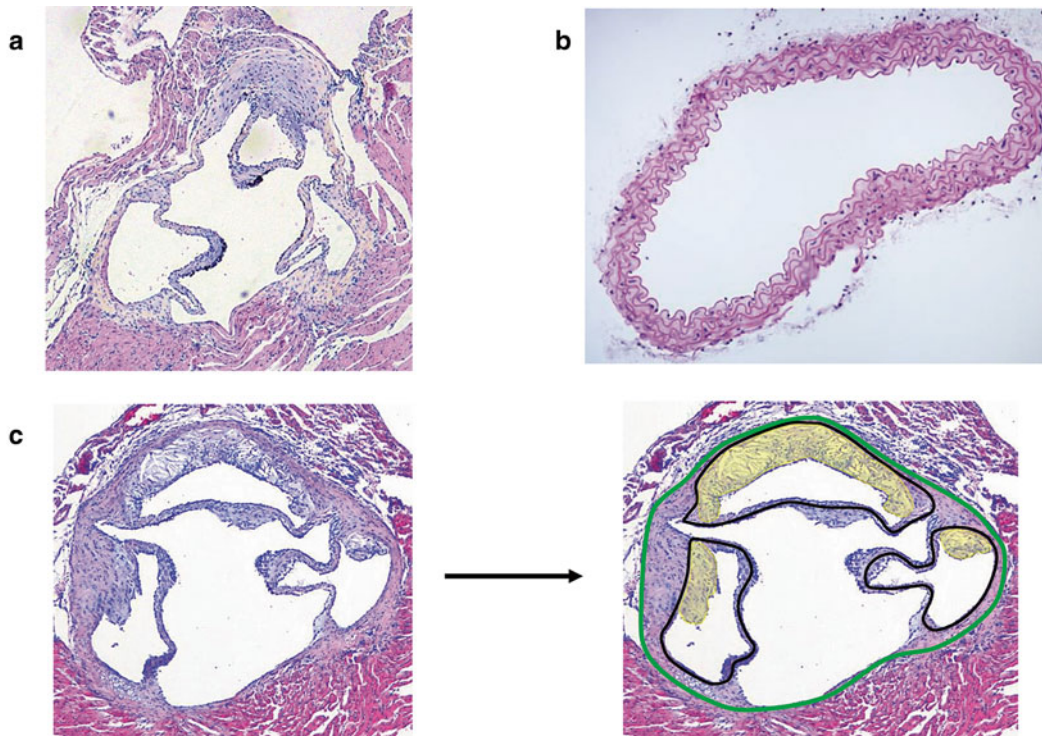

Fig. 5 Examples of hematoxylin and eosin-stained aortic sections. (**a**) Aortic root without atherosclerotic lesions. (**b**) Thoracic aorta without atherosclerotic lesions. (**c**) Aortic root with atherosclerosis plaques. In the image on the right the sinus perimeter is marked in *green* and the valve perimeter in *black*, and the atherosclerotic plaques are marked in *yellow*

11. Wash in running tap water for 5 min.
12. Dehydrate sections through increasing concentrations of EtOH (*see* **Note 27**):
    - 70 % EtOH for 2 min.
    - 95 % EtOH for 2 min.
    - Absolute EtOH for 2 min.
13. Clear in xylene for 2 min (*see* **Notes 28** and **29**).
14. Mount with xylene-based mounting medium.
15. Take pictures of H&E sections with a microscope-mounted camera (*see* Fig. 5).

4 Notes

1. ORO solution can easily precipitate in contact with air. Therefore the solution, whether prepared fresh or from a stock, should always be filtered two or three times before use

to remove precipitated particles that could interfere with the subsequent staining procedure. Use a glass funnel fitted with 0.45 μm filter paper.

2. The fixation of the aorta facilitates the removal of adventitial fat.
3. Hearts can be fixed for longer than 48 h without apparent damage to the tissue or creation of additional difficulties in the subsequent steps.
4. 50–60 min is the optimal time for staining aortic tissue with a 2 % (w/v) ORO working solution. Different ORO concentrations and staining times may be required for tissues other than aorta.
5. Placing the artery on a dark surface during this step increases contrast, making manipulation of the artery under the stereomicroscope easier. A suitable dark surface can be made by fixing adhesive black tape to the silicon pad of the dissecting dish.
6. After capturing bright-field images, we improve the contrast of the image by balancing the background, using the camera software. For this we use the option "white balance" to select a blank area in the picture lying outside the tissue image itself to be used as a reference for background correction.
7. We analyze digital images of ORO-stained arteries with SigmaScan Pro 0.5, which generates an Excel sheet in which marked areas are converted to relative numbers that can be used for graphic representation of the data.
8. Before introducing a heart into a cassette, it is advisable to trim it. This will facilitate subsequent optimal embedding and sectioning, especially if you want to expose the three aortic valves in the same geometric plane.
9. If you are not going to immediately process the tissues after fixation it is better to transfer them to 70 % EtOH. This step will both stop PFA fixation and advance the tissue to the first dehydration step. However, too long a time (more than 3 days) in 70 % EtOH can excessively dehydrate small specimens as aortas and hearts.
10. Always write on histology cassettes with pencil; any mark with regular lab markers will be erased by the EtOH used in the dehydration process.
11. The tissues must be placed loosely in the cassette to allow enough room for ample penetration of paraffin during the embedding procedure.
12. Placing aortas between foam pads in the cassettes prevents loss of these small samples during the dehydration process and is a great help in sectioning.

13. The grade and formulation of the EtOH is important. EtOH can absorb moisture from the air, and the humidity can interfere with proper dehydration and clearing of the slides. Therefore bottles of anhydrous EtOH should be stored in lidded containers and exposure to air should be kept to a minimum.
14. Stepwise increases in EtOH concentration are used to ensure that the replacement of water in the tissue by alcohol is gradual, thereby avoiding excessive distortion of the tissue.
15. Commercial paraffin waxes used for infiltration are solid at room temperature and can be purchased with different melting points. The most common paraffin wax for histological use melts at around 56–58 °C. In our experience it is better to use the paraffin wax at 2 °C above its melting point to decrease its viscosity and improve tissue infiltration.
16. Make sure that there is enough paraffin between the mold and the cassette lid and, if necessary, top up with hot paraffin from the paraffin dispenser. Failure to do this can lead to problems during sectioning, with unstable clamping or undesired differences in section thickness.
17. The paraffin blocks should pop out from the molds easily. If for any reason the blocks crack or the tissues are not aligned as desired inside the block, it is better to melt the blocks and start the paraffin embedding process over.
18. Sectioning is easier when the tissue inside the paraffin block and the paraffin itself are of similar hardness. For this reason, it is usually advisable to place the paraffin-embedded tissue blocks on a cold surface. In addition, if the surface is wet (e.g., melting ice), the water will penetrate slightly into the block, provoking swelling of the tissues which will make them more suitable for cutting. This is particularly important for excessively dehydrated or dry and crumbly tissues. However, placing the blocks in a freezer is not recommended because their surface will break easily.
19. Microtome blades are extremely sharp and can cause serious injury if not handled with care. Replace the microtome blade if sectioning becomes difficult.
20. The goal of trimming is to rapidly remove unwanted tissue until the region of interest is reached.
21. If the block is not ribboning well, place it back on the cool and wet surface to cool and to firm up the paraffin.
22. Flotation should expand the section to its original dimensions and leave it completely flat. If the sections break when they are placed on the water this is probably because the bath is too hot.
23. If the paraffin is not totally removed from the tissues it will interfere with subsequent staining procedures, decreasing

color intensity or producing an irregular color distribution within the section.

24. If the xylene from the deparaffinization step is not completely washed out by the first absolute EtOH step, subsequent carrying over of xylene into the lower EtOH concentrations could, in extreme cases, interfere with hematoxylin staining.
25. Washes are necessary to remove traces of previous solutions and to prepare the sections for the solutions in the subsequent steps. Sections should be fully submerged in liquid at all times.
26. For H&E staining sections thicker than 3–5 μm may require longer exposures to solutions in order to ensure that each reagent fully penetrates the tissue.
27. Inadequate dehydration of the tissue sections will result in slides being milky due to the mixing of water from the EtOH solutions with the xylene of the mounting medium when coverslipping.
28. This step helps to displace the EtOH from the tissue sections, ensuring full miscibility with xylene in the mounting medium. If any alcohol remains in the tissue, the eosin may bleed from the tissue section after coverslipping.
29. Avoid using low-grade xylene; industrial or engineering xylenes may contain petroleum products that can interfere with staining.

Acknowledgements

The authors thank Simon Bartlett for editorial assistance. Work in VA's laboratory is supported by grants SAF2013-46663-R and RD12/0042/0028 from the Spanish Ministerio de Economía y Competitividad (MINECO) with co-funding from the Fondo Europeo de Desarrollo Regional (FEDER), the European Commission (Liphos, Grant Agreement No. 317916), and the Progeria Research Foundation (Established Investigator Award). The CNIC is supported by the MINECO and the Pro-CNIC Foundation.

References

1. Breslow JL (1996) Mouse models of atherosclerosis. Science 272:685–688
2. Fuster JJ, Castillo AI, Zaragoza C et al (2012) Animal models of atherosclerosis. Prog Mol Biol Transl Sci 105:1–23

Chapter 6

Isolation, Culture, and Polarization of Murine Bone Marrow-Derived and Peritoneal Macrophages

Inés Pineda-Torra, Matthew Gage, Alba de Juan, and Oscar M. Pello

Abstract

Macrophages are the most specialized phagocytic cells, and acquire specific phenotypes and functions in response to a variety of external triggers. Culture of bone marrow-derived or peritoneal macrophages from mice represents an exceptionally powerful technique to investigate macrophage phenotypes and functions in response to specific stimuli, resembling as much as possible the conditions observed in various pathophysiological settings. This chapter outlines protocols used to isolate and culture murine bone marrow-derived and peritoneal macrophages. Furthermore, we describe how these macrophages can be "polarized" to obtain specific macrophage subsets with special relevance to atherosclerosis.

Key words Bone marrow-derived macrophages, Peritoneal macrophages, Macrophage polarization, Atherosclerosis

1 Introduction

Macrophages are phagocytic immune cells that play essential roles in homeostasis and orchestrate multiple responses to pathogens [1]. These cells acquire specialized phenotypes and functions depending on their microenvironment and, indeed, several macrophage subtypes have been identified and characterized over the last decade [2]. In the context of atherosclerosis, macrophages are crucial components of atherosclerotic plaques and contribute to the pathogenesis of the disease from its initial stages throughout the progression of the atheroma, and up to the final stages when the plaque becomes vulnerable and may rupture into the bloodstream [3]. During this process, macrophages contribute to a variety of functions depending on their phenotype, which in turns depends on their microenvironment. In an oversimplified classification, Th1 pro-inflammatory cytokines such as IL-2, IL-12, IFNγ, and TNFα and β lead to the activation of macrophages towards the so-called classical inflammatory phenotype (CAMs or M1 macrophages). In addition, Th2 cytokines such as IL-4 and IL-13 as well as

Vicente Andres and Beatriz Dorado (eds.), *Methods in Mouse Atherosclerosis*, Methods in Molecular Biology, vol. 1339, DOI 10.1007/978-1-4939-2929-0_6,

anti-inflammatory molecules like IL-10 and TGFβ activate macrophages towards an alternative phenotype (AAMs or M2 macrophages). While M1s have been described to be involved in the secretion of inflammatory cytokines and vasoactive molecules contributing to atheroma growth, M2 cells participate in a wide range of processes including apoptotic cell clearance or the release of anti-inflammatory molecules and are generally considered anti-atherosclerotic [4, 5]. Although IL-4 is considered "the original" cytokine promoting M2 polarization, its role in atherosclerosis still remains ambiguous, as it has been shown to be involved in both, pro- and anti-atherosclerotic mechanisms [6].

The physiological and pathophysiological processes macrophages participate in make them a very interesting therapeutic target for inflammatory diseases, including atherosclerosis and cancer. Although in recent years there have been major advances in the use of noninvasive techniques to investigate the mechanisms underlying cardiovascular diseases, the systematic study of macrophages in a living organism, specifically within the aorta or a blood vessel by these techniques, is not yet technically feasible [7]. Thus, the isolation and culture of macrophages, which may be subjected to different stimuli ex vivo, has been a very useful and widespread tool to investigate the phenotype and functions of a particular subtype of macrophages. The number, purity and ease of culture of these cells make them a very attractive in vitro model. To investigate in culture the (dys)regulated pathways within a specific macrophage subtype that are playing a role in a particular pathological condition such as atherosclerosis, macrophages are usually activated with IFNγ plus LPS (CAMs or M1) or with IL-4, IL-13, and IL-10 (AAMs or M2) [8]. Due to the complex stimuli milieu present within the atheroma, it is not surprising that other macrophage subtypes have also been described in response to other molecules that affect the pathogenesis of atherosclerosis, including oxidized-LDLs (Mox macrophages) [9], CXCL4 (M4 macrophages) [10], or heme/haemoglobin (Mhem macrophages) [11].

In this chapter we describe the most common protocols used to isolate and differentiate cultured murine bone marrow-derived macrophages and peritoneal macrophages, and outline how these macrophages are traditionally "polarized" to obtain the M1 and M2 subsets that may be relevant to atherosclerosis and other inflammatory diseases.

2 Materials

1. Purified-recombinant proteins
   (a) Murine macrophage colony-stimulating factor (M-CSF or CSF-1). Alternatively, noncommercial L929-M-CSF conditioned medium (LCM) prepared as indicated in Subheading 3.1.

(b) Murine interleukin 4 (IL-4).

(c) Murine interferon γ (IFNγ).

(d) Lipopolysaccharide (LPS).

2. High-glucose DMEM medium (with stable L-glutamine).
3. RPMI-1640 medium with L-glutamine.
4. Sterile phosphate-buffered saline (PBS) 1× suitable for cell culture.
5. Sterile-filtered penicillin/streptomycin (P/S) (10 mg/mL).
6. Sterile-filtered gentamycin (10 mg/mL) in deionized water.
7. Fetal bovine serum (FBS).
8. Complete DMEM medium: High-glucose DMEM, 10 % FBS, 5 % P/S.
9. Complete RPMI medium: RPMI-1640 medium with L-GLUTAMINE, 10 % FBS, 2 % P/S.
10. Differentiation medium: DMEM with stable glutamine + 20 % FBS + 30 % LCM + 20 μg/mL gentamycin (*see* **Notes 1** and **2**).
11. Low (≤10 EU/mL) endotoxin FBS (FBS-LE).
12. Trypsin–EDTA (0.25 % in PBS).
13. Vacuum filter units, 0.45 μm.
14. Sterile dissection tools: scissors, scalpel, and forceps.
15. Needles, 25 gauge.
16. Syringes, 5–10 mL.
17. Sterile 1.5, 15, and 50 mL tubes.
18. Centrifuge/microcentrifuge.
19. Tissue culture T-75 cm^2 and T-175 cm^2 filter cap flasks.
20. Tissue culture dishes (100 × 20 or 150 × 20 mm).
21. Tissue culture sterile polysterene pipettes (10 mL, 2 mL).
22. Plates (6-well) for macrophage culture.
23. Humidified incubator with 5 % CO_2 at 37 °C.
24. Red blood cell lysis buffer (RBC lysis buffer).
25. Mice: mouse models of atherosclerosis.
26. 70 % Ethanol in distilled water.
27. Freezing medium: 90 % FBS + 10 % dimethyl sulfoxide (DMSO).
28. Activation medium M1: 10 % FBS-LE, 20 μg/mL gentamycin, 20 ng/mL IFNγ, 100 ng/mL of LPS.
29. Activation medium M2: 10 % FBS-LE, 20 μg/mL gentamycin, 20 ng/mL IL-4.
30. Hemacytometer.

3 Methods

Before starting the methods please read carefully **Notes 3** and **4**.

3.1 Preparation of L929-Conditioned Medium (LCM)

1. Plate approximately 5×10^5 M-CSF-transduced L929 cells in a 100×20 mm tissue culture dish with 10 mL of complete DMEM medium.
2. Once confluent, split cells into six 100×20 mm dishes or T-75 cm^2 flasks with L929 medium as follows:
   - Remove medium from the tissue culture vessel.
   - Wash cells gently by tipping back and forth with 1× PBS and remove all PBS.
   - Add 0.5–1 mL trypsin–EDTA, tilt flask to cover all cells, and place back to incubator for less than 5 min at 37 °C.
   - Add 6 mL L929 medium and with a 10 mL pipette rinse cells from flask surface and pipette up and down to break up cell clumps.
   - Add 1 mL of this cell suspension to each 100×20 mm dish or T-75 cm^2 flask containing 9 mL or 19 mL L929 medium, respectively (*see* **Note 5**).
3. Once confluent, harvest cells as above and for each flask transfer the entire cell suspension into a T-175 cm^2 tissue culture flask with 40 mL of L929 medium to have a total of six T-175 cm^2 flasks.
4. Once confluent, collect medium (≈40 mL), store in 50 mL tubes, and replace with fresh L929 medium. Repeat this five times every 48 h. After each collection, spin medium at $1000 \times g$ for 5 min to remove cells and store at 4 °C.
5. Pool all collections and filter supernatant through a 0.45 μm filter attached to a vacuum unit under the laminar tissue culture hood. Store in 50 mL aliquots at –20 °C (this is the L929 conditioned medium or LCM to be used in the next step). This procedure will give you about 220–240 mL of LCM per collection and over 1 L of LCM after all collections are carried out.

3.2 Isolation of Total Bone Marrow and Macrophage Differentiation

1. Clean the abdomen and hind legs of mice with 70 % ethanol by soaking all the fur.
2. Make an incision in the midline of the abdomen, dissect the skin from abdomen and hind legs, and dissect the muscles attaching the hind limbs to the pelvis.
3. Remove the hind legs to harvest femur and tibia (thus from each animal two femurs and two tibiae) by cutting through the pelvis close to the hip joint. Remove all muscle tissue from the bones with the aid of a scalpel and dissecting scissors.

Cut the bones at both ends to free them (through beneath the knee joint, and through the foot end of the tibia and the pelvis end of the femur).

4. Collect the bones from each single animal in a 15 mL tube with 5 mL sterile tissue culture grade PBS 1×, wash briefly with 70 % ethanol, and transfer to a laminar flow hood to ensure sterility. Place bones in PBS 1× and remove any remaining tissue attached to the bones if needed.
5. Remove both epiphyses from each bone using sterile scissors and forceps (different from the ones used for dissection) to preserve sterile conditions.
6. There are two options to isolate total bone marrow from mouse tibiae and femurs:
   (a) Cut the top of a 200 μL sterile pipette tip and a 500 μL sterile pipette tip with a sterilized scalpel to make them fit into a 1.5 mL sterile tube. Put the 200 μL tip inside the 500 μL tip and this one inside the 1.5 mL tube with the narrow end of the tip facing the bottom of the tube. With the help of forceps, place the femur and the tibia inside the 200 μL tip and close the tube. Repeat this procedure for each pair of bones (4 bones/mouse = 2 tubes/mouse). To pellet cells, centrifuge tubes 3 min at room temperature at 704 × *g* in a microcentrifuge. Once the bone marrow is expelled the bone becomes transparent.
   (b) Flush each bone with PBS 1× or differentiation medium by inserting a 5 mL syringe attached to a 25-gauge needle into the bone shaft onto a clean 50 mL tube. Collect the bone marrow from all bones from a single mouse on the same tube and centrifuge for 5 min at room temperature at 310 × *g* to pellet cells.
7. Resuspend pellet in 500 μL of RBC lysis buffer, transfer into a fresh 1.5 mL tube and keep it on ice for 5 min. Add 500 μL of PBS 1× or differentiation medium and spin down to pellet cells. At this point the bone marrow pellet may be either frozen in "freezing medium" and stored at −80 °C for later use (*see* **Note 6**) or used fresh.
8. Resuspend fresh (or quickly thawed frozen bone marrow) cells in warm differentiation medium and (optional) count cells.
9. Plate cell suspension in eight tissue culture 100 × 20 mm dishes (or four 150 × 20 mm dishes) or eight 6-well plates or a combination of both (final yield depends on the mouse strain). If cells are counted, adjust the cell suspension as needed in differentiation medium and plate cells as follows: $1.5–2 \times 10^6$ cells with 2 mL in 6-well plate, or $6–8 \times 10^6$ cells with 8 mL in 100 × 20 plate, or $12–15 \times 10^6$ cells with 20 mL in 150 × 20 plate.

10. Culture cells for 6–7 days in a humidified incubator 5 % CO_2 at 37 °C: supplement cells with additional fresh differentiation medium at day 3, remove medium at day 5, wash cells with PBS 1×, and add fresh differentiation medium. Check for cell density and possible contamination (*see* **Note 7**).
11. Macrophages are fully differentiated after 6–7 days (over 90 % cells are positive for the cell type surface marker CD11b). At this point macrophages are considered proliferative non-activated cells (also named M0 macrophages).

3.3 Macrophage Polarization

1. At day 6–7 of culture (from Subheading 3.2, **step 11**), remove medium from M0 macrophages and wash them with PBS 1× (*see* **Note 8**).
2. Add activation medium M1 for M1 polarization or activation medium M2 for M2 polarization for 24 h (for RNA analysis) or 48 h (for protein analysis), or leave cells in activation medium (without the polarizing factors) overnight before adding the activators (*see* **Note 9**).

3.4 Isolation and Polarization of Peritoneal Macrophages

If you are going to perform this method please *see* **Notes 10–12**.

1. Euthanize mice by cervical dislocation or inhalation of carbon dioxide (CO_2) followed by cervical dislocation to ensure death has occurred.
2. Clean the mouse abdomen with 70 % ethanol and make a small incision with a sterile scalpel. Use forceps to remove the abdominal skin to expose the peritoneum.
3. Use a 5 mL syringe with a 25-gauge needle attached to inject 4 mL PBS 1× through the peritoneal wall into the peritoneal cavity being careful not to puncture the intestine or any other organ.
4. Gently massage the mouse abdomen.
5. Use the same 5 mL syringe attached to a 25-gauge needle to slowly recover as much PBS 1× as possible into a 15 mL tube.
6. Centrifuge for 5 min at 4 °C at 310 × *g* to pellet cells.
7. Discard supernatant and resuspend cells in 1 mL complete RPMI medium and count cells on a hemacytometer.
8. Plate cells as needed in complete RPMI medium. Due to the low number of total macrophages within the peritoneal cavity in steady-state conditions, generally $1–3 \times 10^6$ cells can be recovered (two wells in a 6-well plate).
9. Allow macrophages to attach for 1 h in a humidified incubator with 5 % CO_2 at 37 °C.
10. Polarize these macrophages according to the procedure described in Subheading 3.3 (*see* **Note 9**).

4 Notes

1. One of the concerns regarding the variety of protocols used to obtain bone marrow-derived macrophages is the use of purified recombinant M-CSF versus LCM as a source of M-CSF. It should be noted that supernatants from cultured L929 cells could carry different amounts of M-CSF (depending on the batch and procedure) as well as other molecules. Researchers should first ensure whether the proportions of LCM indicated in this protocol give an optimal differentiation of macrophages (cell attachment at day 4 in non-coated petri dishes) before conducting any experimental procedures with them.
2. For the preparation of differentiation medium (Subheading 2, **item 10**), first remove 250 mL medium from a 500 mL DMEM bottle and transfer into a clean and sterile bottle. Store at 4 °C for future preparations. To the remaining DMEM, add 1 mL gentamycin of a 10 mg/mL stock, 100 mL FBS and 150 mL of LCM and mix well. Instead of DMEM, RPMI-1694 may also be used.
3. Techniques should be performed under sterile conditions. Rinse all material with 70 % ethanol before use and sterilize all tools dedicated to dissection. Manipulate cells in a laminar flow hood and culture cells in a humidified incubator 5 % CO_2 at 37 °C.
4. Animals should be maintained in pathogen-free conditions and sacrificed in a designated area for this purpose according to the relevant regulatory laws for animal experimentation. Death must occur without producing pain, the time to produce loss of consciousness and induce death must be as short as possible, and the method must be reliable and nonreversible. To isolate bone marrow, animals are generally sacrificed by cervical dislocation or inhalation of carbon dioxide (CO_2) followed by cervical dislocation to ensure that death has occurred.
5. To obtain macrophages derived from bone marrow cells, progenitor cells from the marrow of femurs and tibiae are propagated in the presence of M-CSF secreted by L929 cells and used in the form of LCM. Alternatively, recombinant M-CSF can be used (*see* **Note 1**).
6. We routinely freeze and store bone marrow till we need to differentiate cells for further experiments. We have not observed any differences in the differentiation or responses to different inflammatory stimuli of macrophages derived from frozen marrow. This has been also documented in more detail in [12].
7. Flasks are preferred to minimize contamination since cells are kept in culture for over a period of approximately 2 weeks.

8. Removal of M-CSF ensures there is no interference with the subsequent activation steps in the protocol. Growth serum that has been certified to contain very low amounts of endotoxin is preferred for the culture of differentiated macrophages when they are going to be activated by inflammatory stimuli such as those mentioned in this chapter.
9. In vitro, macrophages are usually stimulated with a single stimulus, which is only a limited amount of the wide variety of cytokines they may be exposed in their in vivo microenvironment. Thus, M1 and M2 phenotypes represent simplified extremes of a "polarization spectrum," and in vivo, intermediate phenotypes are likely to exist. In addition, the specific stimuli used may vary depending on the pathology. For instance, IL-4 may not be the most suitable cytokine to study the alternative activation of macrophages in atherosclerosis, and hence, new stimuli have been investigated [9–11]. These alternative stimuli could better resemble macrophage activation within the atherosclerotic plaque although studies are still needed to directly assess how similar macrophages polarized in culture resemble those found within atherosclerotic plaques that are positive for some of the commonly used murine M1 or M2 markers such as nitric oxide synthase or arginase 1, respectively. Even alternative macrophages derived from proliferation of tissue resident cells or from recruited inflammatory monocytes appear to have distinct physiological properties [13]. This further highlights the challenges encountered when trying to replicate pathological processes in cultured cells.
10. Phenotypical and functional differences have been described in murine macrophages isolated from different organs [14].
11. Murine macrophages can be additionally isolated from the peritoneal cavity, which provides an easily accessible site to obtain moderate numbers of resident macrophages to be used in subsequent in vitro studies.
12. Due to the relatively low yields of macrophages that can be recovered from a mouse peritoneal cavity in steady-state conditions, intra-peritoneal injection of macrophage-eliciting agents to recruit immature macrophages is generally used to substantially increase macrophage numbers. Injection of thioglycollate broth for instance, recruits larger number of macrophages. However it is controversial whether these macrophages are activated or not since their physiological characteristics may be different from resident cells [15]. Macrophages elicited after intra-peritoneal injection of LPS show an inflammatory/M1 phenotype [16] whereas injection of IL-4 after thioglycollate increases the amount of M2 macrophages that can be directly recovered from the peritoneal cavity [17].

References

1. Wynn TA, Chawla A, Pollard JW (2013) Macrophage biology in development, homeostasis and disease. Nature 496(7446):445–455
2. Molawi K, Sieweke MH (2013) Transcriptional control of macrophage identity, self-renewal, and function. Adv Immunol 120:269–300
3. Andres V, Pello OM, Silvestre-Roig C (2012) Macrophage proliferation and apoptosis in atherosclerosis. Curr Opin Lipidol 23(5): 429–438
4. Murray PJ, Wynn TA (2011) Protective and pathogenic functions of macrophage subsets. Nat Rev Immunol 11(11):723–737
5. Hoeksema MA, Stoger JL, de Winther MP (2012) Molecular pathways regulating macrophage polarization: implications for atherosclerosis. Curr Atheroscler Rep 14(3):254–263
6. Chinetti-Gbaguidi G, Staels B (2011) Macrophage polarization in metabolic disorders: functions and regulation. Curr Opin Lipidol 22(5):365–372
7. Mureddu GF, Brandimarte F, Faggiano P et al (2013) Between risk charts and imaging: how should we stratify cardiovascular risk in clinical practice? Eur Heart J Cardiovasc Imaging 14(5):401–416
8. Pello OM, Silvestre-Roig C, De Pizzol M et al (2011) A glimpse on the phenomenon of macrophage polarization during atherosclerosis. Immunobiology 216(11):1172–1176
9. Kadl A, Meher AK, Sharma PR et al (2010) Identification of a novel macrophage phenotype that develops in response to atherogenic phospholipids via Nrf2. Circ Res 107(6): 737–746
10. Gleissner CA (2012) Macrophage phenotype modulation by CXCL4 in atherosclerosis. Front Physiol 3:1
11. Boyle JJ (2012) Heme and haemoglobin direct macrophage Mhem phenotype and counter foam cell formation in areas of intraplaque haemorrhage. Curr Opin Lipidol 23(5):453–461
12. Marim FM, Silveira TN, Lima DS et al (2010) A method for generation of bone marrow-derived macrophages from cryopreserved mouse bone marrow cells. PLoS One 5(12), e15263
13. Gundra UM, Girgis NM, Ruckerl D et al (2014) Alternatively activated macrophages derived from monocytes and tissue macrophages are phenotypically and functionally distinct. Blood 123(20):e110–e122
14. Wang C, Yu X, Cao Q et al (2013) Characterization of murine macrophages from bone marrow, spleen and peritoneum. BMC Immunol 14:6
15. Ghosn EE, Cassado AA, Govoni GR et al (2010) Two physically, functionally, and developmentally distinct peritoneal macrophage subsets. Proc Natl Acad Sci U S A 107(6): 2568–2573
16. Patel OV, Wilson WB, Qin Z (2013) Production of LPS-induced inflammatory mediators in murine peritoneal macrophages: neocuproine as a broad inhibitor and ATP7A as a selective regulator. Biometals 26(3):415–425
17. Nguyen KD, Qiu Y, Cui X et al (2011) Alternatively activated macrophages produce catecholamines to sustain adaptive thermogenesis. Nature 480(7375):104–108

Chapter 7

Isolation of Mouse Primary Aortic Endothelial Cells by Selection with Specific Antibodies

Pedro Molina-Sánchez and Vicente Andrés

Abstract

Endothelial cells (ECs) are key blood-vessel-wall components that play critical roles in the regulation of many physiological processes, including angiogenesis, coagulation, and vascular tone control, and in pathological events such as vessel inflammation and leukocyte infiltration. EC dysfunction is one of the first events associated with the development of atherosclerosis and is sustained throughout progression of the disease. The study of ECs in vitro has become an invaluable tool for investigating these vascular processes at the molecular level, and is widely used in the search for therapeutic targets and strategies. This chapter describes a protocol for the isolation and culture of primary mouse aortic ECs based on antibody-mediated EC selection.

Key words Endothelial cells, Isolation, Culture, Antibody-mediated selection, Mouse aorta, Atherosclerosis

1 Introduction

The endothelium is the thin cell layer that faces the blood-vessel lumen and is in direct contact with flowing blood. The key functional components of any vascular endothelium are the endothelial cells (ECs). First described as a simple passive barrier, the endothelium is now viewed as a complex and active participant in the regulation of diverse vascular processes, including inflammation and leukocyte infiltration [1], vascular tone [2], and coagulation [3, 4]. In the particular case of atherosclerosis, risk factors such as hypercholesterolemia, diabetes, and smoking trigger an inflammatory response that causes the accumulation of dysfunctional ECs, characterized by the expression of adhesion molecules that promote leukocyte recruitment to the artery wall [5]. This endothelial dysfunction is the first step in atherogenesis, preceding the formation of fatty streaks, and is sustained throughout disease progression, thus contributing to the eventual generation of gross atheromatous plaques [6]. Since the endothelium is also involved in the

Vicente Andrés and Beatriz Dorado (eds.), *Methods in Mouse Atherosclerosis*, Methods in Molecular Biology, vol. 1339, DOI 10.1007/978-1-4939-2929-0_7,

regulation of vascular tone, EC dysfunction may contribute to atherosclerosis development by increasing blood pressure, a well-known proatherogenic risk factor.

Today, a variety of approaches for studying EC function and its relation to vascular disease are available, ranging from ex vivo systems such as wire and pressure myography [7] to highly sophisticated genetically modified mouse models in which gene expression in the endothelium is specifically disrupted or augmented [8–13]. However, in vitro studies with primary EC cultures remain an essential tool for investigating critical processes in EC pathobiology at the molecular level (e.g., proliferation, migration, apoptosis, angiogenesis, release of vasoactive molecules and expression of adhesion molecules). Here we describe a simple procedure for obtaining ECs from mouse aorta based on selection for specific markers.

2 Materials

1. Young mice (8–12 weeks old) (e.g., C57BL/6J).
2. Surgical material: Fine forceps (e.g., Dumont Medical Biology Forceps, FST Cat. No. 11254-20) and scissors (e.g., Extra Fine Bonn Scissors, FST Cat. No. 14084-08).
3. Anesthetics: Ketamine (e.g., Imalgene 1000, Merial) and Medetomidine (e.g., Medeson, Urano). Alternatively, CO_2 chamber.
4. Phosphate-buffered saline (PBS): 8.0 g/L NaCl, 0.2 g/L KCl, 1.44 g/L Na_2HPO_4 in distilled water.
5. Saline solution: 0.90 % (w/v) NaCl in distilled water.
6. Stereo microscope (e.g., Olympus SZX10).
7. DMEM-F12 medium (e.g., Lonza, Cat. No. BE04-687Q).
8. Heparin sodium salt (heparin) from porcine intestinal mucosa (e.g., Sigma, Cat. No. 9041-08-1).
9. Fetal bovine serum (FBS, e.g., Thermoscientific, Cat. No. SV30160.03) inactivated by heating at 56 °C for 30 min.
10. Penicillin and streptomycin (Pen/Strep) solution for culture media (e.g. Pen/Strep stock 10K/10K, Lonza, Cat. No. DE 17-602E).
11. L-Glutamine (e.g., Lonza, Cat. 17-605C).
12. EC growth factor (ECGF) (e.g., Sigma, Cat. No. E2759).
13. EC medium: DMEM-F12 supplemented with 1 % Pen/Strep, 0.4 mM L-glutamine, 10 mM heparin and 50 μg/mL ECGF.
14. HEPES (1 M stock in normal saline; e.g., Lonza, Cat. No. 17-737E).
15. 0.25 % Trypsin/EDTA 1× (e.g., Gibco, Cat. No. 25200-072).

16. Anti-mouse-CD102 antibody (e.g., rat anti-mouse-CD102, BD Pharmingen, Cat. No. 553326).
17. Secondary antibody bound to magnetic beads (e.g., Dynabeads® sheep anti-rat IgG, Life Technologies, Cat. No. 110.35).
18. Magnet (e.g., DynaMag™-15 Magnet, Life Technologies, Cat. No. 12301D).
19. 24-Well culture plates.
20. Matrigel (e.g., Corning, Cat. No. 354234).
21. Gelatin (e.g., Sigma, Cat. No. G9382).
22. Collagen (e.g., Sigma, Cat. No. C8919).
23. Gelatin-coating solution: PBS supplemented with 0.5 % gelatin and 0.1 mg/mL collagen.
24. Ice, fridge, or cold room.
25. Three-dimensional laboratory shaker.

3 Method

1. Euthanize 5–8 mice using any ethically approved method (*see* **Note 1**).
2. Place the mice in *decubitus supine* position and dissect them to remove the thoracic aorta (*see* **Note 2** and Fig. 1a, b).
3. Place the aortas in cold PBS or saline solution (*see* **Note 3** and Fig. 1c).
4. Under a stereomicroscope, use fine forceps to carefully remove all fat tissue from the aorta (*see* **Note 4** and Fig. 1d).
5. Dissect aortas longitudinally with a scalpel to obtain 0.5–0.8-mm-wide strips (*see* Fig. 1e).
6. In sterile conditions (*see* **Note 5**) place the aortic strips lumen-face down in the wells of a 24-well culture plate coated with unset Matrigel. Incubate the plates in a humidified cell culture incubator at 37 °C until the Matrigel solidifies (at least 2 h) (*see* **Notes 6** and 7).
7. Cover the wells with 2 mL of EC medium and culture the aortic strips for a minimum of 1 week (*see* **Note 8** and Fig. 1f). When cell colonies are formed (*see* Fig. 1g), remove the remaining aortic tissue from the well and collect the cells as follows:
   - Wash the attached cells with PBS at least three times.
   - Add trypsin and incubate at 37 °C to detach the cells (usually 5 min).
   - Block trypsin activity by adding EC medium supplemented with 10 % FBS, and pellet the cells by centrifugation at approximately 200 × *g* for 5 min.

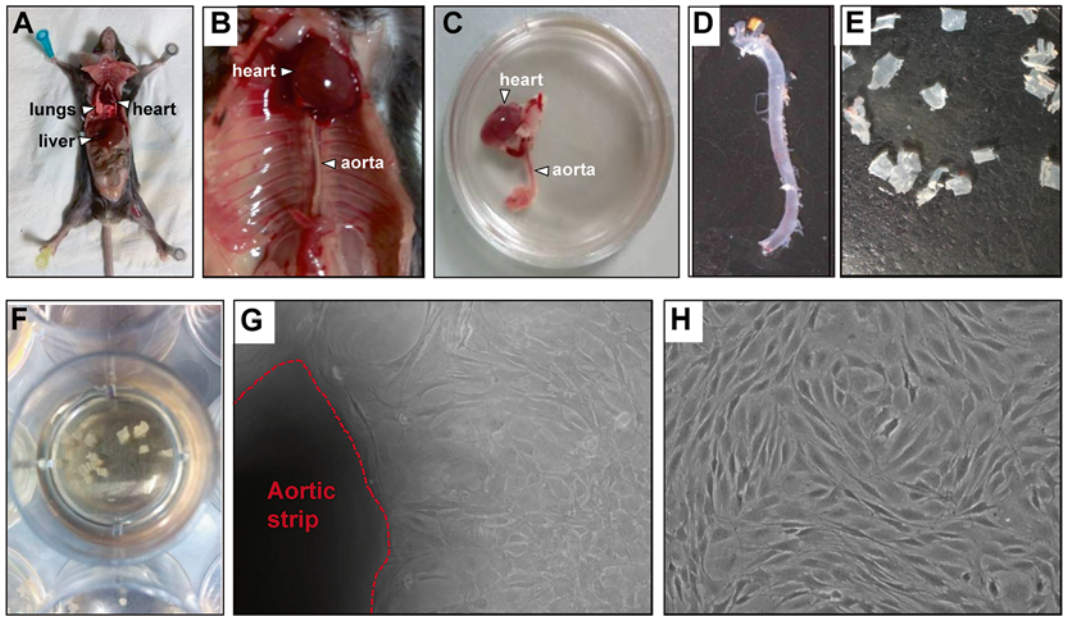

Fig. 1 Steps in mouse aortic endothelial cell extraction and culture. (**a**) Dissection of the animal to expose the thoracic and abdominal cavities. (**b**) Isolation of the aorta and heart in the thoracic cavity. (**c**) Petri dish containing aorta and heart in saline solution or PBS. (**d**) Cleaned aorta. (**e**) Aortic strips in a Petri dish. (**f**) Aortic strips in Matrigel-coated plates. (**g**) Migration of primary cell from an aortic strip (outlined by the *red dashed line*) onto the surface of the culture plate. (**h**) Confluent EC monolayer

8. Resuspend the cells in EC medium containing 10 % of FBS and plate them in gelatin-coated plates (*see* **Note 9**). Incubate the cells to expand the culture (*see* **Note 10**).
9. Select the ECs from the culture as follows:
   - To each well add anti-CD102 antibody (3.5 μL/mL EC medium) and incubate for 30 min at 4 °C in a shaker set at low velocity (*see* **Notes 11** and **12**).
   - Remove the medium containing the anti-CD102 antibody and wash the cells 2–3 times with PBS.
10. To each well add EC medium containing an appropriate secondary antibody linked to magnetic beads (e.g., anti-rat IgG if using rat IgG anti-mouse CD102 as primary antibody). Secondary antibody should be diluted 3.5 μL/mL EC medium. Incubate for 30 min at 4 °C (*see* **Note 13**).
11. Wash the cells with PBS (2–3 times) and detach them with trypsin (as described in **step 7**).
12. Use a magnet to retrieve cells bound to magnetic beads.
13. Wash the ECs retained on the magnet with PBS and culture them in EC medium in gelatin-coated plates (as described in **step 8**).
14. Expand the EC culture as necessary (*see* **Note 14**).

4 Notes

1. For this procedure several euthanasia methods can be used, for example, CO_2 inhalation or chemical anesthetics overdose. Cervical dislocation carries a significant risk of damaging the aorta and therefore of losing useful material for EC extraction.
2. The abdominal aorta can also be used for endothelial cell isolation, but its extraction and cleaning requires additional time that prolongs the protocol. The duration of the procedure strongly influences extraction efficiency and EC viability, and therefore the shorter the dissection and cleaning time the better the result.
3. In many dissection procedures mice are transcardially perfused with buffer to flush out blood from organs and tissues. However, this procedure can damage or even remove the endothelium, and therefore for EC extraction this step should either be omitted or performed with extreme care.
4. For this procedure, it is important that the aorta be dissected as cleanly as possible from the beginning; this avoids excessive handling in subsequent steps and thus increases final cell viability. To maintain endothelium integrity during cleaning, it is important to avoid pinching the aorta as much as possible.
5. Working in sterile conditions is recommended throughout the procedure in order to avoid contamination of the cell culture. Unfortunately, sometimes this is not possible due to technical limitations, especially during aorta isolation and cleaning.
6. Prepare the coated plates ahead of time by chilling them on ice and covering the wells with a solution of 200 μg/mL of cold Matrigel; this will solidify upon incubation at 37 °C in the cell culture incubator once the aortic strips are added.
7. Usually the strips derived from 2 to 3 aortas are pooled together in one well. Correct attachment of the aorta strips to the well surface is critical for the success of the procedure. Therefore try not to shake the culture plates accidentally when placing them in the incubator or transporting them back to the culture hood.
8. EC medium should be changed at least once every 3 days and always with extreme care to avoid detaching the artery explants. Cell colonies should start to appear before day 7; however, due to technical variability, this can take up to 2 weeks.
9. ECs need to be cultured on gelatin-coated plates. The plates can be prepared as follows: pour gelatin coating solution (*see* Subheading 2, **item 23**) into each well to cover the surface (0.5 mL per well for a 24-well plate), place the plates for at least 1 h at 37 °C in a cell culture incubator, and remove the leftover of gelatin by aspiration just before using the plates.

10. ECs are not the most abundant cell type in the aorta, and their proliferation rate is relatively low compared with other cells from the same blood vessel. To ensure a reasonable yield of ECs at the end of the procedure, it is advisable to expand the culture as much as possible before selection. However, it is also important to consider that the other cell types present in the culture can colonize the plate before ECs. In our hands, a good quantity of ECs is obtained by expanding the cells until 60–70 % confluence before selection.
11. ECs can be selected with different antibodies (e.g., CD102, CD31, CD106, or CD146) with similar results. Before choosing an antibody, check that it is optimal for your particular set of experiments. The procedure described here is based on selection with an antibody to CD102, which is specifically expressed in ECs and leukocytes. However, this antibody may not be appropriate if you do not work in an inflammatory context, because expression of CD102 is very low in aorta in basal conditions.
12. Although low temperatures can be harmful to cultured cells, we have found that the final yield of viable ECs increases if the incubation with the specific primary antibody is performed at 4 °C. This temperature improves recognition of the specific antigen at the cell surface and avoids loss of efficiency due to antibody internalization.
13. In addition to selection with magnetic beads as described here, many other systems are available for selection of a specific cell population from a mixture of cell types, for example, use of fluorescent-labeled antibodies followed by flow cytometry sorting.
14. With prolonged time in culture, primary ECs undergo processes of cell senescence and dedifferentiation, and therefore should not be used for in vitro studies after more than 7–8 passages.

Acknowledgements

We thank Simon Bartlett for English editing. Work in V.A.'s laboratory is supported by grants from the Spanish Ministry for Economy and Competitiveness (MINECO) (SAF2013-46663-R), the Fondo Europeo de Desarrollo Regional (FEDER), the Instituto de Salud Carlos III (RD12/0042/0028), the Progeria Research Foundation (Innovator Award 2012, Established Investigator Award 2014), and the European Union (Liphos, Grant Agreement 317916). P.M-S. is supported by an FPU predoctoral fellowship from MINECO. The Centro Nacional de Investigaciones Cardiovasculares (CNIC) is supported by the MINECO and the Pro-CNIC Foundation.

References

1. Pober JS, Sessa WC (2007) Evolving functions of endothelial cells in inflammation. Nat Rev Immunol 7:803–815
2. Félétou M (2011) The endothelium: Part 1. Multiple functions of the endothelial cells—Focus on endothelium-derived vasoactive mediators. Morgan & Claypool Life Sciences, San Rafael (CA)
3. van Hinsbergh VW (2012) Endothelium–role in regulation of coagulation and inflammation. Semin Immunopathol 34:93–106
4. Wu KK, Thiagarajan P (1996) Role of endothelium in thrombosis and hemostasis. Annu Rev Med 47:315–331
5. Libby P, Ridker PM, Hansson GK (2011) Progress and challenges in translating the biology of atherosclerosis. Nature 473: 317–325
6. Hansson GK (2005) Inflammation, atherosclerosis, and coronary artery disease. N Engl J Med 352:1685–1695
7. Spiers A, Padmanabhan N (2005) A guide to wire myography. Methods Mol Med 108: 91–104
8. Alva JA, Zovein AC, Monvoisin A et al (2006) VE-Cadherin-Cre-recombinase transgenic mouse: a tool for lineage analysis and gene deletion in endothelial cells. Dev Dyn 235:759–767
9. Terry RW, Kwee L, Baldwin HS et al (1997) Cre-mediated generation of a VCAM-1 null allele in transgenic mice. Transgenic Res 6:349–356
10. Licht AH, Raab S, Hofmann U et al (2004) Endothelium-specific Cre recombinase activity in flk-1-Cre transgenic mice. Dev Dyn 229: 312–318
11. Gothert JR, Gustin SE, Hall MA et al (2005) In vivo fate-tracing studies using the Scl stem cell enhancer: embryonic hematopoietic stem cells significantly contribute to adult hematopoiesis. Blood 105:2724–2732
12. Gustafsson E, Brakebusch C, Hietanen K et al (2001) Tie-1-directed expression of Cre recombinase in endothelial cells of embryoid bodies and transgenic mice. J Cell Sci 114:671–676
13. Kisanuki YY, Hammer RE, Miyazaki J et al (2001) Tie2-Cre transgenic mice: a new model for endothelial cell-lineage analysis in vivo. Dev Biol 230:230–242

Chapter 8

Isolation and Culture of Aortic Smooth Muscle Cells and In Vitro Calcification Assay

Ricardo Villa-Bellosta and Magda R. Hamczyk

Abstract

Elevated serum phosphorus is a major risk factor for vascular calcification, which is characterized by the presence of calcium phosphate deposits, mainly hydroxyapatite crystals. In vitro studies of phosphate-induced calcification show that vascular smooth muscle cells undergo calcification with features similar to those observed in pathological vascular calcification in vivo, including the presence of hydroxyapatite crystals. Here, we describe the double-collagenase digestion method for isolating vascular smooth muscle cells from aorta, and a method for inducing calcification in vitro using high phosphate concentration.

Key words Vascular smooth muscle cells, Pi-induced calcification, Hydroxyapatite, Calcium phosphate deposits, Aorta, Collagenase

1 Introduction

Cardiovascular complications due to arterial stiffening are the principal cause of morbidity and mortality in patients with chronic kidney disease [1, 2]. Medial calcification, also known as Monckeberg's medial calcinosis [3], occurs within the elastic region of arteries and is almost exclusively associated with vascular smooth muscle cells (VSMCs) [4]. In contrast, intimal calcification occurs in atherosclerotic lesions and is associated with VSMCs and also macrophages [5, 6]. Calcium-phosphate deposition, in the form of hydroxyapatite crystals ($Ca_{10}(PO_4)_6(OH)_2$), is the hallmark of both medial and intimal calcification and can occur in the blood vessels, myocardium, and cardiac valves [7].

Elevated serum phosphorus (in the form of inorganic phosphate, Pi) is a major risk factor for vascular calcification [8, 9]. Investigators in the 1980s discovered links between arterial calcification and bone resorption. Similarities identified at the molecular level between calcified artery and bone led Giachelli et al. [10] and Bostrom et al. [11] to propose that vascular calcification occurs

Vicente Andrés and Beatriz Dorado (eds.), *Methods in Mouse Atherosclerosis*, Methods in Molecular Biology, vol. 1339, DOI 10.1007/978-1-4939-2929-0_8,

essentially through the same molecular mechanisms that govern bone formation during embryonic development.

Vascular calcification has been extensively studied in cell culture models. For example, VSMCs spontaneously produce bone mineral (hydroxyapatite) upon treatment with elevated phosphate (2.7 mM) [12]. Under elevated phosphate conditions, the extracellular matrix surrounding VSMCs undergoes calcification with features similar to that observed in bone and in pathological vascular calcification in vivo, including the presence of hydroxyapatite crystals [7, 13].

There are two major hypotheses regarding the fate of VSMCs in phosphate-induced medial calcification. The first invokes a profound transition to a bone-forming phenotype. Supporting this notion, in vitro studies have shown that elevated phosphate results in loss of VSMCs markers (SM α-actin, SM22α) and induces expression of osteochondrogenic markers (Runx2/Cbfa1) [14]. The transcription factor Runx2/Cbfa1 induces the expression of major components of the bone matrix, including type I collagen, osteocalcin and osteopontin. The second hypothesis involves apoptosis-dependent matrix mineralization, which has been detected both in cultured human VSMCs [15, 16] and in arteries from pediatric dialysis patients [17].

A common experimental approach is to study Pi-induced calcification in VSMCs in vitro. However, many laboratories lack methods to extract these cells from arteries and to induce calcification with high phosphate. This chapter describes these methods in 5 sections: Subheading 3.1. Collagenase preparation; Subheading 3.2. Murine aorta dissection; Subheading 3.3. Vascular smooth muscle cell isolation and culture; Subheading 3.4. Pi-induced calcification induction; and Subheading 3.5. Calcium phosphate deposit detection.

2 Materials

2.1 Collagenase Preparation

1. Collagenase type 2.
2. *sMEM*: Minimal essential medium (MEM) supplemented with 1 mM L-glutamine, 100 IU/mL penicillin and 100 μg/mL streptomycin. Store at 4 °C.
3. Sterile syringe filter 0.22 μm.

2.2 Murine Aorta Dissection

1. 70 % ethanol in distilled H_2O.
2. Dissection material (tweezers and scissors).
3. Phosphate-buffered saline (**PBS**): 1.54 mM KH_2PO_4, 155.17 mM NaCl and 2.70 mM Na_2HPO_4, pH 7.4 (*see* **Note 1**), sterilized by autoclaving.
4. Syringe and needle (25 G).

2.3 Vascular Smooth Muscle Cell Isolation and Culture

1. A pair of microdissection tweezers.
2. PBS (as in Subheading 2.2, **item 3**).
3. Sterile scalpel blade.
4. Magnetic stirrer and a stir bar.
5. Sterile forceps.
6. Heat-inactivated fetal bovine serum (*FBS*). Incubate FBS at 56 °C during 30 min.
7. Pipettes, plates, tubes, and cell culture dishes.
8. Trypsin 1×.

2.4 Pi-Induced Calcification In Vitro

1. 1 M Na_2HPO_4 (disodium phosphate) stock solution in distilled H_2O.
2. 1 M of NaH_2PO_4 (monosodium phosphate) stock solution in distilled H_2O.
3. Distilled H_2O.
4. Sterile syringe filter 0.22 μm.
5. *sMEM* (as in Subheading 2.1, **item 2**).
6. *FBS* (as in Subheading 2.3, **item 5**).

2.5 Calcium Phosphate Deposit Detection

1. 2 % (w/v) Alizarin Red S in distilled H_2O.
2. 10 % NH_4OH (ammonium hydroxide) in distilled H_2O.
3. 3 % (w/v) paraformaldehyde in distilled H_2O.
4. PBS (as in Subheading 2.2).

3 Methods

3.1 Collagenase Preparation

1. Dissolve 30 mg of type 2 collagenase in 15 mL of sMEM (*see* **Note 2**) in a clean non-sterile beaker, to obtain a 2 mg/mL collagenase solution (*see* **Note 3**).
2. Filter the collagenase solution through a sterile 22 μm syringe filter: 10 mL into a 50 mL sterile plastic tube and 5 mL into a 35 mm sterile culture dish. Store the dish and the tube for use in Subheading 3.3, **steps 5** and **11**, respectively (*see* Fig. 1). Use the collagenase solution *on the day of preparation*.

3.2 Mouse Aorta Dissection

1. Select mice from which aortas will be dissected. Usually 5–10 mice are required for one VSMC isolation procedure (*see* **Note 4**). The same protocol can be used for rat aortas.
2. Euthanize the first mouse (*see* **Note 5**).
3. Spray the mouse with 70 % of ethanol and make an initial cut in the lower part of the abdomen.

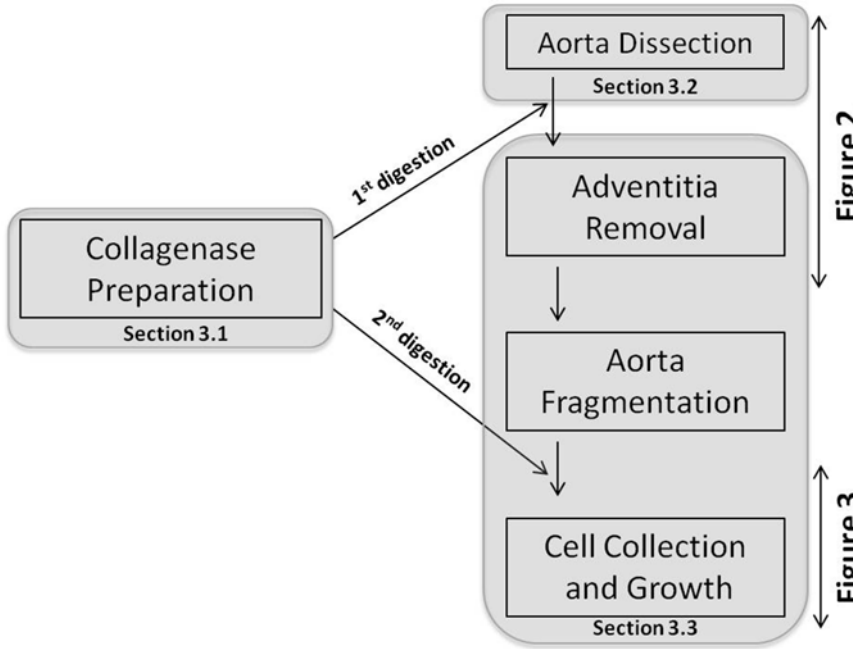

Fig. 1 Double-collagenase digestion procedure for VSMC isolation from aorta

4. Cut the skin from both sides to visualize the organs and the rib cage.
5. Open the chest cavity by cutting the ribs from both sides to access the heart.
6. Remove or move organs (liver, spleen, intestine, etc.) to reach the aorta, which is visible as a white tube running along the spine.
7. With scissors, cut the abdominal aorta below the renal arteries.
8. With a syringe, inject 5 mL of PBS into the left ventricle in order to flush blood out of the aortic lumen.
9. Carefully dissect the aorta away from the vertebral column using small surgical scissors (straight or curved) and forceps (*see* **Note 6**). Start above the abdominal part of the aorta where the diaphragm is attached and work towards the heart.
10. Separate the aorta from the heart; make a cut before the aortic arch to obtain only the thoracic part (*see* **Note 7**). Put the isolated aorta in a culture dish containing PBS (*see* Fig. 2a).
11. Follow the same procedure (**steps 2**–7) for all mice. Store all the dissected aortas in PBS until further use (next Subheading 3.3).

3.3 Vascular Smooth Muscle Cell Isolation and Culture

1. Use a microscope and two microdissection tweezers to remove the tissue surrounding the newly isolated aortas (from Subheading 3.1) and obtain clean aortas (*see* Fig. 2b).

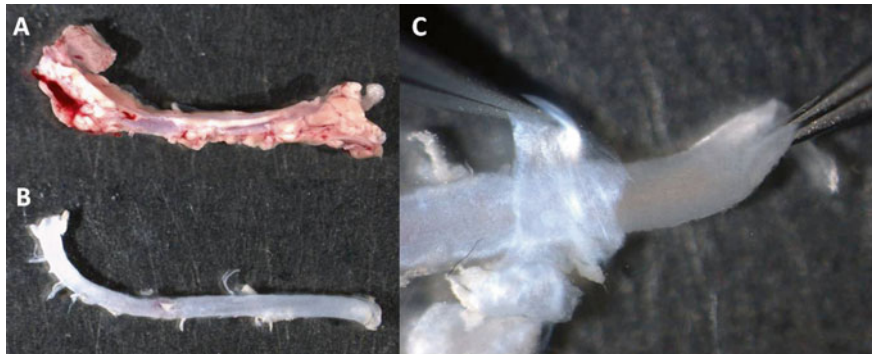

Fig. 2 Cleaning mouse aorta. (**a**) Aorta freshly dissected from a mouse. (**b**) Aorta after removal of the surrounding tissue. (**c**) Removal of the adventitia (held with left tweezers) from the medial layer (held with right tweezers)

2. Transfer clean aortas into a culture dish containing fresh PBS.
3. Put all aortas in a 35 mm dish containing 5 mL of the collagenase solution (Subheading 3.1, **step 2**). Incubate for 15 min at 37 °C in 5 % CO_2 without agitation (*see* **Note 8**).
4. Put one aorta in a culture dish with fresh PBS.
5. Viewing the aorta under a microscope, use two microdissection tweezers to remove the adventitia (*see* Fig. 2c). The adventitia should be rolled off the medial aorta in a manner similar to removing a sock from a foot (*see* **Note 9**).
6. Repeat **steps 4** and **5** for all the aortas.
7. Place the medial aortas in a sterile culture dish containing sterile PBS using a sterile scalpel blade. From this step work in STERILE conditions!
8. Cut each aorta into small fragments using a blade (*see* **Note 10**).
9. To release cells from the aortic fragments, place these in a 50 mL sterile tube containing the remaining collagenase solution (Subheading 3.1, **step 2**) and a magnetic stir bar and incubate at 37 °C for 90 min (*see* **Note 11**) on a magnetic stirrer with gentle mixing (*see* **Note 12**).
10. At the end of the digestion period, remove the stir bar with sterile forceps. Centrifuge the cell/collagenase mixture for 5 min at 300 × *g*. Remove the supernatant and resuspend the cell pellet in 50 mL of sMEM.
11. Centrifuge the suspended cells for 5 min at 300 × *g*. Remove the supernatant and resuspend the cell pellet in an appropriate volume of sMEM supplemented with 10 % FBS (*see* Table 1).
12. Place the cells in two wells of a 12-well plate (*see* **Note 13**). Under the microscope, confirm the presence of round cells in suspension (*see* **Note 14**). Incubate at 37 °C in 5 % CO_2 atmosphere.

Table 1
Growth area and medium volume for selected cell culture vessels

	Approx. growth area (cm^2)	Recommended medium volume (mL)
Multiple-well plates		
6 well	9.5	1.9
12 well	3.8	0.8
24 well	1.9	0.4
48 well	0.95	0.2
Dishes		
35 mm	9	1.8
60 mm	21	4.2
100 mm	55	11
Flasks		
25 cm^2	25	5
75 cm^2	75	15

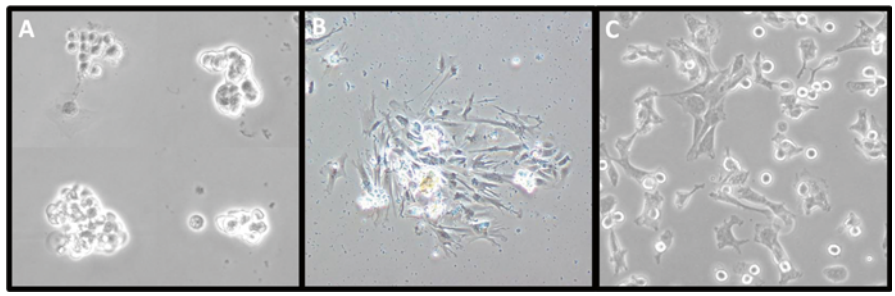

Fig. 3 Primary culture of vascular smooth muscle cells (VSMCs). VSMCs were incubated at 37 °C in 5 % CO_2 with MEM supplemented with 1 mM L-glutamine, 100 IU/mL penicillin, 100 μg/mL streptomycin, and 10 % FBS. (**a**) Groups of VSMCs after 2 days of culture. (**b**) A group of adherent VSMCs after 1 week of culture. (**c**) VSMCs replated after the first trypsinization passage

13. After 2 days, remove the sMEM (with debris) and add fresh sMEM supplemented with 10 % FBS. Under the microscope, confirm the presence of adherent cells (*see* Fig. 3a).
14. Change the medium every 2 days (use sMEM supplemented with 10 % FBS), each time observing cells under the microscope to monitor cell growth.
15. When numerous cell colonies are formed (*see* Fig. 3b), wash cells twice with PBS and add 0.5 mL of 1× trypsin per well (*see* **Note 15**); incubate for ~5 min at 37 °C in 5 % CO_2 until cells detach.
16. As soon as cells detach, collect them in a sterile tube (15 mL) and add sMEM supplemented with 10 % FSB to a final volume of 15 mL to neutralize trypsin action and avoid cell death.

17. Centrifuge the cells for 5 min at 300×*g*. Discard the supernatant and resuspend the pellet in an appropriate volume (*see* Table 1) of sMEM supplemented with 10 % FBS.
18. Transfer the cell suspension to two wells of a 12-well plate. The cells need to be relatively close to each other (*see* Fig. 3c) in order to grow properly. Cells plated at too low a density will eventually die.
19. Change the medium (sMEM, 10 % FBS) every 2 days, and continue culture until the cells reach confluence (*see* **Note 16**). Up to this point cells are considered at passage 0.
20. Trypsinize the cells (according to **steps 15–18**) to obtain successive passages, reseeding cells at a 1:3 ratio (*see* **Note 17**).

3.4 Pi-Induced Calcification In Vitro

1. For calcification experiments use cells between passages 5 and 13. Grow the cells in sMEM supplemented with 10 % FBS until they reach confluence and then aspirate the media, wash with sterile PBS, and incubate overnight with sMEM supplemented with 0.1 % of FBS.
2. Immediately before use, adjust the pH of the 1 M Na_2HPO_4 stock solution to 7.4 using the 1 M of NaH_2PO_4 stock solution, to obtain a 1 M sodium phosphate buffer stock solution (SPBSS) pH 7.4.
3. Dilute 1 M SPBSS in distilled H_2O to a final concentration of 100 mM (*see* **Note 18**).
4. Filter the 100 mM SPBSS through a sterile 22 μm syringe filter in the flow cabinet. Store at 4 °C until use.
5. To make procalcifying medium, add an appropriate volume of 100 mM SPBSS to sMEM to obtain a final phosphate concentration of 2 mM. The phosphate concentration of commercial MEM is normally between 0.9 and 1.1 mM (it is very important to check the medium formulation). Therefore add about 1 mL of 100 mM SPBSS to each 49 mL of sMEM supplemented with 0.1 % FBS.
6. After overnight incubation with sMEM 0.1 % FBS, remove the media and add procalcifying medium. Change the procalcifying medium every day (over 6–7 days). Observe the cells microscopically in order to detect formation phosphate calcium crystals. Usually the deposits can be seen after 3 days of incubation (*see* Fig. 4a).

3.5 Calcium Phosphate Deposit Detection

1. Immediately before use, adjust the pH of Alizarin Red S solution (2 % w/v) to 4.1–4.3 using 10 % NH_4OH (*see* **Note 19**).
2. Remove the procalcifying medium from the culture vessel and wash the cells twice with PBS (*see* **Note 20**).
3. Fix cells by incubating with 3 % paraformaldehyde for 10 min at room temperature (*see* **Note 21**), and then wash the cells

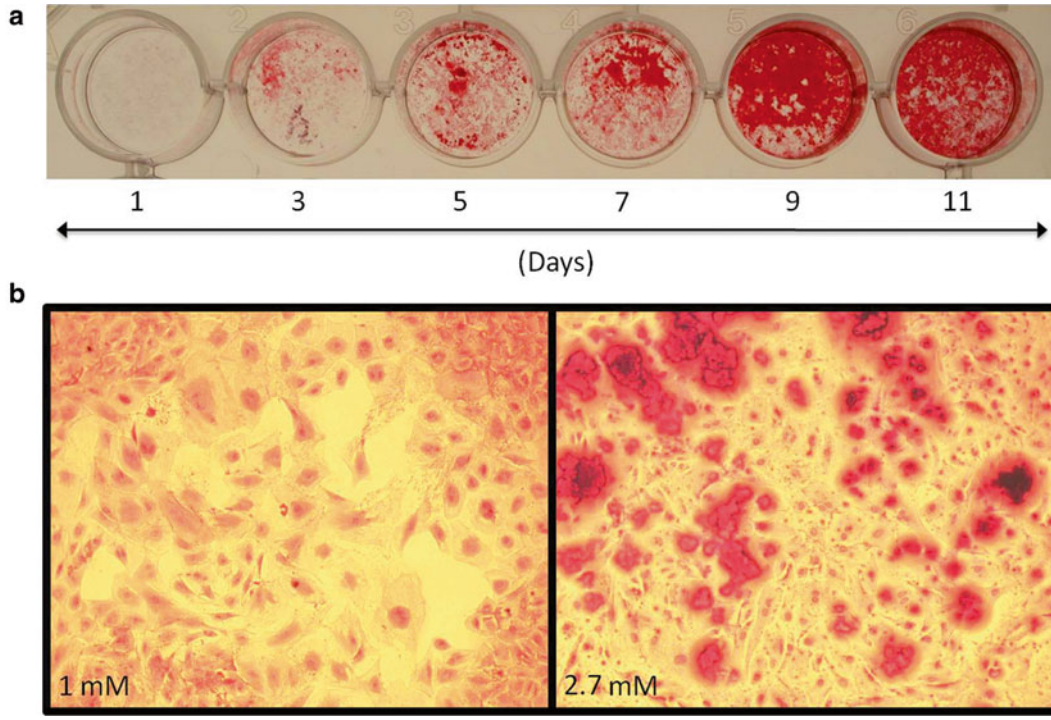

Fig. 4 Alizarin Red S staining of vascular smooth muscle cells. Cultures were incubated with Alizarin Red S solution (2 % w/v, pH 4.1–4.3) for 2 min and washed twice with PBS. Calcium phosphate deposits are visible as red-orange staining. (**a**) VSMCs stained after prior incubation with procalcifying media containing 2.7 mM inorganic phosphate for the indicated periods. (**b**) VSMCs stained after prior incubation with 1 mM (*left*) or 2.7 mM (*right*) inorganic phosphate for 5 days

twice with PBS. From this step, there is no need to work in sterile conditions.

4. Stain the fixed cells with Alizarin Red S Solution, pH 4.1–4.3, from 30 s to 5 min. Usually 2 min will produce a good stain.
5. Discard the Alizarin Red S solution and thoroughly wash the culture vessel with PBS in the sink (*see* **Note 22**).
6. Observe calcium deposits under the microscope; the reaction produces a red-orange staining of calcium (*see* Fig. 4).

4 Notes

1. Alternatively, Hanks' Balanced Salt Solution (HBSS) or Earle's Balanced Salt Solution (EBSS) can be used.
2. Minimal essential medium (MEM) is the best medium for culturing VSMCs, but Dulbecco's modified Eagle's medium (DMEM) can also be used in this step.

3. Collagenase activity is usually about 250 U/mg. For different collagenase activities, adjust the amount of collagenase used accordingly.
4. The greater the number of aortas used for the procedure, the higher the probability of obtaining a good VSMCs primary culture.
5. Euthanasia by cervical dislocation is NOT recommended for this procedure, as it can damage the aorta.
6. Alternatively, slide closed forceps or scissors under the aorta to detach it from the spine.
7. Different VSMC populations can be obtained from different parts of the aorta, such as the abdominal aorta or aortic arch.
8. The first digestion with collagenase makes the removal of the adventitia possible. The adventitia needs to be removed from the medial aorta in order to avoid contamination of VSMCs with fibroblasts. Moreover, all endothelium is lost during this digestion.
9. This first digestion with collagenase makes the aorta more fragile. Removing adventitia from the medial aorta is a tedious procedure, usually taking about 5 min per aorta. It is not an easy task and requires previous training.
10. Alternatively, sterile scissors with microdissection tweezers can be used.
11. The incubation time might need to be adjusted depending on the activity of collagenase.
12. The agitation is very important to ensure release of the cells. Alternatively, an incubator with agitation (200 rpm) can be used.
13. Ten aortas are usually required to provide enough cells for 8 cm^2 of primary culture, but the precise figure depends on the quality of the collagenase digestion.
14. Some wells will contain a few undigested clumps of cells and other debris; this will be aspirated from the dish during the first medium change (Subheading 3.3, **step 13**).
15. The volume of 1× trypsin should be adjusted to the size of the well (*see* Table 1).
16. Primary cultures of VSMCs grow slowly and generally reach confluence in 1 week, but it might take longer depending on the initial density and the quality of the collagenase digestion.
17. Plate cells obtained from each cm^2 of confluent culture on ~3 cm^2. Surface areas of standard flasks, dishes, and plates are indicated in Table 1.
18. Alternatively, 100 mM SPBSS, pH 7.4 can be prepared by mixing 1 M stock solutions according to Table 2.

Table 2
Preparation of 100 mM sodium phosphate buffer stock solution

pH	1 M Na_2HPO_4 (mL)	1 M NaH_2PO_4 (mL)	Distilled H_2O (mL)
6	1.2	8.8	90
6.2	1.78	8.22	90
6.4	2.55	7.45	90
6.6	3.52	6.48	90
6.8	4.63	5.37	90
7	5.77	4.23	90
7.2	6.84	3.16	90
7.4	7.74	2.26	90
7.6	8.45	1.55	90
7.8	8.96	1.04	90
8	9.32	0.68	90

19. The pH is critical, so make the solution fresh or check its pH if it is more than 1 month old.
20. At this point it is possible to use the cells for extraction of RNA or protein; in this case, all subsequent steps should be ignored.
21. At this step other fixation methods can be applied: 100 % methanol at –20 °C for 5 min; 1 % formaldehyde at room temperature for 10 min; or 100 % acetone for 3 min at –20 °C.
22. Alternatively calcium phosphate deposits (CPD) can be quantified by colorimetric assay using any of several commercial kits for calcium quantification. In this case, the CPD should be previously dissolved by incubation in 0.6 N HCl overnight at 4 °C. This procedure is INCOMPATIBLE with Alizarin Red S staining.

Acknowledgements

R.V.-B. is supported by a *Juan de la Cierva* postdoctoral contract from the Spanish Ministry for Economy and Competitiveness (JCI-2011-09663) and M.R.H. by an FPI predoctoral Fellowship from the Spanish Ministry for Science and Innovation (BES-2011-043938).

References

1. London GM, Drueke TB (1997) Atherosclerosis and arteriosclerosis in chronic renal failure. Kidney Int 51(6):1678–1695
2. Rutsch F, Nitschke Y, Terkeltaub R (2011) Genetics in arterial calcification: pieces of a puzzle and cogs in a wheel. Circ Res 109(5): 578–592
3. Monckeberg JG (1902) Uber die reine media-verkalkung der extremitatenarterien und ihr verhalten zur arteriosklerose. Virchows Arch Pathol Anat 171:141–167
4. Villa-Bellosta R, Rivera-Torres J, Osorio FG et al (2013) Defective extracellular pyrophosphate metabolism promotes vascular calcification in a mouse model of Hutchinson-Gilford progeria syndrome that is ameliorated on pyrophosphate treatment. Circulation 127(24):2442–2451
5. Shanahan CM, Cary NR, Metcalfe JC et al (1994) High expression of genes for calcification-regulating proteins in human atherosclerotic plaques. J Clin Invest 93(6):2393–2402
6. Tintut Y, Patel J, Territo M et al (2002) Monocyte/macrophage regulation of vascular calcification in vitro. Circulation 105(5): 650–655
7. Villa-Bellosta R, Millan A, Sorribas V (2011) Role of calcium-phosphate deposition in vascular smooth muscle cell calcification. Am J Physiol Cell Physiol 300(1):C210–C220
8. Alfrey AC, Ibels LS (1978) Role of phosphate and pyrophosphate in soft tissue calcification. Adv Exp Med Biol 103:187–193
9. Block GA, Hulbert-Shearon TE, Levin NW et al (1998) Association of serum phosphorus and calcium × phosphate product with mortality risk in chronic hemodialysis patients: a national study. Am J Kidney Dis 31(4):607–617
10. Giachelli C, Bae N, Lombardi D et al (1991) Molecular cloning and characterization of 2B7, a rat mRNA which distinguishes smooth muscle cell phenotypes in vitro and is identical to osteopontin (secreted phosphoprotein I, 2aR). Biochem Biophys Res Commun 177(2): 867–873
11. Boström K, Watson KE, Horn S et al (1993) Bone morphogenetic protein expression in human atherosclerotic lesions. J Clin Invest 91(4):1800–1809
12. Jono S, McKee MD, Murry CE et al (2000) Phosphate regulation of vascular smooth muscle cell calcification. Circ Res 87(7):E10–E17
13. Villa-Bellosta R, Sorribas V (2009) Phosphonoformic acid prevents vascular smooth muscle cell calcification by inhibiting calcium-phosphate deposition. Arterioscler Thromb Vasc Biol 29(5):761–766
14. Steitz SA, Speer MY, Curinga G et al (2001) Smooth muscle cell phenotypic transition associated with calcification: upregulation of Cbfa1 and downregulation of smooth muscle lineage markers. Circ Res 89(12):1147–1154
15. Proudfoot D, Skepper JN, Hegyi L et al (2000) Apoptosis regulates human vascular calcification in vitro: evidence for initiation of vascular calcification by apoptotic bodies. Circ Res 87(11):1055–1062
16. Ewence AE1, Bootman M, Roderick HL, Skepper JN, McCarthy G, Epple M, Neumann M, Shanahan CM, Proudfoot D (2008) Calcium phosphate crystals induce cell death in human vascular smooth muscle cells: a potential mechanism in atherosclerotic plaque destabilization. Circ Res. 2008 Aug 29;103(5):e28-34. doi: 10.1161/CIRCRESAHA.108.181305. Epub 2008 Jul 31.
17. Shroff RC, McNair R, Figg N et al (2008) Dialysis accelerates medial vascular calcification in part by triggering smooth muscle cell apoptosis. Circulation 118(17):1748–1757

Chapter 9

Immunostaining of Macrophages, Endothelial Cells, and Smooth Muscle Cells in the Atherosclerotic Mouse Aorta

Prashanthi Menon and Edward A. Fisher

Abstract

The atherosclerotic mouse aorta consists of a heterogeneous population of cells, including macrophages, endothelial cells, and smooth muscle cells that play critical roles in cardiovascular disease. Identification of these vascular cells in the vessel wall is important to understanding their function in pathological conditions. Immunohistochemistry is an invaluable technique used to detect the presence of cells in different tissues. Here, we describe immunohistochemical techniques commonly used for the detection of the vascular cells in the atherosclerotic mouse aorta using cell type-specific markers.

Key words Atherosclerosis, Mouse aorta, Immunohistochemistry, Macrophages, Endothelial cells, Smooth muscle cells

1 Introduction

Atherosclerotic lesions in hypercholesterolemic mice develop diffusely in the arteries. Different sites of the aorta, namely the aortic root, ascending aorta, the brachiocephalic artery (BCA), the aortic arch and the abdominal aorta are preferentially susceptible to lesion formation depending on the experimental conditions and the mouse model employed. The undiseased aorta is composed mainly of endothelial cells (ECs) and a medial layer of smooth muscle cells (SMCs). As atherosclerosis advances, lesions contain a heterogenous population of cells, including macrophages, ECs, SMCs, and T- and B-lymphocytes [1, 2]. Immunohistochemistry (IHC) is an invaluable technique used for the detection and localization of these different cell types using labeled antibodies specifically directed against proteins associated with particular cell types. This technique uses the principle of visualization of antigen–antibody interactions either by fluorescent dyes or enzyme conversion of substrates to colored compounds [3].

Vicente Andrés and Beatriz Dorado (eds.), *Methods in Mouse Atherosclerosis*, Methods in Molecular Biology, vol. 1339, DOI 10.1007/978-1-4939-2929-0_9,

IHC is typically performed using frozen sections or fixed and paraffin-embedded sections. The choice between frozen vs. fixed and paraffin-embedded sections depends on the final use of the samples. If the sections are to be used for both IHC and to isolate RNA from cells in the sections using laser capture microdissection (LCM), then frozen sectioning needs to be done [4]. On the other hand, if RNA isolation is not a consideration and maximum retention of tissue architecture is desired, fixation and embedding in paraffin blocks is the better choice. It should be noted that although the final immunostaining protocols are essentially the same for both types of tissue preparation (frozen and paraffin), in practice, a particular antibody might work better with one type of preparation than the other. Sometimes this is noted by the supplier of the antibodies or by a technical specialist at the supplier.

The main aim of immunostaining is to detect the expression of the antigen of interest with the least background and without false positive results. Immunostaining can be done by direct or indirect methods. In the direct method, the primary antibody has directly attached a fluorophore or enzyme, such as alkaline phosphatase or horseradish peroxidase. This enables faster detection in that it is a one-step procedure. The drawback, however, is that each antibody used needs to be conjugated to the fluorophore or enzyme. The indirect method typically involves a two-step process, and sometimes a multistep process. In the two-step detection method, the primary antibody is recognized by a secondary antibody conjugated with a fluorescent group or an enzyme. The primary antibody, which has the specificity for the antigen of interest, is from one species (e.g., a mouse IgM), and the secondary antibody, which has specificity for the source of the primary antibody, is from another species (e.g. a rabbit anti-mouse IgM). Binding of the secondary to the primary antibody is detected by either the fluorescence emitted by the bound fluorescently labeled secondary antibody resulting from being excited at the recommended wavelength, or by adding an adequate colorimetric substrate when using enzyme-conjugated secondary antibodies. In this way, any primary antibody can be used, and commercially supplied secondary antibodies with an adequate detection system are purchased. Alternatively, the avidin–biotin complex (ABC) is commonly used as an indirect multistep detection method, which relies on the strong affinity of avidin or streptavidin for the vitamin biotin. Streptavidin (from Streptomyces avidinii) and avidin (from chicken egg) both possess four binding sites for biotin, which can be easily conjugated to proteins. In the ABC method, secondary antibodies are conjugated to biotin and function as links between tissue-bound primary antibodies and an avidin-peroxidase or phosphatase complex. In general, the sensitivity or signal amplification of the assay increases with its complexity (i.e., multistep > two-step > single-step). As noted earlier, the atherosclerotic mouse aorta

is composed of a heterogenous population of cells. Indirect methods that involve multiple steps where the signal is significantly amplified are commonly used to detect the different cells in atherosclerotic lesions.

This chapter focuses on the methods used to detect macrophages, ECs and SMCs in mouse aortic atherosclerotic plaques using cell type-specific markers. In addition, troubleshooting strategies and optimization notes are provided.

2 Materials

1. Control and experimentally treated mouse models of atherosclerosis (*see* **Note 1**).
2. Forceps.
3. Micro-scissors.
4. Adhesive tape.
5. Gravity flow apparatus to perfuse/fix tissues: We use a simple gravity flow apparatus by suspending the perfusate (saline/sucrose) at a height of 60 cm above the mouse thus maintaining a perfusion pressure of 60–100 mmHg and a flow rate of 1–3 ml/min (Fig. 1) [5].
6. 25-G butterfly needle.
7. Dissecting light microscope.
8. Cotton swabs.
9. Aluminum foil.
10. −80 °C freezer.
11. Cryosection plastic molds.
12. Embedding cassettes.
13. Cryostat or microtome.
14. Poly-L-lysine-coated glass slides (e.g., Fisher scientific, Cat. No. NC9895478).
15. Glass cover slips.
16. Nail polish.
17. Paraffin blocks.
18. Oven.
19. Brush.
20. Water bath.
21. Coplin jar.
22. Microwave oven or pressure cooker.
23. Cleaning wipes (e.g., KimWipes, Kimberly-Clark).
24. Hydrophobic marker.

Fig. 1 Gravity flow apparatus for vascular perfusion. Perfusant is suspended at a height of 60 cm above the mice to be perfused so as to maintain a pressure of 60–100 mmHg and a flow rate of 1–3 ml/min

25. Humidified chamber.
26. Cold room (4 °C) or fridge
27. Anesthetics and equipment for euthanizing mice.
28. Paraffin wax.
29. 70, 80, 95, and 100 % ethanol (dilutions in distilled water).
30. Acetone.
31. Phosphate-buffered saline (PBS) that does not contain calcium or magnesium since the ions may interfere with the detection process.

32. Neutral-buffered formalin or 4 % paraformaldehyde (PFA) diluted in PBS.
33. Isopentane or dry ice.
34. Proteases (e.g., proteinase K, trypsin and pepsin).
35. 10 mM citrate buffer (pH 6.0).
36. 1 mM EDTA buffer (pH 8.0).
37. 3 % hydrogen peroxide (H_2O_2) dissolved in methanol or 0.3 % H_2O_2 dissolved in PBS.
38. Blocking solution: 5 % normal goat or rabbit serum, or ready-to-use protein block serum-free reagent (DAKO, Cat. No. X0909).
39. Biotinylated secondary antibodies raised in species adequate for the primary antibodies used for detection (e.g.: polyclonal rabbit anti-rat antibodies if primary antibody is made in rat).
40. Primary antibodies: rat monoclonal anti-mouse CD68 (e.g., AbSerotec, Cat. No. MCA1957), rat monoclonal anti-CD31 antibody (e.g., BD Pharmingen, Cat. No. 550274), and mouse monoclonal α-SMC actin antibody (e.g., Sigma, Clone1A4, Cat. No. A2547).
41. Vectastain ABC alkaline phosphatase kit (e.g., Vector laboratories, Cat. No. AK 5000), or Vectastain ABC peroxidase kit (Vector laboratories, Cat. No. PK 4000). In both cases, to prepare ABC reagent, add two drops of reagent A to 5 ml PBS, vortex, and add two drops of reagent B.
42. 3,3′ diaminobenzidine (DAB) peroxidase substrate kit (e.g., Vector laboratories Cat. No. SK 4100): mix 2.5 ml double-distilled water (ddH_2O), one drop buffer stock solution, two drops DAB stock solution, one drop H_2O_2 solution, and vortex.
43. Vector red alkaline phosphatase substrate kit (e.g., Vector Laboratories, Cat. No. SK5100): Just before use, add two drops reagent A to 5 ml Tris–HCl buffer, pH 8.5, vortex, and add two drops reagent B.
44. Meyer's hematoxylin (e.g., Sigma Aldrich, Cat. No. MHS1-100 ml).
45. Bluing solution: 250 ml ddH_2O + 500 μl ammonium hydroxide (0.2 % ammonium hydroxide solution).
46. Xylene.
47. Xylene-based mounting media (e.g. DAKO or Permount mounting media).
48. Optimal cutting temperature (OCT) embedding compound (Tissue-Tek, Cat. No. 4583).

3 Methods

3.1 Harvesting Mouse Aorta

1. Euthanize the mouse according to your institutional animal care and use committee approved protocol. We anesthetize the mice using a cocktail of ketamine (100 mg/ml) and xylazine (10 mg/ml). The injectable dose recommended is 0.01 ml/g of the body weight of the animal. After injection, allow 10–15 min for the mice to be completely sedated. Check for loss of reflex response by toe pinching or tail pinching. This is necessary to judge the animal's level of responsiveness to painful stimuli under anesthesia.
2. Once the animal is sedated, secure the four paws to the surface spreading them as far as possible with the help of adhesive tape. Wet with 70 % ethanol the area where the incision is to be made.
3. With the help of forceps and scissors, make an incision by cutting the ribs lateral to the sternum to open the thoracic cavity and thus expose the heart.
4. Perfuse (for frozen sections) or perfuse and fix (for paraffin sections) at a physiological pressure using a gravity flow apparatus (Fig. 1) so as to keep the arteries patent, but not over-distended. Prior to perfusion, flush the tubes of the suspended container with the perfusate (saline) to remove air bubbles. Suspend the perfusate at a height of 60 cm above the mouse maintaining a perfusion pressure of 60–100 mmHg and a flow rate of 1–3 ml/min [5]. This way the arteries are not collapsed or stretched by using excessive or insufficient perfusion pressure, respectively. Insert the 25-G needle attached to the gravity flow apparatus into the left ventricle of the mouse to start perfusion. Make an incision at the right atrium or the hepatic vein. Maintain the flow rate of the perfusate (saline) at 1–3 ml/min so that the pressure is maintained. Perfuse till the liver turns pale in color, which indicates circulating red blood cells have been removed systemically.
5. Remove the lungs, kidneys, and gastrointestinal and reproductive organs.
6. Using a dissection microscope, isolate the aortic arch by carefully dissecting the ascending aorta, aortic arch along with BCA, left common carotid artery and left subclavian artery along with 1 mm of descending aorta attached to the aorta. Remove the excess of fat with the help of a cotton swab.
7. If the aortic root is required, make an incision at the level of the upper level of atria, and cut the heart/aortic root tissue away from the aorta.
8. Proceed to embedding as outlined below in Subheading 3.2 or 3.3 (*see* **Note 2**).

3.2 Preparation of Frozen Sections (*See* Notes 3 *and* 4)

1. Fill separate plastic cryomolds with OCT compound for embedding the heart/aortic tissue and the aortic arch.
2. With the help of forceps, take the heart/aortic root tissue and embed it in the cryomold containing OCT. Place the axis of the aorta perpendicular to the base of the mold.
3. For the aortic arch, make an incision between the left common artery and left subclavian artery. Embed the two portions such that the aortic arches are perpendicular to the mold (i.e., they are facing the user).
4. Freeze the tissues rapidly by placing the molds in dry ice to which isopentane is added.
5. Cover the tissue molds with aluminum foil and store in –80 °C freezer until cryosections are required.
6. To section frozen tissue, cut the tissue at 5–6 μm in thickness with a cryostat. Using a thin brush, gently move the curled portion of the section over the cryostat stage. Pick the sections with the help of a brush and place them on poly-L-lysine-coated slides. Poly-L-lysine-coated slides are used to improve tissue adhesion especially since the aortic sections can easily dislodge from the slides during the staining process. For IHC, place 4–5 sections per slide.
7. Store the cut cryosections in –80 °C freezer immediately. Do not fix the slides before freezing. Fix the slides only if proceeding immediately to immunostaining.
8. Perform IHC to detect different vascular cells (see below). Although we have used uncut frozen tissues for up to one year, once they are sectioned, they should be further processed within a week if RNA is to be isolated from some of the sections.

3.3 Preparation of Paraffin-Embedded Sections (*See* Note 5)

1. Fix the harvested tissues overnight at 4 °C using 4 % paraformaldehyde prepared in PBS or 10 % neutral buffered formalin. Since the aortic tissues are small, overnight tissue fixation is optimal. Usually the fixative volume should be 10× times the tissue volume.
2. Wash the tissues gently with PBS three times, 5 min each.
3. Store the tissues in 70 % ethanol till they are ready to be embedded in paraffin blocks.
4. Transfer tissues to embedding cassettes and dehydrate as follows:
   (a) 70 % Ethanol, two changes, 1 h each.
   (b) 80 % Ethanol, two changes, 1 h each.
   (c) 95 % Ethanol, two changes, 1 h each.
   (d) 100 % Ethanol, three changes, 1 h each.

(e) Xylene, three changes, 1 h each.

(f) Paraffin wax (56–58 °C), two changes, 1.5 h each.

5. Embed the tissues into paraffin blocks.
6. To section paraffin blocks, trim and mount the blocks on to the microtome. Take care to trim the paraffin blocks such that there is an optimal cutting surface area that includes the sample with a small paraffin frame.
7. Using the microtome, cut the tissues in 3–10-μm thick slices. Commonly used thickness for IHC of the mouse aorta is 5–6 μm. Use a brush to gently hold the sections. If the microtome is adjusted properly, the paraffin sections should come out as a ribbon.
8. Place paraffin ribbons or a slice in 40–45 °C water bath using a second wet brush. As the sections expand on the water bath, the wrinkles on the sections vanish.
9. Gently scoop out the floating paraffin sections using microscope glass slides and position the section with the help of a brush.
10. Dry the sections overnight at 37 °C (lower temperatures are better for subsequent antibody detection).
11. Sections are ready for immunostaining (*see* Subheading 3.4) or can be stored at room temperature (RT) for an extended period of time.

3.4 Processing of Paraffin-Embedded Aortic Sections for Immunostaining

1. Bake slides in 56 °C oven for 1 h to melt the wax.
2. Deparaffinize the tissue sections as follows:

   (a) Xylene: three changes, 5 min each.

   (b) 100 % Alcohol: two changes, 2 min each.

   (c) 95 % Alcohol: two washes, 2 min each.

   (d) 70 % Alcohol: three changes, 2 min each.

   (e) ddH_2O: one change, 2 min.
3. Retrieve masked antigens using either protease-induced or heat-induced method (*see* **Note 6**):

   (a) Protease-induced epitope retrieval: Incubate with proteases (e.g., proteinase K, trypsin and pepsin) to cleave the peptides that mask the epitopes in paraffin sections. The optimal time and duration of this protocol should be predetermined for each antibody.

   (b) Heat-induced epitope retrieval: Heating is performed using a microwave oven or a pressure cooker. This protocol typically involves 5-min periods of heat followed by replacement of the buffer. The heat-induced method is especially time, temperature, buffer, and pH sensitive; therefore the optimal conditions must be determined

empirically by the user. For aortic tissue, heat-induced epitope retrieval is usually performed in 10 mM citrate buffer (pH 6.0) or 1 mM EDTA buffer (pH 8.0) for a total of 15 min. Slides must be cooled for 30–40 min before proceeding to immunostaining.

4. Wash sections in PBS, three changes, 5 min each.
5. Block endogenous peroxidase activity by incubating with 3 % H_2O_2 dissolved in methanol or 0.3 % H_2O_2 dissolved in PBS (10 min at RT). Prepare this solution just before use (*see* **Note 7**).
6. Wash slides once in ddH_2O for 5 min.
7. Rinse in PBS for 5 min with two changes. Carefully dry slides with Kimwipes without touching the tissue sections.
8. Outline sections with a hydrophobic marker.
9. Block nonspecific binding by incubating for 20 min at RT with blocking solution (DAKO protein block serum-free buffer or 5 % normal goat or rabbit serum).
10. Gently remove excess liquid off the slides and wipe around tissues.
11. Incubate with specific primary and secondary antibodies to proceed with the detection of different vascular cells as outlined in Subheadings 3.6, 3.7, or 3.8 (*see* **Note 8**).

3.5 Preparation of Frozen Aortic Sections for Immunostaining

1. Take frozen slides out of −80 °C freezer and let them warm up to RT for 2 min.
2. Fix sections in ice-cold acetone for 10 min.
3. Air-dry sections for 30 s at RT. Do not let the sections dry out.
4. Transfer slides to a Coplin jar and wash in PBS three times for 5 min each.
5. Block endogenous peroxidase activity by incubating with freshly prepared 3 % H_2O_2 dissolved in methanol or 0.3 % H_2O_2 dissolved in PBS (10 min at RT) (*see* **Note 7**).
6. Wash slides once in ddH_2O for 5 min.
7. Rinse in PBS for 5 min with two changes. Carefully dry sections with Kimwipes without touching the tissue sections.
8. Outline sections with a hydrophobic marker.
9. Block nonspecific binding by incubating for 20 min at RT with blocking solution (DAKO protein block serum-free buffer or 5 % normal goat or rabbit serum).
10. Gently remove excess liquid off the slides and wipe around tissue sections.
11. Incubate with specific primary and secondary antibodies and proceed to the detection of different vascular cells as outlined in Subheadings 3.6, 3.7, or 3.8 (*see* **Note 8**).

3.6 CD68 Immunostaining Protocol for Macrophages

CD68 is a macrophage marker frequently used in mouse atherosclerosis studies. Other markers for macrophages include F4/80, CD64 (FCγR1), MerTK, and CD115 (CSF1R) [6]. Here we outline the protocol for CD68 staining of frozen mouse aortic sections.

1. Follow **steps 1–10** under Subheading 3.5 for frozen sections.
2. Primary antibody (*see* **Note 9**): For routine staining, incubate frozen sections for 1 h with rat monoclonal anti-mouse CD68 diluted 1:250 in 4 % normal rabbit serum. This step is critical since over-incubation would result in false positive results. For rapid CD68 stain for LCM purposes, incubate sections at RT for 1 min using an antibody concentration of 1:50. Proceed as follows for either application (routine or LCM).
3. Rinse sections in PBS, three times, 5 min each.
4. Secondary antibody: Incubate sections for 20 min with biotinylated rabbit anti-rat antibody diluted 1:200 in blocking solution.
5. While the tissues are incubated with secondary antibody, prepare Vectastain ABC alkaline phosphatase solution in PBS (to be used in **step 7** below) (*see* **Note 10**). The ABC complex solution needs to be prepared 30 min prior to be used.
6. Rinse in PBS, three times, 5 min each.
7. Incubate sections for 20 min with Vectastain ABC alkaline phosphatase solution (20 min for routine staining, 5 min for LCM).
8. Rinse in PBS, three times, 5 min each for routine staining or 2 min each for LCM.
9. Incubate sections in freshly prepared Vector red solution to get the desired stain intensity (approximately 8–10 min).
10. Place slides in ddH_2O for 5 min to stop the reaction.
11. Counter stain with hematoxylin and dehydrate sections as follows:

(a) Hematoxylin: 1 min.

(b) Bluing solution: 30 s.

(c) 70 % Ethanol: one change, 2 min.

(d) 95 % Ethanol: one change, 2 min.

(e) 100 % Ethanol: one change, 2 min.

(f) 100 % Xylene, three changes, 2 min.

12. Mount section with DAKO or Permount mounting media and cover slip.
13. Seal around the edges of the section with nail polish and place slides horizontal to dry.

Using this protocol, the macrophages are stained red and are easy to identify in the light background. An example of the CD68 immunostaining is shown in Fig. 2.

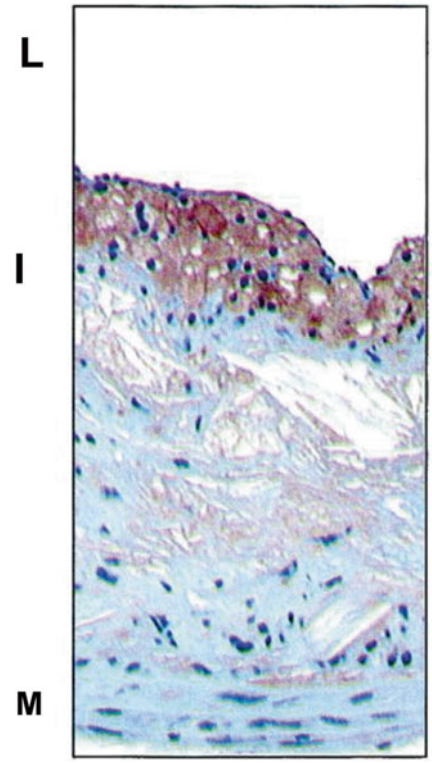

Fig. 2 Immunostaining of macrophages in the mouse atherosclerotic lesions. Atherosclerotic lesions from ApoE-/- mice fed Western diet for 16 weeks were immunostained for the macrophage-specific marker CD68 (*reddish-brown stain*). *L* lumen, *I* intima, *M* media. From *Rong JX et al. Circulation.2001; 104:2447–2452*

3.7 CD31/PECAM1 Immunostaining Protocol for Endothelial Cells

CD31 is a 130-kDa transmembrane glycoprotein also designated as PECAM-1 (platelet endothelial cell adhesion molecule 1). It is a constituent of the endothelial intercellular junction which plays a major role in the adhesion cascade between ECs and the circulating monocytes, promoting their entry into atherosclerotic sites, where they become macrophages. CD31 is commonly used as a standard marker of ECs. Other commonly used EC markers in the mouse aorta include VE-Cadherin, Von Willebrand factor (VWF), and VEGFR2 /Flk1/KDR [7, 8]. The protocol outlined below is for CD31 immunostaining using DAB peroxidase substrate, but a similar design can be used for any EC marker using the appropriate primary and secondary antibodies.

1. Follow **steps 1–10** under Subheading 3.5 for frozen sections.
2. Primary antibody (*see* **Note 9**): Incubate sections with rat monoclonal anti-CD31 antibody (diluted 1:100 in blocking buffer) for 1 h at RT or at 4 °C overnight, in a humidified chamber.

3. Rinse in PBS, three changes, 5 min each.
4. Secondary antibody: Add biotinylated anti-rat antibody diluted 1:200 in PBS and incubate for 30 min at RT in a humidified chamber.
5. Rinse in PBS, three changes, 5 min each.
6. Incubate sections with Vectastain ABC peroxidase reagent for 30 min at RT in a humidified chamber (*see* **Note 10**).
7. Rinse in PBS, three changes, 3 min each.
8. Stain slides with DAB peroxidase substrate for 2–5 min till the desired intensity. Prepare the DAB solution just prior to use (*see* **item 42** in Subheading 2, and **Note 11**).
9. Counterstain with hematoxylin for 1–2 min. Wash slides in ddH_2O. Staining time is important to reduce intensity of hematoxylin. If required, an extra wash may be performed to remove excess stain.
10. Dehydrate slides and mount them with mounting media. Seal the edges as outlined for CD68 staining in Subheading 3.6, **steps 10–13**.
11. Using this protocol, ECs appear as a thin monolayer of cells lining the luminal surface of the vessel wall. An example of CD31 staining in the mouse atherosclerotic lesion is shown in Fig. 3.

3.8 α-Smooth Actin Immunostaining Protocol for SMC

α-Smooth muscle (α-SMC) actin is an isoform typical of contractile SMCs that is present in high amounts in microfilament bundles of vascular SMCs (VSMCs) and in pericytes (cells surrounding small vessels, such as capillaries), thus representing the contractile capacity of these cell types. α-SMC actin is considered one of the best

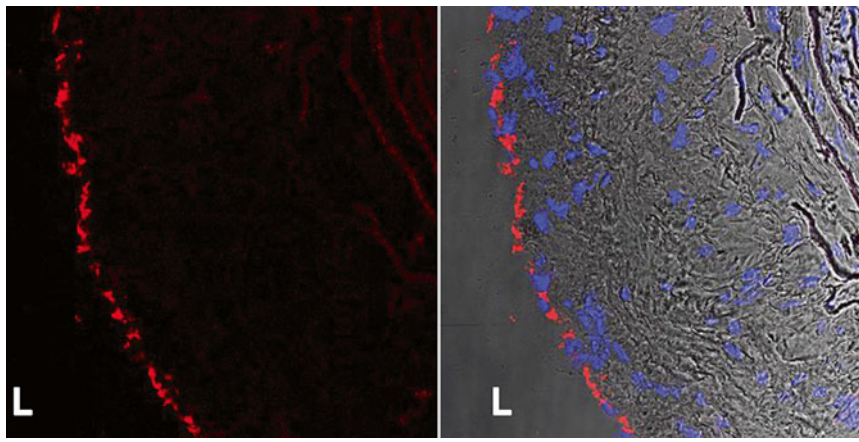

Fig. 3 Immunostaining of endothelial cells in the mouse atherosclerotic lesions. Frozen sections were prepared from the aorta of ApoE-/- mice fed Western diet for 16 weeks. *Left*: Confocal images of CD31 immunofluorescent stain. *Red*: Nuclei are stained blue with DAPI and overlaid with CD31 in the bright-field image. *L* lumen. *P. Menon and E. Fisher, unpublished data*

markers of VSMCs. Other markers for VSMCs include myosin heavy chain, α-tropomyosin, and calponin [9, 10]. Normally, α-SMC actin stains the medial layer of an artery, but staining can be found within complex atherosclerotic plaques because of migration of VSMC from the media. Note though that the differentiation status of intimal VSMCs can change and the expression of any marker of the contractile state can therefore decrease during atherosclerosis. The protocol outlined below will be for α-SMC actin immunostaining in frozen sections, but a similar design can be used for any VSMC marker using the appropriate primary and secondary antibodies.

1. Follow **steps 1–10** outlined in Subheading 3.5 for frozen sections.
2. Incubate sections with mouse monoclonal α-SMC actin antibody diluted 1:400 in blocking solution (1 h or overnight at 4 °C in a humidified chamber) (*see* **Note 9**).
3. Rinse in PBS, three changes, 5 min each.
4. Add biotinylated anti-mouse secondary antibody diluted to 1:200 in PBS. Incubate for 30 min at RT in a humidified chamber.
5. Rinse in PBS, three times, 5 min each.
6. Add Vectastain ABC peroxidase solution and incubate sections for 30 min at RT in humidified chamber (*see* **Note 10**).
7. Rinse in PBS, three times, 3 min each.
8. Stain slides with DAB peroxidase substrate for 2–5 min till the desired intensity. Prepare the DAB solution just prior to use (*see* **item 42** in Subheading 2 and **Note 11**).
9. Counterstain for 1–2 min with 1× hematoxylin. Wash slides in ddH_2O. Perform an extra wash to remove excess stain.
10. Dehydrate and mount with cover slip as described for CD68 staining in Subheading 3.6, **steps 10–13**.

Using this protocol, membrane/cytoplasmic stain of α-smooth muscle actin is observed. An example of smooth muscle α-actin immunostaining is shown in Fig. 4.

3.9 Troubleshooting Strategies

Antibody standardization for IHC applications can be challenging, especially in a mouse aorta where tissue surface area is small. The following troubleshooting protocol assumes that aortic tissues are frozen sections and fixed in acetone.

3.9.1 Tissue Detachment from Slides

1. Use poly-L-lysine-coated glass slides to increase adherence.
2. Inadequate fixing of sections: Increase fixing time in acetone. Rinse well with PBS to remove residual acetone. Inadequate or over fixing will impair the binding of primary antibody to specific epitopes.

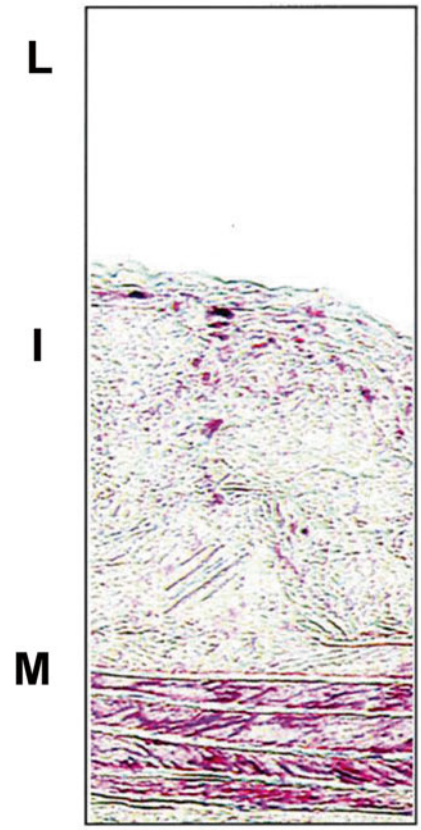

Fig. 4 Immunostaining of smooth muscle cells in the mouse atherosclerotic lesions. Immunostaining of smooth muscle α-actin (*red stain*) in atherosclerotic lesions of ApoE-/- mice fed Western diet for 16 weeks. *L* lumen, *I* intima, *M* media. Note the two positive areas, at the *bottom* of the section, where the bands of the internal elastic laminae are visible, are the VSMC in the medial layer (*M*) of the artery. In the intimal area (*I*) are VSMCs that migrated from the media and continue to express smooth muscle α-actin. From *Rong JX et al. Circulation.2001*; *104:2447–2452*

3. Drying out of tissues: Incubate sections in a humidified chamber throughout the staining process to prevent tissues from drying.
4. Transfer slides gently between washes to avoid sections from coming off the slides.

3.9.2 High Background

1. Endogenous enzyme activity not quenched (for peroxidase-based detection on antigen-epitope complexes): Block endogenous activity by increasing the incubation time or the concentration of the blocking reagent.
2. When using normal serum as blocking reagent, make sure that it is from the same species in which the secondary antibody is generated. For example, normal goat serum is used as a blocking reagent when the secondary antibody is generated in goat.

Alternatively, if high background still persists, DAKO protein block serum-free reagent can be used.

3. Primary antibody concentration is too high: Decrease the concentration and/or incubation time, and/or increase wash times.
4. Secondary antibody concentration is too high: Decrease the concentration and/or incubation time, and/or increase wash time. Secondary antibodies can sometimes recognize endogenous tissue immunoglobulins. To rule out false-positive results, run control experiments in which tissue sections are incubated with secondary antibody only to observe background stain (*see* **Note 8**).
5. Chromogen concentration is high (for enzyme-based detection systems): Reduce concentration and incubation time.
6. Buffer washes are not sufficient: Add an extra wash or extend the time of each wash.
7. Counterstain stain too strong: decrease incubation time or increase wash time. Counterstains can sometime obscure the IHC reaction. Use a counterstain that does not interfere with the IHC staining.

3.9.3 Weak Staining in Samples

1. Over or under--fixed tissue: Optimize fixing protocol by increasing/decreasing fixing times.
2. Primary antibody concentration is too low: Increase concentration or incubation time, or both.
3. Secondary antibody concentration is too low: Increase concentration or incubation time, or both.
4. Chromogen incubation time is too short: Increase incubation till desired intensity is obtained.

4 Notes

1. Typically a mouse based on deficiency of either apolipoprotein E (apoE-/-) or the LDL receptor (LDLr-/-), or their variants, is fed a high-fat and cholesterol-enriched diet (Western diet) for a period long enough to develop the desired stage of atherosclerosis to be studied. In our lab, we use a 16-week diet period so that the lesions that develop are complex and similar to those in people with coronary artery disease, with multiple cell types present and with a necrotic core beginning to form [11, 12].
2. Mouse aorta embedding and processing is a critical step to get consistent results. All aortic tissues (control and experimental) should be processed exactly the same way since variations in this process can lead to inconsistencies.

3. Frozen tissues can be prepared by embedding them in OCT compound before freezing them quickly in the presence of isopentane on dry ice. Tissues can be snap-frozen. This method is beneficial especially when tissues are used for detecting post-translational modifications of proteins, such as phosphorylation. Frozen tissue sections fixed in acetone are also frequently used when direct or indirect immunofluorescence is the detection method of choice, in cases where formalin fixation can sometimes produce weaker results depending on the antibody.
4. Molds with frozen tissues can be stored at −80 °C for up to 1 year. They can then be trimmed and cut into cryosections with the help of a cryostat. They can be re-processed in acetone and re-hydrated in buffer before IHC. One of the primary reasons for using frozen tissue or sections is a faster examination that eliminates the time required for processing and de-waxing compared to paraffin sections. Moreover, frozen tissue sections are typically fixed using acetone or alcohol, thus avoiding the requirement to retrieve epitopes masked by formaldehyde cross-linking in paraffin sections. More importantly, RNA isolation can also be performed by LCM in frozen sections if gene expression profiling is necessary. In paraffin sections, antigen-retrieving methods can sometimes destroy the epitopes, thus making the antibodies unusable.
5. Paraffin embedding is the best method to preserve tissue morphology. However, before embedding, tissues have to be treated in fixatives like neutral buffered formalin or 4 % paraformaldehyde in PBS overnight at 4 °C. Inadequately fixed tissues can dehydrate during tissue processing, resulting in hard and brittle specimens. Once embedded in paraffin, tissue blocks can be stored at RT for a long time (i.e., years). Paraffin sections can then be obtained by cutting the tissue blocks with the help of a microtome. As noted above, two limitations of paraffin sections are that it is hard to isolate RNA (though special kits are now available), and antigen retrieval processes can sometimes destroy the epitope of interest.
6. Antigens can become masked during the preparation of the tissue. In such cases, "antigen retrieval" methods are used to achieve better access to the epitopes recognized by the primary antibody. The method of antigen retrieval usually depends on the target antigen and the type of antibody used.
7. The presence of endogenous peroxidases in the tissue can severely limit the interpretation of immunoperoxidase staining in frozen tissues. Hence it is necessary to quench the endogenous peroxidase activity in aortic tissue sections.
8. Negative control experiments to rule out false-positive results due to unspecific binding of primary and secondary antibodies or to artifacts of the detection system, as well as positive control

experiments should be performed for all IHC studies. Different non-mutually exclusive strategies can be used for negative control studies, such as incubating with isotype-matched immunoglobulins instead of adding primary antibodies, or omitting the secondary antibody. For positive control experiments, IHC should be performed with sections of a tissue known to contain the cells of interest. Control tissue should be from the same species as the experimental tissues.

9. Incubation time for the primary antibody usually depends on the antigen of interest. The protocols outlined here are based on a default incubation time of 30–60 min. When increasing or decreasing the antibody concentration, incubation times may have to be adjusted accordingly. To obtain best results, it is recommended that each user performs titration assays to determine the optimum primary working dilution of both the primary and secondary antibodies.
10. The ABC reagent is best when freshly prepared. Allow 30 min at RT for complex formation before incubation with sections.
11. Incubation time with DAB depends on several factors, including the concentration and incubation time of antibodies used and the amount of the antigen of interest present in the tissue. Optimize time accordingly to prevent over staining and high background. DAB gives a brown reaction product. If a black reaction product is required, add one drop of nickel solution to the DAB solution. The solution should be prepared fresh. DAB and nickel chloride are toxic and carcinogenic; therefore gloves, eye protector, and lab coat must be worn while performing the experiment. Dispose according to institutional regulations.

Acknowledgments

This work is supported by NIH HL 084312 and HL098055 to E.A.F, and NIH T32 grant 5T32HL098129-05 to P.M.

References

1. Reddick RL, Zhang SH, Maeda N (1994) Atherosclerosis in mice lacking apo E. Evaluation of lesional development and progression. Arterioscler Thromb 14:141–147
2. Rong JX, Li J, Reis ED et al (2001) Elevating high-density lipoprotein cholesterol in apolipoprotein E-deficient mice remodels advanced atherosclerotic lesions by decreasing macrophage and increasing smooth muscle cell content. Circulation 104: 2447–2452
3. Ramos-Vara JA (2011) Principles and methods of immunohistochemistry. Methods Mol Biol 691:83–96
4. Trogan E, Choudhury RP, Dansky HM et al (2002) Laser capture microdissection analysis of gene expression in macrophages from atherosclerotic lesions of apolipoprotein E-deficient mice. Proc Natl Acad Sci 99:2234–2239
5. Gage GJ, Kipke DR, Shain W (2012) Whole animal perfusion fixation for rodents. J Vis Exp 65:3564

6. Gautier EL, Shay T, Miller J et al (2012) Gene-expression profiles and transcriptional regulatory pathways that underlie the identity and diversity of mouse tissue macrophages. Nat Immunol 13:1118–1128
7. Gimbrone MA Jr (1995) Vascular endothelium: an integrator of pathophysiologic stimuli in atherosclerosis. Am J Cardiol 75: 67B–70B
8. Muller AM, Hermanns MI, Skrzynski C et al (2002) Expression of the endothelial markers PECAM-1, vWf, and CD34 in vivo and in vitro. Exp Mol Pathol 72:221–229
9. Skalli O, Ropraz P, Trzeciak A et al (1986) A monoclonal antibody against alpha-smooth muscle actin: a new probe for smooth muscle differentiation. J Cell Biol 103:2787–2796
10. Yoshida T, Owens GK (2005) Molecular determinants of vascular smooth muscle cell diversity. Circ Res 96:280–291
11. Feig JE, Rong JX, Shamir R et al (2011) HDL promotes rapid atherosclerosis regression in mice and alters inflammatory properties of plaque monocyte-derived cells. Proc Natl Acad Sci U S A 108:7166–7171
12. Breslow JL (1996) Mouse models of atherosclerosis. Science 272:685–688

Chapter 10

Immunostaining of Lymphocytes in Mouse Atherosclerotic Plaque

Anton Gisterå and Daniel F.J. Ketelhuth

Abstract

Immunostaining can be defined as a method for identification of constituents in situ, e.g., proteins, using specific antigen–antibody interactions, visualized by color or fluorescence. In experimental research of atherosclerosis, immunostaining is a key method used for the characterization of the cellular composition in the atherosclerotic plaques. This includes the quantification of macrophages, smooth muscle cells, and lymphocytes—especially T lymphocytes. In this chapter we focus on basic protocols for characterization of lymphocytes and/or local T lymphocyte-related antigens in mouse atherosclerotic lesions.

Key words Immunostaining, Immunohistochemistry, Immunofluorescence, Lymphocytes, T lymphocytes, Atherosclerosis

1 Introduction

Atherosclerosis is a chronic inflammatory condition initiated by retention and accumulation of apolipoprotein B100 (ApoB100)-containing lipoproteins in the artery wall, in particular LDL, leading to maladaptive responses of macrophages and lymphocytes and the formation of atherosclerotic plaques [1].

Different genetically modified mice are fundamental instruments for experimental atherosclerosis research, e.g., *Apoe*$^{-/-}$ and *Ldlr*$^{-/-}$ mice. These models simulate the human disease and are the most commonly used experimental models of atherosclerosis, initiating the disease with fatty streaks that develop to fibroproliferative plaques with relative abundance of T lymphocyte infiltration and necrotic cores [2, 3]. T lymphocytes are in fact found in all stages of disease, while B lymphocytes only can be occasionally found in the vessel wall, and are more prevalent in the connective tissue surrounding the advanced atheroma, or where tertiary lymphoid organs are formed [4, 5].

Immunostaining is a potent method to demonstrate both the presence and location of particular cells or molecules of interest.

Vicente Andrés and Beatriz Dorado (eds.), *Methods in Mouse Atherosclerosis*, Methods in Molecular Biology, vol. 1339, DOI 10.1007/978-1-4939-2929-0_10,

Immunostaining has been instrumental to understand and characterize the atherosclerotic process. This has led to formulation of new concepts concerning the pathogenesis of atherosclerosis, and to proposals of new targets for prevention, diagnosis, and therapy [6]. Immunohistochemistry (IHC) and immunofluorescence (IF) are the main immunostaining techniques employed for the detection of lymphocytes in mouse atheromas. Both techniques refer to the specific antigen–antibody interactions where the antibody can be tagged with a "visible label," e.g., an antibody tagged with an enzyme that catalyzes the formation of a precipitate from a specific substrate in situ, and which can be visualized by light microscopy; or a "fluorescent label," e.g., an antibody tagged with a fluorochrome that emits light after being excited with light of a certain wavelength, and can be visualized by fluorescent or confocal microscopy.

This chapter describes the IHC and IF methods for the detection, characterization, and quantification of lymphocyte-related antigens in mouse atherosclerotic plaques: CD3, pan T lymphocyte marker; CD4, T-helper lymphocyte marker, CD8, T-cytotoxic lymphocyte marker; FoxP3, regulatory T lymphocyte (Treg) marker; IA^b (H2b haplotype of MHC-II), cell surface molecule needed for antigen presentation to T-helper CD4 lymphocytes, and CD19, B lymphocyte marker. Further, a short description for standardized tissue preparation is provided.

2 Materials

Prepare all solutions using ultrapure water (prepared by purifying deionized or distilled water, typically 18.2 MΩ·cm at 25 °C), and analytical grade reagents.

1. Mounting medium for cryosectioning (e.g., Tissue-Tek O.C.T.—Optimal Cutting Temperature—compound, Sakura) (*see* **Note 1**).
2. Microscope slides: ready-to-use microscope slides are suggested for the described protocols (e.g., Menzel-Gläzer SuperFrost Plus—Thermo Scientific).
3. Fixation reagent: Pure ice-cold acetone.
4. Peroxidase-antiperoxidase (PAP) pen for immunostaining (5 mm tip width).
5. Rinsing buffer: Tris-buffered saline (TBS—50 mM Tris–Cl, 150 mM NaCl), pH 7.6.
6. Staining buffer: 5 % horse serum in rinsing buffer (*see* **Note 2**).
7. Quenching solution: 0.3 % hydrogen peroxide solution in rinsing buffer (*see* **Note 3**).

8. Avidin and biotin blocking solutions (e.g., Avidin/Biotin blocking kit, Vector).
9. Avidin-biotin complex (e.g., Vectastain ABC kit, Vector) (*see* **Note 4**).
10. Developing solutions: For example, 3, 3′-diaminobenzidine (DAB) peroxidase substrate kit—brown color (Vector); Nova Red substrate kit—red color (Vector) (*see* **Note 5**). All necessary reagents are provided in the kits. DAB solution is prepared by mixing 468 µl ultra-pure H_2O, 8 µl buffer, 16 µl DAB, and 8 µl H_2O_2, or as specified by the manufacturer. Nova Red solution is prepared by mixing 464 µl ultra-pure H_2O, 12 µl reagent 1, 8 µl reagent 2, 8 µl reagent 3, and 8 µl H_2O_2, or as specified by the manufacturer.
11. Hematoxylin solution: Hematoxylin QS (Vector), or Mayer's Hematoxylin solution (*see* **Note 6**).
12. Dehydration solutions: 95 and 99 % ethanol solutions in ultra-pure water, and pure Xylene (*see* **Note 7**).
13. Mounting media: For example, Pertex (Histolab), rapid drying mounting medium; or Kaisers Glycerinegelatine (Merck), water-soluble mounting medium (*see* **Note 8**).
14. Autofluorescence blocking solution: 0.03 % Sudan Black in 70 % ethanol.
15. 4′, 6-Diamidino-2-phenylindole (DAPI) working solution: DAPI (e.g., D8417, Sigma) diluted 1:20,000 times in Rinsing buffer (*see* **Note 9**).
16. Fluorescence mounting medium (e.g., S3023, Dako).
17. Sealing agent: Transparent nail polish.
18. Primary and secondary antibodies: Suggested primary antibodies are described in Table 1, secondary antibodies in Table 2, and streptavidin conjugates in Table 3 (*see* **Note 10**).

Table 1
Suggested primary antibodies to evaluate lymphocyte-related antigens

Target antigen	Host species (label)	Clone	Dilution	Comment
Mouse CD3	Hamster	500A2	1:100	Permeabilization step required
Mouse CD4	Rat	H129.19	1:100	
Mouse CD8	Rat	53-6.7	1:100	
Mouse FoxP3	Rat	FJK-16s	1:50	Permeabilization step required
Mouse I-Ab	Mouse (biotinylated)	KH74	1:300	
Mouse CD19	Rat	1D3	1:100	

Table 2
Suggested secondary antibodies

Target antibody	Host species (label)	Cat. no.	Source	Dilution
Rat IgG	Rabbit (biotinylated)	BA-4001	Vector	1:200
Hamster IgG	Goat (biotinylated)	BA-9100	Vector	1:200

Table 3
Suggested streptavidin conjugates

Target	Conjugates	Cat. no.	Source	Dilution
Biotin	Streptavidin-DyLight 488	SA-5488	Vector	1:400
Biotin	Streptavidin-DyLight 594	SA-5594	Vector	1:400

19. Phosphate-buffered saline (PBS): 1.54 mM KH2PO4, 155.17 mM NaCl and 2.71 mM Na_2HPO_4, pH 7.4, sterilized by autoclaving.
20. Tepid water.

3 Methods

3.1 Sectioning of Aortic Roots and Slide Preparation

In order to optimize the results of the immunostaining, the collection, preservation, and processing of organs should be performed in a standardized way.

1. After dissection, the hearts should be kept in PBS on ice until the mounting, or be directly mounted in mounting medium and being snap frozen. The embedded hearts should be kept at −80 °C until the cryosectioning is performed.
2. For sectioning of the aortic roots, it is recommended to use the method described by Nicoletti et al. [7]. Briefly, the proximal 800 μm of the aortic root is serially sectioned on a cryostat, with each section 10 μm thick. "Point Zero," where the aortic root begins, is located where the cusps of the aortic valves start to be visible and is found by sectioning the heart in an upstanding position in a caudal-to-cranial direction. From this point, 10 μm thick sections, starting at the 90–880 μm levels (distance from "Point Zero") are collected to slides following scheme of Fig. 1. The first 90 μm of sections are used to adjust the angle to get all three cusps visible and aligned.

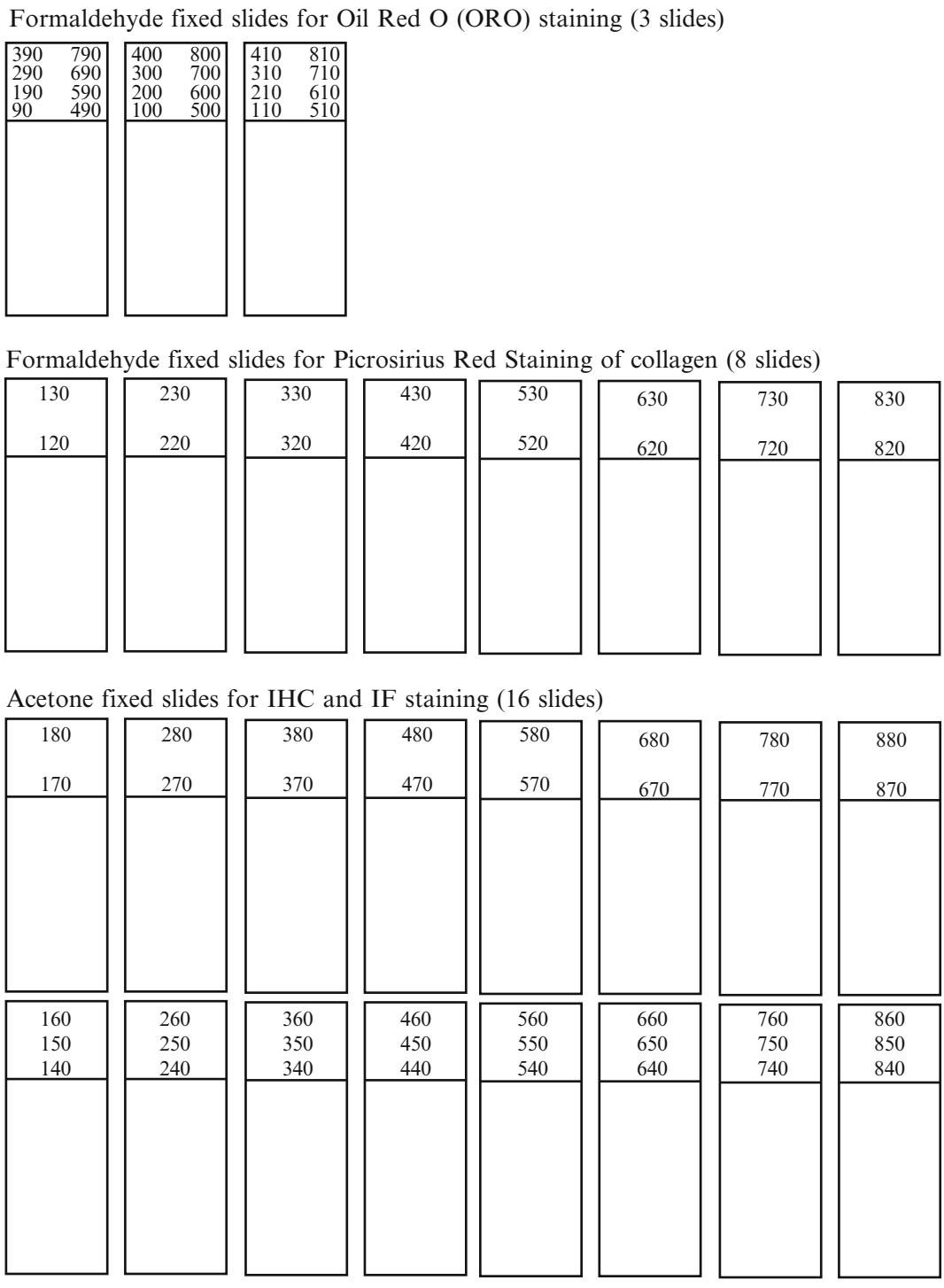

Fig. 1 Template for aortic root sectioning and organization of slides

3.2 Tissue Fixation

1. Immerse the slides into fixation reagent for 10 min on ice (*see* **Note 11**).
2. Remove the slides from fixation reagent and let them dry, at room temperature, for 1 h.
3. After fixation, slides should be stored at −20 °C until staining.

3.3 Immunostaining

All steps are conducted in room temperature unless otherwise stated.

3.3.1 Immunohistochemistry of Acetone-Fixed Frozen Sections

1. Encircle sections on slides with a PAP pen (*see* **Note 12**).
2. Equilibrate sections with rinsing buffer for 5 min (*see* **Note 13**).
3. Add Quenching solution for 15–30 min (*see* **Note 3**).
4. Rinse sections with rinsing buffer, three times for 5 min (*see* **Note 14**).
5. Incubate sections with avidin solution (from Avidin and Biotin blocking solution, Vector, **item 8** in Subheading 2) for 15 min. Rinse briefly after incubation.
6. Incubate sections with biotin solution (from Avidin and Biotin blocking solution, Vector, **item 8** in Subheading 2) for 15 min.
7. Rinse with rinsing buffer, three times for 5 min.
8. Block the sections with staining buffer for 30 min. Remove the excess of staining buffer from sections, but do not rinse the slides after the incubation.
9. Add the primary antibody diluted in Staining buffer (*see* **Note 15**).
10. Incubate the slides overnight at 4 °C, or 1 h at room temperature.
11. Rinse with rinsing buffer, three times for 5 min.
12. Add secondary antibody (biotinylated) diluted in staining buffer. Incubate the slides for 30 min.
13. Rinse with rinsing buffer, three times for 5 min.
14. Incubate sections with avidin-biotin complex for 30 min (*see* **Note 4**).
15. Rinse the slides with rinsing buffer, three times for 5 min.
16. Add the developing solution of your choice. Color development takes typically 3–10 min with DAB solution, and 5–15 min with Nova Red solution (*see* **Note 16**).
17. Rinse the sections with ultra-pure water.
18. Stain with hematoxylin for 30–60 s (*see* **Notes 6** and **17**).
19. Rinse with tepid tap water (*see* **Note 17**).
20. Dehydrate the sections by adding the slides into 95 % ethanol solution for 5 min. Next, transfer the slide to 99 % ethanol

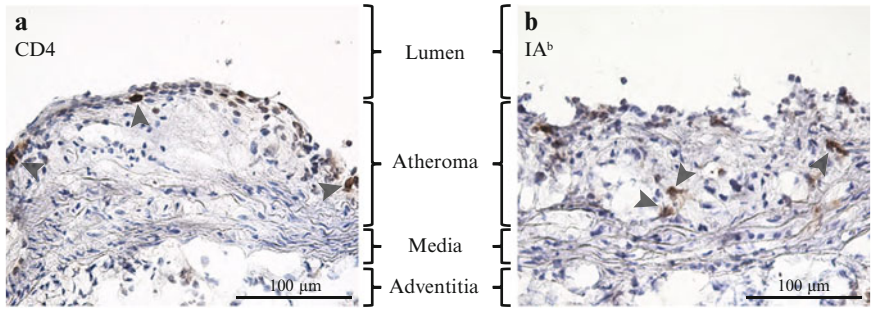

Fig. 2 Sample photomicrographs of immunostained acetone-fixed aortic root sections from *Apoe*$^{-/-}$mice. (**a**) Shows CD4, and (**b**) IA^b immunostaining of acetone-fixed cryosections. Cell nuclei are stained in blue by hematoxylin. Positive examples of DAB-stained cells (*brown*) are indicated with *arrows*. Images were acquired using a light microscope at 200× magnification

solution for an additional 5 min. Lastly, transfer the slides to pure xylene for 1 min.

21. Carefully add mounting medium to the slides in order to avoid air bubble formation. Cover the slides with cover slips and let them dry for 24 h, in a ventilated hood.
22. Analyze the slides using a light microscope. Representative IHC stainings of CD4 and IA^b are shown in Fig. 2.

3.3.2 Immunofluorescence Staining of Acetone-Fixed Frozen Sections

All steps are conducted at room temperature unless otherwise stated.

1. Encircle sections on slides with a PAP pen (*see* **Note 12**).
2. Equilibrate sections with rinsing buffer for 5 min (*see* **Note 18**).
3. Add quenching solution for 15–30 min (*see* **Note 3**).
4. Rinse sections with rinsing buffer, three times for 5 min (*see* **Note 14**).
5. Incubate sections with avidin solution (from Avidin and Biotin blocking solution, Vector, **item 8** in Subheading 2) for 15 min. Rinse briefly after incubation.
6. Incubate sections with biotin solution (from Avidin and Biotin blocking solution, Vector, **item 8** in Subheading 2) for 15 min.
7. Rinse slides with rinsing buffer, three times for 5 min.
8. Block the sections with staining buffer, for 30 min. Remove the excess of staining buffer from sections, but do not rinse the slides after the incubation.
9. Add the primary antibody diluted in staining buffer (*see* **Note 15**).
10. Incubate the slides overnight at 4 °C, or 1 h at room temperature.

11. Rinse with rinsing buffer, three times for 5 min.
12. Add secondary antibody (biotinylated) diluted in staining buffer. Incubate the slides for 30 min.
13. Rinse with rinsing buffer, three times for 5 min.
14. Add streptavidin fluorochrome conjugates diluted in staining buffer. Incubate the slides for 45 min (*see* **Notes 18** and **19**).
15. Rinse with rinsing buffer, three times for 5 min.
16. Add autofluorescence blocking solution for 5–15 min.
17. Rinse the slides with rinsing buffer, three times for 5 min.
18. Incubate with DAPI for 20 min.
19. Rinse with rinsing buffer, three times for 5 min.
20. Add fluorescence mounting medium to the slides, and be careful to avoid air bubble formation. Cover the slides with cover slips and let them dry for 24 h.
21. Surround the cover slip with sealing agent and store the slides at 4 °C.
22. Analyze the slides using fluorescence or confocal microscope.

4 Notes

1. The O.C.T. mounting medium contains water-soluble glycols and resins, which provides a supportive matrix for cryostat sectioning, it surrounds but do not infiltrate the tissue, and leaves no residue on slides during the staining procedure. It freezes at approximately –20 °C. Paraffin-embedded tissues are easier to cut and preserve better their morphology. However, it is not recommended to perform immunostaining of lymphocytes on paraffin-embedded tissues using the described protocol.
2. Prepare as much staining buffer as you need for your experiment. The solution is stable for 1 week at 4 °C. It is advisable to store frozen horse serum aliquots at –20 °C that can be quickly thawed for the preparation of the staining solution. Frozen horse serum aliquots are stable for at least 6 months at –20 °C. Do not refreeze serum remains. Staining of some antigens requires cell permeabilization with the addition of 0.1 % Tween to the staining buffer (1 ml Tween-20 in 1000 ml staining buffer).
3. Endogenous peroxidase activity is blocked by treatment of tissue sections with hydrogen peroxidase prior to incubation with HRP, which reduces the staining background. Cell surface markers such as CD4 could be destroyed during the hydrogen peroxide quenching, therefore it is only recommended to use a low concentration of it, diluted in rinsing buffer. Note that precaution is needed in order to handle and use hydrogen

peroxide. The incubation time with the quenching solution can be determined visually—quenching can be considered finished when the formation of gas bubble diminishes.

4. Vectastain ABC kit (Vector) contains the reagents required for the preparation of the complex. The Complex should always be freshly prepared, at least 30 min prior to its use, following the manufacturer's instructions.
5. DAB is toxic and harmful; be sure to work in adequate ventilated environment, and wear eye protection and chemical-resistant gloves. When choosing which Developing solution to use, it should be noticed that Nova Red is less toxic than DAB.
6. Hematoxylin QS provides ready-to-use solution in a drip-type bottle, which facilitates its direct application to the sections in the slide. This is convenient when staining small batches of slides. For larger slide batches, the use of Mayer's Hematoxylin is recommended.
7. Xylene is an aromatic solvent, flammable of modest acute toxicity. Its handling should be conducted in a fume-hood.
8. Kaisers Glycerinegelatine is a water-soluble mounting medium. It eliminates the need for dehydrating the slides, which can damage some developing solutions (not DAB and Nova Red). This mounting medium does not preserve the hematoxylin staining adequately over time. Therefore, the use of Pertex is preferable. Further, the low viscosity of Pertex can prevent the formation of air bubbles that interferes with analysis.
9. DAPI is a fluorescent dye that binds to DNA and stains the nucleus of cells. DAPI has absorption maximum at 358 nm and its emission maximum at 461 nm.
10. Dilution recommendations are given in the tables. Indeed, all antibodies should be tested individually when setting up the method. It is suggested to perform serial dilutions of the primary antibodies, e.g., 1:100, 1:200, 1:400, 1:800, and 1:1600, and select the best dilution based on the intensity and specificity of the stainings.
11. For immunostaining of lymphocytes, acetone fixation of the sections is strongly recommended. Formaldehyde (4 % aqueous solution, phosphate buffered) is another convenient fixation reagent, but it creates cross-linking of amino groups which most often destroys the epitopes recognized by the antibodies described in this protocol. Nevertheless, formaldehyde is the fixation of choice for Oil Red O staining of lipids and Picrosirius Red staining of collagen (Fig. 1).
12. PAP pen provides a water repellant barrier to define the area of staining which is especially important for the staining of multiple targets on slides with multiple sections. The PAP pen markings are removed in xylene, used in the dehydration step.

13. Use a pipette to add 50–70 μl liquid per section. Make sure that the whole section is covered—the tissue section should never dry out during the staining procedure.
14. Always use large amounts of rinsing buffer. Remove the prior reagent by carefully dripping some rinsing buffer over the section with a pipette before putting slides in a common beaker filled with rinsing buffer. This step needs to be very carefully performed after the primary antibody incubation.
15. IA[b] staining described in this protocol utilizes a directly conjugated biotinylated primary antibody—no secondary antibody is needed. In case this staining is performed in parallel with antigens that need secondary antibodies, add staining buffer "without antibody" during the secondary antibody step.
16. The incubation times of the developing solutions need to be adjusted in order to obtain perfect results. It is recommended to start with a short incubation time with immediate evaluation under the microscope. If the staining is not satisfactory, continue the incubation of the slides with the developing solution. Notice that all slides should be incubated the same time in order to obtain comparable staining intensity between samples.
17. Hematoxylin stains negatively charged sites, in particular nuclear DNA. The acidic hematoxylin solution gives a reddish hematein staining of the nucleus, which is converted to a blue complex after washing with water, and gives a good contrast as a counterstain. For Mayer's Hematoxylin solution, the recommended staining time ranges between 1 and 5 min. The exact time needs to be determined by evaluation of the staining results under a microscope.
18. Protect the slides from light when performing immunofluorescence staining because the fluorochromes will be bleached if exposed to light. Keep the slides at 4 °C and in the dark if analysis will be performed later.
19. Choosing which fluorochrome to use will depend of the available detection possibilities. In Table 3, two recommendable fluorochromes are listed. DyLight 488 excited with blue laser, at 493 nm, emits a green fluorescence, at 518 nm. Dylight 594 excited with an orange laser, at 592 nm, emits a red fluorescence, at 617 nm.

Acknowledgements

We gratefully acknowledge Inger Bodin and Linda Haglund for their technical assistant, standardization, and optimization of immunostaining methods at our Unit. We thank Konstantinos Polyzos for preparation of representative micrographs. We thank

Antonino Nicoletti, Xinghua Zhou, Anna-Karin Robertson, and Inger Bodin for the implementation of the laboratory's sectioning protocol.

References

1. Hansson GK (2005) Inflammation, atherosclerosis, and coronary artery disease. N Engl J Med 352:1685–1695
2. Nakashima Y, Plump AS, Raines EW et al (1994) ApoE-deficient mice develop lesions of all phases of atherosclerosis throughout the arterial tree. Arterioscler Thromb 14:133–140
3. Ishibashi S, Goldstein JL, Brown MS et al (1994) Massive xanthomatosis and atherosclerosis in cholesterol-fed low density lipoprotein receptor-negative mice. J Clin Invest 93: 1885–1893
4. Ketelhuth DF, Hansson GK (2011) Cellular immunity, low-density lipoprotein and atherosclerosis: break of tolerance in the artery wall. Thromb Haemost 106:779–786
5. Zhou X, Stemme S, Hansson GK (1996) Evidence for a local immune response in atherosclerosis. CD4+ T cells infiltrate lesions of apolipoprotein-E-deficient mice. Am J Pathol 149:359–366
6. Libby P, Ridker PM, Hansson GK (2011) Progress and challenges in translating the biology of atherosclerosis. Nature 473:317–325
7. Nicoletti A, Kaveri S, Caligiuri G et al (1998) Immunoglobulin treatment reduces atherosclerosis in apo E knockout mice. J Clin Invest 102:910–918

Chapter 11

Flow Cytometric Analysis of Immune Cells Within Murine Aorta

Breanne N. Gjurich, Parésa L. Taghavie-Moghadam, and Elena V. Galkina

Abstract

The immune system plays a critical role in the modulation of atherogenesis at all stages of the disease. However, there are many technical difficulties when studying the immune system within murine aortas. Common techniques such as PCR and immunohistochemistry have answered many questions about the presence of immune cells and mediators of inflammation within the aorta yet many questions remain unanswered due to the limitations of these techniques. On the other hand, cumulatively the flow cytometry approach has propelled the immunology field forward but it has been challenging to apply this technique to aortic tissues. Here, we describe the methodology to isolate and characterize the immune cells within the murine aorta and provide examples of functional assays for aortic leukocytes using flow cytometry. The method involves the harvesting and enzymatic digestion of the aorta, extracellular and intracellular protein staining, and a subsequent flow cytometric analysis.

Key words Atherosclerosis, Mouse aorta, Flow cytometry, Leukocytes

1 Introduction

Atherosclerosis is characterized by the formation of calcified plaques in the large- and medium-sized blood vessels due to changes in lipid metabolism, the activation of vascular wall components, and an increased pro-inflammatory immune response within the aortic wall. Mice are common models for atherosclerotic studies because of the ease of genetic manipulation and relatively quick progression of disease, where atherosclerotic plaques can be detected in aged or high-fat diet-fed animals [1]. However, the murine model also poses several challenges for immunological analysis due the size and the number of cells obtained from the aorta.

The aorta contains a heterogeneous population of endothelial cells, smooth muscles cells, and leukocytes. Leukocytes play a pivotal role in modulating disease pathogenesis and inflammation.

Vicente Andrés and Beatriz Dorado (eds.), *Methods in Mouse Atherosclerosis*, Methods in Molecular Biology, vol. 1339, DOI 10.1007/978-1-4939-2929-0_11,

Several leukocyte populations and their corresponding subsets including macrophages, dendritic cells, neutrophils, mast cells, and T and B lymphocytes reside within the aortic intima, media, and adventitia [2]. Interestingly, small numbers of leukocytes are found within healthy, non-inflamed aortas but this number increases with the progression of atherosclerosis [3]. The change in aortic leukocyte populations is due to altered influx and efflux rates of leukocytes as well as changes in the proliferation and apoptotic rates of specific leukocyte subsets within the aorta [2]. Thus, it is not only difficult to identify these small numbers of cells within minimal amounts of available tissue, but understanding the dynamic phenotype and functions of these leukocytes is another challenge.

Techniques such as polymerase chain reaction (PCR) and immunohistochemistry (IHC) offered a firm foundation for our understanding of the immunological composition of the aorta. However, both of these techniques have several limitations that are further highlighted when studying atherosclerosis in the murine model. The small quantities of material needed for analysis makes PCR useful; however, to study the immune composition several markers are often needed to identify one cell type. On the other hand, immunohistochemistry offers the ability to use several cell markers simultaneously to identify single cell populations, their location within the aortic tissue, and any interacting partners. However, when performing immunohistochemistry on aortic tissue samples, functions of a specific cell population cannot be explored, and the data is only semiquantitative, which may be difficult to analyze when addressing questions focused on small numbers of cells.

With the advancements of flow cytometry, studying the immune composition of mouse aortas has become increasingly feasible. Flow cytometry provides a method to identify and quantify subpopulations within a heterogeneous sample. Additionally, flow cytometry can be used to analyze certain functional properties of cells such as proliferation, apoptotic state, or cytokine production. Flow cytometry has been successfully used to analyze the immune response with several solid tissues including kidney, skin, and heart [4–6]. Several investigators attempted to use flow cytometry to analyze the aorta, but remnant tissue debris, high auto-fluorescence, and loss of cells [7–9] made the analysis challenging. Recently, Galkina et al. developed a flow cytometry-based method using a combination of multiple enzymes to analyze aortic leukocytes [3]. The use of CD45, a common leukocyte marker, significantly improved the quality of samples permitting the exclusion of highly autofluorescent non-CD45 vascular cells from leukocyte analysis. Since then, several modifications for this protocol and varying enzyme combinations were proposed for flow cytometry analysis [10–13].

Despite the benefits of flow cytometry, this technique also has limitations, some of which are common with PCR and IHC. The amount of material required for quantification of aortic leukocytes by flow cytometry is larger than PCR, but like PCR, the specific location of analyzed cells cannot be identified. Furthermore, the enzymatic digestion of samples can alter the expression of surface markers and may increase autofluorescence that must be accounted for during analysis [9]. Despite these limitations, flow cytometry allows the simultaneous use of multiple markers to identify a cell type resulting in a more detailed analysis of the aortic sample. Additionally, flow cytometry provides quantitative and qualitative results.

Here, we describe the method to prepare and complete flow cytometric analysis on leukocytes isolated from atherosclerotic *Apolipoprotein E-null* (*Apoe*$^{-/-}$) murine aortas (Fig. 1). This includes harvesting the aorta, treatment by enzymatic digestion, cell retrieval, flow cytometric preparation, and sample collection, followed by a detailed description of the analysis performed to identify the aortic leukocyte populations and potential functional applications.

2 Materials

2.1 Harvest Aorta

1. Microdissection tools.
2. Surgical microscope (e.g., Diagnostic Instruments Inc., Sterling Heights, Michigan).
3. 1× Phosphate-buffered saline (PBS): 2.7 mM potassium chloride, 1.5 mM potassium phosphate monobasic, 137.9 mM sodium chloride, 8.1 mM sodium phosphate dibasic.
4. 2 % heparin diluted in PBS.
5. 12 × 75 mm, 5 mL polystyrene round-bottom test tube (FACS tubes).

2.2 Enzymatic Digestion

1. Collagenase, Type I (e.g., Worthington Biochemicals, Lakewood, New Jersey).
2. Collagenase, Type XI (e.g., Sigma Aldrich, St. Louis, Missouri).
3. Deoxyribonuclease I (DNase) from bovine pancreas, type II (e.g., Sigma Aldrich).
4. Hyaluronidase from bovine testes, type 1-s (e.g., Sigma Aldrich).
5. Water bath.

2.3 Cell Suspension

1. 70 μm nylon cell strainer.
2. Syringe without needle.
3. Table-top, swinging bucket centrifuge 5810R.

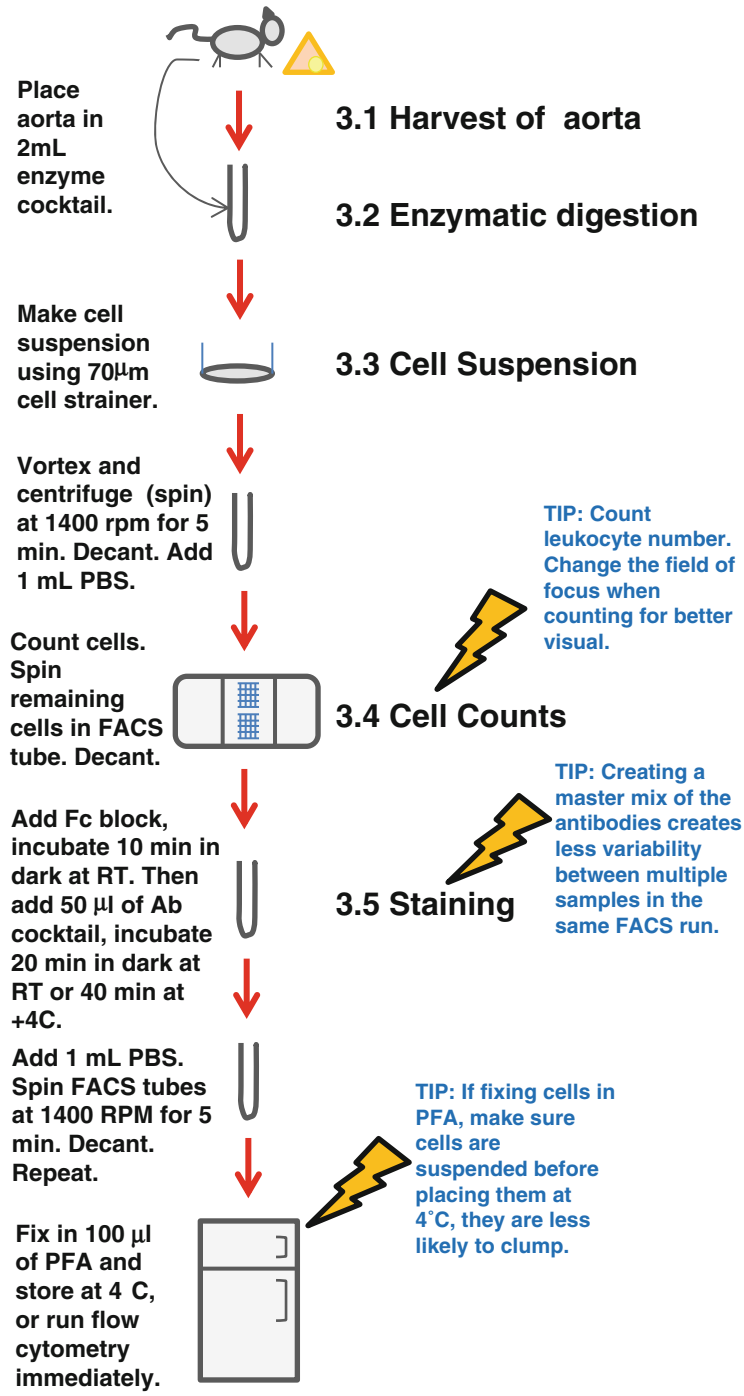

Fig. 1 Schematic describing aortic flow cytometry protocol

4. Red blood cell lysis buffer: 155 mM ammonium chloride (NH_4Cl), 10 mM potassium bicarbonate ($KHCO_3$), and 1.27 mM ethylenediaminetetraacetic acid (EDTA) diluted in distilled water, pH 7.4. Others are commercially available.

2.4 Cell Counting

1. 0.4 % solution Trypan blue.
2. Bright-line hemacytometer.
3. Light microscope.

2.5 Extracellular Staining

1. Fc blocking antibodies (CD16/CD32).
2. Antibodies applicable for flow cytometry.
3. Fixable Viability Dye (eBioscience, CA).
4. 2 % Paraformaldehyde (PFA).

2.6 Intracellular Staining

1. RPMI-1640 medium supplemented with 10 % fetal bovine serum, heat inactivated (FBS), and 1 % penicillin-streptomycin.
2. Phorbol 12-myristate 13-acetate (PMA).
3. Ionomycin calcium salt from *Streptomyces Conglobatus*.
4. Golgi Plug solution containing brefeldin A (BD Biosciences).
5. Humidified incubator with CO_2 tank.
6. Cytofix/Perm kit (BD Biosciences).

2.7 Aortic Sample Acquisition and Analysis

1. Flow cytometry acquisition instrument (e.g., 8-color updated BD FACS Calibur, BD Biosciences/Cytek).
2. FACS tubes with cell strainer caps.
3. Flow cytometry analysis software (e.g., FlowJo).

3 Method

3.1 Harvest Aorta

1. After euthanizing the mouse, remove all blood via cardiac puncture (*see* **Note 1**).
2. Open the abdominal and chest cavities and gently perfuse the aorta with PBS containing 2 % heparin to remove blood from the vessels.
3. Carefully remove any surrounding adipose tissue and dissect aorta (including branches within the arch), keeping the adventitia intact (*see* **Note 2**).
4. Place aorta in a FACS tube in 2 mL of PBS on ice.
5. Collect the spleen to prepare single-control samples for flow cytometer parameter settings (*see* **step 4** in Subheading 3.3 and **step 1** in Subheading 3.5 for details).

3.2 Enzymatic Digestion

1. Place 35 μL of enzyme digestion solution in the FACS tube containing the aorta and 2 mL of PBS. Aortas can be cut into small pieces to improve digestion of the tissues.

   Final enzyme digestion solution concentration (diluted in PBS) is:

450 U/mL collagenase type I.

125 U/mL collagenase type XI.

60 U/mL hyaluronidase type I-s.

60 U/mL DNase-I.

2. Incubate for 45–60 min at 37 °C, and cover tubes with caps (*see* **Note 3**).

3.3 Cell Suspension

1. Use 70 μm cell strainer and syringe to release cells from digested aortic tissue returning cells to FACS tube.
2. Centrifuge at 368 rcf at 4 °C for 5 min, and then decant supernatant (*see* **Notes 4** and **5**).
3. Resuspend in 1 mL of PBS and place on ice.
4. For splenic tissue: Prepare single-cell suspension using a 70 μm cell strainer, remove red blood cells using lysis buffer, wash cells twice with PBS, then centrifuge, and decant as done with aortic samples. Resuspend in PBS.

3.4 Cell Counts

1. Pipet or vortex the cell suspension to ensure that it is homogenous.
2. Count the number of aortic leukocytes using trypan blue to exclude nonviable cells.
3. Calculate the number of aortic leukocytes (*see* **Note 6**).
4. Centrifuge cells at 368 rcf, 4 °C for 5 min and then decant supernatant (*see* **Note 5**).
5. Following the same procedure, count the number of splenic leukocytes.

3.5 Extracellular Staining

1. *See* **Note 7** for an explanation of the appropriate controls to use.
2. If interested in intracellular staining, *see* Subheading 3.6 before proceeding with extracellular staining.
3. Perform staining on aortic cell suspension using a standard flow cytometry protocol. Briefly, incubate $1.0–1.5 \times 10^6$ cells with 10 μg/ml of Fc blocking buffer (*see* **Note 8**) ($0.5–1.0 \times 10^6$ splenic cells should be used for each control sample).
4. Incubate for 10 min at room temperature to inhibit nonspecific binding of antibodies.
5. Add antibodies of interest at appropriate dilutions to 100 μL of diluted Fc blocking buffer and briefly vortex (*see* **Notes 8–12**).
6. If completing the viability staining, incorporate with the extracellular antibody staining here.
7. Incubate samples in the dark for 20 min at room temperature or 40 min at 4 °C.

8. After the antibody incubation, add 1 mL of PBS to wash.
9. Centrifuge at 368 rcf at 4 °C for 5 min and decant the supernatant (*see* **Note 5**).
10. Repeat **steps 8** and **9**.
11. If completing intracellular staining, go to Subheading 3.6.
12. After washing, fix cells in 100 μL of 2 % PFA (*see* **Note 13**).
13. Store overnight at 4 °C in the dark (*see* **Note 14**).

3.6 Intracellular Cytokine Staining

1. After counting cells, resuspend cells in FACS tube or cell culture plate with RPMI-1640 medium supplemented with 10 % FBS and 1 % Penicillin/Streptomycin.
2. Add to the medium 10 ng/mL PMA, 500 ng/mL ionomycin C, and 500 ng/mL Golgi Plug (final concentrations in medium) to stimulate cytokine production.
3. Plate cells at a concentration of 1×10^6 cells/mL.
4. Incubate at 37 °C with 5 % CO_2 for 5 h.
5. If incubating in a cell culture plate, wash and remove cells, placing them in FACS tube.
6. Centrifuge at 368 rcf for 5 min in 4 °C, and then decant the supernatant (*see* **Note 5**).
7. Wash the cells once with PBS.
8. Centrifuge at 368 rcf for 5 min in 4 °C and decant the supernatant (*see* **Note 5**).
9. Stop here and complete Subheading 3.5.
10. After completing extracellular staining without fixation, use CytoFix/Perm kit to prepare cells for intracellular cytokine staining (follow the manufacturer's protocol and *see* **Note 8**).
11. After BD protocol completion, fix cells in 2 % PFA (*see* **Note 14**).

3.7 Aortic Sample Acquisition

1. Set up flow cytometer and settings according to the manufacturer's protocol (*see* **Note 15**) and filter the samples using the cell strainer.
2. Use unstained and single samples prepared from the spleen to set the appropriate forward (FSC) and side (SSC) scatter as well as gain values for the fluorescent channels to depict clear negative and positive populations for each fluorophore used. Then, begin collecting control samples (*see* **Note 17**).
3. Run samples of interest (*see* **Notes 16–19**). For aortic samples, first ensure that the FSC and SSC thresholds are set appropriately (Fig. 2).
4. When sample volume reaches lower limit, add sheath fluid to sample, briefly vortex, and place back for collection. Continue collecting cells to ensure that all cells are recorded (*see* **Note 19**).

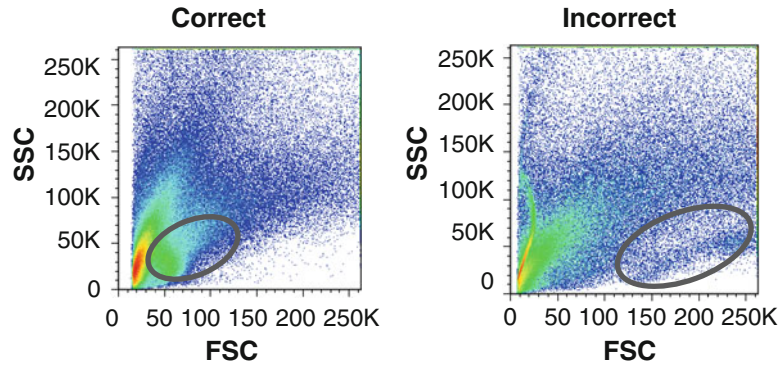

Fig. 2 Setting of appropriate FSC and SSC for aortic tissue sample. FSC and SSC can be slightly altered between different tissue samples. Depicted here are representative FACS plots of the FSC and SSC of aortic cell suspensions, in which different gains were used to set up FSC/SSC parameters. (*Left*) Correctly positioned leukocytes between 50 and 100 K on FSC and between 25 and 50 K on SSC versus (*right*) incorrect positioning where the leukocyte population is shifted too much to the *right*

3.8 Analysis

1. Using flow cytometric analysis software set the appropriate compensation values using the single controls.
2. For the aortic samples, gate out cellular debris less than ~40 K on the FSC axis (Fig. 3a, Plot #1).
3. From the gated cells, identify CD45$^+$ cells as leukocytes (Fig. 3a, Plot #2) using the unstained aorta and/or the CD45 isotype control staining (Fig. 3a, Plot #4) as control references.
4. Once appropriately identified, check the FSC and SSC of the CD45$^+$ gated cells and again gate out cellular debris less than 40 K on the FSC axis (Fig. 3a, Plot #3).
5. If viability staining was used, identify all live cells (Fig. 3b, *left*). A sample that was heat shocked at 70 °C can be used as a positive control to set the appropriate gates (Fig. 3b, *right*).
6. Begin analyzing the aortic immune composition by first establishing where the populations are located on the FACS plots using the isotype and FMO gates (Fig. 4, *right panels*). Apply these gates directly to the samples of interest. Total leukocyte populations can be detected from the CD45$^+$ population (Fig. 5) and more specific analysis of leukocyte subset populations can be detected using additional markers (Figs. 4 and 5) (*see* **Note 20**).
7. If cell types express various levels of a specific marker of interest, use the histogram feature to identify low/intermediate/high populations (*see* Fig. 4c).

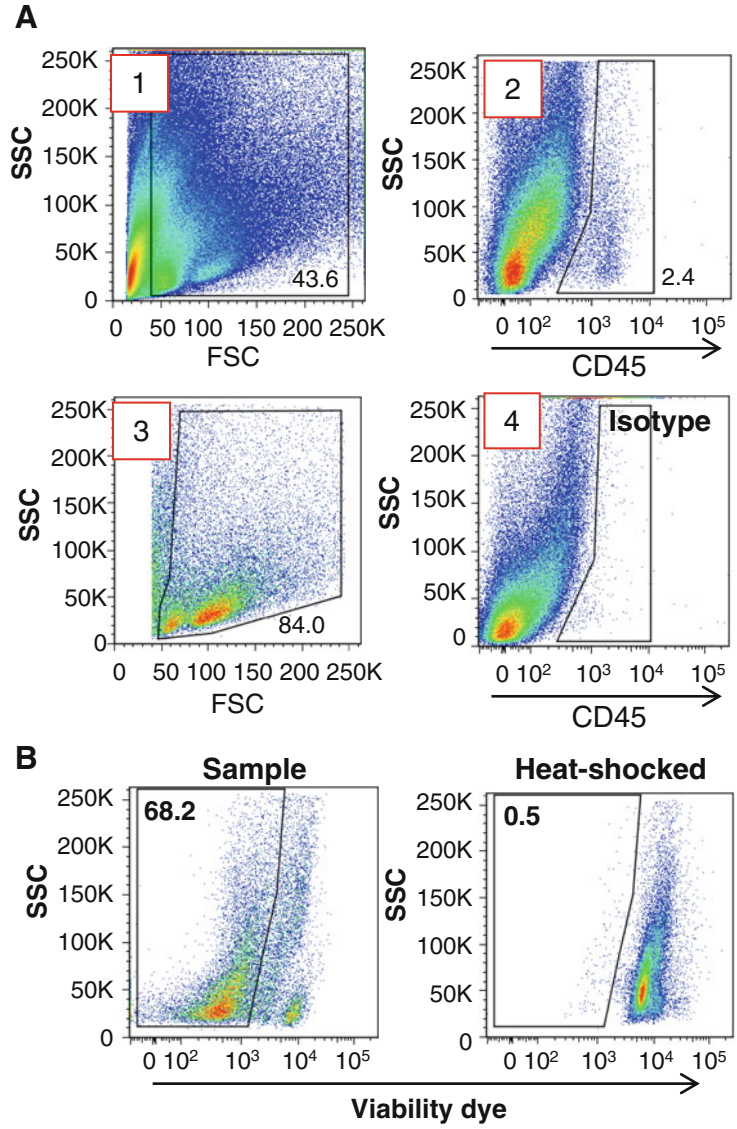

Fig. 3 Initial gating scheme for aortic cell samples (**a**) (1) Gate out events that are less than 40 K on the FSC axis. (2) Next, establish the gate for CD45 positive staining using the unstained aortic sample and/or isotype control staining for CD45 in aortic tissues (*see* Fig. 3a (4) as an example). (3) From the established $CD45^+$ population, gate out additional events that are less than 40 K on the FSC axis. (**b**) To avoid high autofluorescent background and nonspecific staining for aortic cells, a viability dye can be used. (*Left*) Representative FACS plot for aortic sample with Fixable Viability Dye ef506 demonstrates 68.2 % of viable aortic cells within the analyzed sample. (*Right*) Gates for nonviable and viable cells can be determined by using heat shocked positive control sample

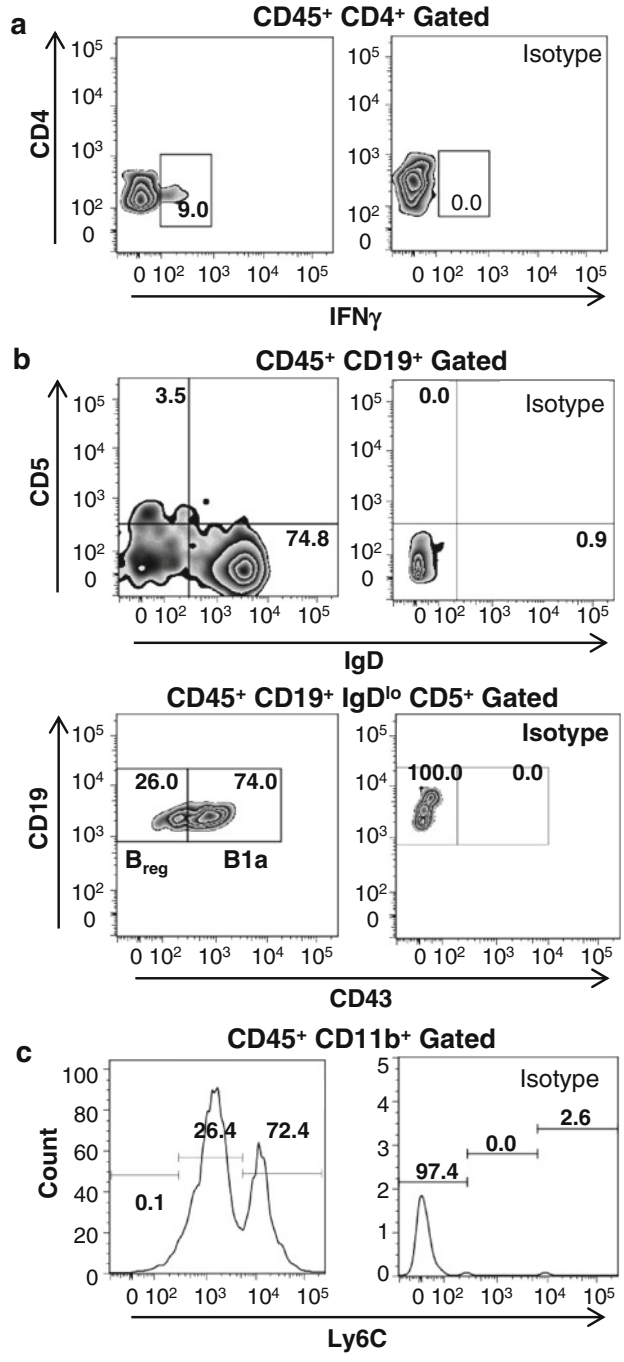

Fig. 4 Characterization of several subpopulations of leukocytes within the murine aorta. Flow cytometric analysis of aortas allows analyzing the distribution of leukocyte subpopulations within the murine aortas using both extracellular and intracellular markers. Aortic cell suspensions were prepared from a whole *Apoe*$^{-/-}$ aorta and stained with various antibodies against CD45, CD4, IFNγ, CD19, IgD, CD5, CD43, CD11b, and Ly6C. Cells were gated on CD45^{+} cells and debris was excluded based on the FSC/SSC profiles. (**a**) To distinguish the T helper 1

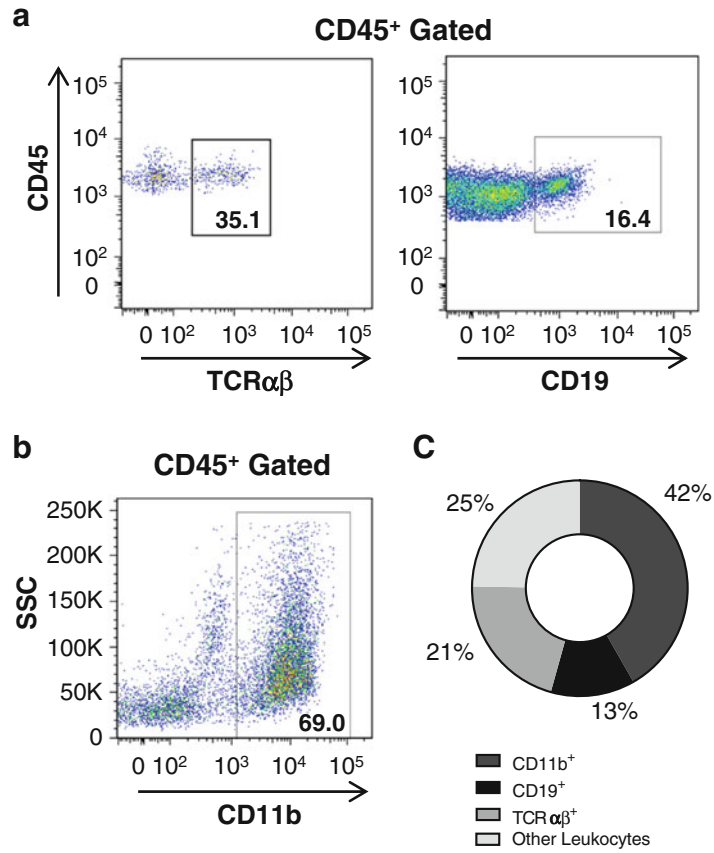

Fig. 5 Variety of immune cells present within the murine aorta. Identification of several leukocyte subpopulations and the characterization of the immune composition of the aorta can be provided by flow cytometry. Aortic cell suspensions were prepared from a whole *Apoe*$^{-/-}$ aorta (as we described in the text) and stained for CD45, TCRαβ, CD19, and CD11b. Cells were gated on CD45^{+} leukocytes and debris was excluded based on the FSC/SCC profiles. Representative FACS plot of aortic cells isolated from *Apoe*$^{-/-}$ aortas stained with (**a**) anti-TCRαβ, CD19, and (**b**) anti-CD11b Abs. Gates set up are based on FMO and isotype controls (not shown). (**c**) Composition of immune cells (%) in aortas of 40–50-week-old *Apoe*$^{-/-}$ mice ($n=12$)

Fig. 4 (continued) subset (Th1) of CD4^{+} cells within *Apoe*$^{-/-}$ aortas, PMA-stimulated CD4^{+} cells were stained with anti-IFNγ antibodies (*left*) and analyzed based on isotype control staining (*right*). (**b**) Detection of several B cell subsets within *Apoe*$^{-/-}$ aortas. Regulatory B cells are identified as CD19^{+}CD5^{+}IgD^{lo}, then gated as CD43^{-}, whereas B1a are CD43^{+} cells. Gating is determined by isotype staining (*right*). (**c**) Distinction of monocyte subsets within CD11b^{+} population. Pro-inflammatory monocytes were identified as Ly6C^{hi} myeloid cells and Ly6C^{low} myeloid cells as patrolling monocytes. Positive Ly6C staining is based on isotype control staining [14]

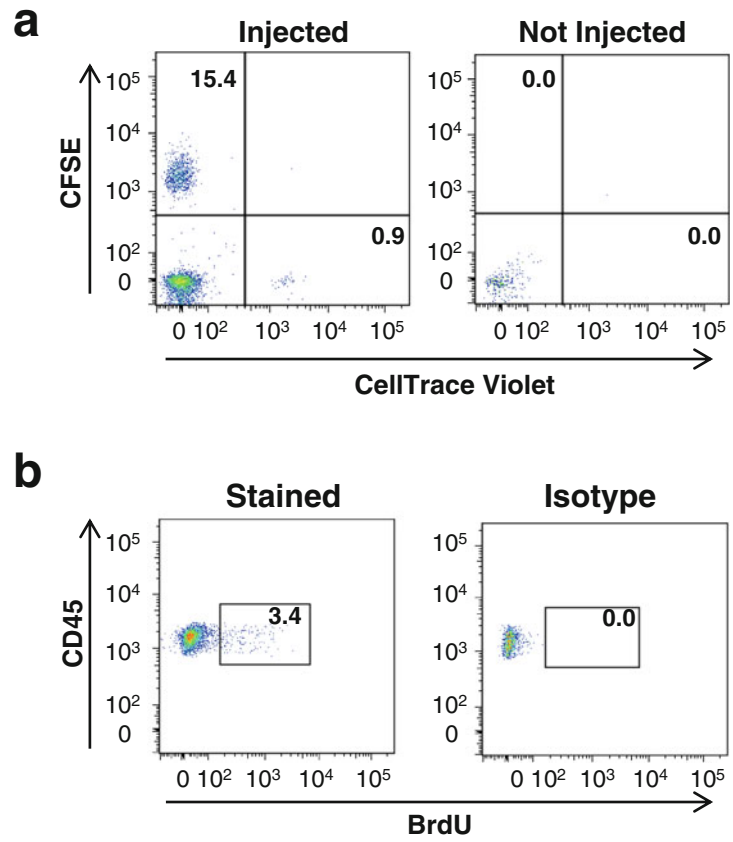

Fig. 6 Functional applications of flow cytometry on aortic tissue. (**a**) L-Selectin-sufficient and -deficient splenic B cells were individually labeled with carboxyfluorescein succinimidyl ester (CFSE) and CellTrace Violet (Invitrogen), respectively, and then intravenously injected via tail vein into a 50-week old *Apoe*$^{-/-}$ recipient fed chow diet. After 16 h post-injection, aortas were harvested and stained with antibodies against CD45 and CD19. Migrated L-selectin-sufficient B cells were identified as CD45^{+}CD19^{+}CFSE^{+} and L-selectin–deficient B cells as CD45^{+}CD19^{+}CellTrace Violet^{+} (*left*). The migration is analyzed by gates set from a non-injected mouse (*right*). (**b**) 50-week-old *Apoe*$^{-/-}$ mice were intraperitoneally injected with BrdU every 12 h, aortas harvested 24 h after the initial injection. Aortas were digested and aortic cell suspensions were prepared and stained with antibodies against CD45, CD19, and BrdU (3). Proliferating CD45^{+}CD19^{+} B cells were identified by positive BrdU staining (*left*) in comparison to the isotype control (*right*)

8. For functional assays, the gating scheme will be dependent on the experimental design (*see* Fig. 6 for examples of possible functions of leukocytes measured by flow cytometry).
9. Data can be represented as a percentage or cell number.

4 Notes

1. Additional aortas may need to be harvested to prepare the appropriate amount of control samples (refer to **Note 7** for details about controls).
2. For adventitial removal, the aorta must be incubated in an enzyme solution [10, 13] to loosen the adventitial layer prior to the enzymatic digestion referred to in Subheading 3.2. Avoid freeze-thawing the enzyme solutions as this reduces their activity.
3. Vortex occasionally throughout incubation. If aorta is not completely digested after 45–60-min incubation, incubate for another 10 min and check again. When resuspending, it should not be difficult to break apart the aorta, if it is this is a sign that the digestion is not complete. Important: Do not over digest.
4. After centrifugation, there should be a light hazy pellet at the bottom of the tube.
5. Do not disrupt the pellet while decanting.
6. Typically, a 50-week-old *Apoe*$^{-/-}$ mouse fed chow diet has $0.91 \pm 0.08 \times 10^6$ total aortic leukocytes. This number is increased in comparison to C57BL/6 mice [3]. If cell numbers are low, it may be beneficial to pool several aortas together to have sufficient numbers for running on the flow cytometer.
7. Appropriate controls for flow cytometry:
   - Unstained splenic and aortic cell suspensions.
   - "Singles": prepared from splenic cell suspension. Each tube contains only one fluorophore-conjugated antibody that is used in the antibody cocktail for the samples of interest.
   - "FMO" (fluorescent minus one): prepared from aortic cell suspension. This sample contains all the appropriate fluorophore-conjugated antibodies except one.
   - "Isotypes" prepared from aortic cell suspension. This sample contains all the appropriate fluorophore-conjugated antibodies, but one is replaced by the appropriate isotype (containing the same fluorophore) which is recommended by the manufacturer of each antibody. Be sure to use the same amount of isotype antibody that is actually used in the sample of interest.
8. To reduce variability, make a master mix for all appropriate samples for the Fc block and for staining.
9. Optimization of the antibody concentration should be determined prior to staining using practice tissue.

10. Enzymatic digestion of the aorta does interfere with the antigen sensitivity of some antibodies [3]. Determine if antigens of interest are affected by enzymatic digestion prior to experiment.
11. Prepare all controls (singles, FMOs, isotypes) simultaneously with samples of interest.
12. Incorporating a red blood cell marker such as TER-119 will help to identify levels of blood contamination within the analyzed samples [3].
13. Some fluorophore-conjugated antibodies are not stable upon PFA fixation; test during optimization.
14. If running within several hours after staining, resuspend cells in PBS rather than PFA.
15. For our acquisition, we use an 8-color updated BD FACS Calibur.
16. FSC, SSC, and antibody intensity will likely be different between tissues (Fig. 2).
17. Vortex each sample prior to running on flow cytometer to ensure homogeneity.
18. When starting to collect the first aortic sample, make sure that the distribution of leukocytes on FSC and SSC looks appropriate. Ideally this is done by using an unstained aortic sample. Lymphocyte populations are typically set at the following values: FSC: 50 K, SSC: 25 K (*see* Fig. 2).
19. Occasionally run water between samples to clean the instrument.
20. In some cases it may be necessary to concatenate several files or analyzed samples to increase the number of events seen. This will generate a clearer larger population and is often useful when studying a small leukocyte population.

Acknowledgements

We thank the EVMS Flow Cytometry Facility for their excellent technical support. This work was funded through NHLBI RO1HL107522 (to E.G.) and NHLBI HL112605 supplemental grant 02S1 (to P.T.M.).

References

1. Getz G, Reardon C (2012) Animal Models of Atherosclerosis. Arterioscler Thromb Vasc Biol 32:1104–1115
2. Galkina E, Ley K (2009) Immune and inflammatory mechanisms of atherosclerosis. Annu Rev Immunol 27:165–197

3. Galkina E, Kadl A, Sanders J et al (2006) Lymphocyte recruitment into the aortic wall before and during development of atherosclerosis is partially L-selectin dependent. J Exp Med 203:1273–1282
4. Afanasyeva M, Georgakopoulos D, Belardi F et al (2004) Quantitative analysis of myocardial inflammation by flow cytometry in murine autoimmune myocarditis. Am J Pathol 164: 807–815
5. Hammond T (1992) Analysis and isolation of renal tubular cells by flow cytometry. Kidney Int 42:997–1005
6. Wu H, Smith M, Millenson M et al (2003) Contribution of flow cytometry in the diagnosis of cutaneous lymphoid lesions. J Invest Dermatol 121:1522–1530
7. Mattsson L, Bondjers G, Wiklund O (1991) Isolation of cell populations from arterial tissue, using monoclonal antibodies and magnetic microspheres. Atherosclerosis 89:25–34
8. Bonanno E, Mauriello A, Partenzi A et al (2000) Flow cytometry analysis of atherosclerotic plaque cells from human carotids: a validation study. Cytometry 39:158–165
9. Liu-Wu Y, Svenningsson A, Stemme S et al (1997) Identification and analysis of macrophage-derived foam cells from human atherosclerotic lesions by using a “mock” FL3 channel in flow cytometry. Cytometry 29: 155–164
10. Butcher M, Herre M, Ley K et al (2011) Flow cytometry analysis of immune cells within murine aortas. J Vis Exp 53, pii 2848 doi: 10.3791/2848
11. Weber C, Meiler S, Döring Y et al (2011) CCL17-expressing dendritic cells drive atherosclerosis by restraining regulatory T cell homeostasis in mice. J Clin Invest 121:2898–2910
12. Koltsova E, Chodaczek G, Landau M et al (2012) Dynamic T cell–APC interactions sustain chronic inflammation in atherosclerosis. J Clin Invest 122:3114–3126
13. Smith E, Prasad K, Butcher M et al (2010) Blockade of interleukin-17A results in reduced atherosclerosis in apolipoprotein E-deficient mice. Circulation 121:1746–1755
14. Taghavie-Moghadam P, Butcher M, Galkina E (2014) The dynamic lives of macrophage and dendritic cell subsets in atherosclerosis. Ann N Y Acad Sci 1319:19–37

Chapter 12

In Vitro Differentiation of Naïve CD4+ T Cells: A Tool for Understanding the Development of Atherosclerosis

Salvador Iborra and Jose M. González-Granado

Abstract

A complete knowledge of atherosclerosis requires a better understanding of how innate and adaptive immunity operate systemically and locally within the arterial wall. T-helper 1 (Th1) lymphocyte responses have proatherogenic effects in mice, contrasting with the responses of T regulatory cells (Tregs), which can suppress growth of atherosclerotic lesions. An imbalance in the differentiation of T-helper cells may therefore impact the development, size, and stability of atherosclerosis plaques. This chapter describes a method to isolate naïve CD4+ T cells from atherosclerosis-prone mouse peripheral blood lymphocytes and to differentiate these CD4+ T cells in vitro to various T helper cell lineages. These techniques allow the analysis of T lymphocytes in vitro, a necessary step in the study of molecular mechanisms involved in the inflammatory responses that trigger atherosclerosis.

Key words T cell differentiation, Th1, Th2, Th17, Atherosclerosis, Immunomagnetic isolation

1 Introduction

Atherosclerosis is the leading cause of morbidity and mortality worldwide. Accumulated evidence shows that the immune system is a major contributor to chronic atherosclerotic lesion development and the destabilization of established arterial lesions, leading to acute clinical events such as myocardial infarction and stroke [1]. Analysis of human and animal lesions and the experimental manipulation of animal models confirm that atherosclerotic lesions originate in chronic inflammatory responses to lipoprotein depositions in the arterial intima. These inflammatory responses are attributable to the activation of the two main branches of the immune system, the innate and adaptive immune responses. A full knowledge of atherosclerosis therefore requires better understanding about how innate and adaptive immunity operate systemically and locally within the arterial wall at all stages of disease progression. Important information about the contribution of adaptive immunity to atherosclerosis has come from several genetically

Vicente Andrés and Beatriz Dorado (eds.), *Methods in Mouse Atherosclerosis*, Methods in Molecular Biology, vol. 1339, DOI 10.1007/978-1-4939-2929-0_12,

modified animal models. For example, depletion of $CD4^+$ T cells using monoclonal antibodies in C57BL/6 mice fed a high-fat diet rich in cholesterol reduces the size of aortic lesions, suggesting a proatherogenic effects of $CD4^+$ T cells [2]. Consistent with this finding, $CD4^+$ T cells are found in early and advanced lesions of apolipoprotein E-deficient (*Apoe*$^{-/-}$) mice fed standard chow or a high-fat diet. These cells express the activation marker CD25 and are surrounded by major histocompatibility complex (MHC) class II expression in the lesion, suggesting local antigen presentation to $CD4^+$ T cells and their activation within plaques [3].

Naïve $CD4^+$ T cells are activated upon recognition of a peptide derived from a cognate antigen presented in the context of class II MHC on dendritic cells (DCs). This interaction triggers a process of division and differentiation into at least four possible T-helper (Th) cell subsets: Th1, Th2, Th17, and induced T-regulatory (iTreg) cells. This classification is based on the pattern of cytokines these cells produce: Th1 cells produce interferon γ (IFN-γ) and tumor necrosis factor β (TNF-β); Th2 cells produce interleukin 4 (IL-4), IL-13, IL-5, and IL-10; Th17 cells produce IL-17A, IL-17F, and IL-22; and iTreg cells produce IL-10 and transforming growth factor β (TGF-β) [4]. The fate decision of naive $CD4^+$ T cells towards the distinct Th subsets is determined by a combination of factors that include the initial profile of cytokines released by the activated $CD4^+$ T cells themselves and cues from the innate immune system and other cell types present during the course of differentiation in the early phase of the immune response [4].

The role of adaptive immunity in atherosclerosis has been studied by deleting the entire adaptive immune system in atherosclerosis-prone models such as *Apoe*$^{-/-}$ or low-density lipoprotein receptor–deficient (*Ldlr*$^{-/-}$) mice. This is achieved by crossing these mice with strains lacking B and T cells, for example *Rag1*$^{-/-}$ or *Rag2*$^{-/-}$ mice, which lack the V(D)J recombinase required to form lymphocyte antigen receptor genes, or SCID mice, which carry mutations in a gene encoding a DNA repair enzyme required for antigen receptor gene formation. *Apoe*$^{-/-}$ *Rag1*$^{-/-}$ or *Apoe*$^{-/-}$*Rag2*$^{-/-}$ mice fed regular chow have moderate levels of plasma cholesterol and fewer lesions than the parent *Apoe*$^{-/-}$ strain [5, 6]. Levels of atherosclerosis below controls are also found in *Apoe*$^{-/-}$ SCID mice fed regular chow and *Ldlr*$^{-/-}$ *Rag2*$^{-/-}$ mice fed a high-fat diet [7]. These studies suggest a significant proatherogenic role for the adaptive immune system; however, the approaches used in these studies removed both the pro- and anti-inflammatory effects of T cells, B cells, and antibodies, and clarification of the role of individual components therefore required more selective genetic manipulations. Studies in *Ldlr*$^{-/-}$ mice also deficient for the genes encoding IL-18 [8], IFN-γ receptor [9], IFN-γ [10], or the Th1 lineage-defining transcription factor T-bet [11] have shown that Th1 responses have a proatherogenic effect in mice. These findings correlate with the

presence of IFN-γ and activated CD4+ T cells in human lesions [12, 13]. Contrasting with this effect, studies in Apoe$^{-/-}$ and Ldlr$^{-/-}$ mice show that iTregs suppress atherosclerotic lesion growth [14]. Effects on the growth of atheromas are not limited to Th cell subsets; cytokines themselves also have pro- and anti-atherogenic properties, as demonstrated by the pro-atherogenic effect of the genetic ablation of IL-10 in C57BL/6 mice [15] and of the reconstitution of irradiated *Ldlr*$^{-/-}$ mice with *Il10*$^{-/-}$ bone marrow [16]. Similar effects have been observed for TGF-β, with the T-cell-restricted expression of a dominant-negative TGF-β receptor increasing inflammation and atherosclerosis development in *Apoe*$^{-/-}$ mice [17].

The development and characterization of additional mouse models in future years will improve our knowledge of the role of T helper cells in the pathophysiology of atherosclerosis. The continued use of tissue culture systems is essential for analysis of the phenotype and cytokine profile of CD4+ Th cells, in order to better define the individual roles that these cells play in atherosclerosis. This chapter describes protocols for the in vitro differentiation of mouse-derived naïve CD4+ T cells into polyclonal T helper cells (Th1, Th2, Th17).

2 Materials

All buffers and stock solutions should be prepared with distilled and deionized water and analytical grade reagents.

1. Phosphate-buffered saline (PBS): 1.9 mM NaH_2PO_4 (anhydrous), 8.1 mM Na_2HPO_4 (anhydrous), 154 mM NaCl. Adjust to pH 7.2–7.4 with 1 M NaOH or 1 M HCl and autoclave or filter through sterile 0.2-μm filter. Store at room temperature.
2. PBS + BSA + EDTA: PBS containing 0.5 % (w/v) bovine serum albumin (BSA) and 5 mM EDTA.
3. Complete medium (RPMI + FBS + Na-Pyr + 2-ME + Pen/Str): RPMI-1640 culture medium (RPMI), 10 % (v/v) fetal bovine serum (FBS), 1 % (v/v) penicillin/streptomycin solution (Pen/Str), 50 μM 2-mercaptoethanol (2-ME),1 mM sodium pyruvate (Na-Pyr).
4. Red blood cell lysing buffer: 0.15 M NH4Cl, 10 mM $KHCO_3$, 0.1 mM Na_2EDTA.
   Adjust to pH 7.2–7.4 with 1 N HCl. Filter through sterile 0.2-μm filter and store at room temperature.
5. Intracellular permeabilization buffer: PBS containing 0.1 % (w/v) BSA, 0.01 M HEPES, 0.3 % (w/v) saponin.
6. PFA + sucrose: 2 % (w/v) paraformaldehyde, 1 % (w/v) sucrose. Warm to 60 °C to facilitate dissolution and adjust to pH 7.2–7.4 with 1 M NaOH.
7. 70 % ethanol.

8. Scissors (straight or angled).
9. Curved forceps.
10. 60 × 15 mm Petri-dish.
11. Frosted microscopy slides.
12. Freshly removed organs from mice.
13. 6-ml syringe with 19-G needle or 70 μm cell strainer.
14. 0.4 % trypan blue (store in dark bottle and filter after prolonged storage).
15. Hemocytometer (also known as Neubauer chamber).
16. Light microscope.
17. Streptavidin-coated magnetic microbeads.
18. Magnet (i.e. MACS separator, Miltenyi Biotec).
19. Biotinylated monoclonal antibodies against CD4, IgM, B220, CD19, MHCII, CD11c, CD11b, CD44, CD8α, and DX5.
20. Mouse recombinant interleukins (IL-2, IL-4), (IL-6), (IL-12).
21. Transforming growth factor β (TGF-β (10 ng/ml).
22. Phorbol 12-myristate-13-acetate (PMA) (10 ng/ml).
23. Ionomycin (1 μg/ml).
24. Brefeldin A (3–10 μg/ml).
25. 6-, 12-, 48-, and 96-well plates.
26. 15- or 50-ml disposable conical tubes with screw caps.
27. Fluorescent-labeled primary antibodies against CD4 and CD3.
28. Primary antibodies against CD3, CD28, IL-4, IL-12, and interferon-γ (IFN-γ).
29. Centrifuges.
30. Water bath.
31. Cytometer.
32. Cell culture incubator.
33. Cell culture hood.
34. 0.1 % saponin.

3 Methods

3.1 Dissection of Spleen and Lymph Nodes

1. Euthanize mice by CO_2 inhalation in a CO_2 chamber with lid.
2. Place the mice face up on absorbent paper.
3. Wet the fur with 70 % ethanol to minimize fur entering the peritoneum.
4. Using forceps, make a skin incision in the abdomen to separate the skin from the body. Make an incision in the peritoneal wall to access to the peritoneum.

5. Remove the spleen using forceps.
6. Clean the spleen from the connective tissue and place it in cold PBS + BSA + EDTA on ice.
7. Remove the lymph nodes using curved forceps and place them in cold PBS + BSA + EDTA on ice (*see* **Notes 1** and **2**).
8. Place each lymphoid organ in a 60 × 15-mm petri dish with 5 ml cold PBS + BSA + EDTA (dish on ice) for single-cell suspension preparation.

3.2 Preparation of Single-Cell Suspensions

1. Disaggregate the tissues (spleen or lymph nodes) by placing them between the frosted areas of two microscope slides and applying pressure in a circular motion (*see* **Notes 3** and **4**).
2. Filter the cell suspension through a 70-μm cell strainer, collecting the dispersed cells in a 50-ml or 15-ml dispensable conical tube (*see* **Notes 5** and **6**).
3. Add 5 ml cold PBS + BSA + EDTA.
4. Centrifuge for 10 min at 200 × *g* at 4 °C and discard the supernatant.
5. Resuspend the pellet in 30 ml (spleen) or 5 ml (lymph node) cold PBS + BSA + EDTA.
6. Centrifuge for 10 min at 200 × *g* at 4 °C and discard supernatant.
7. Resuspend the lymph node pellet in 4 ml cold PBS + BSA + EDTA for counting; resuspend the spleen pellet in 10 ml of cold PBS + BSA + EDTA for removal of red blood cells (*see* **Note 7**).

3.3 Removal of Red Blood Cells from the Single-Cell Spleen Preparation

1. Centrifuge spleen suspension for 10 min at 4 °C at 200 × *g* and discard supernatant.
2. Resuspend the pellet in 1 ml cold erythrocyte lysis buffer and maintain on ice for 5 min with intermittent manual shaking.
3. Add 10 ml of cold PBS + BSA + EDTA.
4. Centrifuge for 10 min at 4 °C at 200 × *g* and discard supernatant.
5. Resuspend the pellet in 10 ml cold PBS + BSA + EDTA.
6. Centrifuge for 10 min at 4 °C at 200 × *g* and discard supernatant.
7. Resuspend the pellet in 10 ml cold PBS + BSA + EDTA for counting.

3.4 Viable Cell Counting by Trypan Blue Exclusion (See Note 8)

1. Centrifuge an aliquot of cell suspension for 5 min at 100 × *g* and discard supernatant.
2. Resuspend the pellet in 1 ml PBS or serum-free complete medium (*see* **Note 9**).

3. Mix 10–20 μl of the cell suspension with the same amount of 0.4 % trypan blue and incubate for 3 min at room temperature (*see* **Note 10** and **11**).
4. Put the glass cover on the hemocytometer (*see* **Note 12**).
5. With a micropipette, take up 10 μl of the trypan-blue-stained cell suspension.
6. Place the micropipette tip close to the edge of the glass cover at the center of the hemocytometer. Apply the solution slowly to allow the liquid to enter the chamber uniformly by capillarity action (*see* **Note 13**).
7. Place the hemocytometer on the microscope stage and illuminate the sample with visible light.
8. Count the number of trypan-blue positive and negative cells in the squares and calculate the concentration according to the hemocytometer manufacturer's instructions (*see* **Notes 14** and **15**).

3.5 Immunomagnetic Selection of Naïve CD4⁺ T Cells

The protocol is illustrated in Fig. 1. *See* **Notes 16–19** before starting the procedure.

1. Calculate the amount of streptavidin-coated magnetic microbeads required, based on the number of cells and the capacity of the beads as indicated by the manufacturer.

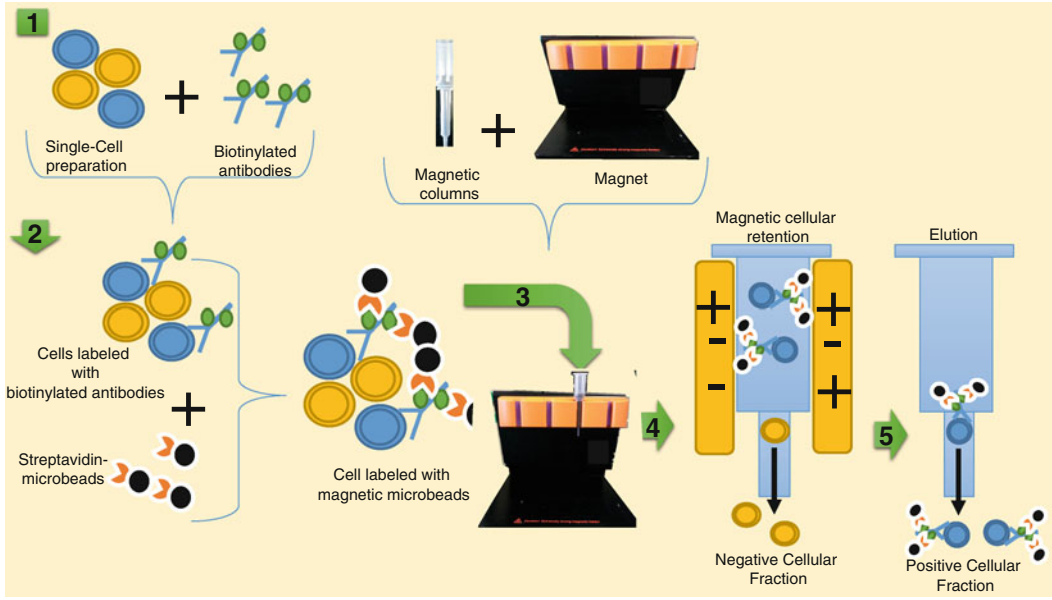

Fig. 1 Immunomagnetic selection of cells. (1) The biotinylated antibodies are bound to the positive cells. (2) The streptavidin-microbeads bind to the biotinylated antibodies. (3) The magnetic columns are placed in the magnet. The solution containing the antibody-bound single-cell suspension and the streptavidin-microbeads is passed through the column. (4) The complex formed by cells, biotinylated antibodies and streptavidin microbeads is retained on the columns, while the negative cell fraction is recovered. (5) Columns are separated from the magnet and the positive cell fraction can be eluted and recovered

2. Transfer the desired volume of magnetic beads to a tube.
3. Add the same volume of cold PBS + BSA + EDTA.
4. Place the tube on a magnet for 1 min and carefully discard the supernatant by aspiration while the tube is still attached to the magnet.
5. Remove the tube from the magnet and resuspend the washed beads in 1 ml of cold PBS + BSA + EDTA.
6. Transfer the desired number of cells to a 15-ml conical tube.
7. Centrifuge the sample for 10 min at 200 × *g* and 4 °C.
8. Discard the supernatant.
9. Add the mixture of biotinylated antibodies to the cell pellet in a small volume of cold PBS + BSA + EDTA (*see* **Note 19**). Incubate on ice for 15 min (*see* **Note 20**).
10. Add 1–3 ml of cold PBS + BSA + EDTA.
11. Centrifuge the sample for 10 min 200 × *g* and 4 °C.
12. Discard the supernatant containing the unbound antibodies.
13. Resuspend the cell pellet in the solution containing the optimal amount of washed streptavidin-coated magnetic beads (obtained in **step 5** above) (*see* **Note 21**).
14. Incubate for 15 min at 4 °C. Filter the dissociated tissue through a cell strainer with 30-μm pore size (*see* **Notes 22**).
15. Pass the suspension through a magnetic column bound to a magnet (*see* **Note 23**).
16. Recover the flow-through in a 15-ml conical tube. This fraction contains the cells that were not bound to the mixture of antibodies. In the case of negative selection, this fraction will contain the $CD4^+$ T cells.
17. Fill the column with a proper volume of PBS + BSA + EDTA, following the manufacturer instructions, and remove the column from the magnet to recover the positive fraction. In the case of positive selection, this fraction will contain the $CD4^+$ T cells (*see* **Notes 24** and **25**).
18. Add RPMI + FBS + Na-Pyr + 2-ME + Pen/Str to adjust cell concentration to 8×10^5 cells/ml.
19. Count the cells, following the protocol described in Subheading 3.4 (Fig. 2).

3.6 Activation and Differentiation of Naïve $CD4^+$ T Cells to Different Th Subsets

1. Add PBS to the anti-CD3 antibody to reach a final concentration of 10 μg/ml.
2. Coat 96-well round-bottom plates with anti-CD3 antibody by adding 30 μl/well of the anti-CD3 solution. Fill control wells with 30 μl of PBS (*see* **Notes 26** and **27**).
3. Incubate plates for 90 min at 37 °C (*see* **Note 28**).

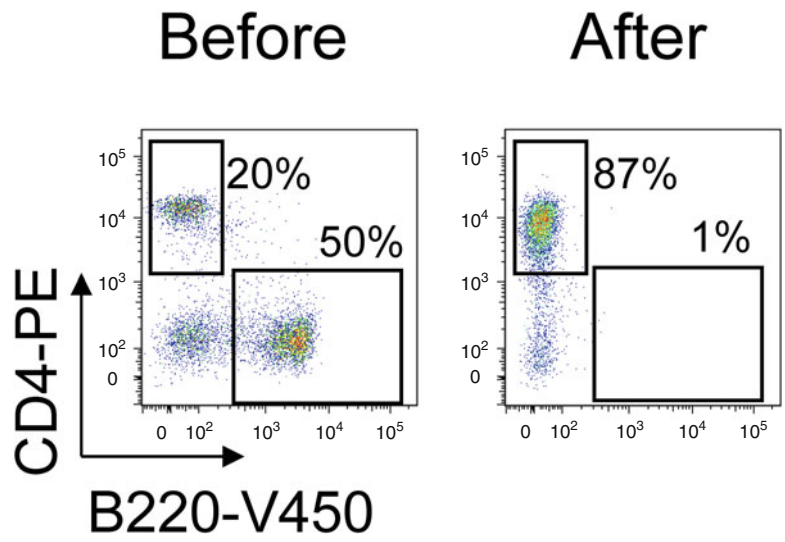

Fig. 2 Flow cytometry plots showing the percentage of CD4+ and B220+ lymphocytes before and after immunomagnetic separation

4. Fill the wells with 200 µl of cold PBS to wash out the excess antibody. Invert the plates quickly to empty the wells and refill them with PBS. Repeat this step two or three times.
5. Block the wells by adding 100 µl of 3 % FBS in PBS for 15 min at room temperature.
6. To complete medium containing 1 µg/ml anti-CD28, add the appropriate mix of cytokines and antibodies for the differentiation to each Th subset, as follows.
   (a) For Th0 differentiation: anti-IFNγ (4 µg/ml) and anti-IL-4 (4 µg/ml) antibodies and cytokine IL-2 (10 ng/ml).
   (b) For Th1 differentiation: anti-IL-4 antibody (4 µg/ml) and cytokines IL-2 (10 ng/ml) and IL-12 (10 ng/ml).
   (c) For Th2 differentiation: anti-IFNγ antibody (4 µg/ml) and cytokines IL-4 (10 ng/ml) and IL-2 (10 ng/ml).
   (d) For Th17 differentiation: anti-IFNγ (4 µg/ml) and anti-IL-4 antibodies (4 µg/ml), and cytokines IL-6 (20 ng/ml), TGF-β (10 ng/ml), and IL-23 (10 ng/ml).
7. Remove the blocking solution from the CD3-coated wells (**step 5** above) and to each well add 2×10^5 cells and 200 µl of medium containing the corresponding mix of cytokines and antibodies.
8. Incubate the cells at 37 °C, 5 % CO_2 for 4–5 days.
9. Check the cultures every 1 or 2 days. If the medium starts to turn yellow, replace it with fresh medium containing the corresponding antibody and cytokine mix but excluding the anti-CD3 and anti-CD28 antibodies.

10. On day 5, centrifuge the plates for 10 min at 200 × *g*.
11. Discard the supernatant by aspiration and resuspend the cells at 2×10^5 cells/ml in complete medium supplemented with IL-2 (5 ng/ml). Expand the culture for a further 2–3 days.

3.7 Quantification of Th Populations by Intracellular Staining

The percentage of each Th cell subset can be determined from the profile of cytokines they produce.

1. Plate 200 µl of cell suspension (2×10^6 cells/ml) in each well of a 96 well plate and stimulate them with ionomycin (1 µM) and PMA (10 ng/ml) for 4–6 h at 37 °C in the incubator.
2. Add Brefeldin A (3–10 µg/ml) for the last 4 h to block cytokine secretion to the medium. Incubate the cells with fluorophore-conjugated anti-CD4 antibody for 15 min and 4 °C.
3. Add 200 µl of PBS.
4. Centrifuge the plates for 10 min at 200 × *g* and 4 °C.
5. Fix the cells by adding 100 µl of 2 % paraformaldehyde/1 % sucrose for 20 min at room temperature.
6. Add 1 ml of PBS.
7. Centrifuge for 10 min 200 × *g* and 4 °C.
8. Discard supernatant.
9. Permeabilize the cells by adding 50 µl of intracellular permeabilization buffer and incubating for 30 min at 4 °C.
10. Add 2 ml of PBS.
11. Centrifuge for 10 min at 200 × *g* and 4 °C.
12. Discard supernatant by aspiration or by quickly inverting the 96-well plate.
13. Add 30 µl of a mixture of diluted fluorophore-conjugated antibodies against IFNγ, IL-4, and IL17 (in PBS + 0.1 % saponin) and incubate for 30 min (*see* **Note 29**).
14. Add 2 ml of PBS + 0.1 % saponin.
15. Centrifuge for 10 min 200 × *g* and 4 °C.
16. Discard supernatant by aspiration or by quickly inverting the 96-well plate.
17. Analyze cell populations by flow cytometry (Fig. 3).

4 Notes

1. In naïve mice, lymph nodes are smaller and more difficult to dissect than spleen. Lymph nodes are nonetheless the most abundant lymphatic organs and the frequency of CD4+ T cells in them is two to threefold higher than in spleen.

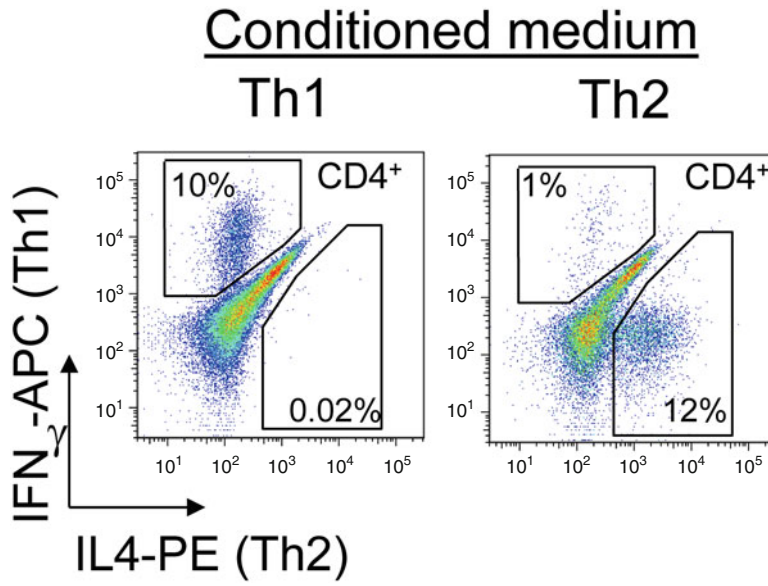

Fig. 3 Flow cytometry plots showing the percentage of IFNγ$^+$ and IL4$^+$ CD4$^+$ cells after selection. Isolated naïve CD4$^+$ T cells were stimulated with plate-bound anti CD3 and soluble anti-CD28 antibodies in medium containing an antibody and cytokine cocktail for differentiation to the Th1 or the Th2 subset. Cells were examined after 4 days

2. The major lymph nodes are the axillary, cervical inguinal, and mesenteric lymph nodes.
3. This action must be performed in an ice container to keep cells in cold PBS + BSA + EDTA at all times.
4. Wet the frosted area of the microscope slides with PBS before disaggregating the organs.
5. To maximize cell recovery, the cell strainer should be wetted before filtering the cell suspension; use 1 ml of PBS containing 0.5 % BSA and 5 mM EDTA.
6. Alternatively, the cells can be dispersed by drawing the suspension up and down several times through a19-G needle attached to a 6-ml syringe.
7. 50–150 × 10^6 cells can be recovered from the spleen of a healthy 6–8 week-old mouse.
8. This assay allows the number of live cells present in a cell suspension to be counted; trypan blue cannot penetrate in cells with an intact plasma membrane, so only nonviable cells will be clearly stained.
9. Staining must be performed in serum-free conditions because trypan blue binds with greater affinity to serum proteins than to cellular proteins, and this can interfere with cell counting.

10. Longer incubations will affect cell viability and can distort the results.
11. The correct range for counting with this method is between 250,000 cells/ml and 2.5×10^6 cells/ml, with 10^6 cells/ml being optimal.
12. Hemocytometers are also known as Neubauer chambers.
13. Repeat the operation if bubbles appear or the glass cover moves.
14. Concentrations below 250,000 cells/ml will not give an accurate estimate of the original concentration. Concentrations above 2.5×10^6 cells/ml increase the probability of counting errors. In this case it is better to dilute the sample to obtain a final concentration closer to the optimal 10^6 cells/ml.
15. The formula used for counting in the large squares of the hemocytometer is usually Concentration=Number of cells × 10,000/Number of squares.

    If the sample is diluted before counting, the concentration should be multiplied by the dilution factor to obtain the original concentration.
16. CD4+ T cells are isolated by negative or positive selection with a mixture of biotinylated monoclonal antibodies against surface markers. Cells are stained with biotinylated primary antibodies and then bound to streptavidin-coated magnetic microbeads. Cells pass through a column of the magnetic beads, and positively marked cells are retained upon exposure to a magnetic field, whereas negatively marked cells are recovered in the elute. The magnetic field is then removed and the positively marked cells can be recovered.
17. Positive selection yields a purer population of recovered cells, but the recovered cells will be bound to the antibodies used for selection. In contrast, negative selection yields a less pure population, but the desired cells are antibody-free.
18. All solutions and equipment used in the selection procedure must be sterile.
19. The cocktail used for negative selection can include antibodies against IgM, B220, CD19, MHCII, CD11c, Cd11b, CD44, CD8α, and DX5. For positive selection, use anti mouse CD4.
20. The optimal concentration of antibodies should be determined empirically or be that recommended by the manufacturer.
21. The optimal amount of beads should be determined empirically or be that recommended by the manufacturer.
22. It is essential to use single-cell suspensions for cell separation to prevent clogging up of the magnetic column.
23. Cell separation columns are fast separators suitable for any cell type labeled with microbeads, and do not compromise cell

function. A well-known brand is MACS cell separation columns, from Miltenyi.

24. $CD4^+$ T cell purity can be determined by staining a small aliquot of the positive and negative fractions with fluorophore-labeled anti mouse $CD4^+$ and $CD3^+$ antibodies for 15 min at 4 °C and checking the cells by flow cytometry.
25. Do not use fluorescent streptavidin and biotinylated $CD4^+$ antibodies to determine purity because fluorescent streptavidin will bind any cell-bound biotinylated antibody remaining from the fractionation.
26. Round bottom plates are usually more efficient than flat-bottom plates in centrifugation and washing processes.
27. Check that the bottom of the well is completely covered.
28. Plates can be incubated at 37 °C for 90 min, washed, and maintained in 150 μl of PBS at 4 °C until the next day.
29. Saponin must be included in every antibody staining and washing step in order to maintain membrane permeability.

Acknowledgements

The authors thank Simon Bartlett, Marta Blanco-Berrocal and Raquel Toribio-Fernández for editorial and technical assistance. This work is supported by ISCIII (Miguel Servet Program, CP11/00145 and PI14/00526) with co-funding from the Fondo Europeo de Desarrollo Regional (FEDER) and by the Fundación Ramón Areces. The CNIC is supported by the MINECO and the Pro-CNIC Foundation.

References

1. Witztum JL, Lichtman AH (2014) The influence of innate and adaptive immune responses on atherosclerosis. Annu Rev Pathol 9:73–102
2. Emeson EE, Shen ML, Bell CG et al (1996) Inhibition of atherosclerosis in CD4 T-cell-ablated and nude (nu/nu) C57BL/6 hyperlipidemic mice. Am J Pathol 149:675–685
3. Zhou X, Stemme S, Hansson GK (1996) Evidence for a local immune response in atherosclerosis. CD4+ T cells infiltrate lesions of apolipoprotein-E-deficient mice. Am J Pathol 149:359–366
4. Yamane H, Paul WE (2013) Early signaling events that underlie fate decisions of naive CD4(+) T cells toward distinct T-helper cell subsets. Immunol Rev 252:12–23
5. Dansky HM, Charlton SA, Harper MM et al (1997) T and B lymphocytes play a minor role in atherosclerotic plaque formation in the apolipoprotein E-deficient mouse. Proc Natl Acad Sci U S A 94:4642–4646
6. Daugherty A, Pure E, Delfel-Butteiger D et al (1997) The effects of total lymphocyte deficiency on the extent of atherosclerosis in apolipoprotein E-/- mice. J Clin Invest 100: 1575–1580
7. Zhou X, Nicoletti A, Elhage R et al (2000) Transfer of CD4(+) T cells aggravates atherosclerosis in immunodeficient apolipoprotein E knockout mice. Circulation 102:2919–2922
8. Elhage R, Jawien J, Rudling M et al (2003) Reduced atherosclerosis in interleukin-18

deficient apolipoprotein E-knockout mice. Cardiovasc Res 59:234–240

9. Gupta S, Pablo AM, Jiang X et al (1997) IFN-gamma potentiates atherosclerosis in ApoE knock-out mice. J Clin Invest 99:2752–2761
10. Buono C, Come CE, Stavrakis G et al (2003) Influence of interferon-gamma on the extent and phenotype of diet-induced atherosclerosis in the LDLR-deficient mouse. Arterioscler Thromb Vasc Biol 23:454–460
11. Buono C, Binder CJ, Stavrakis G et al (2005) T-bet deficiency reduces atherosclerosis and alters plaque antigen-specific immune responses. Proc Natl Acad Sci U S A 102: 1596–1601
12. Frostegard J, Ulfgren AK, Nyberg P et al (1999) Cytokine expression in advanced human atherosclerotic plaques: dominance of pro-inflammatory (Th1) and macrophage-stimulating cytokines. Atherosclerosis 145:33–43
13. Hansson GK, Holm J, Jonasson L (1989) Detection of activated T lymphocytes in the human atherosclerotic plaque. Am J Pathol 135:169–175
14. Nilsson J, Wigren M, Shah PK (2009) Regulatory T cells and the control of modified lipoprotein autoimmunity-driven atherosclerosis. Trends Cardiovasc Med 19:272–276
15. Mallat Z, Besnard S, Duriez M et al (1999) Protective role of interleukin-10 in atherosclerosis. Circ Res 85:e17–e24
16. Potteaux S, Esposito B, van Oostrom O et al (2004) Leukocyte-derived interleukin 10 is required for protection against atherosclerosis in low-density lipoprotein receptor knockout mice. Arterioscler Thromb Vasc Biol 24:1474–1478
17. Robertson AK, Rudling M, Zhou X et al (2003) Disruption of TGF-beta signaling in T cells accelerates atherosclerosis. J Clin Invest 112:1342–1350

Chapter 13

Quantification of Apoptosis in Mouse Atherosclerotic Lesions

Nichola L. Figg and Martin R. Bennett

Abstract

Apoptosis is a key process occurring in atherosclerosis, both in humans and in animal models. Apoptosis occurs in all cell types studied thus far, and thus lineage marking is often necessary. Apoptosis should be ascertained using a combination of morphological features and activation of specific pathways (e.g., terminal UTP nick end labeling—TUNEL). Both TUNEL and cryptic epitope antibodies (e.g., cleaved caspase 3) can be used, although they will often give different frequencies. Apoptotic frequency but not rate can be estimated from these methods, as we do not know the timing of apoptosis or how much of the process is marked by each method. We describe the morphological and immunohistochemical methods used in our laboratory to detect apoptotic cells in animal and human atherosclerotic plaques.

Key words Apoptosis, Atherosclerosis, TUNEL, Caspase

1 Introduction

Apoptosis describes an evolutionarily conserved mode of cell death with characteristic morphological and biochemical features. These features underpin the criteria used for identifying and measuring apoptosis in any tissue, including in atherosclerotic plaques. Apoptosis is accompanied by condensation of the nuclear chromatin, resulting in a very dark (pyknotic) nucleus, often with nuclear fragmentation (Fig. 1). Apoptosis is regulated by activation of caspases, cysteine proteases responsible both for transmitting the apoptotic signals and also for cleaving important intracellular substrates that act as markers, for example other caspases and DNA (reviewed in ref. [2]).

The most frequently used markers for apoptosis are terminal UTP nick end labeling (TUNEL) which assays unprotected DNA ends (Fig. 2), and antibodies to neo-epitopes that appear due to caspase cleavage, including caspases themselves (Figs. 3 and 4). However, the markers of apoptosis (for example TUNEL and cleaved caspase 3) measure frequency, mark different points or

Vicente Andrés and Beatriz Dorado (eds.), *Methods in Mouse Atherosclerosis*, Methods in Molecular Biology, vol. 1339, DOI 10.1007/978-1-4939-2929-0_13,

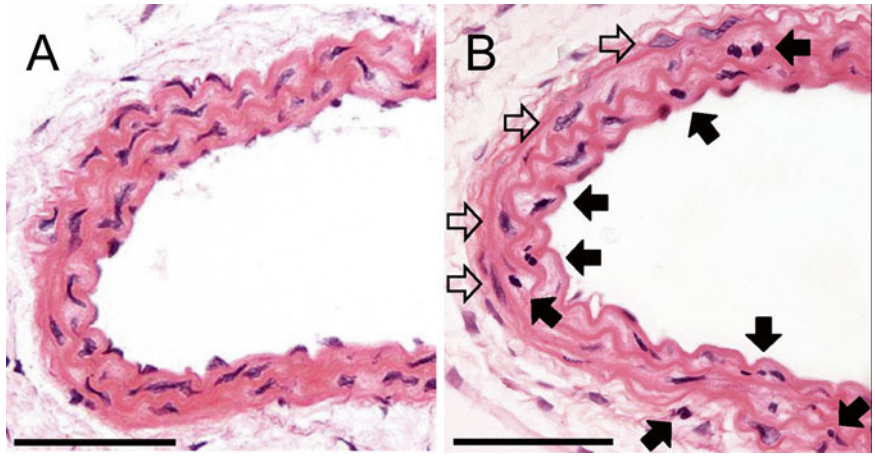

Fig. 1 Morphology of normal and apoptotic smooth muscle cell nuclei. (**a**) Control mouse carotid artery demonstrating normal nuclear morphology. (**b**) Carotid artery showing nuclear condensation (*filled arrows*) compared to normal nuclei (*open arrows*) on H and E staining. Scale bars represent 50 μm. From ref. [1] with permission

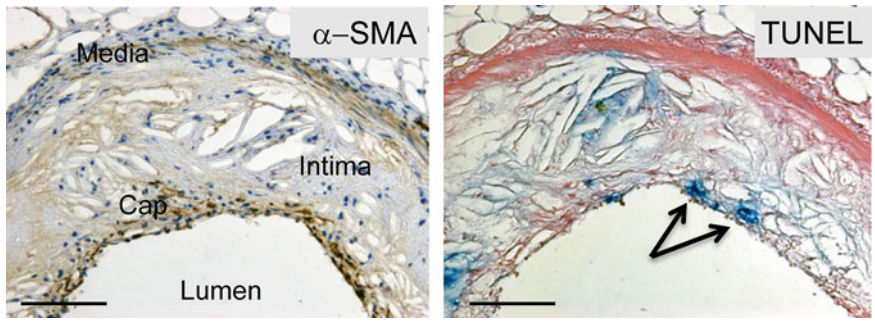

Fig. 2 Apoptosis of smooth muscle cells by TUNEL. α-SMA (*left panel*) and TUNEL (*right panel*) in mouse plaque. *Arrows* indicate TUNEL-positive cells in the fibrous cap. Scale bars represent 200 μm. From ref. [3], with permission

durations of the process, and may even be positive in cells long after the process has finished, for example if the apoptotic body is not cleared [5]. As in most cases we do not know how long apoptosis takes in vivo, and how much of the process is identified by the markers, we cannot ascribe rates of apoptosis. If either the duration of apoptosis or the length of time marked differs between tissues or even the same tissue under different conditions, then the measured 'frequency' may not be an accurate assessment of how much apoptosis is occurring.

This caveat is also important when ascribing changes in death frequencies to changes in apoptotic body clearance; clearance is a kinetic process that needs to be measured at least at two separate time points for a rate to be calculated, and assumes no change in generation of bodies, and no change in the duration of the process

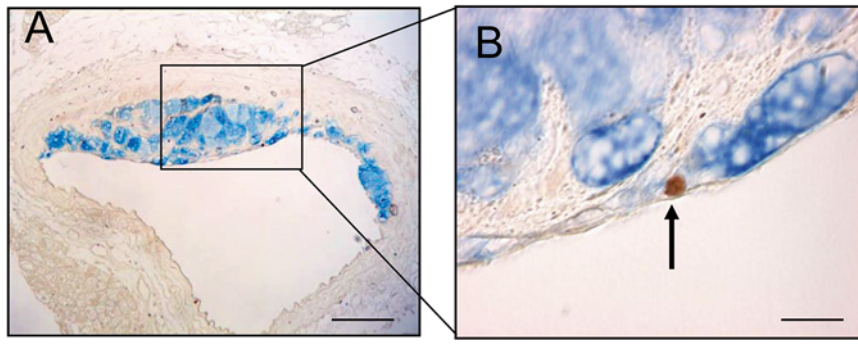

Fig. 3 Apoptosis of macrophages by cleaved caspase 3. (**a**, **b**) Double labeling for mac-3 (*blue*) and cleaved caspase 3 (*brown*) demonstrating apoptotic macrophage. From ref. [4], with permission

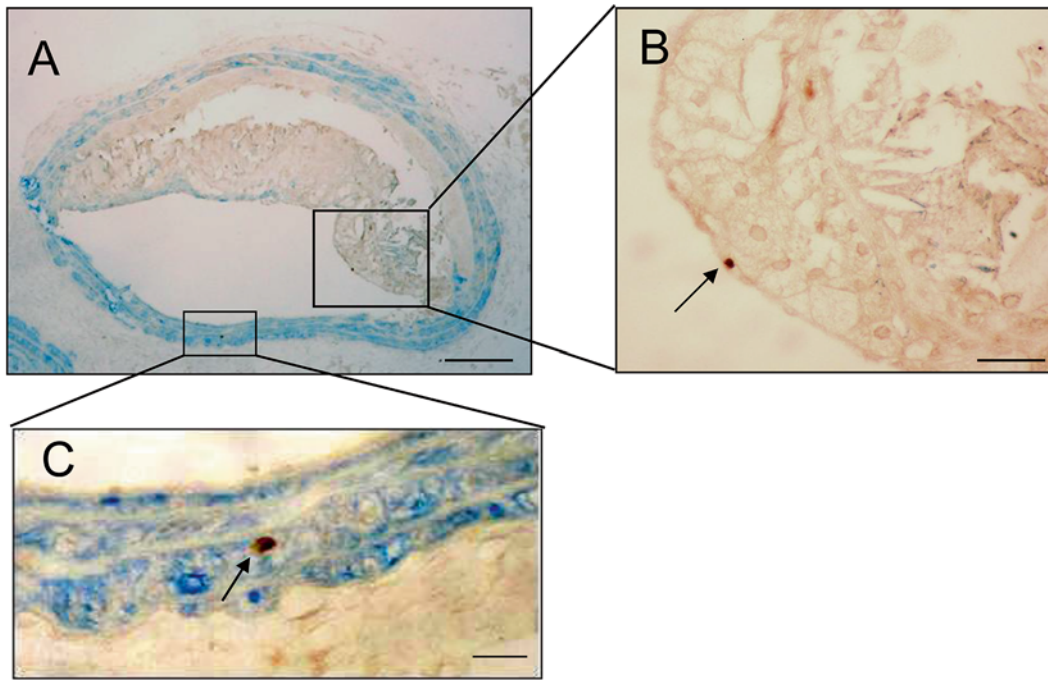

Fig. 4 Apoptosis of smooth muscle cells by cleaved caspase 3. (**a**) Brachiocephalic artery plaque double-labeled for cleaved caspase 3 (*brown*) and SMA (*blue*). (**b**) and (**c**), High power of area outlined in (**a**) showing caspase 3-positive, SMA-negative cell (**b**) or caspase 3 positive, SMA-positive cell (**c**) (*arrows*). Reproduced from ref. [4], with permission

that is marked. We recently described a system whereby the kinetics of vascular smooth muscle cell clearance can be estimated in vivo. The system relies upon a single, defined, time-limited stimulus to induce apoptosis. We found that the half-life of apoptotic body clearance in the vessel wall was approximately 3 days, which could be delayed by challenging animals with a high-fat diet [6], confirming that the frequency of apoptosis observed depends upon the generation rate and the clearance rate.

Detection and particularly quantification of apoptosis generally requires a combination of techniques, as each is prone to artifact (*see* **Notes 1** and **2**), particularly in certain regions of the plaque where non-apoptotic debris collects, such as the necrotic core. Typical nuclear morphology together with TUNEL and/or cleaved caspases is usually sufficient. Identification of the lineage of the cell undergoing apoptosis is also difficult, as morphological features and lineage markers may be lost during cell death, and identification of a dead cell on adjacent sections is challenging (*see* **Notes 3** and **4**). Double labeling of apoptosis and a lineage marker is therefore preferred. Although apoptosis can also be detected in tissue sections using vital dyes (e.g., propidium iodide administered shortly before death [7]), or internucleosomal DNA fragmentation, these assays are not suitable for banked tissue, and therefore will not be considered here.

2 Materials

1. Human and mouse paraffin sections mounted on glass slides suitable for microscopic examination.
2. Proteinase K.
3. Digoxigenin-dUTP.
4. Cleaved caspase 3 antibody (e.g., Cell Signaling, cat. no. 9661).
5. TUNEL assay kit (e.g., Roche Diagnostics, cat. no. 03 333 574 001). Contains:
   (a) Terminal Transferase (TdT) in 60 mM K-phosphate, 150 mM KCl, 1 mM 2-mercaptoethanol, 0.5 % Triton X-100, 50 % glycerol.
   (b) TdT Reaction Buffer 5× concentration: 1 M potassium cacodylate, 125 mM Tris–HCl, 1.25 mg/ml bovine serum albumin (BSA).
   (c) 25 mM $CoCl_2$ solution.
6. Tris-buffered saline (TBS) buffer: 50 mM Tris–HCl, 150 mM sodium chloride, pH 7.6 (6.05 g Tris and 8.76 g sodium chloride in 800 ml of double distilled water, adjust pH, then make up volume to 1 L).
7. Antigen unmasking solution, citrate-based (e.g., Vector Antigen Unmasking Solution, cat. no. H3300).
8. Diaminobenzidine (DAB) solution.
9. 5-bromo-4-chloro-3-indolyl phosphate (BCIP)/Nitro blue tetrazolium (NBT) (e.g., Vector Kit SK5400). Prepared as follows:
   (a) To 5 ml of 100 mM Tris–HCl, pH 9.5 buffer add 2 drops of Reagent 1. Mix well.
   (b) Add 2 drops of Reagent 2. Mix well.

(c) Add 2 drops of Reagent 3. Mix well.

10. Phosphate-buffered saline (PBS) (e.g., Sigma, cat. no. D8537).
11. Blocking buffer in Subheading 3.1. 10 % BSA in TBS.
12. Blocking buffer in Subheading 3.2. 5 % BSA in PBS.
13. Anti-digoxigenin alkaline phosphatase (anti-sheep F′ab fragments) (e.g., Roche Diagnostics: 11 093274 910).
14. α-smooth muscle actin antibody (e.g., Dako M0851).
15. Horse anti-mouse secondary antibody (e.g., Vector Laboratories BA2000).
16. Alkaline phosphatase substrate III (e.g., Vector Kit SK-5300). Prepared as follows:
    (a) To 5 ml of 100 mM–200 mM Tris–HCl, pH 8.2–8.5 buffer.
    (b) Add two drops (80 μl) of Reagent 1.
    (c) Add two drops (80 μl) of Reagent 2.
    (d) Add two drops (45 μl) of Reagent 3.
    (e) Mix well before use.
17. Aqueous mountant solution (e.g., VectaMount H-5000. Vector Laboratories).
18. Microscope.
19. Xylene.
20. Descending series of ethanol: 100 %, 90 %, 70 % ethanol (e.g., Fisher: E/0650DF/P17).
21. 0.3 % hydrogen peroxide in PBS.
22. 5 % goat serum in PBS.
23. ABC complex (e.g., VECTASTAIN RTU Elite PK 7100 Vector Laboratories).
24. Goat anti-rabbit secondary antibody.

3 Methods

3.1 TUNEL

1. Deparaffinize human or mouse paraffin sections mounted on slides with xylene. Use xylene, two times 5 min each.
2. Rehydrate in descending series of ethanol solutions. 2 × 100 % ethanol × 5 min, 1 × 90 % ethanol × 5 min, 1 × 70 % ethanol × 5 min, 2 × double distilled water × 5 min.
3. Wash in tap water, then double-distilled water. Two times × 2 min each.
4. Incubate with 50 μg/ml proteinase K; 3–5 min at room temperature, pH 7.5.
5. Wash in double-distilled water for 2 min, four times.

6. Immerse in TdT buffer for 5 min at room temperature.
7. Remove excess TdT buffer with filter paper, but still leaving the section with a minimum coverage of buffer.
8. Incubate with TdT enzyme (0.05–0.2 U/μl) + Digoxigenin-dUTP in TdT buffer in a lidded box lined with wet paper and place in a regulated oven-incubator at 37 °C for 30 min.
9. Terminate the reaction by transferring the slides to TB buffer for 15 min at room temperature.
10. Wash in double-distilled water with a rinser bottle.
11. Place slides in TBS for 5 min.
12. Cover sections with blocking buffer (10 % bovine serum albumin in TBS) for 10 min at room temperature.
13. Incubate with anti-digoxigenin alkaline phosphatase (e.g., anti-sheep F′ab fragments in blocking buffer) 1:100/1 h at room temperature.
14. Wash with TBS for 5 min two times.
15. Incubate with a chromogenic substrate solution for alkaline phosphatase (e.g., BCIP/NBT). Develop the reaction product microscopically until visible staining develops.
16. Wash in double-distilled water with a rinser bottle, then place slides in a rack and wash in double distilled water two times for 2 min each.
17. Counterstain if required with 1 % eosin. Dip slides for 15 s in eosin, dehydrate rapidly through water, alcohols, and xylene. Provides a background morphology stain.
18. Mount sections with aqueous mountant.
19. The % of apoptotic cells is quantified by eye as the % of cells that demonstrate the apoptotic nuclear phenotype together with a specific marker (TUNEL or cleaved caspase)—*see* Figs. 1, 2, 3, and 4. Positive control tissue should also be included as proof that the method has worked (detection of apoptotic cells) (*see* **Note 5**).

3.2 Double-Labeling Protocols (TUNEL with Lineage-Specific Antibody)

1. Block sections with 5 % bovine serum albumin in PBS for 10 min at room temperature.
2. Tip off excess (as indicated in Subheading 3.1, **step 7**).
3. Incubate sections with α-smooth muscle actin antibody (starting dilution as indicated by your supplier, you may have to optimize) in 10 % BSA for 1 h at room temperature (e.g., Dako M0851 diluted 1:500).
4. Wash sections in PBS buffer, 3 × 5 min.
5. Incubate sections with horse-anti mouse secondary antibody (starting dilution as indicated by your supplier, you may have

to optimize) for 30 min at room temperature (e.g., Vector BA-1400 diluted 1:500).

6. Wash sections in PBS buffer, 3 × 5 min.
7. Incubate sections with pre-prepared Vector ABC-Alkaline Phosphatase (SK-5000) solution for 30 min at room temperature.
8. Wash sections in PBS buffer, 3 × 5 min.
9. Incubate sections with alkaline phosphatase substrate. Monitor the reaction using a microscope. Stop reaction when visible chromogen of desired intensity appears (*see* Figs. 2 and 3).
10. Wash briefly in PBS.
11. Wash in double-distilled H_2O.
12. Coverslip and mount with aqueous mounting medium.
13. Look for nuclear staining of TUNEL and cytoplasmic staining of surrounding cell under the microscope (*see* Figs. 2, 3, and 4). Quantify as % cells having a TUNEL-positive nucleus/total number of that lineage of cells.

3.3 Cleaved Caspase 3

Positive Control: Human Tonsil Sections.

Negative Control: Human Tonsil with Antibody Peptide Block or Rabbit IgG (*see* **Note 5**).

1. Deparaffinize in xylene. Rehydrate in descending series of ethanol solutions (as Subheading 2, **item 1**). Rinse in tap water, then double-distilled water.
2. Microwave sections in antigen unmasking solution for 1 min on full power followed by 9 min at medium power.
3. Cool to room temperature for 20 min.
4. Wash sections in double-distilled water twice for 5 min each.
5. Incubate sections in 3 % hydrogen peroxide in methanol for 10 min.
6. Wash sections twice for 5 min each in PBS.
7. Incubate sections with 5 % goat serum for 1 h at room temperature.
8. Tip off excess serum and incubate sections with primary cleaved caspase 3 antibody in 5 % goat serum overnight at 4 °C (e.g., Cell Signaling, cat. no. 9661 diluted 1:50).
9. Wash twice for 5 min each in PBS.
10. Incubate sections with secondary antibody according to supplier (e.g., Dako Goat anti-Rabbit in 5 % Goat Serum at 1: 400 for 30 min).
11. Wash twice for 5 min each in PBS.
12. Incubate sections with ABComplex for 30 min.

13. Wash twice for 5 min each with PBS.
14. Apply DAB solution and monitor reaction closely using a microscope. Stop reaction when easily visible cytoplasmic stain appears. Wash thoroughly with double distilled water for 5 min.
15. Counterstain as required.
16. Dehydrate, clear in two changes of xylene, coverslip and mount (e.g., Histomount, National Diagnostics HS-103 or DPX, Sigma 44581).

4 Notes

1. It is exceedingly easy to get high TUNEL frequencies in atherosclerotic plaques due to artifact, most likely because dead cells release DNA that reacts under the TUNEL conditions. Indeed, some early papers described apoptosis frequencies of up to 40 % in some parts of the plaque [8]. Other papers have revised these numbers in mouse animal models and humans to 1–2 % under normal circumstances [4, 9–11]. Artifact is particularly common in the necrotic core region where there are many dead cells and interpretation of apoptosis frequencies in this region should be particularly careful. For this reason, TUNEL must be combined with other morphological features before definitive quantification, including nuclear condensation and fragmentation (Fig. 1). TUNEL-positive cells also appear to be above the plane of the section.
2. Cleaved caspase 3 is less prone to artifact, but the frequencies are much lower than TUNEL, most likely because it only marks a small part of the apoptotic process.
3. Although single labeling with serial sections can help identify the lineage of the apoptotic cell, double labeling is preferable. Both TUNEL and cleaved caspase 3 work well with lineage-specific antibodies in plaques.
4. Apoptosis in atherosclerotic plaques is mostly around the "necrotic core" region. This does not automatically mean that the most frequent cell that undergoes apoptosis in the plaque is the macrophage, as many cells lose their lineage markers either in atherosclerosis (e.g., VSMCs) or as they die.
5. Positive control tissues should be included in any assay for TUNEL or cleaved caspases. Tissues with a rapid turnover such as tonsil or gut are appropriate. For human tonsil, look for apoptotic bodies in tingle-body macrophages within germinal centers. For gut, most apoptosis occurs at the tips of villi. Negative controls are the same tissues, but prior peptide blocking of the primary antibody or use of rabbit IgG instead of the primary antibody.

Acknowledgement

This work was supported by British Heart Foundation Grant RG/08/009/25841 and the Cambridge NIHR Biomedical Research Centre.

References

1. Clarke MC, Figg NK, Maguire JJ et al (2006) Apoptosis of vascular smooth muscle cells induces features of plaque vulnerability in atherosclerosis. Nat Med 12:1075–1080
2. Bennett M, Boyle J (1998) Apoptosis in cardiovascular disease. Heart 79:313–318
3. Gorenne I, Kumar S, Gray K et al (2013) Vascular smooth muscle cell Sirtuin 1 protects against DNA damage and inhibits atherosclerosis. Circulation 127:386–396
4. Mercer J, Figg N, Stoneman V et al (2005) Endogenous p53 protects vascular smooth muscle cells from apoptosis and reduces atherosclerosis in ApoE knockout mice. Circ Res 96:667–674
5. Schrijvers DM, De Meyer GR, Kockx MM et al (2005) Phagocytosis of apoptotic cells by macrophages is impaired in atherosclerosis. Arterioscler Thromb Vasc Biol 25:1256–1261
6. Clarke M, Talib S, Figg N et al (2010) Vascular smooth muscle cell apoptosis induces IL-1-directed inflammation; effects of hyperlipidemia-mediated inhibition of phagocytosis. Circ Res 106:363–372
7. Cho A, Courtman D, Langille L (1995) Apoptosis (programmed cell death) in arteries of the neonatal lamb. Circ Res 76:168–175
8. Han D, Haudenschild C, Hong M et al (1995) Evidence for apoptosis in human atherosclerosis and in a rat vascular injury model. Am J Pathol 147:267–277
9. Isner J, Kearney M, Bortman S et al (1995) Apoptosis in human atherosclerosis and restenosis. Circulation 91:2703–2711
10. Lutgens E, de Muinck ED, Kitslaar PJ et al (1999) Biphasic pattern of cell turnover characterizes the progression from fatty streaks to ruptured human atherosclerotic plaques. Cardiovasc Res 41:473–479
11. Clarke MC, Littlewood TD, Figg NL et al (2008) Chronic apoptosis of vascular smooth muscle cells accelerates atherosclerosis and promotes calcification and medial degeneration. Circ Res 102:1529–1538

Chapter 14

Quantification of Cellular Proliferation in Mouse Atherosclerotic Lesions

José J. Fuster

Abstract

Excessive cell proliferation within atherosclerotic plaques plays an important role in the progression of atherosclerosis. Macrophage proliferation in particular has become a major focus of attention in the cardiovascular field because it appears to mediate most of macrophage expansion in mouse atherosclerotic arteries. Therefore, quantification of cell proliferation is an essential part of the characterization of atherosclerotic plaques in experimental studies. This chapter describes two variants of a simple immunostaining protocol that allow for the quantification of cellular proliferation in mouse atherosclerotic lesions based on the detection of the proliferation-associated antigen Ki-67.

Key words Cellular proliferation, Atherosclerosis, Ki-67, Mac3, SM-α-actin

1 Introduction

Exacerbated cellular proliferation in atherosclerotic arteries has been identified in both humans and experimental animals [1–4]. Furthermore, studies with genetically modified mice support its major role in the growth of atherosclerotic plaques [5–9]. Consistently, a recent study elegantly showed that macrophage burden in murine atherosclerosis is mediated predominantly by local macrophage proliferation rather than monocyte recruitment and differentiation [10]. However, the stimuli that induce macrophage proliferation in the plaque, and how typical cardiovascular risk factors affect lesional cell proliferation, remain largely unknown. Therefore, quantification of cellular proliferation has become an essential part of the characterization of atherosclerotic plaques in preclinical studies.

Quantification of cellular proliferation in tissues is typically achieved by immunological techniques that use monoclonal antibodies to specifically detect proliferation-associated antigens. One of the most popular methods involves the detection of bromodeoxyuridine (BrdU), a synthetic thymidine analog that is

Vicente Andrés and Beatriz Dorado (eds.), *Methods in Mouse Atherosclerosis*, Methods in Molecular Biology, vol. 1339, DOI 10.1007/978-1-4939-2929-0_14,

incorporated into the DNA of dividing cells. However, this technique requires the administration of BrdU, and therefore it cannot be used in humans and is not a valid option for the retrospective analysis of tissue specimens. The alternatives described here use a monoclonal antibody to detect the proliferation-associated antigen Ki-67, a nuclear protein that is expressed exclusively in proliferating cells [11]. In contrast to other endogenous proliferation markers that are expressed at specific stages of the mitotic cell cycle, Ki-67 is expressed during all active phases of the cell cycle (G1, S, G2, and M). Therefore it represents an excellent tool to evaluate the total amount of proliferating cells in a given sample.

This chapter describes two variants of a simple immunostaining protocol that allows the quantification of cellular proliferation in mouse atherosclerotic plaques based on the detection of Ki-67 in formalin-fixed paraffin-embedded histological sections. The first protocol described here uses immunohistochemistry to detect total Ki-67-positive cells in tissue sections. The second protocol describes a triple immunofluorescent staining that has been previously used to specifically evaluate the proliferation of macrophages and vascular smooth muscle cells (VSMCs) [12], the most abundant cell types in atherosclerotic lesions.

2 Materials

2.1 Common to Subheadings 3.1 and 3.2

1. Histology equipment: Paraffin embedding station, embedding molds, microtome, heated water bath, microscope slides and coverslips, staining racks and dishes, oven.
2. Xylene.
3. Ethanol, histological grade (100 % and 95 %).
4. Deionized water (dH_2O).
5. Phosphate Buffered Saline (PBS): 137 mM NaCl, 2,7 mM KCl, 10 mM Na_2HPO_4, 1.8 mM KH_2PO_4 in dH_2O. For 1 L, add 8 g NaCl, 0.2 g KCl, 1.44 g Na_2HPO_4, and 0.24 g KH_2PO_4 to 800 ml dH_2O. Adjust the pH to 7.4 with HCl, and then add dH_2O to 1 L. PBS can also be made as a 10× stock solution.
6. Antigen unmasking solution: 10 mM sodium citrate, pH 6 buffer. 1.5–2 L are required per experiment. This unmasking solution is commercially available as a concentrate (e.g., Vector Labs, H-3300), or it can be prepared as follows: For 2 L, add 5.88 g sodium citrate trisodium salt dihydrate to 2 L dH_2O, and adjust pH to 6.0 with 1 M HCl.
7. Blocking Solution: 5 % Normal Horse Serum (Cat. No. S-2000, Vector Labs) in PBS.

8. Ki-67 antibody (rabbit monoclonal, clone SP6). Available from different vendors (e.g., Cat. No. VP-RM04, Vector Labs). Recommended dilution: 1/100.
9. Pressure cooker.
10. Liquid repellent pen (e.g., Cat. No. H-4000, Vector Labs).

2.2 Specific to Subheading 3.1

1. 3 % hydrogen peroxide. For 200 ml, add 20 ml 30 % H_2O_2 to 180 ml PBS.
2. Biotinylated horse anti-rabbit IgG antibody (e.g., Cat. No. BA-1100, Vector Labs, recommended dilution: 1/500).
3. Streptavidin–horseradish peroxidase (HRP) conjugate. Available from different vendors, both as a concentrate (1 mg/ml) or as a ready-to-use working solution (1 μg/ml, e.g., Cat. No. SA-5004, Vector Labs).
4. 3,3′-Diaminobenzidine (DAB), available from different vendors (e.g., Cat. No. SK-4100, Vector Labs).
5. Harris Hematoxylin solution (e.g., Cat. No. HHS80, SIGMA). Filter immediately before use.
6. Differentiation Solution: 1 % Acid Alcohol Solution. For 200 ml, add 2 ml HCl to 200 ml 70 % ethanol and mix well.
7. Mounting medium 1 (e.g., Eukitt®, Cat. No. 03989, Sigma, or VectaMount, Cat. No. H-5000, Vector Labs).
8. Ethanol, histological grade (70 % and 50 %).
9. Light microscope equipped with a digital camera.

2.3 Specific to Subheading 3.2

1. Mac3/LAMP2 antibody (rat monoclonal, clone M3/84). Available from different vendors (e.g., Cat. No. sc-19991, Santa Cruz Biotechnologies, recommended dilution: 1/300) (*see* **Note 1**).
2. α-SMA antibody (mouse monoclonal), Cy3-conjugated (e.g., Cat. No. C6198, Sigma, recommended dilution: 1/50) (*see* **Note 2**).
3. Alexa Fluor® 633-conjugated goat anti-rabbit IgG (e.g., Cat. No. A-21071, Life Technologies, recommended dilution: 1/500).
4. Alexa Fluor® 488-conjugated goat anti-rat IgG, preadsorbed against mouse IgG (e.g., Cat. No. A-11006, Life Technologies, recommended dilution: 1/500) (*see* **Note 3**).
5. Diamidino-2-phenylindole (DAPI) nuclear counterstain. Available from multiple vendors (e.g., Cat. No. EN62248, Thermo Scientific Pierce). Recommended working concentration: 1 μg/ml in PBS.

6. Mounting medium 2 (e.g., Slowfade® Gold Antifade Reagent, Cat. No. S36937, Life Technologies).
7. Confocal fluorescent microscope.

3 Methods

These protocols allow the quantification of cellular proliferation in histological sections of atherosclerotic arteries obtained from hyperlipidemic mice (e.g., LDLR-deficient, apoE-deficient mice). Similar protocols can be used for the analysis of human samples (*see* **Note 4**). Information on basic histology methods can be found elsewhere [13]. Carry out all procedures at room temperature unless otherwise specified. Do not let the sections dry; this would cause nonspecific antibody binding and therefore high background staining.

3.1 Immunohistochemical Staining of Ki-67 in Mouse Aorta

1. *Deparaffinization*. Before immunostaining, sections must be deparaffinized and rehydrated. Incomplete removal of paraffin can cause poor staining. Place the slides in a rack and warm the sections at 55 °C for 10 min or until paraffin starts to melt. Then treat the slides in staining dishes as follows (*see* **Notes 5** and **6**):
   - Xylene: 3 washes, 4 min each
   - 100 % ethanol: 3 × 4 min
   - 95 % ethanol: 2 × 4 min
   - 70 % ethanol: 2 × 2 min
   - 50 % ethanol: 2 × 2 min
   - dH_2O; 2 × 5 min (*see* **Note 7**)
2. *Antigen unmasking*. Ki-67 staining requires heat-mediated antigen unmasking. This works best in a pressure cooker, especially with old specimens (*see* **Note 8**). Pour 1.5–2 L of antigen unmasking solution into the cooker, and cover it, but do not lock lid. Bring solution to a boil, and put the slides into the cooker. Cover and lock lid. As soon as the cooker has pressurized, start timing, and remove the cooker from the heat source after 2 min, then run under cold water until it is safe to open. Let slides cool in the cooker for 30 min, and then wash in a staining dish with PBS for 5 min.
3. *Inactivation of endogenous peroxidase activity*. Incubate the slides in 3 % hydrogen peroxide for 30 min. Wash in PBS for 5 min.
4. *Blocking of nonspecific interactions*. Wipe off excess buffer from slides and, using a liquid repellent pen, draw a circle around each tissue section (this will minimize the volume of solution required to cover the tissue). Add to each section 40 μl of blocking solution and incubate for 60 min.

5. *Incubation with primary antibody.* Drain the blocking solution from slides and apply to each section 40 µl of diluted anti-Ki-67 antibody (1/100 in blocking solution). Incubate for 2 h at room temperature or overnight at 4 °C.
6. Wash in PBS, 3×5 min.
7. *Incubation with secondary antibody.* Apply to each section 40 µl of diluted biotinylated anti-rabbit IgG antibody (1/500 in blocking solution). Incubate for 30 min at room temperature.
8. Wash in PBS, 3×5 min.
9. *Incubation with streptavidin–HRP.* Apply to each section 40 µl of HRP-conjugated streptavidin working solution. Incubate for 30 min at room temperature.
10. Wash in PBS, 3×5 min.
11. *Signal development.* Add to each section 40 µl of DAB working solution and incubate until brown precipitates are formed. This should be monitored under a light microscope. Stop the reaction with dH_2O as soon as brown nuclei can be detected in the tissue (typically after 2–10 min incubation).
12. *Nuclei counterstaining.* Incubate slides in a staining dish with hematoxylin solution for 1–2 min. Rinse slides for 5 min in running tap water. Remove background by immersing in differentiation solution for 1–2 s. Rinse for 5 min in running tap water.
13. *Dehydration*. Wash slides in staining dishes as follows:
    - 70 % ethanol: 2 min.
    - 95 % ethanol: 2 min.
    - 100 % ethanol: 2 min
    - Xylene: 2 min
14. *Mount slides using mounting medium 1.*
15. *Observation* under light microscope, image acquisition and analysis (*see* **Note 9**). Figure 1 shows a representative image of this immunohistochemical staining.

3.2 Combined Immunofluorescent Staining of Ki-67 and the Cell-Type Specific Markers Mac3 (Macrophages) and α-SMA (VSMCs)

1. Perform **steps 1**, **2** and **4** of Subheading 3.1.
2. *Incubation with primary antibodies.* Drain the blocking solution from slides. Use a liquid repellent pen to draw a circle around each tissue section. Apply to each section 40 µl of diluted primary antibody solution. Best results are obtained by combining all three primary antibodies in the same solution (1/100 Ki-67, 1/50 α-SMA, 1/300 Mac3 in blocking solution). Incubate for 2 h at 37 °C or overnight at 4 °C.

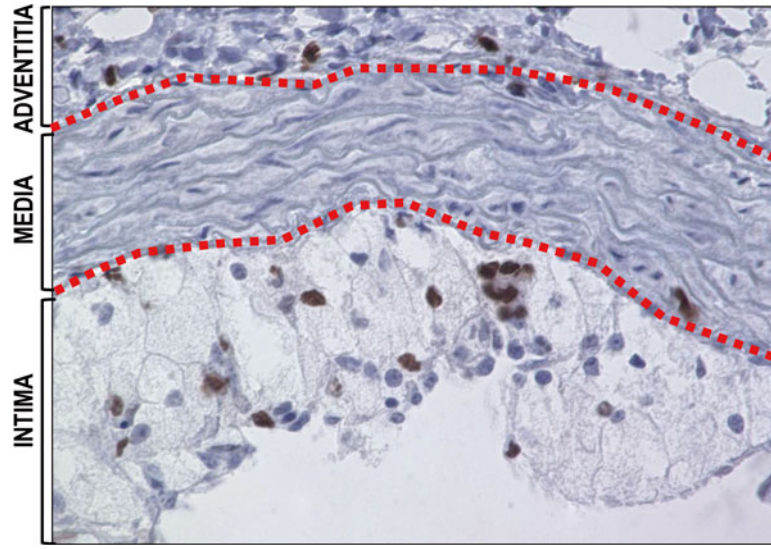

Fig. 1 Representative image of Ki-67 immunohistochemical staining in mouse early-stage atherosclerotic plaques. apoE-KO mice were fed a high-fat/high-cholesterol diet for 6 weeks. 6 μm-thick histological sections were obtained from the ascending aorta and stained as described in the text. The media of the vascular wall is delineated by discontinuous lines. Ki-67-positive nuclei corresponding to proliferating cells are stained *dark brown* with DAB

3. Wash in PBS, 3 × 5 min.
4. *Incubation with secondary antibodies.* Apply to each section 40 μl of diluted secondary antibody solution (containing 1/500 Alexa Fluor® 633-conjugated anti-Rabbit IgG, and 1/500 Alexa Fluor® 488-conjugated anti-Rat IgG in blocking solution) (*see* **Note 10**). Incubate for 30 min at room temperature.
5. Wash in PBS, 3 × 5 min.
6. *Nuclei counterstaining.* Apply to each section 40 μl of DAPI working solution and incubate for 5 min (*see* **Note 11**).
7. *Mount slides using mounting medium 2.*
8. *Observation* under confocal fluorescence microscope, image acquisition and analysis (*see* **Notes 12–15**). Figure 2 shows representative images of this immunofluorescent staining.

4 Notes

1. Mac3 is one of the most popular murine macrophage markers. However, there are other antibodies specific for macrophage markers that can be used with this same protocol, such as anti-F4/80 (e.g., rat monoclonal, clone Cl:A3-1, Cat. No. MCA497,

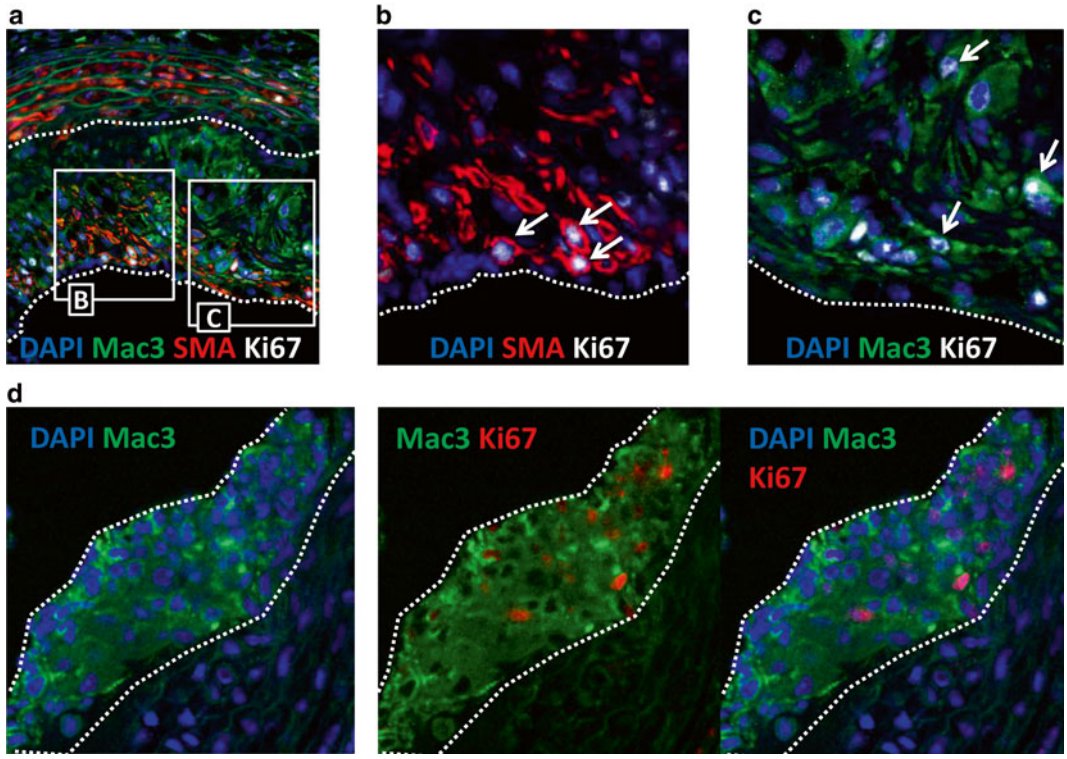

Fig. 2 Representative images of triple immunofluorescent staining of Ki-67 and the cell type-specific markers Mac3 and α-SMA in mouse atherosclerotic plaques. apoE-KO mice were fed a high-fat/high cholesterol diet for 12 weeks (**a**–**c**) or 6 weeks (**d**). 6 μm-thick histological sections were obtained from the ascending aorta and stained as described in the text. Atherosclerotic plaques are delineated by discontinuous lines. (**a**) Immunofluorescent staining of an advanced atherosclerotic plaque exhibiting Mac3-positive macrophages (*green*), α-SMA-positive VSMCs (*red*), Ki-67-positive nuclei (*white*) and total nuclei stained with DAPI (*blue*). *Squared* regions are shown at higher magnification (**b**, **c**). *Arrows* point to Ki-67-positive cells. (**d**) Immunofluorescent staining of an early lesion (fatty streak) consisting almost exclusively of Mac3-positive macrophages (*green*). Proliferating macrophages are positive for Ki-67 (*red*)

Serotec MCA497) or anti-CD68 (e.g., rat monoclonal, clone A-11, Cat. No. MCA1957, Serotec).

2. α-SMA (smooth-muscle specific α-actin isoform) is the best VSMC marker in mouse tissues, but the intensity of its staining varies depending on the differentiation state of the cells. Atherosclerosis progression is known to involve a phenotypic switching of VSMCs, from a contractile to a synthetic phenotype, which is paralleled by a reduction in the expression of α-SMA. Consistently, the intensity of α-SMA staining in atherosclerotic arteries is typically much stronger in medial than intimal VSMCs. While dilutions of this antibody higher than 1/50 will allow the detection of medial VSMCs, they may not stain intimal VSMCs properly.

3. Given the high cross-reactivity between mouse and rat IgG and the abundance of immunoglobulins in atherosclerotic lesions, it is essential to use secondary antibodies that have been adsorbed against mouse IgG and/or mouse serum.
4. The same Ki-67 and α-SMA antibodies listed here can be used for the analysis of human samples. However, Mac3 is not a good marker of human macrophages, so it should be replaced by antibodies specific to human macrophages (e.g., anti-CD68).
5. Do not wash slides for longer periods of time, particularly in xylene or 100 % ethanol solutions, since this would negatively affect tissue integrity and adhesion to the slide.
6. Solvent solutions used for deparaffinization can be reused several times. I typically replace them after 10 uses.
7. After deparaffinization and rehydration, sections can be kept in dH_2O at 4 °C for up to 2 days, if required.
8. Although best results are achieved with a pressure cooker, a conventional water bath can also be used for heat-mediated antigen unmasking. To do this, preheat the water bath with staining dish containing citrate buffer until temperature reaches 95–100 °C. Then immerse slides and incubate for 30 min.
9. Cellular proliferation in the atherosclerotic artery can be expressed as the number of Ki-67-positive cells per mm^2 of plaque area. However, when there are clear differences in lesion cellularity (e.g., due to changes in cell death within the plaque, or different stages of plaque development) is essential to also calculate the percentage of Ki-67-positive cells in the entire cell population. In addition, since typically there are marked differences in the amount of proliferating cells in the different layers of the vascular wall, it is generally advisable to evaluate separately the percentage of Ki-67-positive cells in the intima (plaque), the media, and the adventitia. Cellular proliferation is typically abundant in the intima and the adventitia, and much less frequent in the media. It is also highly recommended to analyze cellular proliferation in different aortic segments (e.g., aortic root and ascending thoracic aorta), and in at least three sections per vascular region.
10. Most immunohistochemical protocols recommend blocking nonspecific interactions with a 3–5 % solution of serum from the same host species as the secondary antibody. However, I find that a 5 % horse serum solution works well for most immunostainings, including Ki-67 staining, regardless of the host species of the secondary antibody. Alternatively, a 3 % goat serum solution in PBS can be used.
11. The choice of fluorescent nuclear stain greatly depends on the laser lines available in the confocal microscope being used for image acquisition. In confocal microscopes lacking the proper

laser line to excite DAPI, TO-PRO3 (Cat. No. T3605, Life Technologies) is a good alternative. However, because of its emission wavelength (661 nm), it requires the use of different fluorescently labeled secondary antibodies and is not compatible with the triple Ki-67/Mac3/α-SMA staining. Two independent double stainings (Ki-67/Mac3 and Ki-67/α-SMA) are required in this case.

12. Confocal microscopy is essential for observation and image acquisition in these experiments, since it typically allows a better discrimination of the different fluorophores, eliminates blur and flare from out-of-focus planes, and greatly improves axial resolution. Best results are generally obtained with 40× or 63× oil immersion objectives.
13. Bleed-through of fluorescence emission due to spectral overlap of the different fluorophores can sometimes be a problem. The phenomenon is usually manifested by the emission of one fluorophore being detected in the channel assigned for a second fluorophore. In the protocol described here, bleed-through is particularly frequent with Alexa Fluor® 488 and Cy3 given their clear spectral overlap and the very high intensity of α-SMA-Cy3 staining. Bleed-through can be reduced by using optimized fluorescence filter sets or confocal microscopes with spectral detection capability, which allows the user to define precisely the wavelength detection range for each fluorophore. In addition, it is recommended to excite and collect the emission of individual fluorophores sequentially. Finally, every experiment should include one single stain control for each fluorophore, in order to set up the imaging conditions accordingly.
14. Elastic fibers in the media exhibit strong autofluorescence, which is usually detected in the same channel as the Alexa Fluor® 488 fluorophore used for Mac3 staining. However, this generally does not affect the quantification of Mac3-positive macrophages. On the contrary, the autofluorescence is sometimes useful, since it helps to identify the media in the tissue section.
15. Fluorescently labeled Ki-67-positive cells in the atherosclerotic plaque can also be detected by flow cytometry, although this requires the digestion of the aorta immediately after harvest in order to produce single-cell suspensions [14], which may affect cellular phenotype. In addition, some cell types are difficult to extract from tissues, so some cell populations within the aorta may not be properly analyzed. Furthermore, this approach typically involves the digestion of the entire aortic wall, and therefore it doesn't allow the quantification of cellular proliferation in its different layers, namely intima, media, and adventitia, which typically exhibit markedly different rates of cellular proliferation.

Acknowledgements

The author is supported by American Heart Association grant 13POST17060028. The author is also grateful to Susan Maclauchlan and Maria A. Zuriaga for insightful discussion and constructive comments on this chapter.

References

1. Gordon D, Reidy M, Benditt E et al (1990) Cell proliferation in human coronary arteries. Proc Natl Acad Sci U S A 87:4600–4604
2. Lutgens E, de Muinck ED, Kitslaar PJ et al (1999) Biphasic pattern of cell turnover characterizes the progression from fatty streaks to ruptured human atherosclerotic plaques. Cardiovasc Res 41:4600–4604
3. Rekhter MD, Gordon D (1995) Active proliferation of different cell types, including lymphocytes, in human atherosclerotic plaques. Am J Pathol 147:668
4. Rosenfeld M, Ross R (1990) Macrophage and smooth muscle cell proliferation in atherosclerotic lesions of WHHL and comparably hypercholesterolemic fat-fed rabbits. Arteriosclerosis 10:680–687
5. Díez-Juan A, Andrés V (2001) The growth suppressor p27Kip1 protects against diet-induced atherosclerosis. FASEB J 15:1989–1995
6. Díez-Juan A, Pérez P, Aracil M et al (2004) Selective inactivation of p27Kip1 in hematopoietic progenitor cells increases neointimal macrophage proliferation and accelerates atherosclerosis. Blood 103:158–161
7. Fuster JJ, Fernández P, González-Navarro H et al (2010) Control of cell proliferation in atherosclerosis: insights from animal models and human studies. Cardiovasc Res 86:254–264
8. Guevara NV, Kim H-S, Antonova EI et al (1999) The absence of p53 accelerates atherosclerosis by increasing cell proliferation in vivo. Nat Med 5:335–339
9. Mercer J, Figg N, Stoneman V et al (2005) Endogenous p53 Protects Vascular Smooth Muscle Cells From Apoptosis and Reduces Atherosclerosis in ApoE Knockout Mice. Circ Res 96:667–674
10. Robbins CS, Hilgendorf I, Weber GF et al (2013) Local proliferation dominates lesional macrophage accumulation in atherosclerosis. Nat Med 19:1166–1172
11. Gerdes J, Lemke H, Baisch H et al (1984) Cell cycle analysis of a cell proliferation-associated human nuclear antigen defined by the monoclonal antibody Ki-67. J Immunol 133:1710–1715
12. Fuster JJ, González-Navarro H, Vinué A et al (2011) Deficient p27 Phosphorylation at Serine 10 Increases Macrophage Foam Cell Formation and Aggravates Atherosclerosis Through a Proliferation-Independent Mechanism. Arterioscler Thromb Vasc Biol 31:2455–2463
13. Hewitson TD, Wigg B, Becker GJ (2010) Tissue preparation for histochemistry: fixation, embedding, and antigen retrieval for light microscopy. Methods Mol Biol 611: 3–18
14. Butcher MJ, Herre M, Ley K et al (2011) Flow cytometry analysis of immune cells within murine aortas. J Vis Exp 53, e2848

Chapter 15

Quantification of In Vitro Macrophage Cholesterol Efflux and In Vivo Macrophage-Specific Reverse Cholesterol Transport

Joan Carles Escolà-Gil, Miriam Lee-Rueckert, David Santos, Lídia Cedó, Francisco Blanco-Vaca, and Josep Julve

Abstract

Promotion of reverse cholesterol transport (RCT) is thought to be a major HDL-mediated mechanism for protecting against atherosclerosis. Preclinical studies support the concept that increasing cholesterol efflux from macrophages may confer atheroprotective benefits independently of the plasma HDL-cholesterol concentration. The application of the macrophage-to-feces RCT method in genetically engineered mice has provided evidence that this major HDL property correlates closely with changes in atherosclerosis susceptibility. This chapter provides details on the methodologies currently used to measure in vitro cholesterol efflux from macrophages or in vivo macrophage-specific RCT. The general principles and techniques described herein may be applied to measure the in vitro cholesterol efflux capacity of human serum in macrophage cultures and to evaluate the effect of different experimental pathophysiological conditions or the efficacy of different therapeutic strategies on the modulation of in vivo macrophage-RCT in mice.

Key words Cholesterol, Cholesterol efflux, HDL, Macrophage, Method, Reverse cholesterol transport

1 Introduction

High-density lipoproteins (HDLs) show a broad range of biological activity [1]. The promotion of reverse cholesterol transport (RCT) from arterial wall macrophages is widely considered a major mechanism responsible for HDL-mediated atheroprotection [2]. The classic steps of the biliary RCT pathway comprise cholesterol efflux from lipid-laden macrophages located in the arterial wall, followed by transfer of the cholesterol to the liver from where it is partly eliminated via bile into the intestine and ultimately to feces [3] (Fig. 1).

The efflux of macrophage cholesterol to HDL occurs by passive diffusion, facilitated by scavenger receptor class B type I (SR-BI) or, more efficiently, by a unidirectional mechanism mediated by the

Vicente Andrés and Beatriz Dorado (eds.), *Methods in Mouse Atherosclerosis*, Methods in Molecular Biology, vol. 1339, DOI 10.1007/978-1-4939-2929-0_15,

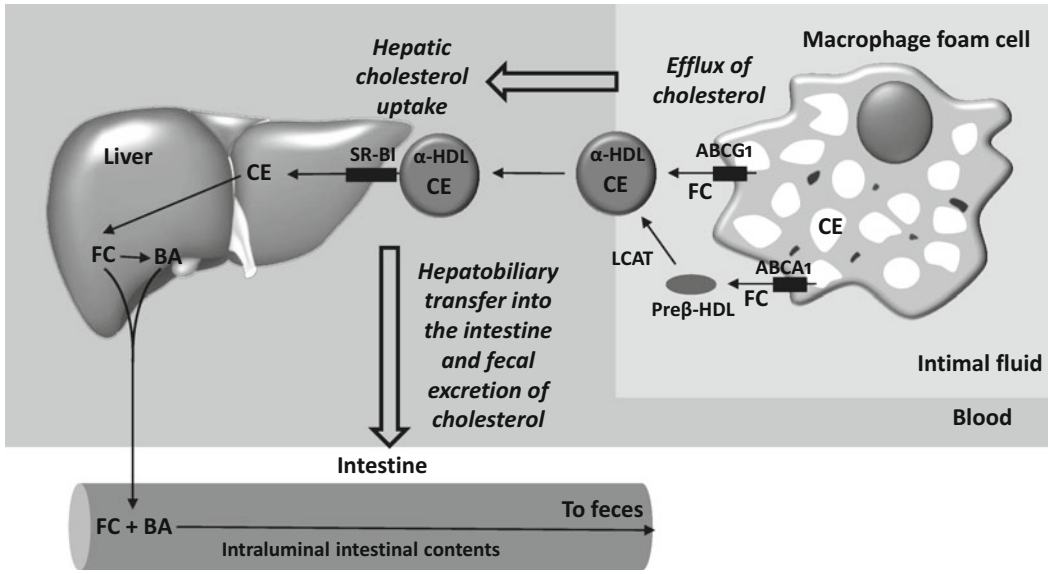

Fig. 1 Schematic diagram of the biliary macrophage-RCT pathway. Cholesteryl esters (CE) stored in lipid droplets of macrophage foam cells are hydrolyzed by neutral cholesteryl ester hydrolases. Lipid-poor nascent preβ-migrating HDL particles acquire free cholesterol (FC) from macrophage foam cells via ABCA1, whereas the ABCG1 transporter facilitates cholesterol efflux from macrophages to α-HDL particles. FC is esterified to CE within nascent HDL particles by lecithin-cholesterol acyltransferase (LCAT), thereby generating mature α-HDL. The liver selectively takes up HDL-associated CE via scavenger receptor class B member 1 (SR-BI) and excretes HDL-derived cholesterol into the bile as FC or as bile acids (BA) after conversion. An alternative non-biliary route for the transfer of cholesterol from the blood directly to the intestinal lumen is thought to contribute to fecal macrophage-derived cholesterol excretion (not shown)

ATP-binding cassette transporters ABCA1 and ABCG1 [4]. Functional analysis of the cholesterol efflux capacity of serum may provide useful data to assess the impact of particular clinical and experimental situations that induce qualitative or quantitative changes in the biological activity of key physiological cholesterol acceptors, such as HDL particles and apolipoprotein (apo) A-I, which is the main protein component of HDL. Recent data [5] have revealed that the HDL-mediated cholesterol efflux ability from macrophages, a metric of HDL function, may be clinically relevant since it displays a strong inverse association with both the carotid intima-media thickness and the presence of angiographically confirmed coronary disease, independently of the plasma HDL-cholesterol concentration.

The in vitro cholesterol efflux method allows the determination of the rate of cholesterol efflux from cultured cells to plasma acceptors (*see* Fig. 2 for a schematic diagram of the method steps). Radioactive labeling of cholesterol and its incorporation in cholesterol-donor cells provides an effective and sensitive method for detecting total cholesterol efflux from cultured human monocyte-derived macrophages or mouse macrophages.

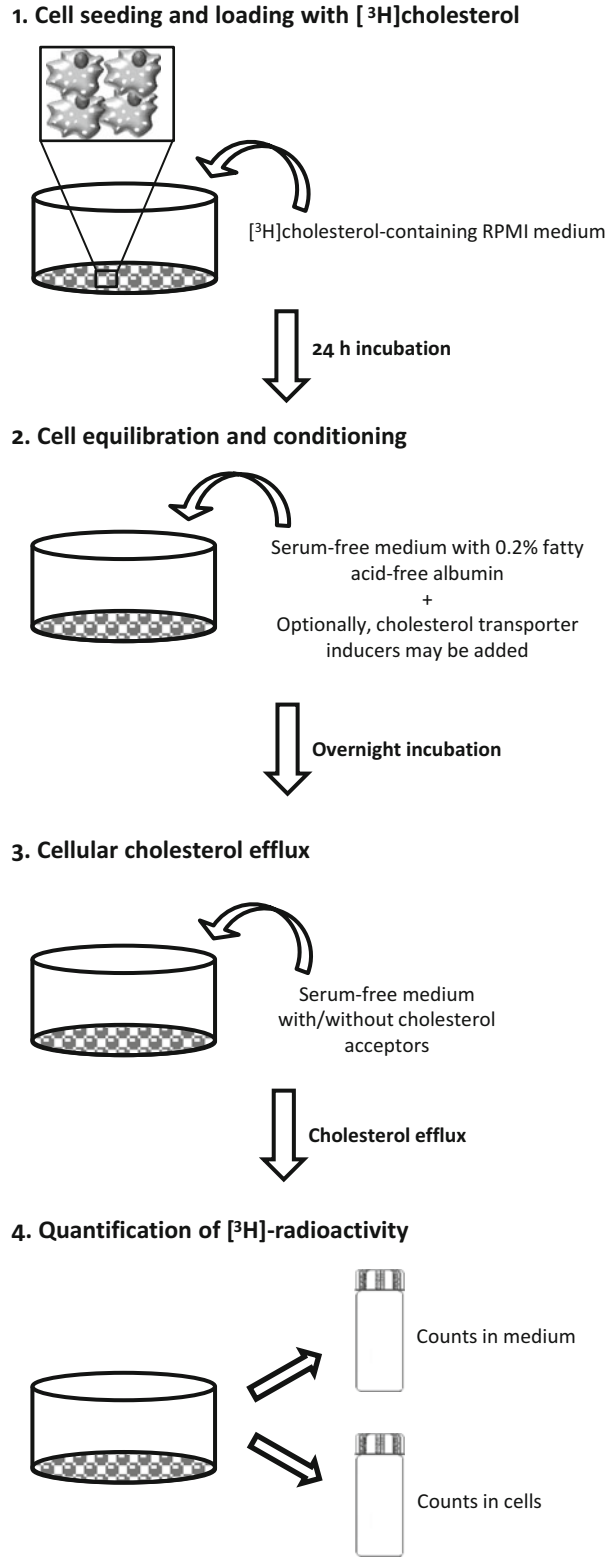

Fig. 2 Steps of cholesterol efflux method. *1*: Macrophages are seeded and grown for two days in RPMI growth medium. If the starting cell typed are monocytes, the cells must be differentiated into macrophages by adding PMA to the macrophage growth medium. The differentiation of monocytes into macrophages typically

However, it should be noted that the efflux of labeled cholesterol from the radiolabeled cells does not necessarily represent the release of cholesterol mass but rather reflect the bidirectional exchange of cholesterol. Sankaranarayanan et al. [6] showed that net movement of cholesterol occurs when the cholesterol donor cells are cholesterol enriched, but not when they are cholesterol normal. The fractional release of label from cholesterol-enriched cells provides an estimate of the "efflux efficiency" of the studied acceptor. However, to quantify the mass movement of the cholesterol, changes in the cell cholesterol mass must be measured [6]. Rodent macrophages expressing preferentially specific cholesterol efflux pathways are usually used in the efflux method. However, the regulation of cholesterol efflux transporters appears to differ among cells from different species. This is the case of cAMP, which strongly stimulates lipid efflux in mouse macrophages but not in human macrophages [7]. Differentiation of human monocytes into macrophages requires incubation of the cells for several days with different polarizing factors. This may affect the expression of ABC transporters in the differentiated macrophages and, accordingly, the cholesterol efflux efficiency of the generated cells [8].

For cholesterol efflux assays, cells are usually seeded in multiwell plates and maintained in growth medium until labeling with [^{3}H] cholesterol. For cell labeling, [^{3}H]cholesterol is added to the cells in growth medium, and the cells are incubated for 24 or 48 h, depending on the study. Cell labeling with [^{3}H]cholesterol is followed by equilibration of the radiolabeled cholesterol among all intracellular cholesterol pools with serum-free medium, supplemented with fatty acid free-albumin for 18 h. When appropriate, the induction of the expression of specific cellular cholesterol transporters may be considered during this step. After equilibration, cholesterol efflux is

Fig. 2 (continued) stops the cells growing, and the cells are then prepared for radiolabeled cholesterol loading. Macrophages or monocyte-derived macrophages are incubated for 24 h with a loading medium containing radiolabeled cholesterol. *2*: Excess radiolabeled cholesterol is then removed, and the cells are washed and incubated with a serum-free medium, which is supplemented with fatty acid-free BSA for 18 h to allow equilibration of the radiolabeled cholesterol with the intracellular cholesterol pools. If required, the cells can be treated during this step to modulate the expression of specific cholesterol transporters (cell conditioning). *3*: After equilibration, the medium is removed, and the cell cultures washed before adding the cholesterol acceptors. The incubation of the macrophages in serum-free cell culture medium in the presence or absence of the acceptors for a specific period allows the estimation of the acceptor-induced release rate of radiolabeled cholesterol from macrophages. *4*: The relative cholesterol efflux is calculated as the percentage of the [^{3}H] counts released in the medium divided by the total [^{3}H] counts (medium + cells)

measured by incubating the cholesterol-labeled cells in the presence of extracellular cholesterol acceptors. To calculate the relative release of acceptor-mediated radiolabeled cholesterol from the cells, the radioactivity in the medium corresponding to the effluxed cholesterol and that remaining in the cells is quantified. Although macrophages are most frequently used, the assay can also be applied to other types of cells, such as Fu5AH hepatoma cells and adipocytes, to obtain mechanistic information; Fu5AH hepatoma cells efflux cholesterol mainly via SR-BI and aqueous diffusion [9], and adipocytes efflux cholesterol via the SR-BI and ABCA1 but not the ABCG1 pathways [10].

The efflux of cellular cholesterol to HDL initiates RCT in all tissues, but the fraction that originates from the macrophage foam cells located in the intima is considered the only RCT component directly involved in atherosclerosis [2]. The key methodological problem for quantifying in vivo RCT from macrophages, which are the most important cholesterol-accumulating cell type in atherosclerosis, is that the macrophage cholesterol pool is a minor contributor to the total RCT from peripheral cells. To overcome this quantitative problem, Zhang et al. [11] developed an assay for measuring in vivo macrophage-to-feces RCT (macrophage-RCT) by tracing the reverse [^{3}H]cholesterol transport from lipid-laden macrophages to feces in mice. In this assay, mouse macrophages or macrophage-like cells were loaded with acetylated low-density lipoproteins (LDL) and [^{3}H]cholesterol and then injected intraperitoneally into recipient animals. After injection, the appearance of [^{3}H]tracer in serum was determined at different time points and, most importantly, collected continuously in the feces during the time frame of the assay. The time course of such experiments is usually 48 h. This method distinguishes between the amount of fecal radioactivity in neutral sterols and bile acids (a schematic outline of this methodology is depicted in Fig. 3). The method can be used to study the role of different therapies and pathways relevant for RCT and HDL-mediated atheroprotection [12, 13]. Under certain experimental settings, the macrophage-RCT rate should be measured within a time spam shorter than 48 h. Therefore, a modified method has been used with pharmacological studies involving short-term transient activation of in vivo events that affect the cholesterol efflux capacity of HDL or acute pathophysiological conditions induced in mice [14, 15]. To evaluate the macrophage-RCT rate within a short time (i.e., in a period not sufficient to support the transfer of macrophage-derived cholesterol into feces), the tracer radioactivity in the intraluminal intestinal contents can be quantitated. The assay follows the same steps used in radiolabeling, injection of the macrophages, and processing of serum and liver samples. The only difference is that the macrophage-derived radioactivity of the intraluminal contents of the intestine is quantitated rather than that of the excreted feces. It should be noted that these

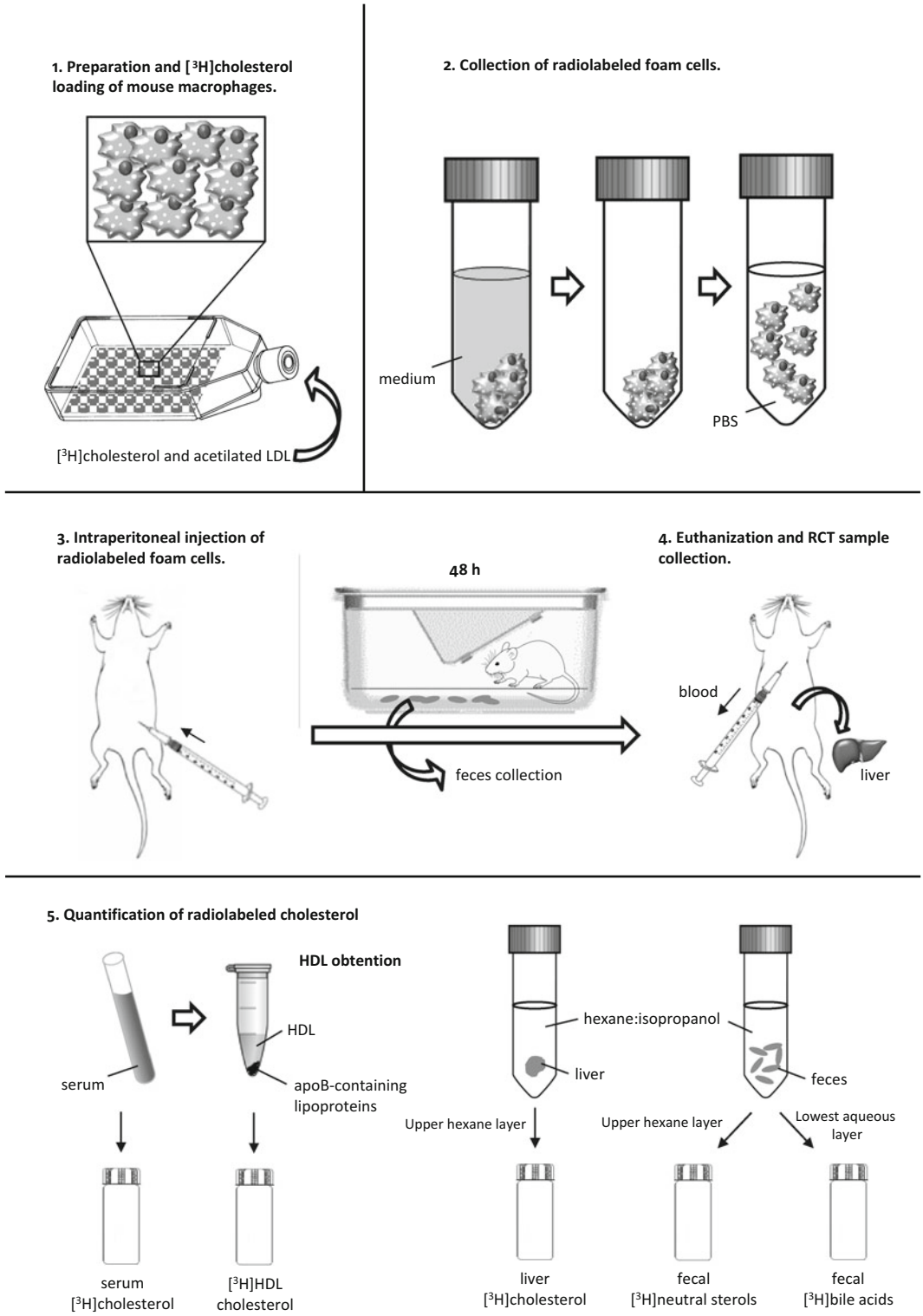

Fig. 3 Steps of the macrophage-to-feces RCT method. This method follows the fate of [^{3}H]cholesterol from mouse macrophages injected into the peritoneal cavity of the mouse. *1*: Mouse macrophages or macrophage-like cells are loaded with ac-LDL and [^{3}H]cholesterol to become foam cells. *2*: Radiolabeled foam cells are gently detached from the plastic surface of 75 cm^2 flasks and resuspended in sterile PBS. *3*: The radiolabeled mouse macrophages are then injected intraperitoneally into the mouse, and the mouse is placed in

macrophage-specific methods do not measure the net flux of cholesterol mass from the macrophages, but rather the unidirectional efflux of the radiolabeled cholesterol from the macrophages to plasma and the intestinal contents or feces. Moreover, this outward flow may be affected by exchange with endogenous tissue cholesterol pools. In addition, although the labeled macrophages in these assays are injected into the peritoneal cavity, which is considered a surrogate of the intimal space, the amount of the cholesterol acceptors in the intraperitoneal compartment and in the arterial intima may differ. The macrophage-RCT method described above has also been applied by injecting the labeled macrophages into extra-peritoneal compartments, such as the skin. However, the RCT fraction that originates from macrophages injected subcutaneously (e.g., in the rostral back), into the mouse requires longer time to be transferred to the intestine/feces in comparison with the faster macrophage-RCT rates obtained when the labeled cells are intraperitoneally injected [15]. Injecting labeled macrophages in other body locations, such as the tail skin, also appears to render a much less robust RCT signal [16].

2 Materials

2.1 Cell Culture

1. Human THP-1 monocyte cell line (ATCC® TIB-202™) and mouse J774A.1 (ATCC® TIB-67™) or P388D1 (ATCC® TIB-63™) macrophage-like cells.
2. Roswell Park Memorial Institute medium (RPMI) 1640 supplemented with 2 mM glutamine.
3. Growth medium for macrophages: RPMI 1640, glutamine, 10 % heat-inactivated FCS, 100 U/mL of penicillin, and 100 μg/mL of streptomycin (P/S) (*see* **Note 1**).
4. 75 cm^2 cell culture flasks.
5. Multiwell cell culture plates.
6. 10 mL serological pipettes.
7. 70 % ethanol in water.
8. Sterile scissors and forceps.
9. Dissecting board.

Fig. 3 (continued) a cage with a metal grid floor for 48 h for feces collection. *4*: At 48 h, the mouse is euthanized, the blood is collected by cardiac puncture, and the liver is removed. *5*: [^{3}H]-radioactivity is measured in serum and HDL after precipitating apoB-containing lipoproteins. Lipids from the liver and feces are extracted with hexane–isopropanol and partitioned against Na_2SO_4. Liver [^{3}H]-radioactivity is determined in the upper layer, which contains the [^{3}H]cholesterol. In the feces extract, the amount of [^{3}H]-radioactivity is determined in the upper layer (neutral sterols) and the lowest layer (bile acids)

10. Sterile phosphate-buffered saline (PBS).
11. 10 mL syringe and 25 G needle.
12. 50 and 15 mL polypropylene tubes.
13. Cell scrapers.
14. Sterile filters with a 0.2 μm pore size.
15. Counting chamber (Fast read 102, Biosigma).
16. Prepare Difco™ fluid thioglycollate medium (Becton Dickinson Labware) (3 % w/v) and autoclave for 15 min at 121 °C. Place the aliquots in 50 mL bottles. Keeping the solution in a dark room at room temperature (RT) for 1–2 months before use will increase the yield of inflammatory cells. Ensure that the broth is clear. Any cloudiness indicates contamination.
17. 1 mg/mL of phorbol 12-myristate 13-acetate (PMA) (Sigma), stored at −80 °C until use.
18. 10 mg/mL of 8-(parachlorophenylthio) cyclic-3′, 5′-AMP (CTP-cAMP; Sigma) in water, stored at −20 °C until use.
19. Liver X receptor agonist (1 g/mL) T0901317 (Cayman Chemical) in ethanol, stored at −20 °C until use.

2.2 Macrophage Radiolabeling and Injection

1. ApoA-I (Sigma) and HDL isolated by sequential ultracentrifugation at a density gradient of 1.063–1.21 g/mL from total plasma (or serum). Although the apoA-I prediluted with serum-free RPMI 1640 medium can be used directly, the isolated HDL must be desalted and incorporated into serum-free RPMI 1640 medium before using it. Incorporate the HDL into RPMI 1640 using a PD-10 desalting column, eluted by gravity. Before adding 2.5 mL of HDL, equilibrate the column with 25 mL of serum-free RPMI 1640 medium. Elute the mixture with 3.5 mL of RPMI 1640, and collect the whole eluate, which contains the HDL, in a separate tube. Whole plasma (or serum) or apoB-depleted plasma (or serum) can be used as acceptors to measure the efflux of the macrophage cholesterol.
2. 40–60 Ci/mmol [1α,2α(n)-^{3}H]cholesterol (Perkin Elmer).
3. 0.2 N of NaOH.
4. PD-10 desalting column (GE Healthcare).
5. Ultracentrifugation tubes.
6. Human LDL: isolate by sequential ultracentrifugation at a density of 1.019–1.063 g/mL and dialyze at 4 °C against 10 mM Tris–HCl, 1 mM EDTA, pH 7.4.
7. Lipoprotein-depleted serum (LPDS): isolate by sequential ultracentrifugation at a density ≥1.21 g/mL and dialyze at 4 °C against 10 mM Tris–HCl, 1 mM EDTA, pH 7.4. To inactivate the LPDS, place it in a 56 °C water bath for 1 h.

8. Acetylated LDL (ac-LDL): adjust the isolated LDL to 2 mg/mL of LDL protein (i.e., apoB or total protein content), and add an equivalent volume of saturated sodium acetate. Next, add 1 μL of acetate anhydride, and gently shake the mixture in an ice-water bath for 30 min. Add another 1 μL of acetate anhydride, and stir the mixture for 30 min. Finally, dialyze the mixture at 4 °C against 10 mM Tris–HCl, 1 mM EDTA, pH 7.4. Before using the mixture for the radiolabeling of mouse macrophages, incorporate the ac-LDL into RPMI 1640 using a PD-10 desalting column, eluted by gravity. To do so, equilibrate the PD-10 column first with 25 mL of RPMI 1640 before adding 2.5 mL of ac-LDL. Elute with 3.5 mL of serum-free RPMI 1640 medium, and collect by gravity the ac-LDL-containing eluate into a separate tube. Filter the suspension through a sterile filter with 0.2 μm diameter pores to avoid aggregated ac-LDL. Ensure that the ac-LDL suspension contains approximately 0.7–1 mg/mL of apoB.
9. Absolute ethanol (>99.9 %).
10. Bovine serum albumin (BSA), essentially fatty acid-free.
11. 2 mL plastic Pasteur pipettes.
12. Liquid scintillation fluid (Optiphase Hisafe 2, Perkin Elmer).
13. Scintillation 20 mL vials.
14. 0.4 % Trypan blue solution (w/v).
15. 1 mL syringes and a 26 G needles.

2.3 RCT Sample Collection and Quantification

1. Isoflurane.
2. Scalpel blade (Carbon steel 21, Swann-Morton).
3. 1.1 mL, Z-gel microtubes for serum separation (Sarstedt).
4. Phosphotungstate precipitant reagent: 0.44 mM phosphotungstic acid and 20 mM $MgCl_2$ (for precipitating apoB-containing lipoproteins).
5. Reusable feeding needle—20 G/30 mm long.
6. Solvent for lipid extraction: hexane–isopropanol (3:2, v:v). Store in a glass sealed bottle.
7. Solution of 0.47 M Na_2SO_4 in bidistilled water.
8. 5 mL glass tubes.
9. Thin layer chromatography (TLC) plates, size 6×20 cm (Whatman).
10. TLC running solvent hexane–diethyl ether–ethyl acetate (50:50:1.5; v:v:v).
11. Iodine crystals.
12. Cholesterol reference standard: 10 mg/mL of cholesterol (Sigma) and 10 mg/mL of cholesterol stearate (Fluka) in chloroform, stored at −20 °C until use.

3 Methods

3.1 In Vitro Cholesterol Efflux Assays

Established cell lines of monocytes are currently used (e.g., THP-1 cells) for cholesterol efflux assays. Alternatively, monocyte-derived macrophages may be used (*see* **Note 2**). Primary human monocytes should be freshly collected with serum containing medium, Ficoll-Hypaque®, or Lympholyte® gradients from whole blood (*see* **Note 2**). The macrophages can be generated by supplementing the growth medium with PMA (i.e., THP-1 cells). In the case of primary human monocytes, they can be supplemented with granulocyte-macrophage colony-stimulating factor (GM-CSF) or macrophage colony-stimulating factor (M-CSF). Various established cell lines of mouse macrophages (e.g., J774 or P388D1 cells) are used to assess the rate of cholesterol efflux to specific extracellular acceptors. Apart from these cell sources, primary mouse macrophages can be isolated from the resident peritoneal macrophage pool either directly or after the injection of thioglycollate broth into the peritoneal cavity of mice.

3.1.1 Seeding and Differentiation of Human THP-1 Monocytes into Macrophages

1. Culture THP-1 in growth medium in 75 cm^2 cell culture flasks, and keep in a humidified cell incubator (5 % CO_2) at 37 °C. Refeed every 2 days with fresh growth medium by adjusting the cell density between 0.8 and 1.2 million cells per milliliter.
2. Sediment the cells at approximately 200 × *g* at RT for 10 min. Aspirate the supernatant and resuspend cells in macrophage growth medium.
3. Count the THP-1 cells in a counting chamber.
4. Seed the monocytes at a cell density of one million cells per well (in a final volume of 1 mL) in 12-well plates (*see* **Note 3**), and allow them to differentiate into macrophages in the presence of 0.05 μg/mL of PMA (*see* **Note 4**) in a humidified cell incubator (5 % CO_2) at 37 °C for 4 days. After differentiation, the cells can be directly used for cholesterol efflux assay (continued in Subheading 3.1.4; *see* **Note 5**).

3.1.2 Seeding of J774 or P388D1 Macrophage-Like Cells

1. Mouse J774 or P388D1 macrophage-like cells are typically seeded and expanded in 75 cm^2 flasks in macrophage growth medium and kept in a humidified cell incubator (5 % CO_2) at 37 °C until use.
2. Change the macrophage growth medium every 2 days. To do so, pour the macrophage growth medium from the flasks, and wash the cells twice with 10 mL of warm PBS. Following this step, add fresh, warm macrophage growth medium and keep in a humidified cell incubator (5 % CO_2) at 37 °C.

3. Maintain the cells until the cell culture reaches about 90 % of confluence (*see* **Note 6**).
4. At a cell culture confluence of 90 %, the cells are ready for subculture. Wash the cells twice with warm PBS, and add the macrophage growth medium as described in Subheading 2.
5. Gently scrape the cells from the plastic surface with a cell scraper.
6. Place the cell suspension into a polypropylene tube. Count the cells in the counting chamber, seed at a cell density of 300,000 cells per milliliter (*see* **Note 7**) and add growth medium up to 1 mL per well in 12-well plates.
7. Keep in a humidified cell incubator (5 % CO_2) at 37 °C for 1 day (continued in Subheading 3.1.4).

3.1.3 Isolation and Seeding of Primary Peritoneal Macrophages

Resident peritoneal mouse macrophages can be isolated via an intraperitoneal injection of thioglycollate into the mice. This produces an inflammatory response, resulting in the release of large numbers of macrophages, which can then be purified. The peritoneal inflammatory cells can be recovered from euthanized mice at various time points after the injection. Davies and Gordon [17] previously described this process in detail. It should be noted that inflammatory macrophages may respond differently to several stimuli than the resident primary macrophages.

1. Inject 2.5 mL of complete thioglycollate medium using a 26 G needle into the peritoneal cavity of the mouse.
2. At 72 h, euthanize the mice by overdose of isoflurane. Pin the mice onto a dissection board, with their abdomens up. Clean the surface of the abdomen with 70 % ethanol.
3. Perform a small off-center skin incision over the caudal half of the abdomen with scissors, and expose the underlying abdominal wall by retraction.
4. Inject 10 mL sterile PBS into the peritoneal cavity using a 25 G needle. Gently massage the abdomen for 30 s (*see* **Note 8**).
5. Slowly withdraw the PBS containing the peritoneal cells from the peritoneal cavity. Try to avoid omental fat zones because they usually block the needle. Repeat this process twice, without removing the needle. Store the cell suspension in a Falcon tube, and keep on ice until required. One thioglycollate-injected mouse may produce 15–20 million macrophages.
6. Sediment the cells at approximately $200 \times g$ at 4 °C for 10 min.
7. Place the cell suspension in a polypropylene tube with 5 mL of growth medium. Count the cells in a counting chamber, seed at a cell density of one million per milliliter (*see* **Note 9**), and add growth medium up to 1 mL per well in 12-well plates.

8. After 2–4 h, remove the nonadherent cells by washing twice with 1 mL of warm PBS. Pour out the PBS, and add 1 mL of radiolabeled medium into each well as described in Subheading 3.1.4.

3.1.4 Cell Labeling

1. Prepare the labeling medium by dispensing 1 μCi of [^{3}H]cholesterol per milliliter of RPMI 1640 medium, supplemented with 5 % FCS and P/S (*see* **Notes 10** and **11**).
2. Measure the apoB levels in the ac-LDL preparation (or alternatively protein content), and add ac-LDL to produce a final concentration of 50 μg/mL in the labeling medium (*see* **Note 12**).
3. Filter the radiolabeled growth medium containing ac-LDL through a sterile filter with a 0.2 μm pore size.
4. Incubate the human monocyte-derived macrophages (after 4 days in culture), J774 or P388D1 macrophage-like cells (1 day after subculture), and peritoneal macrophages (the same day as collection) with the ac-LDL-containing labeling medium for 24 h (*see* **Note 13**).

3.1.5 [^{3}H]Cholesterol Equilibration and Cell Conditioning

1. Pour out the labeling medium, wash the macrophages twice with warm sterile PBS, and incubate with serum-free RPMI 1640 supplemented with 0.2 % BSA (*see* **Note 14**) for 18 h. In this step, the macrophages can be incubated in the presence or absence of specific compounds to manipulate the expression of particular cholesterol transporters in the cultured macrophages (*see* **Note 15**).
2. Remove the medium.
3. Gently wash the macrophages twice with warm sterile PBS.

3.1.6 Promotion of Cholesterol Efflux

1. Prepare the serum-free RPMI 1640 medium, supplemented or not with cholesterol acceptors (*see* Subheading 2.2 and **Note 16**).
2. Incubate the cells with or without cholesterol acceptors for 4 h (*see* **Note 17**).

3.1.7 [^{3}H]Cholesterol Content in the Medium and Cells

1. At the end of the incubation, collect the medium from each well, and centrifuge at approximately 750 × *g* at RT for 10 min to remove detached cells. Then, transfer the cell-free medium to a scintillation vial. For radioactivity counting, to avoid removing sedimented cells from the bottom of the centrifugation vials, take a fixed volume aliquot from the upper fraction of the supernatant. The total counts in the total volume of the medium are then calculated by a correction factor.
2. Add 4 mL of scintillation fluid to each vial. Cap the vials and vortex, and mix the scintillation fluid with the medium.
3. Place the vials in a scintillation rack, and measure the amount of [^{3}H]-radioactivity in the cell culture medium (*see* **Note 18**).

4. Gently wash the cultured macrophages twice with PBS.
5. Add 500 μL of 0.2 N NaOH (*see* **Note 19**) to the cell monolayer, and incubate on a shaker at 4 °C overnight. Transfer the cell extract from each well to a scintillation vial.
6. Repeat the previous step at RT for 30 min, and pool the cell extract from the same well together.
7. Add 4 mL of scintillation liquid to each scintillation vial, cap the vials, vortex vigorously to resuspend the cell extracts, and store the samples overnight in the dark.
8. Measure the amount of [^{3}H] radioactivity in the cell extracts. Repeat the counting every 24 h until the counts are stable (*see* **Note 20**).
9. The cholesterol efflux is expressed as a percentage of total cholesterol using the following formula: % cholesterol efflux = (medium [^{3}H]-radioactivity [cpm])/[(medium [^{3}H]-radioactivity [cpm] + [^{3}H]-radioactivity from cell extract [cpm])] × 100, where cpm = counts per minute. The efflux of the labeled cholesterol can also be expressed as the percentage of radiolabeled cholesterol in the medium relative to that present in the cells prior to the incubation with cholesterol acceptors.

3.2 In Vivo Macrophage-to-Feces RCT in Mice

3.2.1 Seeding of J774 or P388D1 Macrophage-Like Cells

1. Culture the mouse J774 or P388D1 macrophage-like cells in 75 cm^2 flasks until 90 % of confluence, as described in Subheading 3.1.2 (follow **steps 1–3**).
2. Wash the cells with warm PBS twice, and replace the macrophage growth medium.
3. Scrape the cells gently from the plastic surface with a cell scraper.
4. Place the cell suspension in a polypropylene tube. Count the cells in a counting chamber, and place the cells in new flasks, adding five million cells per flask. It should be noted that one flask of cells provides enough macrophages for injecting three mice.
5. Add growth medium to bring the volume up to 10 mL. Grow the cells for 5 days, changing the media every second day (continued in Subheading 3.2.3 and *see* **Note 21**).

3.2.2 Isolation and Culture of Primary Peritoneal Macrophages

1. Inject 2.5 mL of complete thioglycollate medium into the peritoneal cavity of the mouse to obtain the maximum number of peritoneal macrophages, as described in Subheading 3.1.3 (follow **steps 1–6**).
2. Count and seed the peritoneal cells in the growth medium at 20×10^6 cells per flask and incubate for 4 h in a humidified cell incubator (5 % CO_2) at 37 °C.
3. After 4 h, remove the nonadherent cells by washing twice in 10 mL of warm PBS. Pour out the PBS, and add 10 mL of radiolabeled media into each flask, as described in Subheading 3.2.3.

3.2.3 Radiolabeling of Mouse Macrophages

1. Measure the apoB levels (or alternatively the protein content) of the ac-LDL, and add it to RPMI 1640 containing 10 % LPDS and P/S to produce a final concentration of 0.1 mg/mL. Filter the media through a sterile filter with a pore size diameter of 0.2 μm.
2. Evaporate the [^{3}H]cholesterol solution under nitrogen gas in a fume hood. After evaporation, reconstitute the [^{3}H]cholesterol in absolute ethanol (e.g., dissolve 50 μCi of [^{3}H]cholesterol in 20 μL of absolute ethanol when 50 μCi of [^{3}H] cholesterol is the amount needed for radiolabeling the cells of one flask). Add 5 μCi/mL of [^{3}H]cholesterol to the RPMI 1640 containing the ac-LDL, 10 % LPDS, and P/S.
3. For J774 or P388D1 macrophage-like cells, wash the flasks with warm PBS twice.
4. Pour out the PBS, and add 10 mL of RPMI 1640 containing the LPDS, P/S, 1 mg of ac-LDL and 50 μCi of [^{3}H]cholesterol to each flask.
5. Incubate the mixture in a humidified cell incubator (5 % CO_2) at 37 °C for 48 h.

3.2.4 Equilibration and Collection of Radiolabeled Foam Cells

1. Pour out the radiolabeled media, wash twice with warm PBS, and add 10 mL of serum-free RPMI 1640 supplemented with 0.2 % BSA to each flask. Equilibrate the cells for 4 h in a humidified cell incubator (5 % CO_2) at 37 °C.
2. Pour out the RPMI from the flasks, and wash cells twice with 10 mL of PBS.
3. Add 5 mL of PBS to each flask, and keep in a cell incubator for 10 min.
4. Detach the cells from the plastic surface with a plastic Pasteur pipette. Gently wash the bottom of the flask with a brushing motion with a Pasteur pipette. Use the fluid in the flask to flush the cells.
5. Put the PBS containing the cells into one polypropylene tube (pool the cells of all flasks in one tube).
6. Sediment the cells at approximately 200 × *g* at RT for 10 min.
7. Pour out the supernatant, and resuspend the cell pellet with the required amount of PBS (The injection dose for each mouse usually comprises one million cells in 500 μL of PBS). Aliquot the cells to vials, with 500 μL in each.
8. Retain an extra volume to measure the radioactivity and the viability of the cells. To measure the radioactivity, add 100 μL of cell suspension to two scintillation vials. Add 4 mL of scintillation fluid to each vial. Cap the vials, and vortex briefly. Place the vials in a scintillation rack, and measure the

[^{3}H]-radioactivity for 4 min. The total injected dose in 500 μL should be 1–2 million of cpm (*see* **Note 22**).

9. Mix 30 μL of cell suspension, and add 30 μL of Trypan blue. Count the viable (white, clear, and round) and dead (blue and misshapen) cells in a counting chamber (*see* **Note 22**).

3.2.5 Intraperitoneal Injection of Radiolabeled Foam Cells

1. Use a 1 mL syringe with a 26 G needle to withdraw the radiolabeled macrophages.
2. Anesthetize each mouse with isoflurane. Inject 500 μL of radiolabeled cells into the peritoneal cavity of each mouse (*see* **Note 23**).
3. Place each mouse individually in a cage with a metal grid floor for 48 h (for RCT method at 48 h). Water and food should be provided ad libitum (*see* **Note 24**).
4. Collect a small amount of blood from the tail vein at different time points (usually 6 and 24 h; *see* **Note 25**).
5. Transfer the blood to ready-made commercial serum tubes. Centrifuge the blood at approximately 9,000 × *g* at 4 °C for 10 min. Remove 25 μL to measure the serum radioactivity. Add 4 ml of scintillation fluid, and measure the radioactivity as described in **step 8** in Subheading 3.2.4.

3.2.6 Euthanization and RCT Sample Collection at 48 h

1. At 48 h, euthanize the mice by overdose of isoflurane.
2. Perform a cardiac puncture with a 1 mL syringe, and use a 26 G needle to collect a single, good quality, large volume of blood from each mouse (*see* **Note 26**). Put the blood in ready-made commercial serum tubes, and centrifuge at approximately 9,000 × *g* at 4 °C for 10 min.
3. Pin the mice onto a dissection board, with their abdomens up. Open the abdominal cavity using a cut along the median axis of the muscular wall. Remove the whole liver and mince into small pieces (without gallbladder, *see* **Note 27**).
4. Wash the liver samples in containers with saline.
5. Collect feces on the cage floor.

3.2.7 Euthanization and RCT Sample Collection at 3 h

The entire intestine is used for collection of its intraluminal contents. Depending on the aim of the study, the parts corresponding to the small and large intestine can be split into two separate samples. In studies that involve changes in cholesterol absorption, the intraluminal contents of the small intestine are essential [3].

1. At 3 h, euthanize the mice by overdose of isofluorane, and collect the blood as described in **step 2** in Subheading 3.2.6.
2. Open the abdominal cavity of the mouse, pull the skin back on the sides, and locate the stomach pylorus. From this initial

point, using scissors, cut away the small intestine. Remove it from the abdominal cavity by carefully cutting any fatty anchors around its coiled loops.

3. Locate the caecum, and cut out the small intestine where the ileum joins the large intestine (*see* **Note 28**).
4. Collect the intraluminal contents from the intact small intestine by flushing the intestine gently with 5 mL of saline using a syringe and a feeding 20 G needle. Collect the fluid in a 15 mL tube (glass or polypropylene tubes resistant to hexane).
5. Take the large intestine out of the abdominal cavity with forceps, and locate the rectum. Cut out the entire large intestine from this point. Collect the intraluminal contents from the large intestine. Use a forceps to gently retrieve the semisolid material inside, and place the material in a 15 mL tube.
6. Remove the whole liver as described in **step 3** in Subheading 3.2.6.

3.2.8 Quantification of Radiolabeled Cholesterol

1. Divide the serum in two parts: (a) Take 100 μL to measure the serum radioactivity. (b) Take 100 μL and mix well with 200 μL of phosphotungstate precipitant reagent for precipitating apoB-containing lipoproteins in a 1.5 mL tube. Leave for 10 min at RT, and centrifuge at approximately 9,000 × *g* at RT for 2 min. Separate the supernatant (approximately 280 μL) containing the HDL from the precipitate. In both cases add 4 mL of scintillation fluid and count radioactivity as described in Subheading 3.2.4 (**step 8**).
2. Take the whole liver and feces samples obtained in the 48 h RCT method (Subheading 3.2.6), and place each sample in a 15 mL tube (glass or polypropylene tubes resistant to hexane).
3. In the case of the 3 h RCT method, use the 15 mL tubes containing the intraluminal contents of the intact small intestine and large intestine (Subheading 3.2.7).
4. Add 10 mL of hexane–isopropanol for lipid extraction, and rotate the samples on a multitube rotator overnight at 4 °C (*see* **Note 29**).
5. Transfer the fluid carefully to a new tube, taking care to prevent the entry of solid particles.
6. Add 3 mL of 0.47 M Na_2SO_4 to separate the hexane and isopropanol into two layers.
7. Rotate the samples for 10–15 min.
8. Centrifuge at approximately 200 × *g* at 4 °C for 10 min.
9. In the case of liver, transfer the upper layer containing the lipids into the vial to measure [^{3}H]-radioactivity. The upper layer

contains approximately 6 mL, and 5 mL are used to quantify the radioactivity. Put 1 mL into a 5 mL glass tube for TLC analyses.

10. In the cases of feces, transfer the upper layer (neutral sterols) and the lower layer (bile acids) to separate vials.
11. Dry the vials containing the upper layer (mainly hexane) for 48–72 h in a fume hood. Use a nitrogen stream to aid rapid drying. Retain the lowest aqueous layer in the vial until the radioactivity is measured.
12. Add 4 mL of scintillation fluid to each vial, cap the vials, vortex vigorously to resuspend lipid extracts, and store the samples for 30 min. Vortex again, place the vials in a scintillation rack, and measure the [^{3}H]-radioactivity for 4 min. Liver and fecal [^{3}H]-radioactivity are expressed as the % of the injected dose in the liver, feces or intraluminal intestinal contents of each mouse. In the case of serum, the calculation is expressed as the % of injected dose per milliliter of serum.

3.2.9 Liver TLC Analysis

The following TLC method can be used to separate [^{3}H]cholesterol from [^{3}H]cholesterol ester, enabling measurement of the distribution of hepatic [^{3}H]cholesterol.

1. Dry the glass tube containing the 1 mL of the whole liver lipid extract (*see* **step 9** in Subheading 3.2.8 for details) for 24 h in a fume hood.
2. Resuspend liver lipid extract in 50 μL of chloroform and apply 20 μL of sample onto a TLC plate on the line near the bottom (*see* **Note 30**).
3. Apply a standard mixture containing the unlabeled cholesterol and cholesteryl esters onto one lane of each TLC plate (*see* **Note 31**).
4. To run the TLC, prepare solvent hexane–diethyl ether–ethyl acetate (50:50:1.5; v:v:v). Pour 100 mL into a glass tank. Cap the tank, and let the solvent vapors saturate the tank chamber. Line the wall inside with filter paper.
5. Add approximately 50 g of iodine crystals to another tank, and cap the tank to form iodine vapor.
6. Put the TLC plates into the glass tank containing the running solvent against the wall. Run the solvent front until it is 3 cm away from the top line (approximately 45 min).
7. Remove the TLC plates from the tank, and dry them in a fume hood. Place the TLC plates in the iodine tank until the spots are clearly stained (yellow and brown).
8. With a tip of a pipette, carefully scratch off the silica gel containing the stained cholesterol bands (*see* **Note 32**). Transfer the powder of each band to a scintillation vial and count radioactivity as described in Subheading 3.2.8 (**step 12**).

4 Notes

1. To inactivate the FCS, place in a water bath at 56 °C for 1 h. Dulbecco's Modified Eagle's Medium (DMEM), low glucose, supplemented with 10 % FCS, 2 mM glutamine, 100 U/mL penicillin, and 100 μg/mL streptomycin can also be used.
2. Several commercially available gradient separation methodologies can be used to isolate and collect peripheral blood-derived mononuclear cells. Among them, Ficoll-Hypaque® (GE Healthcare®) [18] and Lympholyte®—H (Cedarlane®) density gradient separation methods are specifically designed for the isolation of viable monocytes from different mammalian blood. Monocytes can also be obtained by directly enriching $CD14^+$ cells using a magnetic sorting system (Miltenyi Biotec) [19]. Macrophages can then be produced by differentiating nonadherent macrophage precursors with growth medium, supplemented with M-CSF or GM-CSF. Resident bone marrow macrophages can also be isolated following enzymatic separation of cells from bone marrow plugs and enriched on 30 % FCS-containing medium [20].
3. The number of cells per milliliter in the mentioned plate support is currently used for THP-1 cells and corresponds to a cell density of approximately 300,000 cells per cm^2. If using 6-well (9.5 cm^2/well) or 24-well (1.9 cm^2/well) plates, the number of cells per well may be scaled up or down, respectively. With this cell type, it is important to maintain a cell density of between 0.8 and 1.2 million cells per milliliter. If peripheral blood mononuclear cells are the starting cell source, the recommended working cell density (cells per cm^2) is higher (i.e., approximately 800,000 cells/cm^2) than that indicated for the THP-1 cells.
4. To prepare the working solution of PMA, thaw a stock aliquot (20 μL; 1 mg/mL) of PMA. To yield a working aliquot at a concentration of 75 μg/mL, add exactly 247 μL of DMSO just before use. The working aliquot of PMA at 75 μg/mL in DMSO should be protected from light and maintained at RT until use. The final concentration of PMA in the growth medium should be adjusted to 0.05 μg/mL. Although the indicated concentration of PMA works fine, other concentrations of PMA, ranging from 0.05 to 0.1 μg/mL can be used. When using peripheral blood mononuclear cells, macrophages are produced by culturing primary monocytes with growth medium, supplemented with M-CSF (50 ng/mL) or GM-CSF (10 ng/mL) (Biosite Ltd.). The cells are then maintained in growth medium, which is supplemented with M-CSF or GM-CSF for 6–7 days, refeeding the growth medium with growth factors every 2–3 days. After 6–7 days in culture, the

cells are ready for the assay as judged by phenotypical conversion into macrophages.

5. To maintain these cells, pour out the growth medium from the flasks, and wash the cells twice with 10 mL of warm PBS every second day. Add fresh PMA-containing macrophage growth medium, and maintain the medium in a humidified cell incubator (5 % CO_2) at 37 °C.
6. Monitor the cell growth closely because too great density may cause cell detachment.
7. Various cell densities can be used to start the experiments, with the selection depending on the cell type, cell culture conditions, and plate support used. For instance, an appropriate starting cell density for J774 cells for optimal cholesterol efflux results may range between 75,000–100,000 cells/cm^2, depending on the study.
8. Care should be taken when penetrating the peritoneal cavity with the needle. The syringe plunger should be pushed as soon as the peritoneal cavity is entered. During insertion of the needle into the peritoneal cavity, it is important to prevent red cell contamination and intestinal perforation.
9. Primary differentiated macrophages do not further divide. Thus, the seeding density is calculated to run directly the cholesterol efflux.
10. Although 1 μCi per milliliter of [^{3}H]cholesterol is usually required for a standard assay, other amounts of [^{3}H]cholesterol may also be used. For instance, a range from 0.5 to 4 μCi of [^{3}H]cholesterol per milliliter can be used, depending on the study [21]. At this stage, an Acyl-CoA cholesterol acyltransferase (ACAT) inhibitor (e.g., Sandoz 58-035, Sigma; at a concentration of 2 μg/mL) can be added to prevent the formation of radiolabeled cholesterol ester pools, which complicate the determination of the release of labeled cholesterol or estimates of the specific activity of cell cholesterol [22].
11. If [^{3}H]cholesterol is provided in toluene, the necessary amount should be dried completely under a nitrogen stream and resuspended with absolute ethanol to a final concentration of 2 μCi/μL to minimize the potentially harmful effect of ethanol in cells. If [^{3}H]cholesterol is provided in ethanol, about half the solvent should be evaporated under nitrogen gas to reduce the ethanol concentration in the labeling medium.
12. Depending on the study, the concentration of ac-LDL can range from 0 to 100 μg/mL of growth medium. The addition of ac-LDL to the labeling medium enriches the cells with cholesterol [22].
13. Depending on the study, the incubation of cells with [^{3}H]cholesterol can range from 24 to 48 h. Usually, 24 h is sufficient

for labeling. Labeling for longer periods may result in higher specific activity of intracellular cholesterol.

14. This step allows equilibration of the radiolabeled cholesterol in all the intracellular cholesterol pools. An ACAT inhibitor can also be added during the equilibration period.
15. The addition of CTP-cAMP (at a final concentration of 0.3 mM) induces the specific expression of ABCA1 in mouse macrophage cell lines, whereas liver X receptor (LXR) agonists (e.g., T0901317; 1–4 μM) induce the expression of ABCA1 and ABCG1 transporters. On the other hand, the addition of probucol inhibits ABCA1-mediated efflux. Therefore, ABCA1-specific cholesterol efflux can be determined following the addition of probucol to the equilibration medium by calculating the difference in the efflux in the presence and absence of probucol in the CTP-cAMP-treated cells [23].
16. Cholesterol efflux to cholesterol acceptors occurs via several active transport pathways in macrophages. Lipid-free apolipoproteins (e.g., apoA-I and apoE) and HDL particles induce cholesterol efflux via ABCA1 and ABCG1, which are upregulated by LXR agonists. A "blank" condition, in which no acceptor is added, is included in the efflux assay to determine nonspecific cholesterol efflux from the cells to the media. Such nonspecific efflux can occur due to the secretion of apoE by the cultured cells.
17. Depending on the study, cholesterol acceptors include the following: apoA-I (Sigma) at a final concentration of 0–50 μg/mL; freshly isolated, serum-free RPMI—dialyzed HDL at a final concentration (protein) of 25–100 μg/mL; plasma (or serum) at a final concentration of 1–5 %. Lipid-free apoA-I is commonly used to assess ABCA1-dependent cholesterol efflux, whereas HDL subfractions (HDL_2 or HDL_3) are used mainly to stimulate ABCG1- and SR-BI-dependent cholesterol efflux. The incubation time of the cholesterol donor cells with the extracellular cholesterol acceptors in the efflux assay can vary, usually from 30 min to 18 h.
18. The scintillation counter should be set to measure the [^{3}H]-radioactivity for 4 min, and the average value expressed as cpm should be recorded. If more than one scintillation counter is used, the cpm should be converted to disintegrations per minute (dpm) using the following equation: dpm = cpm sample − cpm background/detector efficiency.
19. Alternatively, cellular lipids can be extracted with 500 μL of hexane–isopropanol (3:2, v:v). A volume of 500 μL should be added to the cell monolayer and incubated on a shaker for 20 min. The solvent should then be transferred from each well to a scintillation vial under a fume hood. This last step is

repeated, and the cell extract from the same well is pooled together. The solvent is then dried overnight in a fume hood before adding the scintillation cocktail. Another method based on the use of bidistilled water can also be used. In this case, the plates are placed in a freezer at –80 °C for 1 h. A volume of 500 μL of bidistilled water is then added to each well. The cells should be checked under a microscope to ensure that cell detachment is completed. If attached cells are observed, the plates with the bidistilled water can be maintained at 4 °C overnight on a shaker, or the wells can be scraped. The cell extract is then transferred from each well to a scintillation vial. Alternatively, an extra volume of bidistilled water can be added to each well, and the cell extract from the same well can be pooled together. The scintillation cocktail is then added and [^{3}H]-radioactivity counted.

20. Allow 4–12 h to ensure that the [^{3}H]cholesterol is fully resuspended and equilibrated in the scintillation fluid. The samples should be counted at least twice, 24 h apart. If [^{3}H]cholesterol is not fully equilibrated, the readings will continue to rise. The counts should be recorded when the readings have stabilized.
21. The cells should be grown until they reach 80 % of confluence.
22. The points eight and nine are carried out to determine the amount of cells and radioactivity injected into mice. These results are used to normalize results from other experiments. The percentage of viable cells should be higher than 70 %.
23. Narcosis of mice should be checked to avoid excess cardiac and respiratory suppression.
24. Animal metabolic cages are preferable, but a standard cage with a grid floor can be used. In the latter, filter paper should be placed under the grid floor to absorb urine.
25. The cut should be made 0.5 cm from the tip of the tail using a scalpel blade, and 50–100 μL of blood should be obtained per sample blood. The blood flow can be stopped by dabbing the tail tip.
26. The needle should be inserted 0.5 cm from the center of the thorax toward the animal's chin, holding the syringe 25°–30° away from the chest. The plunger should be pulled back gently to obtain the maximum amount of blood available (usually 1 mL).
27. To remove the liver, the falciform and coronary ligaments that keep the organ intimately connected with the diaphragm should be cut. The liver can then be removed, together with the inferior vena cava and the liver vessels. The weight of the whole liver is approximately 1–1.5 g.
28. Care should be taken not to lose any of the semifluid mass of the chymus by accidental pouring.

29. The presence of solid food residues in the intraluminal contents may require filtering of the extracts to more accurate separation of the solvent phases.
30. For each sample, 10 μL should be loaded and allowed to evaporate before applying more of the sample.
31. Free cholesterol band is located near the start position, whereas cholesteryl esters band is close to the front of the running solvent.
32. Outline the bands with a pencil. Note that the bands rapidly disappear when the plate is removed from the tank.

Acknowledgments

This work was partly funded by the European Cooperation in Science and Technology (COST) Action BM0904, Ministerio de Sanidad y Consumo, Instituto de Salud Carlos III, CP13-00070 (to J.J.), FIS 11-0176 (to F.V-B.), and FIS 12-00291 (to J.C.E-G). CIBER de Diabetes y Enfermedades Metabólicas Asociadas is an Instituto de Salud Carlos III Project. JJ is recipient of a Miguel Servet Type 1 contract. The Wihuri Research Institute is maintained by the Jenny and Antti Wihuri Foundation.

References

1. Camont L, Chapman MJ, Kontush A (2011) Biological activities of HDL subpopulations and their relevance to cardiovascular disease. Trends Mol Med 17:594–603
2. Cuchel M, Rader DJ (2006) Macrophage reverse cholesterol transport: key to the regression of atherosclerosis? Circulation 113:2548–2555
3. Lee-Rueckert M, Blanco-Vaca F, Kovanen PT et al (2013) The role of the gut in reverse cholesterol transport: focus on the enterocyte. Prog Lipid Res 52:317–328
4. Rothblat GH, Phillips MC (2010) High-density lipoprotein heterogeneity and function in reverse cholesterol transport. Curr Opin Lipidol 21:229–238
5. Khera AV, Cuchel M, de la Llera-Moya M et al (2011) Cholesterol efflux capacity, high-density lipoprotein function, and atherosclerosis. N Engl J Med 364:127–135
6. Sankaranarayanan S, de la Llera-Moya M, Drazul-Schrader D et al (2010) Importance of macrophage cholesterol content on the flux of cholesterol mass. J Lipid Res 51:3243–3249
7. Kiss RS, Maric J, Marcel YL (2005) Lipid efflux in human and mouse macrophagic cells: evidence for differential regulation of phospholipid and cholesterol efflux. J Lipid Res 46:1877–1887
8. Wolfs IM, Donners MM, de Winther MP (2011) Differentiation factors and cytokines in the atherosclerotic plaque micro-environment as a trigger for macrophage polarisation. Thromb Haemost 106:763–771
9. Adorni MP, Zimetti F, Billheimer JT et al (2007) The roles of different pathways in the release of cholesterol from macrophages. J Lipid Res 48:2453–2462
10. Zhang Y, McGillicuddy FC, Hinkle CC et al (2010) Adipocyte modulation of high-density lipoprotein cholesterol. Circulation 121: 1347–1355
11. Zhang Y, Zanotti I, Reilly MP et al (2003) Overexpression of apolipoprotein A-I promotes reverse transport of cholesterol from macrophages to feces in vivo. Circulation 108:661–663
12. Escola-Gil JC, Rotllan N, Julve J et al (2009) In vivo macrophage-specific RCT and antioxidant and antiinflammatory HDL activity measurements: new tools for predicting HDL atheroprotection. Atherosclerosis 206:321–327
13. Annema W, Tietge UJ (2012) Regulation of reverse cholesterol transport: a comprehensive appraisal of available animal studies. Nutr Metab (Lond) 9:25

14. Lee-Rueckert M, Silvennoinen R, Rotllan N et al (2011) Mast cell activation in vivo impairs the macrophage reverse cholesterol transport pathway in the mouse. Arterioscler Thromb Vasc Biol 31:520–527
15. Silvennoinen R, Escola-Gil JC, Julve J et al (2012) Acute psychological stress accelerates reverse cholesterol transport via corticosterone-dependent inhibition of intestinal cholesterol absorption. Circ Res 111:1459–1469
16. Martel C, Li W, Fulp B et al (2013) Lymphatic vasculature mediates macrophage reverse cholesterol transport in mice. J Clin Invest 123: 1571–1579
17. Davies JQ, Gordon S (2005) Isolation and culture of murine macrophages. Methods Mol Biol 290:91–103
18. Ferrante A, Thong YH (1978) A rapid one-step procedure for purification of mononuclear and polymorphonuclear leukocytes from human blood using a modification of the Hypaque-Ficoll technique. J Immunol Methods 24:389–393
19. Verreck FA, de Boer T, Langenberg DM et al (2004) Human IL-23-producing type 1 macrophages promote but IL-10-producing type 2 macrophages subvert immunity to (myco)bacteria. Proc Natl Acad Sci U S A 101:4560–4565
20. Pascual-Garcia M, Rue L, Leon T et al (2013) Reciprocal negative cross-talk between liver X receptors (LXRs) and STAT1: effects on IFN-gamma-induced inflammatory responses and LXR-dependent gene expression. J Immunol 190:6520–6532
21. Yancey PG, Bortnick AE, Kellner-Weibel G et al (2003) Importance of different pathways of cellular cholesterol efflux. Arterioscler Thromb Vasc Biol 23:712–719
22. Weibel GL, Drazul-Schrader D, Shivers DK et al (2014) Importance of evaluating cell cholesterol influx with efflux in determining the impact of human serum on cholesterol metabolism and atherosclerosis. Arterioscler Thromb Vasc Biol 34:17–25
23. Favari E, Zanotti I, Zimetti F et al (2004) Probucol inhibits ABCA1-mediated cellular lipid efflux. Arterioscler Thromb Vasc Biol 24:2345–2350

Chapter 16

In Vitro Macrophage Phagocytosis Assay

Magda R. Hamczyk, Ricardo Villa-Bellosta, and Vicente Andrés

Abstract

The key roles of macrophages in atherosclerosis include the phagocytosis of apoptotic and necrotic cells and cell debris, whose accumulation in atherosclerotic lesions exacerbates inflammation and promotes plaque vulnerability. Evidence is accumulating that macrophage phagocytic functions peak at the early stages of atherosclerosis and that the reduced phagocytosis at the late stages of disease leads to the generation of necrotic cores and a defective resolution of inflammation, which in turn promotes plaque rupture, thrombus formation, and life-threatening acute ischemic events (myocardial infarction and stroke). The impaired resolution of inflammation in advanced lesions featuring loss of macrophage phagocytic activity may be in part due to an imbalance between M1 and M2 subsets of polarized macrophages. A better understanding of the mechanisms that regulate macrophage phagocytic activity in the context of atherosclerosis may therefore help identify novel therapeutic targets. This chapter presents a protocol for establishing primary mouse macrophage cultures, a method for polarizing macrophages to the M1 and M2 states, and a method for the in vitro study of macrophage phagocytosis of IgG-opsonized or IgM/complement component 3-opsonized erythrocytes.

Key words Phagocytosis, Macrophage, Opsonization, IgG, IgM, Complement component 3, Red blood cells

1 Introduction

Atherosclerosis is the main feature of atherothrombotic vascular disease, the leading cause of death in developed countries which may soon acquire this status worldwide [1]. Atherogenesis is initiated by the accumulation of lipoproteins in the subendothelial space of the arterial wall followed by the activation of endothelial cells [2, 3]. Activated endothelium secretes chemokines that attract monocytes, which once within the lesion differentiate into macrophages upon exposure to macrophage colony-stimulating factor (M-CSF) [4, 5]. Once differentiated, lesional macrophages begin to ingest deposited lipoproteins through the scavenger receptor pathway [6]. This process drives the transformation of macrophages into foam cells, which augment the inflammatory response and thus promote the recruitment of more monocytes and other

Vicente Andrés and Beatriz Dorado (eds.), *Methods in Mouse Atherosclerosis*, Methods in Molecular Biology, vol. 1339, DOI 10.1007/978-1-4939-2929-0_16,

inflammatory cells. Cytotoxic substances produced by foam cells cause the death of lesion-resident endothelial and smooth muscle cells [7, 8], producing enlarged lesions that contain dead cells, cell debris, lipids, and extracellular matrix. A major function of macrophages is to ingest these components through phagocytosis. Macrophage phagocytic activity is high in the initial stages of atherosclerosis, but in advanced plaques, it is defective, and macrophages fail to engulf dead cells and cell debris, compromising the resolution of inflammation. Necrotic cores then accumulate and generate life-threatening vulnerable plaques that can easily undergo rupture, causing thrombus formation and myocardial infarction or stroke.

Phagocytosis is a receptor-mediated process by which cells ingest large particles (≥0.5 μm). Since macrophages can encounter a great variety of particles, they express many receptors that can mediate phagocytosis. Moreover, some molecules, such as antibodies and complement components (e.g., complement component 3, C3), facilitate phagocytosis by tagging particles for recognition, in a process called opsonization. The two best-studied phagocytic receptors are Fcγ receptor (FcγR) and C3 receptor (CR3), which recognize IgG- and C3-opsonized particles, respectively. In this chapter, we describe a protocol for the in vitro study of these two phagocytic routes using macrophage primary cultures. Because an imbalance between pro-inflammatory M1 and anti-inflammatory M2 macrophages in large lesions is thought to contribute to impaired resolution of inflammation [9], we describe an optional step for the polarization of macrophages to the M1 (classical activation) and M2 (alternative activation) phenotypes. The work flow for the complete protocol is shown in Fig. 1.

2 Materials

2.1 Establishing Macrophage Primary Culture

1. Mice.
2. 70 % ethanol in distilled H_2O.
3. Dissection materials: tweezers, scissors, and sterile scalpel blades.
4. Conical sterile polypropylene centrifuge tubes (15 mL).
5. Phosphate-buffered saline (PBS): 1.54 mM KH_2PO_4, 155.17 mM NaCl, and 2.71 mM Na_2HPO_4, pH 7.4, sterilized by autoclaving.
6. Roswell Park Memorial Institute (RPMI) 1640 medium with antibiotics: 100 U/mL penicillin and 100 μg/mL streptomycin (*see* **Note 1**).
7. Cell culture dishes (60 mm and 100 mm).

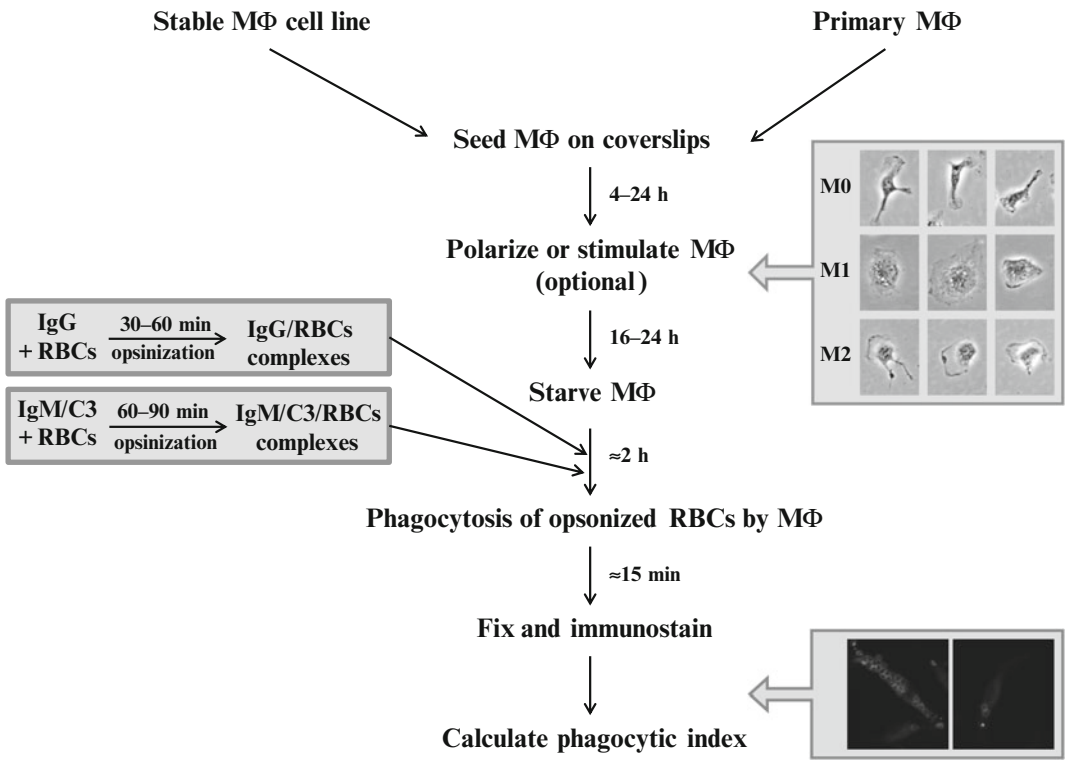

Fig. 1 Work flow of the phagocytosis assay with estimated times for each step. MΦ, macrophages; RBCs, red blood cells; C3, complement component 3

8. Paper towels.
9. Syringes (10 mL) and needles (25G).
10. Distilled H_2O.
11. Heat-inactivated (30 min at 56 °C) fetal bovine serum (FBS).
12. Differentiation medium: RPMI 1640 supplemented with 10 % heat-inactivated FBS, 20 % L-cell conditioned medium (*see* **Note 2**), 2 mM L-glutamine, 100 U/mL penicillin, and 100 μg/mL streptomycin.

2.2 Seeding Macrophages on Coverslips

1. 24-well cell culture plates.
2. Round coverslips (matching the well size, e.g., 12 mm for 24-well plates).
3. PBS (as in Subheading 2.1, **item 5**).
4. Differentiation medium (as in Subheading 2.1, **item 12**).
5. Sterile cell scrapers.
6. Conical sterile polypropylene centrifuge tubes (50 mL).
7. Cell counting chamber.

2.3 Macrophage Polarization (Optional)

1. M1 polarization medium: RPMI 1640 supplemented with 10 % heat-inactivated FBS (*see* Subheading 2.1, **item 11**), 2 mM L-glutamine, 100 U/mL penicillin, 100 μg/mL streptomycin, 100 ng/mL lipopolysaccharide (LPS), and 10 ng/mL interferon γ (INFγ).
2. M2 polarization medium: RPMI 1640 supplemented with 10 % heat-inactivated FBS (*see* Subheading 2.1, **item 11**), 2 mM L-glutamine, 100 U/mL penicillin, 100 μg/mL streptomycin, and 10 ng/mL interleukin 4 (IL-4).
3. Differentiation medium (as in Subheading 2.1, **item 12**).
4. PBS (*see* Subheading 2.1, **item 5**).
5. Permanent marker.

2.4 Phagocytosis Assay

1. PBS (*see* Subheading 2.1, **item 5**).
2. Starvation medium: RPMI 1640 medium containing 0.1 % heat-inactivated FBS (as in Subheading 2.1, **item 11**), 2 mM L-glutamine, 100 U/mL penicillin, and 100 μg/mL streptomycin.
3. Sheep red blood cells (RBCs) in Alsever's solution (*see* **Note 3**) (e.g., Cat. No. SR0053, Oxoid).
4. Polypropylene microcentrifuge tubes (1.5 mL).
5. 20 mM glucose in HBSS (*see* **Note 4**).
6. Rabbit IgM fraction anti-sheep RBCs (e.g., Cat. No. CL9000-M, Cedarlane) (*see* **Note 5**).
7. Rabbit IgG fraction anti-sheep RBCs (e.g., Cat. No. 55806, Cappel) (*see* **Note 5**).
8. Complement component 5 (C5)-deficient serum (e.g., Cat. No. C1163, Sigma) (*see* **Note 6**).
9. Conical sterile polypropylene centrifuge tubes (50 mL).
10. Ice.

2.5 Cell Fixing and Immunostaining

1. PBS (as in Subheading 2.1, **item 5**).
2. 4 % formaldehyde in PBS (for 500 mL: in a fume hood, heat 400 mL of PBS to aprox. 60 °C on a hot plate with magnetic stirrer, add 20 g of paraformaldehyde and incubate with mixing, add dropwise 1 M NaOH until all powder is dissolved, fill up with PBS up to 500 mL, cool the solution, filter and adjust pH to 7.4, and use fresh or freeze at −20 °C).
3. 0.5 % (v/v) Triton X-100 in PBS.
4. 0.1 % (v/v) Triton X-100 in PBS.
5. Blocking solution: PBS supplemented with 1 % (w/v) bovine serum albumin (BSA) and 0.1 % (v/v) Triton X-100.

6. Anti-rabbit secondary antibody conjugated with a fluorochrome of choice (e.g., FITC, AlexaFluor488, etc.).
7. Mounting medium of choice containing diamidino-2-phenylindole (DAPI; e.g., ProLong Gold Antifade Mountant with DAPI, Molecular Probes; *see* **Note 7**).
8. Microscope glass slides (e.g., 76 × 26 mm).
9. Fluorescence or confocal microscope.

3 Methods

3.1 Establishing Macrophage Primary Culture

1. Euthanize a mouse, from which the lower limbs will be obtained (*see* **Note 8**).
2. Spray the mouse with 70 % ethanol to disinfect.
3. Using tweezers and scissors, remove the skin from both legs (*see* **Note 9**).
4. Cut away each leg at the hip joint (where the head of the femur meets the pelvis) and place them in a 15 mL tube containing PBS.
5. In a flow cabinet, transfer the legs to a paper towel (*see* **Note 10**) and remove muscles with a sterile blade to obtain clean femurs and tibias.
6. Put the bones on a 60 mm dish containing RPMI medium with antibiotics.
7. Hold one bone with sterile tweezers and cut both joints with sterile scissors to gain access to the bone marrow (*see* **Note 11**).
8. Aspirate RPMI medium with antibiotics into a 10 mL syringe and fit a 25G needle.
9. Introduce the needle into the bone lumen and flush out the bone marrow into a new 60 mm dish until the bone color turns white.
10. Aspirate the medium containing the bone marrow using the same syringe and pass through the needle to disaggregate cells.
11. Repeat **steps 7–10** for all the bones.
12. Transfer the cell suspension from the dish to a 15 mL tube and centrifuge at 300 × *g* for 5 min at room temperature.
13. Discard the supernatant and add 1 mL of distilled H_2O to lyse RBCs. Pipette up and down for 10 s and add PBS to 15 mL.
14. Centrifuge at 300 × *g* for 5 min at room temperature. Repeat the lysis step if after centrifugation the pellet still contains RBCs.
15. Discard the supernatant and resuspend the pellet in 45 mL differentiation medium (*see* **Note 12**).

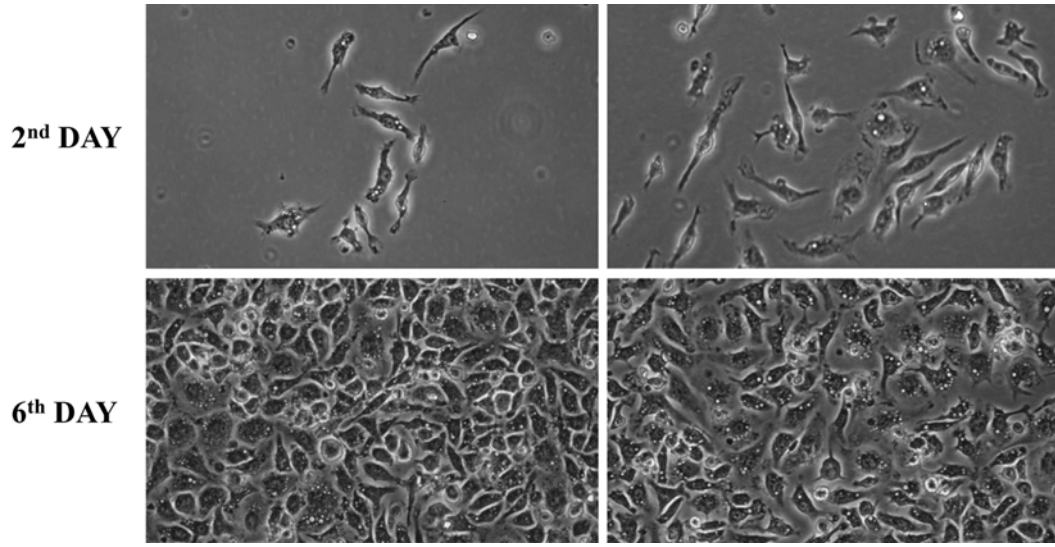

Fig. 2 Primary macrophage cell culture. Mouse bone marrow progenitors were cultured in RPMI 1640 medium containing 10 % heat-inactivated fetal bovine serum, 20 % L-cell conditioned medium, 2 mM L-glutamine, 100 U/mL penicillin, and 100 μg/mL streptomycin. Pictures show representative cell cultures after 2 days (*top*) and 6 days (*bottom*)

16. Plate the cells on four 100 mm dishes (10 mL of cell suspension per dish).
17. Incubate at 37 °C in a 5 % CO_2 atmosphere.
18. After 48 h (day 2) of culture, add 10 mL of fresh differentiation medium (*see* **Note 13**) to each plate. At this point, some attached cells can be observed (*see* Fig. 2, top).
19. After further 48 h (day 4) of culture, discard the medium and add 10 mL of fresh differentiation medium to each plate.
20. After a further 48 h (day 6) of culture, discard the medium and add 10 mL of fresh differentiation medium to each plate. At this point, the attached cells usually reach confluence (*see* Fig. 2, bottom).
21. After 7 days in culture, bone marrow precursors are considered fully differentiated to macrophages (M0 state) and are ready for experiments.

3.2 Seeding Macrophages on Coverslips

1. In the flow cabinet, prepare a 24-well plate (*see* **Note 14**).
2. Put a glass coverslip in each well and expose the plate to UV light for 20 min in order to sterilize it.
3. Aspirate medium from one 100 mm dish containing a confluent monolayer of primary macrophages (*see* **Note 15**) and wash twice with PBS to remove dead and unattached cells.
4. Add fresh differentiation medium and gently scrape off the macrophages with a cell scraper (*see* **Note 16**).

5. Transfer the medium containing cells to a 50 mL tube and centrifuge at $260 \times g$ for 5 min at room temperature.
6. Discard the supernatant and resuspend the cell pellet in differentiation medium.
7. Count the cells in a cell counting chamber (*see* **Note 17**).
8. Prepare a suspension containing 5×10^4 cells per mL of differentiation medium (e.g., for one 24-well plate, prepare around 1.25×10^6 cells in 25 mL).
9. Transfer 1 mL of the cell suspension (around 5×10^4 cells, *see* **Note 18**) into each well containing a coverslip (prepared in **step 2**) and briefly shake plates to distribute the cells evenly.
10. Incubate cells at 37 °C in a 5 % CO_2 atmosphere for a few hours (or overnight) to allow cells to attach.
11. If phagocytic activity is to be examined in polarized macrophages, proceed as indicated in Subheading 3.3. For phagocytic assays with M0 macrophages, go directly to Subheading 3.4.

3.3 Macrophage Polarization (Optional)

1. Prepare polarization medium for macrophages (1 mL for each well of a 24-well plate) just before use (*see* **Note 19**).
2. Remove medium from all wells (from **step 10** in the previous section) and wash them once with PBS.
3. Add the appropriate polarization (M1 and M2) or differentiation (M0) medium to each well. Identify wells on the plate cover using a marker.
4. Incubate at 37 °C in a 5 % CO_2 atmosphere for 16–24 h.

3.4 Phagocytosis Assay

1. Wash the macrophages once with PBS and incubate with starvation medium for 2 h (*see* **Note 20**) at 37 °C in a 5 % CO_2 atmosphere.
2. Mix sheep RBC solution by flipping the tube and transfer an appropriate volume (depending on the design of your experiment) to two 1.5 mL tubes, one for IgM opsonization and another for IgG opsonization. Use 0.5 μL RBC solution for each well of a 24-well plate. Remember to leave some control wells free of RBCs.
3. Wash RBCs by adding 1 mL of 20 mM glucose in HBSS, centrifuge at $1500 \times g$ for 4 min at room temperature, and discard the supernatant.
4. Repeat **step 3** (*see* **Note 21**).
5. Resuspend each RBC pellet in 0.25 mL of 20 mM glucose in HBSS.
6. Prepare the IgM and IgG solutions: add 3 μL of anti-sheep RBC IgM or 0.1 μL of anti-sheep RBC IgG per μL of RBC solution used in **step 2** to 0.25 mL of 20 mM glucose in HBSS.

7. Mix RBC solutions (obtained in **step 5**) with IgG or IgM solution (obtained in **step 6**).
8. Incubate for 30–60 min at room temperature with gentle mixing to enable opsonization (*see* **Note 22**).
9. Centrifuge at 1500 × *g* for 4 min at room temperature, discard the supernatant, and resuspend each pellet in 1 mL of 20 mM glucose in HBSS (*see* **Note 23**).
10. Centrifuge at 1500 × *g* for 4 min at room temperature, and discard the supernatant. Store the pellet of IgG-opsonized RBCs at 4 °C while performing **steps 11–13** with the IgM-opsonized RBCs.
11. Mix 20 μL of C5-deficient serum (containing C3) with 180 μL of 20 mM glucose in HBSS to obtain 200 μL of diluted C5-deficient serum.
12. Resuspend IgM-opsonized RBC pellet in 200 μL of diluted C5-deficient serum (containing C3) and incubate at 37 °C for 30 min with mixing.
13. Add 1 mL of 20 mM glucose in HBSS to the same tube (IgM/RBCs sample), centrifuge at 1500 × *g* for 4 min at room temperature, and discard the supernatant.
14. Resuspend in 50 mL tubes the complexes containing RBC/IgG (obtained in **step 10**) or RBC/IgM/C3 (obtained in **step 13**), using an appropriate volume of starvation medium (calculate 1 mL of starvation medium for each well).
15. Aspirate the starvation medium from plates containing cultured macrophages (prepared in Subheading 3.4, **step 1**) and add 1 mL per well of medium containing RBC/IgG or RBC/IgM/C3 complexes (*see* **Note 24**). Incubate for 15 min at 37 °C in 5 % CO_2 atmosphere. Remember to leave some wells without RBCs.
16. Place the plates on ice and wash wells two to three times with 1–2 mL PBS to arrest the phagocytosis process. Proceed directly to **step 1** in Subheading 3.5.

3.5 Cell Fixing and Immunostaining

1. Fix the macrophages (from **step 16** in Subheading 3.4) by incubating with 4 % formaldehyde (in a fume hood) for 10–15 min at room temperature (*see* **Note 25**).
2. Rinse twice with PBS (*see* **Note 26**).
3. Permeabilize the cells with 0.5 % Triton X-100 in PBS for 10 min at room temperature.
4. Wash three times with 0.1 % Triton X-100 in PBS for 5 min.
5. To block nonspecific binding of the antibodies, incubate coverslips with blocking solution for 30 min at room temperature.

6. Prepare a dilution of the antibody conjugated to a fluorochrome in blocking solution; allow around 150–200 μl per coverslip (*see* **Note 27**).
7. Remove the blocking solution by holding each coverslip on its edge with forceps and touching a paper towel.
8. Immediately incubate the coverslips with diluted antibody for 1 h at room temperature in a humidified chamber in the dark.
9. Aspirate the antibody solution and wash coverslips three times with 0.1 % Triton X-100 in PBS, then once with PBS (5 min each wash).
10. Using tweezers, take each coverslip and remove liquid by touching the corner of a paper towel. Invert the coverslip on a drop of mounting medium (with DAPI) placed on a glass slide. Mount 2–3 coverslips per glass slide.
11. Allow the slide to dry in the dark overnight at 4 °C or proceed directly to the next step, depending on the mounting medium used (see supplier instructions).
12. Under a fluorescence or confocal microscope, count the number of phagocytized RBCs in individual macrophages.
13. Calculate the phagocytic index, which is usually given as the average number of erythrocytes per 100 macrophages. You can also determine the percentage of macrophages that engulfed at least one erythrocyte.

4 Notes

1. Medium can also contain L-glutamine and heat-inactivated fetal bovine serum (medium composition is not crucial at this point). Instead of medium, sterile PBS can be used.
2. L-cell conditioned medium (LCM) is a source of macrophage colony-stimulating factor (M-CSF) which drives differentiation of progenitor cells to macrophages. Differentiation medium can be supplemented with 100 U/mL recombinant M-CSF instead of 20 % LCM. This increases the cost of the experiment but gives more reliable and reproducible results.
3. Alsever's solution is an isotonic, balanced salt solution widely used as a blood preservative, permitting prolonged storage under refrigeration and preserving the antigenic properties of erythrocytes. Sheep RBCs in Alsever's solution are available normally in 20 mL vials and have quite short expiry date (around 2–3 months), so before each experiment, make sure that the reagent has not expired.
4. Alternatively, glucose can be dissolved in PBS.

5. Many suppliers do not give the exact concentrations of the IgG and IgM fractions, so the amount of antibodies used for opsonization normally requires optimization.
6. Complement C5-deficient serum contains C3, which binds to IgM antibodies on the RBC surface and can then be recognized by CR3 (also called Mac-1) on macrophages. Serum used for the experiment should lack C5 to avoid activation of the alternative complement pathway, which would result in erythrocyte lysis.
7. It is also possible to use mounting medium without nuclear stain and perform an additional staining step (after **step 9** in Subheading 3.5) with DAPI or Hoechst.
8. The protocol description is for one mouse. Adjust amounts and volumes to the number of mice required for your experiment.
9. Femurs and tibias are the richest source of murine bone marrow. If the number of mice is limited, extract additional marrow from the upper limbs.
10. To minimize the risk of contamination, you can incubate the legs in 70 % ethanol for 1 min and wash once with PBS just before removing the muscles.
11. In the case of tibia, it is necessary to cut away almost half of the bone (from the side where the foot and the leg meet). To avoid contamination after opening a bone, do not put it down until the bone marrow is flushed out.
12. Bone marrow progenitors have a high proliferation potential, and normally one animal is enough to yield sufficient macrophages for a phagocytosis assay. For all experiments, maintain similar seeding density, but if counting cells, bear in mind that bone marrow consists of different progenitors, and macrophage precursors are just a fraction of this. We typically resuspend the bone marrow in 45 mL medium to seed on four 100 mm dishes, but the volume can differ depending on the experiment.
13. At this point, it is better to add medium (instead of changing it) because there are still many unattached macrophage progenitors.
14. Although the protocol is given for 24-well plates, it can be adjusted for other formats. In any case, remember to dedicate some wells as technical controls for immunostaining, e.g., do not add RBCs to some wells to have negative controls (wells where no fluorescence should be detected). These wells will be a reference of unspecific fluorescence or background.
15. Instead of primary cell cultures, some established macrophage cell lines can be used, such as RAW264.7; however, the phagocytosis

period needs to be extended, usually up to 30 min. The phagocytic activity of some cell lines might need to be augmented by stimulation with phorbol myristate acetate (PMA).

16. Alternatively, wash the cells twice with PBS and detach them with 2× or 4× trypsin. Bear in mind that macrophages are strongly attached to the plate surface so do not use 1× trypsin as it may be ineffective.
17. A Neubauer chamber can be used, or any other cell counting chamber available in your laboratory.
18. The number of macrophages seeded on each well can vary from 2.5×10^4 to 1.5×10^5 cells and may require some optimization depending on the cell type and mouse genotype. Seeding densities that are too high or too low can make it difficult to quantify RBC-to-macrophage ratios. If cells are too close to each other, it is difficult to assess which of the adjacent cells engulfed a particular erythrocyte. On the other hand, if cells are seeded too sparsely, many photographs are needed to obtain sufficient numbers of cells for RBC/macrophage quantification.
19. Macrophage polarization is an optional step that depends on the experimental strategy. As an alternative, other stimuli or drugs can be applied before the phagocytosis assay.
20. It is also possible to starve macrophages in medium without FBS. The duration of starvation may be extended, but the same duration must be maintained for all experiments.
21. The purpose of these washes is to eliminate broken cells from the RBC stock solution before using it. At the end of **step 4**, the supernatant should be free of signs of hemolysis. Two washes are normally enough.
22. If available, use a noria mixer as it will provide the best conditions for opsonization.
23. It normally takes a while to resuspend the pellet, but this is a sign that the opsonization was successful.
24. At this point, it is possible to add a short centrifugation step ($300 \times g$ for 1 min at room temperature) to synchronize the phagocytosis process.
25. In order to save time, perform **steps 1–5** (Subheading 3.5) directly on the 24-well plate containing coverslips (since volumes of the fixation, permeabilization, and blocking solutions do not have to be exact).
26. Plates can be stored at 4 °C for quite a long time before processing. It is important to fill up all the wells with PBS and wrap each plate with parafilm to avoid evaporation.
27. The antibody dilution may vary depending on the source and normally needs to be optimized. Remember to use an antibody

that recognizes antibodies involved in the opsonization process, e.g., if rabbit IgGs and IgMs were used to form complexes with RBCs, for the detection, use a secondary antibody anti-rabbit IgG/IgM made in a different species, e.g., donkey or goat.

Acknowledgments

We thank Simon Bartlett for English editing. M.R.H. is supported by an FPI predoctoral fellowship from the Spanish Government (BES-2011-043938) and R.V-B. by a *Juan de la Cierva* postdoctoral contract from the Spanish Government (JCI-2011-09663). Work in V.A.'s laboratory is supported by grants from the Spanish Ministry of Economy and Competitivity (MINECO) (SAF2013-46663-R), Fondo Europeo de Desarrollo Regional (FEDER), Instituto de Salud Carlos III (RD12/0042/0028), the Progeria Research Foundation (Innovator Award 2012, Established Investigator Award 2014), and the European Union (Liphos, Grant Agreement 317916). The Centro Nacional de Investigaciones Cardiovasculares (CNIC) is supported by the MINECO and the Pro-CNIC Foundation.

References

1. Lloyd-Jones D, Adams RJ, Brown TM et al (2010) Executive summary: heart disease and stroke statistics—2010 update: a report from the American Heart Association. Circulation 121(7):948–954
2. Williams KJ, Tabas I (1995) The response-to-retention hypothesis of early atherogenesis. Arterioscler Thromb Vasc Biol 15(5):551–561
3. Tabas I, Williams KJ, Boren J (2007) Subendothelial lipoprotein retention as the initiating process in atherosclerosis: update and therapeutic implications. Circulation 116(16): 1832–1844
4. Glass CK, Witztum JL (2001) Atherosclerosis. the road ahead. Cell 104(4):503–516
5. Mestas J, Ley K (2008) Monocyte-endothelial cell interactions in the development of atherosclerosis. Trends Cardiovasc Med 18(6): 228–232
6. Greaves DR, Gordon S (2005) Thematic review series: the immune system and atherogenesis. Recent insights into the biology of macrophage scavenger receptors. J Lipid Res 46(1):11–20
7. Kockx MM, Knaapen MW (2000) The role of apoptosis in vascular disease. J Pathol 190(3): 267–280
8. Boyle JJ, Weissberg PL, Bennett MR (2002) Human macrophage-induced vascular smooth muscle cell apoptosis requires NO enhancement of Fas/Fas-L interactions. Arterioscler Thromb Vasc Biol 22:1624–1630
9. Johnson JL, Newby AC (2009) Macrophage heterogeneity in atherosclerotic plaques. Curr Opin Lipidol 20(5):370–378

Chapter 17

Glucose and Insulin Tolerance Tests in the Mouse

Ángela Vinué and Herminia González-Navarro

Abstract

In vivo metabolic tests are highly valuable to determine whether atherosclerosis progression in mouse models is accompanied by carbohydrate metabolism alterations such as glucose intolerance and insulin resistance. In this chapter, we describe protocols to perform in the mouse glucose and insulin tolerance tests, two metabolic assays which evaluate the glucose tolerance and the insulin sensitivity, respectively.

Key words Insulin, Glucose, Metabolism, Intraperitoneal injection, Metabolic test

1 Introduction

Type 2 diabetes mellitus (T2DM) is one of the main cardiovascular risk factors and enhances from 2 to 10 times the risk of developing cardiovascular disease and atherosclerosis [1, 2]. Its relevance is due to the increasing incidence provoked by the acquisition of unhealthy life habits [3, 4]. Glucose homeostasis alterations such as glucose intolerance and reduced insulin sensitivity are characteristic of T2DM. In vivo metabolic tests are designed to identify glucose metabolism derangements in mice due to genetic or dietary manipulations [5, 6]. The use of these metabolic techniques in animal models has resulted in important advances in the understanding of atherosclerosis progression associated to T2DM [7, 8].

The glucose tolerance test (GTT) measures the clearance by the body of an injected glucose load [9]. A solution of glucose is administered by intraperitoneal injection in overnight-fasted mice, and subsequently plasmatic glucose levels are measured at different time points during the following 2 h [10]. Blood samples are also collected to determine plasmatic insulin levels during the glucose test. The insulin tolerance test (ITT) evaluates insulin sensitivity by monitoring endogenous glucose disappearance over time in response to an injection of human insulin. To avoid hypoglycemia induced by the insulin injection, the test is conducted in mice fasted between 4 and 6 h. Glucose clearance rate indicates the

Vicente Andrés and Beatriz Dorado (eds.), *Methods in Mouse Atherosclerosis*, Methods in Molecular Biology, vol. 1339, DOI 10.1007/978-1-4939-2929-0_17,

action of insulin in periphery tissues showing their sensitivity to the hormone [10]. The metabolic tests change over age and display sexual dimorphism; thus, these must be performed in age- and sex-matched mice [11, 12]. Husbandry, diet, mouse handling, and circadian rhythm have also a major impact in these tests [10]. Therefore, to obtain reproducible results, mice must be housed in the same conditions of light; housing and feeding and tests should be performed by experienced personnel and at the same time frame of the day.

2 Materials

1. 20 % D-glucose solution (analytical grade).
2. Insulin 100 U/ml.
3. Saline solution (0.9 % NaCl).
4. 25-gauge needles (0.5 mm × 16 mm).
5. 1 ml syringes.
6. Sharp scalpel blade.
7. Glucometer.
8. Glucose test sticks.
9. Sterile alcohol pads.
10. Microfuge tubes.
11. Refrigerated microfuge.
12. Heparinized capillaries.
13. Heparin.
14. Scale.
15. Timer.
16. Clean mouse cages.

3 Methods

3.1 Intraperitoneal Glucose Tolerance Test (IPGTT)

1. Prepare a maximum of 5 mice per cage, separated by sex, and bring them to the metabolic assay room the day before the fasting (*see* **Note 1**).
2. Fast mice 16 h before the IPGTT in clean cages with no food or feces in the bedding (*see* **Note 2**) with standard light–dark cycle and free access to water.
3. Start the procedure between 8 and 9 am (*see* **Note 3**).
4. Prepare an experimental record table to annotate body weight (BW), glucose solution volume to be injected, and the glucose

levels at the different time points ($t=0$, $t=15$, $t=30$, $t=60$, $t=120$ min) (*see* **Note 4**).

5. Weigh mice and report BW in the record table.
6. Calculate and record in the table the volume of the 20 % glucose stock solution required for intraperitoneal injection of a final dose of 2 g of glucose/kg of BW, for each mouse as follows:

   volume of glucose (20 % solution) to inject (μl) = 10 × BW (g).
7. Prepare syringes loaded with the required volume of glucose solution (according to **step 6**), needles, glucometer, and glucose sticks for measurements (*see* **Note 5**).
8. Clean with alcohol pads the tip of mouse tails.
9. Cut 1–2 mm of tissue from the tail tip distal to the bone with a sharp scalpel.
10. Let blood flow directly into the glucose test stick inserted into the glucometer and report the glucose value in the experimental table ($t=0$). Collect 10 μl of blood using heparinized capillaries, place in a test tube with 2 μl heparin, and keep at 4 °C (*see* **Notes 6** and **7**).
11. To avoid excessive blood loss, apply pressure to the incision after each measurement.
12. Clean intraperitoneal area using sterile alcohol pads and inject mice with syringes loaded with glucose according to **step 6** (*see* **Note 8**).
13. Start timer in mode "count up".
14. After 15 min of glucose injection, repeat measurement of blood glucose levels and collect blood as in **step 10** by gently removing the scab and by massaging the tail tip.
15. Record the glucose values in the experimental table ($t=15$).
16. Repeat **steps 14** and **15** at 30, 60, and 120 min ($t=30$, $t=60$, and $t=120$) after glucose injection.
17. At the end of the experimental session, clean with sterile pads the mouse tail tips and place the mice in clean cages with free access to food and water.
18. Monitor the animals during the following 2 h to report any abnormal behavior.
19. Centrifuge blood at 4 °C during 5 min at 8000 × *g* speed followed by 20 min at 14,000 × *g* speed to obtain plasma from the different time points.
20. Collect plasma into a new labeled tube and measure insulin concentration by ELISA (*see* **Note 9**).
21. The IPGTT results are represented in a graph depicting glucose levels versus time (*see* **Note 10**).

3.2 Insulin Tolerance Test

1. Prepare maximum 5 mice per cage, separated by sex, and bring them to the metabolic assay room the day before the fasting (*see* **Note 1**).
2. Fast mice 4 h before the test in clean cages with no food or feces in the bedding with standard light–dark cycle and free access to water (*see* **Notes 2** and **3**).
3. Weigh mice and report BW in the record table.
4. Prepare an experimental record table to annotate BW, insulin solution volume to be injected, and the glucose levels at the different time points ($t=0$, $t=15$, $t=30$, $t=45$, $t=60$, $t=90$ min) (*see* **Notes 4** and **6**).
5. Calculate the volume of insulin to be injected to each mouse for a dose of 0.5 U/kg of BW and annotate in the report table. For a working solution of 0.1 U/mL, the following formula can be used (*see* **Note 11**):

   volume of insulin (0.1 U/mL) to inject (μL) = BW (g) × 5.
6. Load 1 ml syringes with the insulin solution and prepare glucose test strips and glucometer (*see* **Note 5**).
7. Clean with alcohol pads the tip of mouse tails.
8. Cut 1–2 mm of tissue from the tail tip distal to the bone with a sharp scalpel.
9. Collect the blood by direct flow directly into the glucose test stick inserted into the glucometer and annotate the glucose value in the experimental table ($t=0$) (*see* **Notes 6** and **7**).
10. Clean intraperitoneal area using sterile alcohol pads and inject mice with syringes loaded with insulin according to **step 5** (*see* **Note 8**).
11. Start timer in mode "count up".
12. After 15 min of insulin injection, repeat measurement of blood glucose levels as in 9 by simply gently removing the scab and by massaging the tail tip and placing a small blood drop in a new test stick.
13. Record the glucose values in the record table ($t=15$).
14. Repeat glucose measurements as in 9 at 30, 45, 60, and 90 min ($t=30$, $t=45$, $t=60$, $t=90$) after insulin injection.
15. At the end of the experimental session, clean with sterile pads the mouse tail tips and place the mice in clean cages with free access to food and water.
16. Monitor the animals to report any abnormal behavior during the following 2 h.
17. The ITT results are represented in a graph depicting relative glucose levels in percentage versus time (*see* **Note 12**).

4 Notes

1. Mouse metabolic assays are diet, age, sex, and strain sensitive; thus, it is important to keep these parameters comparable throughout each independent experiment. It is recommended to carry out the test in no more than 10–12 mice per experiment to avoid stress conditions which affect glucose disposal and consumption and insulin release. Although anesthesia might appear to be a suitable method to reduce stress in the mice, it affects heart rate and induces hyperglycemia in mice. Therefore, glucose metabolism tests must not be performed in anesthetized mice. Mouse handling by experienced personnel is highly recommended in order to reduce anxiety levels in the mice.
2. For fasting, it is very important to remove all food and feces to avoid pellet and stool intake. If available, fasting cages can be used.
3. It is recommended that metabolic studies are performed at approximately the same hour in the morning because physiological and biochemical parameters change throughout the day.
4. An example for experimental record table is displayed in Table 1. A similar table can be used for the ITT.
5. Store sterile 20 % glucose solution and human insulin solution (100 U/mL) at 4 °C and bring them to room temperature for the tests. Prepare one syringe per mouse with the volume of glucose or insulin according to BW. Using two or more glucometers is also recommended in order to avoid overlapping of measurements.

Table 1
Example of an experimental record table for a GTT

Mouse number	BW (g)	Glucose solution volume (μl) to inject	Glucose levels (mg/dL)				
			0 min	15 min	30 min	60 min	120 min
1							
2							
3							
4							
5							
6							

6. Blood sampling for small volumes is most commonly obtained from the tip of the tail, and the subsequent samples are obtained by gently removing the scab and repeating the massaging procedure. Avoid excessive bleeding as it might affect mouse welfare and results.
7. Fasting basal glucose levels will be $t=0$ in the GTT and the ITT curve.
8. Space the injections of each mouse about 1–2 min to facilitate glucose measurements and to avoid overlapping of timings and take into account for the following bleedings. Remove all air bubble from the syringes. Make the injection with an angle of 25° to avoid subcutaneous injection and below the visceral area. In obese mice, make sure to avoid fat pad areas to successfully inject the glucose or insulin load.
9. For measurement of insulin levels by ELISA, use an ultrasensitive commercially available kit and follow the instructions. Usually 5 μl of plasma is enough for determination of insulin concentration, but if a larger volume is required for the ELISA, plasma can be diluted in saline solution. Plasma samples can be also stored at -20 °C until later ELISA determination.
10. Results are depicted as glucose levels (mg/dL) in the Y-axis versus time (min) in the X-axis (Fig. 1). For comparisons among different mouse groups, the Area Under the Curve parameter ($AUC_{glucose}$) is typically used. This parameter is obtained by calculating the area generated by the glucose disappearance versus time over a period of 2 h in the GTT.

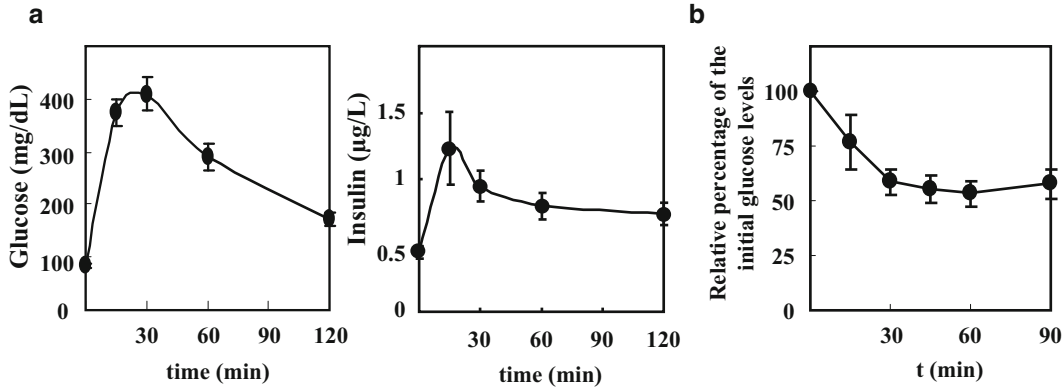

Fig. 1 Glucose tolerance test (GTT) and insulin tolerance test (ITT). (**a**) The left graph displays the average glucose levels ($n=6$ mice) at time 0 (fasting plasma levels) and at 15, 30, 60, and 120 min after the glucose load (2 g/kg BW). The right graph shows insulin levels measured by ELISA at the different time points after glucose load. (**b**) Graph depicts the average glucose levels relative to initial glucose levels in percentage ($n=6$ mice) at time 0 (100 %, 4 h fasting plasma levels) and at times 15, 30, 45, 60, and 90 min after the insulin infusion (0.5 U/kg BW). For GTT, mice were fasted 16 h and for ITT mice were fasted 4 h. Data is shown as mean ± sem

Higher $AUC_{glucose}$ parameter compared to a control group indicates increased glucose intolerance; in contrast, smaller $AUC_{glucose}$ value indicates faster glucose disappearance and therefore improved glucose tolerance. To analyze the glucose-stimulated insulin secretion during the test, insulin results from the ELISA are also depicted as insulin levels (μg/L) in the Y-axis versus time (min) in the X-axis (Fig. 1). For comparisons among different mouse groups, the AUC parameter ($AUC_{insulin}$) obtained by calculating the area generated by the insulin versus time over a period of 2 h in the GTT can be used. Higher $AUC_{insulin}$ parameter compared to a control group might indicate increased capacity of pancreatic islets to secrete insulin induced by the glucose load, the so-called glucose-stimulated insulin release. However, additional studies are needed to reach such a conclusion, such as β-cell area measurement in the pancreas and in vitro insulin secretion by isolated islets.

11. To inject a dose of 0.5 U/kg of BW, prepare an insulin solution of 0.1 U/mL by making a dilution (1/1000) in saline solution 0.9 % from a human insulin stock concentrate (100 U/ml). Be aware that injection of insulin will rapidly induce glucose clearance; therefore, the insulin dose used will depend on the sensitivity to insulin of the mice to be studied. We have found that 0.5 U of insulin per kg of BW is an optimal dose for mice fed a regular chow diet with a moderate insulin resistance. For high-fat-fed mice with severe insulin resistance, higher doses might be used (e.g., 0.75 U/kg). For very mild insulin resistance, a dose of 0.25 U/kg of BW can be used.
12. For ITT, results are depicted as percentage of the initial glucose levels (percentage at $time_X$ = (glucose level value at $time_x$/glucose level value at $time_0$) × 100) in Y-axis versus time (min) in the X-axis. For comparisons among different mouse groups, the Area Under the Curve parameter ($AUC_{glucose}$) is typically used. This parameter is obtained by calculating the area generated by the glucose values of glucose disappearance curve versus time for a period of 90 min. For the ITT, as the most relevant values to asses differences among mice are those within the first 30 min of insulin infusion, $AUC_{glucose}$ parameters might also be calculated at 45 min.

Acknowledgments

This work was supported by grants from the Carlos III Health Institute (CP10/00555, PI13/00834) and from the European Regional Development Fund (FEDER). H. González-Navarro is a "Miguel Servet" Program researcher, and A. Vinué received salary support from Proyecto Paula.

References

1. Benetos A, Thomas F, Pannier B et al (2008) All-cause and cardiovascular mortality using the different definitions of metabolic syndrome. Am J Cardiol 102:188–191
2. Zambon S, Zanoni S, Romanato G et al (2009) Metabolic syndrome and all-cause and cardiovascular mortality in an Italian elderly population: the Progetto Veneto Anziani (Pro.V.A.) Study. Diabetes Care 32:153–159
3. Beckman JA, Creager MA, Libby P (2002) Diabetes and atherosclerosis: epidemiology, pathophysiology, and management. JAMA 287: 2570–2581
4. Nunn AV, Bell JD, Guy GW (2009) Lifestyle-induced metabolic inflexibility and accelerated ageing syndrome: insulin resistance, friend or foe? Nutr Metab (Lond) 6:16
5. Burks DJ, de Mora JF, Schubert M et al (2000) IRS-2 pathways integrate female reproduction and energy homeostasis. Nature 407:377–382
6. Gonzalez-Rodriguez A, Mas Gutierrez JA, Sanz-Gonzalez S et al (2010) Inhibition of PTP1B restores IRS1-mediated hepatic insulin signaling in IRS2-deficient mice. Diabetes 59:588–599
7. Gonzalez-Navarro H, Vinue A, Sanz MJ et al (2013) Increased dosage of Ink4/Arf protects against glucose intolerance and insulin resistance associated with aging. Aging Cell 12: 102–111
8. Gonzalez-Navarro H, Vinue A, Vila-Caballer M et al (2008) Molecular mechanisms of atherosclerosis in metabolic syndrome: role of reduced IRS2-dependent signaling. Arterioscler Thromb Vasc Biol 28:2187–2194
9. Andrikopoulos S, Blair AR, Deluca N et al (2008) Evaluating the glucose tolerance test in mice. Am J Physiol Endocrinol Metab 295: E1323–E1332
10. Ayala JE, Samuel VT, Morton GJ et al (2010) Standard operating procedures for describing and performing metabolic tests of glucose homeostasis in mice. Dis Model Mech 3: 525–534
11. Carvalho CR, Brenelli SL, Silva AC et al (1996) Effect of aging on insulin receptor, insulin receptor substrate-1, and phosphatidylinositol 3-kinase in liver and muscle of rats. Endocrinology 137:151–159
12. Macotela Y, Boucher J, Tran TT et al (2009) Sex and depot differences in adipocyte insulin sensitivity and glucose metabolism. Diabetes 58:803–812

Chapter 18

Wire Myography to Study Vascular Tone and Vascular Structure of Isolated Mouse Arteries

Lara del Campo and Mercedes Ferrer

Abstract

Atherosclerosis is characterized by endothelial dysfunction and alterations in vascular reactivity, which can be investigated by wire myography. The method allows ex vivo monitoring of the transversal isometric tension developed by a vessel segment in response to different pathophysiological stimuli. Here we describe in detail how to use the wire myograph to evaluate endothelial function and vasoconstrictor or vasodilator properties of the vessel, as well as to identify and characterize different factors and molecular pathways that control vascular tone. We also describe how to use the wire myograph to analyze biomechanical and passive properties of vessels such as diameter and elasticity.

Key words Wire myograph, Vascular reactivity, Endothelial function, Vascular tone, Isolated mouse arteries, Vascular structure

1 Introduction

Wire myography is a laboratory technique used to study vascular function in ex vivo mounted vessels. The method was developed in 1977 by Mulvany and Halpern [1] to measure vasomotor responses (i.e., vasoconstriction or vasodilation) to different substances or procedures. Vessel segments are maintained in an organ bath setting and mounted between two wires that go through the lumen. One wire is connected to a force transducer that records the isometric tension developed by the vessel, and the other is connected to a micrometric screw that allows setting up the initial distension.

Wire myography is a very useful and reliable technique to evaluate endothelial function and vasoconstrictor or vasodilator properties of the vessel, as well as the participation of different factors and molecular pathways in the control of vascular tone. Endothelial function, one of the most studied vessel functions using wire myography, is typically determined by performing relaxation–response curves to acetylcholine in vessel segments precontracted

Vicente Andrés and Beatriz Dorado (eds.), *Methods in Mouse Atherosclerosis*, Methods in Molecular Biology, vol. 1339, DOI 10.1007/978-1-4939-2929-0_18,

with a vasoconstrictor (e.g., phenylephrine). Acetylcholine induces the release of nitric oxide (NO) in the endothelial cells, which diffuses within the vessel wall and causes vasodilation by inducing the relaxation of smooth muscle cells [2]. NO has other important effects, such as inhibition of platelet activation and aggregation, reduction of leukocyte adhesion, and inhibition of endothelial cell permeability, vascular smooth muscle cell proliferation, and endothelial cell apoptosis. Importantly, in the presence of endothelial cell dysfunction, NO release induced by acetylcholine is inhibited and acetylcholine acts on vascular smooth muscle cells directly causing constriction [3].

The nervous system also plays a crucial role in the regulation of vascular tone in some vascular beds, specifically in resistance vessels [4]. The net vasomotor effect of perivascular nerve activation is the result of the integration of vasoconstrictor and vasodilator influences [5–7], such as adrenergic and nitrergic innervations, respectively. Neuronal function can also be analyzed in the wire myograph by performing frequency–response curves to electrical field stimulation.

Vascular caliber and therefore vascular resistance are modulated not only by vascular tone but by vascular structure as well. Wire myography can also be used to analyze passive biomechanical properties of vessels, by performing passive diameter–tension curves [8].

This chapter describes how to perform wire myography experiments to analyze endothelial function, phenylephrine-induced contractile responses, electrical field stimulation-induced responses, and some passive biomechanical properties of vessels (such as diameter and elasticity) (*see* **Note 1**).

2 Materials

1. Stereomicroscope, preferably equipped with an eyepiece reticule.
2. Dissection instruments: microdissection scissors, a pair of fine forceps, regular surgical forceps and scissors, and a small screwdriver (Fig. 1).
3. Wires of 2 cm in length and either 40 μm of diameter (for arteries between 200 and 1000 μm) or 25 μm of diameter (for arteries with inner diameters less than 200 μm) (Fig. 1).
4. Wire myograph (e.g., Multi Wire Myograph System, Model 620M, Danish Myo Technology, DMT) (Fig. 2) (*see* **Note 2**).
5. Data acquisition hardware unit (e.g., PowerLab, ADInstruments) (*see* **Note 3**).
6. Computer with specific installed software (e.g., LabChart 7, ADInstruments) (*see* **Note 4**).

Fig. 1 Tools to dissect and mount the vessels into the wire myograph. The small petri dish contains 2-cm-long wires. The blue mark on the petri dish marks a length of 2 cm to facilitate cutting the wires

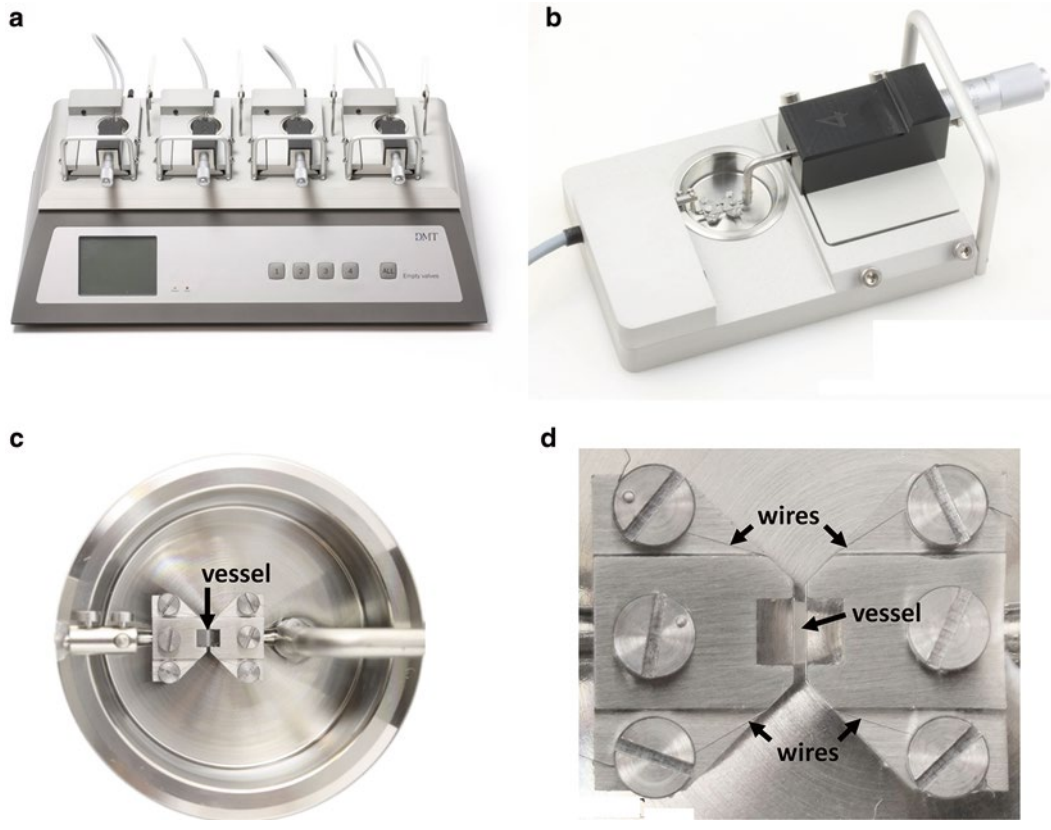

Fig. 2 The wire myograph. (**a**) DMT multi-chamber 620M Wire Myograph. The wire myograph interface holds four myograph units. (**b**) Each myograph unit contains a force transducer (*left*) and a micrometer (*right*), which are both connected to corresponding jaws to support the vessel inside the chamber. (**c**) Detail of the chamber with the jaws and a mounted vessel segment. The upper and lower jaws are connected to the micrometer screw and to the force transducer, respectively. (**d**) Detail of the jaws, screws, wires, and a mounted vessel segment. Adapted from www.dmt.dk with permission from Danish Myo Technology A/S

7. Vacuum connection or vacuum device (*see* **Note 5**).
8. Krebs–Henseleit (KH) solution: 115 mM NaCl, 2.5 mM $CaCl_2$, 4.6 mM KCl, 1.2 mM KH_2PO_4, 1.2 mM $MgSO_4$, 25 mM $NaHCO_3$, 11.1 mM glucose, and 0.01 mM EDTA (*see* **Note 6**).
9. Bath with heating system (for incubations at 37 °C) (*see* **Note 7**).
10. Carbogen gas mixture (95 % O_2 and 5 % CO_2), tubing, and connectors (*see* **Note 8**).
11. Saturated KCl solution (4.61 M at 20 °C).
12. Acetylcholine. Prepare stock solutions: 0.1 μM, 1 μM, 10 μM, 0.1 mM, 1 mM, and 10 mM, dissolved in KH solution.
13. Phenylephrine or norepinephrine. Prepare stock solutions: 0.1 μM, 1 μM, 10 μM, 0.1 mM, 1 mM, and 10 mM, dissolved in KH solution (*see* **Note 9**).
14. Other drugs (*see* **Note 10**).
15. Accessories for analyzing responses to electrical field stimulation: electrical stimulator (e.g., CS14-4BO, Cibertec), plastic mounting jaws, and connecting cable for the wire myograph (they should be mounted in each channel before mounting the vessels).

3 Methods

3.1 Vessel Dissection

1. Before starting, please *see* **Notes 11** and **12**.
2. Euthanize mice by CO_2 inhalation.
3. Excise the artery immediately without stretching it (*see* **Note 13**).
4. Place artery immediately in 4 °C KH solution (*see* **Note 14**).
5. Remove connective tissue (*see* **Note 12**).
6. Cut the artery into ~2-mm-long segments.
7. Renew 4 °C KH solution, to minimize the artery being in contact with rests of blood (*see* **Note 15**).
8. Try to eliminate blood clots inside the artery, if present (*see* **Note 16**).
9. If desired, remove the endothelium (*see* **Note 17**) as follows:
   (a) For mouse aorta: place the artery segment on a paper tissue, and let the inner walls touch. Pull the artery with a piece of absorbent laboratory countertop paper, making the segment roll throughout one turn, and place the artery again in cold KH solution.
   (b) For smaller vessels: introduce a thin stick or even a human hair through the arterial lumen and gently rub the luminal surface [9].

3.2 Vessel Mounting

1. Switch on the wire myograph.
2. Fill in the chamber with 5 mL of KH solution.
3. Switch on the heater in the wire myograph display and set it at 37 °C (*see* **Note 18**).
4. Put 500–600 mL of KH solution in the heated bath and continuously bubble it with carbogen. This buffer will be used to wash and refill the chambers during the experiment.
5. Open the carbogen supply (*see* **Note 19**).
6. Cut a 2-cm-long wire and pass it through the lumen of the artery segment minimizing contact with the artery wall.
7. Take the wire with the artery and place it into one of the chambers of the myograph, between the two jaws, alongside the space for the artery (Fig. 3a).
8. Clamp the wire with the jaws by moving the jaws closer (Fig. 3b). One of the jaws is fixed and connected to the force transducer, and the other is mobile. The distance between the jaws can be changed with a micrometric screw connected to the mobile jaw. Let the jaws come together to clamp the wire.
9. Wrap the wire clockwise around the screws of the jaw and clamp it by closing the screws (Fig. 3c and *see* **Note 20**).

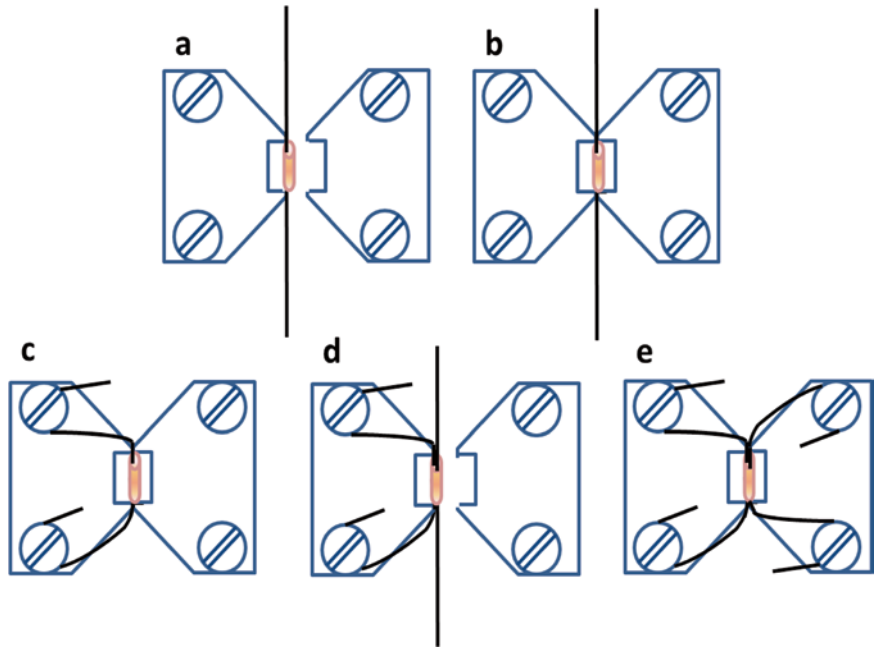

Fig. 3 Mounting procedure. See details in Subheading 3.2

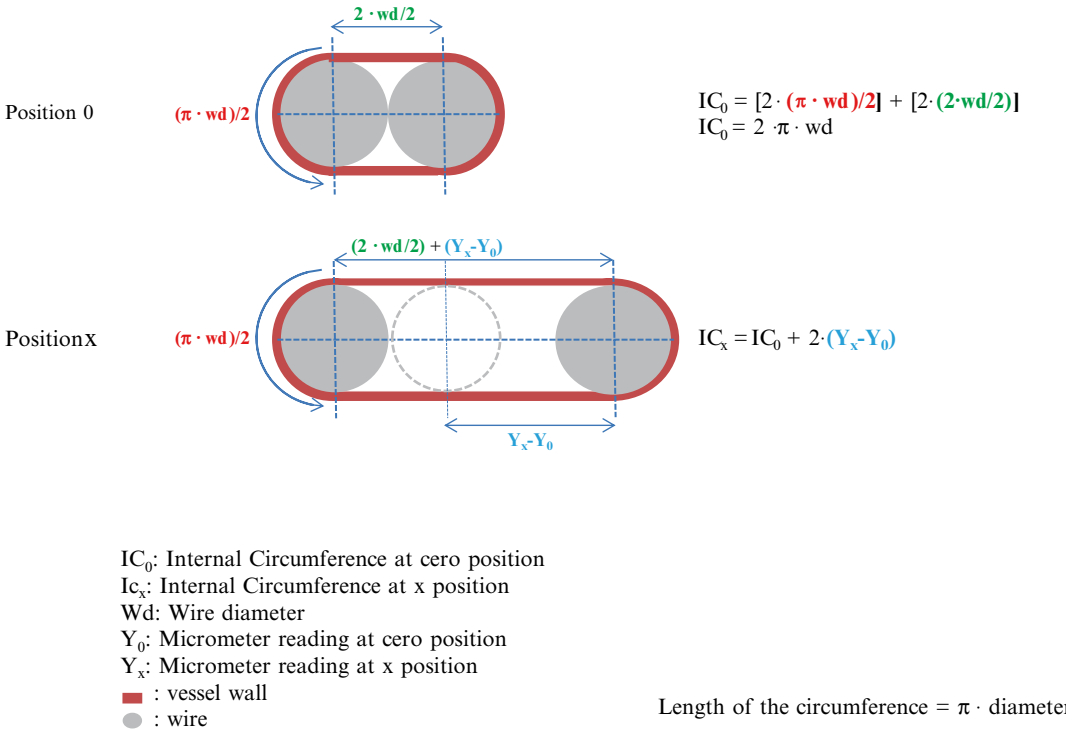

Fig. 4 Procedure to calculate the Internal Circumference. The diagram shows how to measure the length of the internal circumference of the artery mounted on the wire myograph. The DMT normalization module of LabChart automatically calculates it according to these principles. See details in **Note 22**

10. Separate the jaws and carefully insert another 2-cm-long wire through the lumen of the artery minimizing contact with the wall (Fig. 3d).
11. Clamp the second wire by moving jaws together again. Wrap clockwise and clamp the second wire to the screws of the second jaw (Fig. 3e).
12. Move away the wires so that they are as close to each other as possible but not touching.
13. Place the chamber into its place in the wire myograph and plug the transducer cables into the back of the wire myograph.
14. Renew the 5 mL of KH solution using 37 °C bubbled KH solution (*see* **Note 21**).
15. Cover each channel with its chamber cover, put the plastic funnels, and wait for 30 min approximately to allow stabilization of the vessels and bath heating before starting the normalization protocol.

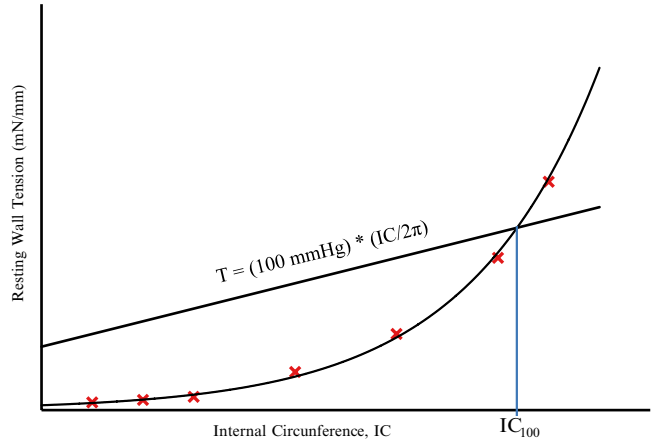

Fig. 5 Curve fitting for the determination of IC100. Internal Circumference (IC) corresponding to an effective pressure of 100 mmHg (IC_{100}) is estimated by the insertion point of the exponential fitting curve of the different points on the normalization procedure and the isobar at 100 mm Hg according to the Laplace´s equation. This curve and the IC_{100} value is automatically plotted and calculated during the normalization procedure by the DMT normalization module of LabChart, which gives the micrometer reading value in which the artery should be set to perform the experiment. See details in **Note 22**

3.3 Normalization

1. Before starting, please *see* **Note 22**.
2. Switch on the computer and open your LabChart settings file (*see* **Note 23**).
3. Press the "Start" button on the "Chart View" window to run the experiment and start recording. Save the experiment as a "LabChart data file," with a new name to avoid overwriting the original settings file (*see* **Note 24**).
4. Move very slowly the jaws together until the wires just touch. At this point, the force displayed on the wire myograph will suddenly fall to a negative reading (*see* **Note 20**). Then slightly move the jaws apart to just separate the wires. This position corresponds to the zero force point where the artery wall is not subjected to any force.
5. In the myograph display, set the chamber force to the zero point. Force recorded in the LabChart should automatically change to zero.
6. In LabChart, press the "DMT" flap, go to "Normalization Settings," and fill the boxes as indicated below:

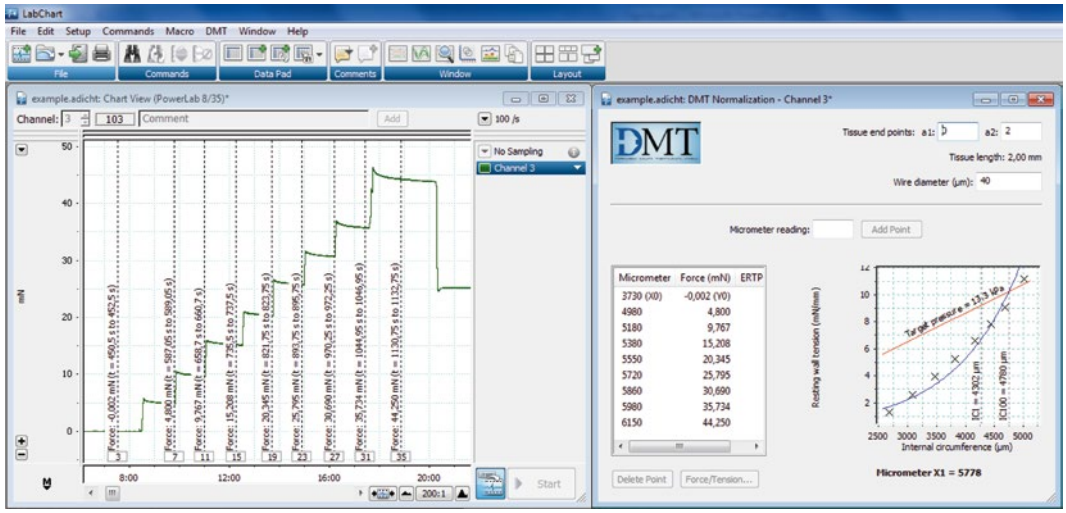

Fig. 6 Example of output recordings during the normalization procedure. *Left*: The Chart View window shows the force recordings along the time in one channel. *Right*: The DMT Normalization window shows the data of force and micrometer readings, and also plots the automatically-calculated internal circumference and resting wall tension data. When the artery has reached the tension corresponding to the target pressure of 100 mmHg (13.3 KPa), the program gives a definitive Micrometer X1 value. The artery is then set to the distension corresponding to the Micrometer X1 value (IC1 = 0.9 · IC100). The software used is LabChart 7 from ADInstruments. Reproduced with permission from ADInstruments

(a) "Eyepiece calibration (mm/div)": 1.

(b) "Target pressure (KPa)": 13.3 (*see* **Note 25**).

(c) "IC1/IC100": 0.9 (*see* **Note 26**).

(d) "Online averaging time (seconds)": 2.

(e) "Delay time (seconds)" (*see* **Note 27**): 60.

(f) The window also offers the possibility of playing a sound when the delay time has been completed.

7. Press the "OK" button on the "DMT Normalization Settings" window. The window will close.

8. Click the "DMT" flap and select the channel of interest. The normalization window for the channel will open (channel 3 in the example of Fig. 6). Fill in the boxes for the constant values (*see* **Note 28**):

   (a) "Tissue end point a1": 0

   (b) "Tissue end point a2": 2

   (c) "Wire diameter (µm)": 40

9. Introduce the actual micrometer reading value in the box and press "Add Point." This first value is the zero point, the first

point of the exponential fitting curve for normalization. Wait for the 60-s delay until the program records the force measurement corresponding to the first point, which should be close to zero. After this time, the box for "micrometer reading" values becomes active again (Fig. 6).

10. Slightly stretch the vessel by moving jaws apart until you see an increase in the force in the wire myograph display (*see* **Note 29**). Introduce the value of the micrometer in the box and press "Add Point." Wait for the 60-s delay time.
11. Repeat this step until the program gives you the "Micrometer X1" value (the micrometer reading corresponding to the 0.9 of the estimated IC_{100}) (*see* **Note 30** and Fig. 6).
12. Set micrometric screw to the "Micrometer X1" value.
13. Change KH solution buffer on each chamber. Wait for 15 min before starting to induce vasomotor responses in order to let the arteries stabilize at their new distension.

3.4 Assessment of Vessel Viability (See Note 31)

An example of the output recordings for a contractile response to KCl is shown in Fig. 7.

1. Add 120 mM KCl and let the artery contract for 5 min.
2. Wash out four times with fresh, warm, and bubbled KH solution.

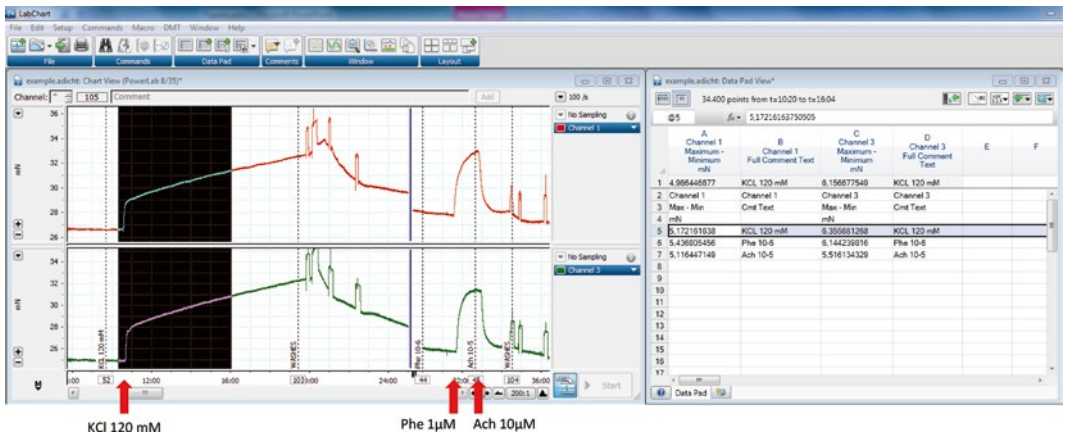

Fig. 7 Example of output recordings during the assessment of vessel viability and endothelium integrity. *Left*: Chart View window showing the force recordings along the time in two channels. Vertical dotted lines correspond to comments that are entered by the operator to indicate the substance added before any induced vasomotor effect. Shown from left to right are the contraction induced by 120 mM KCl, the relaxation after washes, the precontraction induced by 1 µM phenylephrine (Phe 10-6), and the relaxation induced by 10 µM acetylcholine (Ach 10-5). *Right*: Data Pad View window showing data measurements in each channel and the corresponding comments. The black area in the chart window shows the raw data selected to calculate the maximum-minimum force values in the Data Pad. Corresponding counted values are in the row highlighted in grey in the Data Pad view. The software used is LabChart 7 from ADInstruments. Reproduced with permission from ADInstruments

3. Wait ≈15 min to let the artery recover its basal tone. Some vessels may need more time or more washes in order to recover the basal tone (*see* **Note 32**).

3.5 Assessment of Endothelium Integrity (See Note 33)

An example of the output recordings of the procedure for the assessment of the endothelium integrity is shown in Fig. 7.

1. Add 1 μM phenylephrine (final concentration) to the bath. Let the artery contract until it has reached a stable contraction (*see* **Notes 34** and **35**).
2. Add 10 μM acetylcholine (final concentration) to the bath. Let the artery vasodilate until it reaches its maximum level of vasodilation (*see* **Notes 33** and **36**). Wash out 3–4 times with fresh, warm, and bubbled KH solution. Wait around 15 min to let the artery recover its basal tone.
3. Measure both the contraction (force from basal tone to maximum contraction) and the relaxation (force from maximum contraction to the end of the relaxation induced by acetylcholine). Calculate the % of relaxation induced by acetylcholine in relation to the previous contraction induced by phenylephrine.

3.6 Vasodilator Response to Acetylcholine

To study acetylcholine-induced vasorelaxation, vessels are first precontracted with phenylephrine. An example of the output recordings for a vasodilation–response curve to acetylcholine is shown in Fig. 8.

1. Mark in the comments box of the Chart View window, 1 μM phenylephrine (or the corresponding dose, in the following steps) just before adding phenylephrine (*see* **Note 37**).
2. Add 1 μM phenylephrine (final concentration) to the bath. Let the artery contract until it has reached a stable contraction (*see* **Notes 34** and **35**).
3. Mark and add 0.1 nM acetylcholine (final concentration). Let the artery dilate until a steady response has been reached (*see* **Note 38**).
4. Repeat **step 3** with increasing concentrations of acetylcholine (1 nM, 10 nM, 0.1 μM, 1 μM, and 10 μM, final concentrations in the bath) (*see* **Note 39**).
5. Wash three times with fresh KH solution.
6. Let the artery stabilize for at least 30 min before performing any additional procedure.

3.7 Contractile Response to Phenylephrine

An example of the output recordings for a contractile response to phenylephrine is shown in Fig. 9.

1. Mark in the comments box of the Chart View window, 1 nM phenylephrine (or the corresponding in the following steps) just before adding phenylephrine (*see* **Note 37**).

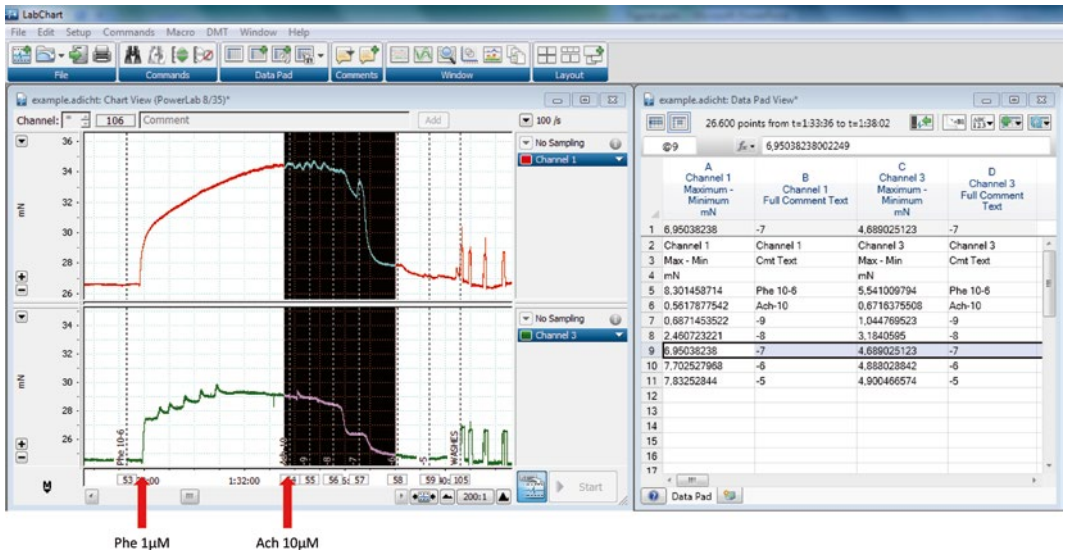

Fig. 8 Example of output recordings during the vasodilator response to acetylcholine to analyze endothelial function. *Left*: Chart View window showing the force recordings along the time in two channels. Vertical dotted lines correspond to comments that are entered by the operator to indicate the substance added before any induced vasomotor effect. Shown from left to right are the precontraction induced by 1 µM phenylephrine (Phe 10-6), and a cumulative concentration-response vasodilator curve to acetylcholine (Ach-10, -9, -8, -7, -6, and -5). *Right*: Data Pad View window showing force measurements and corresponding comments in each channel. The black area in the chart window shows the raw data selected to calculate in Data Pad the vasodilation induced by 0.1 µM acetylcholine. Corresponding counted values are in the row highlighted in grey in the Data Pad view. The software used is LabChart 7 from ADInstruments. Reproduced with permission from ADInstruments

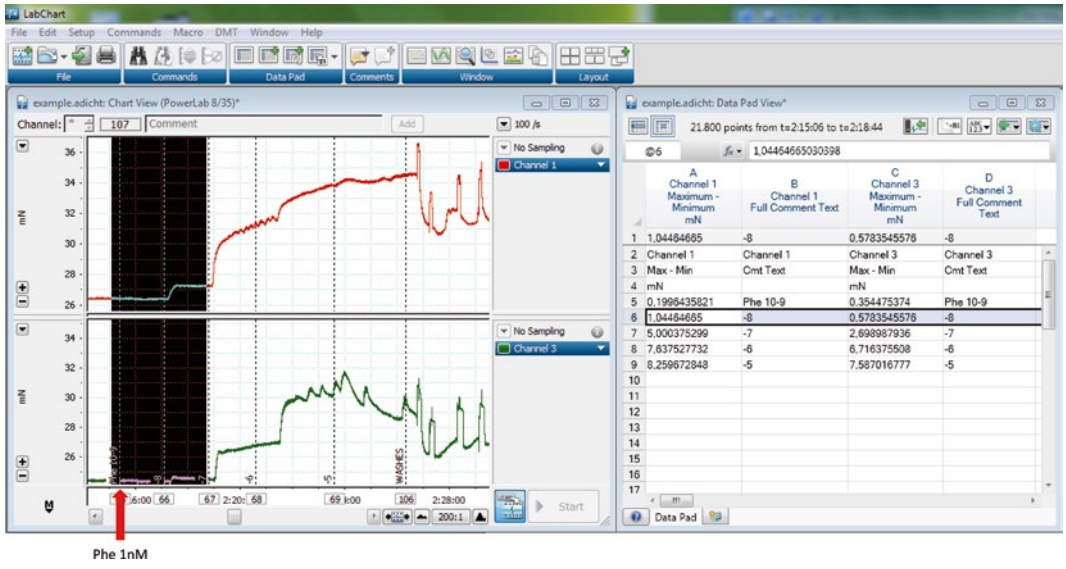

Fig. 9 Example of output recordings during the vasoconstrictor response to phenylephrine to analyze contractile function. *Left*: Chart View window showing the force recordings along the time in two channels. Vertical dotted lines correspond to comments that are entered by the operator to indicate the substance added before any induced vasomotor effect. The plot shows a cumulative contractile concentration-response curve to phenylephrine (Phe -9, -8, -7, -6, and -5). *Right*: Data Pad View window showing force measurements and corresponding comments in each channel. The black area in the chart window shows the raw data selected to calculate in Data Pad the vasoconstriction induced by 10 nM Phenylephrine. Corresponding counted values are highlighted in grey in the Data Pad view. The software used is LabChart 7 from ADInstruments. Reproduced with permission from ADInstruments

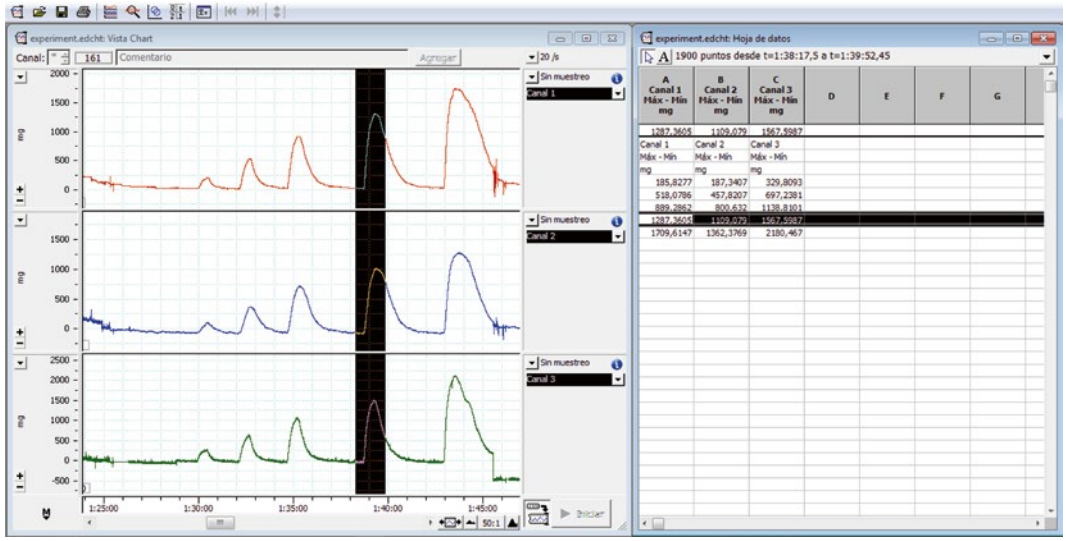

Fig. 10 Example of output recordings during a frequency-response curve to electrical field stimulation to analyze the innervation function. *Left*: force recordings along the time in three channels showing from left to right the non-cumulative contractions induced by 1, 2, 4, 8 and 16 Hz electrical stimuli (30 seconds each). *Right*: force measurements in each channel. The black area in the left window shows the raw data selected to calculate the vasoconstriction induced upon stimulation with 8 Hz. Corresponding counted values are highlighted in black in the right window. Force values are given in mg instead of mN. The software used is Chart from eDAQ. Reproduced with permission from eDAQ

2. Add 1 nM phenylephrine (final concentration) to the bath. Let the artery contract until it has reached a stable contraction (*see* **Note 35**).
3. Repeat the **steps 1** and **2** with increasing concentrations of phenylephrine (10 nM, 0.1 μM, 1 μM, and 10 μM, final concentrations in the bath).
4. Wash three times with fresh KH solution.
5. Let the artery stabilize for at least 30 min before performing any additional procedure.

3.8 Contractile Response Induced by Electrical Field Stimulation (See Note 40)

An example of the output recordings for a frequency–response curve to electrical field stimulation is shown in Fig. 10.

1. Mount the plastic mounting jaws on the chambers.
2. Set the following parameters in the electrical stimulator: 30 s of stimulation at 200 mA, 0.3 ms (pulse duration), and an interval of 1 min between each stimulus (*see* **Note 41**).
3. Connect the electrodes to the jaws.
4. Enter 1 Hz in the comments box of the "Chart View" window (or the corresponding frequency, in the following steps) just before applying electrical stimulation (*see* **Note 37**).

5. Set the frequency in the electrical stimulator to 1 Hz and switch on the stimulator.
6. After the stimulus has finished (each stimulus lasts 30 s), set the frequency to 2 Hz.
7. Repeat **step 6** for the next frequencies (4, 8, and 16 Hz).
8. Wash once or twice with fresh KH solution.
9. Let the artery stabilize for at least 30 min before performing any additional procedure.

3.9 Counting Responses and Data Analysis

For better understanding the method, please *see* **Note 42**. Responses can be semiautomatically counted using the Data Pad tool in LabChart.

1. Press the "Data Pad View" button on the "Data Pad" panel. A new window will open. Each column can be arranged to show given data of each channel (Figs. 7, 8, and 9).
2. Click on the first cell of column A and select "statistics" and "maximum–minimum." Also select "calculate from source channel: channel 1."
3. Do the same in following columns for channels 2–4.
4. In column E, "comments" and "Full Comment Text" can be selected for a given channel in order to associate each measurement with the corresponding dose.
5. Go to the "Chart View" window and select the recordings corresponding to the response induced by a given dose, taking care to cover the data just before adding the dose and the maximum response induced by the drug. Press the button "Add to Data Pad" in the "Data Pad" panel (or press Control + D). The difference between the maximum and the minimum force values of the selected data will appear in the corresponding column for each channel in the "Data Pad" window (*see* **Note 43**).
6. These data can be copied into other data manager programs to analyze and plot them.

3.10 Passive Properties (See Note 44)

1. After normalization, the program gives the IC_{100} value (the internal circumference corresponding to a transmural pressure of 100 mmHg) (*see* **Note 22**). The internal diameter corresponding to an IC_{100} (D_{100}) can be calculated from the following equation: diameter = circumference/π. Thus, $D_{100} = IC_{100}/\pi$.
2. Take the data of micrometer reading vs. force from the DMT Normalization window for each channel (Fig. 6).
3. Calculate the diameter corresponding to each micrometer reading. Internal circumference with wires just touching (at zero position) is considered to be equal to $2 \times \pi \times$ wire diameter = 205.664 µm (when using wires of 40 µm diameter).

Thus, internal diameter for each micrometer reading is equal to $205.664 + 2 \times$ (micrometer reading at position x – micrometer reading at position zero)$/\pi$ (*see* **Note 22**).

4. With this data, you can plot the diameter–tension curve.
5. Calculate the distension fraction corresponding to each micrometer reading using the following equation: distension fraction = diameter/D_{100}.
6. With this data, you can plot the distension–tension curve.

4 Notes

1. Many other agents and inhibitors can be used to analyze the participation of the corresponding factor in vasomotor responses.
2. This wire myograph allows the testing of four vessels at the same time.
3. It should be connected within the wire myograph and the computer to amplify and filter the analogic signal from the wire myograph.
4. LabChart 7 records and processes the data obtained with the wire myograph. Some extra features can be added to this software, such as the DMT Normalization Module, which is very useful to carry out the normalization protocol (*see* Subheading 3.3).
5. The vacuum is used to remove the buffer in the chambers when washing.
6. This buffer is used at 4 °C to maintain the vessels before mounting and can be stored for 24 hours at 4 °C. During the experiment, vessels are submerged in 37 °C KH solution continuously bubbled with carbogen. For one single experiment with four vessels, around 700 mL of KH solution may be necessary. The duration of the whole experiment and the nature of the substances used can increase the amount of KH solution needed up to 2 L.
7. The bath heater allows maintaining the KH solution warm, ready to use over the vessel, during the experiment.
8. Carbogen maintains KH solution at pH 7.4 and keeps the buffer oxygenated. Tubes will bring the gas to the wire myograph and to the KH solution in the bath heater.
9. Both norepinephrine and phenylephrine are commonly used as contractile agents, but other vasoconstrictors can be used. The election of any of these compounds will depend on the nature of the investigation, the vascular bed under study, and the animal model used. Norepinephrine is an unspecific adrenoceptor

agonist and it is a good option to use as contractile agent in mesenteric superior and resistance vessels, while phenylephrine is a specific α_1-adrenoceptor agonist commonly used in mouse or rat aorta. On the other hand, the target of phenylephrine is more specific than the target for norepinephrine; thus the contraction induced by phenylephrine will avoid interactions with other vasodilator adrenoceptors, such as the β-adrenoceptors. However, the use of norepinephrine allows to study a more integrated and physiological response to all the adrenergic molecular machinery. In our experience, the use of norepinephrine works well in the mesenteric bed (which is densely innervated and, thus, a good choice to study the role of innervation), but it is difficult to manage in the aorta, where high doses of norepinephrine can induce in mice vasodilation instead of vasoconstriction.

10. Depending on the experiments, other drugs may be used to activate or inhibit target factors. For example, to study the role of NO, inhibitors of NO synthase (to analyze the involvement of NO in any specific response) or NO donors (to analyze the sensitivity to NO) can be used.

11. The method described here uses mouse aorta or mesenteric arteries, although other vascular beds from this or other species can also be analyzed. The choice of which vascular bed is best to study will depend on the nature of the investigation and the size of the animal model used. Regarding the size, the wire myograph was designed to study vessels from ≈50 to ≈600 μm. However, bigger arteries (even up to 5–10 mm in diameter) can be studied in the wire myograph by changing the mounting supports, i.e., substituting the jaws by pins.

    Regarding the nature of the investigation, it must be noted that the endothelium function is important for local control of vascular tone, while innervation plays a crucial role in the control of global peripheral resistances [4]. Since small arteries constitute the main source of resistance to blood flow in the vascular system [10], it would be a good choice to use small mesenteric vessels in studies focused on the role of innervation and hypertension. For studies concerning more local alterations, such as aneurysms and atherosclerosis, the vessels in which these alterations have been observed should be used. In fact, the most commonly used vessel for mouse atherosclerosis studies is the aorta, which is a conductance vessel easy to mount. However coronary and cerebral arteries and almost any other artery can also be studied with the wire myograph as long as they fulfill the size requirements and it can be properly excised.

12. For wire myography, the maintenance of the whole tissue integrity is mandatory to preserve vasomotor responses. Thus, it is important to avoid excessive manipulation of the artery to

leave it intact, in particular the segments that are going to be mounted. Another important tip is not to stretch the artery. The artery should preferably be cleaned of connective tissue and perivascular fat before being mounted, but the researcher should come up to equilibrium between minimal manipulation and maximal cleanliness. Perivascular fat can also modulate vascular tone. Thus, unless it is the focus of the study, it is preferable to remove it out completely to avoid differences in the responses due to different amounts of fat.

13. It is advisable to excise the artery immediately after sacrifice, preferably while the heart is still beating, in order to avoid the formation of clots inside the artery. These clots can be sometimes hard to extract, and if they are retained into the artery, they can cause damage to the endothelium. In aortas, the clot can be removed by carefully shaking the artery while submerged in physiological solution. Careful perfusion of the artery with saline solution prior to excision is another option, but this may remove or damage the endothelium.
14. Cold saline solution (0.9 % sodium chloride solution) can also be used to submerge the arteries just after dissection. However, arteries should be moved to cold KH solution as soon as possible because saline does not contain an anticoagulant.
15. In these conditions, arterial segments can be maintained at 4 °C during a few hours before mounting them, although it is always better to mount the vessels just after dissection. Besides, it must be noted that within a single set of experiments, both the control and the target samples should be managed in the same conditions.
16. Blood clots in large arteries such as the aorta can be removed by gently shaking the vessel segment in KH solution buffer trying to avoid contacts with the walls or the bottom of the recipient. This cannot be done in small resistance arteries.
17. Removal of the endothelium, as well as mounting, needs some training. It should be done very gently to avoid damaging the underlying smooth muscle layer and thus preserve the contractile properties, but hard enough to avoid any acetylcholine-induced vasodilation (*see* **Note 33**).
18. The whole system will take around 30 min to heat up, but you can mount the vessel segments while reaching 37 °C.
19. The amount of bubbling occurring in each chamber can be regulated by needle valves on the back of the wire myograph. Bubbling should not be too strong in order to avoid interference on the force measurements.
20. Wires should be screwed quite tight, to avoid undue compliance, but be careful not to tighten them too much or they will break.

This could also damage the jaws. Besides, jaws should not be pressed against each other too much, just the enough to clamp the wires. Force should not fall beyond −50 mN.

21. Chambers can be drained individually or all together by pressing the corresponding buttons in the front of the myograph interface.

22. Normalization is used to standardize the initial conditions of the vessels, which should mimic the basal physiological distension. Resting tension strongly determines the amount of the vasomotor responses induced by the vessel [11]. Thus, it is very important that all the vessels are set up to the same initial conditions, which can be specifically estimated for each segment. Normalization allows estimating the internal diameter when the vessel is fully relaxed under a transmural pressure of 100 mmHg (the IC_{100} value).

    The procedure for normalization consists of stretching stepwise a mounted vessel and recording the force exerted by the vessel at each point of distension. Force is automatically recorded by the DMT Normalization Module in LabChart, while distension (in length) is read from the micrometric screw and keyed by the operator at each step. Internal circumference and thus internal diameter (circumference = π × diameter) are calculated from the difference between two readings from the micrometric screw and the known diameter of the mounted wires (Fig. 4).

    Since wall tension is the measured force divided by the wall length (usually 2 mm) and the thickness of the vessel is constant throughout the experiment, the effective pressure corresponding to each distension is automatically calculated using the Laplace equation [tension = (pressure × radius)/thickness]:

$$\text{Effective Pressure} = \text{Wall Tension} / \left(\text{Internal Circumference} / 2\pi \right).$$

    The stepwise stretching is stopped when the effective pressure raises 100 mmHg. An exponential curve is fitted to the internal circumference/effective pressure data points. IC_{100} is the point of intersection between the exponential curve fit and the isobar corresponding to 100 mmHg: $T = (100\ \text{mmHg}) \times (\text{internal circumference}/2\pi)$ (*see* Fig 5).

23. Before the first experiment, the whole system (myograph and software) should be calibrated according to manufacturer instructions. After calibration, you will have a LabChart settings file (*.adiset), which you will use every time you run a new experiment. Once this file is opened to start an experiment, it should be now saved as a LabChart data file (*.adicht), in order to maintain the original LabChart settings for future experiments until a new calibration is performed.

24. It is advisable to save the document several times during the experiment.
25. 13.3 KPa corresponds to a target effective pressure of 100 mmHg.
26. The distance between the wires is arranged to the 0.9 fraction of the IC_{100} value for each vessel. This fraction is usually set at the point in which contractile force produced by the artery is maximal, in order to enhance the resolution of the technique. The optimal IC_{100} fraction can change between vascular bed and species. It is usually set to 0.9 and we also set it to 0.9 for mouse aorta.
27. This is the delay on the time in which the program acquires the force measurement after entering the micrometer reading at a given point in order to draw the exponential curve fitting. This delay is set up to 1 min to allow the vessel to stabilize after stretching it. The vessel develops a myogenic tone in response to stretch. This myogenic tone disappears after some seconds.
28. The program automatically calculates the segment length from the given eyepiece calibration (mm/div) value stated in the DMT Normalization Settings window and the a1 and a2 tissue end point values in the corresponding channel normalization window. However, if the vessels are always cut into 2-mm-long segments, then it is easier to set the eyepiece calibration (mm/div) in 1, the tissue end point a1 in 0, and tissue end point a2 in 2. The 40-μm-diameter wire is usually used for vessels ranging between 200 and 1000 μm in diameter. For smaller vessels, a 25-μm-diameter wire can be used. In this case, it should be indicated here.
29. The experience will give the operator an idea of the amount of stretch that will have to apply in each step. In the first step, the increase in the distance between the wires is usually the bigger. In our experience with adult mouse aortas, we initially stretch the artery up to ≈4–5 mN and then increase the distension 5 mN each time. Usually the normalization finishes when the artery reaches ≈35–40 mN.
30. The program automatically plots the values as they are recorded (Fig. 5). During the process, an "(extrapolated result)" for the "Micrometer X1" value appears below the chart. This value shows where the micrometer should be set to arrange the optimal distension, in this case corresponding to the 0.9 fraction of IC_{100}. When the artery reaches the tension corresponding to an effective pressure of 100 mmHg (13.3 KPa), the plot shows the place of the IC_{100} and IC1 (in this case, $0.9 \times IC_{100}$) values and the final "Micrometer X1" value (Fig. 5).
31. The first part of every protocol consists of assessing the vessel integrity to check whether the vessel has been damaged during

dissection or mounting. A contractile response induced by 120 mM KCl allows to reactivate the mechanical and functional contractile properties of the vessel wall, as well as to check that the tissue is alive and functional. The values of the contraction induced by KCl will be used later to normalize other specific contractile responses.

The concentration of KCl used to perform this first part of the protocol can be optimized depending on the vessel or the animal chosen. For mouse aorta and mesenteric vessels, we typically use 120 mM KCl, while 75–80 mM is a commonly chosen option for rat aortas and mesenteric arteries. The duration of the stimuli should be also standardized, since the contraction usually continues increasing for more than 10 min until it reaches the maximum value. In any event, the range of the normal values for the KCl contraction should be clarified for each set of data in order to be able to detect damaged segments. Some studies have described a characterization of the vasomotor responses in thoracic aorta of the C56/BL/6J mouse [12, 13].

32. Endothelium-denuded vessels usually need more time to recover the basal tone after a contraction.

33. Endothelial cell integrity must be assessed before analyzing responses to vasomodulators. In this step, the viability or the absence of endothelium is checked. For this, relaxation of vessels precontracted with phenylephrine is induced with a single dose of acetylcholine (10 μM). Endothelium can be considered to be intact when acetylcholine fully relaxes the contraction induced by phenylephrine. On the other hand, vessels can be considered free of endothelium when acetylcholine falls to relax the vessel precontracted with phenylephrine.

34. Since aorta and mesenteric arteries do not show spontaneous tone in the wire myograph, arteries should be previously precontracted to analyze vasodilator responses. This applies for both the acute responses, such as the acetylcholine dose response for endothelium assessment or the multiple dose–response curve to acetylcholine. The optimal level of precontraction is the ≈80 % of the maximum contraction, which should be optimized for each preparation. In mouse aorta, 1 μM phenylephrine is usually chosen to precontract.

35. Precontraction usually takes between 3 and 10 min. Spontaneous relaxation is a common problem when using certain contractile agonists in some vessels. If the vessel fails to contract or shows relaxation not due to the addition of the vasodilator agent, a second attempt can be made after washing the vessel with fresh KH solution and letting it recover to its basal tone. However, using another vasoconstrictor should be considered if the problem is frequent.

Additionally, some vessels can undergo vasomotion, usually when contracting. Vasomotion occurs when there are rhythmic oscillations in the vessel tone. Its physiological role and its underlying mechanism remain poorly understood [14]. Counting the responses may be difficult when the vessel has developed vasomotion, so the researcher should decide whether to exclude the arteries undergoing vasomotion from the study or just apply systematic standard criteria to count the responses, such as taking into account the maximum, the minimum, or the midpoint level of tone.

36. This response is usually very quick; it may not take more than 2 min. In endothelium-denuded segments, very small or no effect is observed after acetylcholine addition.
37. This is useful for counting and measuring all the responses at the end of the experiment. *See* Subheading 3.9.
38. The first dose should induce no effect or a very weak effect. This is to be sure that we are covering all the range of vasoreactivity induced by the drug.
39. If maximal resolution of the technique is needed, intermediate doses can be added. As an example:
    (a) Add 5 μL of 1 μM to get 1 nM in the bath.
    (b) Add 2.0 μL of 10 μM to get 5 nM in the bath (intermediate dose).
    (c) Add 2.5 μL of 10 μM to get 10 nM in the bath.
40. Responses to electrical field stimulation can be measured in the wire myograph in order to study the function of perivascular innervation. Neuronal activation is performed by applying frequency–response curves to electrical field stimulation (1, 2, 4, 8, and 16 Hz) (*see* Fig. 10).
41. The 1-min interval between each frequency stimuli is set in order to recover basal tone. In case the vessel needs more time to recover basal tone, this period can be increased. The optimal intensity (mA value) should be supramaximal (0.9 fraction of the intensity in which the maximal response is obtained) and should be previously determined in each vascular bed.
42. To normalize data, contractile response curves are usually expressed as the percent of the tone induced by KCl, whereas vasodilator responses, which are induced after precontracting the vessel segment, are expressed as the percent of dilation with respect to the precontractile tone. However, additional information can be obtained if responses are expressed in absolute values (mN), especially in the case of detecting differences in the response to KCl or differences in the response induced by the agent used to precontract when examining vasorelaxing responses. Dose–response curves are also often expressed and

compared in terms of the EC_{50} (or $logEC_{50}$) and the E_{max} values. EC_{50} is the concentration of agonist that provokes a response halfway between the minimum and the maximum response. E_{max} is the maximum response.

43. Sometimes recordings need to be counted manually to avoid including background noise as a specific signal (which could change the values of maximum or minimum points). In these cases, take the marker from the bottom left corner in the "Chart View" window and place it at any point in the recording. The program will display (at the top right corner of that channel in the "Chart View" window) the value of the difference between the marker and the place where you have positioned the cursor (i.e., place the marker before adding the dose and the cursor at the point of maximum effect of that dose).
44. Data obtained from the normalization procedure can be used to get some information about the passive properties of the vessel, such as the estimated diameter at 100 mmHg (D_{100}), diameter–tension curves (which will give information about the size of the lumen), and distension–tension curves (which will give information about the elasticity of the wall).

Acknowledgments

We thank Erick NTP Bakker for teaching the use of the wire myograph to Lara del Campo. This work was supported by grant to M.F. from the *Fondo de Investigaciones Sanitarias* (PI1100406) and Fondo Europeo de Desarrollo Regional and Comunidad de Madrid (S2013/ABI-2783, "INSPIRA1-CM"). L.C. receives salary support from Instituto de Salud Carlos III (Red de Investigación Cardiovascular, RD12/0042/0028). The CNIC is supported by the Ministerio de Economía y Competitividad and by the Pro-CNIC Foundation.

References

1. Mulvany MJ, Halpern W (1977) Contractile properties of small arterial resistance vessels in spontaneously hypertensive and normotensive rats. Circ Res 41:19–26
2. Ignarro LJ, Buga GM, Wood KS et al (1987) Endothelium-derived relaxing factor produced and released from artery and vein is nitric oxide. Proc Natl Acad Sci U S A 84: 9265–9269
3. Herrmann J, Lerman A (2008) The endothelium: the cardiovascular health barometer. Herz 33:343–353
4. Burnstock G, Ralevic V (1994) New insights into the local regulation of blood flow by perivascular nerves and endothelium. Br J Plast Surg 47:527–543
5. Kawasaki H (2002) Regulation of vascular function by perivascular calcitonin gene-related peptide-containing nerves. Jpn J Pharmacol 88:39–43
6. Vanhoutte PM, Verbeuren TJ, Webb RC (1981) Local modulation of adrenergic neuroeffector interaction in the blood vessel well. Physiol Rev 61:151–247

7. Toda N, Okamura T (2003) The pharmacology of nitric oxide in the peripheral nervous system of blood vessels. Pharmacol Rev 55:271–324
8. Tuna BG, Bakker EN, Van Bavel E (2013) Relation between active and passive biomechanics of small mesenteric arteries during remodeling. J Biomech 46:1420–1426
9. Osol G, Cipolla M, Knutson S (1989) A new method for mechanically denuding the endothelium of small (50–150 microns) arteries with a human hair. Blood Vessels 26:320–324
10. Kreulen DL (2003) Properties of the venous and arterial innervation in the mesentery. J Smooth Muscle Res 39:269–279
11. Dobrin PB (1973) Influence of initial length on length-tension relationship of vascular smooth muscle. Am J Physiol 225:664–670
12. Russell A, Watts S (2000) Vascular reactivity of isolated thoracic aorta of the C57BL/6J mouse. J Pharmacol Exp Ther 294:598–604
13. Horvath B, Orsy P, Benyo Z (2005) Endothelial NOS-mediated relaxations of isolated thoracic aorta of the C57BL/6J mouse: a methodological study. J Cardiovasc Pharmacol 45:225–231
14. Nilsson H, Aalkjaer C (2003) Vasomotion: mechanisms and physiological importance. Mol Interv 3:79–89

Chapter 19

Pressure Myography to Study the Function and Structure of Isolated Small Arteries

Olav L. Schjørring, Rune Carlsson, and Ulf Simonsen

Abstract

Small arteries play an important role in regulation of peripheral resistance and organ perfusion. Here we describe a series of methods allowing measurements in pressurized segments of small arteries from the systemic and coronary circulation of mice as well as other species. The pressure myography techniques described include measurements of wall structure, wall stress, strain, and myogenic tone. The pressurized perfused small arteries also allow evaluation of responses to increases in pressure, flow, and drugs, where the main readout is changes in vascular diameter.

Key words Endothelium, Flow, Microvasculature, Mice, Myogenic tone, Structure, Pharmacology, Pressure, Small arteries, Stiffness

1 Introduction

Small arteries play an important role in regulation of peripheral resistance and organ perfusion [1]. Pressure myography is used to study in vitro vascular tone and structure of small vascular segments under isobaric conditions [2]. The vessel segment studied is cannulated and intraluminally pressurized and hence to a large degree mimics the conditions of the vessel in vivo. For pharmacological purposes, microvascular segments mounted on wire myographs seem advantageous, since they allow several preparations to be studied simultaneously [3]. However, due to the geometry of the pressurized vascular segments, pressure myography bears the closest resemblance to the in vivo conditions, and several studies have provided evidence that functional responses may differ in wire-mounted versus pressurized vascular segments [4, 5]. Therefore, pressure myography remains an invaluable method of investigating basal physiological and pathophysiological alterations in the microvasculature. The technique allows the study of the effects of drugs, pressure, and/or flow on vascular diameter and hence whether they would lead to vasodilation or vasoconstriction.

Vicente Andrés and Beatriz Dorado (eds.), *Methods in Mouse Atherosclerosis*, Methods in Molecular Biology, vol. 1339, DOI 10.1007/978-1-4939-2929-0_19,

Pharmacological characterization uses endothelium-dependent agonists for vasodilation in combination with blockers of the different known pathways involved in endothelium-dependent vasodilation. The flow exchange mediated for induced response is characterized by use of the same blockers, including blockers of the cyclooxygenase (COX), of the nitric oxide synthase (NOS) [6], and of the endothelium-derived hyperpolarization (EDH) pathway. The EDH-derived response is the most elusive and least known, though intensively studied. To characterize this latter pathway, we used blockers of various calcium-activated potassium channels that are known to take part in the EDH-derived vasodilation [7–9]. The pressure myograph is essential as an in vitro setup for evaluating a flow-mediated response, which, in combination with pharmacological characterization, remains a unique way of characterizing the endothelial function, revealing the autoregulative properties of the endothelium as a response to an enhanced or diminished flow of blood.

In this chapter, we describe a pressure myograph method for investigating both flow-induced and acetylcholine-induced vasodilation, as well as methods to obtain responses to increasing pressures, to enlighten the vessels' degree of myogenic tone, and to characterize the structural features of the arterial segment in passive calcium-free conditions. The methods described are basic protocols; any pharmacological or physiological intervention can be incorporated. This is especially usable in the persuasion of new pharmacotherapeutics that modulate endothelial vascular function.

2 Materials

The setup for the described protocols is outlined in Fig. 1.

1. Regular microscope.
2. Micro-forceps, micro-scissors, and petri dish for dissection.
3. Glass pipettes with an outer tip diameter of 80–200 μm (at least 20 μm smaller than the mounted artery's internal diameter).
4. Monofilament nylon sutures (15-μm diameter).
5. Pressure myograph (e.g., model 110P, Danish Myo Technology, Aarhus, Denmark).
6. Two pressure columns (up to 150 mmHg) mechanically adjusted or an interface with buffer-filled containers (e.g., 110P, Danish Myo Technology, Aarhus, Denmark).
7. Computer and software: frame grabber and dimension-analyzing program (e.g., Vessel View, Danish Myo Technology, Aarhus, Denmark).

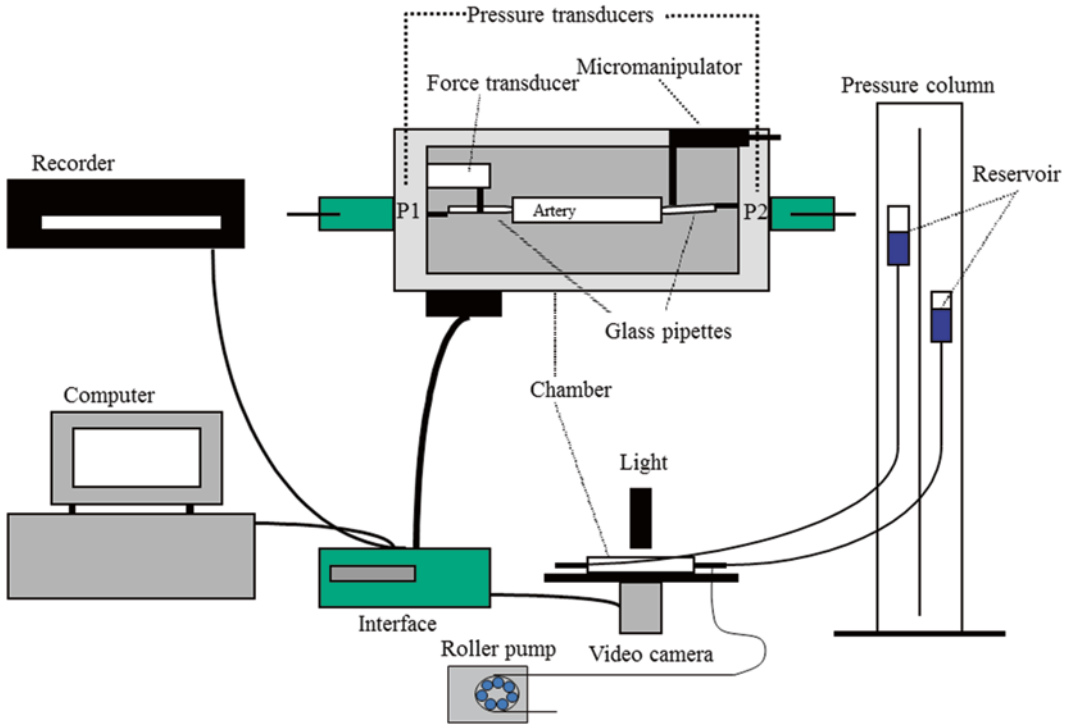

Fig. 1 Schematic drawing of the pressure myograph setup used for the described protocols

8. Inverted microscope, magnification × 100 (e.g., Telaval 31, Zeiss, Oberkochen, Germany).
9. Video camera.
10. A graphic writer is optional to record the pressure and diameter outputs and found useful in teaching students the setup.
11. Electric thermometer.
12. 2 × 50-ml syringes without pistons, attached to the pressure columns. These syringes represent the inflow and outflow reservoirs in Fig. 1.
13. Silicone tubing (1 mm in diameter, Danish Myo Technology, Aarhus, Denmark) for myograph setup.
14. Two 3-way valves connected to each end of the pressure myograph.
15. Air mixture of 95 % O_2 and 5 % CO_2.
16. Roller pump (e.g., Alita Watson Marlow 400, VS2-10R-Midi, 2.5–50 rpm).
17. Roller pump tubing (e.g., Gilson, gas-tight PVDF), different sizes adequate for the given artery diameters, roller pump, and wanted flow levels.

18. Physiological saline solution, 1.6 mM calcium ($PSS_{1,6}$): 1.6 mM $CaCl_2$, 119 mM NaCl, 4.7 mM KCl, 5.5 mM glucose, 7.0 mM $MgSO_4$, 25 mM $NaHCO_3$, 1.18 mM KH_2PO_4, and 0.026 mM ethylenediaminetetraacetic acid (EDTA).
19. Physiological saline solution, 0.0 mM calcium ($PSS_{0,0}$): composition as $PSS_{1,6}$ but without $CaCl_2$ and with 0.1 mM ethylene glycol tetraacetic acid (EGTA) instead of EDTA.
20. Thromboxane analogue 9,11-di-deoxy-11α, 9α-epoxymethanoprostaglandin $F_{2\alpha}$ (U46619).
21. Acetylcholine.
22. Papaverine.
23. Acetic acid.
24. Demineralized water.

3 Methods

3.1 Mounting

The mounting procedure is conducted under a regular microscope.

1. Fill pressure myograph tubing, chamber, and roller pump tubing with 4 °C $PSS_{1,6}$ (*see* **Note 1**) and set pressure to 0 mmHg.
2. Advance the outflow pipette so that the tips of the outflow and inflow pipettes are barely touching each other. The pipettes are aligned and the distance on the micrometer gauge is noted (*see* **Note 2**). Retract again the outflow pipette.
3. Place four nylon sutures loosely over the shaft of each glass pipette (*see* **Note 3**).
4. Transfer the isolated artery to the chamber of the pressure myograph.
5. Cannulate the proximal end of the artery with the inflow pipette (*see* **Note 4**).
6. Tighten two of the sutures around the vessel and pipette (*see* **Note 5**).
7. Cut the distal end of the artery to produce an arterial segment of 1.5–3 mm of length (*see* **Note 6**).
8. Raise the pressure of the inflow pipette to 20–25 mmHg to wash out the remaining blood in the artery. Afterwards the pressure is lowered to 0 mmHg again (*see* **Note 7**).
9. Advance the outflow pipette toward the inflow pipette to allow cannulation of the distal end of the artery without stretching it.
10. Cannulate the distal end of the artery with the outflow pipette and tighten two of the sutures around the vessel and pipette (*see* **Note 5**).

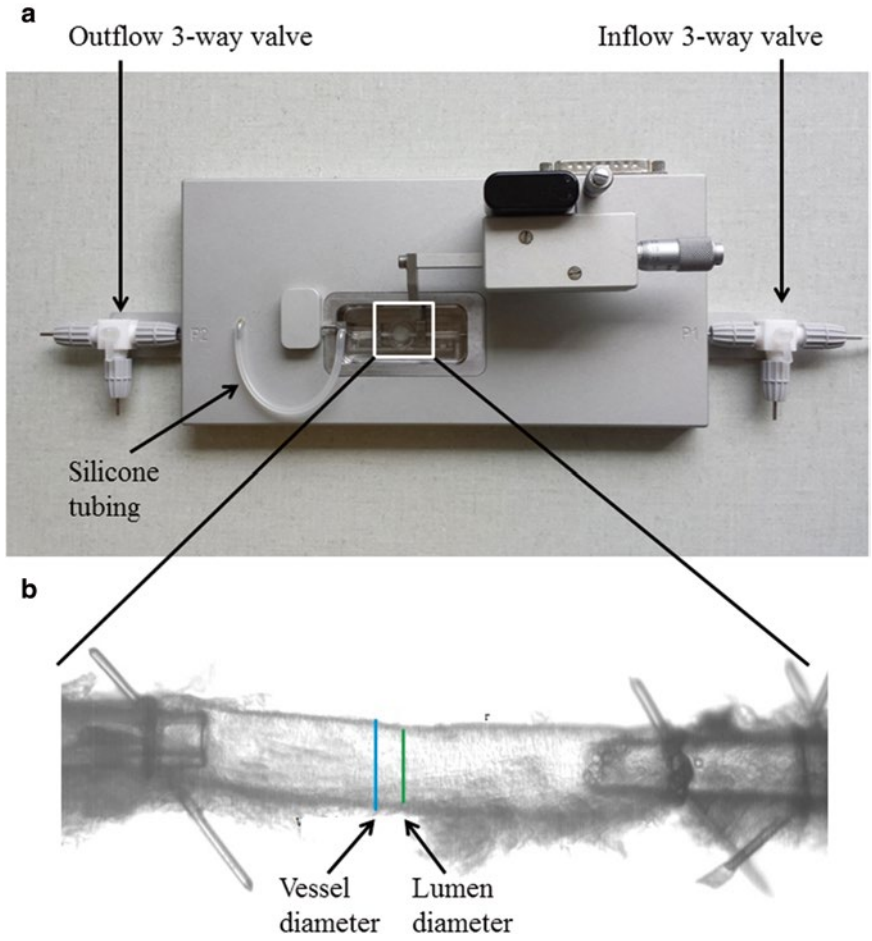

Fig. 2 (**a**) Pressure myograph (P110) used for functional and structural studies. The inflow and outflow 3-way valves as well as the silicone tube in between the pressure transducer and the mounting pipette. This silicone tubing can be used to administer drugs intraluminally (*see* Subheading 3.3). (**b**) Mouse left anterior descending coronary artery (ID ~120 μm) mounted on two glass micropipettes in a pressure myograph for structural measurements. Bars show outer diameter (vessel diameter) and inner diameter (lumen diameter). It is important that the adhering myocardium is carefully removed before mounting

11. Raise the pressure to 30 mmHg, remove the $PSS_{1,6}$ by suction, and inspect the artery through the microscope to identify leaks (*see* **Note 8**).
12. Refill the chamber with 5 ml 4 °C $PSS_{1,6}$.
13. Close the 3-way valve on the outflow side of the set up (Fig. 2a). Pressure should henceforth be managed from only one side at a time (*see* **Note 9**).
14. Place the pressure myograph lid over the myograph chamber and connect an air tube to the air connection in the lid. The myograph bath is henceforth bubbled with an air mixture of 95 % O_2 and 5 % CO_2.

15. Turn on the heat and warm the chamber to 37 °C (*see* **Note 10**).
16. Raise the pressure to 60 mmHg while stretching the artery to avoid bulging.
17. Stretch the arterial segment longitudinally to 110 % of its passive, non-bulging length.
18. Transfer the chamber with the artery to the inverted microscope and turn on the light and video camera.
19. Adjust the frame grabber on the computer of the pressure myograph setup to continuously monitor the internal diameter (*see* **Note 11**).
20. Turn on the graph writer. This will continuously monitor the internal diameter and median pressure over the artery at 3 Hz, correlating to the numeric registrations in the computer log.
21. Mounting is now complete (Fig. 2).

3.2 Structural Studies Under Passive Conditions on the Pressure Myograph

The structural studies are considered as separate protocols and can be combined with the other described protocols in an experiment.

1. Mount the artery (mouse mesenteric or coronary artery) in calcium-free PSS ($PSS_{0,0}$).
2. Heat the chamber to 37 °C.
3. Raise the intraluminal pressure to 100 mmHg to unbuckle the artery.
4. Measure the distance between the sutures. In case of the mesenteric artery, it is stretched to 110 % in longitudinal direction to correspond to in vivo conditions and avoid buckling. The coronary artery segments are kept at the same length.
5. Lower the intraluminal pressure to 70 mmHg and equilibrate for 60 min at 37 °C in $PSS_{0,0}$ gassed with an air mixture of 95 % O_2 and 5 % CO_2.
6. After equilibration, lower the intraluminal pressure to 10 mmHg.
7. Increase the intraluminal pressure in steps from 10 to 20 mmHg and then in 20-mmHg increments from 20 to 140 mmHg. Take a picture and obtain data by continuous measurements of the internal and external diameters (*Di* and *De*) for 3 min per step using the MyoVIEW software. The mean of the data from the last 30 s is used for the calculations.
8. Using a previously described procedure [10], calculate the structural and mechanical parameters from the D_i and D_e measured under passive conditions at intraluminal pressures ranging from 10 to 140 mmHg. The following three equations describe structural parameters and give information about arterial remodeling:

Equation 1 (wall thickness, WT):

$$\mathrm{WT} = \frac{\left(D_e - D_i\right)}{2}.$$

Equation 2 (cross-sectional area, CSA):

$$\mathrm{CSA} = \frac{\pi}{4} \cdot \left(D_e^2 - D_i^2\right).$$

Equation 3 (wall/lumen ratio, W:L):

$$\mathrm{W:L} = \frac{\left(D_e - D_i\right)}{2 \cdot D_i}.$$

The next three equations describe the mechanical parameters and give information about the elasticity and stiffness of the artery:

Equation 4 (incremental distensibility, ID), which represents the percentage of change in the D_i of the artery for each mmHg change in the intraluminal pressure:

$$\mathrm{ID} = \frac{\Delta D_i}{\left(D_i \cdot \Delta P\right)} \cdot 100.$$

Equation 5 (circumferential wall stress, σ):

$$\sigma = \frac{\left(P \cdot D_i\right)}{2 \cdot \mathrm{WT}}.$$

The relationship between the circumferential wall stress and strain can be used to quantify the arterial stiffness.

Equation 6 (circumferential wall strain, ε):

$$\varepsilon = \frac{\left(D_i - D_{i@10\,\mathrm{mmHg}}\right)}{D_{i@10\ \mathrm{mmHg}}}.$$

Equation 7 (exponential growth). By using the Young's elastic modulus, $= \frac{\sigma}{\varepsilon}$, the arterial stiffness can be determined independently of geometry. Since the stress–strain relationship is nonlinear, an incremental elastic modulus (E_{inc}) is obtained by determining the slope of the stress–strain curve. This can be done by fitting the stress–strain curve to an exponential curve, as illustrated in Fig. 3, using the exponential growth equation:

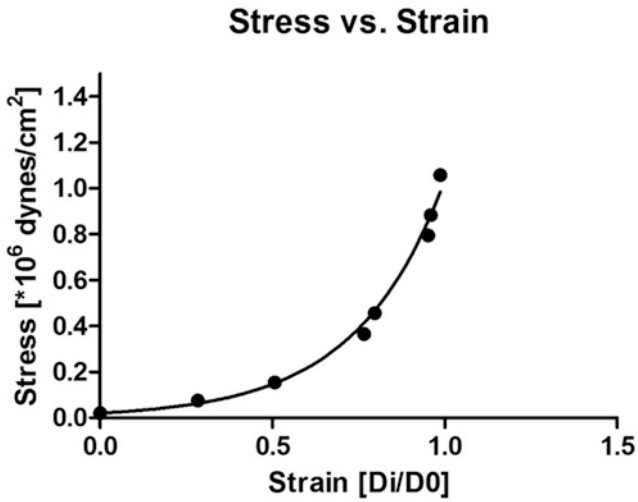

Fig. 3 Stress–strain curve in mouse coronary artery. The *black dots* represent increments in intraluminal pressure

$$\sigma = \sigma_{10\,\mathrm{mmHg}} e^{\beta\varepsilon}.$$

By taking the derivatives to Equation 7, which equals $E_{\mathrm{inc}} = \beta\sigma$. This means that for a given σ-value, E_{inc} is directly proportional to β. Thus, an increase in β would imply an increase in E_{inc}, corresponding to an increase in arterial stiffness [10, 11].

3.3 Incubation

At any point of the study, it may be necessary to incubate the preparation with a given substance (*see* **Note 12**). If the protocol does not incorporate a flow-induced response, the incubation is straightforward and the substance is only added to the pressure myograph chamber (passive diffusion will ensure intraluminal incubation as well). In a protocol incorporating a flow-induced response however, there is a need for adding the substance intraluminally as well as extraluminally to avoid washout. Intraluminal application of a given substance is conducted during the incubation period of typically 30 min after the extraluminal concentration has been added. The following protocol is used:

1. Make sure the pressure on the outflow pipette is 60 mmHg, corresponding to the inflow pressure. Open the 3-way valve on the outflow pipette toward the pressure column. The preparation is now pressurized from two sides.
2. With a clamp, slowly close the inflow tubing at the level closest to the pipette (the small piece of regular tubing protruding from the pressure myograph) (*see* **Note 13**).

3. Add the incubation substance to the inflow reservoir, according to the volume of $PSS_{1,6}$ remaining here, to achieve the desired concentration equivalent of the extraluminal incubation concentration. Mix shortly with a clean spatula.
4. Carefully remove the clamped piece of tubing from its proximal joint on the inflow side of the clamp attached in **step 2**, thereby disconnecting it from the inflow reservoir.
5. Remove 10 ml of $PSS_{1,6}$ from the inflow tubing by suction through the disconnected joint. This will ensure that the inflow system down to the clamped tubing is filled with $PSS_{1,6}$ containing the incubation substrate.
6. Reattach the clamped tubing to its proximal joint, making sure that no air is introduced. Adjust the inflow pressure to 60 mmHg.
7. Attach 10 cm of empty silicone tubing to the distal end of the roller pump tube (*see* **Note 14**).
8. Slowly open the clamp to pressurize the system from two sides.
9. Turn the outflow 3-way valve, so that it is open toward the roller pump.
10. Start the roller pump slowly (from lowest rounds per minute (%RPM)) and, while simultaneously raising the inflow pressure to keep the median pressure at 60 mmHg, increase the %RPM to a shear stress level of maximally 22 dynes/cm^2 (*see* **Note 15**).
11. When the 10 cm of tubing attached in **step 7** is filled with $PSS_{1,6}$, it is ensured that the entire lumen of the arterial segment is now filled with $PSS_{1,6}$ containing the incubation substrate. Depending on the artery's internal diameter, this may take up to 15 min. Stop the pump by slowing down %RPM while adjusting the pressure accordingly.
12. Allow at least 10 min of rest after the flow stop (*see* **Note 16**).
13. If the extraluminal incubation period of 30 min has passed, the incubation is complete and the experiment can proceed.

3.4 Flow-Induced Responses

Prior to conducting the actual experiment on a mounted arterial segment (**steps 3–10** below), some specific preparations indicated in **steps 1** and **2** need to be made to conduct the flow-induced response.

1. Conduct a curve for each roller pump tube of volume per time (μl/min) of $PSS_{1,6}$ at different levels of %RPM (*see* **Note 17**).
2. Calculate the shear stress (τ) of different internal diameters of the artery using the following equation: $\tau = 4\eta Q / \pi r^3$ (*see* **Note 18**). A separate graph for the wanted level of shear stress is made with each roller pump tube. The graph should express the %RPM (y-axis) to achieve the given level of shear stress at different internal diameters (x-axis) (*see* **Note 19**).

3. Make sure the outflow pipette is connected directly to the roller pump, which is acting as a clamp (*see* **Note 9**).
4. Contract the artery by adding U46619 to the pressure myograph chamber at a concentration equivalent of the U46619 concentration in the inflow tube (*see* **Note 20**).
5. When stable contraction is achieved, start the roller pump slowly (from lowest %RPM) and, while simultaneously raising the inflow pressure to keep the median pressure at 60 mmHg, increase the %RPM to the desired level of shear stress (use the graph produced in **step 2**) (*see* **Note 21**).
6. Leave the pump rolling for 5 min to achieve a 5-min flow response (*see* **Note 22**).
7. Slowly stop the roller pump by decreasing the %RPM while lowering the inflow pressure to keep the median pressure at 60 mmHg in a manner opposite to the flow start (*see* **step 5**).
8. Allow 10 min of rest after the flow stop. In this period, the arterial segment should attain stable contraction once again (*see* **Note 23**).
9. If the protocol incorporates a higher flow level, repeat **steps 5–8** with this level of flow (*see* **Note 24**).
10. The protocol can now proceed.

3.5 Concentration–Response Curve for Acetylcholine

1. Contract the mounted arterial segment by adding U46619 in rising concentrations from 0.02 to 0.1 μM until a stable contraction with a reduction of the internal diameter of at least 25 % is obtained (*see* **Note 25**).
2. Dilate the arterial segment with consecutive rising acetylcholine concentrations added extraluminally to the pressure myograph chamber in intervals of 5 min. Concentrations are as follows: 0.003, 0.01, 0.03, 0.1, 0.3, and 1.0 μM.
3. Washout after the last 5 min of dilation is done as follows: Remove the $PSS_{1,6}$ in the myograph chamber through suction and add 10 ml of fresh 37 °C $PSS_{1,6}$. This is done three times in a row. Wait for 10 min and wash again three times with $PSS_{1,6}$. Wait for another 10 min and repeat the change three times. Ten minutes after the last change, the protocol can be continued (*see* **Note 26**).

3.6 Pressure–Diameter Curve to Obtain a Measure of Myogenic Tone

1. During the mounting procedure (*see* Subheading 3.1), skip **step 16** so that the pressure remains at 30 mmHg.
2. Conduct a pressure–diameter curve by raising the pressure in consecutive steps of 10 mmHg, 3 min at each level, from 30 to 140 mmHg (*see* **Note 27**).
3. To obtain a measure of myogenic tone, **step 2** is repeated in $PSS_{0,0}$ (*see* **Note 28**). Myogenic tone is calculated as the

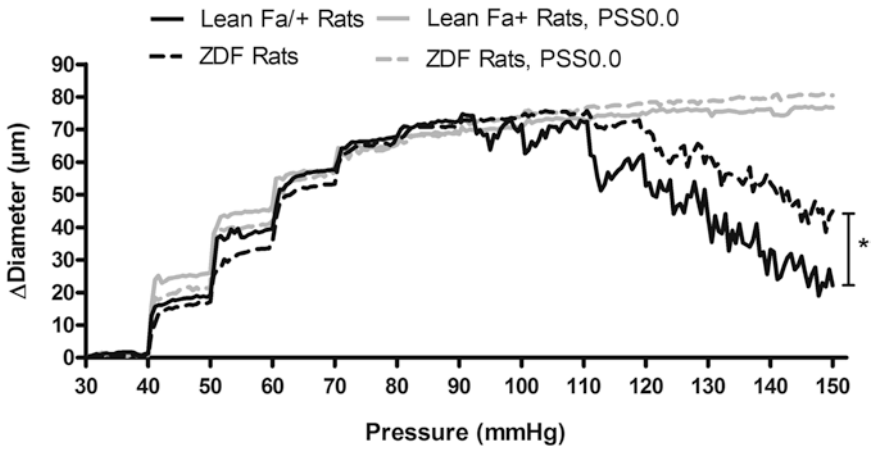

Fig. 4 Average changes in internal diameter in penile arterial segments with (*black lines*) and without calcium (PSS0.0 plus EGTA, *gray lines*) from lean control animals and from Zucker diabetic fatty (ZDF) rats leading to dilation in response to increases in pressure until 90 mmHg. Further pressure increases results in constriction (myogenic tone) in the arteries from the lean control animals, while myogenic constriction is markedly depressed in arteries from diabetic animals (*$P < 0.05$, $N = 6–8$)

difference in internal diameter in the presence of PSS with ($PSS_{1,6}$) and without ($PSS_{0,0}$) calcium. Figure 4 shows that the myogenic response is impaired in diabetic animals [9].

4. Lower the pressure slowly to 60 mmHg (*see* **Note 29**) and exchange $PSS_{0,0}$ solution to $PSS_{1,6}$ (*see* **Note 28**).
5. Allow 30 min of equilibration.
6. Stretch the arterial segment longitudinally to 110 % of its passive, non-bulging length. The protocol can now proceed.

3.7 Denudation of the Endothelium

Removing the endothelium of an arterial segment mounted in a pressure myograph is a bothersome procedure not easily conducted (*see* **Note 30**) [12, 13]. We used the following protocol:

1. In the mounted arterial segment, make sure the pressure on the outflow pipette is 60 mmHg, corresponding to the inflow pressure. Open the 3-way valve on the outflow pipette. The preparation is now pressurized from two sides.
2. With a clamp, slowly close the inflow tubing at the level closest to the pipette (the small piece of regular tubing protruding from the pressure myograph) (*see* **Note 13**).
3. Turn the inflow 3-way valve to act as a clamp toward the inflow reservoir.
4. Carefully remove the clamped piece of tubing from its proximal joint on the inflow side of the clamp attached in **step 2**, thereby disconnecting it from the inflow reservoir.

5. Insert a 5-cm piece of regular tubing prefilled with air bubbles (*see* **Note 31**) between the clamped tubing and its proximal joint on the pressure myograph. This bubble-filled tubing is an insertion of tubing; it is therefore not replacing the regular tubing protruding from the pressure myograph (clamped in **step 2**) but merely extending it.
6. Open the 3-way valve on the inflow side.
7. Slowly open the clamp. The system is now pressurized from two sides.
8. Turn the outflow 3-way valves open toward the roller pump.
9. Start the roller pump slowly from the lowest %RPM and, while simultaneously raising the inflow pressure to keep the median pressure at 60 mmHg, increase the %RPM to a shear stress level of maximally 22 dynes/cm^2 (*see* **Note 15**).
10. When the bubbles of the inserted 5-cm tubing have run through the arterial segment, stop the pump by slowing down %RPM while adjusting the pressure accordingly.
11. Repeat **step 1**–**10** with the next piece of 5-cm tubing prefilled with air bubbles.
12. When the last air bubbles have run through the arterial segment, leave the pump running until the bubbles have all passed the outflow 3-way valve. Stop the pump by slowing down %RPM while adjusting the pressure accordingly.
13. Inspect the arterial segment thoroughly to make sure no air is stuck within.
14. Switch the 3-way valve to block the outflow side of the setup and remove the air bubbles by sucking fresh $PSS_{1,6}$ into the roller pump tubing (*see* **Note 32**).
15. Allow at least 10 min of rest after the flow stop.
16. Contract the mounted arterial segment raising U46619 concentrations from 0.02 to 0.1 μM until a stable contraction with a reduction of the internal diameter of at least 25 % is obtained (*see* **Note 33**).
17. Add acetylcholine to the pressure myograph chamber at a final concentration of 1 μM. If the arterial segment does not dilate in response to this concentration, the endothelium has been removed successfully and the protocol can proceed.

3.8 End of Experiment and Cleaning

This procedure should be conducted after a complete pressure myographic protocol of any kind.

1. Dilate the arterial segment maximally by adding 0.1 mM papaverine to the pressure myograph chamber and wait for 5 min (*see* **Note 34**).

2. Remove the artery and thoroughly rinse the whole system with adequate amounts of demineralized water (*see* **Note 35**).
3. Clean the pressure myograph chamber (but not tubing and pipettes) with 10 % acetic acid and rinse thoroughly with demineralized water.

4 Notes

1. If the experiment has a flow protocol incorporated, the inflow tubing should be filled with $PSS_{1,6}$ containing the thromboxane analogue U46619. This is done to avoid intraluminal washout of the vasoconstrictor during flow, thus mimicking flow-mediated vasodilation. The concentration of U46619 should reflect the concentration expected to cause stable contraction of the arterial segment when added extraluminally. This concentration may vary depending on the type of vascular bed and type of animal. Interindividual variations between each preparation also occur. We used a start concentration of 0.05 μM (mesenteric and penile rat arteries) but concentrations from 0.02 to 0.1 μM are acceptable. If stable contraction cannot be obtained at the estimated concentration, it may be necessary to change the intraluminal concentration during the experiment (*see* **Note 12**). To hit the correct concentration of vasoconstrictor can be very bothersome and time consuming. It is advisable to conduct pilot studies to establish the adequate concentration of a vasoconstrictor. The pressure myograph chamber and the outflow tubing, including the roller pump, should not contain U46619. Theoretically, any vasoconstrictor can be used for the experiment. We examined noradrenaline as well as U46619, but our experience was that noradrenaline even in low concentrations elicited too high a level of contraction obliterating the internal lumen and the contraction level was not stable. Noradrenaline was therefore not found usable as a vasoconstrictor in our experiments.
2. The distance will serve as baseline when the length of the arterial segment is calculated (*see* Subheading 3.1, **step 17**). Be careful not to fracture the pipettes in this process.
3. Sutures are best done in advance. Under a microscope using two micro-forceps, produce adequate amounts of loosely tied overhand knots on 15-μm diameter monofilament nylon sutures (best done and kept on the edge of the sticky side of regular office adhesive tape). The use of four sutures on each pipette when only two is needed is to ensure spare sutures if a suture falls off or a leak is detected. The knots are much harder to tie around the pipette after the artery is mounted.

4. If, when isolating the artery, the in vivo orientation of the artery is identifiable, it is advisable to leave a small piece of interstitial tissue at the distal end of the isolated artery. This will allow mounting in the correct orientation, so that flow application will follow the in vivo flow direction. To which degree the flow direction does actually affect the outcome of the experiment remains unclear, but it seems appropriate to take this precaution to mimic in vivo conditions as much as possible.
5. The sutures should not be too tight, since that may damage the arterial segment producing a leak.
6. Beware that the arterial segment is of the right length. Too long a segment may (depending on the length of the glass pipettes) instigate a problem. The artery will lengthen when pressurized, and on top of this, it is necessary to stretch it to 110 % of its passive length later on (*see* Subheading 3.1, **step 17**) which might not be possible then.
7. Beware of negative pressure which will collapse the artery and thereby disrupt the endothelium.
8. If a leak is detected at one of the ends of the artery, refill with 4 °C $PSS_{1,6}$ and add another suture closer to the tip of the pipette, which may stop the leak. If the arterial segment is long enough, another option may be to cut the artery and remount the affected end. If a leak persists in spite of extra sutures or remounting the arterial segment, then the experiment should be discarded.
9. If pressure is managed from both sides at once, the slightest differences in the water columns will cause unnoticeable, unwanted flow through the artery, possibly disrupting the experiment. Both pressure columns should only shortly be opened at the same time when shifting the pressure from one side to the other.

   If the experiment has a flow protocol incorporated, instead of closing the 3-way valve, open the tubing toward the roller pump. The pump will then function as a clamp until it is turned on. This is recommendable to avoid the slight pressure drop that is caused by turning the 3-way valve in itself. The slightest change in pressure may disrupt a stable contraction when flow is applied (*see* Subheading 3.3, **step 5**).
10. Meanwhile place a bowl of $PSS_{1,6}$ in a heated bath at 37 °C: from now on, only heated $PSS_{1,6}$ is used.
11. When conducting the experiment, it is necessary to continuously adjust the frame grabber to follow the precise internal diameter visually. Try to keep the frame grabber located at approximately the same point of the artery throughout the experiment, since the artery may vary slightly in internal diameter throughout its length.

12. Substances that are typically used in pressure myograph experiments include various blockers of either the nitric oxide, the prostaglandin, or the endothelium-derived hyperpolarizing factor-elicited vasodilation. We have conducted experiments using indomethacin, asymmetric dimethylarginine, iberiotoxin, apamin,, and charybdotoxin.

    Regarding changing concentrations of thromboxane analogue U46619 in the tubing of the inflow pipette and intraluminally in the arterial segment (in circumstances described in Subheading 3.4, **step 4**, **Notes 20** and **33**), the intraluminal incubation protocol is followed from **step 1**, only adding the adequate amount of U46619 to the inflow reservoir instead of an incubation substance.

13. The clamping of the small piece of silicone tubing will disrupt the pressure registration. This happens because the inflow pressure gauge is placed proximally of this piece of tubing; therefore, disregard the registered pressures while the pean is on. The pressure of 60 mmHg from the outflow water column ensures stable pressure through the preparation.

14. The attached tubing will serve as a marker of liquid passed through the arterial segment when starting the roller pump.

15. Since the artery is now relaxed, the flow of liquid through the vessel needed to attain a shear stress level of 22 dynes/cm^2 is much higher than on the contracted artery. A shear stress of 22 dynes/cm^2 is not necessary. In general, we used the amount of flow needed to give a shear stress of 22 dynes/cm^2 in the contracted artery. This ensures a much lower amount of shear stress here than in the experiment. A shear stress level of 22 dynes/cm^2 though is regarded safe for the endothelium (for shear stress calculations, *see* Subheading 3.3, **step 2**).

16. Usually this can be accomplished within the 30 min of extraluminal incubation time.

17. This is done with an electronic scale (capable of weighing μg), by letting the $PSS_{1,6}$ run through the pump, dripping down onto the scale (e.g., 5 min per %RPM level). At some point, the relation between %RPM and volume/min is no longer directly proportional. Since this point is depending on the resistance through the tube, it is important to suck the $PSS_{1,6}$ up through a glass pipette of the same diameter that you plan on using for the experiment. The point where direct proportionality subsides should be noted. This signifies the maximum %RPM for this specific roller pump tube. If a larger flow is needed, it is necessary to change the pump tubing to a larger diameter. This may be necessary to do in the experiment (*see* **Note 21**). Theoretically, the pump tubing can be used beyond this point, but it will make further calculations much more

complex since then you cannot just multiply a coefficient to calculate the difference between %RPM and the volumetric flow rate.

18. τ = shear stress, Q = volumetric flow rate (volume/time), r = internal radius of the artery, and η = viscosity of the liquid (the viscosity of water at 37 °C is 0692 mPa × s; the viscosity of $PSS_{1,6}$ is assumed to be negligibly different than the viscosity of water).
19. If two levels of flow are needed, the high flow level can be easily calculated without a separate graph. Since shear stress is directly proportional to %RPM, you can multiply the %RPM of the low flow level with the factor difference between the flow levels (e.g., low flow 5.5 dynes/cm^2 and high flow 22 dynes/cm^2 equals a factor 4). Just beware not to go beyond the maximum %RPM for the specific roller pump tubing (*see* **Note 17**).
20. If this concentration fails to provide stable contraction with a reduction of the arterial segments internal diameter of at least 25 %, it is necessary to change the U46619 concentrations in the inflow system as well as intraluminally (*see* **Notes 1** and **12**) and then try with a larger U46619 concentration.

    Depending on the vascular bed and type of animal, the arterial segment may elicit spontaneous vasomotion upon U46619 application. The experiment can continue if vasomotion does not recede spontaneously as long as the vasomotion is in a cyclic manner and the average diameter can be assessed.
21. This should be done in seconds, just slowly enough to keep the pressure steady. If the pump is started directly at the desired level of shear stress, the abrupt flow start will course a partial vacuum possibly sucking the artery together mimicking a contraction and thus distracting the experiment.

    You may be in a situation where the roller pump tube chosen before mounting will not suffice. To achieve the desired level of shear stress, the tube will have to be changed. This can be done as follows: very carefully clamp the regular tubing leading to the roller pump with a clamp. Change the roller pump tube to the appropriate size and fill it with $PSS_{1,6}$ by running the roller pump. Connect it carefully to the clamped regular tubing, avoiding introduction of air. Slowly remove the clamp. The tube is now changed. If the small pressure variations caused by clamping the regular tube leading to the roller pump have disrupted the otherwise stable contraction, it may be necessary to wait for stable vasoconstriction once again.
22. The roller pump will cause small cyclic pressure variations, the extent of these depending of the type of roller pump and the size of roller pump tubing. Keep the median pressure at 60 mmHg.

23. To obtain stable vasoconstriction once again may require more than 10 min.
24. To attain the higher level of flow, it may at this time be necessary to change the roller pump tube to a larger diameter (*see* **Note 21**).
25. If at this point the artery is already contracted with U46619 after a flow-induced response, just allow 10 min to rest, awaiting stable contraction once again and proceed to **step 2** (see also [14]).
26. If the dose–response curve is conducted with an incubated arterial segment, the incubation substance should be added to the pressure myograph chamber after each three times $PSS_{1,6}$ is changed before each 10 min of rest.
27. As the pressure rises, the arterial segment will start bulging. When this happens, stretch the segment accordingly to keep it straight.
28. The corresponding pressure–diameter curve without calcium present should be done after a complete washout procedure (*see* Subheading 3.5, **step 3**) with $PSS_{0,0}$ with 0.1 mM EGTA and a change of intraluminal PSS likewise to $PSS_{0,0}$ containing 0.1 mM EGTA (*see* Subheading 3.3 from **step 1**).
29. When decreasing the pressure, simultaneously slack the arterial segment to the point where it starts bulging. Otherwise it may be overstretched.
30. The main problem with the denudation of the endothelium is introducing the correct amount of air needed to remove the endothelium without affecting the smooth muscle layer of the artery wall. Often the endothelium has not been removed completely, so when adding acetylcholine (*see* Subheading 3.7, **step 17**), the artery will dilate, signifying viable endothelium is still in the artery. At other times, the smooth muscle layer has been disrupted to a degree where stable contraction cannot be obtained even with 0.1 μm U46619.
31. Before the procedure, two pieces of 5 cm of regular tubing should be filled with $PSS_{1,6}$ and a string of five small air bubbles of approximately 1.5 mm of length each. This is best done by sucking air into the tubes with the roller pump.
32. If a flow response is conducted after the denudation of the endothelium, turn the outflow 3-way valve after reattaching the roller pump to the system, so it is again open toward the roller pump that is now acting as a clamp.
33. If a flow response is conducted after the denudation of the endothelium, the U46619 concentration should be equivalent to its concentration in the inflow tube. The concentration needed after denudation of the endothelium may be larger

than that needed to provide stable contraction before the denudation. If so, the inflow and intraluminal concentrations should be changed (*see* **Notes 1** and **12**).

34. Papaverine is added for two reasons. The first is to ensure that the artery is still viable and the second is to provide the maximal dilated internal diameter to serve as a baseline for calculations later on and to be able to compare the size of the artery between different animals in an experimental row. The resting diameter of the artery after mounting may vary significantly especially if intraluminal U46619 is added before mounting to be able to conduct a flow-mediated response (*see* **Note 1**).
35. The pipettes are in risk of clotting, if salt crystals form in the system between experiments. Check the tips of the glass pipettes for the presence of crystals before mounting again. The lifetime of a glass pipette is usually no more than 2–3 experiments before fracturing or clotting, so if in doubt, better be safe than sorry and change to new pipettes before mounting again.

Acknowledgment

Ulf Simonsen is supported by the Danish Heart Foundation and is part of LiPhos (Living Photonics: Monitoring light propagation through cells), which is funded by the EC Seventh Framework Programme.

References

1. Mulvany MJ, Aalkjaer C (1990) Structure and function of small arteries. Physiol Rev 70: 921–961
2. Duling BR, Gore RW, Dacey RG Jr et al (1981) Methods for isolation, cannulation, and in vitro study of single microvessels. Am J Physiol 241: H108–H116
3. Mulvany MJ, Halpern W (1977) Contractile properties of small arterial resistance vessels in spontaneously hypertensive and normotensive rats. Circ Res 41:19–26
4. Buus NH, VanBavel E, Mulvany MJ (1994) Differences in sensitivity of rat mesenteric small arteries to agonists when studied as ring preparations or as cannulated preparations. Br J Pharmacol 112:579–587
5. Schubert R, Wesselman JP, Nilsson H et al (1996) Noradrenaline-induced depolarization is smaller in isobaric compared to isometric preparations of rat mesenteric small arteries. Pflugers Arch 431:794–796
6. Paniagua OA, Bryant MB, Panza JA (2001) Role of endothelial nitric oxide in shear stress-induced vasodilation of human microvasculature: diminished activity in hypertensive and hypercholesterolemic patients. Circulation 103:1752–1758
7. Edwards G, Dora KA, Gardener MJ et al (1998) K+ is an endothelium-derived hyperpolarizing factor in rat arteries. Nature 396: 269–272
8. Miura H, Wachtel RE, Liu Y et al (2001) Flow-induced dilation of human coronary arterioles: important role of Ca(2+)-activated K(+) channels. Circulation 103:1992–1998
9. Schjorring O, Kun A, Flyvbjerg A et al (2012) Flow-evoked vasodilation is blunted in penile arteries from Zucker diabetic fatty rats. J Sex Med 9:1789–1800
10. Hernanz R, Martin A, Perez-Giron JV et al (2012) Pioglitazone treatment increases COX-2-derived prostacyclin production and reduces oxidative stress in hypertensive rats:

role in vascular function. Br J Pharmacol 166:1303–1319

11. Roque FR, Briones AM, Garcia-Redondo AB et al (2013) Aerobic exercise reduces oxidative stress and improves vascular changes of small mesenteric and coronary arteries in hypertension. Br J Pharmacol 168:686–703
12. Thorsgaard M, Lopez V, Buus NH et al (2003) Different modulation by Ca2+-activated K+ channel blockers and herbimycin of acetylcholine- and flow-evoked vasodilatation in rat mesenteric small arteries. Br J Pharmacol 138: 1562–1570
13. Stankevicius E, Dalsgaard T, Kroigaard C et al (2011) Opening of small and intermediate calcium-activated potassium channels induces relaxation mainly mediated by nitric-oxide release in large arteries and endothelium-derived hyperpolarizing factor in small arteries from rat. J Pharmacol Exp Ther 339:842–850
14. Christensen FH, Hansen T, Stankevicius E et al (2007) Elevated pressure selectively blunts flow-evoked vasodilatation in rat mesenteric small arteries. Br J Pharmacol 150: 80–87

Chapter 20

Generation of Aorta Transcript Atlases of Wild-Type and Apolipoprotein E-null Mice by Laser Capture Microdissection-Based mRNA Expression Microarrays

Changjun Yin*, Sarajo Mohanta*, Zhe Ma, Christian Weber, Desheng Hu, Falk Weih, and Andreas Habenicht

Abstract

Atherosclerosis is a transmural chronic inflammatory disease of medium and large arteries. Though it is well recognized that immune responses contribute to atherosclerosis, it remains unclear whether these responses are carried out in secondary lymphoid organs such as the spleen and lymph nodes and/or within the arterial wall. Arteries are composed of three major layers, i.e., the laminae intima, media, and adventitia. However, each of these layers may play different roles in arterial wall biology and atherogenesis. We identified well-structured artery tertiary lymphoid organs (ATLOs) in the abdominal aorta adventitia but not in the intima of aged apolipoprotein E-null ($ApoE^{-/-}$) mice. These observations suggested that disease-associated immune responses are highly territorialized within the arterial wall and that the adventitia may play distinct and hitherto unrecognized roles. Here, we set out to apply laser capture microdissection (LCM) to dissect plaque, media, adventitia, and adjacent aorta-draining lymph nodes (LN) in aged $ApoE^{-/-}$ mice in attempts to establish the territoriality of atherosclerosis immune responses. Using whole-genome mRNA expression microarrays of arterial wall tissues, we constructed robust transcript atlases of wild-type and $ApoE^{-/-}$ mouse aortas. Data were deposited in the National Center for Biotechnology Information's gene expression omnibus (GEO) and are accessible to the public through the Internet. These transcript atlases are anticipated to prove valuable to address a wide scope of issues ranging from atherosclerosis immunity and inflammation to the role of single genes in regulating arterial wall remodeling. This chapter presents protocols for LCM of mouse aorta and microarray expression analysis from LCM-isolated aorta laminae.

Key words Atherosclerosis, Laser capture microdissection (LCM), Gene expression omnibus (GEO), Microarrays, Transcriptome atlas, Artery tertiary lymphoid organ (ATLO)

*These authors contributed equally to this work.
After submission of this manuscript Falk Weih deceased.

Vicente Andrés and Beatriz Dorado (eds.), *Methods in Mouse Atherosclerosis*, Methods in Molecular Biology, vol. 1339, DOI 10.1007/978-1-4939-2929-0_20, © Springer Science+Business Media New York 2015

1 Introduction

Atherosclerosis research in the past has largely focused on the plaque in the intima and on smooth muscle cells of the media, whereas the adventitia, i.e., the connective tissue that surrounds arteries, has received less attention [1–3]. Recently, however, the adventitia gained interest as it had become apparent that atherosclerosis in apolipoprotein E-null ($ApoE^{-/-}$) aortas is associated with the accumulation of major types of immune cells in the adventitia over time [4–10]. Indeed, the immune system was shown to selectively organize well-structured artery tertiary lymphoid organs (ATLOs) containing separate T cell areas and activated germinal centers of B cells adjacent to arterial wall segments afflicted with atherosclerotic plaques. Previous studies had already established protective roles of T regulatory cells, pro- and antiatherogenic impacts of distinct T and B cell and dendritic cell subtypes, and various innate immune cells [1–5]. However, it remained uncertain where atherosclerosis immune responses are carried out and what the contributions of individual immune cell lineages are to promote or attenuate the disease. Together with the discovery of various subtypes of dendritic cells and macrophages, follicular dendritic cells (FDCs), proliferating T and B cells, newly formed high endothelial venules (HEVs) and blood vessels, lymph vessels, and conduits in ATLOs, our results indicated that these lymphoid aggregates may participate in atherosclerosis-specific adaptive immune responses locally rather than systemically [4, 5, 7]. Detailed immunohistochemical and fluorescent-activated cell sorter analyses of immune cells and structural constituents in arterial wall laminae had revealed major differences between plaque and adventitia cellularity and between wild-type and $ApoE^{-/-}$ adventitia [4, 7] (Fig. 1). However, these analyses were limited in their scope as they cannot fully reflect the complexity of gene expression that is present in each cell lineage in the various arterial wall compartments. To understand immune responses within the normal and diseased arterial wall better and to apply an unbiased rather than a hypothesis-driven approach to arterial wall biology, we set out to employ laser capture microdissection (LCM), which had previously been used to examine distinct mRNAs by reverse transcription polymerase reaction analyses in plaques [11–13]. These and other advances of LCM techniques together with the establishment of algorithms to avoid cross contamination of arterial wall lamina-specific mRNAs allowed us to generate robust transcriptome maps of high specificity and considerable predictive power [12]. Microarray data were deposited in the National Center for Biotechnology Information's (NCBI) gene expression omnibus (GEO) (www.ncbi.nlm.nih.gov/geo/info/MIAME.html; accession no. GSE40156). The maps were assembled to construct comprehensive transcript atlases of wild-type and $ApoE^{-/-}$ aortas

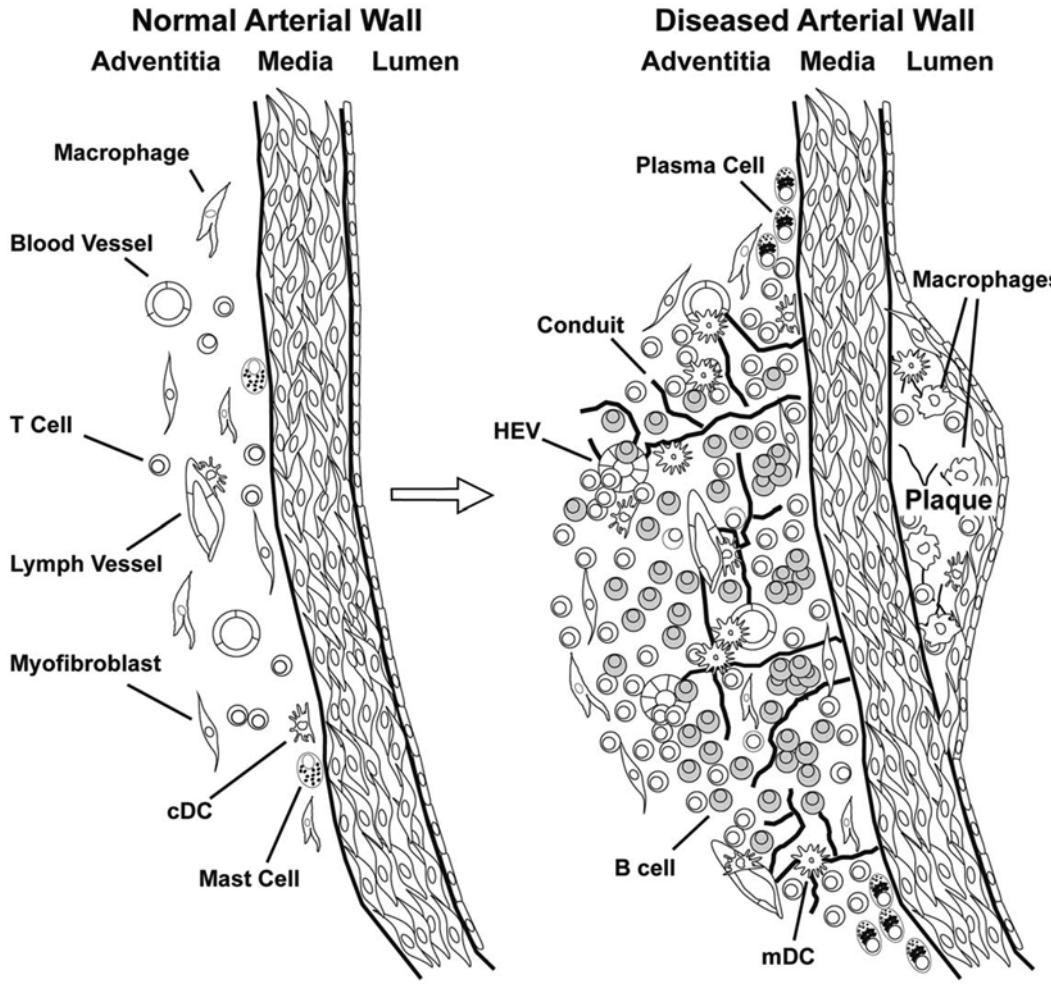

Fig. 1 Atherosclerotic arteries harbor distinct immune cell infiltrates in plaques and adventitia. The adventitia of the normal arterial wall (*left*) constitutively contains *vasa vasorum*, lymph vessels, tissue macrophages, few T cells, mast cells, conventional dendritic cells (cDCs), and myofibroblasts. In response to transmural arterial wall inflammation during early stages of atherosclerosis, T cells and other immune cells such as B cells and monocyte-derived DCs (mDCs) infiltrate the adventitia. Throughout disease progression, extensive reorganization of adventitia segments adjacent to atherosclerotic plaques can be observed in the abdominal aorta of ApoE $^{-/-}$ mice resulting in ATLOs (*right*). Reorganization of the adventitia includes both the connective tissue-derived cells such as myofibroblasts and neogenesis of lymph vessels, angiogenesis, conduit formation, and high endothelial venule (HEV) formation. Concomitantly, monocytes are recruited through blood vessels, cDCs are recruited through lymph vessels, and naïve T and B cells are recruited through newly formed HEVs. Moreover, survival niches are populated by plasma cells that secrete immunoglobulins in situ. In contrast to the adventitia, advanced atherosclerotic plaques are comparably acellular and show a limited set of adaptive immune cells. Adapted from Mohanta et al. 2014, *Circulation Research*, 114 (11):1772–1787

(Fig. 2) and are now available to the public through the Internet. The atlases can be used to address a wide range of issues in arterial wall remodeling and atherogenesis. When transcriptome data are combined with other techniques such as in situ hybridization, immunohistochemistry, fluorescence-activated cell sorter analyses,

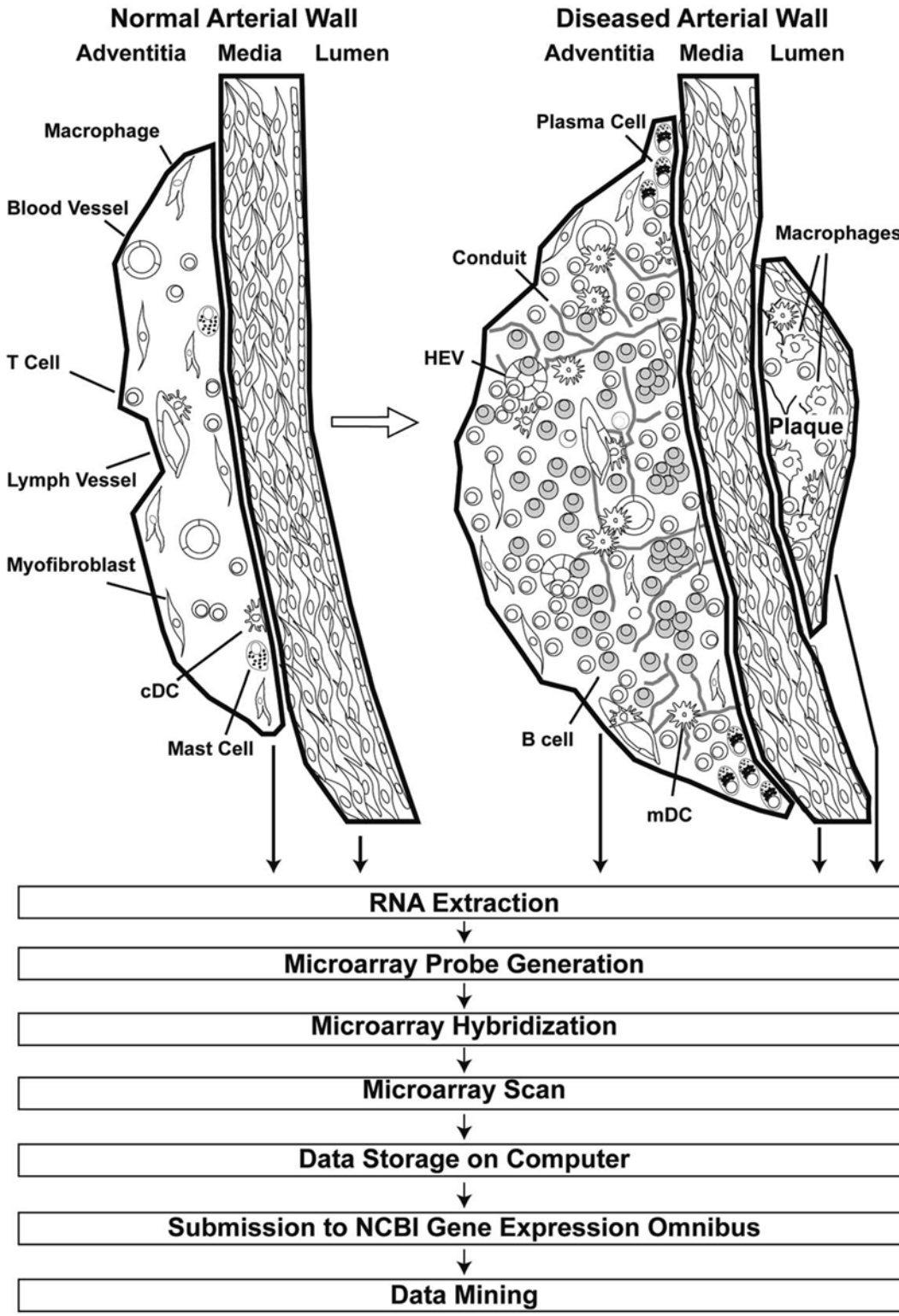

Fig. 2 Approach to construct transcript atlases of wild-type and ApoE$^{-/-}$ aortas from LCM-derived arterial wall laminae. Thick lines delineate the laser track to dissect and collect tissue compartments of the arterial wall laminae (*see* Fig. 1) from which total RNA is extracted for the preparation of mRNA expression microarrays. Subsequently, microarray probes are generated as described previously, hybridized to the microarray, scanned, and subsequently stored as CEL files in the NCBI GEO data bank. Various mining tools are available in the Internet to address a large number of issues; see [4–7]. Adapted from Mohanta et al. 2014, *Circulation Research*, 114 (11):1772–1787

and transgenic mouse generation, progress into new facets of atherogenesis may be achievable.

2 Materials

2.1 LCM Procedure

1. O.C.T.® compound (Sakura Finetek, Germany).
2. Membrane slides (e.g., MembraneSlide 1.0 PEN, Carl Zeiss MicroImaging GmbH, Jena).
3. Oil Red O (e.g., Sigma-Aldrich, Germany).
4. Hematoxylin (e.g., Dako, Germany).
5. Isopropanol.
6. Acetone.
7. PALM MicroBeam system (Carl Zeiss MicroImaging GmbH, Munich, Germany).
8. Trizol (e.g., Invitrogen, Carlsbad, CA).
9. Eppendorf cup (Eppendorf, Germany).
10. Vacuum desiccator (e.g., Schott, Germany).
11. Stereomicroscope (e.g., Carl Zeiss, Germany).

2.2 Preparation of RNA and Quality Control

1. RNeasy® Micro Kit (Qiagen, Valencia, CA).
2. NanoDrop ND spectrophotometer device (Thermo Fisher Scientific, Pittsburgh, PA).
3. Agilent RNA 6000 Pico Kit (Agilent, Santa Clara, CA).
4. Agilent 2100 Bioanalyzer (Agilent Technologies, Germany).
5. Vortexer for Pico chip (e.g., IKA®-Werke GmbH & Co. KG, Germany).
6. Ladder for RNA 6000 Pico chip (e.g., Ambion, Austin, TX).
7. Chloroform.
8. Ethanol.
9. RNase-free H_2O (e.g., DEPC H_2O, Ambion, Austin, TX).
10. Nonstick tubes (e.g., Ambion, Austin, TX).

2.3 Preparation of Microarrays from Small Amounts of RNA

1. SuperScript II enzyme (Invitrogen, Carlsbad, CA).
2. *E.coli* ligase (e.g., Invitrogen, Carlsbad, CA).
3. RNase H (e.g., Invitrogen, Carlsbad, CA).
4. T4 DNA polymerase (e.g., Invitrogen, Carlsbad, CA).
5. T7-oligo(dT) Primer (e.g., Affymetrix, Santa Clara, CA).
6. p(A) RNA (component of the RNeasy Micro Kit, Qiagen, Germany).
7. ENZO™ High Yield In Vitro Transcription Kit (ENZO Life Sciences, Switzerland).

8. Concentrated T7 polymerase (e.g., Ambion, Austin, TX).
9. RNeasy® Mini kit (Qiagen, Germany).
10. Phenol–chloroform (Ultra Pur) isoamyl alcohol (e.g., Ambion, Austin, TX).
11. 10× fragmentation buffer: 400 mM Tris-Ac, 1 M KOAc, 300 mM MgOAc.
12. NH_4Ac (e.g., Sigma-Aldrich, Germany).
13. GeneChip® Hybridization Control Kit (Affymetrix, Santa Clara, CA).
14. Control oligoB2 (Affymetrix, Santa Clara, CA).
15. Herring sperm DNA (e.g., Promega, Madison, USA).
16. Acetylated BSA, 50 mg/ml (e.g., Sigma-Aldrich, Germany).
17. Tween-20 (10 % Surfact-Amps 20) (e.g., Thermo Fisher Scientific, Pittsburg, PA).
18. GeneChip® Hybridization, Wash, and Stain Kit (Affymetrix, Santa Clara, CA).
19. GeneChip® Mouse Genome 430A 2.0 Arrays (Affymetrix, Santa Clara, CA).
20. GeneChip® Hybridization Oven (Affymetrix, Santa Clara, CA).
21. GeneChip® Fluidics Station 450 (Affymetrix, Santa Clara, CA).
22. GeneChip® Scanner (Affymetrix, Santa Clara, CA).

2.4 Microarray Data Analysis

1. R and Bioconductor software (http://www.bioconductor.org/).

2.5 Mice

1. $ApoE^{-/-}$ and wild-type mice (e.g., C57BL/6J background, The Jackson Laboratory, Bar Harbor, Maine, USA) (*see* **Note 1**).

3 Methods

3.1 LCM Procedure

1. Euthanize mice.
2. Perfuse the aorta in situ using EDTA/PBS for 10 min to remove blood taking care of preserving the adventitia.
3. Remove adipose tissue and para-aortic ganglia but not LNs using forceps with the help of a dissection microscope (*see* **Note 2**).
4. Embed aorta in Tissue-Tek and store at −80 °C.
5. Heat membrane slides to 180 °C for 4 h to remove RNase.
6. Store RNase-free membrane slides at −20 °C.
7. Prepare fresh-frozen cryotome sections (10 μm) from aorta embedded in Tissue-Tek (maintained at −80 °C); use every

tenth section for Oil Red O/hematoxylin staining to identify ATLOs or other arterial wall structures (*see* **Note 3**).

8. Transfer five sections into Eppendorf cup to examine RNA integrity using Bioanalyzer electrophoresis (first RNA integrity control to test RNA quality before LCM) (*see* **Note 4**).
9. Place 5×20 µm sections onto cooled membrane slides (*see* **Note 5**).
10. Save 3×10 µm sections for immune fluorescence analyses; store at –20 °C.
11. Fix membrane slides for 25 s in ice-cold acetone within cryotome chamber.
12. Dry section on warm plate for 5–10 min at 37 °C under argon. Place dry sections in a vacuum desiccator until LCM to avoid moisture uptake. Prepare approximately 200 sections on an appropriate number of membrane slides to get a yield of approximately 30–120 ng RNA for each of the arterial wall laminae.
13. Use the PALM MicroBeam system to microdissect the adventitia, the media, and the plaque according to their position of appearance under the LCM microscopy using phase contrast objective.
14. Separate manually isolated LCM material using forceps, and transfer into Eppendorf cup containing 900 µl Trizol.
15. Subsequent to completion of the LCM procedure of an individual mouse aorta, transfer five sections into separate Eppendorf cup to examine RNA integrity using Bioanalyzer electrophoresis (second RNA integrity control to test RNA degradation during LCM).

3.2 Preparation of RNA

1. Collect all LCM samples plus samples for RNA quality control in individual 900 µl Trizol (if necessary, store them for up to 48 h at 4 °C to assemble a complete set).
2. Add 180 µl chloroform and shake.
3. Centrifuge for 15 min, 15,000×*g*, 12 °C.
4. Transfer clear supernatant into an Eppendorf tube; add 280 µl ethanol.
5. Transfer to RNeasy® MinElute column (component of the RNeasy® Micro Kit).
6. Centrifuge for 1 min, 10,000×*g*, at room temperature (RT).
7. Discard flowthrough and wash column with 500 µl of RW1 buffer (component of the RNeasy® Micro Kit).
8. Centrifuge for 1 min, 10,000×*g*, RT.
9. Change tube and wash column with 500 µl of RPE buffer (component of the RNeasy® Micro Kit).

10. Centrifuge for 1 min, 10,000 × *g*, RT.
11. Discard flowthrough and wash columns with 500 µl of 80 % ethanol.
12. Centrifuge for 1 min, 10,000 × *g*, RT.
13. Discard flowthrough and open cap.
14. Centrifuge for 2 min, 13,000 × *g*, RT.
15. Add 12 µl RNase-free H_2O to column, and place a 1.5 ml nonstick tube under the column.
16. Centrifuge for 2 min, 13,000 × *g*, RT to collect eluted RNA into the nonstick tube.
17. Apply a 1:5 dilution of RNA to an Agilent RNA6000 Pico Chip to determine RNA quality and estimate concentration (*see* **Note 6**).
18. Store RNA at –80 °C.

3.3 Preparation of Microarrays from Small Amounts of RNA

1. Reverse-transcribe 30–120 ng RNA using SuperScript II. T7 promoter is introduced by tailed T7-oligo(dT) Primer (5 µM) and SuperScript II enzyme (10 U/µl) in total 20 µl reaction mixture.
2. Synthesize second strand with the help of DNA polymerase I (4 µl, 10 U/µl), RNase H (1 µl, 2 U/µl), and *E. Coli* ligase (1 µl, 10 U/µl) in total 150 µl reaction mixture. To obtain blunt ends, T4 DNA polymerase (2 µl, 5 U/µl) is used at the end of the reaction (10 µl EDTA (0.5 M, pH = 8.0) is used to terminate the reaction).
3. Centrifuge for 1 min, 13,000 × *g*, RT.
4. Transfer sample into a new 0.5 ml tube, and add 170 µl phenol–chloroform isoamyl alcohol (pH = 7.9). Vigorously shake for 1 min.
5. Centrifuge for 5 min, 13,000 × *g*, RT.
6. Transfer 165 µl of supernatant into a 1.5 ml tube.
7. Precipitate ammonium acetate by adding 5 µg of p(A) RNA as a carrier, 420 µl ethanol, and 85 µl NH_4Ac (7.5 M), shake, and incubate for 20 min at –20 °C.
8. Centrifuge for 20 min, 13,000 × *g*, 4 °C.
9. Remove supernatant, and then add 1 ml 75 % ethanol.
10. Shake for 5 min, 900 × rpm RT, in Eppendorf shaker.
11. Centrifuge for 20 min, 13,000 × *g*, 4 °C.
12. Remove 970 µl of supernatant.
13. Centrifuge for 10 min, 13,000 × *g*, 4 °C.
14. Remove the rest of the supernatant, dry under the hood, and then store at 4 °C.

15. Perform in vitro transcription using ENZO™ High Yield In Vitro Transcription Kit according to the standard kit protocol. To obtain optimal linear amplification from the low-starting LCM material, run in vitro transcription for 68 h: After 16, 24, 40, 48, and 64 h, add concentrated T7 polymerase and nucleotides to the reaction mixture.
16. Purify cRNA using the RNeasy® Mini Kit. Measure yield with NanoDrop ND-1000 spectrophotometer. Estimate cRNA yield by subtracting 4 μg for the carrier added in **step 7**.
17. Fragment probe (0.5–12 μg cRNA) in the 1× fragmentation buffer for 30 min at 94 °C. Make sure that the amount of cRNA does not differ more than twofold for different probes within one experiment.
18. Hybridize arrays for 20 h in hybridization buffer (component of the GeneChip® Hybridization Control Kit) containing control oligoB2, herring sperm DNA, acetylated BSA, and Tween-20 at 45 °C under vigorous agitation according to the standard kit protocol. With cRNA yields less than 2 μg, hybridization time is extended to 24 h, and temperature is reduced to 43 °C.
19. Stain in the Fluidics Station (400 or 450) according to Affymetrix protocols using the Affymetrix staining kit.
20. Scan the arrays by GeneChip® Scanner immediately after staining. Scale raw data to 500 and export for further processing.

3.4 Microarray Data Analysis

1. Calculate signal intensities from the raw data and scale to an array trimmed mean of 500. For all further steps, use R and Bioconductor software [14, 15].
2. Normalize logarithmized signals across arrays using quantile normalization [16].
3. Filter data prior to statistical analyses to remove genes with low expression or without significant changes between control group and analyzing group. For upregulation, include probe sets if a minimum of 2 arrays (of three) or 3 arrays (of four) are present (detection p value $P \leq 0.05$) and a minimum of 2 arrays show a log signal $\geq \log2(200)$. For downregulation, include probe sets if a minimum of 2 or 3 arrays are present in the control group (detection p value $P \leq 0.05$) and a minimum of 2 arrays show a log signal $\geq \log2(200)$. Recorded genes are required to be upregulated or downregulated with a fold change of at least log2 (2.0).
4. Use data from two groups and subject the resulting up-list or down-list to t-test. Use data after applying filters with more than two groups, and subject the resulting up-list or down-list to one-factor variance analysis (ANOVA). Tests with p values $P \leq 0.01$ are corrected with Benjamini and Hochberg correction for multiple testing [17].

3.5 Model to Improve the Predictive Power of Microarray Expression Data from LCM-Isolated Aorta Laminae

1. Analyze cross RNA contamination on a genome-wide scale by determining relative abundance of genes on the microarrays of adventitia and their corresponding media in four individual mice.
2. Use probe sets of myelin basic protein (mbp) as marker for adventitia-selective genes.
3. Determine cross contamination as ratio of media expression to the sum of media expression and adventitia expression (relative media expression).
4. Generate means of four pairs and determine SD.
5. Devise a correction algorithm of RNA carryover between LCM-separated tissues as described in [12].

4 Notes

1. Mice should be housed in a pathogen-free environment on a 12 h light–dark cycle and fed a standard rodent chow (e.g., Altromin, Germany). Animal procedures must be approved by the Animal Care and Use Committee.
2. Secondary lymphoid organs including spleen and lymph nodes organize adaptive immune responses under normal conditions. However, when chronic inflammatory reactions emerge such as those observed in atherosclerosis and autoimmune diseases, tertiary lymphoid organs emerge within or adjacent to the diseased tissue. We identified ATLOs in the adventitia of aged $ApoE^{-/-}$ mice afflicted with advanced atherosclerosis [7]. To examine where immune responses are carried out in atherosclerosis, we isolated the adventitia, media, and plaque as well as lymph nodes that drain the aorta.
3. High RNA quality is critical to obtain robust microarrays and reduce the number of false-positive mRNAs. RNA quality needs to be examined repeatedly during the different experimental steps to avoid any RNA degradation before LCM (first RNA integrity control) and thereafter (second RNA integrity control). The LCM procedure for one slide (before transferring the LCM tissue into Trizol) requires around 60 min at room temperature. Moreover, lasers produce high energy which in turn raises the temperature of the adjacent tissues. In order to examine the degree of RNA degradation during LCM, RNA integrity needs to be examined after LCM (second round of integrity control). The RNA integrity number (RIN) is used to determine the RNA quality ($1 < RIN < 10$) and is calculated by Agilent 2100 Bioanalyzer automatically. For the first RNA integrity control, RIN should be set at the minimum of 7.0; for the second RNA integrity control, the RIN should

be set at > 5.0. Applying these rules and discarding any RNA that does not meet these criteria, we created microarray triplets or quadruplets that met stringent statistical tests and fulfilled MIAME criteria [12].

4. To reduce RNA degradation to produce high-quality mRNA microarrays from small amounts of total RNA, we used phase contrast optics to avoid histology staining. However, it is important to stain parallel sections with Oil Red O and hematoxylin to identify and outline ATLOs.
5. To improve transfer and attachment of cold tissue sections to the membrane slide, briefly warm the membrane slide on the glass side opposite to the site where the tissue section is attached by touching this site using a fingertip for 3 s.
6. Agilent RNA 6000 Pico Kit was used to prepare RNA 6000 Pico chip according to the standard protocol (Agilent RNA 6000 Pico kit quick start guide is available online: https://www.chem.agilent.com/Library/usermanuals/Public/G2938-90037_RNA6000Nano_QSG. pdf). The reagents, ladder, reference RNA (mouse liver RNA with known concentration and quality), and samples were properly added to the specific wells of the Pico chip, and then the Pico chip was vortexed for 60 s and analyzed by Agilent 2100 Bioanalyzer.

References

1. Weber C, Noels H (2011) Atherosclerosis: current pathogenesis and therapeutic options. Nat Med 17(11):1410–1422
2. Libby P, Ridker PM, Hansson GK (2011) Progress and challenges in translating the biology of atherosclerosis. Nature 473(7347): 317–325
3. Hansson GK, Hermansson A (2011) The immune system in atherosclerosis. Nat Immunol 12(3):204–212
4. Mohanta SK, Yin C, Peng L et al (2014) Artery Tertiary Lymphoid Organs Contribute to Innate and Adaptive Immune Responses in Advanced Mouse Atherosclerosis. Circ Res 114(11):1772–1787
5. Weih F, Grabner R, Hu D et al (2012) Control of dichotomic innate and adaptive immune responses by artery tertiary lymphoid organs in atherosclerosis. Front Physiol. doi:10.3389/fphys.2012.00226
6. Lotzer K, Dopping S, Connert S et al (2010) Mouse aorta smooth muscle cells differentiate into lymphoid tissue organizer-like cells on combined tumor necrosis factor receptor-1/lymphotoxin beta-receptor NF-kappaB signaling. Arterioscler Thromb Vasc Biol 30(3): 395–402
7. Grabner R, Lotzer K, Dopping S et al (2009) Lymphotoxin beta receptor signaling promotes tertiary lymphoid organogenesis in the aorta adventitia of aged ApoE-/- mice. J Exp Med 206(1):233–248
8. Galkina E, Kadl A, Sanders J et al (2006) Lymphocyte recruitment into the aortic wall before and during development of atherosclerosis is partially L-selectin dependent. J Exp Med 203(5):1273–1282
9. Moos MP, John N, Grabner R et al (2005) The lamina adventitia is the major site of immune cell accumulation in standard chow-fed apolipoprotein E-deficient mice. Arterioscler Thromb Vasc Biol 25(11):2386–2391
10. Zhao L, Moos MP, Grabner R et al (2004) The 5-lipoxygenase pathway promotes pathogenesis of hyperlipidemia-dependent aortic aneurysm. Nat Med 10(9):966–973
11. Feig JE, Fisher EA (2013) Laser capture microdissection for analysis of macrophage gene expression from atherosclerotic lesions. Methods Mol Biol 1027:123–135
12. Beer M, Doepping S, Hildner M et al (2011) Laser-capture microdissection of hyperlipidemic/ApoE-/- mouse aorta atherosclerosis. Methods Mol Biol 755:417–428

13. Trogan E, Fisher EA (2005) Laser capture microdissection for analysis of macrophage gene expression from atherosclerotic lesions. Methods Mol Biol 293:221–231
14. R Development Core Team (2009) R: A language and environment for statistical computing. R Foundation for Statistical Computing. http://www.r-project.org/. Accessed 9 July 2014
15. Gentleman RC, Carey VJ, Bates DM et al. (2004) Bioconductor: Open software development for computational biology and bioinformatics. Genome Biol **5**:R80
16. Bolstad BM, Irizarry RA, Astrand M et al (2003) A comparison of normalization methods for high density oligonucleotide array data based on variance and bias. Bioinformatics 19(2):185–193
17. Benjamini Y, Hochberg Y (1995) Controlling the false discovery rate—a practical and powerful approach to multiple testing. J Roy Stat Soc B Met 57(1):289–300

Note added in proof, after submission of this article the following manuscript has been published: Hu D, Mohanta S, Yin C et al (2015) Artery Tertiary Lymphoid Organs Control Aorta Immunity and Protect against Atherosclerosis via Vascular Smooth Muscle Cell Lymphotoxin β Receptors. Immunity 42:1100–1115

Chapter 21

Analysis of Gene and Protein Expression in Atherosclerotic Mouse Aorta by Western Blot and Quantitative Real-Time PCR

José Rivera-Torres

Abstract

Atherosclerosis involves changes in gene and protein expression patterns in affected arteries. Quantification of these alterations is essential for understanding the molecular mechanisms underlying this pathology. Western blot and real-time PCR—used to quantify protein and messenger RNA levels, respectively—are invaluable molecular biology tools, particularly when material is limited. The availability of many genetically modified mouse models of atherosclerosis makes the mouse aorta an ideal tissue in which to carry out these expression pattern analyses. In this chapter, protocols are presented for mRNA and protein extraction from mouse aorta and for the accurate quantification of mRNA expression by RT-PCR and of proteins by western blot.

Key words Protein, RNA, Western blot, Reverse transcription, cDNA, Real-time PCR, SYBR Green

1 Introduction

Atherosclerosis is a highly prevalent disease and is one of the main causes of death and morbidity in developed countries. The main risk factors contributing to the development and progression of the disease are hypercholesterolemia, hypertension, diabetes mellitus, and smoking tobacco. The disease involves alterations in complex patterns of cell to cell interaction and paracrine signaling mechanisms that start in the vascular endothelium. Central roles in inflammation and atherosclerosis have been reported for several proteins [1]. Some of these proteins, such as C-reactive protein, are validated markers of disease risk [2], whereas others represent primary targets for therapy and drug development, for example, the endoglin receptor, PPARα, squalene synthase, thyroid hormone analogues, and scavenger receptor [3].

Proteins and the messenger RNA (mRNA) molecules that encode them are essential for all cell processes, including proliferation, differentiation, and death. Even minimal alterations in the

Vicente Andrés and Beatriz Dorado (eds.), *Methods in Mouse Atherosclerosis*, Methods in Molecular Biology, vol. 1339, DOI 10.1007/978-1-4939-2929-0_21,

homeostatic levels of RNA and proteins result in alterations in essential cellular functions and can lead to disease [4]. Quantification of the expression changes affecting known or novel genes and proteins can therefore provide valuable information about the molecular mechanisms involved in atherosclerosis. Gene and protein expression changes can be analyzed directly in tissues isolated from animal models, and this in vivo approach has clear advantages over in vitro studies in cell lines. However, the use of animal tissues also presents drawbacks that can limit or impair protein and mRNA extraction, such as cell heterogeneity and the presence of nonprotein elements (e.g., lipids), fibrous components, and extracellular matrix. The most important issue for reproducible expression analysis in tissues is therefore the availability of a rigorous and reliable method for efficient sample preparation (RNA or protein), with all steps and buffers optimized to ensure robust downstream analysis.

Western blot, also known as immunoblotting, is one of the widely used and informative techniques used for the analysis of protein expression. The technique involves protein gel electrophoresis, transfer of proteins from the gel to a protein-binding membrane, and incubation of the membrane with antibodies specific for the proteins of interest.

Another pivotal tool in research and molecular diagnosis is gene expression profiling by quantitative reverse transcription polymerase chain reaction (qRT-PCR). This technique allows accurate and reproducible measurement of specific mRNA expression levels with extremely high sensitivity over a wide dynamic range. The sensitivity is sufficient to detect low-abundance mRNA in a single cell, making the technique especially applicable when sample sources are scarce [5]. The qRT-PCR method requires a special thermal cycler equipped with a sensitive system to monitor fluorescence emission at frequent intervals during the PCR reaction. The chemistry of the detection system depends on the nature of the fluorophore used [6]. The SYBR Green dye is a DNA-intercalating fluorescent reagent that preferentially binds to newly synthesized double-stranded DNA during the PCR reaction, such that the fluorescence intensity is directly proportional to the amount of DNA. Among the probe-based chemistries, the TaqMan method (also known as fluorogenic 5′ nuclease chemistry) requires also an additional fluorogenic probe. This probe consists in a specific oligonucleotide containing a fluorescent reporter with quencher dyes attached to its 5′ and 3′ ends. These dyes are so close to each other that fluorescence emission is prevented. After hybridization of the primer and the TaqMan probe to the complementary DNA strand and subsequent extension, the 5′ endonuclease activity of the DNA polymerase cleaves the TaqMan probe, splitting apart the reporter dye from the quencher and producing fluorescence. This technique is especially applicable when higher accuracy and reliability are required. Other chemistries

available include dual hybridization probes, molecular beacons, and Scorpions [6].

Here I present validated protocols for mRNA and protein extraction from the aorta of genetically modified mouse models of atherosclerosis [7, 8] and for the accurate quantification of mRNA expression by qRT-PCR and of proteins by western blot.

2 Materials

2.1 Tissue Disruption and RNA and Protein Extract Preparation

1. Tissue disruptor/homogenizer (e.g., Polytron, VWR; TissueLyser, Qiagen).
2. Calibrated and autoclaved pipettes and RNase-free fitting tips.
3. Water bath with adjustable temperature.
4. Refrigerated centrifuge (achieving $\geq 16{,}000 \times g$).
5. Spectrophotometer for estimation of protein concentration.
6. Plastic cuvettes (or plates) for measuring protein absorbance.
7. Quartz cuvettes (4 mm width, 1 cm path length) to measure RNA light absorption at 260 and 280 nm (A260/280). Optional: NanoDrop spectrophotometer.
8. Tube rotator/vortex.
9. Freezer and cold room.
10. Stainless steel beads (5 mm).
11. Dry ice (or liquid nitrogen).
12. Screw-cap propylene tubes, 2 ml.
13. Round-bottom propylene tubes, 2 ml.
14. Specific lab area exclusively dedicated to work with RNA (recommended).
15. RNase-free disposable glassware and plasticware.
16. RNase-free water or water treated with 0.05 % diethylpyrocarbonate (DEPC).
17. Monophasic solution of phenol and guanidine thiocyanate (e.g., QIAzol).
18. 75 % ethanol.
19. Chloroform.
20. Protease inhibitor cocktail tablets (e.g., Roche) containing 0.02 mg/ml pancreas extract; 0.0005 mg/ml thermolysin, 0.002 mg/ml chymotrypsin; 0.02 mg/ml trypsin and 0.33 mg/ml papain at 1× dilution.
21. Phosphatase inhibitor cocktail tablets (e.g., Roche) containing 14 U/ml calf alkaline phosphatase, 0.2 U/ml potato acidic phosphatase, 64 U/ml human acidic phosphatase, 20 U/ml

rabbit PP1, 50 U/ml human PP2A, 50 U/ml human PTP at 1× dilution.

22. Protein lysis buffer: 150 mM NaCl, 10 mM Na_2HPO_4, 2 mM KH_2PO_4, 2.7 mM KCl, 50 mM EDTA, 2.5 mM EGTA, 0.1 % SDS, 1 % NP-40, 0.5 % sodium deoxycholate.

2.2 SDS Polyacrylamide Gel Electrophoresis (SDS-PAGE)

1. Hand gel casting system of your choice.
2. Electrophoresis power pack.
3. Glass plates, combs, and spacers of your choice.
4. Water-saturated isobutanol.
5. Pasteur pipettes.
6. Whatman 3MM paper.
7. Ammonium persulfate (APS): 10 % w/v in water. Prepare fresh before use.
8. *N*, *N*, *N*′, *N*′-Tetramethylethylenediamine (TEMED).
9. Prestained protein molecular weight markers of your choice.
10. Stock solutions for preparing SDS-PAGE gels: 1.5 M Tris–HCl, pH 8.8 (at 25 °C); 0.5 M Tris–HCl pH 6.8 (at 25 °C), 30 % acrylamide/bis-acrylamide solution in water (29:1 ratio), 20 % (w/v) sodium dodecyl sulfate (SDS) solution.
11. 1× SDS Running Buffer: 25 mM Tris base, 0.192 M glycine, 0.1 % (w/v) SDS.
12. 5× Sample Buffer: 10 % (w/v) SDS, 10 mM DTT (or β-mercaptoethanol), 20 % (v/v) glycerol, 200 mM Tris–HCl pH 6.8 (at 25 °C), 0.075 % (w/v) bromophenol blue.

2.3 Western Blotting

1. Gel transfer device and accessories (e.g., iBlot® Invitrogen).
2. TBS: 49 mM Tris–HCl pH 7.6 (at 25 °C), 150 mM NaCl.
3. TBS-T: 0.2 % (v/v) polyoxyethylene sorbitan monolaurate (Tween-20) in TBS.
4. Blocking buffer: 5 % (w/v) nonfat dry milk in TBS-T.
5. Bovine serum albumin (BSA).
6. Enhanced chemiluminescent reagents.
7. Stripping Buffer: 62.5 mM Tris–HCl pH 6.8, 0.1 M β-mercaptoethanol, 2 % SDS.

2.4 Reverse Transcription (RT)

1. Reverse transcriptase to generate cDNA from an RNA template (100 U/μL).
2. 10× RT buffer: 0.5 M Tris–HCl, pH 8.3, 0.75 M KCl, 30 mM $MgCl_2$, 50 mM DTT.
3. Random hexamer, oligo (dT) or sequence-specific primers (50 μM).

4. High-quality deoxynucleotide triphosphates (dNTPs) (1 mM).
5. RNase inhibitor (10 U/μL).
6. Optional: commercially available first cDNA synthesis kit (e.g., the High Capacity cDNA Reverse Transcript Kit from Applied Biosystems) containing: 10× RT buffer, 10× RT random primers, 100 mM dNTP mix, 50 U/μL MultiScribe™ reverse transcriptase and 100× RNase inhibitor.
7. Thermal cycler.
8. 0.2 ml flat cap tubes fitting your thermal cycler.

2.5 Quantitative Real-Time PCR

1. Template DNA (cDNA).
2. High-quality dNTPs (1 mM).
3. Hot-start DNA polymerase.
4. 10× DNA polymerase buffer.
5. Forward and reverse gene-specific primers.
6. Forward and reverse primers for the housekeeping gene(s) of your choice. Options include β-actin, 18S ribosomal RNA (18SrRNA), cyclophilin A (CYC), glyceraldehyde phosphate dehydrogenase (GAPDH), β-2-microglobulin (B2M), β-glucuronidase (GUS), hypoxanthine phosphoribosyltransferase (HPRT), and TATA-box-binding protein (TBP).
7. Fluorescent DNA dye: SYBR Green.
8. Optional: in place of materials 2, 3, and 4, you can use commercially available working mixtures for SYBR Green reactions (e.g., Power SYBR® Green Master Mix from Applied Biosystems).
9. 384-well clear optical reaction plates.
10. Clear adhesive film for 384-well plates.
11. Thermocycler (e.g., ABI PRISM® 7900HT/FAST Real-Time PCR System).
12. ABI Prism 7000 SDS software (or other supplied with your thermocycler).
13. 2–3 % agarose gel.
14. RNA molecular weight markers (0.28–6.58 kb).
15. Agarose gel electrophoresis apparatus.
16. Electrophoresis power supply.

3 Methods

3.1 Tissue Disruption and Protein Lysate Preparation

1. Pool 2–3 frozen mouse aortas (maximum 100 mg tissue/tube) in prechilled screw-cap tubes containing a 5 mm stainless steel bead for processing with a TissueLyser homogenizer (Option A)

or in a round-bottom tube for processing with a Polytron rotor-stator homogenizer (Option B) (*see* **Notes 1–3**).

2. Disrupt tissues in 500 µL of cold protein lysis buffer for 2 min at 50 Hz (Option A) or at 15,000 rpm, starting at the lowest power and increasing gradually to the target speed (Option B). Keep tubes on ice throughout the process (*see* **Notes 4–6**).
3. Repeat the process until complete tissue disruption is achieved (*see* **Notes 7** and **8**).
4. Transfer homogenate to a precooled tube and leave it on a rocker in a cold room for 20–30 min.
5. Centrifuge at 16,000 × *g* for 15 min at 4 °C.
6. Save supernatant and measure protein concentration by your preferred method. Use 0, 1, 2.5, 5, and 10 µL BSA (1 mg/ml) to generate a standard curve.
7. Store at −20 °C or lower until use.

3.2 SDS-PAGE for Protein Analysis

1. Mount the assembled gel casting unit upright to facilitate pouring of the gel.
2. Prepare the appropriate % SDS-PAGE solution for the resolving gel (1 mm thickness) as indicated in Table 1, and pour it (*see* **Notes 9–15**).
3. Carefully cover the top of the gel with water-saturated isobutanol (or any other tertiary amyl alcohol), and allow complete gel polymerization (30–60 min) (*see* **Note 16**).
4. Meanwhile, prepare 4 % stacking solution (recipe in Table 1).
5. Remove the isobutanol top layer and rinse the gel extensively with distilled water.
6. Dry the inner sides of the glass plates thoroughly with Whatman 3MM paper.
7. Add 10 µL of TEMED to the stacking gel solution; mix and pour immediately.
8. Insert the desired clean comb (1 mm thickness), and allow the gel to polymerize completely (approximately 20 min). Check for leaks.
9. Remove the comb and rinse extensively with distilled water (*see* **Note 17**).
10. Place the gel sandwich in the appropriate electrophoresis apparatus.
11. Fill the tank and cassette holder reservoir with 1× SDS Running Buffer. Ensure that there are no leaks and remove bubbles.
12. Boil samples at 95 °C in 1× final SDS Sample Buffer for 4–5 min and briefly spin down.

Table 1
Recipes for SDS polyacrylamide gels and their linear molecular mass resolution

Resolving gel (%)	*5*	*7.5*	*10*	*12*	*15*
Total vol	8 ml	8 ml	8 ml	8 ml	8 ml
ddH_2O	4.5 ml	3.8 ml	3.2 ml	2.6 ml	1.8 ml
30 % Acry/Bis	1.33 ml	2 ml	2.67 ml	3.2 ml	4 ml
1.5 M Tris–HCl (pH 8.8)	2 ml	2 ml	2 ml	2 ml	2 ml
20 % SDS	40 µL	40 µL	40 µL	40 µL	40 µL
10 % APS	80 µL	80 µL	80 µL	80 µL	80 µL
TEMED	8 µL	8 µL	8 µL	8 µL	8 µL
Mr (kDa)	25–200		15–70		12–45
Stacking gel (%)	*4*				
Total vol	5 ml				
ddH_2O	3				
30 % Acry/bis	0.67 ml				
0.5 M Tris pH 6.8	1.25 ml				
20 % SDS	25 µL				
10 % APS	50 µL				
TEMED	5 µL				

13. Load samples (~20 µg/lane), including one well with prestained molecular weight markers.
14. Run gels at 90 V (8–15 milliamps current) until the dye front has moved through the stacking gel. The current can then be increased (25–35 milliamps), and the gel run until the dye front reaches the bottom of the gel.
15. Remove the glass plates and use the gel for western blot (*see* **Note 18**).

3.3 Western Blotting

1. Transfer the proteins from the 1 mm thick gel to a PVDF membrane by using the iBlot® Gel dry transfer system which allows ultra-rapid protein transfer in 7 min (P3 program) (*see* **Notes 19–22**).
2. Immerse membrane in blocking buffer and incubate with gentle agitation for 2 h at room temperature or overnight at 4 °C (*see* **Note 23**).
3. Wash membrane three times in abundant volumes of TBS-T for 5 min each time, rocking (*see* **Note 24**).

4. Add diluted appropriately primary antibody in blocking buffer and incubate overnight at 4 °C (unless otherwise specified), with gentle agitation (*see* **Notes 25** and **26**).
5. Wash three times in TBS-T for 5 min each time.
6. Dilute secondary antibody in blocking buffer (as recommended by the manufacturer), and incubate with the membrane for 1 h at room temperature with gentle agitation.
7. Wash three times for 5 min each with an excess of TBS-T.
8. Detect proteins with a chemiluminescence kit according to the manufacturer's recommendations.

3.4 Membrane Stripping

If samples are limited, bound antibody can be stripped from membranes, which can then be reprobed with a different first antibody.

1. Immerse the membrane in Stripping Buffer and incubate at 50 °C for 30–60 min (*see* **Note 27**).
2. Wash membranes extensively with TBS-T at least five times for 5 min each time.
3. Block membranes in the appropriate blocking buffer based on the requirements of your first antibody (*see* **Note 23**).

3.5 RNA Isolation

1. Disrupt mouse aortic tissue (maximum 100 mg of tissue) in sterilized screw-cap RNAase-free tubes with 700 μL of phenol-based RNA Lysis Reagent (e.g., QIAzol) for 2 min at 50 Hz speed (CAUTION! *See* **Notes 28–31**).
2. Repeat the process until complete tissue disruption is achieved (*see* **Notes 7** and **8**).
3. Transfer homogenate to a new tube and leave for 5 min at room temperature.
4. Add 140 μL (1/5 v:v) chloroform and shake vigorously for 15 s or until a uniform pink suspension is obtained.
5. Leave for 2 min at room temperature until phase separation is achieved (*see* **Note 32**).
6. Centrifuge at 12,000 × *g* for 15 min at 4 °C.
7. Transfer the RNA-containing upper aqueous phase to a new tube.
8. Add 1/2 volume of isopropanol, vortex, and leave at room temperature for 10 min (*see* **Note 33**).
9. Centrifuge at 10,000 × *g* for 20 min at 4 °C (*see* **Note 34**).
10. Discard supernatant and wash the RNA pellet with 1–2 ml of 75 % ethanol (in RNase-free water). Mix by vortexing.
11. Spin down at 7000 × *g* for 5 min at 4 °C and allow the RNA pellet to air-dry briefly.

12. Dissolve the RNA in RNase-free water by pipetting up and down.
13. Determine the RNA concentration by measuring absorbance at 260 nm (OD_{260} nm) (*see* **Note 35**).
14. Check RNA purity by assessing the 260/280 nm absorbance ratio (*see* **Note 36**).
15. Check RNA integrity by running a 2–3 % agarose gel (*see* **Note 37**).
16. If samples are not for immediate use, store them at –80 °C.

3.6 Reverse Transcription

Although RT-PCR can be achieved in a single step in which all the components are mixed and assayed, a traditional two-step protocol is recommended here (*see* **Note 38**).

1. Thaw kit components (e.g., High Capacity cDNA Reverse Transcript Kit from Life Technologies) on ice (*see* **Note 39**).
2. Prepare enough 2× RT master mix according to the following volumes.

Components (stock)	Volume/reaction (μL)
RT buffer (10×)	2
dNTP Mix (25×)	0.8
Random primers (10×)	2
RT enzyme (50 U/μL)	1
RNase inhibitor (20 U/μL)	1

Bring to 10 μL with RNase-free water

3. Mix gently. DO NOT vortex. Spin down briefly.
4. Pipette 10 μL of 2× RT master mix per tube; use tubes compatible with your thermal cycler.
5. Add 10 μL (1–2 μg) of RNA sample in RNase-free water.
6. Mix gently by pipetting and briefly spin tubes down.
7. Perform the RT reaction in a thermal cycler using the following conditions (*see* **Note 40**):
   10 min at 25 °C/120 min at 37 °C/5 min at 85 °C.
8. Store cDNA at 4 °C or lower until use.

3.7 Quantitative Real-Time PCR

1. Prepare oligonucleotide mix containing 0.5× Power SYBR® Green PCR Master Mix and 50–100 nM of forward and reverse primers; prepare sufficient mix for triplicate loadings of each sample plus controls (*see* **Note 41**).
2. Load 5.6 μL of the oligo mix per well in a 384-well plate. Keep the plate on ice throughout the process (*see* **Notes 42–44**).

3. Add 4.4 μL diluted cDNA (1–10 ng) to each well, omitting the negative control well (*see* **Note 41**).
4. Seal the plate with clear adhesive film and spin it down briefly.
5. Use the specific software provided with your thermal cycler (e.g., SDS 2.1 for the ABI PRISM® 7900HT/FAST Real-Time PCR System) to program your PCR reaction to the following cycling conditions: 2 min at 50 °C followed by10 min at 95 °C for polymerase activation and then 40 cycles of 95 °C for 15 s and 60 °C for 1 min for primer annealing and extension. An optional dissociation stage (95 °C 15 s/60 °C 15 s/95 °C 15 s) can be used to assess PCR specificity (*see* **Note 45**).

3.8 Quantitative Real-Time PCR Data Analysis

qRT-PCR data are generally quantified in two ways:

1. Absolute quantification based on a standard curve generated from an internal control.
2. Relative quantification of a target gene compared to internal standards (housekeeping genes such as 18S rRNA, GAPDH, β-actin, HPRT, etc.). This method is particularly useful for gene expression analysis and is one of the most commonly used [9]. An improved commercial version (Biogazelle) is also available of the free qBASE software [10] that validates reference genes and performs normalization of target genes with the geometric mean of the different validated housekeeping genes (*see* **Note 46**).

4 Notes

1. The Polytron system processes a single sample at a time, whereas TissueLyser is a low-medium-throughput sample homogenizer that allows simultaneous disruption of multiple samples (up to 192 depending on the model), ensuring reproducibility between samples.
2. Before starting, ensure that all the parts of the Polytron apparatus that will be in contact with your sample are clean and free of any contaminants from previous experiments. Polytron components are easily disassembled and can be sterilized by all the usual methods, including autoclave. Remaining aggregates can be removed by running in an adequate solvent, water, or a rinsing solution. Alternatively, an ultrasonic bath is a very effective way of cleaning. Wash the Polytron with water between samples.
3. Wear gloves, safety glasses, and ear protection.
4. If using TissueLyser, it is recommended to cool the tube holder for at least 24 h before starting. Screw tube caps securely

to avoid sample spills and balance them for proper homogenizer operation.

5. When required, add protease/phosphatase inhibitors to cold protein lysis buffer just before proceeding with the lysis.
6. Depending on your protein of interest and the buffer stringency needed for its recovery, choose the appropriate detergent concentration for the homogenization buffer. RIPA buffer contains 0.1 % SDS, 1 % NP-40, and 0.5 % Na deoxycholate, and is a fairly stringent buffer. Alternatively, you can use 1 % NP-40, 1 % Tween-20, 1 % SDS, or 1–2 % CHAPS, depending on your specific extraction requirements and downstream usages.
7. Rotate the TissueLyser rack to allow even homogenization.
8. The duration of disruption/homogenization depends on the tissue being processed and can be extended until no tissue debris is visible.
9. CAUTION! Acrylamide/bis-acrylamide solution is a biohazard (neurotoxic by contact in liquid state). Always handle with gloves.
10. If acrylamide/bis-acrylamide liquid mixture is not available, dissolve 29 g of acrylamide and 1 g of bis-acrylamide in 100 ml of water and then filter the solution through Whatman 3MM filter paper and store at 4 °C in a light-protected bottle. Manipulate the reagents wearing gloves and a protective mask, and if possible, work under a biosafety hood.
11. Bis-acrylamide cross-links acrylamide in the gel. APS drives acrylamide/bis-acrylamide polymerization, and TEMED catalyzes the formation of free radicals from APS, speeding up the polymerization process.
12. Acrylamide/bis-acrylamide percentages can vary. This general protocol describes recipes for different SDS acrylamide/bis-acrylamide resolving and stacking gels. Percentages can be adjusted to suit the molecular weight range of the proteins to be resolved.
13. 10 % APS solution should be freshly prepared as its activity decays when stored.
14. Polymerization starts as soon as TEMED is added: work without delay.
15. For separation of high molecular weight proteins, an acrylamide/bis-acrylamide 37.5:1 ratio is recommended instead of 29:1.
16. It prevents oxidation of the polyacrylamide, which inhibits polymerization.
17. Do not dispose of any remaining acrylamide/bis-acrylamide mixture until it has completely polymerized.
18. Alternatively, gels can be stained.

19. Alternatively, semidry and wet blotting transfer systems are commonly available and work well.
20. Different current and transfer times can be used; the choice depends on the intrinsic properties (molecular size and shape) of your protein of interest and should be empirically optimized. Efficient transfer depends, among other factors, on the percentage of acrylamide, the gel thickness, and the transfer system used (semidry, wet).
21. Wear gloves for handling the gel and PVDF membrane to prevent fingertip contamination.
22. To make it easy to orient the membrane later, cut one corner or mark it with a pencil.
23. For detection of phospho-specific antibodies, use BSA-based blocking buffer instead.
24. Alternatively, you can use PBST: 0.2 % (v/v) Tween-20 in PBS (137 mM NaCl; 2.7 mM KCl; 10 mM Na_2HPO_4, 2 mM KH_2PO_4).
25. Very small volumes can be used for antibody incubations so long as you ensure that the membrane remains wet throughout the incubation (e.g., by placing the membrane in sealed plastic bags). This minimal volume reduces the amount of antibody used per blot.
26. After incubation, the diluted primary antibody can be kept and reused. The effectiveness of each antibody on reuse should be empirically tested. For storage, it is recommended to add 0.02 % sodium azide to the diluted antibody as preservative. To avoid freeze/thawing of the primary antibody, add glycerol at a 1:1 v/v ratio and store at –20 °C.
27. The β-mercaptoethanol stock concentration is 14.3 M.
28. When isolating RNA, avoid freeze/thaw steps to prevent degradation. The protocol can start with aortic tissue which has been stored in an ultrafreezer or with fresh tissue. When using fresh aortas, it is recommended to disrupt the tissue using a mortar, razor blades, scissors, etc.
29. Rinse plasticware thoroughly with 0.1 N NaOH/1 mM EDTA and then with DEPC-treated water. Lab-made solutions should be treated with 0.05 % DEPC overnight at room temperature, and then autoclaved for 30 min to degrade the DEPC. Bake glassware overnight at 250 °C. DEPC cannot be used to treat Tris-based buffers because it reacts with the free amino group, annulling the buffering capacity of Tris-based formulations.
30. CAUTION! QIAzol reagent contains phenol and guanidine thiocyanate, which are toxic and corrosive agents.
31. Increase buffer volume in proportion to the tissue weight. The tissue should not exceed 10 % (w/v) of the RNA lysis buffer.

32. Phases separate faster when tubes are incubated on ice.
33. At this step, samples can be left overnight at −20 °C.
34. RNA has a gel-like appearance.
35. 1 OD_{260} Unit = 40 μg/ml RNA.
36. A ratio of ~2.0 is generally accepted as "pure" for RNA.
37. When the RNA sample is not degraded, the 28S rRNA subunit band (~5 kb) is approximately twice as intense as the 18S rRNA subunit band (~2 kb), and no smearing should be seen between the rRNA bands and below the 18S rRNA.
38. One-step qRT-PCR is recommended when processing large numbers of samples since it minimizes carryover contamination. It also provides greater sensitivity. Two-step qRT-PCR allows the archiving of cDNA for further analysis and is useful for detection of multiple messengers from a single RNA sample.
39. Alternatively, use a mixture containing the reverse transcriptase enzyme, its associated buffer, dNTPs, and random hexamer oligonucleotides at their appropriate concentration and the conditions indicated by your supplier.
40. These thermal conditions have been optimized for this specific kit and can be changed if a different kit is used.
41. Inclusion of a no-template control, in which all components of a reaction are included except the template of interest, is always recommended in order to validate specificity. Any amplification in these samples is due either to primer-dimers or contaminating template. Another control to be considered is a no-reverse-transcriptase control, in which all components except the reverse transcriptase are present. Amplification from this control indicates DNA contamination of the RNA sample, which can make expression levels look higher than they are.
42. Primer concentration should be optimized for each newly designed primer pair.
43. The following public databases are excellent sources for validated primers: PrimerBank (http://pga.mgh.harvard.edu/primerbank/), RTPrimerDB (http://medgen.ugent.be/rtprimerdb/), and Real-Time PCR Primer Sets (http://www.realtimeprimers.org). When validated primer sequences are not available, primers should be designed according to standard procedures [11].
44. Free primer design software is also available, such as Primer3 from the Whitehead Institute at MIT (http://bioinfo.ut.ee/primer3/); *see* also http://eu.idtdna.com/PrimerQuest/Home/Index. Online design tools also exist for TaqMan probes (https://www.genscript.com/ssl-bin/app/primer).
45. Alternatively, run 5 μL from each PCR reaction in a 3 % agarose gel to check specificity.

46. Many biotech companies bundle data analysis software packages with their real-time PCR instruments. qPCR data analysis tools are also freely available from either public sources (http://bioinformatics.gene-quantification.info/) or private sources (http://www.lifetechnologies.com/es/en/home/technical-resources/software-downloads/dataassist-software.html).

References

1. Libby P, Ridker PM, Maseri A (2002) Inflammation and atherosclerosis. Circulation 105:1135–1143
2. Tomiyama H, Okazaki R, Koji Y et al (2005) Elevated C-reactive protein: a common marker for atherosclerotic cardiovascular risk and subclinical stages of pulmonary dysfunction and osteopenia in a healthy population. Atherosclerosis 178:187–192
3. Jamkhandea PG, Chandaka PG, Shashikant C et al (2013) Therapeutic approaches to drug targets in atherosclerosis. Saudi Pharm J. doi:10.1016/j.jsps.2013.04.005
4. Wu SC, Zhang Y (2010) Active DNA demethylation: many roads lead to Rome. Nat Rev Mol Cell Biol 11:607–620
5. Stahlberg A, Bengtsson M (2010) Single-cell gene expression profiling using reverse transcription quantitative real-time PCR. Methods 50:282–288
6. Arya M, Shergill IS, Williamson M et al (2005) Basic principles of real-time quantitative PCR. Expert Rev Mol Diagn 5:209–219
7. Getz GS, Reardon CA (2012) Animal models of atherosclerosis. Arterioscler Thromb Vasc Biol 32:1104–1115
8. Vasquez EC, Peotta VA, Gava AL et al (2012) Cardiac and vascular phenotypes in the apolipoprotein E-deficient mouse. J Biomed Sci 19:22
9. Bustin SA, Benes V, Garson JA et al (2009) The MIQE guidelines: minimum information for publication of quantitative real-time PCR experiments. Clin Chem 55:611–622
10. Hellemans J, Mortier G, De Paepe A et al (2007) qBase relative quantification framework and software for management and automated analysis of real-time quantitative PCR data. Genome Biol 8:R19
11. Nolan T, Hands RE, Bustin SA (2006) Quantification of mRNA using real-time RT-PCR. Nat Protoc 1:1559–1582

Chapter 22

Bone Marrow Transplantation in Mice to Study the Role of Hematopoietic Cells in Atherosclerosis

Vinatha Sreeramkumar and Andrés Hidalgo

Abstract

Hematopoietic stem cell transplantation or bone marrow transplantation is a common approach to reconstitute the immune system of mice that have been subjected to marrow-ablative doses of radiation. This method can be used in the field of atherosclerosis to assess the contribution of hematopoietic cells of a desired genotype to disease pathogenesis. The engraftment of atherosclerosis-prone mice with donor cells that contain genetic alterations in cells of the innate or adaptive immune system has been invaluable to define the role of multiple gene products in atherosclerosis. Here, we describe the different steps involved in the bone marrow transplantation protocol along with specific guidelines regarding the theoretical and technical details of the procedure.

Key words Bone marrow transplantation, Atherosclerosis, Irradiation, Macrophages, Apolipoprotein-E, Low-density lipoprotein, Atherogenic, Plaque, Chimerism, Transgenic, Engraftment

1 Introduction

Hyperlipidemia triggers the local accumulation of lipoproteins on the vessel wall of large arteries. The lipid deposits induce the recruitment of cells from the innate and adaptive immune system causing the formation of atherosclerotic lesions that eventually grow in size and become unstable, and may finally elicit formation of thrombi, occlusion, and death of the tissue [1]. Hematopoietic cells, especially those of the myeloid and lymphoid lineages, along with cells of the vessel wall participate in the atherogenic process [2, 3]. All these events lead to the development of atherosclerosis, a chronic inflammatory disorder affecting medium and large arteries which represents the underlying cause of most cardiovascular, cerebrovascular, and peripheral vascular diseases [4]. Murine models have considerably contributed to our understanding of the process of atherogenesis owing to their relative ease in handling and reasonable time frame for atherosclerotic plaque development

Vicente Andrés and Beatriz Dorado (eds.), *Methods in Mouse Atherosclerosis*, Methods in Molecular Biology, vol. 1339, DOI 10.1007/978-1-4939-2929-0_22,

and subsequent monitoring [5, 6]. While genetically altered (transgenic and gene targeted-deletion) mouse models have afforded great progress in the study of the cellular and genetic basis of atherosclerosis, the use of bone marrow transplantation (BMT) to specifically exchange the genetic makeup of hematopoietic cells (but not the parenchymal tissues) has been and continues to be essential to dissect the contribution of defined cells and genes to atherosclerosis [7].

Murine atherosclerosis models are generated by inducing hypercholesterolemia, which is facilitated by the use of mice with specific genetic deletions, typically mice deficient for apolipoprotein-E (*Apoe*$^{-/-}$) or low-density lipoprotein receptor (*Ldlr*$^{-/-}$) in combination with diets with a high content in fat and cholesterol [1]. BMT studies in these mice have aided in the generation of insights into the cellular sources of these particular receptors and their contribution to the different phases of atherogenesis. For example, while the reconstitution of *Apoe*$^{-/-}$ mice with wild-type BM cells resulted in virtually complete protection from diet-induced atherosclerosis, the presence of LDLR on BM-derived cells that are transplanted into *Ldlr*$^{-/-}$ mice did not have a significant impact on the development of atherosclerosis or hyperlipidemia in these mice [8–12]. Conversely, wild-type mice reconstituted with *Apoe*$^{-/-}$ BM cells exhibit increased atherosclerosis [13]. Therefore the *Apoe*$^{-/-}$ mouse model has helped in the attribution of specific roles for macrophage/monocyte-derived *ApoE*, whereas *Ldlr*$^{-/-}$ mice have the advantage of remaining susceptible to atherogenesis when reconstituted with bone marrow with an intact LDLR [14]. Thus, irradiation of atherosclerosis-prone mice followed by BM reconstitution from donors with genetic alterations in the innate and acquired immune systems have been employed to identify the role of BM-derived cells and their genes in atherosclerosis, particularly in the *Ldlr*$^{-/-}$ model. The BMT approach can also be used experimentally to decipher the complex cytokine and chemokine signatures involved in the recruitment and adherence of various cell types to the arterial wall during atherogenesis. An additional advantage of this method is that it allows discrimination of the pathogenic effects on atherosclerosis development derived specifically from the hematopoietic compartment (or more accurately, the transplantable cells) relative to the "parenchymal" components that remain of host origin, including the endothelial and smooth muscle cells and extrahepatic lipoproteins [2, 3].

Among the various means of employing BMT in atherosclerosis research, there are three main purposes for which it can be utilized: (1) to define the role of hematopoietic-borne (intrinsic) mutations, in which case the mutant mouse would serve as the donor while the atherosusceptible mouse (*Ldlr*$^{-/-}$) lacking that particular mutation would serve as a recipient; (2) to detect non-hematopoietic-derived (extrinsic) effects of genetic alterations for

which the donors would be the wild-type mice and the recipient mice would bear the mutation/s; and (3) to compare the behavior of different donor-derived blood cells within the same atherogenic microenvironment by generating mixed chimeras with either two mutant donors or one mutant and one wild-type donor which are transplanted into atherosusceptible recipient mice. In addition, with major advances in the field of imaging of the atherosclerotic plaque [15] and the development of reporter mice that tag specific myeloid or leukocyte populations with fluorescent markers (e.g., $Lyz2^{GFP}$, $CX3CR1^{GFP}$, $Actb^{DSRED}$) which could be used as either donors or recipients in BMT studies, it is now possible to assess the behavior of single cells, their incorporation into the plaque, and their contribution to disease at a very high resolution. Another obvious advantage of using BMT is the relative ease in obtaining a large number of sex- and age-matched animals for single experiments while also rendering unnecessary the time-consuming procedure of genetic backcrossing to introduce a defined mutation in the atherosusceptible mouse lines.

However, there are some caveats and concerns with the use of BMT for research in atherosclerosis. For example, some studies propose that irradiation does not eliminate tissue-resident macrophages that may be involved in atherogenesis; this is the case of Kupffer cells which can be nonetheless removed from the recipient mice using clodronate liposomes [16]. Other studies have demonstrated significant differences in atherosclerotic lesion size and composition in BM-transplanted mice [17]. While considering these disadvantages, the use of BMT in atherosclerosis continues to be extremely useful for further exploration of this complex disease if the procedure is done under optimal conditions and taking into account several critical parameters that will ensure the reproducibility of the method.

In this chapter we detail an optimized protocol for hematopoietic stem cell transplantation with several tips and guidelines in order to warrant a successful study of atherogenesis using BMT (Fig. 1).

2 Materials

1. Irradiator: A commercial irradiator of X-rays or gamma rays with a cesium/cobalt source.
2. Atherosusceptible recipient mice (e.g., *Apoe*$^{-/-}$, or *Ldlr*$^{-/-}$).
3. Sterile phosphate-buffered saline (PBS).
4. Saline solution or cell culture medium (e.g., RPMI) without antibiotics.
5. Scalpel.
6. Petri dishes.

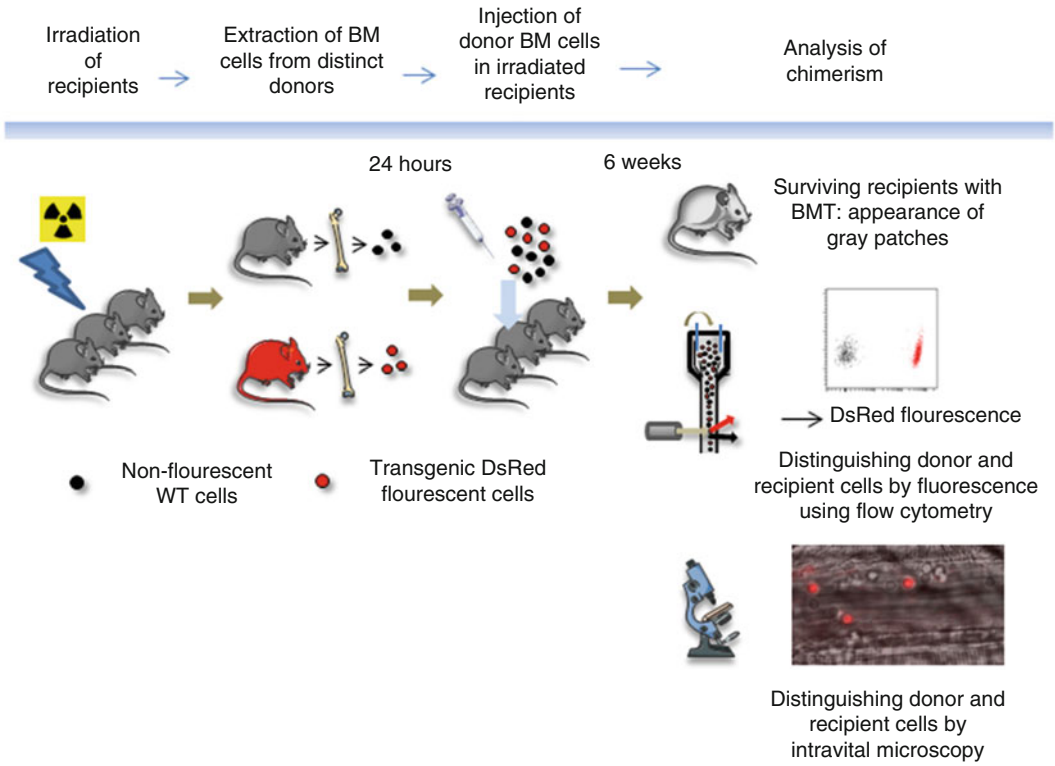

Fig. 1 Illustrative example of bone marrow transplantation to generate mixed chimeras in mice. Six- to eight-week-old recipient mice are irradiated with myeloablative doses of radiation. In this example, femurs from non-fluorescent and transgenic fluorescent DsRed donors are extracted following euthanasia. One day after irradiation, BM cells are processed and mixed in equal numbers and are injected intravenously in recipient mice. Six weeks following BMT, chimerism in surviving recipients is analyzed. Irradiated mice exhibit visual signs such as the appearance of grey patches of hair on skin. Reconstitution can be confirmed by analyzing the blood counts of the recipient mice using a hematological counter. In this example, the engrafted donor cells can be distinguished as derived from the DsRed transgenic- or the wild-type donor mice based on their fluorescence in the DsRed channel by flow cytometry or by intravital microscopy. Flow cytometry allows for standardized quantification and characterization of relative numbers of the different donor-derived cells in the recipients. Intravital microscopy allows the direct visualization of their relative numbers and to detect possible differential behaviors of distinct donor-derived hematopoietic cell subtypes. Both protocols could therefore be used to visualize not only the efficiency of engraftment of irradiated recipients but also for the analysis of functional differences between the donor cell subsets during atherosclerosis

7. Hemocytometer.
8. 0.5–1 ml syringes.
9. 21 and 25–27 G needles.
10. Automatic pipettes for resuspension.
11. General anesthetic (e.g., isoflurane 2 %).
12. Flow cytometer: To check bone marrow reconstitution by staining blood cells with antibodies for specific markers (e.g., CD45.1).

13. Hematological cell counter: For analysis of blood parameters.
14. Optional: Microscope and surgical tools if intravital microscopy needs to be performed.

3 Methods

3.1 Preparation of Donor BM Cells

1. Sacrifice donor mice and obtain femurs (and tibiae if necessary). For reference, up to 30×10^6 cells can be obtained from one femur of a healthy donor. BM cellularity increases with age, but declines in very old mice. Hence the age of the donor mice should be preferably between 6 and 14 weeks (*see* **Note 1**).
2. Use a scalpel to make an incision at the head of the bones.
3. Flush bone marrow in a laminar flow hood, using PBS or cell culture medium (containing no serum). Use a 21 G needle for femurs, and 25–27 G for tibiae (*see* **Note 2**).
4. Homogenize marrow gently with a p1000 pipette or a 1-mL syringe with 21 G needle, taking care not to break cells. Make a single-cell suspension. Lysis of red blood cells using hypotonic buffers is possible but not recommended in order to preserve the full viability of BM cells.
5. Count cells with the hemacytometer and adjust with PBS or sterile saline solution to have 1×10^6 BM cells in 100 μL (the volume to be injected in the recipient mice). This number should be adjusted depending on existing information about the quality of hematopoietic stem cells in the donor mice (*see* **Notes 3** and **4**).

3.2 Irradiation of Mice and Injection of Donor BM Cells

1. Recipient male or female mice of at least 6 weeks of age (to be able to survive the irradiation) are irradiated with two doses of 650 rads (6.5 Gy) each (total irradiation of 1300 rads, 13 Gys). Regarding the various parameters of irradiation and veterinary care of irradiated animals *see* **Notes 5–9**.
2. Anesthetize irradiated recipient mice and inject intravenously (retro-orbital or tail vein) with at least 10^6 BM cells resuspended in 100 μl of sterile saline or culture media without serum (*see* **Notes 10** and **11**).
3. Transplanted mice should be allowed to recover for at least 1 month post-BMT.
4. Confirm reconstitution by analysis of blood parameters (*see* **Note 12**).
5. Draw 50 μl of blood for flow cytometric analysis to detect the degree of chimerism. Depending on the experiment, the analysis can be done at different times post-transplantation (*see* **Notes 13–17** for guidelines concerning analysis of chimerism following BMT).

4 Notes

1. While preparing donor BM cells, if the amount of cells obtained from two femurs and two tibias is not sufficient, additional cells can also be harvested from the humerus, radius, and sternum.
2. The cell-culture medium used for flushing of BM can be supplemented with antibiotics to avoid contamination but should not contain fetal calf serum. Alternatively, BM cells can be frozen and reutilized at a later time. For this purpose, donor BM cells are washed and resuspended in 1 ml of DMEM or RPMI medium containing 20 % fetal calf serum and 10 % DMSO (a cryopreservant) at a density of 10^7 cells/ml/vial. Cells are frozen in cryotubes at a temperature of –70 °C or in liquid nitrogen. When the BM cells need to be used again for transplantation, they should be thawed quickly in a water bath at 37 °C, washed several times with plain RPMI medium/sterile saline solution in order to get rid of the serum and DMSO, and resuspended in PBS or saline solution, prior to injection into the recipient/s.
3. Before engraftment, it must be assured that the donor hematopoietic stem cells have no defect or deficiency in the homing molecules associated with their migration to the bone marrow, the lack of which would result in a failure of reconstitution. If the donor cells do have this deficiency alternatives such as orthotopic graft delivery (directly into the bone marrow) or wild-type BM cell supplements could be considered.
4. Necrotic or apoptotic BM cells from donors will not survive the transplant. In this case the degree of cell death in the donor inoculum should be tested by measuring necrotic and apoptotic cell content using Annexin-V or propidium iodide staining, prior to being injected into the recipients.
5. The dose of radiation required for recipient mice needs to be calculated based on the strain of the mice used. While C57/BL6 mice can be irradiated with the above-indicated doses, mice that are immunodeficient such as the RAG KO mice should receive a dose that is no higher than 600 rad. BALB/C mice are extremely sensitive to irradiation and should ideally be subject to a total radiation dosage of 900 rads in order to be lethally irradiated. This dosage should be administered as two split doses of 450 rads each with a 2–3-h time interval. Separating both sessions with an interval of at least 3 h reduces the toxicity associated with total body irradiation. Some studies have documented the use of an 800 Gy dosage that was well tolerated by BALB/C recipients [18].
6. Sufficient evidence from literature shows that irradiation doses of 700–1300 Gy are myeloablative. While higher doses increase

the probability of irradiation-induced toxicity, lower doses may reduce the chances of achieving full donor chimerism. Therefore, the choice of dosage is important in determining the success of the study and might differ considerably. It will need to be adjusted based on the experimental setup and the researcher's specific objectives [19]. For example, when a stable mixed chimera needs to be generated with the recipient's immune system composed of both donor and recipient cells, a lower dose of irradiation needs to be chosen. The overall goal of transplantation studies will consequently require the identification of a dose that permits full (or partial) immune ablation while minimizing radiation-induced toxicity.

7. The amount of time spent by animals within the irradiator depends on a number of parameters such as radioisotope decay tables, extent of irradiation required, and source of ionizing energy (X-rays versus gamma rays, for which a cesium or cobalt source is needed). The size of the irradiator is another factor to be considered since the space within the irradiator and the amount of animals receiving the radiation within every cycle need to standardize to ensure uniform distribution of ionizing energy within the entire group of animals. As a reference we use a cesium source with an activity of 1000 Ci, 2 animal containers with 12 mice arranged perpendicularly within an irradiator that has irradiation cycles that last for 12 min.
8. The veterinary care of irradiated animals following BMT is vital for their survival and well-being. The immunosuppression induced in mice by irradiation can persist for a period of time after BMT and therefore need to be housed in strict specific pathogen-free/barrier conditions with a supply of sterilized food and water. The immunocompromised state of transplanted animals makes them susceptible to *Pneumocystis carinii* and *Pseudomonas aeruginosa* infection if they are not housed in a barrier facility. If this is the case, mice should be treated with acidified water or water that is supplemented with antibiotics in order to prevent infection [20]. The commonly used antibiotics include metronidazole, neomycin, ciprofloxacin and tetracyclines [21].
9. In addition to infectious disease, mice that are subject to long-term experiments after BMT have increased incidence of neoplasia [22]. Considering their increased risk for tumor development, mice belonging to these experiments should be monitored regularly and subject to post-irradiation-specific conditions.
10. Intravenous injection of mice through the tail vein is a technique that requires extensive practice and one needs to be trained in the procedure prior to performing the BMT, to be

certain regarding the size and uniformity of the inoculum in the recipient mice. Technical errors during injection will result in either a failed, inadequate, or inconsistent BM reconstitution within the recipient.

11. To minimize stress of the recipient mice following irradiation and to ensure maximum survival, we perform BMT between 1 and 24 h after irradiation.
12. Peripheral blood screening allows for detection of donor-derived cells from 2 weeks after transplantation although optimal detection is possible only at 4 weeks post-BMT. Blood can be drawn using standard methods from each animal facility and analyzed in a hematological counter that gives absolute leukocyte, erythrocyte, and platelet counts.
13. When analyzing chimera in recipient mice, those that have been adequately irradiated can be visually distinguished by the appearance of gray patches of hair on the surface of their skin after several weeks. Irradiated recipients that received a marrow-ablative dose of radiation and no transplantation with donor bone marrow cells will not survive for more than 12–14 days after irradiation. While those that did receive BMT should be able to survive a normal life-span and in turn be reconstituted with peripheral blood cells that are almost entirely derived from the donor bone marrow.
14. Analysis of blood from the same animal can be followed up over time after BMT. However, care should be taken not to bleed the mouse too often and maintain an interval of at least 7 days between each bleed.
15. Amongst the various methods used to discriminate donor versus recipient-derived hematopoietic cells after BMT, the most widely utilized and practical approach is flow cytometry. When donor hematopoietic cells are derived from transgenic fluorescent mice, for example LysMGFP or DsRed mice, they can be distinguished easily based on their fluorescence in the respective fluorescent channels. When using congenic mice, antibodies that specifically identify the specific isoforms of surface receptors such as CD45.1 and CD45.2 can be employed to distinguish between donor- and recipient-derived cells.
16. Irradiation of mice eliminates the recipient's BM but fails to eliminate tissue-resident macrophages. In this case, injection of a macrophage-depleting agent such as clodronate can be used to remove subsets of donor-derived macrophages [16].
17. There has been considerable speculation over the past 10 years regarding the presence of donor-derived epithelial cells in lungs, skin, intestine, liver, and buccal and nasal mucosa of recipients. However, research in this area has demonstrated that the highest epithelial engraftment obtained was 0.02 %,

deemed too low to be of any significant relevance in BMT-associated therapies or experimental studies unless combined with special strategies (e.g., use of 1-day-old mice or additional preparative regimens with specific chemical agents such as busulfan) [23, 24].

References

1. Whitman SC (2004) A practical approach to using mice in atherosclerosis research. Clin Biochem Rev 25:81–93
2. Getz GS, Reardon CA (2012) Animal models of atherosclerosis. Arterioscler Thromb Vasc Biol 32:1104–1115
3. Linton MF, Fazio S (1999) Macrophages, lipoprotein metabolism, and atherosclerosis: insights from murine bone marrow transplantation studies. Curr Opin Lipidol 10:97–105
4. Ross R (1999) Atherosclerosis – an inflammatory disease. N Engl J Med 340:115–126
5. Allayee H, Ghazalpour A, Lusis AJ (2003) Using mice to dissect genetic factors in atherosclerosis. Arterioscler Thromb Vasc Biol 23:1501–1509
6. Daugherty A (2002) Mouse models of atherosclerosis. Am J Med Sci 323:3–10
7. Aparicio-Vergara M, Shiri-Sverdlov R, de Haan G et al (2010) Bone marrow transplantation in mice as a tool for studying the role of hematopoietic cells in metabolic and cardiovascular diseases. Atherosclerosis 213:335–344
8. Boisvert WA, Spangenberg J, Curtiss LK (1995) Treatment of severe hypercholesterolemia in apolipoprotein E-deficient mice by bone marrow transplantation. J Clin Invest 96:1118–1124
9. Boisvert WA, Spangenberg J, Curtiss LK (1997) Role of leukocyte-specific LDL receptors on plasma lipoprotein cholesterol and atherosclerosis in mice. Arterioscler Thromb Vasc Biol 17:340–347
10. Fazio S, Hasty AH, Carter KJ et al (1997) Leukocyte low density lipoprotein receptor (LDL-R) does not contribute to LDL clearance in vivo: bone marrow transplantation studies in the mouse. J Lipid Res 38:391–400
11. Herijgers N, Van Eck M, Groot PH et al (1997) Effect of bone marrow transplantation on lipoprotein metabolism and atherosclerosis in LDL receptor-knockout mice. Arterioscler Thromb Vasc Biol 17:1995–2003
12. Linton MF, Atkinson JB, Fazio S (1995) Prevention of atherosclerosis in apolipoprotein E-deficient mice by bone marrow transplantation. Science 267:1034–1037
13. Fazio S, Babaev VR, Murray AB et al (1997) Increased atherosclerosis in mice reconstituted with apolipoprotein E null macrophages. Proc Natl Acad Sci U S A 94:4647–4652
14. Linton MF, Babaev VR, Gleaves LA et al (1999) A direct role for the macrophage low density lipoprotein receptor in atherosclerotic lesion formation. J Biol Chem 274:19204–19210
15. Chevre R, Gonzalez-Granado JM, Megens RT et al (2014) High-resolution imaging of intravascular atherogenic inflammation in live mice. Circ Res 114:770–779
16. Bradshaw G, Gutierrez A, Miyake JH et al (2005) Facilitated replacement of Kupffer cells expressing a paraoxonase-1 transgene is essential for ameliorating atherosclerosis in mice. Proc Natl Acad Sci U S A 102:11029–11034
17. Schiller NK, Kubo N, Boisvert WA et al (2001) Effect of gamma-irradiation and bone marrow transplantation on atherosclerosis in LDL receptor-deficient mice. Arterioscler Thromb Vasc Biol 21:1674–1680
18. Duran-Struuck R, Tawara I, Lowler K, Clouthier SG, Weisiger E, Rogers C, Luker G, Kumanogoh A, Liu C, Ferrara JL, Reddy P (2007) A novel role for the semaphorin Sema4D in the induction of allo-responses. Biol Blood Marrow Transplant 13:1294–1303
19. Down JD, Tarbell NJ, Thames HD, Mauch PM (1991) Syngeneic and allogeneic bone marrow engraftment after total body irradiation: dependence on dose, dose rate, and fractionation. Blood 77:661–669
20. Duran-Struuck R, Dysko RC (2009) Principles of bone marrow transplantation (BMT): providing optimal veterinary and husbandry care to irradiated mice in BMT studies. J Am Assoc Lab Anim Sci 48:11–22
21. Velders GA, van Os R, Hagoort H, Verzaal P et al (2004) Reduced stem cell mobilization in mice receiving antibiotic modulation of the intestinal flora: involvement of endotoxins as cofactors in mobilization. Blood 103:340–346
22. Schwartz RS, Beldotti L (1965) Malignant lymphomas following allogenic disease: transition from an immunological to a neoplastic disorder. Science 149:1511–1514

23. Bruscia EM, Ziegler EC, Price JE et al (2006) Engraftment of donor-derived epithelial cells in multiple organs following bone marrow transplantation into newborn mice. Stem Cells 24:2299–2308

24. Khan FM, Sy S, Louie P et al (2012) Epithelial cells in PBSC grafts: source of donor-type epithelial cells after allogeneic transplantation? Bone Marrow Transplant 47:461–462

Chapter 23

Tandem Stenosis to Induce Atherosclerotic Plaque Instability in the Mouse

Yung Chih Chen, Jennifer Rivera, and Karlheinz Peter

Abstract

Despite the number of animal models of atherosclerosis, a major limitation in research on mechanisms of plaque rupture is the lack of appropriate atherosclerotic mouse models where lesions develop and progress to a vulnerable and thus rupture-prone phenotype that is typically observed in humans. Most animal models of atherosclerosis typically represent a few but not the full combination of the characteristics seen in human unstable/ruptured plaques. Such characteristics most importantly include a thin and ruptured fibrous cap, plaque inflammation, neovascularization within the plaque (vasa vasorum), plaque hemorrhage, and intravascular (often occlusive) thrombus formation. Ideally, an animal model of plaque instability/rupture would respond to current pharmacological interventions known to reduce the risk of plaque rupture, such as statins. Here we describe a mouse model of plaque instability/rupture that is based on the surgical introduction of a tandem stenosis in the carotid artery. This model results in the formation of unstable atherosclerotic plaques that reflect human plaque pathology. It will allow to further understanding of plaque instability/rupture, to identify the participating factors such as specific proteins, genes and microRNAs, and to develop imaging methods towards the detection of vulnerable, rupture-prone atherosclerotic plaques.

Key words Acute myocardial infarction, Angiogenesis animal models of human disease, Arterial thrombosis, Atherosclerosis, Gene expression profiling, Inflammation, MicroRNA profiling, Plaque rupture

1 Introduction

The rupture of inflammation-driven, unstable atherosclerotic plaques is the main cause of atherothrombotic complications such as myocardial infarction, making it a major health burden and a leading cause of mortality and morbidity. Atherosclerosis is well characterized as a progressive, chronic, inflammatory disease with specific, localized manifestations in the arterial wall. Human atherosclerotic plaques preferentially occur at vessel bifurcations, where shear stress is low and varies significantly over a small distance. Similarly, in apolipoprotein E-deficient ($ApoE^{-/-}$) mice fed a high-fat diet (HFD) atherosclerotic plaques preferentially

Vicente Andrés and Beatriz Dorado (eds.), *Methods in Mouse Atherosclerosis*, Methods in Molecular Biology, vol. 1339, DOI 10.1007/978-1-4939-2929-0_23,

develop in areas of low shear stress. Low shear stress upregulates adhesion molecule and protease expression, increases the accumulation of macrophages and other inflammatory cells, reduces stabilizing collagen fibers, increases necrotic core volume, causes thinning of fibrous caps, and promotes lipid accumulation [1]. However, while low shear stress promotes the formation of vulnerable plaques, it does not seem to be sufficient to induce plaque rupture. As a plaque progresses and intrudes into the lumen, shear stress around the plaque is altered to increase tensile stress [2]. Tensile stress, which is higher by several magnitudes than wall shear stress, appears to be an important trigger for plaque rupture to occur. Indeed, plaque rupture occurs more frequently in the proximal coronary arteries, where the tensile stress is higher compared with the periphery of the coronary artery system [3]. On the basis of these observations, we used computational fluid dynamics (CFD) to design an animal model of plaque rupture. We developed a surgical approach whereby tandem stenosis (TS) is applied to the right carotid artery of HFD diet-fed ApoE$^{-/-}$ mice, which creates high tensile stress upstream of the proximal stenosis, while the rest of the arterial system within the vicinity of the TS exhibit low shear stress (*see* Fig. 1). This facilitates the formation of plaques with an unstable, rupture-prone phenotype within a defined vessel segment. For representative morphological descriptions of each

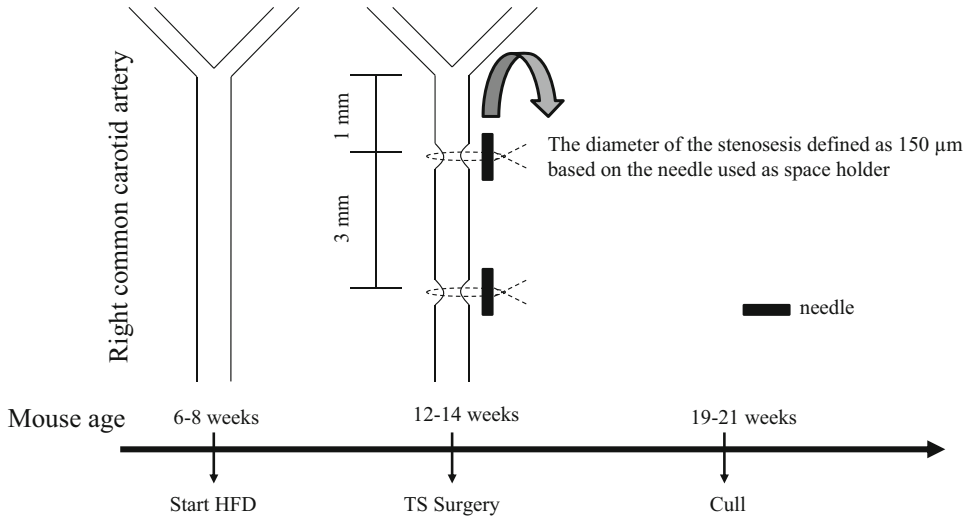

Fig. 1 Schematic drawing of the tandem stenosis. ApoE$^{-/-}$ mice at 6–8 weeks of age are fed with Western diet containing 22 % fat and 0.15 % cholesterol and tap water ad libitum. At 12–14 weeks of age, including 6 weeks of Western diet, the animals are anesthetized for TS surgery. The fur is removed around the surgical site and mice are placed on a 37 °C heater mat to prevent hypothermia. Vascular stenoses are created by two sutures on the common carotid artery using a 6-0 blue braided polyester fiber. The distal point is 1 mm apart from the carotid artery bifurcation. The proximal point is 3 mm apart from the distal point. The stenosis diameter is defined by the needle applied as a space holder

vessel segment and the characteristics of atherosclerotic plaque composition and quantification, please refer back to original paper [4]. Extensive characterization using histology, expression profiling, hierarchical clustering, quantitative polymerase chain reaction (PCR) and pharmacological intervention allowed us to demonstrate that plaques generated using the TS model closely resembled human unstable, vulnerable plaques [4–6]. In addition, we have provided proof-of concept examples demonstrating that the TS mouse model can be used to define and discover novel pathophysiological mechanisms relevant to atherosclerotic plaque rupture in humans [4]. In this chapter, we provide methodological detail of the tandem stenosis surgical procedure, which reliably generates unstable, rupture-prone atherosclerotic plaques.

2 Materials

Prepare all solutions using medical grade saline or autoclaved phosphate-buffered saline (PBS).

1. PBS: 137 mM sodium chloride, 2.7 mM potassium chloride, 10 mM disodium hydrogen phosphate, 1.8 mM monopotassium phosphate, pH 7.2.
2. HFD: Mouse chow supplemented with 22 % fat and 0.15 % cholesterol (e.g., SF00-219, Specialty Feeds, Western Australia).
3. Anesthetic: Mixture of ketamine (80–100 mg/kg), xylazine (16–20 mg/kg), atropine (0.96–1.2 mg/kg).
4. Post-anesthetic: Atipamezole HCl (e.g., antisedan, 0.2 mg/kg, s.c.).
5. Pain relief: Bupivacaine (marcaine, 2 mg/kg).
6. Surgical instruments and accessories: High-precision tweezers (e.g., 4*Dumont Tweezers: T0545-811 Tweezers, style 5/45, Inox 08, high precision, polished), straight Castroviejo scissors (e.g., 1*TS1092 Castroviejo scissors, 420SS, straight, 100 mm), straight dissecting scissors (e.g., 1*TS1044 dissecting scissors, 420SS, straight, 115 mm), 150 μm diameter needles (e.g., Ethicon 8-0, Virgin Silk blue: W1782), 450-μm diameter needles (e.g., Terumo 26 G×½″: NN*2613R), suture (e.g., 6-0 TI.CRON coated, braided polyester blue, 0.7 metric, Kendall), dissecting microscope, heater mat, depilatory hair removal cream, gauze, cotton tips, 1 mL syringe (Terumo), 30 G needle (Terumo).

3 Methods

1. Use 6–8-week-old male ApoE$^{-/-}$ mice that weigh around 20–23 g, and maintain them on a high-fat diet and tap water ad libitum for 6 weeks prior to the surgery.
2. At the day of surgery, weigh mice on a scale and record weight.
3. It is recommended that at least semi-sterile conditions are maintained during the whole surgical procedure. Wear a surgical gown, gloves, mask, and hair cap. Sterilize surgical instruments using ultra-heat beads or autoclave the surgical instruments before use.
4. Administer bupivacaine (2 mg/kg) 10–15 min prior to anesthesia. Anesthetize mice by i.p. administration of a mixture of ketamine, xylazine and atropine in saline according at a volume of 0.1 ml per 10 g of body weight, using a 30 G needle (*see* **Note 1**).
5. Monitor the depth of anesthesia by the response to toe pinch. Movement or an increased breathing rate indicates inadequate anesthesia. In this situation, a top-up dose (half of initial dose) of anesthetic mixture should be given and it should be waited for at least 5–10 min without further stimulation. If the animal still responds to toe pinch, consider the option of using gas anesthetics.
6. After anesthesia has taken effect, lay the animals down in the dorsal to ventral position on a 37 °C heat mat, disinfect the surgical area with 70 % ethanol, and clear the neck region of fur using hair removal cream.
7. A small incision (~1 cm) of the skin is made directly on top of the left common carotid artery region. It is highly recommended that from this step onwards, the procedure is performed under a dissecting microscope to help increase accuracy and avoid unnecessary bleeding.
8. Bluntly dissect the connective tissue underneath the skin using curved forceps.
9. Expose a segment of the left common carotid artery.
10. Lift up the common carotid artery and blunt dissect away from the surrounding tissue.
11. Separate the vagus nerve from the common carotid artery (*see* **Note 2**).
12. Induce vascular stenosis by suturing two points on the common carotid using 6-0 blue braided polyester fibre. Distal point is defined as 1 mm from the carotid bifurcation. Proximal point is defined as 3 mm from the distal point (Fig. 1) (*see* **Note 3**).

13. Perform carotid stenosis by tying against a probe made of a needle, with the probe promptly removed to attain a narrowing of the carotid from the needle used (*see* **Note 4**).
14. Tie the suture twice to generate a stable stenosis. Cut off any excess filament.
15. When required, a less severe stenosis can be induced by using either 26 G needles or any other needle with a higher diameter (*see* **Note 5**).
16. Close the wound using a 6-0 monofilament suture in the single interrupted or continuous method.
17. Give mice bupivacaine (2 mg/kg, s.c.) close to the surgical site and atipamezole HCl (antisedan, 0.2 mg/kg, s.c) (*see* **Note 6**).
18. Monitor mice to ensure recovery from anesthesia. Typically, mice will recover within 15 min after atipamezole HCl.
19. Place cage half-on/half-off a heat pad to allow mice to sustain their body temperature for the next 24 h (*see* **Note 7**).
20. Mice should be monitored and placed under post-surgical care in the next 48 h according to your institutional animal guidelines.

4 Notes

1. Gas anesthesia (e.g., halothane or isoflurane) is also recommended. Some mice do not respond well to the mixture of ketamine and xylazine. It is recommended that both liquid and gas anesthetics are included in the animal ethics. If using gas anesthesia, 4 % isoflurane induction rate and 2 % isoflurane maintenance rate supplied via a small rodent mask work well.
2. Be careful when performing this step to avoid breaking or punching a hole in the vessel. The vagus nerve loosely sits next to the carotid artery. Some mice will have the middle thyroid vein coming on top of the carotid artery. Bluntly dissect this from the carotid artery. If major bleeding happens at this stage, it is recommended that the mouse be euthanized.
3. Due to bio-variability, the distal point to the carotid bifurcation varies between animals. However, the distance between the proximal point and distal point should be fixed at 3 mm. If there is not enough space for the distal point position, it can be adjusted by placing the distal point on top of the carotid bifurcation.
4. The proper control experiment for TS surgery will be changing the probe size to a higher diameter (non-stenotic) or a sham control (make an incision in the neck and close the wound without performing stenosis surgery).

5. If a higher diameter probe (450 μm) is used, due to the arterial pulse, the distal suture spot may be pushed away from its original ligation. In this situation, fix the proximal and distal sutures to its surrounding tissue to stabilize the stenosis positions.
6. Administration of other pain relief (e.g., general opioids like buprenorphine) is also recommended. The use of non-steroidal anti-inflammatory agents is not recommended as these drugs may cause atherosclerotic plaque compositional changes.
7. Some animals may show symptoms of pain after 48 h. Additional pain relief should be given. If the symptoms of pain persist, it is suggested that the mouse be euthanized immediately or according to your local institutional animal guidelines.

References

1. Cheng C, Tempel D, van Haperen R et al (2006) Atherosclerotic lesion size and vulnerability are determined by patterns of fluid shear stress. Circulation 113(23):2744–2753
2. Slager CJ, Wentzel JJ, Gijsen FJ et al (2005) The role of shear stress in the generation of rupture-prone vulnerable plaques. Nat Clin Pract Cardiovasc Med 2(8):401–407
3. Cheruvu PK, Finn AV, Gardner C et al (2007) Frequency and distribution of thin-cap fibroatheroma and ruptured plaques in human coronary arteries: a pathologic study. J Am Coll Cardiol 50(10):940–949, doi:S0735-1097(07)01931-6 [pii]10.1016/j.jacc.2007.04.086
4. Chen YC, Bui AV, Diesch J et al (2013) A novel mouse model of atherosclerotic plaque instability for drug testing and mechanistic/therapeutic discoveries using gene and microRNA Expression Profiling. Circ Res 113(3):252–265. doi:10.1161/CIRCRESAHA.113.301562
5. Jain MK, Ridker PM (2005) Anti-inflammatory effects of statins: clinical evidence and basic mechanisms. Nat Rev Drug Discov 4(12):977–987, doi:nrd1901 [pii] 10.1038/nrd1901
6. Finn AV, Nakano M, Narula J et al (2010) Concept of vulnerable/unstable plaque. Arterioscler Thromb Vasc Biol 30(7):1282–1292, doi:30/7/1282 [pii] 10.1161/ATVBAHA.108.179739

Chapter 24

Detection of Intraplaque Hemorrhage in Mouse Atherosclerotic Lesions

Judith C. Sluimer, Marion J. Gijbels, and Sylvia Heeneman

Abstract

Intraplaque hemorrhage is defined as the presence of fresh or lysed erythrocytes, iron deposits in macrophages, and/or a fibrin clot in an atherosclerotic plaque. These features can be detected by hematoxylin and eosin, Martius scarlet Blue, and Perl's iron histological stainings.

It is noteworthy that intraplaque hemorrhage is only present in murine atherosclerotic plaques after additional interventions or additional genetic traits affecting matrix degradation or thrombosis. In this chapter, we describe methods to detect intraplaque hemorrhage in mouse atherosclerotic lesions.

Key words Intraplaque hemorrhage, Erythrocytes, Iron, Fibrin, Hematoxylin and eosin, Martius scarlet Blue, Perl's Prussian blue

1 Introduction

Specific features of an atherosclerotic plaque in humans are associated with an increased risk of plaque rupture, and thus subsequent clinical symptoms such as myocardial infarction and stroke. These features include inflammatory infiltrate, a lipid/necrotic core, and intraplaque hemorrhage [1]. Intraplaque hemorrhage includes the leakage of erythrocytes into the plaque presumably from leaky intraplaque microvasculature, medial dissection, or a plaque rupture [1, 2]. This evokes infiltration of macrophages and erythrophagocytosis, leading to intracellular deposits of iron derived from the erythrocytes hemoglobin content. Often, coagulation is instigated resulting in the formation of a fine-meshed network of fibrin fibers. Therefore, intraplaque hemorrhage is defined as the presence of lysed erythrocytes, iron deposits in macrophages, and/or a fibrin clot.

In murine models of atherosclerosis, such as apolipoprotein E-deficient (apoE−/−) mice, the presence of intraplaque hemorrhage is not commonplace (Table 1). The occurrence of hemorrhage depends on the arterial location and rarely occurs in

Vicente Andrés and Beatriz Dorado (eds.), *Methods in Mouse Atherosclerosis*, Methods in Molecular Biology, vol. 1339, DOI 10.1007/978-1-4939-2929-0_24,

Table 1
Frequency of intraplaque hemorrhage in apoE−/− mice

Intervention [reference]	Age[a] (weeks)	Diet	Brachiocephalic artery (%)	Carotid artery (%)
None [3, 4]	20	WTD	8	0
Age [5]	42–50	Chow	66–75	n.d.
Collar [7]	52	WTD	n.a.	8
Ligation + collar [6]	13	WTD	n.a.	100
Irradiation 14y [3]	44–52	Chow	n.d.	85
Collar + Ad.MMP9 [7]	18–20	WTD	n.a.	90
adMMP bone marrow transplant [8]	52	chow	50	n.d.
Thrombomodulin$^{pro/pro}$ + collar [10]	18	WTD	n.d.	unk
Fibrillin1$^{C1039G+/-}$ [4]	20	WTD	88	92

[a]Age at the time of analysis, *WTD* western-type diet (high fat/cholesterol), *n.a.* not applicable, *n.d.* not done, *unk* unknown/not analyzed

the carotid artery [3, 4] while being slightly more common in the brachiocephalic artery, i.e., 8 % at 20 weeks of age [4]. In contrast, frequencies rise with age up to 75 % in brachiocephalic arteries of 1-year-old apoE−/− mice [5], up to 100 % after additional surgical interventions [6] or around 50–90 % with additional genetic traits enhancing matrix degradation [4, 7, 8] or thrombosis [9, 10]. Of note, in mice intraplaque hemorrhage and plaque rupture are not synonymous, the latter occurring even less frequently.

The detection of intraplaque hemorrhage, be it in mice or man, involves histology to identify the components of intraplaque hemorrhage. This chapter describes the protocols for hematoxylin and eosin (HE) and Martius Scarlet Blue (MSB) staining, able to discriminate erythrocytes and fibrin, and the Perl's Prussian blue staining identifying ferric iron. The protocols in this chapter should preferably be used together to achieve maximal reliability in the detection of intraplaque hemorrhage.

1.1 Hematoxylin and Eosin

The widely used combination of hematoxylin and eosin allows the discrimination between nuclei and cytoplasm/connective tissue, respectively. Hematoxylin itself does not stain nuclei, but rather its oxidation product hematein. In this protocol, Meyer's hematoxylin is used, which is chemically oxidized by sodium iodate. Hematein is anionic, as is nuclear chromatin, and will thus only stain nuclei in the presence of a mordant, in this case aluminium salt. The mordant/metal cation will positively charge hematein, providing a net charge able to bind and stain the anionic nucleic

Table 2
Colors identifying tissue components after each staining

	Staining		
Structure	**HE**	**MSB**	**Perl's**
Nuclei	Blue	Black	Red
Cytoplasm	Varying shades of pink	Yellow	Light red
Erythrocytes	Orange/red	Yellow	Red
Fibrin	Fuchsia	Red	n.a.
Collagen	Pink	Blue	n.a.
Iron	Brown-yellow	n.a.	Blue

n.a. not applicable

acids in chromatin in an acidic environment. The color change from red to blue occurs in alkaline pH, which is achieved by washing in a weak alkaline solution, such as tap water.

Eosin distinguishes the cytoplasm of different cell types and types of connective tissues by staining them different shades of red (Table 2). Fibrin is very acidophilic and is thus strongly stained by eosin and appears as distinctly pink (Fig. 1a, b) [11].

1.2 Martius Scarlet Blue

The MSB procedure includes application of Martius yellow, Brilliant Scarlet red, and Alcian blue dyes to easily distinguish erythrocyte cytoplasm, fibrin, and collagen, respectively, while nuclei appear black (Table 2, Fig. 1) [11]. Nuclei are first stained black with Weigert's iron hematoxylin, a solution allowing stable and acid-resistant nuclear detection if compared to alum hematoxylins, such as Meyer's hematoxylin. Martius yellow is then applied together with phosphotungstic acid in alcoholic solution to stain the cytoplasm of erythrocytes yellow. Mature fibrin will then be stained by brilliant crystal scarlet (Fig. 1c, d). Phosphotungstic acid will subsequently fix the dye in fibrin fibrils while removing any red stain from the collagen and blocking staining of muscle, collagen and connective tissue. Aniline blue subsequently stains collagen [11]. The MSB staining is selective for fibrin, but not entirely specific. Bone tissue, granulae in Paneth's cells, and other cytoplasmic vesicles may stain. The combination of the three histological stains described in this chapter will resolve the detection of fibrin.

1.3 Perl's Prussian Blue for Ferric Iron

Perl's iron visualizes ferric iron ions in hemosiderin, which is hydrated, protein-bound iron oxide ($Fe(OH)_3$). Hemosiderin is always located within cells and an intraplaque hemorrhage can result in hemosiderin deposits in the macrophages. In unstained or HE-stained tissue sections, hemosiderin presents as yellow-brown,

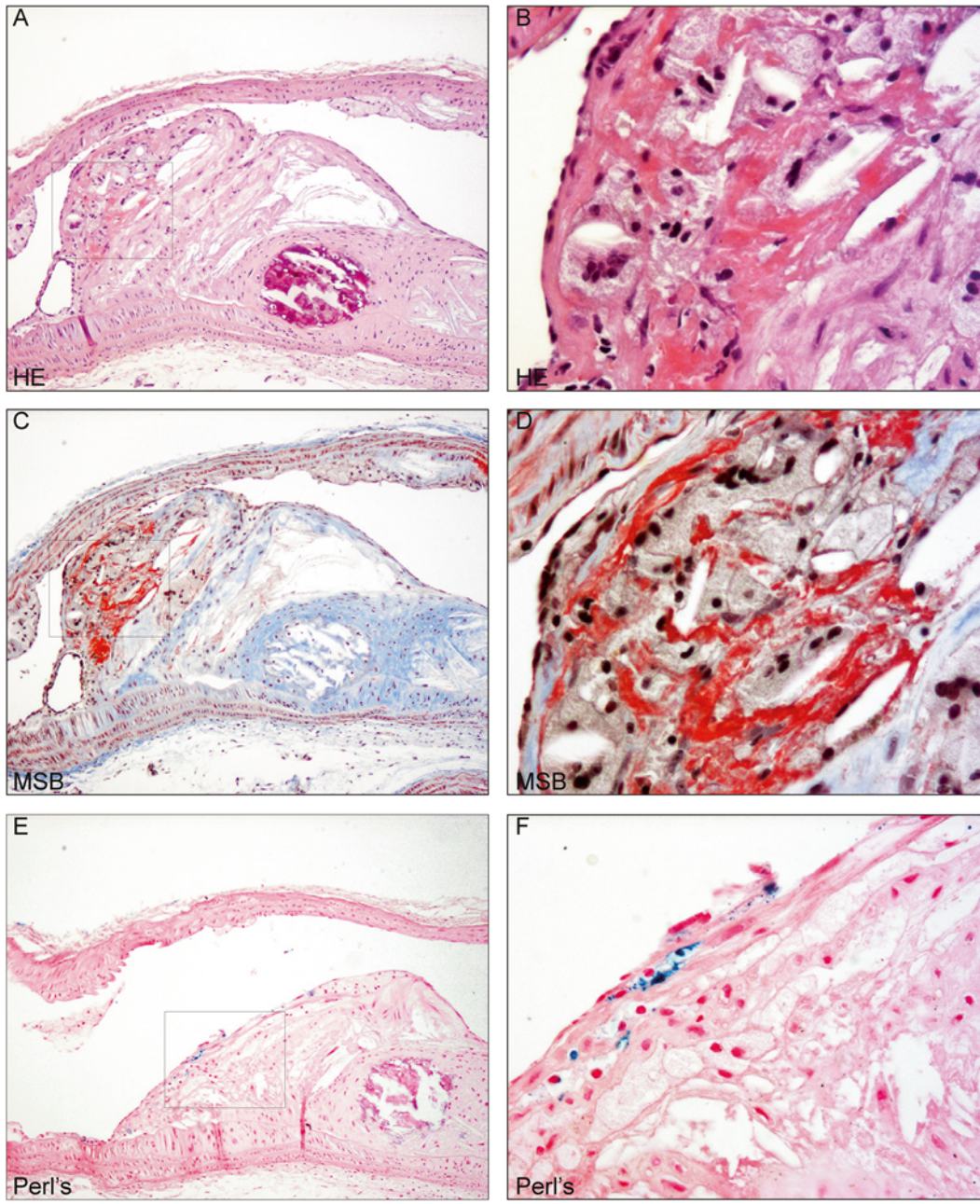

Fig. 1 Murine intraplaque hemorrhage detection using HE, MSB, and Perl's ferric iron (**a**). Atherosclerotic plaque in the aortic arch of ApoE–/– mice fed chow for 30 weeks after single irradiation dose of 14y [3] stained with hematoxylin and eosin. *Bright pink* indicates fibrin. Magnification 100×. Boxed region is shown in higher magnification in (**b**). Detail of fibrin indicating intraplaque hemorrhage. Magnification 400×. (**c**). Section of same plaque stained with MSB protocol detecting fibrin in *bright red*. Magnification 100×. Boxed region is shown in higher magnification in (**d**). Detail of fibrin indicating intraplaque hemorrhage. Magnification 400×. (**e**). Section of same plaque stained with Perl's Prussian *blue* for ferric iron detection in *blue*, counterstained with nuclear fast *red*. Magnification 100×. Boxed region is shown in higher magnification in (**d**). Detail of iron in macrophage indicating intraplaque hemorrhage. Magnification 400×

coarse-grained pigment, which is more easily identified upon Perl's Prussian blue staining [11]. Ferric iron in hemosiderin reacts with potassium ferrocyanide to yield insoluble blue ferric ferrocyanide precipitate (Prussian Blue, Fig. 1e, f). This reaction takes place in an acidic milieu to liberate iron from its protein carrier, such as hemoglobin, as follows: $4Fe(OH)_3 + 3K_4Fe(CN)_6 + 12HCl$ $Fe_4[Fe(CN)_6]^3 + 12KCl + 12H_2O$ [11].

2 Materials

1. Formalin-fixed, paraffin-embedded murine arterial sections (4–5 μm) on adhesive, silane-coated glass slides (*see* **Note 1**).
2. Xylene.
3. Alcohol 100 %.
4. Alcohol 96 %.
5. Alcohol 70 %: 700 ml alcohol 100 %, 300 ml distilled water.
6. Alcohol 50 %: 500 ml alcohol 100 %, 500 ml distilled water.
7. Distilled water.
8. Tap water.
9. Containers for solutions (*see* **Note 2**).
10. Rack to place glass slides in and transfer between containers.
11. Glass cover slips (*see* **Note 3**).
12. Water-free mounting medium for the permanent mounting of specimen for microscopy (*see* **Note 4**).
13. Microscope.
14. Timer.
15. Flow cabinet (*see* **Note 5**).
16. Stir plate.
17. Stir Bar.
18. Flasks.
19. Filter paper or equivalent for blotting or filtration.
20. Funnel.
21. Bottles.

2.1 Hematoxylin and Eosin

1. Meyer's hematoxylin.
2. Eosin, 0.2 % alcoholic solution, ready to use (*see* **Note 6**).

2.2 Martius Scarlet Blue

1. Weigert's iron hematoxylin solution A: 10 g hematoxylin, 1000 ml alcohol 96 % (*see* **Note 7**).
2. Weigert's iron hematoxylin solution B: 11.6 g $FeCl_3$, 10 ml HCl, 1000 ml distilled water.

3. Martius yellow solution: 0.5 g martius yellow, 2 g phosphotungstic acid, 98 ml alcohol 95 % (*see* **Note 8**).
4. Brilliant crystal scarlet 6R 1 %: 1 g Brilliant crystal scarlet, 2.5 ml acetic acid, 97.5 ml distilled water (*see* **Note 9**).
5. Phosphotungstic acid 1 %: 1 g phosphotungstic acid, 100 ml distilled water (*see* **Note 10**).
6. Aniline blue 1 %: 1 g Aniline blue, 1 ml acetic acid, 99 ml distilled water.
7. Acetic acid 1 %: 1 ml acetic acid, 99 ml distilled water.

2.3 Perl's Prussian Blue for Ferric Iron

1. Potassium ferrocyanide 2 %: 2 g potassium ferrocyanide, 100 ml distilled water.
2. Hydrochloric acid 2 %: 54 ml HCl 37 %, 946 ml distilled water.
3. Perl's solution: Potassium ferrocyanide 2 %:hydrochloric acid 2 % (1:1) (*see* **Note 7**).
4. Nuclear Fast Red (Kernechtrot) Solution, ready to use.

3 Methods

3.1 Hematoxylin and Eosin

1. Deparaffinize slides:
   - Place slides in container with xylene and incubate for 2 min.
   - Transfer to second container with xylene and incubate for 2 min.
2. Rehydrate slides:
   - Transfer slides to container with 100 % alcohol and incubate for 2 min.
   - Transfer slides to second container with 100 % alcohol and incubate for 2 min.
   - Transfer to container with 96 % alcohol and incubate for 2 min.
   - Transfer to container with 70 % alcohol and incubate for 2 min.
   - Transfer to container with 50 % alcohol and incubate for 2 min.
   - Transfer to container with distilled water and incubate for 2 min.
3. Transfer to container with hematoxylin and incubate for 3 min.
4. Transfer to container with tap water and develop blue for 10 min.
5. Transfer to container with eosin 0.2 % and incubate for 3 min.

6. Transfer to container with tap water running until solution is clear (*see* **Note 11**).
7. Dehydrate slides (*see* **Note 12**):
   - Transfer to container with 70 % alcohol and incubate for 2 min.
   - Transfer to container with 96 % alcohol and incubate for 2 min.
   - Transfer to container with 100 % alcohol and incubate for 2 min.
   - Transfer slides to second container with 100 % alcohol and incubate for 2 min.
   - Transfer to container with xylene and incubate for 2 min (see Note 13).
   - Transfer to second container with xylene and incubate for 2 min (*see* **Note 13**).
8. Place drop of mounting medium on slide and cover with cover slip.
9. Air-dry for 15 min under flow cabinet to evaporate xylene.
10. Examine slides under microscope.

3.2 Martius Scarlet Blue

1. Deparaffinize slides:
   - Place slides in container with xylene and incubate for 2 min.
   - Transfer to second container with xylene and incubate for 2 min.
2. Rehydrate slides:
   - Transfer slides to container with 100 % alcohol and incubate for 2 min.
   - Transfer slides to second container with 100 % alcohol and incubate for 2 min.
   - Transfer to container with 96 % alcohol and incubate for 2 min.
   - Transfer to container with 70 % alcohol and incubate for 2 min.
   - Transfer to container with 50 % alcohol and incubate for 2 min.
   - Transfer to container with distilled water and incubate for 2 min.
3. Transfer to container with a mix of Weigert's solutions A and B (1:1) (*see* **Note 14**) and incubate for 3 min.
4. Transfer to container with tap water.
5. Place container under running tap water for 5 min.

6. Transfer to container with 96 % alcohol and incubate for 2 min.
7. Transfer to container with Martius Yellow and incubate for 2 min.
8. Transfer to container with distilled water and incubate for 10 s.
9. Transfer to container with Briljant crystal scarlet and incubate for 10 min.
10. Transfer to container with distilled water and incubate for 10 s.
11. Treat with phosphotungstic acid for 1–5 min until no red remains in the collagen.
12. Transfer to container with distilled water and incubate for 10 s.
13. Transfer to container with Aniline blue and incubate for 4–10 min (*see* **Note 15**).
14. Transfer to container with Acetic acid 1 % and incubate for 10 s.
15. Blot dry by tapping slide rack on filter paper.
16. Dehydrate slides (*see* **Note 12**):
    - Transfer to container with 70 % alcohol and incubate for 2 min.
    - Transfer to container with 96 % alcohol and incubate for 2 min.
    - Transfer to container with 100 % alcohol and incubate for 2 min.
    - Transfer slides to second container with 100 % alcohol and incubate for 2 min.
    - Transfer to container with xylene and incubate for 2 min (*see* **Note 13**).
    - Transfer to second container with xylene and incubate for 2 min (*see* **Note 13**).
17. Place drop of mounting medium on slide and cover with cover slip.
18. Air-dry for 15 min under flow cabinet to evaporate xylene.
19. Examine slides under microscope.

3.3 Perl's Prussian Blue for Ferric Iron

1. Deparaffinize slides:
    - Place slides in container with xylene and incubate for 2 min.
    - Transfer to second container with xylene and incubate for 2 min.
2. Rehydrate slides:
    - Transfer slides to container with 100 % alcohol and incubate for 2 min.
    - Transfer slides to second container with 100 % alcohol and incubate for 2 min.

- Transfer to container with 96 % alcohol and incubate for 2 min.
- Transfer to container with 70 % alcohol and incubate for 2 min.
- Transfer to container with 50 % alcohol and incubate for 2 min.
- Transfer to container with distilled water and incubate for 2 min.

3. Transfer to container with 2 % HCl-2 % ferrocyanide mixture (*see* **Note 16**) and incubate for 30 min.
4. Transfer to container with distilled water and incubate for 10 s.
5. Counterstain with neutral fast red for 5 min.
6. Transfer to container with distilled water and incubate for 10 s.
7. Dehydrate slides (*see* **Note 12**):
   - Transfer to container with 70 % alcohol and incubate for 2 min.
   - Transfer to container with 96 % alcohol and incubate for 2 min.
   - Transfer to container with 100 % alcohol and incubate for 2 min.
   - Transfer slides to second container with 100 % alcohol and incubate for 2 min.
   - Transfer to container with xylene and incubate for 2 min (*see* **Note 13**).
   - Transfer to second container with xylene and incubate for 2 min (*see* **Note 13**).
8. Place drop of mounting medium on slide and cover with cover slip.
9. Air-dry for 15 min under flow cabinet to evaporate xylene.
10. Examine slides under microscope.

4 Notes

1. For excision, fixation, and sectioning refer to Daugherty et al. [12] or De Waard et al. [13].
2. If used often prepare containers for each solution, change solutions weekly.
3. Dimensions depending on section size.
4. Entellan, permount, or similar.
5. Work under flow cabinet to avoid inhaling xylene fumes.
6. Be careful to use the alcoholic not the aqueous solution.

7. Filter solution with filter paper to remove undissolved precipitate.
8. Dissolve martius yellow in alcohol before adding phosphotungstic acid.
9. Synonym: Crystal Ponceau acid red 44.
10. Synonym: Dodecatungstophosphoric acid.
11. Maximum 30 s to avoid washing out eosin from tissue.
12. Avoid any water carry over. Change alcohols every week. Blot dry after each alcohol change by tapping slide rack on filter paper.
13. Change xylene if contaminated with water drops to avoid remaining water in tissue, hindering examination with light microscopy.
14. Prepare fresh daily; in contrast to Meyer's hematoxylin, Weigert's hematoxylin is resistant to acidic washout.
15. Examine under the microscope after 4 min and check after successive 2-min intervals to avoid overstaining collagen.
16. Prepare fresh.

References

1. Michel JB, Virmani R, Arbustini E et al (2011) Intraplaque haemorrhages as the trigger of plaque vulnerability. Eur Heart J 32(16): 1977–1985
2. Falk E, Nakano M, Bentzon JF et al (2013) Update on acute coronary syndromes: the pathologists' view. Eur Heart J 34(10):719–728
3. Stewart FA, Heeneman S, Te Poele J et al (2006) Ionizing radiation accelerates the development of atherosclerotic lesions in ApoE−/− mice and predisposes to an inflammatory plaque phenotype prone to hemorrhage. Am J Pathol 168(2):649–658
4. Van der Donckt C, Van Herck JL, Schrijvers DM et al (2015) Elastin fragmentation in atherosclerotic mice leads to intraplaque neovascularization, plaque rupture, myocardial infarction, stroke, and sudden death. Eur Heart J 36:1049–1058
5. Rosenfeld ME, Polinsky P, Virmani R et al (2000) Advanced atherosclerotic lesions in the innominate artery of the ApoE knockout mouse. Arterioscler Thromb Vasc Biol 20(12): 2587–2592
6. Sasaki T, Kuzuya M, Nakamura K et al (2006) A simple method of plaque rupture induction in apolipoprotein E-deficient mice. Arterioscler Thromb Vasc Biol 26(6):1304–1309
7. de Nooijer R, Verkleij CJ, von der Thusen JH et al (2006) Lesional overexpression of matrix metalloproteinase-9 promotes intraplaque hemorrhage in advanced lesions but not at earlier stages of atherogenesis. Arterioscler Thromb Vasc Biol 26(2):340–346
8. Gough PJ, Gomez IG, Wille PT et al (2006) Macrophage expression of active MMP-9 induces acute plaque disruption in apoE-deficient mice. J Clin Invest 116(1):59–69
9. Eitzman DT, Westrick RJ, Shen Y et al (2005) Homozygosity for factor V Leiden leads to enhanced thrombosis and atherosclerosis in mice. Circulation 111(14):1822–1825
10. Borissoff JI, Otten JJ, Heeneman S et al (2013) Genetic and pharmacological modifications of thrombin formation in apolipoprotein e-deficient mice determine atherosclerosis severity and atherothrombosis onset in a neutrophil-dependent manner. PLoS One 8(2):e55784
11. Suvarna K, Layton C, Bancroft J (2008) Bancroft's theory and practice of histological techniques, 7th edn. Churchill Livingston, London
12. Daugherty A, Whitman SC (2003) Quantification of atherosclerosis in mice. Methods Mol Biol 209:293–309
13. de Waard V, Gijbels M, Lutgens E et al (2012) Models and analysis of atherosclerosis, restenosis, and aneurysm formation in the mouse. Curr Protoc Mouse Biol 2(4):317–345

Chapter 25

Mechanical Stabilization of Mouse Carotid Artery for In Vivo Intravital Microscopy Imaging of Atherogenesis

Raphaël Chèvre

Abstract

We present here a procedure that allows real-time high-resolution multichannel imaging of early atherosclerotic lesions of live mice, by dramatically reducing the respiratory and pulsatile movements of the athero-susceptible carotid artery, without significantly altering blood flow dynamics. This surgical preparation can be combined with the use of various fluorescent probes and reporter mice to simultaneously visualize the dynamics of inflammatory leukocytes, platelets, or even subcellular structures. Stabilization of the tissue renders it suitable for two-photon laser scanning microscopic imaging and allows tracking the behavior of inflammatory cells in three dimensions.

Key words Intravital fluorescence microscopy, Mouse carotid artery surgery, Atherogenesis, Leukocyte recruitment, Inflammation

1 Introduction

Atherosclerosis is a chronic inflammatory disease of large arteries and a major cause of mortality in Western societies [1]. Despite intense research in the field, many outstanding questions related to the initiation and propagation of inflammation in athero-prone arteries (e.g., aorta and carotid arteries) remain open. This is in large part due to the difficulty of performing real-time imaging of athero-prone arteries subjected to respiratory and pulsatile movements, which greatly limit the temporal and spatial resolution.

Attempts to directly image leukocyte recruitment in athero-prone regions of explanted arteries by applying epifluorescent or two-photon laser scanning microscopy (TPLSM) have yielded important mechanistic information on the processes that underlie disease progression, including a role of adhesion receptors in leukocyte recruitment [2], accumulation of activated platelets [3], or local presentation of antigens by dendritic cells to T lymphocytes [4].

Vicente Andrés and Beatriz Dorado (eds.), *Methods in Mouse Atherosclerosis*, Methods in Molecular Biology, vol. 1339, DOI 10.1007/978-1-4939-2929-0_25,

While these studies with explanted arteries dramatically improved image quality, they have failed to provide the complex rheological and immune context present in the arterial lumen of live animals.

Direct visualization of exposed carotid arteries in vivo at low magnification allowed analysis of leukocyte rolling or even the identification of cellular clusters [5, 6]. However, visualization at higher resolution or in 3D was prevented by the pulsatile motion of the arterial wall, which prevented analysis of the dynamics of leukocytes and platelets in the atherogenic environment, or the identification of subcellular structures [2, 5–7]. Synchronization of acquisition with arterial wall motion allowed nonetheless an increase in spatial resolution in the *z*-axis at the cost of temporal resolution [6]. Other studies in which the artery was fully immobilized allowed imaging of the arterial wall at high spatial resolution but completely abrogated the physiological blood flow and could not be used to study the dynamic inflammatory events that occur intravascularly [8].

We recently demonstrated that mechanical stabilization of carotid artery in the vertical plane dramatically increases imaging quality at subcellular and sub-second resolutions in both 2D or in 3D using TPLSM [9], comparable to the resolutions achieved in the microvasculature of many tissues [3, 10, 11]. In this chapter, we describe a method for the stabilization of the mouse carotid artery which allows the quantification of leukocyte and platelet dynamics during early atherogenesis, and of subcellular events, such as adhesion molecule reorganization during rolling and arrest phases [9].

2 Materials

1. Athero-susceptible transgenic mice challenged with a high-fat diet (*see* **Note 1**).
2. Intravital fluorescence microscopy platform with perfusion system (e.g., water-jacketed heating coil, Radnoti, Monrovia, CA) (*see* **Note 2**).
3. Custom plastic platform for mouse immobilization and tissue perfusion (*see* **Note 3**).
4. Fluorescent probes or fluorescent transgenic mice (*see* **Note 4**).
5. Anesthetics: 50 mg/kg ketamine (e.g., Imalgene 1000, Merial) + 0.5 mg/kg medetomidine (e.g., Medeson, Urano) in 0.9 M NaCl prepared with distilled water.
6. Phosphate-buffered saline (PBS): 8.0 g/L NaCl, 0.2 g/L KCl, and 1.44.g/L Na_2HPO_4 prepared with distilled water.
7. Ethanol 70 % in distilled water.
8. Razor.
9. Stereo microscope (e.g., Olympus SZX10).
10. Fine and dull forceps.

11. Sharp/blunt serrated-edge scissors.
12. Water-resistant tape.
13. Intraperitoneal injection syringe.
14. Small size/high gauge sutures (e.g., C-7 12 mm 6/0 USP).
15. Custom tissue spreaders (basically sutures hung with pieces of tape to separate tissue).
16. Custom mechanical stabilizer: water-resistant modeling clay, flat metal piece with a beveled edge (e.g., back end of a surgical blade), plastic stick (e.g., cotton swab cut in half), and glass cover 12 mm in diameter (Fig. 1).

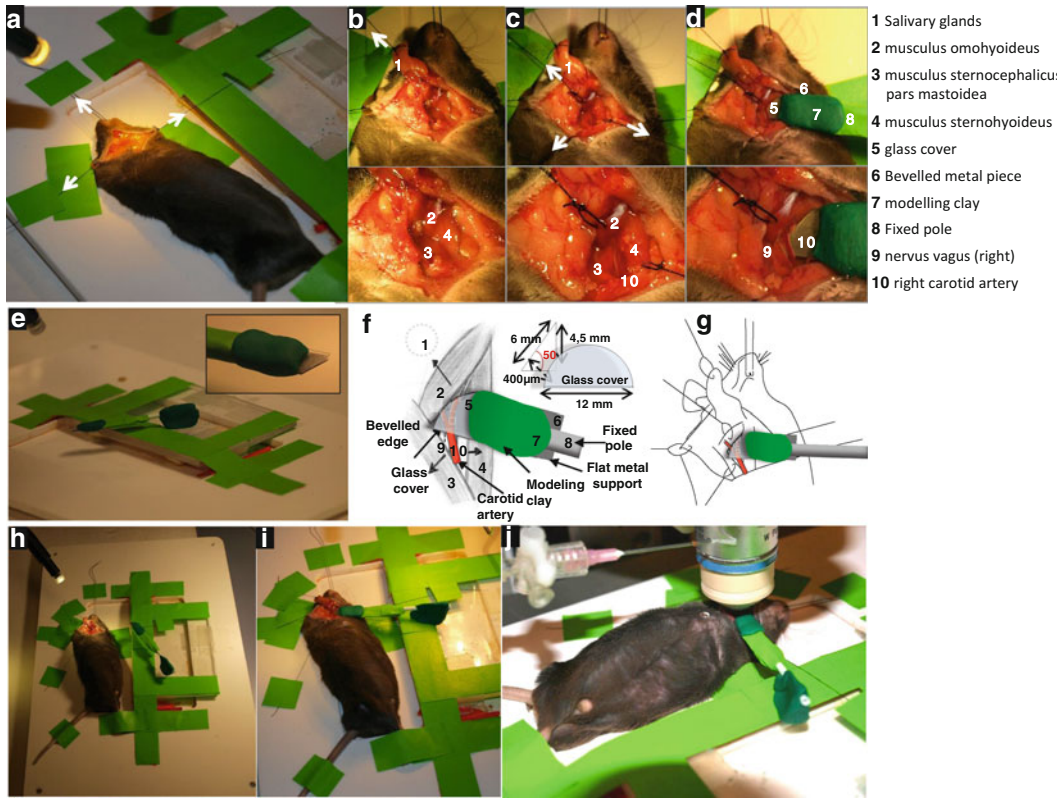

Fig. 1 Surgical preparation and stabilization of the mouse carotid artery. *Numbers* indicate the different elements and tissues involved in the procedure. (**a**) Mice are immobilized in decubitus position, the carotid artery area is exposed, and skin around the surgical wound is fixed with sutures (*white arrows*). (**b**) The salivary gland (*1*) is fixed above the preparation with sutures (*white arrows*). (**c**) Hyoid muscles surrounding the carotid artery are separated and fixed with sutures (*white arrows*). Detail of hyoid muscles: omohyoid muscle (*2*), mastoid part of sternocephalic muscle (*3*), sternothyroid muscle (*4*). (**d**) Positioning of the metal support and glass coverslip for stabilization of the artery. The right vagus nerve (*9*) is carefully separated from the carotid artery (*10*). A flat metal piece with a beveled edge (*6*) is placed under the vessel, while the other side of the piece is fixed to a lateral holder (*8*). An image-grade round coverslip cut in half (*5*) is then placed above the artery and flexibly fixed to the bottom support using water-insoluble modeling clay (*7*). (**e**) General and detailed views of the stabilizer and of the platform. (**f**) Schematic representations of the stabilizer and tissues. (**g**) Schematic showing the positioning of the stabilizer. (**h** and **i**) General view of the mouse on the platform without (**h**) and with (**i**) the stabilizer positioned on carotid artery. (**j**) Image of the mouse prepared for observation under the microscope

3 Methods

3.1 Mouse Preparation

1. Inject intraperitoneally the anesthetic mixture (ketamine + medetomidine) and wait approximately 15 min until the mouse losses reflex response to toe or tail pinching (*see* **Note 5**).
2. Shave the neck and clean with 70 % ethanol to prevent contamination at the surgical site.
3. Immobilize mouse in decubitus position on the custom plastic platform as shown in Fig. 1 using water-resistant tape. Immobilize the head of the mouse by attaching its teeth to the platform using sutures and tape (Fig. 1a and *see* **Note 6**).

3.2 Surgery for Carotid Artery Exposure

Apply warm saline to the tissues throughout the procedure.

1. Using sharp/blunt serrated-edge scissors, make an ≈1-cm-long straight incision on the right part of the neck region, parallel to the trachea, from just below the chin to the top of the sternum just above the rib cage (*see* **Note 7**).
2. Using dull forceps, separate and blunt-dissect the skin on both sides of the incision and dissect the underlying tissue away from the skin circumferentially around the entire incision wound. Using sutures hung with water-resistant tape, maintain the skin away from incision wound (Fig. 1a and *see* **Note 8**).
3. Using the forceps, bluntly dissect the connective tissue away from the mouse's right jugular (*see* **Note 9**).
4. Using the forceps, separate the fascia overlying the glandular tissue to expose the underlying glands, and gently dissect glandular tissue apart via blunt dissection to expose the muscular layer. Using sutures and tape, maintain the salivary gland away from the wound (Fig. 1b).
5. Using sutures and tape, maintain surrounding muscles (omohyoid muscle, mastoid part of the sternocephalic muscle, and the sternothyroid muscle) away from the carotid artery (Fig. 1c, f).
6. Expose the right carotid artery and carefully dissect it from the surrounding tissues (Fig. 1c, f and *see* **Note 10**).
7. Carefully separate the right vagus nerve from the carotid artery and surrounding tissues using dull forceps (Fig. 1c, f and *see* **Note 11**).

3.3 Carotid Artery Mechanical Stabilization for Intravital Imaging

1. Prepare the stabilizer (Fig. 1d–j). Fix the front end of the surgical blade to the plastic stick using water-resistant tape. Cut the image-grade round coverslip in half, and put it on the top of the back end of the surgical blade. Fix both elements flexibly using modeling clay (*see* **Note 12**). Using forceps, gently separate the coverslip from the surgical blade to obtain a separation of approximately 0.5–1 mm (Fig. 1f).

2. Place the beveled edge of the flat metal piece under the carotid artery, with the coverslip on its top (*see* **Note 13**).
3. Attach flexibly the stabilizer to the platform using modeling clay, as shown in Fig. 1f.
4. Using the back end of forceps, press gently on the coverslip and on the modeling clay to visually restrain motion in *z*-plane without interrupting blood flow (*see* **Note 14**, Fig. 1d–f).
5. Place the stabilized region of the artery under the water-dipping objective of a multichannel epifluorescence microscope or a two-photon microscope (Fig. 1j and *see* **Note 15**).

4 Notes

1. Athero-susceptible mice should be used (e.g., *ApoE*$^{-/-}$, or *Ldlr*$^{-/-}$). For diet-induced atherosclerotic studies, 6- to 8-week-old male mice can be fed with atherogenic high-fat diet (e.g., 10.8 % total fat, 0.75 % cholesterol, S8492-E010, Ssniff, Germany). Primary lesions typically appear after 2 weeks of fat feeding in *ApoE*$^{-/-}$ mice [9].
2. Intravital fluorescence microscopy or TPLSM platforms can be used. The humidity and temperature of the tissue can be maintained through constant dripping of saline at 37 °C delivered onto the objective through a water-jacketed heating coil.
3. A custom plastic support similar to the supports used for cremaster muscle intravital microscopy is used to maintain the mouse immobility and to easily transport it to the intravital microscope stage after surgery. It consists basically of a plastic support which allows the elimination of perfused liquids.
4. As intravital imaging of the carotid artery does not allow bright-field visualization (contrary to cremasteric arterioles or venules), structures of interest should be fluorescently labeled. Luminal cells of the carotid artery can be easily labeled by injecting intravenously 50 μg of rhodamine 6G (Sigma) in PBS [9]. Fluorescent mice (e.g., *Lysm*$^{egfp/egfp}$*ApoE*$^{-/-}$ mice [9, 12] or Mafia: *ApoE*$^{-/-}$ mice [9, 13]) can be used to visualize myeloid cells. Other molecules and cells of interest in atherosclerosis studies can be visualized using multiple fluorescent probes that are commercially available (e.g., antibodies or fluorogenic substrates), as well as other reporter murine strains. For example, it should be possible to examine the specific recruitment and behavior of regulatory and interleukin 17-producing T cells, patrolling or inflammatory populations of monocytes, neutrophils, or platelets during atherosclerosis using existing reporter mice [14–17].
5. It is recommended to use sterile instruments and solutions and a sterile surgical field and surgical attire (gloves, face masks, head

and hair covering, and/or surgical gown). Diligently follow all waste disposal regulations when disposing waste material.

6. Make sure mouse is immobilized from teeth to tail to attenuate respiratory movements.
7. Use scissors only at this step of the procedure. All other surgery steps should be performed by using dull forceps to limit tissue damage.
8. Prepare in advance a set of 0.5–1-cm pieces of tape. Doing this now will save you time during the surgery procedure.
9. Be extremely careful when working near the jugular vein because its wall is quite thin and easy to damage. You don't need to clear everything off the jugular, just clear away enough to see what's going on. Doing this step now will save you time later.
10. Carotid surgical exposure for imaging [9, 18] is similar to preparations for balloon and wire injury and remodeling studies after ligation in rat or mice [19]. Nevertheless, preparation for imaging requires to be particularly careful when working near the carotid artery. The artery wall is easy to damage and should not be touched directly to limit surgery-caused inflammation.
11. If the vagus nerve is too intimately adhered to the carotid artery, don't separate it from the vessel wall, just separate it from the surrounding tissues.
12. Use the smallest amount of modeling clay you can; otherwise the resulting stabilizer will be too big and the objectives of the microscope may not reach the appropriate focal distance. Keep in mind that you will have to place the coverslip under the microscope. Therefore, check the shape/size of the objectives and estimate the focal distance ahead of time.
13. To stabilize the carotid artery, the flat metal piece of the stabilizer is placed underneath the vessel and the glass cover on top (≈0.5-mm distance between metal piece and glass cover). Modeling clay should be flexible to allow modulation of the distance between the metal piece and glass cover but also sufficiently rigid to maintain the artery between both supports to avoid motion in z-plane.
14. Gentle pressing on the coverslip should lead to a separation of approximately 400 ± 50 μm between both supports which should visually restrain the vertical pulsatile movements without significantly compressing the artery. This step is critical as you should attempt to reach the better immobilization without significant alterations of blood flow. If you abrogate blood flow and compress too much the artery, even for a short period of time (seconds), the carotid artery will not be suitable for imaging. For example, accumulation of platelets and neutrophils can be dramatically affected by artery compression.

15. The humidity and temperature of the tissue should be maintained through constant dripping of saline at 37 °C delivered onto the microscope objective.

Acknowledgments

I thank R. Villa-Bellosta for photography.

Competing financial interests: The author declares no competing financial interests.

References

1. Roger VL, Go AS, Lloyd-Jones DM et al (2011) Heart disease and stroke statistics--2011 update: a report from the American Heart Association. Circulation 123(4): e18–e209
2. Ramos CL, Huo Y, Jung U et al (1999) Direct demonstration of P-selectin- and VCAM-1-dependent mononuclear cell rolling in early atherosclerotic lesions of apolipoprotein E-deficient mice. Circ Res 84(11):1237–1244
3. Huo Y, Schober A, Forlow SB et al (2003) Circulating activated platelets exacerbate atherosclerosis in mice deficient in apolipoprotein E. Nat Med 9(1):61–67
4. Koltsova EK, Garcia Z, Chodaczek G et al (2012) Dynamic T cell-APC interactions sustain chronic inflammation in atherosclerosis. J Clin Invest 122(9):3114–3126
5. Eriksson EE, Xie X, Werr J et al (2001) Direct viewing of atherosclerosis in vivo: plaque invasion by leukocytes is initiated by the endothelial selectins. FASEB J 15(7): 1149–1157
6. Megens RT, Kemmerich K, Pyta J et al (2011) Intravital imaging of phagocyte recruitment. Thromb Haemost 105(5):802–810
7. Drechsler M, Megens RT, van Zandvoort M et al (2010) Hyperlipidemia-triggered neutrophilia promotes early atherosclerosis. Circulation 122(18):1837–1845
8. Yu W, Braz JC, Dutton AM et al (2007) In vivo imaging of atherosclerotic plaques in apolipoprotein E deficient mice using nonlinear microscopy. J Biomed Opt 12(5):054008
9. Chevre R, Gonzalez-Granado JM, Megens RT et al (2014) High-resolution imaging of intravascular atherogenic inflammation in live mice. Circ Res 114(5):770–779
10. Clark SR, Ma AC, Tavener SA et al (2007) Platelet TLR4 activates neutrophil extracellular traps to ensnare bacteria in septic blood. Nat Med 13(4):463–469. doi:10.1038/nm1565
11. Hidalgo A, Chang J, Jang JE et al (2009) Heterotypic interactions enabled by polarized neutrophil microdomains mediate thromboinflammatory injury. Nat Med 15(4):384–391
12. Rotzius P, Soehnlein O, Kenne E et al (2009) ApoE(-/-)/lysozyme M(EGFP/EGFP) mice as a versatile model to study monocyte and neutrophil trafficking in atherosclerosis. Atherosclerosis 202(1):111–118
13. Burnett SH, Kershen EJ, Zhang J et al (2004) Conditional macrophage ablation in transgenic mice expressing a Fas-based suicide gene. J Leukoc Biol 75(4):612–623
14. Auffray C, Fogg D, Garfa M et al (2007) Monitoring of blood vessels and tissues by a population of monocytes with patrolling behavior. Science 317(5838):666–670
15. Esplugues E, Huber S, Gagliani N et al (2011) Control of TH17 cells occurs in the small intestine. Nature 475(7357):514–518
16. Faust N, Varas F, Kelly LM et al (2000) Insertion of enhanced green fluorescent protein into the lysozyme gene creates mice with green fluorescent granulocytes and macrophages. Blood 96(2):719–726
17. Zhang J, Varas F, Stadtfeld M et al (2007) CD41-YFP mice allow in vivo labeling of megakaryocytic cells and reveal a subset of platelets hyperreactive to thrombin stimulation. Exp Hematol 35(3):490–499
18. Doring Y, Drechsler M, Wantha S et al (2012) Lack of neutrophil-derived CRAMP reduces atherosclerosis in mice. Circ Res 110(8): 1052–1056
19. Holt AW, Tulis DA (2013) Experimental rat and mouse carotid artery surgery: injury & remodeling studies. ISRN Minim Invasive Surg. doi:10.1155/2013/167407

Chapter 26

Intravital Microscopy in the Cremaster Muscle Microcirculation for Endothelial Dysfunction Studies

Cristina Rius and María J. Sanz

Abstract

The intravital microscopy in the mouse cremaster muscle microcirculation is a method widely used to visualize in vivo blood cells interacting with the endothelium and within the vessels. Therefore, it is a suitable technique to study leukocyte-endothelial cell interactions along every stage of the canonical leukocyte recruitment cascade: rolling, adhesion, intravascular crawling, and migration both in postcapillary venules and arterioles of the mouse cremasteric microcirculation. This technique also enables to assess vessel functionality, since hemodynamic parameters such as shear stress, flow rate, and vasodilatation/vasoconstriction, among other vascular events, can be additionally determined. Furthermore, response to multiple drugs and mechanisms underlying blood cells interactions within the vascular system can be studied in a real scenario. This chapter describes a protocol for intravital microscopy in the mouse cremaster muscle microcirculation.

Key words Atherosclerosis, Endothelial dysfunction, Intravital microscopy, Cremaster muscle, Murine microcirculation, Leukocyte recruitment, Leukocyte migration, In vivo imaging

1 Introduction

The early atherosclerotic lesion involves an inflammatory response consisting of intimal accumulation of T lymphocytes and lipid-laden macrophages, and these events occur continuously throughout the entire atherogenic process [1, 2]. One of the earliest stages of atherogenesis is endothelial dysfunction. Endothelial function has been assessed primarily in terms of endothelium-dependent vasomotion, largely based on the assumption that impaired endothelium-dependent vasomotion reflects alterations of other functions of the endothelium as well. Indeed, endothelial dysfunction leads to a pro-inflammatory and prothrombotic phenotype of the endothelium [3] and, thus, provokes the attachment and the subsequent migration of leukocytes.

Intravital microscopy represents one of the best methods to visualize in real time and in vivo a great deal of biological vascular processes. Since early indications of the use of intravital microscopy

Vicente Andrés and Beatriz Dorado (eds.), *Methods in Mouse Atherosclerosis*, Methods in Molecular Biology, vol. 1339, DOI 10.1007/978-1-4939-2929-0_26,

technique in 1839 [4], the technique has been improved largely due to the upgrading of the optical systems The incorporation of high-resolution microscopes such as confocal or multiphoton and the use of fluorescence-labeled markers, including molecules (dextran-FITC or albumin-FITC) [5] for vascular permeability studies, fluorescence-conjugated antibodies to detect different cell subtypes [6], or even bioluminescent pathogens (usually employed for analyzing mechanisms of host-pathogen interaction) [7], have implemented the quality of the studies since they allow to investigate in detail highly complex pathophysiological processes.

Nowadays, the versatility of this technique has gained increased interest given the development of new fluorescent tools which allow exploring new tissues and organs. The organs or tissues which are commonly examined are: the cremaster muscle [8] to study leukocyte interactions with the venular and arteriolar endothelium; the liver, in order to investigate hepatocellular cancer [9], microbial infections [7], or sterile injury [1], among others; the brain, for cerebrovascular events [10]; the lymph nodes, for immune system trafficking studies [11]; as well as the adipose tissue for chronic metabolic diseases [12].

For cardiovascular pathologies, and specifically in endothelial dysfunction research, the mouse cremaster microcirculation has been widely employed [8, 13, 14]. In fact, in addition to provide a relevant vascular scenario, this technique can be used to study acute local effects through intrascrotal injection of the inflammatory stimulus, drugs, or pathogens, as well as the impact of systemic effects in this vascular territory through the intravenous or intraperitoneal administration of the agents under investigation.

Another advantage of this technique relies in the minimal invasive surgery required since the testicles are external non-vital organs that do not imply a threat for the animal's life. In general, the manipulations do not affect the respiratory or the cardiac system functions if the anesthetics have been properly selected. Additionally, the potential bleeding during surgery manipulation is very low given that the blood vessels that irrigate the testis and have high blood flow are far away from the area under investigation. Furthermore, the cremasteric tissue is very accessible, and the microvascular structures are easily identified; therefore, there is no need of a long training to learn how to exteriorize the muscle.

In addition, and from an optical point of view, the cremaster muscle is a thin layer that allows the direct visualization of vessels and blood flow under a conventional transilluminating microscope, and it is possible to get excellent resolution with bright field [15]. In fact, correct surgical preparations are very stable over time and allow visualizing the vessels in only one plane providing high-quality imaging not affected by striated muscle movements.

Nevertheless, the main obvious limitation of this technique is its restriction to studies in male mice. The use of the murine

mesenteric microcirculation is neither common nor ideal due to the nearly absence of microvessels in this preparation. Therefore, for female studies, it has very recently established the intravital microscopy for the mouse carotid artery visualization [6].

2 Materials

1. Heated surgery tray (Fig. 1) (*see* **Note 1**).
2. Electrothermometer to monitor mouse rectal temperature (*see* **Note 2**).
3. Intravital microscopy system (*see* **Note 3**).
4. Common materials and buffers: all the materials and solutions are prepared under sterile conditions.
   (a) Mouse anesthesia is a mixture of xylazine hydrochloride at the dose 10 mg/kg and ketamine hydrochloride 200 mg/kg.
   (b) Sterile water.

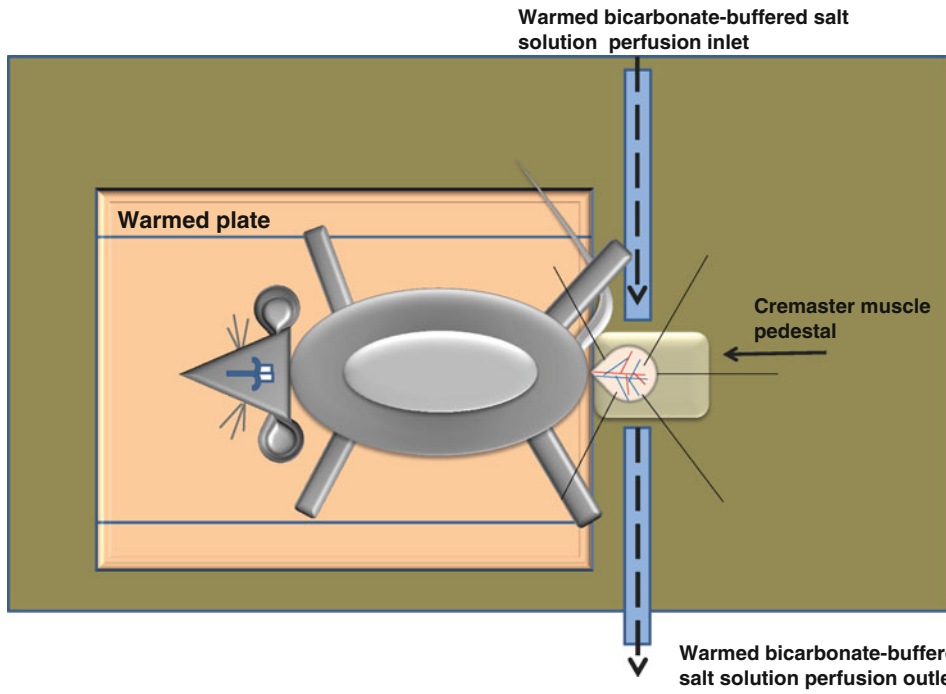

Fig. 1 Mouse board for cremaster muscle intravital microscopy. The board should be maintained in a constant temperature (36.5–37.5 °C) with a heating system. There are two areas in the tray: the warmed plate and the cremaster muscle pedestal. Mouse should be placed in the warmed area, while the cremaster should be externalized and fixed in the cremaster muscle pedestal. The warmed bicarbonate-buffered salt solution should be perfused directly to the cremaster, keeping the muscle wet during the whole study

(c) Sterile physiological saline solution: 0.9 % NaCl.

(d) Sterile bicarbonate-buffered salt solution (BBS): 131.9 mM NaCl, 4.7 mM KCl, 1.2 mM $MgSO_4$, 20 mM $NaHCO_3$, 2.0 mM $CaCl_2$, pH 7.4. The buffer is bubbled with a 95 % N_2/5 % CO_2 gas mixture to reduce the oxygen tension to the physiological level (40–50 mmHg).

5. Surgical materials:
   (a) A pair of sharp-tip tweezers and a small surgical scissors.
   (b) Triangular suture needle.
6. Sterile gauze pads.
7. 1 ml syringe with 25-gauge needles.
8. Thermocautery.
9. Water-resistant surgical tape.
10. Male mice.
11. Electric razor.
12. Optical Doppler velocimeter (Microcirculation Research Institute, Texas A&M University, College Station, Texas).
13. Video caliper to measure vessel diameter (e.g., Microcirculation Research Institute, Texas A&M University, College Station, Texas).

3 Methods

3.1 Surgical Procedure to Access Mouse Cremaster Muscle (Fig. 2)

1. Anesthetize a male mouse by intraperitoneal injection of a mixture of xylazine hydrochloride (10 mg/kg) and ketamine hydrochloride (200 mg/kg).
2. Shave the testicle area, legs, and lower abdomen, using an electric razor.
3. Remove the cut hairs using wet sterile gauze pads moistened in water (*see* **Note 4**).
4. Place the animal in a supine position on the surgery tray taking into account that surgical tape pad should be located close to the cremaster muscle pedestal (area of the plate specially designed for the visualization of the cremaster muscle).
5. Extend each leg of the animal, separating them as much as possible to have enough space to facilitate the manipulation of the testis and exteriorize the cremaster muscle (*see* **Note 5**). Fix them to the plate using water-resistant surgical tape.
6. Press gently the lower abdomen using the fingers to bring down the testicles (*see* **Note 6**).
7. Hold with tweezers the skin testicle apex and use small scissors to make a tangential incision of 1 cm until visualizing the round white tissue that corresponds to epididymis (*see* **Note 7**).

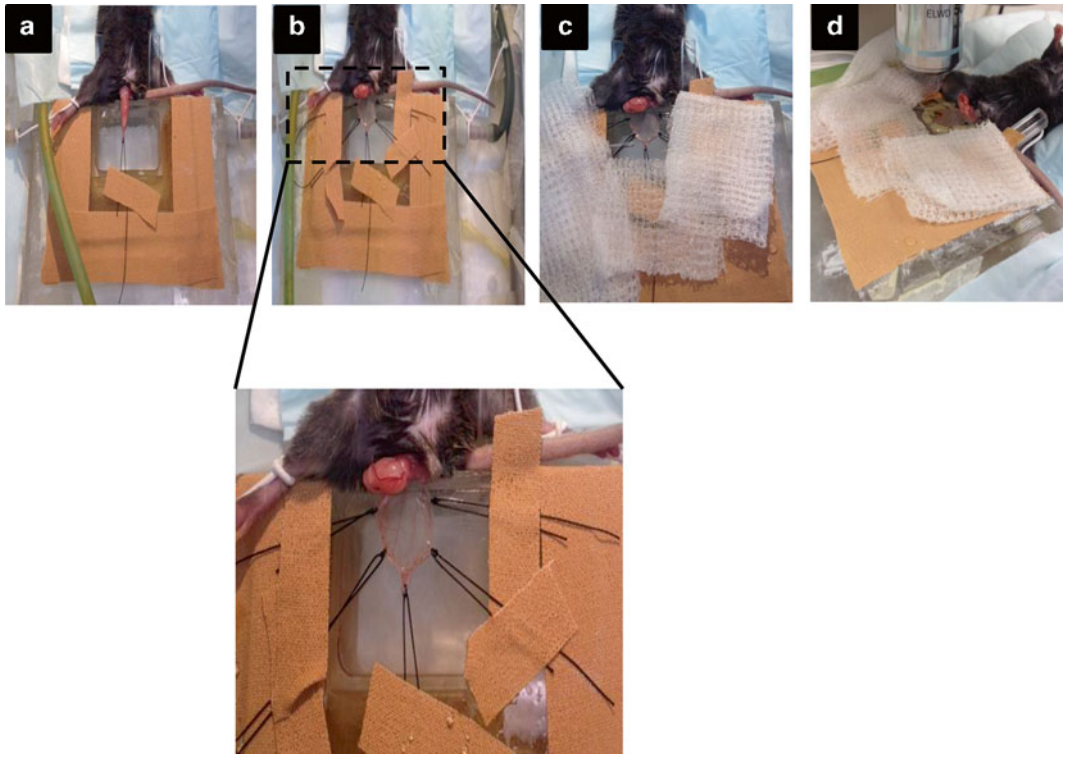

Fig. 2 Main steps during the cremaster muscle surgery. (**a**) Externalization of the testicle and fixation of the apex to the board. (**b**) Exposure of the cremaster muscle and fixation with five stitches to the board, to create a surface as flat as possible (suture at least with 3–5 stitches). (**c**) The preparation must be kept moistened constantly with sterile bicarbonate-buffered salt solution. (**d**) Visualization under the microscope using the 40× objective

8. Gently separate the scrotum sac from the surrounding tissue using sharp-tip tweezers (*see* **Note 8**).
9. Take the end of the scrotal sac with suture and pull it up to exteriorize the testicle completely.
10. Separate tissues surrounding the cremaster muscle using sharp-tip tweezers (*see* **Note 9**).
11. Recognize the prolongation of the femoral artery and iliac vein in the cremaster muscle (*see* **Note 10**).
12. Pin the apex of the cremaster muscle using a suture.
13. Tension the suture that has been inserted in the apex until the testicle is externalized and longitudinally extended onto an optical clear viewing pedestal.
14. Make a small incision with a thermocautery without touching the main vessels.
15. Extend the initial incision using the thermocautery longitudinally along the line drawn by the prolongation of the femoral artery and the iliac vein, until reaching the base of the testicle.

16. Open the cremaster sac carefully with tweezers until the testicle and epididymis are visualized.
17. Keep wet the exposed tissue with a few drops of warm BBS (*see* **Note 11**).
18. Tear testicular ligament with sharp-tip tweezers at the same time that epididymis and testis are separated from the cremaster muscle (*see* **Note 12**).
19. Move the testicle and the epididymis to the pedestal side (*see* **Note 13**).
20. Hold flat the cremaster muscle against the pedestal by attaching silk sutures to the corners of the tissue (*see* **Note 14**).
21. Immediately, perfuse the muscle continuously at a rate of 1 ml/min with warmed BBS (temperature 37 °C).

3.2 Cremaster Muscle Microcirculation Visualization and Data Analysis

1. Let stabilize the cremaster preparation with continuous perfusion of warmed BSS (temperature 37 °C) at a rate of 1 ml/min for at least 30 min (*see* **Note 15**).
2. Select the 40× objective to visualize the microcirculation and identify venules, arterioles, and capillaries (*see* **Note 16**). Avoid for the study the branched cremasteric venules thinner than 20 μm in diameter (*see* **Note 17**). Once you find an appropriate vessel for the study, begin to record a video.
3. Use an optical Doppler velocimeter to measure the centerline red blood cell velocity (V_{rbc}).
4. Calculate the venular blood flow from the product of mean red blood cell velocity ($V_{mean} = V_{rbc}\ 1.6^{-1}$) and cross-sectional area, assuming cylindrical geometry.
5. Calculate the venular wall shear rate (γ) based on the Newtonian definition: $\gamma = 8 \times (V_{mean}\ D_v^{-1})\ s^{-1}$, in which D_v is the vessel diameter [16].
6. Determine the number of rolling, adherent, and emigrated leukocytes off-line during playback of videotaped images (*see* **Note 18**).
7. Sacrifice the animal once you have completed the study.

4 Notes

1. The mouse board for cremaster muscle intravital microscopy studies is a specific device composed of a surgery tray in a warmed plate connected to a heating system to maintain mouse temperature between 36.5 and 37.5 °C along the whole procedure (Fig. 1).

2. Rectal temperature is monitored using an electrothermometer. A dispenser system is required for a continuous perfusion of the cremaster muscle. Ideally, it should be coupled to the pedestal.
3. Different intravital microscopy systems can be employed depending on the researcher needs. Leukocyte trafficking within the cremasteric microcirculation can be visualized using just transillumination of the exposed tissue. Nevertheless, other microscopes with either spinning-disk multichannel-fluorescence confocal or multiphoton microscopes can be also used to image this preparation using fluorescent-labeled antibodies and/or molecules.

   The intravital microscopy system recommended is built by 3i (Intelligent Imaging Innovations, Denver, CO). The system is composed of an AXIO Examiner Z.1 work station (Zeiss, Oberkochen, Germany) mounted on a 3-dimensional motorized stage (Sutter Instrument, Novato, CA) for fast control of the focal plane and precise computer-controlled lateral movement between XY positions. The microscope is equipped with a CoolLED pE widefield fluorescence LED light source system (CoolLED Ltd. UK), and a quad pass filter cube used with a Semrock Di01-R405/488/561/635 dichroic and FF01-446/523/600/677 emitter. The objectives used are Plan-Apochromat 40× NA1.0 and N-Achroplan 10× NA0.3 water-immersion objectives (Zeiss). The images are recorded with CoolSnap HQ2 camera (Photometrics, Tucson, AZ).

   For video and images visualization and analysis, some different softwares can be used, but we recommend the SlideBook software 5.0 (Intelligent Imaging Innovations).
4. Take special care when shaving the testicular area. The animal's penis is very close to the cremaster and can be damaged during shaving. If this happens, stop the bleeding using a sterile gauze pad and press the wound. The manipulator must assess the severity of the injury caused to continue or stop the surgery.
5. If the animal has not been properly placed on the board from the beginning, it can be repositioned removing the water-resistant adhesive plaster and placing the mouse in the correct position.
6. If the bladder is full when the researcher presses the lower abdomen, urine can come out leaving the testicular area wet. In this case, wash properly the area with a sterile gauze moistened in water.
7. Both testes can be used for surgery preparation, because it does not affect the results. Be aware of not touching, damaging, or piercing the internal tissue during the skin incision.

8. Connective and fatty tissues are surrounding and protecting the scrotum sac. They must be removed carefully without damaging the internal tissue.
9. It is very important to remove the connective and fatty tissues surrounding the cremaster muscle as they can interfere with the correct visualization of the blood vessels. Transgenic, old, or fat mice are usually examined by this technique, and fat deposits surrounding the vessels can affect leukocyte visualization. Old or obese mice have fat surrounding the cremaster muscle; therefore, once the testicle is externalized and before starting the cremaster muscle incision, the fat must be carefully removed using the tweezers, to obtain an adequate transillumination of the tissue for microscope examination.
10. The prolongation of the femoral artery and iliac vein in the cremaster muscle can be easily identified since they stand above the rest of the vessels. In addition, they have a bright red color and larger size than the rest of the vessels.
11. Do not ever let the tissue dry. It should be preserved at physiological temperature (37 °C) and humidity conditions (Fig. 2c).
12. The testicular ligament is a thin and transparent tissue which is located below the epididymis and testis.
13. There are two methods for removing the testicle and the epididymis from the cremaster muscle: either they can be internalized back into the abdominal cavity or left on one side of the cremaster muscle.
14. It is recommended to suture at least with 3–5 stitches to extend and properly fix the muscle without damaging the blood vessels.
15. It is important to wait the adequate time to allow stabilization of the microvasculature after the surgical manipulation.
16. Venules can be easily identified since white blood cells can be visualized flowing or interacting within the vessel under basal conditions. In contrast, the high shear rate of the arterioles does not permit leukocyte visualization under the same conditions. Only in a pathological scenario leukocytes can be shown adhered to these vessels. Leukocyte-endothelial cell interactions in the arterioles should be determined at the curvatures where rheological changes occur. Those are the easiest ways to distinguish between arterioles and postcapillary venules (Fig. 3).
17. The vessel diameter is measured using a video caliper.
18. Rolling leukocytes are defined as those white blood cells moving at a velocity less than that of erythrocytes in the same vessel. The white blood cells that are rolling along the endothelial cells differ on their velocity depending on several factors but mostly on the inflammatory state of the blood vessel.

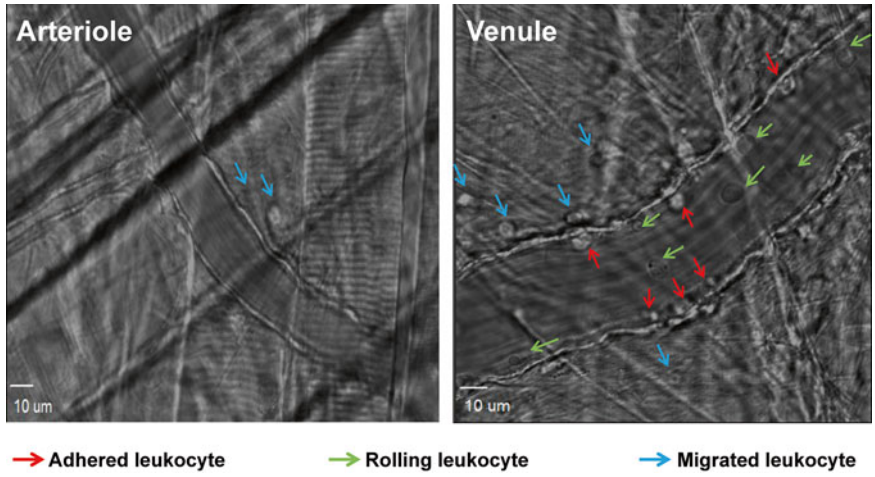

Fig. 3 Visualization of the cremasteric microcirculation. Examples of an arteriole and venule of cremasteric microcirculation. *Arrows* point to adhered leukocytes (*red*), rolling leukocytes (*green*), and migrated leukocytes (*blue*)

The leukocyte rolling velocity (V_{wbc}) is determined from the time required for a leukocyte to move along 100 μm length of the microvessel and is expressed as μm per second. The flux of rolling leukocytes is measured as those cells that could be seen moving past a defined reference point in the vessel. The same reference point is used throughout the experiment because leukocytes may roll for only a section of the vessel before rejoining the blood flow or becoming firmly adhered. A leukocyte is defined as adherent to arteriolar or venular endothelium, if it is stationary for at least 30 s. 20 % of leukocytes that remain halted start to emigrate across the vessel to the extravascular (postcapillary venule) or to the subendothelial (arteriole) space. Leukocyte adhesion is expressed as the number per 100 μm length of vessel during 5 min. Leukocyte emigration is expressed as the number of white blood cells per microscopic field surrounding the vessel. In each animal, leukocyte responses are measured in three to five randomly selected arterioles or postcapillary venules.

Acknowledgments

The CNIC is supported by the Ministerio de Economía y Competitividad and by the Pro-CNIC Foundation. C.R. holds a postdoctoral contract associated with grant RD12/0042/0028 (Red de Investigación Cardiovascular, Instituto de Salud Carlos III).

References

1. Price DT, Loscalzo J (1999) Cellular adhesion molecules and atherogenesis. Am J Med 107:85–97
2. Ross R (1993) The pathogenesis of atherosclerosis: a perspective for the 1990s. Nature 362:801–809
3. Landmesser U, Hornig B, Drexler H (2004) Endothelial function: a critical determinant in atherosclerosis? Circulation 109:II27–II33
4. Wagner R (1839) Information panels on the physiology and evolution. Tab XIV, p. 9
5. McDonald B, Pittman K, Menezes GB et al (2010) Intravascular danger signals guide neutrophils to sites of sterile inflammation. Science 330:362–366
6. Chevre R, Gonzalez-Granado JM, Megens RT et al (2014) High-resolution imaging of intravascular atherogenic inflammation in live mice. Circ Res 114:770–779
7. Lee WY, Moriarty TJ, Wong CH et al (2010) An intravascular immune response to Borrelia burgdorferi involves Kupffer cells and iNKT cells. Nat Immunol 11:295–302
8. Rius C, Piqueras L, Gonzalez-Navarro H et al (2013) Arterial and venous endothelia display differential functional fractalkine (CX3CL1) expression by angiotensin-II. Arterioscler Thromb Vasc Biol 33:96–104
9. Takeichi T, Engelmann G, Mocevicius P et al (2010) 4-dimensional intravital microscopy: a new model for studies of leukocyte recruitment and migration in hepatocellular cancer in mice. J Gastrointest Surg 14:867–872
10. Osswald M, Winkler F (2013) Insights into cell-to-cell and cell-to-blood-vessel communications in the brain: in vivo multiphoton microscopy. Cell Tissue Res 352:149–159
11. Liou HL, Myers JT, Barkauskas DS et al (2012) Intravital imaging of the mouse popliteal lymph node. J Vis Exp (60), e3720
12. Nishimura S, Manabe I, Nagasaki M et al (2008) In vivo imaging in mice reveals local cell dynamics and inflammation in obese adipose tissue. J Clin Invest 118:710–721
13. Rius C, Company C, Piqueras L et al (2013) Critical role of fractalkine (CX3CL1) in cigarette smoke-induced mononuclear cell adhesion to the arterial endothelium. Thorax 68: 177–186
14. Company C, Piqueras L, Naim Abu Nabah Y et al (2011) Contributions of ACE and mast cell chymase to endogenous angiotensin II generation and leucocyte recruitment in vivo. Cardiovasc Res 92:48–56
15. Zarbock A, Ley K (2009) New insights into leukocyte recruitment by intravital microscopy. Curr Top Microbiol Immunol 334:129–152
16. House SD, Lipowsky HH (1987) Microvascular hematocrit and red cell flux in rat cremaster muscle. Am J Physiol 252:H211–H222

Chapter 27

Fluorescent Molecular Tomography for In Vivo Imaging of Mouse Atherosclerosis

Alicia Arranz, Markus Rudin, Carlos Zaragoza, and Jorge Ripoll

Abstract

Optical imaging technologies such as fluorescence molecular tomography (FMT) are gaining great relevance in cardiovascular research. The main reason is the increased number of available fluorescent agents, especially those termed "activatable probes," which remain quenched under baseline conditions and are fluorescent when a specific enzymatic activity is present. A major characteristic of FMT is the possibility of obtaining quantitative data of fluorescence signal distribution in a noninvasive fashion and using nonionizing radiation, making FMT an invaluable tool for longitudinal studies with biomedical applications. Here, we describe a standard procedure to perform FMT experiments in atherosclerosis mouse models, from the handling of the animals to the reconstruction of the 3D images.

Key words Fluorescent agents, Activatable probes, Optical systems, Optical tomography, Whole-body optical imaging, In vivo models, Scattering, Diffusion, Near-infrared probes, 3D imaging

1 Introduction

Microscopic fluorescence techniques are routinely and widely used in biomedical research laboratories. When dealing with in vivo models, however, whole-body imaging technologies are desirable in order to allow longitudinal studies and to reduce the number of animals required for experimentation. From these whole-body imaging approaches, optical imaging systems display a number of advantages such as their high sensitivity, their high throughput, their cost-effectiveness (e.g., when compared with other technologies such as magnetic resonance imaging, MRI, or positron emission tomography, PET), and their safety (due to the nonionizing nature of the wavelengths employed).

Whole-body optical imaging approaches, on the other hand, have to deal with two main characteristics of living tissue which affect light propagation: high scattering and high absorption. When traveling in non-scattering media, as it happens in traditional microscopic techniques, light keeps its directionality and its original

Vicente Andrés and Beatriz Dorado (eds.), *Methods in Mouse Atherosclerosis*, Methods in Molecular Biology, vol. 1339, DOI 10.1007/978-1-4939-2929-0_27,

intensity decays exponentially with the amount of tissue traversed. When considering whole-body optical imaging, however, light loses its directionality due to the high scattering nature of tissue, and its original intensity is absorbed selectively by different tissue constituents, the most important being melanin and blood. Scattering and absorption affect the light source energy differently: scattering simply redistributes light spatially and does not remove any of the energy, even though the energy density diminishes with increasing distance from the light source; absorption, on the other hand, sequesters the energy we need for imaging fluorescence [1, 2].

In order to predict the effect of scattering in propagation, light transport in highly scattering tissue is typically modeled using the diffusion approximation, accounting for the wavelength-dependent absorption of the tissues present. This effectively means that if one needs to recover the spatial distribution of fluorescence in 3D, we need to solve what is termed an "inverse problem," which in the case of diffusion is highly nonlinear as opposed to imaging in microscopy, where there is a direct relationship between the data and the object that one intends to image [1, 3, 4].

On the other hand, the only way to effectively overcome the loss of signal intensity due to absorption is to operate in wavelengths where the main tissue constituents (oxy- and deoxy-hemoglobin, water, and lipids mainly) absorb the least. To that end, near-infrared fluorescent (NIRF) agents and proteins have been developed with excitation maximums above 650 nm, allowing the use of excitation sources and emission spectra in a region of the optical spectrum termed the "optical window" where blood absorption is reduced to a minimum. This region spans from 700 to 900 nm, approximately, increasing exponentially in the Infra-Red due to water absorption [5, 6].

Recently developed NIRF agents are usually classified according to the mechanism involved in the production of the fluorescent signal. Thus, within this framework, we can distinguish the nontargeted, the targeted, and the activatable fluorescent probes. Nontargeted fluorescent imaging agents are nonspecific and are generally used for imaging of perfusion or vascular leakage of the tissue. They typically suffer from severe background signal and require a careful study of the imaging times in order to optimize the signal-to-background ratio. Targeted probes, such as fluorescent-conjugated antibodies, recognize and bind specific ligands and are thus specific, but need some clearing time in order to reduce the signal originating from the unbound portion of the probes. Finally, activatable probes are those fluorescent imaging agents which are designed in such a way that the fluorescent signal is quenched unless a specific enzymatic activity cleaves the probe (e.g., two fluorophores in close proximity would quench each other—if they are joined by a cleavable linker, this system would fluoresce in the presence of the specific enzymatic activity that

cleaves the linker). In cardiovascular studies, nontargeted fluorescent agents are generally used for imaging of vascularization and angiogenesis, whereas targeted fluorescent agents have been used to detect, for example, fibrin deposition in deep vein thrombosis [7] or apoptotic cells after myocardial infarction in a mouse model [8]. In recent years, however, the use of activatable fluorescent agents has witnessed a significant increase in studies of different cardiovascular pathologies [9, 10], including atherosclerosis. More specifically, activatable fluorescent agents have allowed the quantification of protease activity from matrix-metalloproteases (MMPs) [11–13] and different cathepsins [14, 15] in atherosclerosis models.

This chapter describes a method for 3D optical imaging of mouse atherosclerosis using fluorescence molecular tomography (FMT). Variations from this protocol, though, will depend on the specific experimental model and the fluorescent agent used and on the FMT system employed.

2 Materials

2.1 Mice and Diet

1. Atherosclerosis-prone mice. Mouse models for atherosclerosis are based on genetic modifications of lipoprotein metabolism in combination with high-fat dietary changes (*see* **Note 1**). All procedures involving animals should have received the corresponding ethic committee approval.
2. High-cholesterol and high-fat diet (*see* **Note 2**).
3. Chlorophyll-free chow is highly recommended (*see* **Note 3**).

2.2 Anesthesia

1. Inhaled anesthesia: 2 % isoflurane is recommended due to reduced toxicity and reduced recovery time.
2. Equipment for inhalatory anesthesia: a system including an isoflurane vaporizer, a supply of oxygen with a regulator, and a flowmeter will be the minimum equipment required, as well as a filtration system to avoid the exposure of the operator to isoflurane (*see* **Note 4**).
3. Ocular lubricant cream (*see* **Note 5**).

2.3 Hair Removal

1. Hair removal cream for shaving the mice (*see* **Notes 6** and **7**).
2. Cotton swabs.

2.4 Fluorescent Agents

1. NIRF agents: several are available in the market which are suitable for cardiovascular research. Selection depends on the specific objectives of the experimental procedures (*see* **Note 8**).
2. Phosphate-buffered saline (PBS): this is the most common diluent of the fluorescent imaging agents.

3. Tools for mouse tail vein injection of fluorescent agents: mouse restraining device or equipment for anesthetizing the animal, sterile 27–30 G needles, sterile 0.5–1 ml syringe, cannulation tubing, and heating pad (*see* **Note 9**).

2.5 Fluorescence Molecular Tomography

1. FMT system: The commercial systems officially performing FMT are the FMT series offered by PerkinElmer, FMT1000, FMT2000, and FMT4000. Another system capable of performing tomography is the IVIS Spectrum (PerkinElmer).
2. Mouse holder (*see* **Note 10**).
3. Excitation source and emission filters (*see* **Note 11**).
4. Imaging camera (*see* **Note 12**).
5. 3D reconstruction software (*see* **Note 13**).
6. Spectral unmixing software (*see* **Note 14**).

2.6 Validation by Histology

1. Surgical instruments.
2. Tissue-Tek optimal cutting temperature (OCT) compound.
3. Cryotome.
4. Microscope glass slides and coverslips.
5. Mounting medium.
6. Epifluorescence microscope coupled to a digital camera.

3 Methods

3.1 Administration of Fluorescent Agents

1. Reconstitute (when required) and/or prepare a dilution of the specific fluorescent imaging agent in PBS (generally, commercial fluorescent agents are administered at a concentration of 2–4 nmol/25 g body weight).
2. Inject the probe intravenously 24–48 h prior imaging (*see* **Notes 15–17**).

3.2 Mouse Preparation for Imaging Procedure

1. Anesthetize mice with isoflurane.
2. Keep anesthetized mice in a heating pad.
3. Gently cover the area of interest with hair removal cream (*see* **Notes 6** and **7**) and remove it using cotton swabs damped with lukewarm water.
4. Repeat shaving procedure, if needed.
5. Place the mouse in the animal holder of the FMT system (*see* **Note 6**). Make sure that the anesthesia and temperature control systems are correctly located.
6. Add a drop of ocular lubricant cream to both eyes of the animal to prevent corneal desiccation during anesthesia (*see* **Note 5**).

3.3 Image Acquisition

1. Make sure that the system is properly calibrated (*see* **Note 18**).
2. Make sure that the CCD camera is cooled down (*see* **Note 12**).
3. Select the region of interest (ROI). This will be the area scanned by the laser (*see* **Note 19**).
4. If allowed by the FMT system used (*see* **Note 20**), select the number of "sources" (spots where the laser will be focused) that would be registered during the imaging procedure (*see* **Note 21**).
5. Select the excitation laser and the emission filter according to the fluorescent agent used.
6. Acquire the excitation and emission pair which is best suited to the fluorophore or fluorescent protein used. In some commercial systems, this is done sequentially and automatically, ensuring the best signal-to-noise ratio is obtained for each case by varying the excitation power and/or the exposure time of the camera. Whenever possible, acquisition of extra emission wavelengths improves sensitivity (*see* **Note 11**) and simplifies spectral unmixing whenever needed (*see* **Note 14**).
7. When using more than one fluorescent agent, repeat **steps 5** and **6** for each of them.
8. Once the image acquisition is finished, keep the animal warm in a recovery chamber until full recovery.
9. Return the animal to the cage.

3.4 Image Analysis

1. Visualize 2D data. Before analyzing the reconstructed data, there is very valuable information that can be obtained using directly the raw data. Since FMT data consists of a collection of source positions for each excitation/emission pair, by adding these measurements and normalizing by the sum of all excitation measurements, one obtains a semiquantitative image which is independent of the reconstruction algorithm ($\text{Image} = \sum_i [\text{Fluo}]_i \Big/ \left(\sum_i [\text{Exc}]_i + s \right)$, where $[\text{Fluo}]_i$ and $[\text{Exc}]_i$ represent the fluorescence and excitation image for source position i, respectively, and s is a smoothing factor that prevents division by very small excitation values). This resulting image does not provide true quantitative 2D but should correlate spatially with the depth projection of the results obtained in the reconstruction.
2. Quantify 3D fluorophore concentration. If the system has been properly calibrated for imaging the fluorescent probe used, the 3D images should be quantitative (*see* **Note 22**). This is done by using mathematical algorithms to solve the "inverse problem." Some of them are described in [1, 3, 4]. Commercial systems include their own proprietary software for 3D reconstruction of the data (*see* **Note 13**).

3. Unmix spectra. As mentioned previously (*see* **Notes 11** and **14**), whenever the system allows the acquisition of data from several excitation/emission pairs, spectral unmixing helps in reducing the contribution of autofluorescence (*see* **Note 23**) and allows imaging of more than one fluorophore simultaneously, even if there is overlap between the emission curves. It is important to understand that spectral unmixing will not help in elucidating which is the probe that has been activated or bound specifically to the unspecific activation or unbound probe, since both present the same emission spectrum.

3.5 Validation by Histology

It is recommended to validate the results of FMT by performing postmortem histological analysis.

1. Euthanize the animal following the procedures accepted by the ethics committee.
2. Surgically remove the area of interest (i.e., the aortas), embed it in Tissue-Tek (OCT compound), and freeze it at −80 °C.
3. Cut cryo-sections using a cryotome and mount them in glass slides, covered by a small drop of mounting medium and a coverslip.
4. Acquire fluorescent images of the frozen sections with an epifluorescence microscope connected to a digital camera.

4 Notes

1. Among the existent mouse models for atherosclerosis, low-density lipoprotein receptor-deficient mice (LDLR$^{-/-}$ mice) and apolipoprotein E-deficient mice (apoE$^{-/-}$ mice) are the most widely used. LDLR$^{-/-}$ mice show delayed clearance of VLDL and LDL from plasma, developing atherosclerosis on high-fat diet. On the other hand, homozygous deficiency in apoE contains the entire spectrum of lesions observed during atherogenesis and was the first mouse model described to develop lesions similar to those of human. Under normal dietary conditions, apoE$^{-/-}$ mice develop extensive atherosclerotic lesions, and the process can be accelerated on a high-fat diet (*see* **Note 2**). A chronological analysis of atherosclerotic lesions in apoE$^{-/-}$ mice revealed that the sequential events involved in lesion formation in this model are strikingly similar to those in larger animal models and in humans [16].
2. High-cholesterol and high-fat diets are used to accelerate the formation of atherosclerotic plaques in mouse models of atherosclerosis. The atherosclerosis-promoting diet most frequently used in mice contains 0.15 % cholesterol and 21 % fat derived from milk fat. After 10–14 weeks under this diet,

apoE-deficient mice develop complex fibrous plaques in the aortic sinus [16, 19].

3. Providing chlorophyll-free chow to the animals is recommended at least 10 days prior imaging, in order to reduce autofluorescence [20].
4. Human exposure to anesthetic gases has been associated with health risks. Therefore, safety considerations have to be taken into account when using inhaled anesthesia.
5. Applying an ocular lubricant cream in the eyes of the animals during anesthesia is recommended in order to prevent corneal desiccation. Avoid touching the eye with the tip of the ointment dispenser as it may scratch the cornea. Using a small piece of tissue paper to apply the cream is recommended.
6. Hair strongly interferes with light, and therefore hair removal from the skin is highly recommended for FMT experiments when using haired animals. In black haired mice, such as the C57BL/6 strain, the first steps of hair growth are accompanied by strongly dark pigmentation of the skin [21]. This pigmentation will completely ruin the FMT experiment due to light absorption. Therefore, whenever performing a longitudinal study with black haired mice, the time between hair removal and the initiation of skin pigmentation should be considered as the optimal imaging period. Whenever possible, it is recommended to use albino mice (such as albino C57BL/6 mice, which carry a mutation in the tyrosinase gene).
7. Hair removal creams are very irritant for the skin of the mice. They should not be applied for longer than 1 min. We recommend diluting it in lukewarm water (1:2) prior to using it and wash it away right after shaving, keeping always the animal warmed on a heating pad.
8. Apart from the mentioned fluorescent imaging agents, recently developed NIRF proteins [22, 23] are also optimal for FMT imaging.
9. Fluorescent imaging agents are usually administered intravenously. Exceptional cases may require administration via intraperitoneal.
10. Placing the animal in an adequate holder during the imaging procedure is the key to obtaining good quality images. The animal holder of each imaging system might be slightly different; ensure that good coupling between the light source and the exposed tissue takes place in order to avoid the contribution of stray light (i.e., light that has not traveled through the animal) to the detected signal.
11. Depending on the FMT system employed, several laser lines will be available. Choose the laser line and emission filter most

appropriate for the probe under study. Whenever imaging more than one probe, if the setup allows it, take as many combinations of excitation/emission pairs as possible, always making sure that the emission filter used covers a range of wavelengths longer (i.e., lower energies) than the excitation source, always bearing in mind the total duration of the experimental session. Before ordering a fluorescent probe, make sure the FMT setup you have access to has the optimum excitation/emission pair for this particular probe: not all FMT systems have the same laser lines and filters, and most commercially available ones do not provide imaging below 600 nm.

12. Each FMT system might have a different camera attached. The sensitivity of the camera is important, especially when imaging deep signals. Signal-to-noise is increased by cooling the camera; therefore, make sure you always cool the camera to the lowest temperature possible (typically from −80 °C to −100 °C when CCD cameras are used, from −30 °C to −40 °C when sCMOS are employed).
13. Each imaging system will have its own reconstruction software for solving the "inverse problem." If not all, practically all of them will rely on solving the diffusion equation through different approaches, mainly through numerical solvers such as the finite elements method (FEM), *see*, for example, ref. 17, or analytical expressions [1]. Additionally, there are two popular open-source alternatives which require some basic skills in programming but provide the necessary tools to reconstruct in 3D fluorophore distribution given a set of data as long as the geometry is provided. The most popular are TOAST (now TOAST++), developed by S. Arridge and M. Schweiger at UCL (http://web4.cs.ucl.ac.uk/research/vis/toast/) and NIRFAST, developed by H. Dehghani and B. Pogue at Dartmouth (http://www.dartmouth.edu/~nir/nirfast/).
14. In those imaging systems which allow the collection of several excitation/emission pairs (*see* **Note 11**), it is possible to perform spectral unmixing in the data. Note that for this to be effective, one should spectrally unmix the FMT reconstruction and not the raw data [18]. In case your FMT system does not provide spectral unmixing software, open-source alternatives such as ImageJ can be used as long as unmixing is performed on the 3D FMT reconstruction and not on the raw data.
15. Typical timing for commercial fluorescent imaging agents is 24–48 h. The optimal time point should be determined for each imaging agent and the specific application.
16. Total volume administered per injection should not exceed 1 % of the body weight of the animal.
17. When using more than one fluorescent agent, different aspects should be taken into consideration: (1) their emission spectra

should be well separated with the FMT system used—in case of overlap, spectral unmixing will be required, and (2) the timing of injection/imaging procedure of each agent should be well coordinated.

18. Most commercial systems will provide a calibration phantom to ensure the system is working properly. This will automatically provide quantitative data for those probes provided by the same vendor. Whenever using fluorescent proteins or probes from several vendors or research groups, a linear relationship between probe concentration and 3D concentration must be obtained prior to imaging if quantitative results are pursued.
19. Mathematical models of light propagation in high scattering media make use of detected diffused light. Therefore, the ROI should be big enough to cover the expected emitting area and adjacent areas (i.e., allow an extra ~5 mm around the expected area). If the system allows it, there is a possibility of selecting the size of the voxel to be reconstructed. Bear in mind that due to the diffusive nature of light in tissue, voxels smaller than 1 mm cannot be resolved [1] and thus would increase the computational time unnecessarily.
20. Some commercially available systems will automatically select the number of sources present within the ROI.
21. The number of sources directly correlates with the final resolution and inversely with the computing time during the 3D imaging reconstruction.
22. Note that typical artifacts in 3D FMT reconstructions might include signal close to the location of the sources and that spurious artifacts might arise from light reaching the detector through reflections (due, e.g., to bad coupling of the exposed surface to the sources when placing the animal in the FMT holder).
23. Multispectral measurements also serve as a correction for the autofluorescence generated endogenously [1, 24].

References

1. Ripoll J (2012) Principles of diffuse light propagation. World Scientific, Singapore
2. Valeur B, Berberan-Santos M (2012) Molecular fluorescence: principles and applications. Wiley Online Library, Weinheim
3. Arridge SR, Schotland JC (2009) Optical tomography: forward and inverse problems. Inv Probl 25:123010
4. Ntziachristos V, Leroy-Willig A, Tavitian B (eds) (2007) Textbook of in vivo imaging in vertebrates. Wiley Online Library, Chichester
5. Jacques SL (2013) Optical properties of biological tissues: a review. Phys Med Biol 58:5007–5008
6. Ntziachristos V, Ripoll J, Wang LV et al (2005) Looking and listening to light: the evolution of whole-body photonic imaging. Nat Biotechnol 23:313–320
7. Hara T, Bhayana B, Thompson B et al (2012) Molecular imaging of fibrin deposition in deep vein thrombosis using a new fibrin-targeted near-infrared fluorescence (NIRF)

imaging strategy. JACC Cardiovasc Imaging 5:607–615

8. Ale A, Siebenhaar F, Kosanke K et al (2013) Cardioprotective C-kit$^+$ bone marrow cells attenuate apoptosis after acute myocardial infarction in mice - in-vivo assessment with fluorescence molecular imaging. Theranostics 3:903–913
9. Kaijzel EL, van Heijningen PM, Wielopolski PA et al (2010) Multimodality imaging reveals a gradual increase in matrix metalloproteinase activity at aneurysmal lesions in live fibulin-4 mice. Circ Cardiovasc Imaging 3:567–577
10. Tarin C, Lavin B, Gomez M et al (2011) The extracellular matrix metalloproteinase inducer EMMPRIN is a target of nitric oxide in myocardial ischemia/reperfusion. Free Radic Biol Med 51:387–395
11. Deguchi J, Aikawa M, Tung C-H et al (2006) Inflammation in atherosclerosis: visualizing matrix metalloproteinase action in macrophages in vivo. Circulation 114:55–62
12. Rodriguez-Menocal L, Wei Y, Pham SM et al (2010) A novel mouse model of in-stent restenosis. Atherosclerosis 209:359–366
13. Li B, Maafi F, Berti R et al (2014) Hybrid FMT-MRI applied to in vivo atherosclerosis imaging. Biomed Opt Express 5:1664
14. Nahrendorf M, Waterman P, Thurber G et al (2009) Hybrid in vivo FMT-CT imaging of protease activity in atherosclerosis with customized nanosensors. Arterioscler Thromb Vasc Biol 29:1444–1451
15. Chen J (2002) In vivo imaging of proteolytic activity in atherosclerosis. Circulation 105: 2766–2771
16. Zaragoza C, Gomez-Guerrero C, Martin-Ventura JL et al (2011) Animal models of cardiovascular diseases. J Biomed Biotechnol 2011:497841
17. Schweiger M, Arridge S (2014) The Toast++ software suite for forward and inverse modeling in optical tomography. J Biomed Opt 19(4):040801
18. Simantiraki M, Favicchio R, Psycharakis S et al (2009) Multispectral unmixing of fluorescence molecular tomography data. J Innov Opt Health Sci 2:353–364
19. Fuster JJ, Castillo AI, Zaragoza C et al (2011) Animal models of atherosclerosis. In: Conn PM (ed) Progress in molecular biology and translational science - animal models of molecular pathology. Elsevier, Amsterdam, pp 1–23
20. Bhaumik S, DePuy J, Klimash J (2007) Strategies to minimize background autofluorescence in live mice during noninvasive fluorescence optical imaging. Lab Anim 36:40–43
21. Slominski A, Paus R (1993) Melanogenesis is coupled to murine anagen: toward new concepts for the role of melanocytes and the regulation of melanogenesis in hair growth. J Invest Dermatol 101:90S–97S
22. Filonov GS, Piatkevich KD, Ting L-M et al (2011) Bright and stable near-infrared fluorescent protein for in vivo imaging. Nat Biotechnol 29:757–761
23. Shcherbakova D, Verkhusha V (2013) Near-infrared fluorescent proteins for multicolor in vivo imaging. Nat Methods 10:751–754
24. Tichauer KM, Holt RW, El-Ghussein F et al (2013) Dual-tracer background subtraction approach for fluorescent molecular tomography. J Biomed Opt 18:16003

Chapter 28

In Vivo ^{18}F-FDG-PET Imaging in Mouse Atherosclerosis

Jesús Mateo, Izaskun Bilbao, Juan José Vaquero, Jesús Ruiz-Cabello, and Samuel España

Abstract

Positron emission tomography (PET) is an important technique in cardiovascular research. Vascular inflammation detected by fluorodeoxyglucose (FDG)-PET has been shown to predict cardiovascular (CV) events independent of traditional risk factors and is also highly associated with overall burden of atherosclerosis. The use of PET imaging in mouse models of atherosclerosis is challenged by the reduced size of the scanned organs. However, the last generation of dedicated PET scanners has an improved spatial resolution (<1 mm) and increased sensitivity allowing those studies to be performed. Here, we describe a procedure to perform FDG-PET experiments in atherosclerosis mouse models, the required equipment for animal handling and imaging, and the tools and procedures for image analysis and validation of the results.

Key words Positron emission tomography (PET), Fluorodeoxyglucose (FDG), Computed tomography (CT), Vascular imaging, Atherosclerosis, Small animal imaging

1 Introduction

Increased FDG-PET uptake has been demonstrated in a variety of inflammatory processes, which has been typically attributed to FDG uptake by macrophages [1]. FDG-PET enables highly precise measurements of inflammatory activity of atherosclerotic plaques in large- and medium-sized arteries [2]. Vascular inflammation detected by FDG-PET has been shown to predict CV events independently of traditional risk factors and is also highly associated with overall burden of atherosclerosis [3]. Plaque activity by FDG-PET is modulated by known beneficial CV interventions such as statin therapy [4] as well as by long-term therapeutic lifestyle changes [5].

Cardiac preclinical in vivo research using FDG-PET has mainly been done on rabbits [6–8]. As transgenic mouse models have shown their value in atherosclerosis, FDG-PET for in vivo imaging of atherosclerosis [9–12] has been used for in vivo imaging of mice suggesting that this method can be used to follow the development

Vicente Andrés and Beatriz Dorado (eds.), *Methods in Mouse Atherosclerosis*, Methods in Molecular Biology, vol. 1339, DOI 10.1007/978-1-4939-2929-0_28,

of atherosclerosis in murine models. The aorta is typically used as the human coronary artery analog in rodents since the diameter of mouse aorta is ~1 mm, comparable to the size of small arteries in humans [13].

This chapter describes the methodology to obtain reliable values of FDG uptake in mouse atherosclerosis using PET imaging. However, the methodology can vary depending on the specific focus under study and the employed equipment.

2 Materials

1. Atherosclerosis-prone mouse models and wild-type controls (*see* **Notes 1** and **2**).
2. A small animal PET/CT scanner (a combined PET and CT system (Fig. 1) is required in order to fuse functional and anatomical images for the analysis on the PET image of the desired anatomical region).
   (a) CT subsystem (*see* **Note 3**).
   (b) PET subsystem (*see* **Note 4**).
3. Animal bed (the bed support should integrate a mask for the anesthesia and a heating system to keep a constant temperature of the animal during the study, ~38 °C).
4. Anesthetic delivery system (*see* **Notes 5** and **6**).
5. Reconstruction software. The system should include reconstruction software to recover the CT image from the projections and the PET tracer distribution from the measured data.

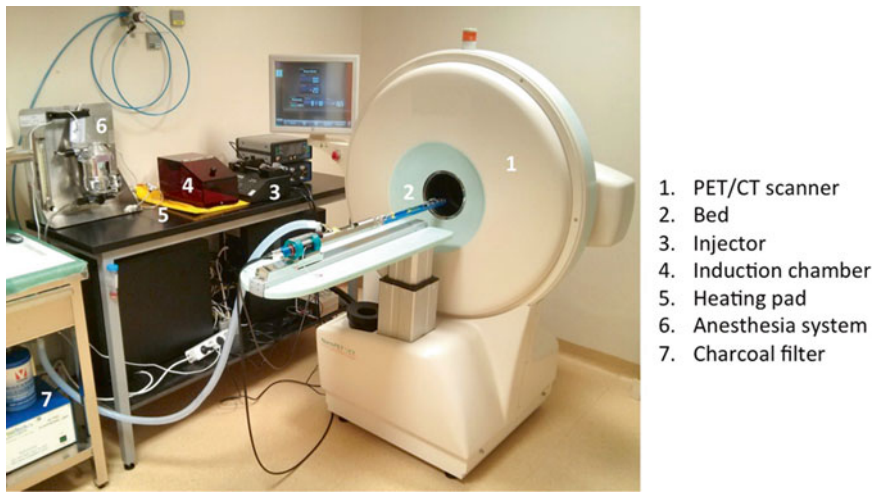

Fig. 1 PET/CT scanner and different equipment needed for anesthesia, injection of CT contrast agent, and temperature control

For PET, different reconstruction methods can be typically chosen: 2D, 3D, analytical (FBP), and iterative (MLEM, OSEM).

6. Contrast agent (*see* **Note 7**).
7. PET tracer (*see* **Note 8**).
8. Activimeter for PET tracer dose calibration.
9. Blood glucose meter.
10. Imaging analysis software (*see* **Note 9**).
11. Materials for radiotracer uptake validation (*see* **Note 10**):
    (a) Surgical instruments to extract the anatomical organ or structure of interest.
    (b) Material for autoradiography: phosphor imaging system equipped with software for data acquisition and image analysis and a phosphor imaging screen or autoradiography films and tools for developing and analysis.
    (c) Automatic gamma counter for tissue gamma counting.
12. Materials for histology/immunohistology validation: phosphate-buffered saline (PBS, pH 7.4), 10 % buffered formalin, dissection tools, Tissue-Tek O.C.T. compound (Sakura), paraffin, hematoxylin, eosin, antibodies (e.g., F4/80 for mouse macrophages), reagents for developing and visualization of immunostaining, microtome (to section tissue specimens embedded in paraffin), cryostat (to section tissue specimens embedded in O.C.T.), and microscope equipped with camera and imaging dedicated software.

3 Methods

A schematic of the animal preparation, imaging procedure, and validation protocol is summarized in Fig. 2.

3.1 Animal Preparation

1. Have mice fasting overnight prior to the FDG-PET/CT scan.
2. Keep the mice warm from 30 min before the injection until the end of the uptake period in order to reduce uptake by fat. Different strategies such as heating pads, IR lamps, or hot air are available.
3. Weigh the animal.
4. Check the fasting serum glucose levels prior to FDG administration using a blood glucose meter to ensure that glucose within the body does not compete with FDG. Values between 80 and 120 mg/dl are typically obtained.

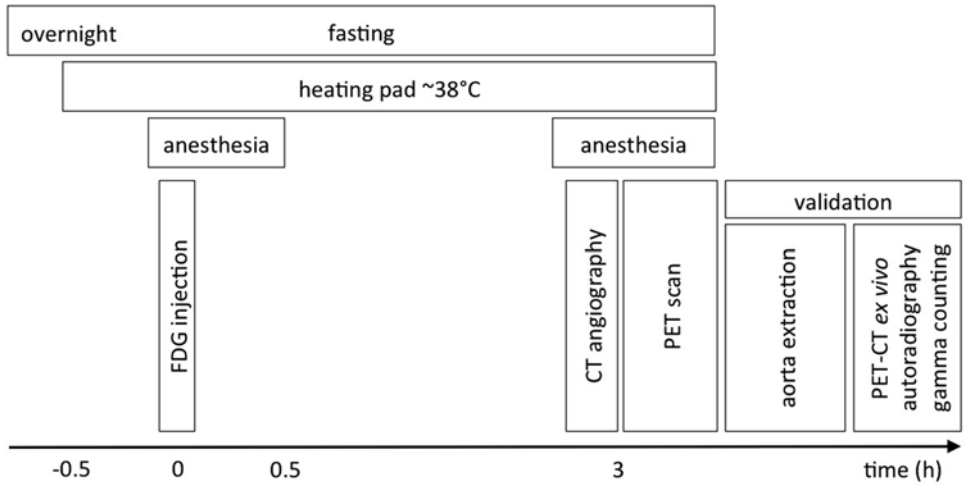

Fig. 2 Protocol for FDG-PET/CT imaging in atherosclerotic mice

5. Anesthetize the animal prior to injection and keep the anesthesia for at least 30 min after injection to reduce the muscular uptake (e.g., isoflurane, sevoflurane).
6. Prepare the FDG dose in an insulin syringe and measure the activity in the activimeter. Subtract the background activity from the obtained value. Write down the background-corrected activity in the syringe and the time at which the measurement is done (*see* **Note 11**).
7. Inject the FDG dose (10–20 MBq) in the tail vein (*see* **Notes 8** and **12**) and allow for an uptake time of 3 h (*see* **Note 13**). Measure in the activimeter the activity left in the syringe and subtract it from the previous obtained values after correcting this last measurement by decay.
8. Put the animal back in the cage in a shielded area to protect the personnel from radiation.
9. Anesthetize the animal again for 20 min before the end of the uptake time and place it in the scanning bed enabling the anesthesia and heating mechanism.
10. Place a drop of ocular lubricant (e.g., Puralube or Lacryvisc gel) on each eye of the mouse during the anesthesia to prevent corneal ulceration.

3.2 PET/CT Acquisition

1. Use the CT detector to obtain a localizer, which consists in a projection image of the entire animal that is used to delimit the region to be scanned with both CT and PET scans.
2. Perform a CT scan using contrast agent before the PET scan in order to avoid any further movement of the animal once the contrast agent is administered. The field of view of the CT scan

should at least cover the one that is imaged with the PET scan to allow for scatter and attenuation correction and to use as an anatomical reference. The CT scan configuration parameters will depend on vendor to vendor, but some reference could be 55 kVp, exposure time 500 ms, projections 180, and isotropic voxel size 0.1 mm. Try to keep a low level of dose (<100 mGy CTDI) by using a larger voxel size instead of an increased dose to avoid producing side effect on the animal.

(a) In case of using continuous infusion of CT contrast agent, place a catheter in the tail vein and administer the contrast using an injector (*see* Fig. 1). In case of using long-circulating contrast, this is directly administered through the tail vein (*see* **Note 14**).

3. Perform the PET scan. The axial extend of the field of view for the PET scan should at least cover from the iliac bifurcation to the neck of the mouse to cover the entire aorta. This requires one or two bed positions depending on the axial extent of the PET scanner. An acquisition time of 10–30 min can be used depending on the scanner sensitivity and the injected dose.
4. Once finished with the image acquisition, return the animal to the cage, resume the food supply, and leave it in a shielded area until most of the activity has decayed (typically 10 half-lives, ~18 h after injection).

3.3 Image Analysis

1. Open PET and CT images on the analysis software.
2. Adjust the contrast level on both images.
3. Make sure that the units in which the PET image is shown are standardized uptake values (SUV), which is the ratio of tissue radioactivity concentration at time point and the injected activity extrapolated to the same time divided by the body weight (*see* **Note 15**).
4. Check the registration between PET and CT images and adjust it in case it is needed using fiducial markers (*see* **Note 16**), in case they were added, or by anatomical references.
5. Localize the aorta or artery of interest navigating through the axial, coronal, and sagittal views.
6. Draw the regions of interest (ROIs) preferably using the axial views of fused PET/CT images (*see* Fig. 3). In that way, the CT provides the anatomical information to localize the artery, and the PET is used to avoid possible influence of neighbor region into the aorta due to partial volume effect (spill-in and spillover), which should be removed from the analysis. A good approach for the aorta is to analyze it from the heart to the kidneys. The aorta in the CT can be identified as it has higher HU values (more white) due to the contrast agent. The ROIs around the vessel should be drawn slightly bigger than is shown

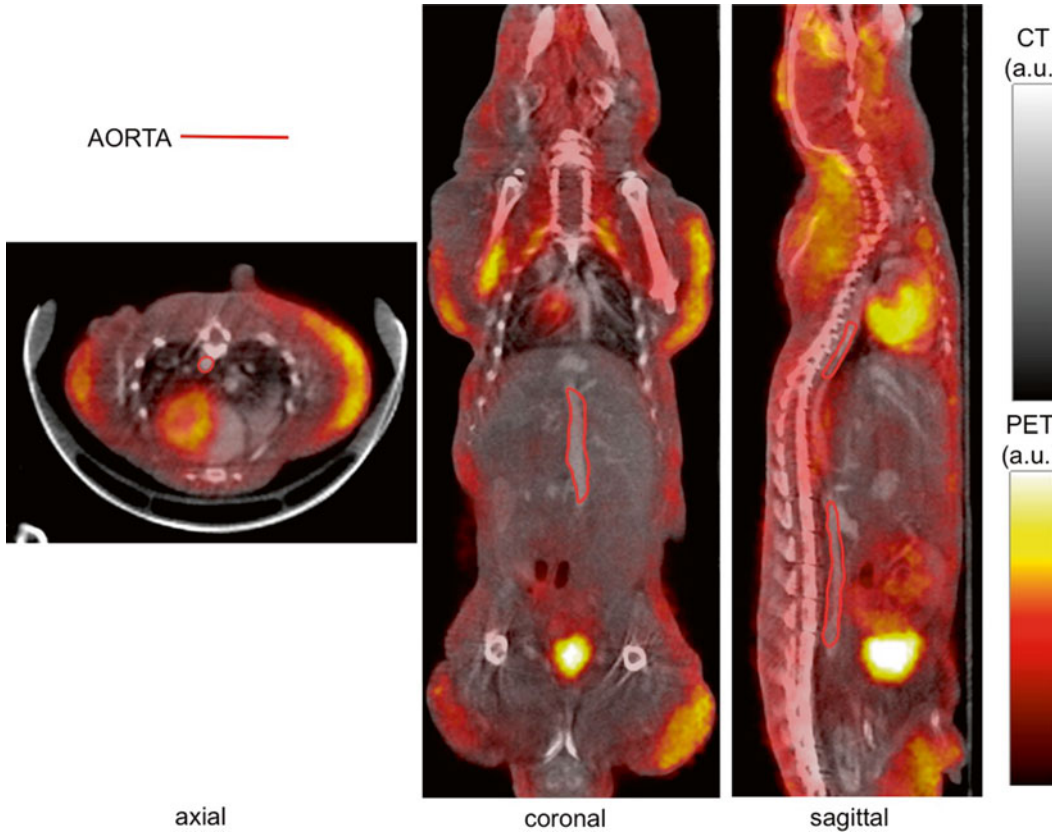

Fig. 3 Axial, coronal, and sagittal views of fused FDG-PET and CT images of an atherosclerotic mouse. Aorta is delineated in *red*

on the CT to account for the spillover of activity due to partial volume effect.

7. Obtain several reporting values for each of the segmented artery or regions. From each slice, the SUV_{mean} (mean uptake in the ROI) and SUV_{max} (maximum uptake in the ROI) values can be obtained. Later, the mean of both parameters for all the slices ($meanSUV_{mean}$, $meanSUV_{max}$) can be computed as a single parameter to characterize the FDG uptake in the artery (*see* **Note 17**).

3.4 Validation

1. Euthanize the animal following the procedures accepted by the ethics committee (*see* **Note 18**).
2. Surgically remove the area of interest (i.e., the aorta) (*see* **Note 19**).
3. Ex vivo PET/CT: place the extracted tissue in the animal bed of the PET/CT scanner and perform a localizer followed by a PET/CT scan. Acquire the PET scan for a longer time than previously for the in vivo study in order to compensate for the extra activity decay during the surgery.

4. Autoradiography: use an exposure time of 1–10 h depending on the employed methodology. Ex vivo PET/CT is not required if autoradiography is performed.
5. Gamma counting: introduce the tissue sample in the gamma counter for 1–5 min.
6. Histological (e.g., hematoxylin and eosin) and/or immunohistological (e.g., anti-F4/80, anti-Mac-3, etc.) validation of the results obtained with noninvasive PET/CT imaging is strongly recommended. Standard and routine histological techniques can be found elsewhere [8, 9, 11].

4 Notes

1. Mouse models for atherosclerosis are based on genetic modifications of lipoprotein metabolism in combination with the use of high-fat diets. The most widely used atherosclerosis models are low-density lipoprotein receptor-deficient mice (LDLR$^{-/-}$) and apolipoprotein E-deficient mice (apoE$^{-/-}$).
2. High-cholesterol and high-fat diet is required to accelerate the formation of atherosclerotic plaques in apoE$^{-/-}$ mice. We use 0.75 % cholesterol and 11 % fat diet (S9167-E010, "Ssniff," Germany), but other compositions with varying percentage of cholesterol/fat are commonly employed.
3. The CT consists of a microfocus x-ray tube source and a semiconductor-based flat panel detector that rotate around the animal in order to record different angular projections of how much the x-ray beam is attenuated through each particular angle position. Different configuration parameters can be adapted to the requirements of each specific acquisition, e.g., the energy and intensity of the x-ray beam, the exposure time, or the number of projections.
4. The most common PET scanners are based on a ring of detectors surrounding the animal, each one based on scintillation crystals coupled to a position-sensitive photosensor. The acquisition time should be adjusted according to the injected dose and PET system sensitivity.
5. Animal anesthesia: inhalant anesthetics (e.g., isoflurane, sevoflurane) using a precision vaporizer, supply of 100 % oxygen with a regulator and a flowmeter (1 l/min), and a filtration system to avoid the exposure of the operator to isoflurane. Expired carbon dioxide can be collected using a charcoal filter (Fig. 1).
6. Animal monitoring is recommended during the scanning time, including temperature, ECG, and respiratory sensors.
7. Blood vessels provide very little inherent contrast for micro-CT imaging, and therefore their localization requires the use of

vascular contrast agents [14]. In vivo CT studies take long scan times (5–40 min) and require either a long-circulating contrast agent or continuous infusion of contrast agent. However, long-circulating agents ease the animal handling and improve the success rate of the study. Some of these long-circulating agents used for preclinical vasculature imaging are Fenestra (Fenestra VCH, ART Advanced Research Technologies Inc., Canada) and ExiTron (Viscover™ ExiTron™ nano; Miltenyi Biotec, Bergisch-Gladbach, Germany). An example of clinical contrast agent for continuous infusion is Ultravist 300® contrast agent (Bayer Schering Pharma, Germany).

8. Fluorodeoxyglucose (^{18}F-FDG) is by far the most commonly employed tracer on PET imaging and also in atherosclerosis. The relatively long half-life of ^{18}F (109.8 min) allows delivering it to sites that are far from the cyclotron where it is produced (<100 km). A dose of 10–20 MBq of FDG is typically administered to the mouse in a volume of 100–150 μl. A calibrated activimeter and a reproducible protocol should be used to prepare the individual doses.
9. The imaging systems usually provide software for image analysis. However, other public domain software can be used as Amide (http://amide.sourceforge.net/) or OsiriX (http://www.osirix-viewer.com/). The software should be able to load and fuse the PET and CT images obtained from the scanner, show them in the proper units, draw ROIs, and provide the quantitative values of the selected ROIs (typically maximum and mean values).
10. Ex vivo counting can be considered devoid of any partial volume and spillover effects, and it is considered as a reference for tracer uptake quantification. Different validation techniques can be used to compare between the measurements done in vivo and ex vivo: Ex vivo PET/CT scan, autoradiography, or gamma counting.
11. Make sure that the time in the clock that you use during the measurement of the activity in the syringe is the same than in the acquisition console.
12. To facilitate i.v. injection into the mouse tail vein, an infrared lamp can be used to allow vasodilatation.
13. To perform vascular PET studies, a longer FDG circulation time than that for oncology PET imaging is advised. This is to allow sufficient FDG accumulation in the arterial wall and to permit blood levels of FDG to become reduced. Early dynamic PET studies determined that the optimum time from FDG injection to imaging was approximately 3 h [15, 16].
14. The circulation time of the contrast agent allowed before the CT scan can be optimized depending on the employed

contrast. In some cases can be administered at the time of the FDG injection [12] or right before the CT scan.

15. SUV units will be only available and valid if the weight of the animal and the activity and time of measurement of the FDG dose have been introduced correctly in the acquisition console during the acquisition procedure. Make sure that you used the proper units (typically grams for weight and MBq for activity) as required by the acquisition console. In addition, the system should have followed all the quality control procedures in order to obtain reliable values.
16. One or two round glass capillaries filled with FDG can be used as fiducial markers. Prepare a diluted amount of FDG and introduce the capillary tube in the dilution from one of its ends and the fluid will get inside the tube by capillarity. Tilt the tube to control the length of the tube that is filled. Seal the tube on the same side that was used to fill it. To have a similar activity concentration than in the animal, divide the amount of injected dose by the weight of the animal and prepare a dilution with a similar concentration assuming a density of 1 g/cm^3. Place the capillary tubes in the scanner bed at the same position where the animal is placed. Make sure that the entire source is scanned with both PET and CT images.
17. In some studies, the FDG uptake is reported as the ratio between the arterial uptake and the uptake in some reference tissue (blood pool, muscle). For example, a small ROI can be drawn in the inner part of the cava vein in order to compute the SUV in the blood pool, and the target-to-background ratio (TBR) can be obtained as the ratio between the arterial SUV and the venous blood pool SUV.
18. A CO_2 chamber and an overdose of anesthetics are common methods for euthanizing mice. CO_2-induced euthanasia is preferred over other mechanical methods (decapitation, cervical dislocation) to avoid displacement of the heart, aorta, etc.
19. It is recommended to leave some reference organs as the heart and/or the kidneys when the aorta is removed for anatomical guidance once the aorta is removed from the animal.

Acknowledgments

JJ Vaquero is partially funded by the Cardiovascular Research Network (RIC, RD12/0042/0057) from the Ministerio de Economía y Competitividad (www.mineco.gob.es/). The funder had no role in study design, data collection and analysis, decision to publish, or preparation of the manuscript.

References

1. Buettner C, Rudd JHF, Fayad ZA (2011) Determinants of FDG uptake in atherosclerosis. J Am Coll Cardiol Img 4:1302–1304
2. Mehta N, Torigian D, Gelfand JM et al (2012) Quantification of atherosclerotic plaque activity and vascular inflammation using [18-F] fluorodeoxyglucose positron emission tomography/computed tomography (FDG-PET/CT). J Vis Exp 63:e3777
3. Rominger A, Saam T, Wolpers S et al (2009) 18F-FDG PET/CT identifies patients at risk for future vascular events in an otherwise asymptomatic cohort with neoplastic disease. J Nucl Med 50:1611–1620
4. Tahara N, Kai H, Ishibashi M et al (2006) Simvastatin attenuates plaque inflammation: evaluation by fluorodeoxyglucose positron emission tomography. J Am Coll Cardiol 48:1825–1831
5. Lee SJ, On YK, Lee EJ et al (2008) Reversal of vascular 18F-FDG uptake with plasma high-density lipoprotein elevation by atherogenic risk reduction. J Nucl Med 49:1277–1282
6. Ogawa M, Ishino S, Mukai T et al (2004) (18) F-FDG accumulation in atherosclerotic plaques: immunohistochemical and PET imaging study. J Nucl Med 45:1245–1250
7. Hyafil F, Cornily JC, Rudd JHF et al (2009) Quantification of inflammation within rabbit atherosclerotic plaques using the macrophage-specific CT contrast agent N1177: a comparison with 18F-FDG PET/CT and histology. J Nucl Med 50:959–965
8. Mateo J, Izquierdo-Garcia D, Badimon JJ et al (2014) Noninvasive assessment of hypoxia in rabbit advanced atherosclerosis using 18F-fluoromisonidazole positron emission tomographic imaging. Circ Cardiovasc Imaging 7(2):312–320
9. Zaragoza C, Gomez-Guerrero C, Martin-Ventura JL et al (2011) Animal models of cardiovascular diseases. J Biomed Biotechnol 2011:497841
10. Silvola JMU, Saraste A, Laitinen I et al (2011) Effects of age, diet, and type 2 diabetes on the development and FDG uptake of atherosclerotic plaques. JACC Cardiovasc Imaging 4(12):1294–1301
11. Wenning C, Kloth C, Kuhlmann MT et al (2014) Serial F-18-FDG PET/CT distinguishes inflamed from stable plaque phenotypes in shear-stress induced murine atherosclerosis. Atherosclerosis 234(2):276–282
12. Hag AMF, Pedersen SF, Christoffersen C et al (2012) (18)F-FDG PET imaging of murine atherosclerosis: association with gene expression of key molecular markers. PLoS One 7(11):e50908
13. Orbay H, Hong H, Zhang Y et al (2013) Positron emission tomography imaging of atherosclerosis. Theranostics 3(11):894–902
14. Zagorchev L, Oses P, Zhuang ZW et al (2010) Micro computed tomography for vascular exploration. J Angiogenes Res 2:7
15. Rudd JHF, Warburton EA, Fryer TD et al (2002) Imaging atherosclerotic plaque inflammation with [18F]-fluorodeoxyglucose positron emission tomography. Circulation 105(23):2708–2711
16. Rudd JHF, Myers KS, Bansilal S et al (2008) Atherosclerosis inflammation imaging with 18F-FDG PET: carotid, iliac, and femoral uptake reproducibility, quantification methods, and recommendations. J Nucl Med 49(6):871–878

Chapter 29

Magnetic Resonance Imaging of the Atherosclerotic Mouse Aorta

Jesús Mateo, Marina Benito, Samuel España, Javier Sanz, Jesús Jiménez-Borreguero, Valentín Fuster, and Jesús Ruiz-Cabello

Abstract

Plaque development has been extensively studied using magnetic resonance imaging (MRI) in animal models of rapidly progressing atherosclerosis, such as apolipoprotein E-knockout (apoE-KO) mice. Preclinical MRI plays a significant role in the study of experimental atherosclerosis. Currently, MRI is capable of detecting luminal narrowing, plaque size, and morphology with high accuracy and reproducibility, providing reliable measurements of plaque burden. Therefore, MRI offers a noninvasive approach to serially monitor the progression of the disease. Compared with other imaging modalities, MRI appears to have the greatest potential for plaque characterization, through the use of multiple contrast weightings (e.g., *T*1, *T*2, and proton density). Here, we illustrate a standard procedure to image the aorta of atherosclerotic mice using noninvasive MRI.

Key words Magnetic resonance imaging (MRI), Atherosclerosis, Plaque, Aorta, apoE-KO mice

1 Introduction

Atherosclerosis is a chronic inflammatory disease characterized by the progressive accumulation of lipid deposits and different cell types (mainly vascular smooth muscle cells that migrate from the tunica media and immune cells recruited from the blood stream) in the subendothelial space to form the so-called plaques. Atherosclerosis is the primary cause of cardiovascular disease, leading to myocardial infarction and stroke [1]. The early detection and characterization of atherosclerotic lesions in humans is critical and is currently under investigation to try to identify potential markers associated with the progression of atherosclerosis [2] as well as the occurrence of clinical cardiovascular events [3]. Conventional X-ray and computed tomographic angiography are well-established techniques in clinical practice for detection of

Vicente Andrés and Beatriz Dorado (eds.), *Methods in Mouse Atherosclerosis*, Methods in Molecular Biology, vol. 1339, DOI 10.1007/978-1-4939-2929-0_29,

stenotic lesions. However, even though the degree of coronary artery stenosis may correlate with ischemic symptoms such as angina, it does not necessarily predict sudden plaque rupture or acute myocardial infarction [4, 5].

High-resolution magnetic resonance imaging (MRI) has emerged as the leading noninvasive in vivo imaging modality for atherosclerotic plaque characterization. The MRI is based on the detection of a signal, typically emitted from water protons, following administration of a radio-frequency (RF) pulse, while the subject is placed in a strong magnetic field. The emitted signal mainly varies according to the water concentration and the relaxation times (*T*1 and *T*2). Using combined analysis of different tissue signal intensities generated by the application of *T*1-weighted (*T*1W), *T*2-weighted (*T*2W), and proton density-weighted (PDW) sequences, it has been possible to determine both plaque anatomy and composition [6]. Thus, MRI differentiates plaque components on the basis of biophysical and biochemical properties such as chemical composition, water content, physical state, molecular motion, or diffusion. MRI does not involve ionizing radiation and can be repeated sequentially over time. Currently, MRI is being used to study atherosclerotic lesions in vivo in humans [7, 8] and in large animal models (e.g., rabbits) [9, 10] by use of conventional MR scanners (1.5–3 T) with a spatial resolution ranging from 300 to 500 μm. To study small structures, such as the abdominal aorta of mice (<1 mm in luminal diameter), it is necessary to increase the signal-to-noise ratio by use of high-magnetic-field scanners equipped with small RF coils and strong magnetic field gradients [11–15]. Yet, the small size of mouse arteries and the presence of cardiac, respiratory, and blood flow induced artifacts make in vivo vascular imaging challenging. In this chapter, we describe a method for noninvasive imaging of mouse atherosclerotic aorta using MRI.

2 Materials

1. Atherosclerosis-prone mouse models and wild-type controls (*see* **Notes 1–3**).
2. MRI equipment:
   (a) Horizontal bore experimental MR scanner (e.g., 7 T 300 MHz Agilent/Varian, Santa Clara, CA) (*see* **Note 4**) equipped with a DD2 (DirectDrive 2) NMR/MRI console, an active shielded 205/120 gradient insert coil with 130 mT/m maximum gradient strength, and a four-channel receiver.
   (b) Transmit/receive RF coils to improve data quality (*see* **Note 5**).

3. Animal holder (*see* **Note 6**).
4. System for monitoring respiration, electrocardiogram (ECG)/heart rate, and body temperature equipped with an MRI-compatible thermocouple (e.g., Model 1025 Monitoring and Gating System for MRI, SA Instruments Inc., New York, NY) (*see* **Note 7**).
5. Anesthetic delivery system (e.g., isoflurane vaporizer with oxygen line).
6. DICOM viewer software (*see* Subheading 3.3).
7. Material for histological validation: phosphate-buffered saline (PBS, pH 7.4), 10 % buffered formalin, dissection tools, Tissue-Tek O.C.T. compound (Sakura), paraffin, hematoxylin, eosin, microtome (for tissue embedded in paraffin), cryostat (for tissue embedded in O.C.T.), and microscope equipped with camera and imaging dedicated software.

3 Methods

3.1 Animal Preparation and Handling

1. Anesthetize mice initially with 2 % isoflurane in oxygen (2–3 min) and maintain anesthesia with 1–1.5 % isoflurane during the MRI experiments (*see* **Note 8**).
2. Place the mouse in the animal holder in prone position using a dental bar to fix the teeth inside the mask (*see* **Note 9**).
3. Enable the warming system.
4. Connect a pair of ECG leads to subdermal needle electrodes positioned in the forepaws.
5. Lubricate the temperature probe and insert it into the rectum of the animal.
6. Place the respiration sensor under the body of the animal near the lungs.
7. Apply a drop of ophthalmic gel in the eyes to prevent corneal drying during scanning time.
8. Make sure that the region-of-interest (ROI) to be scanned is in the center of the coil of the MR scanner.
9. Check that the monitoring system is recording all the signals (ECG/heart rate, respiration, and temperature).

3.2 MRI Acquisition

1. Tune and match the transmit RF coil according to the manufacturer's instructions.
2. Position the scan on x, y, and z to confirm that the region to be scanned is in the center of the coil (*see* **Note 10**).

3. Perform a localizer scan (scout). The default scout protocol in the 7 T Agilent/Varian MR scanner is based on a gradient-echo sequence with a field of view (FOV) = 50 mm, slice thickness = 1 mm, matrix size = 128 × 128, echo time (TE) = 2.6 ms, repetition time (TR) = 32 ms, and number of averages = 2. The scout protocol acquires three slices in each of the three cardinal planes in order: axial, coronal, and sagittal. The scan takes less than 40 s. This acquisition is useful for slice planning of subsequent scans and for serial studies to identify relevant anatomical markers.
4. Calibrate the RF pulses for given pulse shapes and durations.
5. Perform shimming: run auto shim or manual shim to compensate field inhomogeneities.
6. Depending on the scope of the study, perform *T*1- and/or *T*2- and/or proton density (PD)-weighted imaging. MRI parameters should be selected to optimize visualization and characterization of the arterial wall.
7. Typically, a high-resolution *T*1-weighted imaging in coronal and axial orientations can be acquired using a *T*1 fast spin-echo sequence with the following parameters: two-dimensional (2D) acquisition mode (*see* **Note 11**), FOV = 60 mm × 30 mm (for coronal) and 30 mm × 30 mm (for axial), slice thickness = 0.8 mm, TR = 400 ms, TE = 8 ms, acquisition matrix size = 256 × 256, reconstruction matrix size = 256 × 256, 10–20 slices (interleave mode), with 6 signal averages, and ≈5 min average acquisition time (*see* Fig. 1). The resulting spatial resolution is 117 × 117 μm² for axial and 234 × 117 μm² for coronal imaging (*see* **Note 12**).
8. A saturation pulse can be planned to eliminate signals from fat tissue to better delineate the outer boundary of the aortic wall and minimize chemical shift artifacts [11].

3.3 Image Analysis

We recommend to convert images to a standard format such as DICOM. Open source DICOM viewer software packages are available for Apple Macintosh computers (e.g., OsiriX, http://www.osirix-viewer.com), for Windows-based computers (e.g., Sante DICOM viewer, http://www.santesoft.com/dicom_viewer.html; Onis Free Edition, http://www.onis-viewer.com), as well as multiplatform software (e.g., 3D Slicer, http://www.slicer.org; Mango viewers, http://ric.uthscsa.edu/mango). Some of these software packages also provide initial and advanced imaging analysis. Some of the following measurements are commonly obtained after image magnification during the off-line analysis: vessel area, wall thickness, lumen area, and area of the plaque.

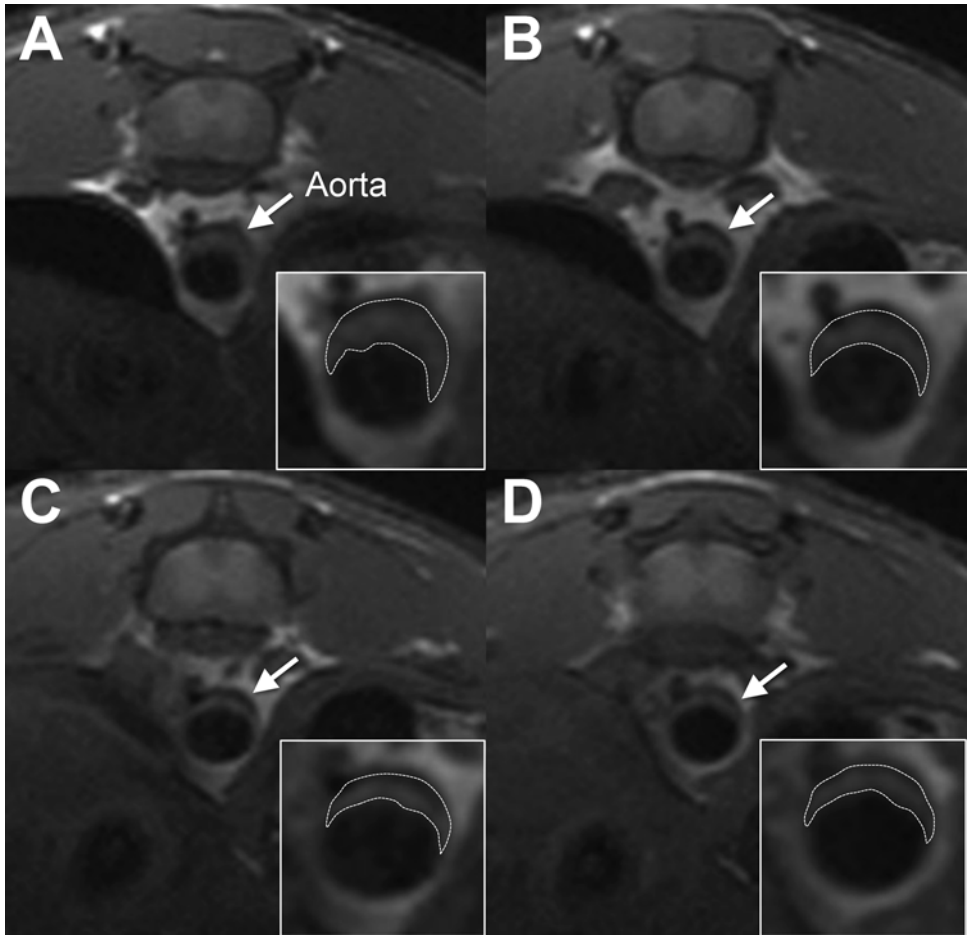

Fig. 1 Representative *T*1-weighted MR serial images showing the abdominal aorta (*white arrow*) above the right renal artery of an apoE-KO mouse demonstrating large atherosclerotic lesions protruding the arterial lumen. Magnification of the aorta outlining the plaque area is displayed at the *bottom right of each image*

3.4 Validation of Results with Histology

Postmortem histological validation of the results obtained with noninvasive MRI is strongly recommended.

1. After the last imaging session, euthanize the animal following the procedures approved by the ethics committee (*see* **Note 13**).
2. Open the chest and cannulate the aorta via the left ventricle.
3. Perfuse the aorta with PBS through an incision in the iliac arteries until complete exsanguination. Continue the perfusion with 5–10 ml of 10 % buffered formalin.
4. Surgically remove the aorta and fix it in 10 % buffered formalin for 24 h. Aortic tissue segments can be embedded in paraffin or frozen using O.C.T. compound.

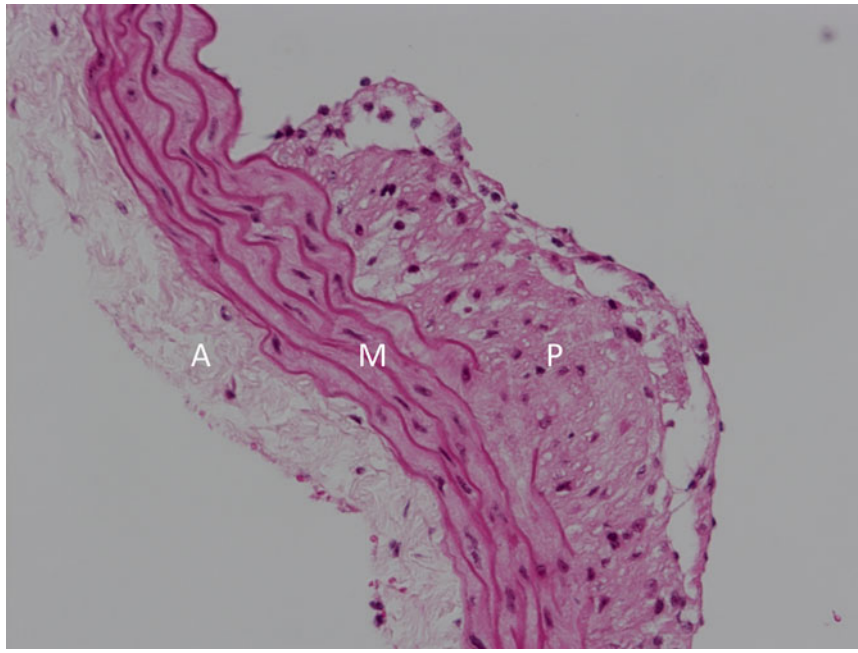

Fig. 2 Representative histological image (200×) of an aortic section from an apoE-KO mouse stained with hematoxylin and eosin (H&E). *A* adventitia, *M* media, *P* plaque

5. Cut 5–10-μm-thick sections using a microtome (paraffin-embedded tissue) or a cryostat (O.C.T.-embedded tissue), and place them onto histology glass slides.
6. Stain the sections with hematoxylin and eosin (H&E) for histopathological examination (*see* **Note 14**). Figure 2 shows an example of an abdominal aortic section stained with H&E demonstrating plaque formation.
7. Acquire photomicrographs with a camera attached to the microscope and perform morphometric measurements using dedicated software.

4 Notes

1. Care of animals should be in accordance with institutional guidelines and regulations, and animal procedures must obtain approval from the Ethics Committee.
2. Mouse models of atherosclerosis are based on genetic modifications of lipoprotein metabolism in combination with high-fat dietary changes [16]. Apolipoprotein E-deficient mice (apoE-KO) and low-density lipoprotein receptor-deficient mice (LDLR-KO) are the most commonly used models. We typically use apoE-KO mice and wild-type controls (both C57BL/6J, Charles River, Lyon, France).

3. High-cholesterol and high-fat diet is required to accelerate the formation of atherosclerotic plaque. We use 0.75 % cholesterol and 11 % fat diet (S9167-E010, "Ssniff," Germany), but other compositions with varying percentage of cholesterol/fat can be employed similarly.
4. In order to provide sufficient signal-to-noise ratio, MRI systems for rodents consist of magnets that generate strong static magnetic fields (7 T, 9.4 T, or even higher).
5. We use a combination of a volume coil operating in transmit-only and a two-channel phased-array coil (RAPID Biomedical GmbH, Rimpar, Germany) operating in receive-only. Different magnet, gradient, and RF coil configurations should also work.
6. The animal holder restrings the animal motion. It should integrate a mask for the anesthesia, a dental bar to fix the teeth, and an MRI-compatible system for thermoregulation (e.g., circulating warm water system, electric warming pad, or forced warm air).
7. Respiration can be monitored using the pressure signal of a respiration balloon sensor (e.g., Graseby Medical Ltd., Hertfordshire, UK). The ECG signal is used to synchronize cardiac movement and MR data acquisition.
8. Reducing fast breathing movements helps to improve image acquisition of the aorta. We recommend adjusting the percentage of isoflurane in order to maintain no more than 60 breaths per minute.
9. The optimal position of the animal (prone or supine) in the animal holder may depend on the specific application and anatomical region to be scanned and should be optimized by the investigator. The best position in our most favorable coil combination (volume coil for TX/two-channel array coil for RX) is when the array coils are proximate to the region to be scanned for better B1-field homogeneity.
10. Make sure the correct RF coil is selected and well positioned.
11. 3D acquisition is also possible. Although it is more demanding technically, it can provide better signal-to-noise ratio and near isotropic resolution [15].
12. Similarly as described for the *T*1W sequence, *T*2W and PDW sequences can be used with good results to image and monitor mouse atherosclerotic lesions [11, 14].
13. A CO_2 chamber and an overdose of anesthetics are two common methods for euthanizing mice.
14. Additional staining protocols might be of interest: oil red O (for plaque lipids), Masson's trichrome (for elastic fibers), von Kossa (for calcifications), etc.

References

1. Libby P (2002) Inflammation in atherosclerosis. Nature 420:868–874
2. Fernández-Ortiz A, Jiménez-Borreguero LJ, Peñalvo JL et al (2013) The Progression and Early detection of Subclinical Atherosclerosis (PESA) study: rationale and design. Am Heart J 166:990–998
3. Falk E, Sillesen H, Muntendam P et al (2011) The high-risk plaque initiative: primary prevention of atherothrombotic events in the asymptomatic population. Curr Atheroscler Rep 13:359–366
4. Little WC, Applegate RJ (1996) Role of plaque size and degree of stenosis in acute myocardial infarction. Cardiol Clin 14:221–228
5. Camici PG, Rimoldi OE, Gaemperli O et al (2012) Non-invasive anatomic and functional imaging of vascular inflammation and unstable plaque. Eur Heart J 33:1309–1317
6. Corti R, Fuster V (2011) Imaging of atherosclerosis: magnetic resonance imaging. Eur Heart J 32:1709–1719
7. Chan SK, Jaffer FA, Botnar RM et al (2001) Scan reproducibility of magnetic resonance imaging assessment of aortic atherosclerosis burden. J Cardiovasc Magn Reson 3:331–338
8. Zavodni AE, Wasserman BA, McClelland RL et al (2014) Carotid artery plaque morphology and composition in relation to incident cardiovascular events: the Multi-Ethnic Study of Atherosclerosis (MESA). Radiology 271:381–389
9. Helft G, Worthley SG, Fuster V et al (2001) Atherosclerotic aortic component quantification by noninvasive magnetic resonance imaging: an in vivo study in rabbits. J Am Coll Cardiol 37:1149–1154
10. Ibanez B, Giannarelli C, Cimmino G et al (2012) Recombinant HDL(Milano) exerts greater anti-inflammatory and plaque stabilizing properties than HDL(wild-type). Atherosclerosis 220:72–77
11. Fayad ZA, Fallon JT, Shinnar M et al (1998) Noninvasive in vivo high-resolution magnetic resonance imaging of atherosclerotic lesions in genetically engineered mice. Circulation 98: 1541–1547
12. Choudhury RP, Aguinaldo JG, Rong JX et al (2002) Atherosclerotic lesions in genetically modified mice quantified in vivo by noninvasive high-resolution magnetic resonance microscopy. Atherosclerosis 62:315–321
13. Hockings PD, Roberts T, Galloway GJ et al (2002) Repeated three-dimensional magnetic resonance imaging of atherosclerosis development in innominate arteries of low-density lipoprotein receptor-knockout mice. Circulation 106:1716–1721
14. Trogan E, Fayad ZA, Itskovich VV et al (2004) Serial studies of mouse atherosclerosis by in vivo magnetic resonance imaging detect lesion regression after correction of dyslipidemia. Arterioscler Thromb Vasc Biol 24:1714–1719
15. Dietrich T, Hucko T, Bourayou R et al (2009) High resolution magnetic resonance imaging in atherosclerotic mice treated with ezetimibe. Int J Cardiovasc Imaging 25:827–836
16. Breslow JL (1996) Mouse models of atherosclerosis. Science 272:685–688

INDEX

Vicente Andrés and Beatriz Dorado (eds.), *Methods in Mouse Atherosclerosis*, Methods in Molecular Biology, vol. 1339, DOI 10.1007/978-1-4939-2929-0, © Springer Science+Business Media New York 2015

D

E

F

M

N

O

P

Q

R

S

T

U

V

W